Hydro-Mechanical Modelling of Preferential Gas Flow in Host Rocks for Nuclear Waste Repositories

Jianxiong Yang

Thesis submitted to the University of Ottawa
in partial Fulfillment of the requirements for the
Doctorate in Philosophy degree in Civil Engineering

Under the supervision of

Prof. Mamadou Fall

Department of Civil Engineering
Faculty of Engineering
University of Ottawa

Abstract

As a safe long-term management of nuclear wastes, deep geological repositories (DGRs) have been proposed or currently being constructed in several countries. The host rocks in DGRs are saturated with water after the geological disposal facilities (GDFs) are closed and sealed. Significant gas can be generated due to several processes, e.g., the metal corrosion, water radiolysis or microbial reaction of organic materials, etc. The generated gas is anticipated to span throughout the long-term disposal of waste, which may jeopardize the stability of host rocks. Correspondingly, the performance of GDF will be affected since the host rocks provide a final impediment to the radionuclide transport. As gas migration in saturated host rocks is a highly coupled hydro-mechanical (HM) process, either gas-induced micro-fracturing or macro-fracturing may contribute to the development of preferential gas pathways, which needs to be concerned to ensure the feasibility and safety of geological disposal.

Current numerical studies on the gas migration behavior devoted to explaining the experimental phenomena in the gas injection tests conducted on the rock materials, in which some behaviors still cannot be well represented, i.e., gas induced fracturing, volulme dilation, anisotropic radial deformation. Therefore, to better represent the actual physical process of preferential gas flow, two modelling frameworks, i.e., macroscopic HM framework and two-scale HM framework, are proposed in the PhD study.

For the macroscopic HM framework, a double porosity model is firstly developed based on the dual continuum method, in which the volumetric strains of the porous continuum (PC) and fractured continuum (FC) are work-conjugated to the respective effective stress level. The treatment in two types of porosity allows us to capture that the opening/closure of the fractures is caused by the interaction between the dilation of the PC and the dilation of the FPM, which is beneficial to describe the gas induced fracturing in an implicit way. Then, an enriched embedded fracture model (EFM) is proposed to address the mechanical behavior of fractures. A hyperbolic relation of fracture deformability is incorporated into the rock matrix, as a result the fractured rock shows a nonlinear elastic behavior, which can capture the stiffness degradation due to fracture opening. The equivalent continuum method is provided to derive the effective compliance tensor, which includes the transverse isotropic matrix and two fracture sets. Using the enriched EFM with a three-dimensional (3D) geometry is able to capture the anisotropic radial deformation during gas migration.

Although the macroscopic HM framework is able to capture the major HM behaviors related to preferential gas flow, the development of gas dilatant pathways is still represented in an implicit way. Therefore, a two-scale HM framework is developed to explicitly simulate the development of preferential gas pathways. Initiating from the periodically distributed microstructures with microcracks, the asymptotic homogenization method is used to derive the macroscopic governing equations coupled with the normalized damage variable. The time-dependent damage evolution law is obtained from the microscopic mechanical energy analysis for evolving microcracks. Both time effect and size effect are incorporated in the damage model that will affect the overall HM behavior of rocks.

The developed two-scale HM framework with single gas flow can qualitatively capture important behaviors, such as the discrete pathways, localized gas flow, unstabilized fracture branching. More specifically, the simulated results demonstrates that the inter-connection of fractures from gas inlet to outlet is a prerequisite for gas breakthrough, accompanied by large amounts of gas flowing out of the sample and a rapid drop in gas injection pressure.

Incorporating water flow in the two-scale framework allows the model to quantitatively reproduce the experimental phenomena observed in the laboratory air injection tests, such as gas pressure evolution and mechanical deformation. More importantly, the model exlpaines that the significant differences in controlling gas breakthrough and mechanical deformation are resulting from the arbitrary nature of microstructural heterogeneities.

To account for the gas-water interaction in the two-scale HM framework, a fully coupled two-phase flow and elaso-damage model is developed to simulate the laboratory and in-situ gas injection experiments. The model can quantitatively capture the experimental behaviors, e.g., gas pressure evolution and non-desaturation phenomenon. Furthermore, model results show that the highly localized fracture pathways are the major places where gas and water interacts each other, and as a result the rock is still kept fully saturated.

As a whole, the obtained numerical results are synthesized and analyzed, the pros and cons of the developed models are discussed. To better improve the model performance, some recommendations are proposed for the future studies.

Acknowledgement

First and foremost, I would like to express my sincere gratitude to my supervisor, Dr. Mamadou Fall, for his enduring supports to my PhD study over the past four years. I can still recall the first meeting with Dr. Fall, how he showed me the step-by-step outline for my first research topic on his DELL monitor. He also prepared a hard copy of my PhD thesis organization and explained how to develop the mathematical models one-by-one, what considerations need to be highlighted in each model, the novelty and originality in doing research, etc. His guidance has led me to be gradually familiar with the PhD research, his encouragement has motivated me to overcome the research difficulties, and his passion has inspired me to be a creative researcher. These inspirations will continue to benefit my future studies.

I am so grateful to Dr. Sai Vanapalli for his constructive suggestions to my career development. He is also the person who sparks my great interest in unsaturated soil mechanics that is important to my PhD study. Although my experiences are not closely associated with Dr. Vanapalli due to my working place as well as the pandemic, each conversation in his office benefits me a lot, especially on my attitude to life.

I would like to extend my appreciation to Dr. Colin Rennie for his good-tempered help on graduate seminar, Dr. Liang Cui at Lakehead University for his constructive advice on my research, Dr. Gongda Lu at Sichuan University for his valuable advice on the working experience. I also thank Dr. Guanlong Guo at Westlake University, who inspired and shared me with so many creative ideas. Each discussion with him benefits me a lot, not only on the research outcomes, but also on the career pursuit.

In the days of endless research, I thank my roommate Dr. Kun Fang for his kindless help and finding ways in enjoying life. Summer time playing basketball with friends, Shaoping, Xichun, Jie, Chunwang is a pleasant momery. Also, I am grateful to Sada, Yibo, Shuaigang and other colleagues and friends for their generous helps to my study and life in the past years.

I gratefully acknowledge China Scholarship Council and University of Ottawa for providing the financial support for my research program.

Last but not least, I wish to deeply thank my family for their unconditional support, and this work could not have been possible without their unceasing love and encouragement throughout the entire four years. Specifically, I own a debt of gratitude to my fiancee, Jingjing Wang, who makes a lot of self-sacrifice, who is not being a family but the connection is more than a family.

Table of Contents

List of Figures

List of Tables

List of Abbreviations

BBM	Barcelona Basic Model
BC	Boundary Condition
BEM	Boundary Element Method
BGR	Back Guard Ring
CRM	Cubic Root Model
CSL	Critical State Line
CZM	Cohesive Zone Model
DEM	Discrete Element Method
DFN	Discrete Fracture Network
DGR	Deep Geological Repository
DTS	Direct Tensile Strength
EBS	Engineered Barrier System
EDZ	Excavation Damaged Zone
EFM	Embedded Fracture Model
FC	Fractured Continuum
FDEM	Finite-Discrete Element Method
FEM	Finite Element Method
FPM	Fractured Porous Medium
GDF	Geological Disposal Facility
HLW	High-Level Waste
HM	Hydro-Mechanical
IF	Injection Filter
IGR	Injection Guard Ring
ILW	Intermediate-Level Waste
LBM	Lattice Boltzmann Method
LEFM	Linear Elastic Fracture Mechanics
LLW	Low-Level Waste
MCM	Mohr-Coulomb Model
NBS	Natural Barrier System
PC	Porous Continuum
PF	Phase Field
PLM	Power Law Model
PSD	Pore Size Distribution
REV	Representative Elementary Volume
SPH	Smoothed Particle Hydrodynamics
STP	Standard Temperature and Pressure
UDEC	Universal Distinct Element Code
vG	van Genuchten
WRC	Water Retention Curve
XFEM	Extended Finite Element Method

Chapter 1 Introduction

1.1 Background

Deep geological repositories (DGRs) have been proposed to contain and isolate the radioactive wastes in several countries, i.e., Canada, China, France, Germany, Switzerland, Sweden, etc. In the post-closure phase of DGR, significant volume of gas can be generated due to several processes, such as the metal corrosion (which produces H_2), water radiolysis (mainly produces H_2) or microbial reaction of organic materials (which may produce CO_2 and CH_4), of which the most noteworthy one is hydrogen (Johnson et al., 2004; Rodwell et al., 1999). The production of gas is anticipated to span throughout the long-term disposal of waste (Harrington et al., 2017). The potential issues related with the gas generation, accumulation, and release have gained much concern by many international research programs related to nuclear waste disposal, i.e., ANDRA project (Andra, 2005), NAGRA project (NAGRA, 2008), FORGE project (Shaw, 2015), etc., since the integrity of host rocks may be impaired by the accumulated gas pressure and in consequence enable the easy transport of contaminants (Guo and Fall, 2021). Therefore, understanding the gas migration behavior in the host rocks is of fundamental importance to the performance assessment of the geological disposal facility (GDF).

In a clay-based GDF, several gas transport processes may be active separately or simultaneously (Pazdniakou and Dymitrowska, 2018). The first gas transport process is the diffusion/advection of dissolved gas within the pore water, which may be able to prevent the form of free gas phase under the condition of limited gas production rate (Cuss et al., 2014). If the gas production rate continuously increases to a solubility limit, a discrete gas phase will form and accumulate that the gas transport is dominated by the visco-capillary two-phase flow process (Cuss et al., 2014; Gerard et al., 2014). As the accumulated gas pressure increases to a certain value, gas induced micro-fracturing may form in the clayey rocks with low tensile strength, which leads to the development of gas dilatant pathways (Johnson et al., 2004; Marschall et al., 2005). The onset of dilatancy controlled gas flow occurred at a gas pressure significantly lower than the minimum principal stress (note: compressive stress is assumed to be positive), which has been observed in various laboratory gas injection tests, see Cuss et al. (2012, 2014); Harrington et al. (2013, 2017); Hildenbrand et al. (2002); Popp et al. (2007). If the combined effects of pore water displacement and micro-fracturing formation cannot counterbalance the gas

production rate, macroscopic fracture will develop for the single gas phase transport (Marschall et al., 2005). The macro-fracture controlled gas flow occurs at abrupt gas pressure build-up that needs sufficient gas source, which may be not expected in the DGR.

The transport of dissolved gas is largely constrained due to the low permeability of host rocks, as a result the contribution by gas dissolution/diffusion is several orders of magnitude lower than the transport capacity of two-phase flow (NAGRA, 2008). Besides, the visco-capillary controlled two-phase flow cannot explain the experimental phenomena in the gas injection tests, e.g., the increase in both sample volume and permeability, no measurable desaturation after significant gas flux is observed at the outlet (Cuss et al., 2014; Harrington et al., 2012a, 2017). These specific experimental behaviors have confirmed the gas induced micro-fracturing, in which the advective movement of gas through saturated clayey rocks is highly localized and the dilatant gas pathways are affected by the gas injection pressure (Harrington et al., 2012b; Wiseall et al., 2015). Therefore, the dilatancy controlled gas flow is the predominant transport mechanism that needs to be specifically concerned.

Field tests have been conducted to investigate the rock mass behavior when gas is injected from the experimental borehole (Jacops et al., 2014), in which the recorded field data is difficult to be analyzed and interpreted when compared with the experimental results (Cuss et al., 2011; De La Vaissière et al., 2014). This might be caused by the scale difference, uncertainties of boundary conditions in the field since gas migration is a highly coupled process (Gerard et al., 2014). Understanding the highly coupled processes in the host rocks is the fundamental requirement in the context of DGR.

1.2 Objectives

In the research work, we focus on the development of several novel and robust numerical models that can represent gas migration in saturated claystone as well as the accompanied HM behaviors. These models are expected to provide in-depth understanding of gas transport process in low permeability media. The main objectives of the thesis are:

a) To make a comprehensive review on the HM models of advective gas movement through rock materials.

b) To develop a macroscopic double porosity model that can represent the coupled HM behavior of gas induced fractures, meanwhile the different HM response between the matrix and

fractures should be identified. The developed model should capture the experimental phenomena, i.e., the sample volume dilation, gas induced fracturing, major gas breakthrough.

c) To extend the double porosity model to the three-dimensional cases and incorporate the fracture opening-induced softening behavior into the HM model, which can capture the anisotropic radial deformation observed in the laboratory gas tests.

d) To improve the HM model from macroscale to microscale that initiates from the microscopic phenomenon considering the subcritical crack propagation, which can explicitly capture the gas dilatant pathways under single phase (gas) flow condition.

e) To extend the two-scale model from single phase flow condition to two-phase (water, gas) flow condition, which can explicitly capture the gas dilatant pathways at laboratory condition.

f) To extend the coupled two-scale HM model to the field application that the model can be used to predict the gas migration behavior through host rocks in the in-situ experiments.

1.3 Research Approaches

Figure 1.1 presents the research approach adopted in the study. First, there is a need to specify the research problems, figure out the mechanism dominating the gas migration behavior through host rocks, determine the involved coupled processes with regard to gas migration and present the experimental phenomena. Secondly, a state-of-art review on previous HM modelling works concerning gas transport in clayey rocks is conducted, which is included in Chapter 3. The review includes material properties and experimental interpretations related to gas migration process, the governing equations for fluid flow and solid deformation, the constitutive models for hydraulic and mechanical processes, a brief discussion on the pre-existing models, the fracture propagation models for simulating the preferential fluid flow. Thirdly, based on the information collected and filtered from the literature review, the tasks on how to step by step achieve the PhD research objectives are defined, which are given in Section 1.4. The reasons for choosing the modelling method as well as capturing the included experimental phenomena are described briefly in Section 1.4. Lastly, the coupled HM models are developed to simulate the laboratory gas injection tests that can partly or fully capture the experimental observations. Then, the two-scale HM model is extended to the field conditions to interpret the results from field gas injection tests, which provides deeper understanding of gas migration behavior in the host rocks of potential DGR.

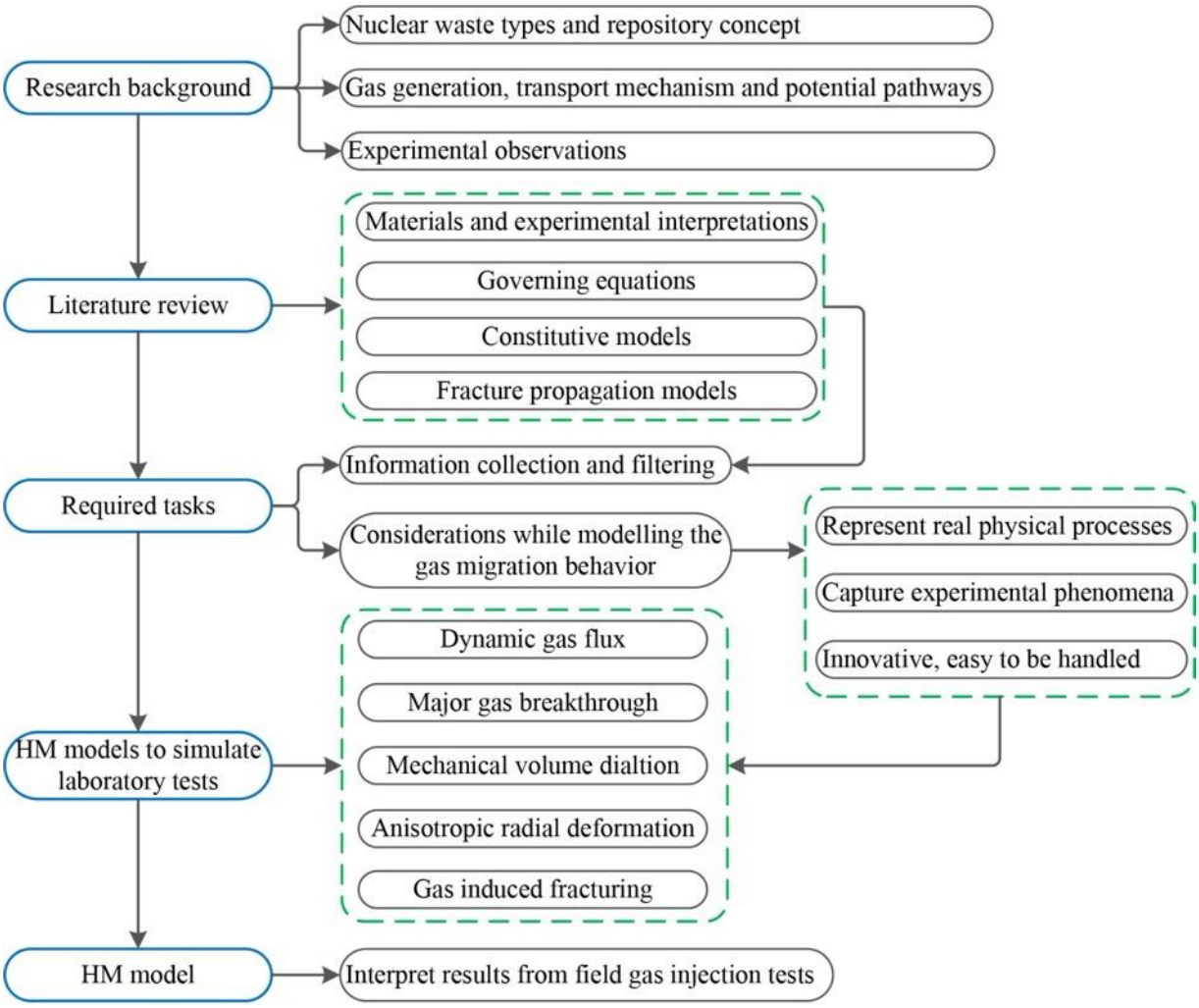

Figure 1.1 Research approach

1.4 Tasks and Organization of the Thesis

Figure 1.2 shows the major objectives of every chapter and the overall organization of the thesis which includes 8 chapters. These chapters are structured into a paper-based thesis format. It should be underlined that this adopted paper-based thesis format will lead to some repetition in the respective articles since each article is independently written and crafted according to manuscript instructions for the specified publication. Detailed descriptions are provided as follows:

Chapter 1 provides a general introduction of the research topic, which describes the research background of the gas migration behavior through host rocks of the DGR. In addition, the objectives of the thesis and adopted approaches for each section are provided.

Chapter 2 presents the background information of nuclear waste types and repository concept. Moreover, the main gas generation, transport mechanisms and the potential gas pathways in the DGR are elucidated. At last, the experimental observations with respect to gas migration in saturated host rocks are summarized.

Chapter 3 provides a comprehensive literature review with regard to the gas flow through host rocks under coupled HM condition (Technical Paper I). Specifically, the material properties and the experimental interpretations related to gas migration process are analyzed. The governing equations, the constitutive models for hydraulic and mechanical processes are summarized. The performances of the pre-existing HM models are discussed in detail, which will give us some fundamental and up-to-date guidance to analyze the preferential fluid flow behavior. Lastly, the fracture theories are reviewed, the existing approaches and potential methods for simulating the preferential fluid flow are discussed.

Chapter 4 focuses on the HM modelling of dilatancy controlled gas flow through clayey rock materials at the macroscale, which is divided into two parts. The first part (Technical Paper II) elucidates the development of a double porosity model that is used to implicitly simulate the development of gas preferential pathways, in which several important phenomena are captured, i.e., the development of preferential gas pathways, mechanical volume dilation (sample volume increases), major gas breakthrough. While for the second part (Technical Paper III), a three-dimensional HM model is developed on the basis of the double porosity model, in which the anisotropic radial deformation accompanied with gas advective transport is well represented.

Chapter 5 focuses on the two-scale HM modelling of advective gas flow behavior, in which the model is initiated from the microscopic phenomenon that studies the gas induced micro-fracturing. The Chapter includes two parts, in which the first part explicitly simulates the development of gas dilatant pathways and fracture propagation under single phase (gas) flow condition (Technical Paper IV), while two-phase (water, gas) flow is incorporated in the second part (Technical Paper V). The two-scale damage model with two phase flow can explicitly capture the development of gas dilatant pathways under laboratory conditions.

In **Chapter 6**, the two-scale HM model is extended to field application (Technical Paper VI), in order to predict the gas migration behavior through host rocks in the in-situ experiments. The model can quantitatively reproduce the in-situ findings, e.g., gas pressure evolution, non-desaturation phenomenon.

In **Chapter 7**, the obtained results are synthesized and discussed to provide valuable insight into the HM modelling of gas migration behaviors in host rocks. Based on the discussion, the originality of the PhD work is highlighted.

Chapter 8 presents the conclusions and recommendations for future research.

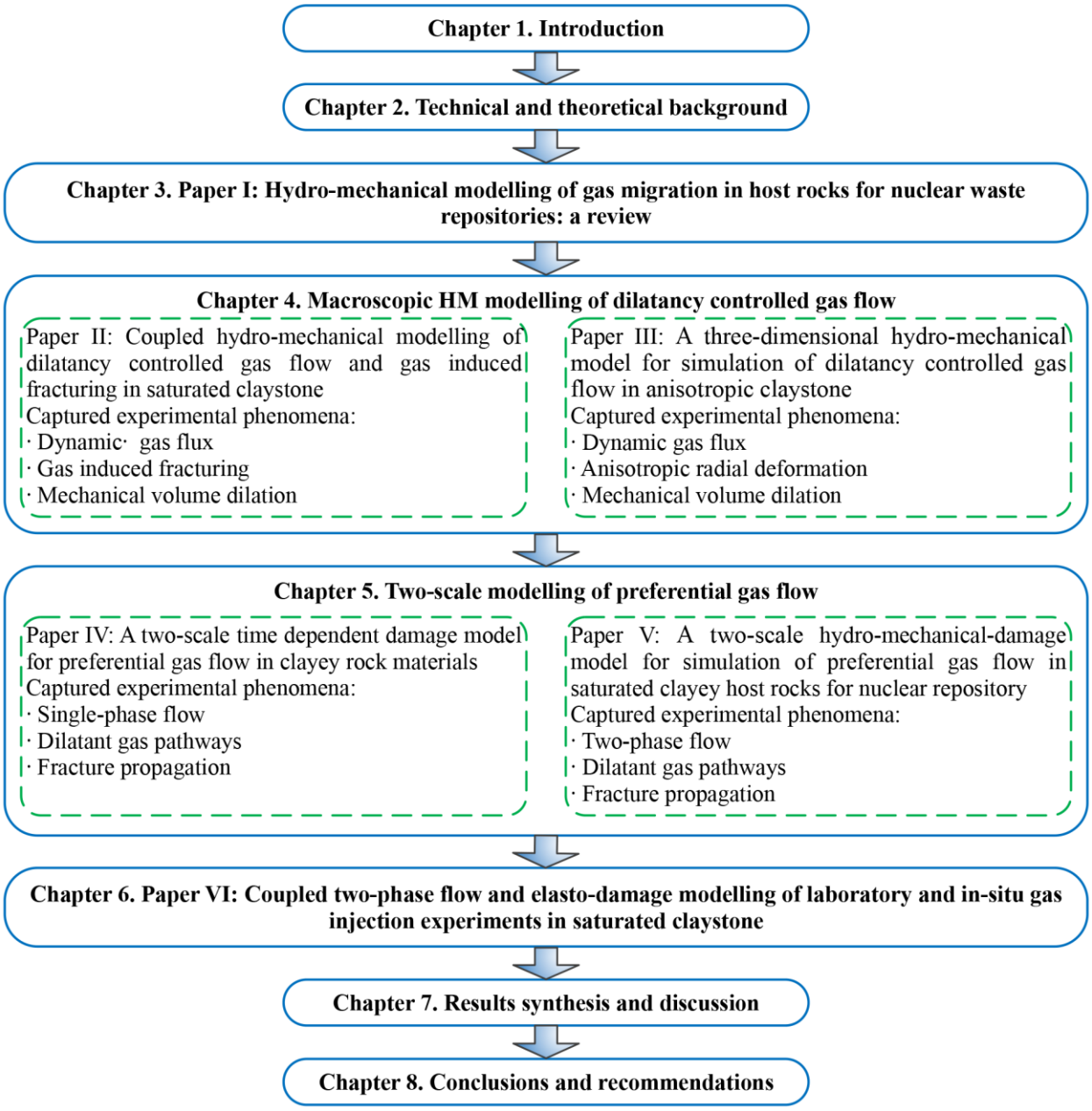

Figure 1.2 Organization of the thesis

1.5 References

Andra, 2005. Synthesis: Evaluation of the feasibility of a geological repository in an argillaceous formation. Andra,

Chatenay-Malabry, France.
Cuss, R., Harrington, J., Giot, R., Auvray, C., 2014. Experimental observations of mechanical dilation at the onset of gas flow in Callovo-Oxfordian claystone. Geological Society Special Publication 400, 507-519.
Cuss, R.C., Harrington, J.F., Noy, D.J., 2012. Final report of FORGE WP4.1.1: The stress-path permeameter experiment conducted on Callovo-Oxfordian Claystone. British Geological Survey Commissioned Report, CR/12/140.
Cuss, R.J., Harrington, J.F., Noy, D.J., Wikman, A., Sellin, P., 2011. Large scale gas injection test (Lasgit): Results from two gas injection tests. Physics and Chemistry of the Earth 36, 1729-1742.
De La Vaissière, R., Gerard, P., Radu, J.-P., Charlier, R., Collin, F., Granet, S., Talandier, J., Piedevache, M., Helmlinger, B., 2014. Gas injection test in the Callovo-Oxfordian claystone: data analysis and numerical modelling. Geological Society, London, Special Publications 400, 427-441.
Gerard, P., Harrington, J., Charlier, R., Collin, F., 2014. Modelling of localised gas preferential pathways in claystone. International Journal of Rock Mechanics and Mining Sciences 67, 104-114.
Guo, G., Fall, M., 2021. A Thermodynamically Consistent Phase Field Model for Gas Transport in Saturated Bentonite Accounting for Initial Stress State. Transport in Porous Media.
Harrington, J.F., Cuss, R.J., Talandier, J., 2017. Gas transport properties through intact and fractured Callovo-Oxfordian mudstones. Geological Society Special Publication 454, 131-154.
Harrington, J.F., de la Vaissière, R., Noy, D.J., Cuss, R.J., Talandier, J., 2012a. Gas flow in Callovo-Oxfordian claystone (COx): Results from laboratory and field-scale measurements. Mineralogical Magazine 76, 3303-3318.
Harrington, J.F., Milodowski, A.E., Graham, C.C., Rushton, J.C., Cuss, R.J., 2012b. Evidence for gas-induced pathways in clay using a nanoparticle injection technique. Mineralogical Magazine 76, 3327-3336.
Harrington, J.F., Noy, D.J., Cuss, R.C., 2013. Callovo-Oxfordian Claystone: processes governing advective gas flow. British Geological Survey Commissioned Report, CR/13/088.
Hildenbrand, A., Schlömer, S., Krooss, B.M., 2002. Gas breakthrough experiments on fine-grained sedimentary rocks. Geofluids 2, 3-23.
Jacops, E., Volckaert, G., Maes, N., Charlier, R., Collin, F., Gerard, P., Levasseur, S., Delavaissière, R., Talandier, J., Granet, S., 2014. WP5 Final Report: Experiments and modelling of gas migration processes in undisturbed rocks. FORGE Report D5.19, p. 146pp.
Johnson, L., Marschall, P., Zuidema, P., Gribi, P., 2004. Effects of post-disposal gas generation in a repository for spent fuel, high-level waste and long-lived intermediate level waste sited in opalinus clay. National Cooperative for the Disposal of Radioactive Waste (NAGRA), NTB 04-06.
Marschall, P., Horseman, S., Gimmi, T., 2005. Characterisation of gas transport properties of the Opalinus clay, a potential host rock formation for radioactive waste disposal. Oil and Gas Science and Technology 60, 121-139.
NAGRA, 2008. Effects of post-disposal gas generation in a repository for low- and intermediate-level waste sited in the Opalinus Clay of Northern Switzerland. National Cooperative for the Disposal of Radioactive Waste (NAGRA).
Pazdniakou, A., Dymitrowska, M., 2018. Migration of Gas in Water Saturated Clays by Coupled Hydraulic-Mechanical Model. Geofluids 2018, 1-25.
Popp, T., Wiedemann, M., Böhnel, H., Minkley, W., Manthei, G., 2007. Untersuchungen zur Barriereintegrität im Hinblick auf das Ein-Endlager-Konzept. Insitut fur Gebirgsmechanik GmbH, Leipzig, Germany.
Rodwell, W.R., Harris, A.W., Horseman, S.T., Lalieux, P., Müller, W., Ortiz Amaya, L., Pruess, K., 1999. Gas migration and two-phase flow through engineered and geological barriers for a deep repository for radioactive waste. Joint EC/NEA Status Report.
Shaw, R.P., 2015. The Fate of Repository Gases (FORGE) project. Geological Society Special Publication 415, 1-7.
Wiseall, A.C., Cuss, R.J., Graham, C.C., Harrington, J.F., 2015. The visualization of flow paths in experimental studies of clay-rich materials. Mineralogical Magazine 79, 1335-1342.

Chapter 2 Technical and Theoretical Background

2.1 Introduction

The concept of geological disposal for the radioactive wastes had been proposed since the late 1950s, in which the underground facility is built at depths varying from 200 to 1000 m, to permanently isolate the wastes (Norris, 2015). The safety concern for the geological disposal facility (GDF) is a key necessity that needs to be addressed during the whole stage of DGR, including the time of disposal and the long-term storage after the facility is closed (Norris, 2015). An important issue of the GDF performance is the safety-relevant gas migration processes in the host rocks.

To get a deep understanding of gas migration induced safety issues in the DGR, the technical and theoretical background information are provided in this chapter. Specifically, background information on the nuclear waste repositories is presented in Section 2.2, which includes the main sources and types of nuclear wastes, and the DGR concept. In Section 2.3, the main gas generation and transport mechanisms, as well as potential gas transport pathways out of the emplacement cavern are briefly discussed. Moreover, some important phenomena with regard to gas migration through clayey rocks are summarized in Section 2.4. Finally, some conclusions will be drawn in Section 2.5.

2.2 Nuclear Waste Types and Repository Concept

2.2.1 Main Sources and Types of Nuclear Wastes

Nuclear wastes are the unwanted by-products generated by various nuclear technology processes. The majority of wastes are generated by nuclear power generation and nuclear weapon construction, while a relatively small amount results from industrial, medical and scientific programmes (Miller et al., 2000). Based on the level of radioactivity, nuclear wastes are commonly categorized into three types: high-level waste (HLW), intermediate-level waste (ILW) and low-level waste (LLW) (Rodwell et al., 1999).

LLW includes all items contaminated with radioactive materials, such as cooling water from nuclear reactors, medical supplies and protective tools in hospitals, etc. It contains around 90% of the volume of all radioactive waste, while accounts for less than 1% of the total radioactivity (Freiesleben, 2013; IAEA, 2018). Due to the very limited amounts of long-lived radionuclides,

no heating is generated during the disposal stage.

ILW includes chemical sludge, resins and contaminated material from reactor decommissioning, which represents around 7% of the volume of all radioactive waste, while contains about 4% of the total radioactivity (IAEA, 2018). No significant heat is generated from its disposal and the temperature increase is less than 3 K (Freiesleben, 2013).

HLW comprises fission products, plutonium and spent fuel generated in the reactor core. It contains around 3% of the volume of all radioactive waste from nuclear power plants, but represents more than 95% of the radioactivity (Freiesleben, 2013). Due to the large amounts of long-lived radionuclides, significant quantities of heat can be released through radioactive decay (Fall and Nasir, 2012; IAEA, 2018).

2.2.2 Deep Geological Repository Concept

As a safe long-term management of nuclear waste, deep geological repositories (DGRs) have been investigated as a favored option internationally (Rodwell et al., 1999). The components of DGR concept include surface and underground facilities, shafts, tunnels, and emplacement rooms for the waste, etc (Rodwell et al., 1999), as shown in Figure 2.1. The waste is sealed in a canister and enclosed in the overpack, then placed in the deposition hole and surrounded by the buffer material. The safe long-term isolation of the waste relies on the stability of a multi-barrier system, which includes an engineered barrier system (EBS) and a natural barrier system (NBS) (Johnson et al., 2004).

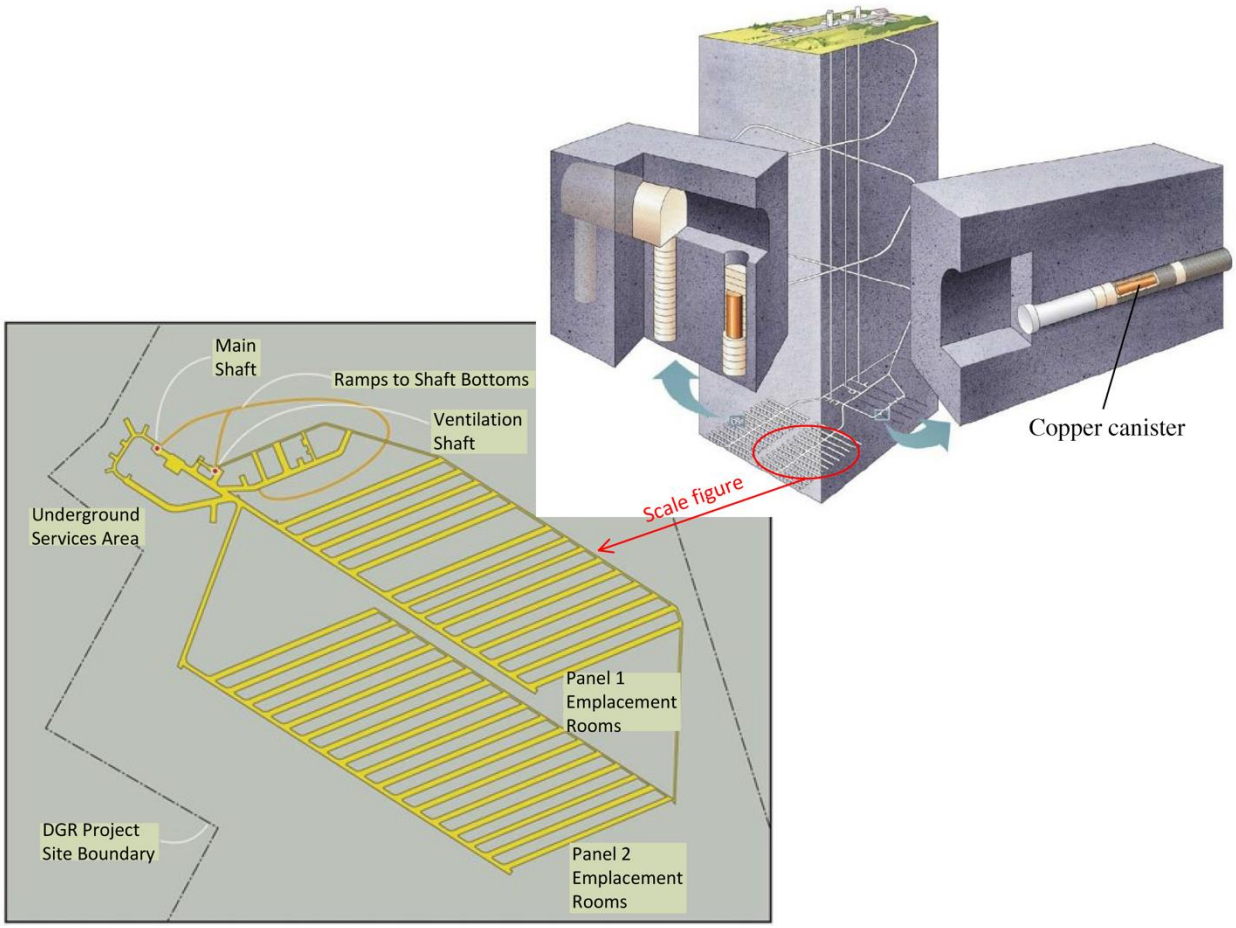

Figure 2.1 Schematic description of DGR concept (adapted from Damnanac et al. (2011); Kronberg (2018))

In the multi-barrier system of DGR, bentonite is generally considered as an ideal buffer material for the EBS (Guo and Fall, 2021), while the host rocks are viewed as natural barriers for the radionuclide transport, see Figure 2.2. To satisfy the requirements of impeding the radionuclide transport, some certain properties of host rocks are favored, e.g., thick formation, low permeability and radionuclide retardation capability, etc. Based on these considerations, the highly consolidated argillaceous formations, i.e., Callovo-Oxfordian (COx) claystone in France, Opalinus (OPA) clay in Switzerland, and Boom Clay in Belgium, are being investigated as potential host rocks (Charlier et al., 2013).

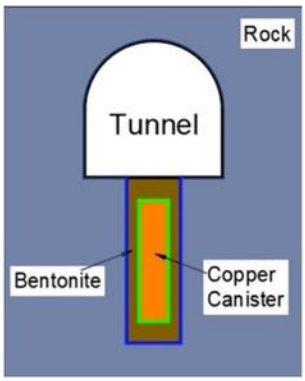

Figure 2.2 Multi-barrier system (Guo and Fall (2018))

2.3 Main Gas Generation, Transport Mechanisms and Potential Pathways

2.3.1 Main Gas Generation Mechanisms

Various processes may contribute to the gas generation in repositories, of which the specific significance depends on the physico-chemical site conditions, the disposal method and the waste types (Rodwell et al., 1999). The main gas generation mechanisms are the corrosion of metals, radiolysis of water and other organic materials, microbial degradation. As the repositories for LLW and ILW contains larger amounts of metals and organic materials than those for HLW, thus the gas generation rates are likely to be higher in the former repositories (Fall and Nasir, 2012; Rodwell et al., 1999).

2.3.1.1 Corrosion of Metals

The gas generation due to metal corrosion has been recognized as the dominant mechanism for nearly all disposal situations (Rodwell et al., 1999). Corrosion as an electrochemical process is characterized by the transformation of metal to a higher oxidation state. In the nuclear waste repositories, the corroding agents for the metallic materials may include oxygen in the repository and air in the porous spaces; residual water in the waste, packaging and backfill materials; groundwater; and porewater contained in host rocks (Rodwell et al., 1999). The involved chemical reactions will take place after the closure of an underground repository, formulated as follows:

$$2Fe+O_2 \rightarrow 2FeO \quad (2.1)$$

$$2Fe+2H_2O+O_2 \rightarrow 2Fe(OH)_2 \quad (2.2)$$

After the oxygen is exhausted by the above processes, hydrogen is generated due to the following processes:

$$Fe+2H^{+} \rightarrow Fe^{2+}+H_2 \quad (2.3)$$

$$Fe+2H^{+}+2OH^{-} \rightarrow Fe(OH)_2+H_2 \quad (2.4)$$

In the repository system, the generation of hydrogen is expected to occur over thousands of years after the closure of DGR (Ye et al., 2014). Correspondingly, it is expected that the host rocks have already reached a fully saturated state and the nuclear waste released heating process has been completed at the onset of gas generation (Rodwell et al., 1999). Considering these specific site situations, the saturated rock samples under isothermal conditions are adopted in most experimental studies, e.g., see Cuss et al. (2012); Harrington et al. (2013); Hildenbrand et al. (2002).

2.3.1.2 Radiolysis

Radiolysis is termed as the decomposition of chemical compounds by radiation, in which the decomposition of water makes the leading contribution to the gas generation of this mechanism. The gas generation by water radiolysis is characterized by the produced hydrogen and the applied radiation dose. Generally, two types of radiolysis processes are distinguished based on the location where the radiolysis takes place, including internal and external radiolysis (Rodwell et al., 1999). The former takes place in the waste product and package, while the latter occurs in the backfill material or the host rocks. Due to the low activity concentration, the gas generation by radiolysis is not as significant as that by corrosion (Fall and Nasir, 2012).

2.3.1.3 Microbial Degradation

There are some prerequisites for microbial gas generation, for example, the existence of micro-organisms, the availability of water and nutrients. The produced amount of gas is influenced by several factors, i.e., pH, temperature, salinity, oxygen supply, radiation, etc. With these conditions taken into account, the microbial gas generation is only an issue for certain ILW and LLW repositories (Rodwell et al., 1999).

2.3.2 Basic Gas Transport Mechanisms

To assess the performance of the clay-rich GDF, it is necessary to recognize the predominant gas migration process that may jeopardize the integrity of host rocks in the DGR. Based on the phenomenological description of the conceptual models defined by Marschall et al.

(2005), see Figure 2.3, four primary gas transport mechanisms are presented in the clay-rich GDF: advective/diffusive movement of dissolved gas, visco-capillary controlled two-phase flow, dilatancy controlled gas flow, macroscopic fracture controlled gas flow. These four mechanisms are explained in detail in the following subsections.

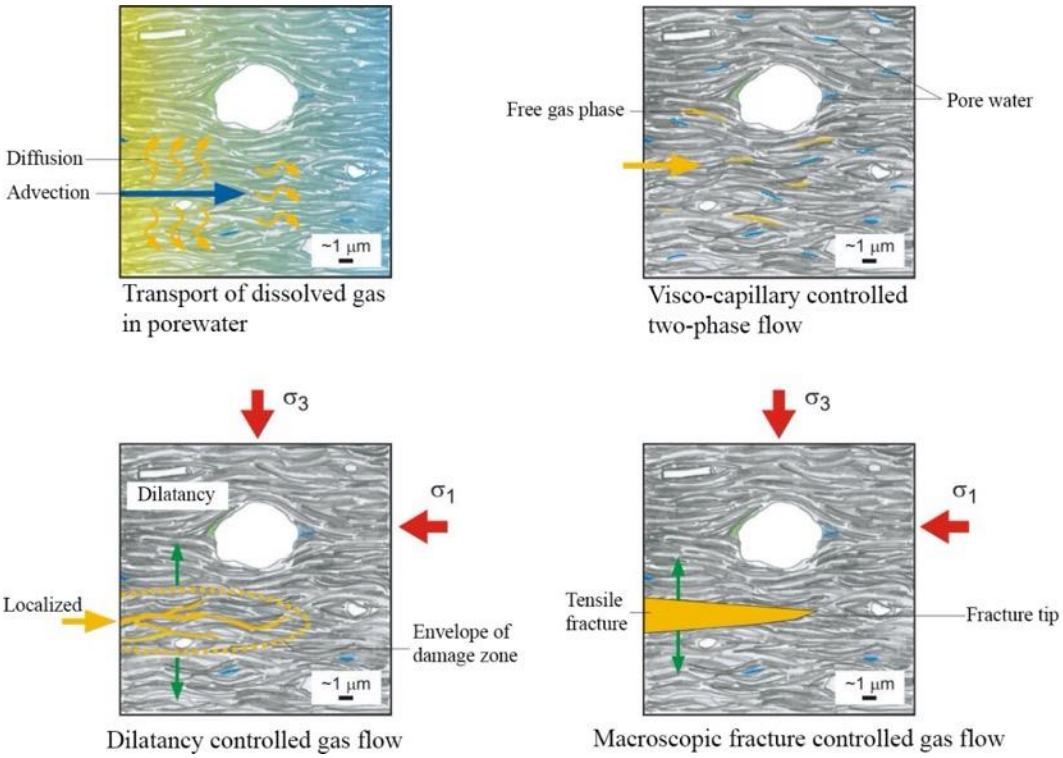

Figure 2.3 Gas transport mechanism in clayey rocks (modified from Marschall et al. (2005))

2.3.2.1 Advective/Diffusive Movement of Dissolved Gas

With the continuous increase of gas production rate during the post-phase of the DGR, the generated gas would be firstly transported by advection/diffusion in a dissolved state. The advective transport of pore water is governed by Darcy's law, while the diffusive transport of gas is governed by Fick's law that mainly depends on the diffusive coefficient. The amount of gas dissolved in the pore water is in equilibrium and proportional with the quantity of dry gas, which is governed by Henry's law that is related to the Henry's coefficient. The key parameters controlling gas advective/diffusive movement include Henry's coefficient, diffusive coefficient, tortuosity, porosity and permeability of the porous material (NAGRA, 2008). The gas transport capacity by advection/diffusion in a dissolved state is significantly restricted by the low permeability of argillaceous host rocks, which is several orders of magnitude lower than other mechanisms (NAGRA, 2008).

2.3.2.2 Visco-Capillary Controlled Two-Phase Flow

Once the gas production rate exceeds the solubility limit, a free gas phase will form that gas will try to displace the water through the largest pore in the host rocks (Norris, 2015). This process of gas transport is dominated by the visco-capillary controlled two-phase flow. The interaction between gas and water may be referred to the water retention curve (WRC); details can be found in Vanapalli et al. (1996, 1999). The primary variable in the capillary model is the capillary pressure. The transport properties, i.e., the intrinsic permeability of porous medium, the air entry value, relative permeability relation are viewed to be not related to the material deformation, which means the fluid flow and mechanical deformation are not coupled.

2.3.2.3 Dilatancy Controlled Gas Flow

As the generated gas amount is sufficient for the micro-fracturing formation, the dilatancy controlled gas flow will dominate the gas transport process. Gas will be transported through the pathways of micro-fracturing and the transport capacity is significantly improved as the hydraulic properties of host rocks are not limited to the invariants of intact materials. In this process, the pathway aperture is related to the solid deformation, which is accompanied by a significant increase in pore space, intrinsic permeability and mechanical volume (Marschall et al., 2005). The fluid flow and mechanical deformation are fully coupled that occurs at the applied gas pressure significantly lower than the minimum principal stress (note: compressive stress is assumed to be positive). This might be caused by the non-uniform distribution of stress state and heterogeneous HM properties of the material (Guo and Fall, 2019), which play an important role in the development of preferential gas pathways.

2.3.2.4 Macroscopic Fracture Controlled Gas Flow

When the gas injection pressure is larger than the sum of material tensile strength and the minimum principal stress, macroscopic tensile fractures are expected to be developed that provide preferential pathways for gas to flow through the macroscopic tensile fractures. This process may be viewed as a single phase (gas) flow process, which is similar to the hydraulic fracturing process. In the argillaceous rock formations with low tensile strength, a macroscopic tensile fracture develops when the gas pressure increases rapidly, i.e., when the gas production

rate exceeds the combined effects of pore-water displacement and the formation of dilatant pathways (Marschall et al., 2005).

2.3.3 Potential Gas Pathways

In the post-closure phase of DGR, the GDF is saturated with water (Pazdniakou and Dymitrowska, 2018). Significant volume of gas can be generated during the long-term lifespan of DGR due to the existence of several processes, such as the metal corrosion (which produces H_2), water radiolysis (mainly produces H_2) and microbial reaction of organic materials (which may produce CO_2 and CH_4), of which the most noteworthy one is hydrogen (Johnson et al., 2004; Rodwell et al., 1999). With the continuous increase of accumulated gas in the emplacement cavern, several potential gas transport pathways may be formed, see Figure 2.4. The potential transport pathways for the gas out of the emplacement cavern can be summarized as:

① along the excavation damaged zone (EDZ) surrounding the tunnel, cavern, or other underground structures.

② along the EBS consisting of sealing materials and cavern plugs, etc.

③ through the host rocks due to pore spaces, pre-existed fractures or induced fractures.

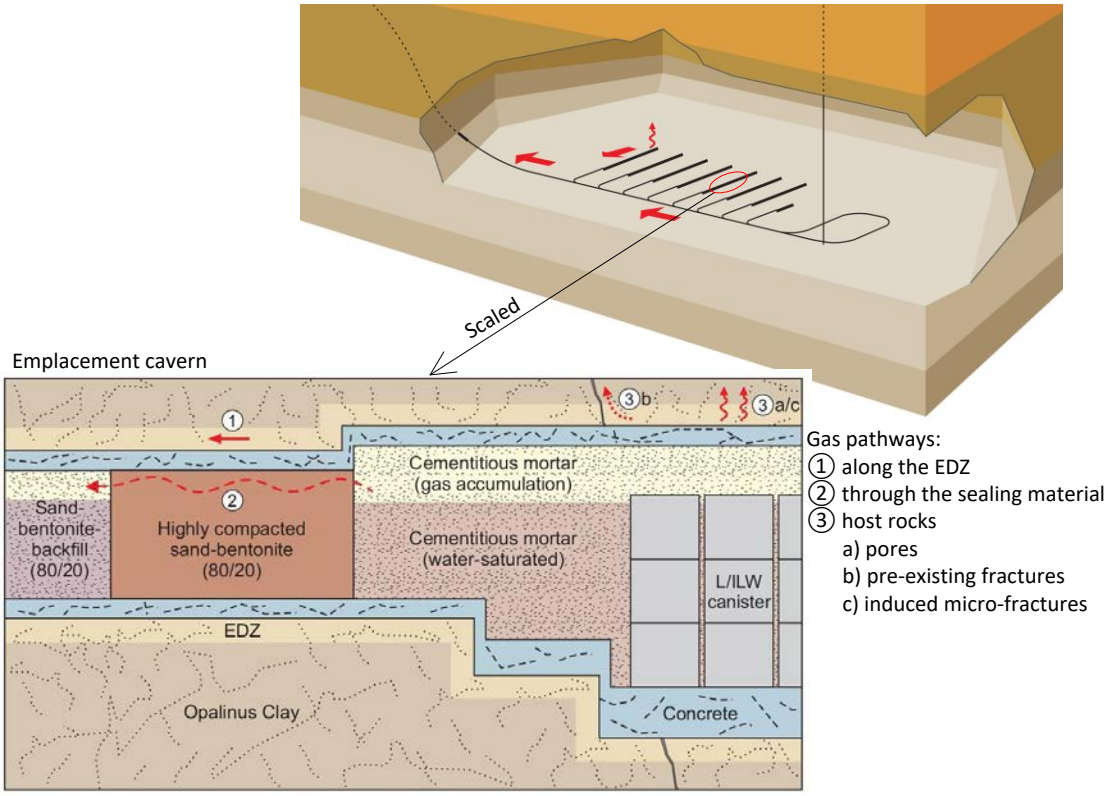

Figure 2.4 Diagram of potential gas transport pathways (adapted from NAGRA (2008))

2.4 Experimental Observations

The commonly investigated host rocks include Callovo-Oxfordian (COx) claystone in France, Opalinus (OPA) clay in Switzerland, and Boom Clay in Belgium. All of the experimental tests are conducted under isothermal conditions, and the tested sample is almost in an initially saturated state.

2.4.1 Dilatant Gas Pathways

To recognize the mechanism controlling the advective movement of gas through host rocks, a series of long-term laboratory gas injection tests were conducted on initially saturated COx claystone, see Cuss et al. (2014); Harrington et al. (2017). A significant phenomenon observed during the tests is the gas induced micro-fracturing, which varies temporarily and spatially with the variation of local effective stress (Cuss et al., 2014; Harrington et al., 2012a, 2012b; Wiseall et al., 2015). The gas induced micro-fracturing is accompanied by the development of gas dilatant pathways, which has been experimentally observed in clay by using the nanoparticle injection technique (Harrington et al., 2012b).

Due to the difficulty in visualizing the gas flow pathways through saturated claystone, a new method developed by the British Geological Survey (BGS) has recorded the development of gas pathways in clay-rich materials. Figure 2.5 shows the captured images at different timing of gas injection test in a clay paste, of which the aim is to provide an insight into gas migration path in clay-rich rocks. As gas is injected from the inlet (circled ring in Figure 2.5(a)), it gradually penetrates the paste and the pathways are localized around the inlet area, see Figure 2.5(b). With the continuous gas injection process, complex gas networks are formed, see Figure 2.5(c), and the pathway aperture seems to be opened larger as gas pressure is increased, see Figure 2.5(d). Detailed descriptions of the new method and experimental phenomena can be referred to Wiseall et al. (2015).

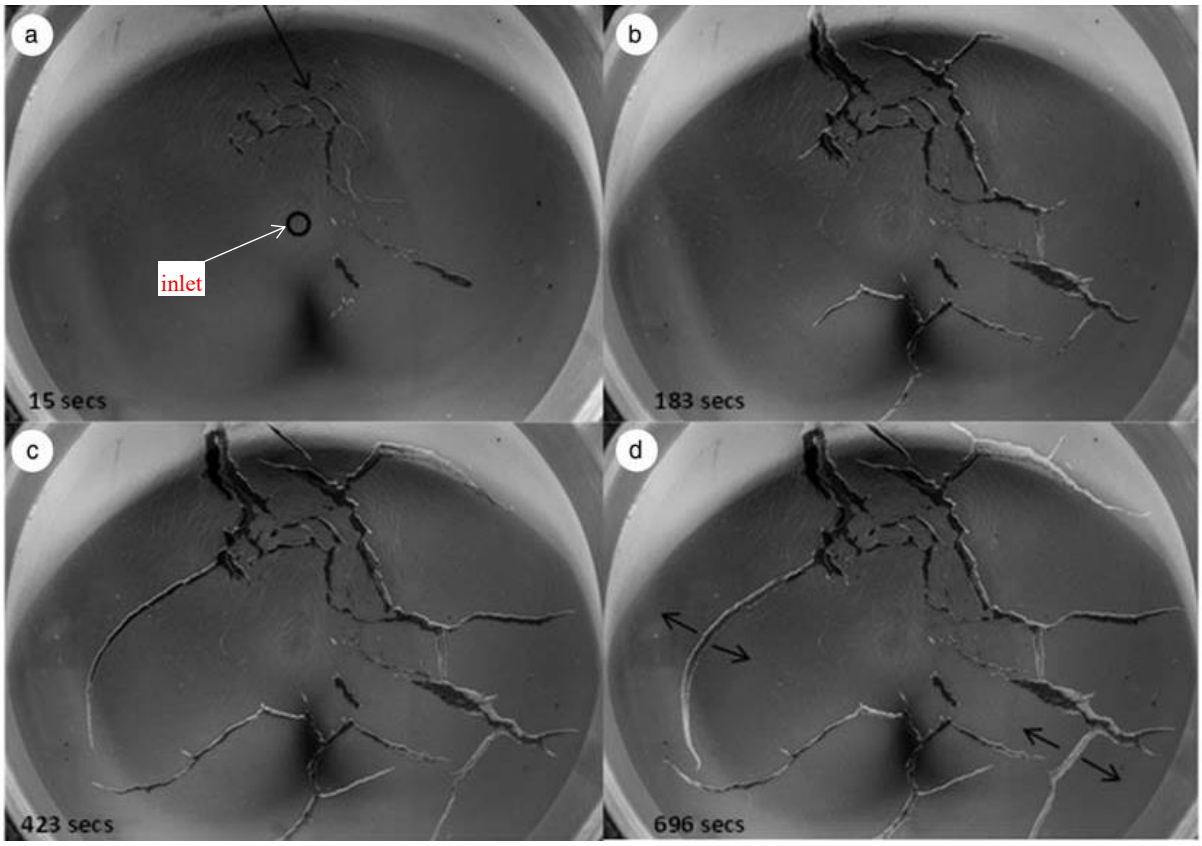

Figure 2.5 Evolution of dilatant pathways (by Wiseall et al. (2015))

To provide the evidence of localized gas pathways in the claystone, the sample COx-1 was heated to discharge the gas after the gas injection test (Harrington et al., 2013). As can be seen from Figure 2.6, gas bubbles are flowing out of the sample through the micro-fracturing formed pore spaces. Another clear visual difference from the images is that more gas bubbles occur in the backpressure face than that of the injection face. We may explain the difference from the following aspects: (i) the COx sample is able to accommodate high pressure gradient over small distances. Once the gas injection is ceased, the gas dilatant pathways close immediately and a pressure difference may exist from the injection face to the backpressure face since the existed pressure difference is not capable to re-open the pathway. When the COx sample is heated, the pathway will re-open that gas will flow along the existed pressure gradient (from the injection to the backpressure face), thus leading to a higher density of gas pathways occurring in the backpressure face. (ii) as explained by Harrington et al. (2013), the dendritic gas networks may expand through the core area of sample, leading to more localized pathways forming in the area close to backpressure face.

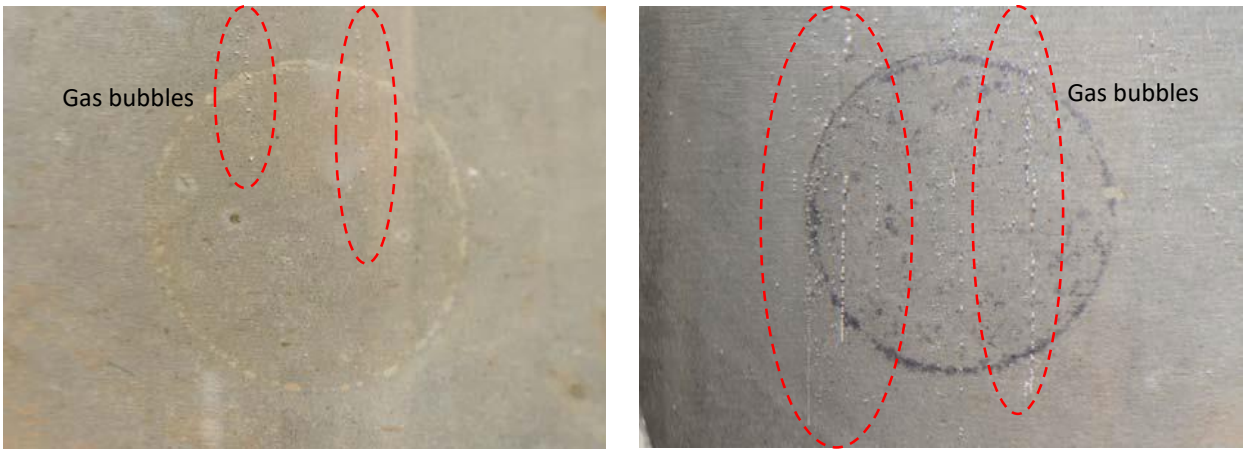

(a) Injection face (b) Backpressure face

Figure 2.6 Gas discharged from sample COx-1 after gas injection test (Harrington et al., 2013)

2.4.2 Dynamic Gas Flux and Gas Breakthrough Behavior

Gas flow through porous medium is generally described by Darcy's law, which was validated to be effective for the pore size even at a nanoscopic to microscopic scale (Kawagoe et al., 2016). The experimentally recorded gas flux was obtained using a generalized Darcy's law from the one-dimensional steady state flow path, details are provided by Harrington et al. (2017). The timing of gas breakthrough is determined when the gas leakage at the outlet is recorded by a sudden increase, followed by a steady state gas flow (Harrington et al., 2013). The interconnection of the gas dilatant pathways can be inferred from the recorded gas flux at the outlet. Figure 2.7 illustrates the experimentally recorded gas flux out of the sample at the standard temperature and pressure (STP) condition, in which the data of COx-1 and COx-4 tests are extracted from Harrington et al. (2017), data of COx-2 and SPP_COx-2 tests are obtained from Harrington et al. (2013) and Cuss et al. (2014), respectively.

As can be seen from the figure, these gas injection tests show a similar behavior that the major gas breakthrough occurs at the applied gas pressure significantly lower than the minimum principal stress, which implies the formed micro-fractures are highly localized. Once the major gas breakthrough occurs, the gas pathways is fully opened and interconnected from the inlet to the outlet. Then the steady state flow dominates the gas transport process, where the opening/closure of dilatant pathways is controlled by the gas injection pressure. Besides, the gas outflow rate increases at a rapid but intermittent rate when the applied gas pressure reaches the observed gas entry pressure, which reflects the unstable and dynamic behavior of gas preferential pathways.

On the other side, the gas migration behavior in different COx sample shows a significant difference, either in the orders of gas flux value or in the breakthrough timing, which may be attributed to the micro-heterogeneity or the arbitrary distribution of the pore networks.

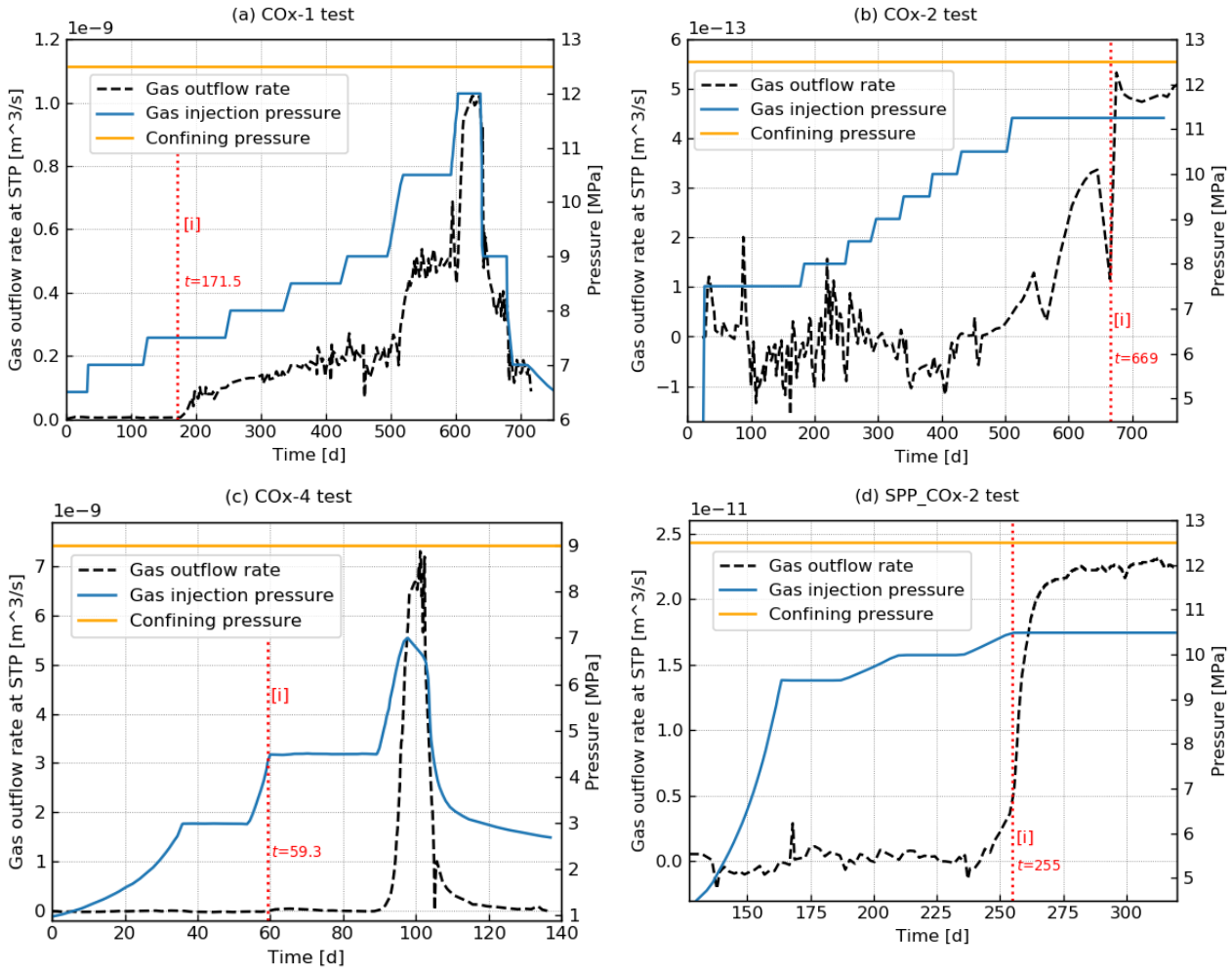

Figure 2.7 Gas outflow rate recorded experimentally at STP condition. Notes: Correlation line [i] represents the onset of major gas breakthrough (data extracted from Cuss et al. (2014); Harrington et al. (2013, 2017))

It should be specified here even the significant gas flux was observed in the outlet, the rock sample shows no measurable desaturation from the post-test analysis (Cuss et al., 2012; Harrington et al., 2013), which indicates the gas was not from the original pore spaces.

2.4.3 Sample Volume Dilation

Accompanied with the micro-fracturing, an obvious and measurable increase in the sample volume has been observed in the experiments, see Figure 2.8, details are referred to Cuss et al. (2014); Harrington et al. (2013). As clarified by Cuss et al. (2012), the volume dilation of the

sample cannot be explained by the compressibility of the pore water alone. Furthermore, the volume change shows a similar evolution trend with the gas flux out of the sample, which implies the coupling between stress, strain, gas breakthrough and permeability.

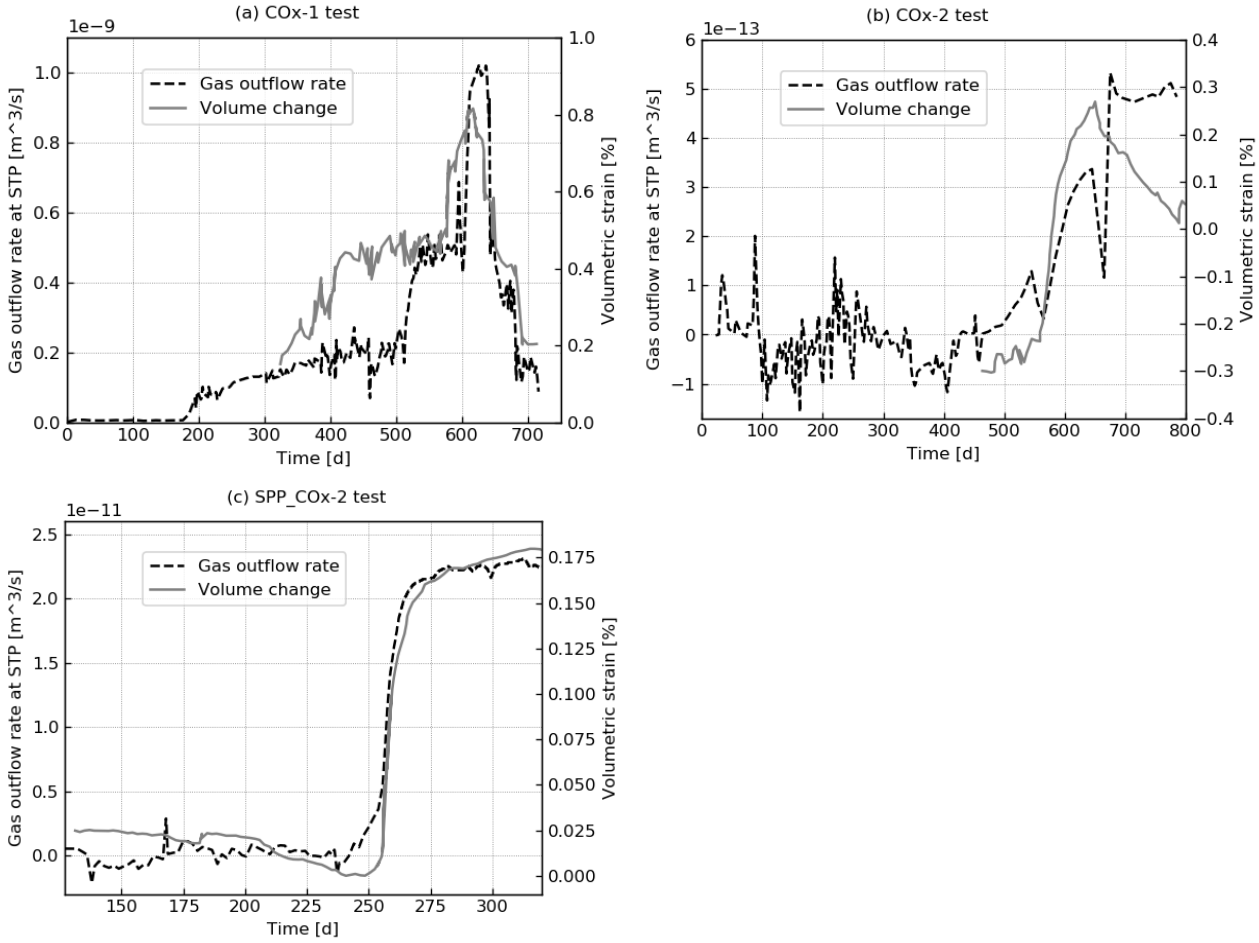

Figure 2.8 Experimentally recorded gas flux and volume change (data extracted from Cuss et al. (2014); Harrington et al. (2013))

2.4.4 Anisotropic Radial Deformation

An important experimental phenomenon is the gas induced anisotropic deformation along the radial direction, as can be seen in Figure 2.9. Radial 1, 2 and 3 represents three different locations in a same radial plane. The anisotropic deformation may be caused by the combined effects of the inherent bedding of rock materials, the micro-heterogeneous properties and the gas induced micro-fracturing, which provide valuable implications for the numerical study.

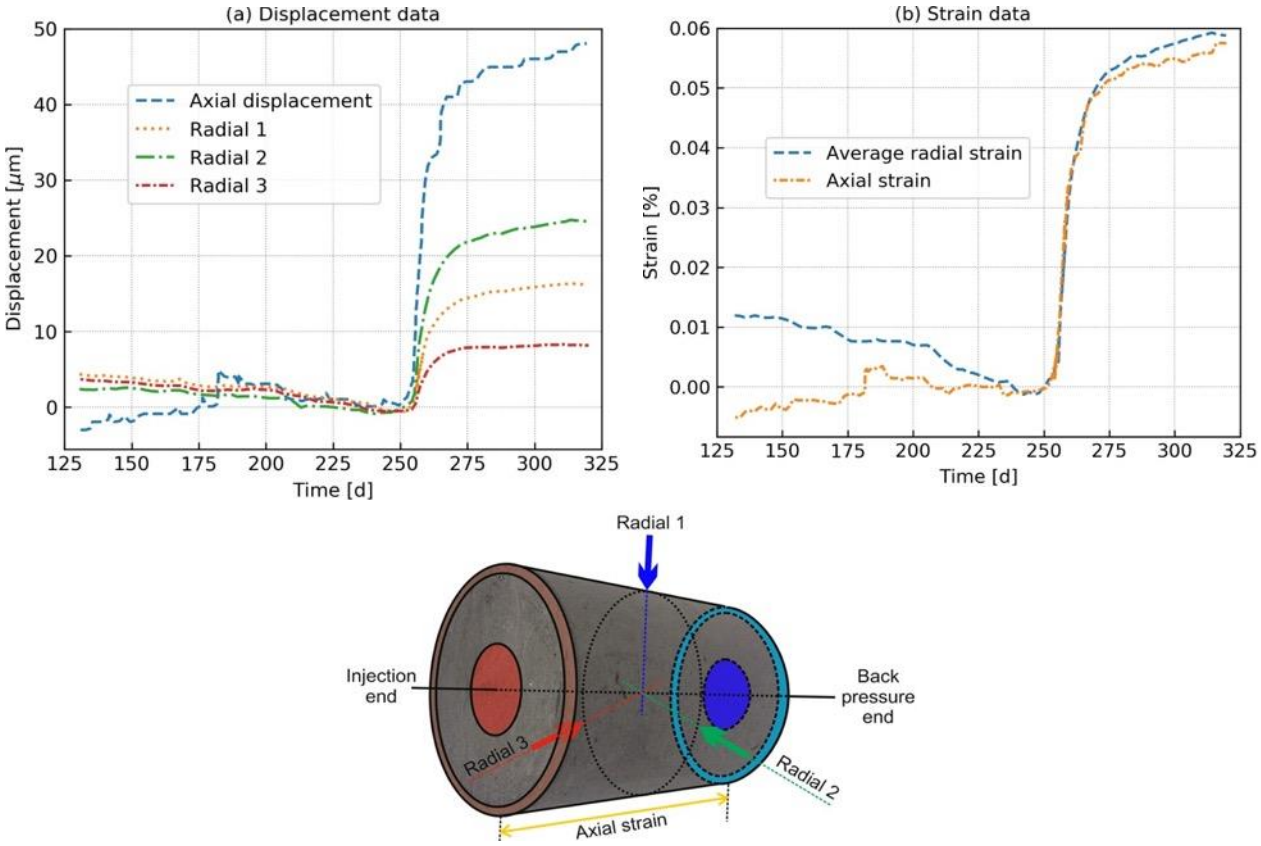

Figure 2.9 Anisotropic deformation and locations in the SPP_COx-2 test (data extracted from Cuss et al. (2014))

2.4.5 Pore Pressure Evolution

In the gas injection tests, the pressure in the injection guard ring (IGR) and back guard ring (BGR) is recorded to provide results on hydraulic anisotropy, which can be seen as the pore fluid pressure within the sample. Accompanied with the major gas breakthrough, both the pore pressure in the IGR and BGR has an abrupt increase, see different experimental results from Figure 2.10. It has to be noted that the pore pressure increase in the COx-2 test occurs ahead of the major gas breakthrough. This may be explained by that the gas front penetrates the guard ring earlier than the time it reaches the outlet, which represents the tortuous pore throat of the porous medium.

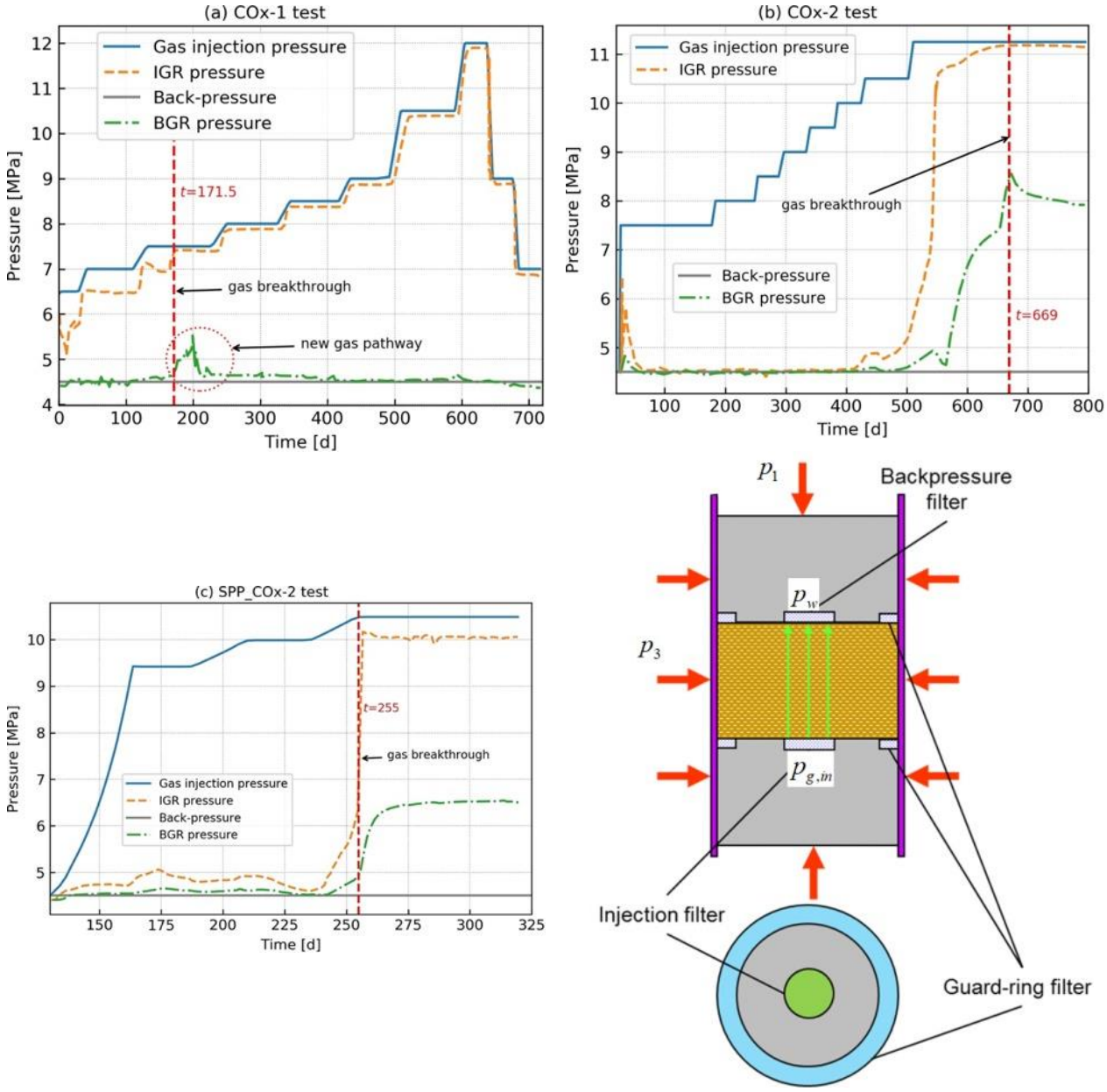

Figure 2.10 Pore pressure evolution (data extracted from Cuss et al. (2014); Harrington et al. (2013))

2.5 Conclusions

In the DGRs for nuclear wastes, significant quantities of gas could be produced due to several physico-chemical processes, i.e., the corrosion of metals, radiolysis and microbial degradation. About 97% of all radioactive wastes are constituted of LLW and ILW, where no significant heat is generated for their disposal. Although significant quantities of heat can be released in the repositories for HLW, it is expected that the onset of gas generation occurs after the heating process has been completed, and the host rocks have reached a fully saturated state.

Thus, the saturated rock samples under isothermal conditions are adopted in most previous experimental studies.

Four basic gas transport mechanisms are briefly discussed, including the advective/diffusive movement of dissolved gas, visco-capillary controlled two-phase flow, dilatancy controlled gas flow and macroscopic fracture controlled gas flow. Either the gas-induced micro-fracturing or macro-fracturing can create preferential pathways for radionuclides to bypass the host confinement, which is a significant safety concern that needs to be investigated in the study.

The gas migration in saturated host rocks is characterized by several HM behaviors, i.e., the development of preferential gas pathways, dynamic gas flow and gas breakthrough, mechanical volume dilation, anisotropic radial deformation, no desaturation after gas injection test. These experimental phenomena provide valuable implications for developing reliable mathematical models.

2.6 References

Charlier, R., Collin, F., Pardoen, B., Talandier, J., Radu, J.P.J.P., Gerard, P., 2013. An unsaturated hydro-mechanical modelling of two in-situ experiments in Callovo-Oxfordian argillite. Engineering Geology 165, 46-63.

Cuss, R., Harrington, J., Giot, R., Auvray, C., 2014. Experimental observations of mechanical dilation at the onset of gas flow in Callovo-Oxfordian claystone. Geological Society Special Publication 400, 507-519.

Cuss, R.C., Harrington, J.F., Noy, D.J., 2012. Final report of FORGE WP4.1.1: The stress-path permeameter experiment conducted on Callovo-Oxfordian Claystone. British Geological Survey Commissioned Report, CR/12/140.

Damnanac, B., Diederichs, M., Leech, R.E.J., 2011. Long-Term Geomechanical Stability Analysis. Itasca Consulting Group, Inc, p. 121.

Fall, M., Nasir, O., 2012. Numerical modeling of gas migration from a DGR in Ontario's sedimentary rocks. University of Ottawa.

Freiesleben, H., 2013. Final disposal of radioactive waste, in: Cifarelli, L., Wagner, F., Wiersma, D.S. (Eds.), New Strategies for Energy Generation, Conversion and Storage. E D P Sciences, Cedex A.

Guo, G., Fall, M., 2018. Modelling of dilatancy-controlled gas flow in saturated bentonite with double porosity and double effective stress concepts. Engineering Geology 243, 253-271.

Guo, G., Fall, M., 2019. Modelling of preferential gas flow in heterogeneous and saturated bentonite based on phase field method. Computers and Geotechnics 116, 103206.

Guo, G., Fall, M., 2021. Advances in modelling of hydro-mechanical processes in gas migration within saturated bentonite: A state-of-art review. Engineering Geology 287, 106123.

Harrington, J.F., Cuss, R.J., Talandier, J., 2017. Gas transport properties through intact and fractured Callovo-Oxfordian mudstones. Geological Society Special Publication 454, 131-154.

Harrington, J.F., de la Vaissière, R., Noy, D.J., Cuss, R.J., Talandier, J., 2012a. Gas flow in Callovo-Oxfordian claystone (COx): Results from laboratory and field-scale measurements. Mineralogical Magazine 76, 3303-3318.

Harrington, J.F., Milodowski, A.E., Graham, C.C., Rushton, J.C., Cuss, R.J., 2012b. Evidence for gas-induced pathways in clay using a nanoparticle injection technique. Mineralogical Magazine 76, 3327-3336.

Harrington, J.F., Noy, D.J., Cuss, R.C., 2013. Callovo-Oxfordian Claystone: processes governing advective gas flow. British Geological Survey Commissioned Report, CR/13/088.

Hildenbrand, A., Schlömer, S., Krooss, B.M., 2002. Gas breakthrough experiments on fine-grained sedimentary rocks. Geofluids 2, 3-23.

IAEA, 2018. Options for Management of Spent Fuel and Radioactive Waste for Countries Developing New Nuclear Power Programmes. INTERNATIONAL ATOMIC ENERGY AGENCY, Vienna.

Johnson, L., Marschall, P., Zuidema, P., Gribi, P., 2004. Effects of post-disposal gas generation in a repository for spent fuel, high-level waste and long-lived intermediate level waste sited in opalinus clay. National Cooperative for the Disposal of Radioactive Waste (NAGRA), NTB 04-06.

Kawagoe, Y., Oshima, T., Tomarikawa, K., Tokumasu, T., Koido, T., Yonemura, S., 2016. A study on pressure-driven gas transport in porous media: from nanoscale to microscale. Microfluidics and Nanofluidics 20.

Kronberg, M., 2018. KBS-3H Heated supercontainer test. Swedish Nuclear Fuel and Waste Management Co (SKB), p. 57.

Marschall, P., Horseman, S., Gimmi, T., 2005. Characterisation of gas transport properties of the Opalinus clay, a potential host rock formation for radioactive waste disposal. Oil and Gas Science and Technology 60, 121-139.

Miller, W., Alexander, R., Chapman, N., McKinley, J.C., Smellie, J., 2000. Geological disposal of radioactive wastes and natural analogues. Elsevier.

NAGRA, 2008. Effects of post-disposal gas generation in a repository for low- and intermediate-level waste sited in the Opalinus Clay of Northern Switzerland. National Cooperative for the Disposal of Radioactive Waste (NAGRA).

Norris, S., 2015. EC FORGE project: Updated consideration of gas generation and migration in the safety case. Geological Society Special Publication 415, 241-258.

Pazdniakou, A., Dymitrowska, M., 2018. Migration of Gas in Water Saturated Clays by Coupled Hydraulic-Mechanical Model. Geofluids 2018, 1-25.

Rodwell, W.R., Harris, A.W., Horseman, S.T., Lalieux, P., Müller, W., Ortiz Amaya, L., Pruess, K., 1999. Gas migration and two-phase flow through engineered and geological barriers for a deep repository for radioactive waste. Joint EC/NEA Status Report.

Vanapalli, S.K., Fredlund, D.G., Pufahl, D.E., 1996. The relationship between the soil-water characteristic curve and the unsaturated shear strength of a compacted glacial till. Geotechnical Testing Journal 19, 259-268.

Vanapalli, S.K., Fredlund, D.G., Pufahl, D.E., 1999. Influence of soil structure and stress history on the soil water characteristics of a compacted till. Géotechnique 49, 143-159.

Wiseall, A.C., Cuss, R.J., Graham, C.C., Harrington, J.F., 2015. The visualization of flow paths in experimental studies of clay-rich materials. Mineralogical Magazine 79, 1335-1342.

Ye, W.M., Xu, L., Chen, B., Chen, Y.G., Ye, B., Cui, Y.J., 2014. An approach based on two-phase flow phenomenon for modeling gas migration in saturated compacted bentonite. Engineering Geology 169, 124-132.

Chapter 3 Paper I: Hydro-Mechanical Modelling of Gas Migration in Host Rocks for Nuclear Waste Repositories: A State-of-the-Art Review

Submitted for publication

Jianxiong Yang, Mamadou Fall

Department of Civil Engineering, University of Ottawa, Ottawa, ON, Canada

Abstract: Host rocks, as the final impediment to waste migration, play a significant role in the nuclear waste repositories. Modelling of gas migration in saturated host rocks as well as its coupled hydro-mechanical (HM) behaviors is of importance to the assessment of geological disposal facilities. A comprehensive literature review is carried out on the models for simulating gas migration in saturated rock materials. Several aspects have been provided and discussed, including the material properties and experimental interpretations, governing equations, constitutive models for hydraulic and mechanical processes, fracture propagation models. Specifically, these models are discussed in detail with respect to their performance in describing the recorded experimental behaviors. It is found that the visco-capillary two phase flow model with enriched intrinsic permeability is commonly used to describe the advective gas transport in saturated host rocks. The embedded fracture model (EFM) or enriched EFM seems to be the most favored model as it accounts for the fracturing mechanism which is more representative to implicitly simulate the preferential gas pathways. To describe the mechanical behavior of rocks during the gas migration process, linear/nonlinear elastic, elastoplastic and damage models have been included in the mechanical processes. The HM models incorporating plasticity or damage may not be applicable in most experimental studies, which are not competent to simulate the key experimental behavior associated with the development of gas preferential pathways. Current models that can explicitly describe the gas induced micro-fracturing are seldomly reported, the existed ones are not able to represent all the key experimental behaviors related to preferential gas flow. Advanced approaches, i.e., phase field (PF) method, extended finite element method (XFEM), discrete element method (DEM), hybrid finite discrete element method (FDEM) can be integrated with cohesive zone model (CZM) to provide some promising aspects in representing the development of preferential gas pathways. Lastly, the conclusions and recommendations for future modelling are given.

Keywords: hydro-mechanical processes; gas flow; model; host rocks; deep geological repository; review.

Nomenclature

Latin symbols

a	fracture spacing
A_i	empirical parameter in intrinsic permeability model
b	fracture aperture
b_{hs}	hydraulic aperture of fracture set s
b_{ij}	Eshelby configurational stress tensor
C_{ijkl}	stiffness tensor
$\boldsymbol{C}$	stiffness tensor in matrix format
d	damage variable
$d_{\max}$	maximum damage
D_g^m	apparent diffusion coefficient of gas mixture
D_g^w	apparent diffusion coefficient of wet gas
$\bar{D}_g^m$	diffusion coefficient of gas mixture
$\bar{D}_g^w$	diffusion coefficient of wet gas
e_i	unit vector along crack propagation direction
E	Young's modulus
f_{tr}	residual tensile strength
$\mathcal{F}$	energy flux
$\boldsymbol{g}$	gravity acceleration in vector format
$\mathcal{G}$	energy release rate at crack tip
H	Henry's constant
$\boldsymbol{i}_g^d$	diffusion flux of dry gas in vector format
$\boldsymbol{i}_g^w$	diffusion flux of wet gas in vector format
$\boldsymbol{i}_w^v$	diffusion flux of water vapor in vector format
k_{in}	isotropic intrinsic permeability
$k_{\max}$	maximum permeability at maximum damage
$k_{r\alpha}$	relative permeability of fluid α
$\boldsymbol{k}_f$	fracturepermeability in matrix format
$\boldsymbol{k}_{in}$	intrinsic permeability in matrix format
$\boldsymbol{k}_m$	porous matrix permeability in matrix format
K	bulk modulus of porous material
$\mathbb{S}$	equivalent compliance tensor in matrix format
$\mathbb{S}_f$	compliance tensor of fracture in matrix format
$\mathbb{S}_m$	compliance tensor of matrix in matrix format
$t_{cn}^{'}$	effective stress traction normal to crack
$\boldsymbol{t}_c^{'}$	effective stress traction in vector format
T	absolute temperature
T_s	surface tension on air-water interface
$\mathbb{T}$	transformation matrix in matrix format
Δu_{ns}	change of mechanical aperture in fracture set s
U	interfacial energy
v	crack velocity
$\boldsymbol{v}_{fs}$	solid velocity in FC in vector format
$\boldsymbol{v}_{ps}$	solid velocity in PC in vector format
$\boldsymbol{v}_{f\alpha}^D$	Darcy's velocity of fluid α in FC in vector format
$\boldsymbol{v}_s$	solid velocity in vector format
$\boldsymbol{v}_\alpha^D$	Darcy's velocity of fluid α in vector format
V_1	material constant

Greek symbols

α_{ij}	Biot's effective stress coefficient tensor
β_{fs}	rotation angle of fracture set s
β_m	rotation angle of bedding plane in matrix
Γ_w	water exchange term between FC and PC
δ_{ij}	Kronecker delta
δ_c	displacement separation at full failure
δ_0	displacement separation at failure initiation
δ_1, δ_2	fitting parameters related to the PSD
ε_n	strain normal to the fracture
$\bar{\varepsilon}_p$	effective plastic strain
ε_{tu}	strain at tensile strength degrades to zero
ε_{t0}	strain corresponding to tensile strength
ε_v	volumetric strain
ε_0	threshold strain controlling fracture opening

K_{fs}	shear stiffness of fracture	$\boldsymbol{\varepsilon}$	strain tensor in matrix format
K_I	type-I stress intensity factor	$\boldsymbol{\varepsilon}_p$	plastic strain tensor in matrix format
K_n	normal stiffness of fracture	μ_α	dynamic viscosity of fluid α
K_s	bulk modulus of solid grain	ν	Poisson's ratio
l	crack length	π	equivalent pore pressure
m	shape parameter in the WRC	ρ	total mass density
M_w	molar mass of water	$\rho_{f\alpha}$	density of fluid α in FC
n_d	subcritical crack growth index	ρ_{pw}	water density in PC
n_i	outward unit vector normal to the contour	ρ_g^w	density of wet gas in dissolved state
$\vec{n}_f, \boldsymbol{n}$	unit vector normal to fracture in vector format	ρ_w^v	density of water vapor
$\vec{n}_{fs}$	unit vector normal to fracture set s in vector format	ρ_α	density of fluid α
p_c	capillary pressure	σ_{ij}	total stress tensor
p_{cr}	critical threshold pressure	σ_t	tensile strength
$\overline{p}_f$	average pore fluid pressure	$\boldsymbol{\sigma}$	total stress tensor in matrix format
p_{gev}	gas entry value	σ'_{ij}	effective stress tensor
p_w^{v0}	water vapor pressure	$\boldsymbol{\sigma}'$	effective stress tensor in matrix format
p_α	pressure of fluid α	τ	tortuosity
p_0	initial air entry value	ϕ	total porosity
Q_π	source term of fluid α	ϕ_f	porosity of FC in double porosity model
R	ideal gas constant	ϕ_p	porosity of PC in double porosity model
S_e	effective saturation degree	ψ_s	elastic strain energy
$S_{f\alpha}$	saturation degree of fluid α in FC	ω_g	mass fraction of dry gas
$S_{\alpha,r}$	residual saturation degree of fluid α	ω_g^w	mass fraction of wet gas
S_α	saturation degree of fluid α	ω_w^v	mass fraction of water vapor

3.1 Introduction

Nuclear power, as a reliable and powerful source of energy, has been widely adopted to meet the electricity expectations by many countries. However, the nuclear plants will generate nuclear wastes containing a number of radioactive isotopes that have a long-term half-lives and high calorific value, which calls for strict disposal requirements (Horseman and Volckaert, 1996). The deep geological repositories (DGRs) have been proposed to manage and isolate the radioactive wastes, without the intention to fetch them (Rodwell et al., 1999). In the post-closure phase of DGR, the geological disposal facilities (GDFs) are saturated with water and significant gas can be generated due to several processes, e.g., the metal corrosion, water radiolysis or

microbial reaction of organic materials (Johnson et al., 2004; Rodwell et al., 1999). The generated gas is anticipated to span throughout the long-term disposal of waste, over which time the gas will flow into the host rocks through molecular diffusion or bulk advection or the two processes simultaneously (Harrington et al., 2017). In the DGR concept, highly consolidated argillaceous formations, such as Callovo-Oxfordian (COx) claystone in France, Opalinus (OPA) clay in Switzerland, and Boom Clay in Belgium, are being investigated as potential host rocks due to their favored properties, i.e., small diffusion rate, low permeability (Senger et al., 2018) and strong radionuclide retardation capability (Altmann et al., 2012). However, these properties significantly restricts the gas movement so that the generated gas can accumulate to a certain pressure value, which may introduce new pathways for gas transport (Angeli et al., 2009; Cuss et al., 2014; Harrington et al., 2017; Hildenbrand et al., 2002; Horseman et al., 1996; Skurtveit et al., 2012). Thus, understanding the gas migration process in the host rocks is of fundamental importance to assess the GDF performance and safety.

To investigate the sealing capacity of host rocks, current analysis of gas migration behavior mainly includes experimental and mathematical methods. The earliest research on this topic may be dated back to about 1990s when many laboratory and in-situ gas injection experiments have been conducted in natural clay samples (Lineham, 1989) and in argillaceous rocks (Harrington and Horseman, 1999; Horseman et al., 1996). The experimental studies devoted to the understanding of the predominant processes governing the advective movement of gas through argillaceous rocks. The basic parameters needed to be recognized include the steady-state permeability, porosity, gas entry pressure (the pressure difference between upstream and downstream value (Hildenbrand et al., 2002)), capillary threshold pressure (the air entry value in the soil mechanics (Fredlund and Rahardjo, 1993)). As the focus of interest is to investigate the long-term gas migration behavior, thus most gas injection experiments are time consuming and the duration generally varies from hours to years. Sometimes, the duration of the tests may be ended in minutes due to specific experimental objectives, i.e., to investigate the influence of confining pressure on the gas flow process, see e.g., the loading cycle test conducted by Popp et al. (2007). Accompanied with the experimentally recorded gas flux at the outlet (Harrington and Horseman, 1999; Hildenbrand et al., 2002; Horseman et al., 1996), some other important results are also observed, i.e., the axial or radial deformation (Angeli et al., 2009; Gonzalez-Blanco et al., 2016; Romero et al., 2013; Skurtveit et al., 2012), the volume dilation and the pore pressure

evolution (Cuss et al., 2014; Cuss et al., 2012; Harrington et al., 2017; Harrington et al., 2013). These laboratory observed phenomena or recorded results provide valuable data to mathematically understand the gas migration behavior through saturated rocks.

In comparison to the experimental methods on gas migration behavior, the mathematical modelling provides a straightforward explanation on the coupled processes with regard to the observed phenomena. Using both specific assumptions and physical laws that govern the gas transport process (e.g., gas mass conservation, generalized Darcy's law governs the gas movement), the mathematical models can be developed and validated against the experimental data, which may be used to capture the real physical processes of gas migration in host rocks. Thanks to the efficiency of numerical methods on the time and resources, the mathematical modelling has been used as an effective tool to investigate the coupled relations (e.g., gas entry value and fracture aperture, deformation and permeability, etc) with regard to the gas migration behavior. Although the mathematical modelling has gained increasing attention for the research topic at hand, the number of publications that addresses the gas migration behavior is still relatively limited. Most stimulating contributions stem from the hydro-mechanical (HM) coupled models, which are developed in the framework of Biot's consolidation theory or mixture theory, as in (Arnedo et al., 2013; Fall et al., 2014; Gerard et al., 2014; Gonzalez-Blanco et al., 2016; Mahjoub et al., 2018; Nguyen and Le, 2015; Olivella and Alonso, 2008; Pazdniakou and Dymitrowska, 2018; Rozhko, 2016; Senger et al., 2014; Senger et al., 2018; Xu et al., 2013; Yang and Fall, 2021a; Yang et al., 2020). As gas migration in saturated clayey rocks concerns very complex behaviors, some conceptual models such as the embedded fracture model (EFM) (Arnedo et al., 2013; Gerard et al., 2014; Gonzalez-Blanco et al., 2016; Olivella and Alonso, 2008), double porosity model (Yang and Fall, 2021a) and enriched EFM (Yang et al., 2020) were proposed. To consider the irreversible deformation due to micro-fracturing, plasticity (Nguyen and Le, 2015; Xu et al., 2013) or damage (Fall et al., 2014) was also incorporated. Since the development of preferential gas pathways directly controls the HM couplings in the saturated rocks, it is desirable to represent this process in an explicit way. Therefore, the modelling approaches which can explicitly simulate preferential gas flow are more favorable recently in the international project for nuclear waste disposal.

To provide a comprehensive understanding of gas migration behavior in saturated rock materials, a state of art review is carried out in this paper. The review work has covered the

material properties and the experimental interpretations related to gas migration process. Then the governing equations for fluid flow and solid deformation are introduced in Section 3.3. In Section 3.4, the constitutive models for hydraulic and mechanical processes are summarized, a brief discussion on the pre-existing models is provided. In Section 3.5, the fracture theories which can represent the fracturing process are reviewed, the existing approaches and potential methods for simulating the preferential fluid flow are discussed. At last, conclusions and recommendations for future works are given.

3.2 Materials and Experimental Interpretations

Although significant quantities of heat can be released in the repositories for high-level wastes, it is expected that the onset of gas generation occurs after the heating process has been completed, and the host rocks have reached a fully saturated state (Rodwell et al., 1999). Thus, the saturated rock samples under isothermal conditions are adopted in most previous experimental studies.

3.2.1 Materials

3.2.1.1 Hydro-Mechanical Properties

Several types of clayey rocks, i.e., Boom clay, OPA clay and COx claystone, have been adopted to conduct gas injection experiments. As different types of minerals exhibit distinct grain size scope, a large proportion of clay contained in the clayey rocks significantly affects its transport properties (Li et al., 2007). Some key HM properties highly depend on the mineralogical component, e.g., water retention capacity, intrinsic permeability, since the distinct grain size determines the microstructure of rock (Marschall et al., 2005). Besides, the inherent bedding induced anisotropy is mainly a result of microstructural heterogeneity (Marschall et al., 2005). Experimentally recorded radial deformation during gas injection experiments was shown to be anisotropic (Cuss et al., 2014), which is closely related to the rock inherent bedding. These HM parameters need to be determined from the microscale, then upscaled to be the effective macroscopic parameters, as has been done in (Ababou et al., 2014). In this way the preferential gas flow can be described in a more physical manner.

3.2.1.2 Micro-fractures

Micro-fractures are ubiquitous in most rock types that clayey rock is one of them (Rodwell

et al., 1999). Two types of micro-fractures can be generally identified, e.g., one type refers to be bedding-parallel and another type forms at an angle to the bedding-parallel micro-fractures (Ougier-Simonin et al., 2016). In water saturated clayey rocks which are fine-grained with low permeability, the existence of micro-fractures may serve as the gas migration pathways when they are connected, regardless of the micro-fractures are closed or opened. This is because the closed micro-fractures could be reactivated during the periods of increased gas pressure, and correspondingly the incipient gas pathways along micro-fractures can dilate and become the preferred pathways.

The highly pressurized gas in saturated claystone leads to the micro-fracturing process mainly affected by stress history, mineralogy, clay content and microstructural heterogeneities (Ougier-Simonin et al., 2016). The fracture propagation is more likely to occur at the tip of existed ones, as the corresponding stress concentration will drive the creation of many smaller features in a nonlinear process zone ahead of the tip (Anderson, 2005). Microscopic observations after gas injection experiment have confirmed the mode-I rupture arising in sample areas of active gas discharge (Harrington et al., 2017). Therefore, accounting for the existence of micro-fractures in the macroscopic modelling framework is beneficial to simulating the gas induced fracturing process when the local stress exceeds the local tensile strength of rock.

3.2.1.3 Pore Structure

It is commonly agreed that the naturally fractured rock can be ideally treated to have a structure of two types of pore networks (Aifantis, 1977; Warren and Root, 1963; Wilson and Aifantis, 1982). The primary porosity refers to the natural pores that are highly connected and correlated with permeability, since its property is mainly dependent on the pore geometry, size distribution and spatial distribution of solid grains (Song et al., 2015; Warren and Root, 1963). While the secondary porosity is dominated by fracturing or jointing, which leads to the anisotropic behavior in parallel/normal directions to the crack plane (Warren and Root, 1963). Microscopic observations on clayey rocks (Ougier-Simonin et al., 2016) allow us to conclude that the typical size of cracks is at least one magnitude larger than the pore size. Although the blurry distinction between elongated pores and micro-fractures is still existed in some cases, what is clear from the observations is that some pores may act as initial flaws for propagation of micro-fractures whose size can become significantly larger than its initial size (Ougier-Simonin

et al., 2016). Under this circumstance the unimodal pore size distribution of intact claystone can become bimodal when fracturing occurs within the material, as seen in Figure 3.1.

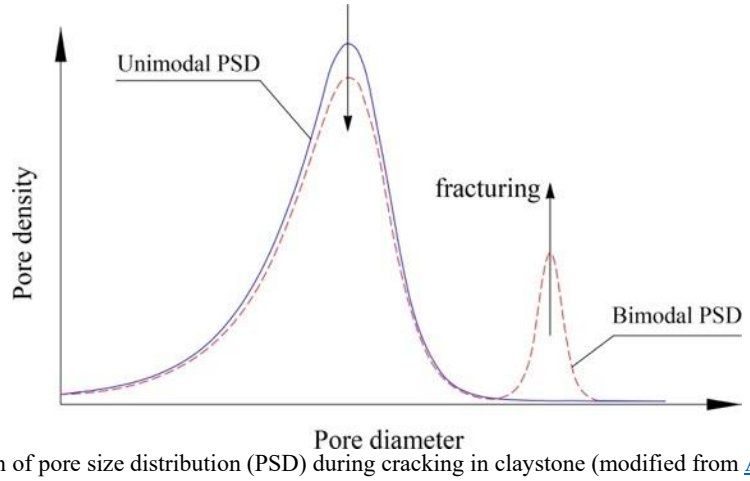

Figure 3.1 Variation of pore size distribution (PSD) during cracking in claystone (modified from Arson and Pereira (2013))

It should be noted that the treatment on the pore network of clayey rocks depends on the specific concern for the physical processes. With regard to the traditional research topics focusing on the overall mechanical behavior of claystone, the existence of limited amounts of large pores may have inessential impact on its behavior. In consequence, it is more appropriate to regard the claystone as a single porosity medium since the mathematical relations can be greatly simplified. With regard to the current topic of gas migration in saturated claystone, any existence of large pores has a significant influence on the transport processes. This is because when saturated claystone is subjected to highly pressurized gas, the large pores may serve as the source of an elastic stress concentration, which is similar to the feature of mechanical notch in fracture mechanics (Rodwell et al., 1999). Therefore, gas entry event is more likely to occur in the structure area with large pores. Driven by the continuous gas pressure, the large pores will be connected gradually and as a result utilized by gas as the preferential flow pathways. In such a situation, it is reasonable to consider the saturated claystone as a porous medium consisting of two pore networks, where the large connected pores serve as the preferential gas pathways while the pore space of matrix keeps to be saturated by water.

3.2.2 Experimental Findings and Interpretations

3.2.2.1 Experimental Findings

Previous laboratory gas injection tests conducted on saturated claystone (Cuss et al., 2014; Cuss et al., 2012; Harrington et al., 2017; Harrington et al., 2013; Hildenbrand et al., 2002;

Skurtveit et al., 2012) have demonstrated that the gas migration is accompanied by a series of characteristic observations, e.g., gas breakthrough, mechanical volume dilation, anisotropic radial deformation, micro-fracture propagation, non-desaturation after gas injection test and self-sealing behaviors. All of these behaviors are recorded at the condition of applied gas pressure significantly lower than the minimum principal stress.

Due to the small pore size of clay matrix in the claystone, the gas entry value is generally so high that the saturated claystone is difficult to be penetrated by gas in the absence of large pores. According to the adhesion theory by Rodwell et al. (1999), gas starts penetrating the saturated claystone when the increase in capillary pressure, resulting from the increase in gas pressure, exceeds the cohesive strength of interparticle water films. If the total maximum burial stress is indicative of force necessary to desorb water molecules from mineral surfaces during the process of consolidation, then the displacement of water in saturated claystone is hardly to occur as the applied gas pressure is much lower than the total stress, of which this value is generally lower than the maximum burial stress for overconsolidated clayey rocks (Rodwell et al., 1999). That is why the experimentally recorded gas entry pressure (0.9-1.3 MPa in COx-1 test, 5.6 MPa in COx-2 test, 1-3 MPa in COx-3 test and 6 MPa in SPP_COx-2 test from (Cuss et al., 2014; Harrington et al., 2013)) is commonly lower than the capillary threshold pressure. This behavior indicates the micro-fracturing is the major mechanism for gas invasion in saturated claystone. The microscopic observation from the sample areas presenting active gas discharge has confirmed the occurrence of opening micro-fractures, as seen from the left image in Figure 3.2.

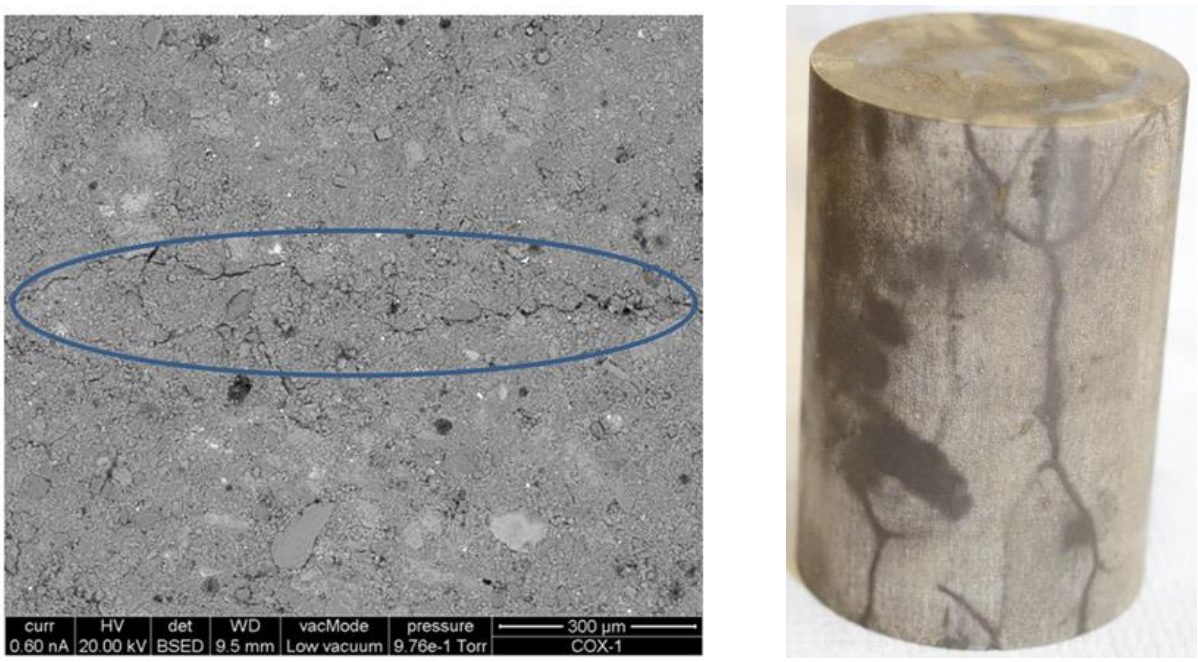

Figure 3.2 Image of observed micro-fractures in COx-1 sample areas presenting active gas discharge (left) from Harrington et al. (2017) and observed gas dilatant pathways in SPP_COx-2 sample (right) from Cuss et al. (2012).

As gas migrates through saturated claystone, strong couplings have been recorded between solid deformation, gas pressure and gas outflow rate (Cuss et al., 2014; Cuss et al., 2012; Harrington et al., 2017; Harrington et al., 2013). Specifically, gas breakthrough is accompanied by the development of pressure induced micro-fractures, which may vary temporally and spatially within the claystone (Harrington et al., 2017). Generally, the perturbation of local stress field precedes the event of major gas breakthrough, as seen from the different timing for maximum axial strain and maximum gas outlet pressure in air test conducted on Boom clay (Gonzalez-Blanco et al., 2016). The strong HM coupling is closely related to the development of preferential gas pathways that are highly instable. The variations in number, orientation, width and aperture of these dilatant pathways are affected by the local gas pressure, clay fabric deformation and gas-water interaction, etc (Harrington et al., 2017). Therefore, the experimentally recorded gas outflow rate, solid deformation and pore pressure will experience significant fluctuations (Cuss et al., 2014; Gonzalez-Blanco et al., 2016; Harrington et al., 2017; Romero et al., 2013).

When the developed gas dilatant pathways are interconnected from the gas inlet to outlet, see the right image from Figure 3.2, large amounts of gas flow out of the sample that leads to the phenomenon of gas breakthrough. It is noted from the experimental recordings that the gas breakthrough in rock samples may take place during the stage of gas pressure increase, such that

in COx-4 test (Harrington et al., 2017) and SPP_CO-2 test (Cuss et al., 2012), or during constant gas pressure stage in COx-1 and COx-2 test (Harrington et al., 2013). Furthermore, the gas breakthrough may even occur when gas pumping is ceased, see the air tests conducted on Boom clay (Gonzalez-Blanco et al., 2016) and on OPA clay (Romero et al., 2013). The exact timing for gas breakthrough is sometimes difficult to be determined (Cuss et al., 2012) due to the unstable behavior of gas pathways and the strong HM couplings in the clay matrix. Besides, the self-sealing capacity of claystone has been examined during the second gas injection history (Harrington et al., 2017). When the applied gas pressure decreases to a certain value, the gas pathways may close or self-seal partly or totally. As a consequence, the previously developed gas pathways may not be utilized by gas in the following testing cycles (Harrington et al., 2017).

3.2.2.2 Conceptual Model of Gas Dilatant Pathways

Gas flow in the clayey rocks is a complicated behavior in which the development of gas dilatant pathways is likely to present a dendritic pattern (Cuss et al., 2014; Hildenbrand et al., 2002), as shown in Figure 3.3. Large amounts of gas flow into the sample, leads to unstabilized branching fractures in the inlet area. When the gas front penetrates a certain area of rock sample, the corresponding HM response will be emerging, such as the increase of pore pressure in the guard ring, sample volume dilation, anisotropic deformation along the radial direction.

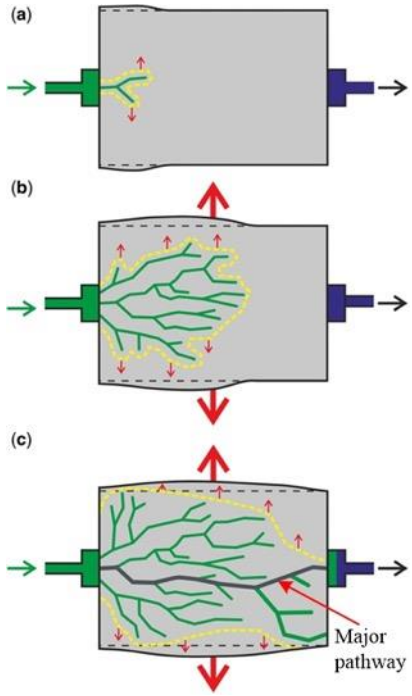

Figure 3.3 Experimental interpretation of gas flow in clayey rocks (Cuss et al., 2014)

Due to the strong adhesion applied by the mineral surfaces, water movement in the saturated claystone is more likely an exchange between clay matrix and developed micro-fractures, depending on the local water pressure values. A general case is that the development of gas dilatant pathways is accompanied by the increase of water pressure in the micro-fractures, thus leading to water movement from fractures to the clay matrix. The coupling between pore-volume and fractures is closely related to the gas entry value, as the increase in capillary pressure resulting from increase in gas pressure represents the degree of gas-water interaction. This specific behavior can be confirmed from the recorded HM responses in laboratory tests, e.g., the obvious distinction of pore pressure evolution between COx-1 and COx-2 test (Harrington et al., 2013), while a similar increasing trend of pore pressure evolution in the first testing cycle from the comparison between COx-2 test (Harrington et al., 2013) and SPP_COx-2 test (Cuss et al., 2012).

After the major pathway is formed from the gas inlet to outlet, gas rapidly flows out of the rock sample that triggers the gas breakthrough phenomenon. If the existed pathways cannot accommodate large amounts of gas flow, a number of auxiliary pathways may be developed and interconnected, as seen from Figure 3.3. In consequence, the gas injection pressure will decrease under the condition of constant injection rate, as observed in (Romero et al., 2013). The variations in gas breakthrough and steady state gas flow are closely associated with the number, orientation, width and aperture of the pressure-induced micro-fractures, which pose great challenges to the numerical work. However, these behaviors need to be appropriately considered in the modelling framework, to get a deeper understanding of gas migration behavior in saturated claystone.

3.3 Governing Equations

Previous HM models are generally developed in the unsaturated framework, which will be briefly revisited and discussed in the following section.

3.3.1 Mass Balance Equations

3.3.1.1 Single Porosity Medium

Most of the previous modelling work has considered the saturated rock as a porous medium consisting of a single pore structure, see (Arnedo et al., 2013; Fall et al., 2014; Gerard et al.,

2014; Nguyen and Le, 2015; Xu et al., 2013). A complete form of mass balance equations can be developed to simulate the gas flow in saturated rock materials, including liquid water and water vapor for water phase, dry gas in gaseous phase and wet gas in dissolved state for gas phase, expressed as follows (Charlier et al., 2013; Gerard et al., 2014):

$$\underbrace{\frac{\partial(\rho_w \phi S_w)}{\partial t} + \nabla \cdot (\rho_w \boldsymbol{v}_w^D + \phi \rho_w S_w \boldsymbol{v}_s)}_{\text{Liquid water}} + \underbrace{\frac{\partial(\rho_w^v \phi S_g)}{\partial t} + \nabla \cdot \left(\rho_w^v \boldsymbol{v}_g^D + \boldsymbol{i}_w^v\right)}_{\text{Water vapor}} = Q_w \tag{3.1}$$

$$\underbrace{\frac{\partial(\rho_g \phi S_g)}{\partial t} + \nabla \cdot (\rho_g \boldsymbol{v}_g^D + \phi \rho_g S_g \boldsymbol{v}_s + \boldsymbol{i}_g^d)}_{\text{Dry gas in gaseous phase}} + \underbrace{\frac{\partial(\rho_g^w \phi S_w)}{\partial t} + \nabla \cdot \left(\rho_g^w \boldsymbol{v}_w^D + \boldsymbol{i}_g^w\right)}_{\text{Wet gas in dissolved state}} = Q_g \tag{3.2}$$

where ϕ is porosity, ρ_w and ρ_w^v are the density of liquid water and water vapor, respectively; ρ_g and ρ_g^w are the density of dry gas and wet gas in dissolved state, respectively; S_w and S_g are the water and gas saturation degree, respectively; $\boldsymbol{v}_w^D$ and $\boldsymbol{v}_g^D$ are the Darcy's velocity vector of water and gas respectively; $\boldsymbol{v}_s$ is solid velocity, Q_w and Q_g are the source term for water and gas; $\boldsymbol{i}_w^v$, $\boldsymbol{i}_g^d$ and $\boldsymbol{i}_g^w$ are the diffusion fluxes for the water vapor, dry gas, wet gas in dissolved state, respectively.

3.3.1.2 Double Porosity Medium

As has been discussed in Section 3.2.1.3, it is reasonable to consider the saturated claystone as a porous medium consisting of two pore networks. In (Yang and Fall, 2021a), the fractured porous rock is conceptualized as a superposition of porous continuum (PC) and fractured continuum (FC). Two-phase flow is assumed to occur in the FC, while water can exchange between the PC and FC. The mass balance equations for water and gas in the FC are respectively expressed as (Yang and Fall, 2021a):

$$\frac{\partial(\rho_{fw} \phi_f S_{fw})}{\partial t} + \nabla \cdot (\rho_{fw} \boldsymbol{v}_{fw}^D + \phi_f \rho_{fw} S_{fw} \boldsymbol{v}_{fs}) = \Gamma_w \tag{3.3}$$

$$\frac{\partial(\rho_{fg} \phi_f S_{fg})}{\partial t} + \nabla \cdot (\rho_{fg} \boldsymbol{v}_{fg}^D + \phi_f \rho_{fg} S_{fg} \boldsymbol{v}_{fs}) = 0 \tag{3.4}$$

The mass balance equation for water in the PC is given as (Yang and Fall, 2021a):

$$\frac{\partial(\rho_{pw} \phi_p)}{\partial t} + \nabla \cdot (\phi_p \rho_{pw} \boldsymbol{v}_{ps}) = -\Gamma_w \tag{3.5}$$

where ρ_{fw} and ρ_{fg} are the density of water and gas in the FC, respectively; S_{fw} and S_{fg} are the saturation degree of water and gas in the FC, $\boldsymbol{v}_{fw}^{D}$ and $\boldsymbol{v}_{fg}^{D}$ are Darcy's velocity for water and gas in the FC, ϕ_f and ϕ_p are the porosity for the FC and PC, respectively; $\boldsymbol{v}_{fs}$ and $\boldsymbol{v}_{ps}$ are the solid velocity in FC and PC; Γ_w is a water exchange term between the FC and PC, which can be expressed by an accurate lumped-parameter model over all time scales from Zimmerman et al. (1996).

3.3.2 Momentum Balance Equation

The momentum balance equation to represent the mechanical behavior of rock materials is expressed as

$$\nabla \cdot \boldsymbol{\sigma} + \rho \boldsymbol{g} = 0 \tag{3.6}$$

where $\boldsymbol{\sigma}$ is the total stress tensor, ρ is the total mass density that can be expressed with regard to the contained mass in the porous medium, $\boldsymbol{g}$ is the gravity acceleration vector.

In the momentum balance equation (3.6), the total stress tensor $\boldsymbol{\sigma}$ can be expressed with respect to the effective stress tensor and contained fluid pressure based on the adopted assumptions in the study. For example, Terzaghi (1923) defined the earliest effective stress formulation for porous materials, as follows:

$$\sigma_{ij}^{'} = \sigma_{ij} + p_w \delta_{ij} \tag{3.7}$$

where $\sigma_{ij}^{'}$ is the component of effective stress tensor, σ_{ij} is the component of total stress tensor, p_w is the pore water pressure, δ_{ij} is the Kronecker delta.

Although the simplified form is not suitable for unsaturated case, the relation has been widely applied in the saturated soil mechanics. To extend the formulation to unsaturated soil mechanics, Bishop (1954, 1959) suggested an alternative closed-from:

$$\sigma_{ij}^{'} = (\sigma_{ij} + p_g \delta_{ij}) - S_w (p_g - p_w) \delta_{ij} \tag{3.8}$$

where p_g is the gas pressure, S_w is the water saturation degree. When the soil is fully saturated ($S_w = 1$), the gas pressure is viewed as the gauge pressure, Eq. (3.8) becomes the Terzaghi effective stress law. This formulation is limited to be used in the soil mechanics where the solid grain of soil is regarded as incompressible, thus it may not be suitable for rock materials as the stiffness difference between rock matrix and solid grain is not so significant.

To consider the compressibility of solid grain in the rock materials, a more general form may be suggested by introducing the Biot's effective stress coefficient (Biot and Willis, 1957), as follows:

$$\sigma_{ij}^{'} = \sigma_{ij} + \alpha_{ij}\bar{p}_f = \sigma_{ij} + \alpha_{ij}(p_g S_g + p_w S_w) \tag{3.9}$$

where α_{ij} is the component of Biot's effective stress coefficient tensor, $\bar{p}_f$ is the average pore fluid pressure. Noted that the Biot's coefficient can be expressed as $\alpha_{ij} = (1 - K/K_s)\delta_{ij}$ for materials with isotropic poroelasticity, in which K is the drained bulk modulus of porous material, K_s is the bulk modulus of solid grain. The ratio K/K_s usually ranges from 0.4 to 0.7 for saturated rocks and concrete (Skempton, 1961). While for soils $\alpha_{ij} = \delta_{ij}$, since the bulk modulus of solid grain is generally assumed to be incompressible, under this condition the general formulation Eq. (3.9) becomes the Bishop effective stress law. For the anisotropic materials, the components of Biot's coefficient tensor can be expressed by (Cheng, 1997):

$$\alpha_{ij} = \delta_{ij} - \frac{1}{3K_s} C_{ijkl}\delta_{kl} \tag{3.10}$$

where C_{ijkl} is the component of elastic stiffness tensor.

In order to consider the thermodynamically irreversible processes such as plasticity, damage etc., Coussy (2004) derived the effective stress law from the seconder law of thermodynamics, as follows:

$$\sigma_{ij}^{'} = \sigma_{ij} + \alpha_{ij}\pi = \sigma_{ij} + \alpha_{ij}(\bar{p}_f - U) \tag{3.11}$$

where π is the equivalent pore pressure, U is the interfacial energy that can be obtained from the integration as $U = \int_{S_w}^{1} p_c dS$, in which $p_c = p_g - p_w$ is the capillary pressure. Note that if the interfacial energy is neglected, the thermodynamically derived formulation (3.11) becomes the Bishop-type effective stress law (3.9).

From the viewpoint of thermodynamics, the total stress and strain, the equivalent pore pressure and porosity, as well as the damage driving force and damage variable are thermodynamically conjugated (Coussy, 2004). The thermodynamically derived formulation (3.11) has several advantages, i.e., applicable in both saturated and unsaturated cases, seamlessly recoverable to be the Terzaghi's effective stress. Therefore, it has been widely adopted to simulate the anisotropic damage propagation coupled with visco-plasticity behavior (Bui et al.,

2016a, 2016b, 2017; Dufour et al., 2012), to analyze the poroplasticity for the unsaturated porous medium (Coussy, 2007; Coussy et al., 2010), to simulate the coupled HM behavior for fractured rock mass (Lu et al., 2020; Nasir et al., 2014; Nasir et al., 2011; Yang et al., 2020).

3.4 Constitutive Models

3.4.1 Hydraulic Models

3.4.1.1 Advection/Diffusion of Dissolved Gas

Gas transport through advection and diffusion in a dissolved state is significantly restricted by the low permeability of host rocks, as a result the capacity is several orders of magnitude lower than the visco-capillary two-phase flow (NAGRA, 2008). Thus this transport process is commonly neglected for modelling the dominant gas flow process in the host rocks, more details about this mechanism are referred to Amann-Hildenbrand et al. (2015). Generally, the advection/diffusion of dissolved gas is controlled by three basic law, i.e., Darcy's law, Fick's law and Henry's law. The diffusion of dissolved gas in the host rocks is driven by the gas concentration gradient, which is represented by Fick's law:

$$\boldsymbol{i}_w^v = -\rho_g D_g^m \nabla \omega_w^v = -\boldsymbol{i}_g^d \;\; ; \;\; \boldsymbol{i}_g^w = -\rho_w D_g^w \nabla \omega_g^w \tag{3.12}$$

where D_g^m is the apparent diffusion coefficient in the gaseous mixture of dry gas and water vapor, D_g^w is the apparent diffusion coefficient of wet gas in dissolved state, ω_w^v and ω_g^w are the mass fraction of water vapor and wet gas in dissolved state, respectively.

The apparent diffusion coefficient can be modelled as (Charlier et al., 2013)

$$D_g^m = \phi S_g \tau \bar{D}_g^m \;\; ; \;\; D_\alpha^\pi = \phi S_w \tau \bar{D}_g^w \tag{3.13}$$

where τ is the tortuosity, $\bar{D}_g^m$ and $\bar{D}_g^w$ are the diffusion coefficient of gaseous mixture and dissolved gas, respectively.

In the unsaturated porous medium, phase transformation exists between gaseous phase and liquid phase by the process of water evaporation and gas dissolution. The mass fraction of water vapor ω_w^v in gaseous phase can be derived by following Charlier et al. (2013):

$$\omega_w^v = \frac{p_w^{v0} M_w}{RT\rho_g} \exp\left(\frac{-p_c M_w}{RT\rho_w}\right) \tag{3.14}$$

where M_w is the molar mass of water, R is the ideal gas constant, T is the absolute temperature,

p_w^{v0} is the water vapor pressure in equilibrium with liquid water pressure.

The mass fraction of gas dissolved in water ω_g^w is determined by Henry's law:

$$\omega_g^w = (\omega_g \rho_g) \frac{RT}{HM_w} \tag{3.15}$$

where H is the Henry's constant, ω_g is the mass fraction of dry gas.

3.4.1.2 Visco-Capillary Two-Phase Flow

In unsaturated porous medium, the visco-capillary two-phase (gas, water) flow is commonly described by the generalized Darcy's law:

$$\boldsymbol{v}_\alpha^D = -\frac{\boldsymbol{k}_{in} k_{r\alpha}}{\mu_\alpha} (\nabla p_\alpha - \rho_\alpha \boldsymbol{g}), \ \alpha = w, g \tag{3.16}$$

where $\boldsymbol{v}_\alpha^D$ is the Darcy's velocity of fluid α, $\boldsymbol{k}_{in}$ is the intrinsic permeability tensor, $k_{r\alpha}$ is the relative permeability of fluid α, μ_α is the dynamic viscosity of fluid α.

Gas migration in saturated host rocks activates complex coupled HM processes, in which the intrinsic permeability will be modified by mechanical effects, i.e., volume dilation, plastic deformation, damage, etc., thus various intrinsic permeability models are developed to represent the specific behavior.

3.4.1.2.1 Intrinsic Permeability

The evolution of intrinsic permeability directly controls the gas transport behaviors in the host rocks, including dynamic gas discharge, major breakthrough and the evolution of pore pressure. The previously developed models are categorized in Table 3-1.

The gas pressure based model (Xu et al., 2013) was proposed based on the experimental phenomenon that the permeability value increases abruptly when the applied gas pressure reaches a critical value p_{cr}. As a result, the gas outflow rate increases abruptly which may represent the gas breakthrough phenomenon. However, as indicated by Eq. (3.17), neither the evolution of pore size nor pore structure is contained, thus the model may not appropriately capture the deformation dependent phenomenon that is caused by the confining pressure change.

Compared to the gas pressure based model, the strain-based model can be well used to address this behavior. Both the volumetric strain and effective plastic strain are incorporated in

the relation, see Eqs. (3.18)-(3.19). The porosity evolution is well represented by the volumetric strain change, while the plastic strain is beneficial to achieve the rapid increase of gas outflow rate once the tensile failure is reached in the gas injection test (Popp et al., 2007). However, the model is limited to be used in the gas fracture cycle test by Popp et al. (2007), in which the plastic deformation can occur when the gas pressure is larger than the minimum principal stress.

By using a well-known exponential law (Eq. (3.20)) in the porosity-based model, the permeability evolution due to pore volume change can be well represented in certain air injection tests within one gas pumping cycle (Senger et al., 2014, 2018). But the pore structure change may not be captured by the simple formulation. To address the behavior, a slightly more complicated formulation (Eq. (3.21)) is proposed to implicitly consider the fracturing induced pore structure change, where fracture initiation, propagation and stabilization are included (Yang and Fall, 2021a). The enriched porosity model has been properly applied in the gas injection tests of complex loading paths. Clearly, the complicated porosity formulation has better performance in the complex loading experiments.

The damage-based permeability model is conceptually close in spirit to the strain-based model where the variables of both volumetric and plastic strain are substituted by the porosity and damage variable. As expressed by Eq. (3.22), the contribution of permeability evolution comes from two parts, where the former part is controlled by the pore volume change while the latter part by the damage variable. This model can capture the reversible process due to gas induced volume change, also it can capture the abrupt increase of permeability caused by the damage propogation (Fall et al., 2014). However, its applicability is limited in the gas fracture cycle test (Popp et al., 2007) where the macroscopic tensile failure can occur. As in other gas injection tests (Cuss et al., 2014; Harrington et al., 2017; Hildenbrand et al., 2002), the mode-I failure may occur locally since the gas injection pressure did not reach the macroscopic minimum principal stress (note: compressive stress is assumed to be positive).

Table 3-1 Intrinsic permeability models for gas migration in host rocks (1, Arnedo et al. (2013); 2, Fall et al. (2014); 3, Gerard et al. (2014); 4, Gonzalez-Blanco et al. (2016); 5, Nguyen and Le (2015); 6, Olivella and Alonso (2008); 7, Senger et al. (2014); 8, Senger et al. (2018); 9, Xu et al. (2013); 10, Yang and Fall (2021a); 11, Yang et al. (2020))

Categories	Intrinsic permeability models	Eq.	References
Gas pressure based model	$\boldsymbol{k}_{in} = \begin{cases} (1 + A_1 p_g)\boldsymbol{k}_{in0}, & p_g \le p_{cr} \\ (A_2(p_g - p_{cr}) + 1 + A_1 p_{cr})\boldsymbol{k}_{in0}, & p_g > p_{cr} \end{cases}$	(3.17)	[9]

Strain-based models	$\boldsymbol{k}_{in} = \begin{cases} 10^{A_3 \Delta\varepsilon_v} \exp(A_4 \Delta\bar{\varepsilon}_p)\boldsymbol{k}_{in0}, & \text{compression} \\ 10^{A_5 \Delta\varepsilon_v} \exp(A_4 \Delta\bar{\varepsilon}_p)\boldsymbol{k}_{in0}, & \text{tension} \end{cases}$	(3.18)	[9]
	$\boldsymbol{k}_{in} = \boldsymbol{k}_{in0}\exp(-A_6\varepsilon_v)\exp(-A_7\bar{\varepsilon}_p)$	(3.19)	[5]
Porosity-based models	$\boldsymbol{k}_{in} = \boldsymbol{k}_{in0}\exp[A_8(\phi/\phi_0 - 1)]$	(3.20)	[7, 8]
	$\boldsymbol{k}_{in} = \boldsymbol{k}_{in0}(\frac{\phi_f}{\phi_{f0}})^3(A_9\{1 + \exp[A_{10}(1 - \frac{\phi_f - \phi_{f0}}{A_{11}})]\}^{-1} - A_9[1 + \exp(A_{10})]^{-1} + 1)$	(3.21)	[10]
Damage-based model	$\boldsymbol{k}_{in} = \boldsymbol{k}_{in0}\exp[A_{12}(\phi/\phi_0 - 1)] + \frac{d}{d_{\max}}\{k_{\max}\boldsymbol{I} - \boldsymbol{k}_{in0}\exp[A_{12}(\phi/\phi_0 - 1)]\}$	(3.22)	[2]
Embedded fracture model	$\boldsymbol{k}_{in} = \boldsymbol{k}_m + \frac{(b_0 + a\langle\varepsilon_n - \varepsilon_0\rangle)^3}{12a}\vec{n}_f \otimes \vec{n}_f$	(3.23)	[1, 4, 6]
	$\boldsymbol{k}_{in} = \boldsymbol{k}_{in0} + \boldsymbol{k}_{f0}(1 + A_{13}\langle\varepsilon_n - \varepsilon_0\rangle)^3(\boldsymbol{I} - \vec{n}_f \otimes \vec{n}_f)$	(3.24)	[3]
Enriched embedded fracture model	$\boldsymbol{k}_{in} = \boldsymbol{k}_{in0}\frac{\phi^3}{(1-\phi)^2}\frac{(1-\phi_0)^2}{\phi_0^3} + \frac{(b_{hs0} + A_{14s}\Delta u_{ns})^3}{12a}(\boldsymbol{I} - \vec{n}_{fs} \otimes \vec{n}_{fs}), s = 1,2$	(3.25)	[11]

Note: $\boldsymbol{k}_{in}$ is the intrinsic permeability tensor, $\boldsymbol{k}_m$ is the permeability tensor of matrix, p_{cr} is a critical threshold pressure in the model, ϕ_f is the porosity of fractures in the double porosity model, ε_V is the volumetric strain, $\bar{\varepsilon}_p$ is the effective plastic strain, d is the damage variable, $d_{\max}$ is the maximum damage, $k_{\max}$ is the maximum permeability corresponding to maximum damage, ε_n is the strain normal to the fracture, ε_0 is a threshold strain controlling fracture opening, $\vec{n}_f$ and $\vec{n}_{fs}$ are the unit vector normal to the fracture plane and fracture set s (=1 or 2), a is fracture spacing, b is fracture aperture, $\boldsymbol{k}_{f0}$ is the initial intrinsic permeability tensor of embedded fractures, b_{hs0} is the initial hydraulic aperture of fracture set s (=1 or 2), Δu_{ns} is the change of mechanical aperture in fracture set s(=1 or 2), notations with subscript '0' denote their corresponding initial values, A_i is the empirical parameter in the model.

Embedded fracture model (EFM) is widely adopted for the research topic at hand, see e.g., (Arnedo et al., 2013; Gerard et al., 2014; Gonzalez-Blanco et al., 2016; Olivella and Alonso, 2008), due to its simplicity and geometric representation of fracture networks. In the model, the rock is conceptualized as a series of parallel fracture sets embedded into a porous matrix, see Figure 3.4. As can be seen from Eq. (3.23), the permeability of matrix is described by Kozeny-Carmen model (former part in the relation (3.23)) (Carman, 1937), while the fracture permeability is described by cubic law (latter part in the relation (3.23)) (Witherspoon et al., 1980). The permeability of porous medium is a combination of matrix permeability and fracture permeability. The opening/closure of fracture is represented by the variation of strain normal to the fracture, which is more representative to the gas induced fracturing.

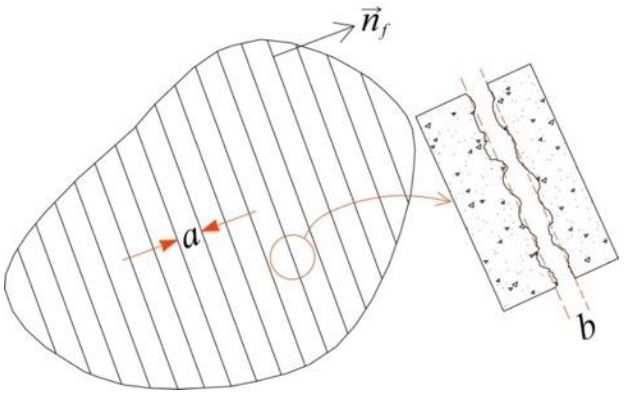

Figure 3.4 Schematic graph of the EFM

It is worth noting that the fracture permeability can be expressed with respect to several variants, and in consequence leading to different formulations, as represented by Eqs. (3.23)-(3.24). However, the EFM only considers the hydraulic behavior of fractures, which cannot describe the stiffness degradation due to fracture opening. To account for the nonlinear mechanical behavior of embedded fractures, Martinez et al. (2013) introduced the normal stiffness of fractures into the equivalent stiffness tensor, and differentiated the mechanical aperture with hydraulic aperture of fractures. This enriched EFM is further improved by Yang et al. (2020) using an equivalent continuum model, where two fracture sets are inserted into the anisotropic matrix. The enriched EFM was demonstrated to be more powerful by reproducing the coupled HM behaviors in the gas injection tests, e.g., gas flow behavior as well as the anisotropic radial deformation.

3.4.1.2.2 Water Retention Curve

As gas starts penetrating the saturated rocks, the interaction between gas and water occurs, which can be represented by the widely used van Genuchten model (van Genuchten, 1980). In the model, the effective saturation degree S_e is defined as:

$$S_e = \begin{cases} \left[1+\left(\dfrac{p_c}{p_{gev}}\right)^{\frac{1}{1-m}}\right]^{-m} & p_c > 0 \\ 1 & p_c \le 0 \end{cases} \tag{3.26}$$

$$p_c = p_g - p_w \tag{3.27}$$

where p_c is the capillary pressure (or matrix suction in the soil mechanics), p_{gev} is the gas entry value, m is the shape parameter.

The water saturation degree S_w and gas saturation degree S_g are coupled by the following relation:

$$S_e = \frac{S_w - S_{w,r}}{1 - S_{w,r} - S_{g,r}} \tag{3.28}$$

$$S_g = 1 - S_{w,r} - S_w \tag{3.29}$$

where $S_{w,r}$ and $S_{g,r}$ are the residual water and gas saturation degree, respectively.

The gas entry value, plays an important role in controlling the gas migration process since it affects the amount of gas penetrated into the saturated porous medium, as a result influencing the HM response of the material. Due to the extremely small pore size of clay matrix, the intact clayey rock has a high gas entry value, while this value will be significantly decreased by the development of gas induced micro-fracturing or macro-fracturing. This desaturation process is commonly described by the capillary model in the unsaturated soil mechanics (Fredlund and Rahardjo, 1993), where the diameter of capillary tube is regarded as equal to the fracture aperture b. Thus the gas entry value can be described by the cubic root model (CRM), which is written in view of the Laplace equation:

$$p_{gev} = \frac{2T_s}{b} = \frac{2T_s}{b_0}\left(\frac{b_0}{b}\right) = p_0\left(\frac{k_{in0}}{k_{in}}\right)^{\frac{1}{3}} \tag{3.30}$$

where p_0 is the initial air entry value, T_s is the surface tension acting on the air-water interface. It is noted that for the rock materials with anisotropic permeability or containing several fracture sets, several values will be obtained based on Eq. (3.30). To account for the actual capillary behavior, the gas entry value should be the minimum one from all the derived values, which represents gas can penetrate the porous medium through the largest pore that corresponds to the samllest gas entry value.

3.4.1.2.3 Relative Permeability

Two groups of relative permeability models are commonly used to simulate the gas flow behavior in saturated host rocks, one of which is the well-known vG model (Mualem, 1976; van Genuchten, 1980), the other one is the power law model.

The vG model is a close-form analytical relation to predict the relative permeability of unsaturated soils, which has been applied in the unsaturated rocks, see (Fall et al., 2014;

Mahjoub et al., 2018; Nguyen and Le, 2015; Senger et al., 2014; Senger et al., 2018; Xu et al., 2013). The relative permeability for water and gas is described with respect to the effective saturation degree:

$$k_{rw} = \sqrt{S_e}[1-(1-S_e^{1/m})^m]^2 \tag{3.31}$$

$$k_{rg} = \sqrt{1-S_e}(1-S_e^{1/m})^{2m} \tag{3.32}$$

The power law model was developed from the experimental approach by Brooks and Corey (1964); Mualem (1978), which has been used in (Arnedo et al., 2013; Gerard et al., 2014; Gonzalez-Blanco et al., 2016; Olivella and Alonso, 2008). The empirical relation is expressed as:

$$k_{rw} = S_e^{\delta_1} \tag{3.33}$$

$$k_{rg} = (1-S_e)^{\delta_2} \tag{3.34}$$

where δ_1 and δ_2 are the fitting parameters related to the pore size distribution of the rock.

The comparison of gas relative permeability between vG model and power law model is illustrated in Figure 3.5 for different model parameters. It is noted that the relative permeability predicted by vG model is higher than that predicted by power law model over the whole range of effective saturation degree. For the saturated host rocks, the gas penetration is difficult at the initial stage, while the desaturation process is accelerated with the fracture opening. Thus, the power law model with higher order can better represent the specific phenomenon. Due to the limited experimental data to validate the power relation, Eq. (3.34) is commonly scaled by a coefficient to improve the flexibility, as seen in (Arnedo et al., 2013; Gonzalez-Blanco et al., 2016). To capture the dynamic evolution of gas flow behavior, these introduced parameters have to be calibrated by fitting the experimental results.

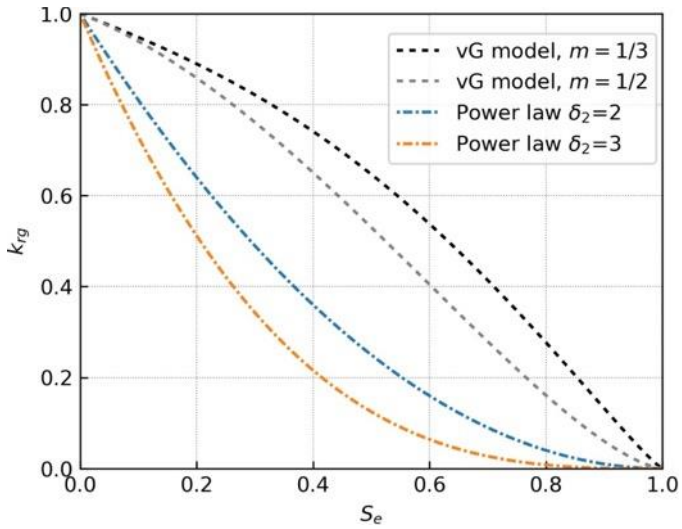

Figure 3.5 Comparison between vG model and power law model

3.4.2 Mechanical Models

Gas migration in saturated host rocks is a complex phenomenon that is accompanied by many specific mechanical behaviors, i.e., gas induced micro-fracturing or macro-fracturing, mechanical volume dilation, and anisotropic deformations. Previous constitutive models have covered the plasticity or damage into the constitutive relation, which can be expressed in the following form:

$$\boldsymbol{\sigma}' = \boldsymbol{C}(d) : (\boldsymbol{\varepsilon} - \boldsymbol{\varepsilon}_p) \tag{3.35}$$

where $\boldsymbol{C}$ is the stiffness tensor, d is the damage variable, $\boldsymbol{\varepsilon}$ is the total strain tensor, $\boldsymbol{\varepsilon}_p$ is the plastic strain tensor.

3.4.2.1 Elastic Models

Bothe linear (Arnedo et al., 2013; Gerard et al., 2014) and nonlinear (Mahjoub et al., 2018; Senger et al., 2014; Senger et al., 2018; Yang and Fall, 2021a; Yang et al., 2020) elastic relations are used to simulate the mechanical behavior of host rocks during the gas transport process. The linear elastic relations are generally adopted in the EFM where only hydraulic aperture is introduced in the fracture set. As the fracture opening induced softening behavior is not incorporated, the linear model cannot capture the phenomenon of mechanical volume dilation. By adding a softening variable into the elastic parameters, the material presents nonlinear mechanical response (Mahjoub et al., 2018). This simplified enrichment can represent the gas induced volume dilation as the material degradation is related to the gas saturation degree. However, the phenomenologically proposed damage law (Mahjoub et al., 2018) is not

thermodynamically consistent as the desaturation process is reversible, more theoretical work needs to be done to validate the damage law. In the nonlinear models by Senger et al. (2014, 2018), the bulk modulus is pressure dependent, and the net mean pressure is not allowed to be negative. Thus the model is limited to representing the macroscopic compressive behavior of rock in the gas injection test.

As there were a lack of models that can flexibly tackle the gas induced micro-fracturing in saturated claystone, the dual-continuum model seems to provide an alternative choice to address the highly coupled problem. Recently, Yang and Fall (2021a) developed a double porosity model that conceptualizes the fractured porous rock as a superposition of PC and FC, the mechanical behaviors of which are described by their specific effective stress law. The respective volumetric of PC and FC are incorporated in the governing equations to get a direct coupling between pores and developed fractures. The mechanical behaviors in PC and FC are coupled through total stress equilibrium, as seen in Figure 3.6. Although several important experimental phenomena were captured by the double porosity model, the fracturing process is still expressed in an implicit way. In addition, the respective physical processes in the PC and FC lead to the production of many model parameters, which are difficult to be determined through experimental methods. The model should be carefully used before finding the appropriate physical background for the model parameters.

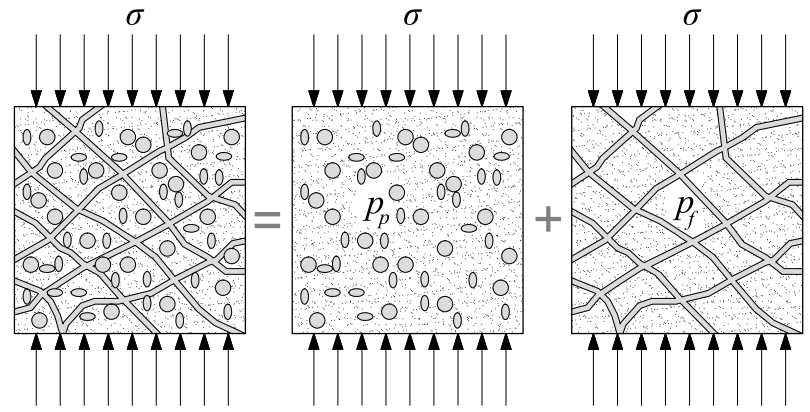

Figure 3.6 Schematic of double porosity model

To address the mechanical behavior of fractures in the EFM, Yang et al. (2020) incorporated the hyperbolic relation of fracture deformability (Bandis et al., 1983) in the matrix, as a result the fractured rock shows a nonlinear elastic behavior. In the enriched EFM, both the inherent bedding and fracture induced anisotropy contribute to the anisotropic radial deformation during

gas migration. A simple superposition method was provided to derive the effective compliance tensor, as presented in Figure 3.7. Thanks to the three-dimensional (3D) geometry, the anisotropic radial deformation in the SPP_COx-2 test (Cuss et al., 2014) was well represented. Besides, the relation between pathway aperture, local gas pressure and effective stress within the solid matrix has been satisfactorily explained. This model seems to be a potential that may be extended to the field condition. But, this approach is still not able to describe the preferential gas flow in an explicit way. Therefore, the non-desaturation phenomenon may not be properly simulated.

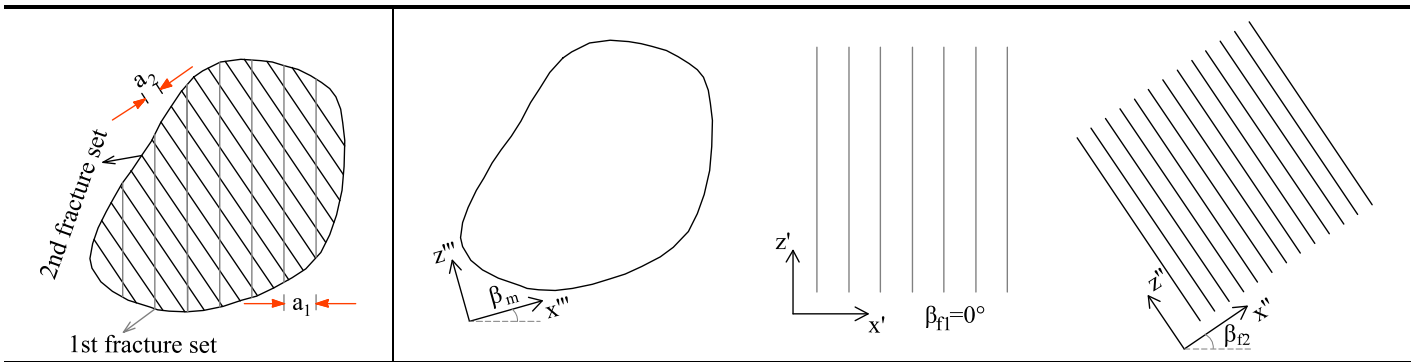

$\mathbb{S} = \mathbb{S}'_m + \mathbb{S}'_f + \mathbb{S}''_f$ Fractured rock

$\mathbb{S}'_m = \mathbb{T}^{-1}(\beta_m)\mathbb{S}_m\mathbb{T}(\beta_m)$ Matrix with bedding

$\mathbb{S}'_f = \mathbb{S}_f$ The 1st fracture set

$\mathbb{S}''_f = \mathbb{T}^{-1}(\beta_{f2})\mathbb{S}_f\mathbb{T}(\beta_{f2})$ The 2nd fracture set

$$\mathbb{S}_m = \begin{bmatrix} \frac{1}{E_\parallel} & -\frac{\nu_{\parallel\parallel}}{E_\parallel} & -\frac{\nu_{\perp\parallel}}{E_\perp} & & & \\ -\frac{\nu_{\parallel\parallel}}{E_\parallel} & \frac{1}{E_\parallel} & -\frac{\nu_{\perp\parallel}}{E_\perp} & & & \\ -\frac{\nu_{\perp\parallel}}{E_\perp} & -\frac{\nu_{\perp\parallel}}{E_\perp} & \frac{1}{E_\parallel} & & & \\ & & & \frac{1}{G_{\parallel\parallel}} & & \\ & & & & \frac{1}{G_{\parallel\perp}} & \\ & & & & & \frac{1}{G_{\parallel\perp}} \end{bmatrix}, \mathbb{S}_f = \begin{bmatrix} \frac{1}{aK_n} & & & & & \\ & 0 & & & & \\ & & 0 & & & \\ & & & \frac{1}{aK_{fs}} & & \\ & & & & 0 & \\ & & & & & \frac{1}{aK_{fs}} \end{bmatrix}, \mathbb{T} = \begin{bmatrix} \cos^2\beta & 0 & \sin^2\beta & 0 & 0 & \sin(2\beta) \\ 0 & 1 & 0 & 0 & 0 & 0 \\ \sin^2\beta & 0 & \cos^2\beta & 0 & 0 & -\sin(2\beta) \\ 0 & 0 & 0 & \cos\beta & \sin\beta & 0 \\ 0 & 0 & 0 & -\sin\beta & \cos\beta & 0 \\ -\frac{1}{2}\sin(2\beta) & 0 & \frac{1}{2}\sin(2\beta) & 0 & 0 & \cos(2\beta) \end{bmatrix}$$

Figure 3.7 Determining the effective compliance tensor of fractured rock (Yang et al., 2020). $\mathbb{S}_m$ and $\mathbb{S}_f$ are compliance tensor of matrix and fracture set, respectively; $\mathbb{T}$ is the transformation matrix.

3.4.2.2 Elastoplastic Models

The elastic models may be not competent to represent the gas induced irreversible behaviors, thus the elastoplastic models, i.e., Mohr-Coulomb Model (MCM) and Barcelona Basic Model (BBM), are introduced into the HM framework.

3.4.2.2.1 BBM

The BBM by Alonso et al. (1990) has been used to simulate the behavior of Boom clay (Gonzalez-Blanco et al., 2016) as well as the behavior of clayed barrier material (Olivella and

Alonso, 2008) during the gas migration process. The yield surface of BBM is illustrated in Figure 3.8.

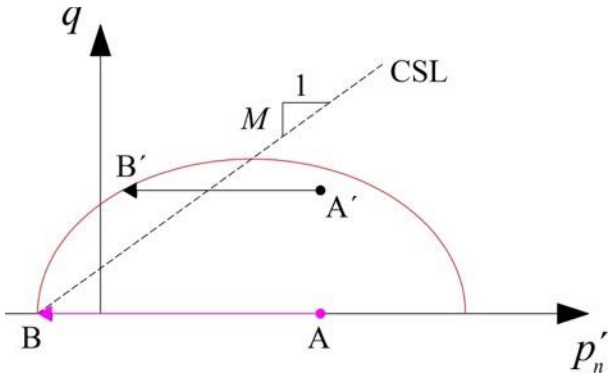

Figure 3.8 Yield surface of BBM

The initial stress state for material under isotropic loading pressures may be referred to point A in Figure 3.8. The stress state at point A may evolve along a specific path with the increase of gas pressure, depending on the external loading conditions. Under constant external loading pressures, the increase of gas pressure only reduces the net mean stress, thus the stress state evolves along A-B. If the gas pressure exceeds the confining pressure and the net mean stress reaches the material tensile strength, the material is expected to experience tensile failure. However, the capability of BBM to represent the material tensile behavior is rarely examined.

If the rock is initially subjected to strong anisotropic stress state, we may refer to Point A' as the initial stress state in Figure 3.8. Under constant external stress condition, the increase of gas pressure will cause the stress state evolving along the path A'-B' until the shear failure occurs. However, a nearly isotropic stress state is expected in most in-situ conditions of geological repositories (Cuss et al., 2014), thus the constant isotropic loading pressures are adopted in most experimental gas injection tests (Harrington et al., 2017; Hildenbrand et al., 2002; Romero et al., 2013). Besides, the plastic deformation due to the rise of gas pressure is rarely reported in the numerical studies of this research topic by using the BBM, as seen in (Gonzalez-Blanco et al., 2016; Olivella and Alonso, 2008). In fact, the BBM is widely adopted in the soil like material, in which the behavior of other host rocks, i.e., OPA clay, COx claystone may be not appropriately represented by the BBM.

3.4.2.2.2 MCM

The MCM has been used to simulate the plastic behavior of OPA clay in the gas fracture

cycle experiment by Popp et al. (2007), as seen in (Nguyen and Le, 2015; Xu et al., 2013). The Mohr circles in Figure 3.9 represent different stress states, and the size of circle represents the difference of maximum and minimum principal stress. The circle of larger size means the material is subjected to a more significant anisotropic stress state. With the increase of gas pressure, the Mohr circle will move towards left. Once the circle touches the MC failure line, shear failure occurs that the failure zone will serve as the preferential path for gas migration. This situation is likely to happen prior to the onset of tensile failure in case of initially anisotropic stress state and fracture zones pre-existing in the rock formations, where the gas flow prefers in a certain direction, see the CO_2 injection induced shear slip in caprock (Rutqvist and Tsang, 2002). However, the exact failure characteristics, the boundary between shear and tensile failure needs to be further verified experimentally. In contrast, small mode-I type fractures have been observed at the injection port area in the gas injection test by Cuss et al. (2012). Under a nearly isotropic loading condition, stress state may be referred to the Mohr circle of small size in Figure 3.9, the increase of gas pressure is more likely to cause tensile failure. To account for this mechanism, a tension cutoff line needs to be incorporated in the MCM. The enriched MCM is suitable to simulate the tensile failure behavior in the gas injection test under the condition of gas pressure exceeding the minimum principal stress.

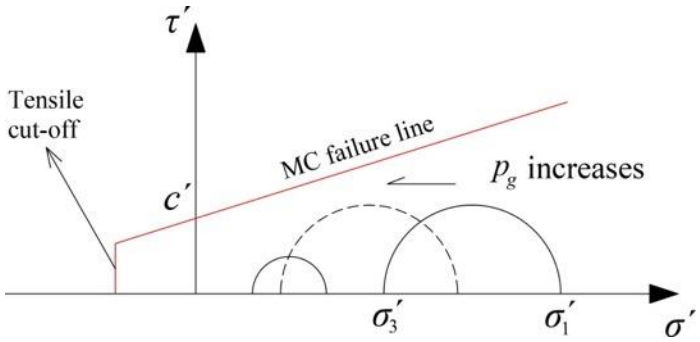

Figure 3.9 Stress state with the increase of gas pressure in the MCM

3.4.2.3 Damage Models

The development of gas dilatant pathways is accompanied by the gas induced micro-fracturing or macro-fracturing (Popp et al., 2007; Wiseall et al., 2015), which have a degradation effect on the material stiffness. Explicitly simulating the fractures is mathematically complex, thus the damage models are developed to implicitly simulate the fracturing process. The material damage is generally expressed by the degradation of Young's modulus for an isotropic damage

model, as follows:

$$E(d) = (1-d)E_0 \tag{3.36}$$

where $E(d)$ is the damaged Young's modulus.

The damage model was originally developed by Tang et al. (2002), considering both compressive/shear damage and tensile damage. The damage variable was introduced with respect to material compressive and tensile strength, respectively. As the increase of gas pressure is equivalent to an unloading process, the gas induced fracturing belongs to tensile damage behavior, of which the damage variable is defined as follows:

$$d = \begin{cases} 0 & \varepsilon < \varepsilon_{t0} \\ 1 - \dfrac{f_{tr}}{E_0 \varepsilon} & \varepsilon_{t0} \le \varepsilon < \varepsilon_{tu} \\ 1 & \varepsilon \ge \varepsilon_{tu} \end{cases} \tag{3.37}$$

where f_{tr} is the residual tensile strength, ε_{t0} is the strain corresponding to tensile strength, ε_{tu} is the strain at tensile strength degrades to zero.

As can be seen from Eq. (3.37), two displacement jumps occur at $\varepsilon = \varepsilon_{t0}$ and $\varepsilon = \varepsilon_{tu}$, which may cause some convergence problems in the simulation. In addition, the isotropic damage model has been adopted to represent the gas induced fracturing process in OPA clay under the experimental condition that gas pressure exceeds the minimum principal stress (Fall et al., 2014; Pazdniakou and Dymitrowska, 2018). However, the applied gas pressure is generally lower than the confining pressure and nearly no shear stress is provided for most laboratory gas injection tests on host rocks, see e.g., (Cuss et al., 2012; Harrington et al., 2013, 2017; Hildenbrand et al., 2002). The application of this damage model to other tests seems to be infeasible.

It is noted that the gas induced fracturing occurs highly localized, which might be caused the heterogeneities, initially contained micro-fissures of the rock sample, etc., (Wiseall et al., 2015). Furthermore, the gas dilatant pathways may evolve in a dendritic pattern along the preferential pathways (Cuss et al., 2014; Hildenbrand et al., 2002). However, the mechanical behavior predicted by the previously mentioned damage model is isotropic that cannot represent the actual physical behavior. To realistically capture the gas dilatant pathways, more advanced damage models considering the material heterogeneities, the direction of micro-fissures and fissure density need to be developed.

3.4.3 Discussions on the Pre-Existing Numerical Models

To provide a detailed comparison of different models, we summarize the existing models of simulating gas migration behavior in saturated host rocks in Table 3-2. It is noted that all numerical models adopted the visco-capillary two-phase flow to simulate gas migration through saturated host rock. Different intrinsic permeability models are introduced to couple the fluid flow and mechanical deformation, except anisotropic constant permeability was adopted by Mahjoub et al. (2018). The favorable permeability model is the EFM or enriched EFM as the model can convey more information about the characteristics of fracture sets. The PLM and vG model are commonly used in the relative permeability models, while the CRM or constant value is selected to predict the gas entry value except the model by Fall et al. (2014), where the Leverett relation (Leverett, 1941) was used. Compared with the constant gas entry value, the CRM is more representative of the gas penetration process as gas induced fracture opening can significantly reduce the gas entry value and accelerate the desaturation process.

To implicitly simulate the gas induced fracturing process, plastic and damage models have been incorporated into the HM framework. As analyzed in Section 3.4.2.2, with the increase of gas pressure, tensile failure is more likely to occur if the gas pressure can exceed the macroscopic minimum principal stress. However, this condition is only fulfilled in the gas fracture cycle experiment by Popp et al. (2007). The gas breakthrough in saturated host rocks occurs at the gas pressure significantly lower than the macroscopic minimum principal stress (note: compressive stress is assumed to be positive) (Cuss et al., 2014; Harrington et al., 2017; Hildenbrand et al., 2002), and small mode-I fractures were observed around the injection port area (Cuss et al., 2012). From a viewpoint of local stress state, these mode-I fractures are highly localized that may be caused by the heterogeneously distributed stress state due to contained micro-fissures or heterogeneous structure in the real materials. Except for the model by Mahjoub et al. (2018), the previous plastic or damage models provide an alternative way to implicitly simulate the fracturing process under specific conditions, which may not be applicable in other experimental studies. The model by Mahjoub et al. (2018) defined the damage variable with respect to gas saturation based on the assumption that gas penetration has a direct degradation on the rock stiffness. This phenomenologically proposed model provided an innovative way to interpret gas induced damage, but more theoretical works based on thermodynamics need to be performed to validate the damage evolution law.

Table 3-2 Summary and comparison of existing HM models for gas migration in saturated host rocks

Source	Hydraulic models			Mechanical models		
	$\boldsymbol{k}_{in}$	k_r	p_{gev}	Elastic ($\boldsymbol{\varepsilon}_e$)	Plastic ($\boldsymbol{\varepsilon}_p$)	Damage (d)
Olivella and Alonso (2008)	EFM	PLM	CRM	Isotropic nonlinear	BBM	/
Arnedo et al. (2013)	EFM	PLM	CRM	Anisotropic linear	/	/
Xu et al. (2013)	$\boldsymbol{k}_{in}(p_g)$ or $\boldsymbol{k}_{in}(\varepsilon_v, \bar{\varepsilon}_p)$	vG	Const	Isotropic linear	MCM	/
Fall et al. (2014)	$k_{in}(d, \phi)$	vG	$p_{gev}(k_{in}, \phi)$	Isotropic linear	/	$d(\varepsilon_t, \varepsilon_c)$
Gerard et al. (2014)	EFM	PLM	CRM	Isotropic linear	/	/
Senger et al. (2014, 2018)	$k_{in}(\phi)$	vG	Const	Isotropic nonlinear	/	/
Nguyen and Le (2015)	$\boldsymbol{k}_{in}(\varepsilon_v, \bar{\varepsilon}_p)$	vG	Const	Anisotropic nonlinear $\boldsymbol{E}(t)$	MCM	/
Gonzalez-Blanco et al. (2016)	EFM	PLM	CRM	Isotropic nonlinear	BBM	/
Mahjoub et al. (2018)	Const	vG	Const	Linear	/	$d(S_g)$
Pazdniakou and Dymitrowska (2018)	$k_{in}(\phi)$	/	/	Isotropic linear	/	$d(\varepsilon_t, \varepsilon_c)$
Yang and Fall (2021a)	$\boldsymbol{k}_{in}(\phi)$	PLM	CRM	Anisotropic nonlinear	/	/
Yang et al. (2020)	Enriched EFM	PLM	CRM	Anisotropic nonlinear	/	/

Note: EFM=Embedded fracture model; PLM=Power law model; CRM= Cubic root model; MCM=Mohr-Cohr model; vG=van Genuchten-Mulaem model

3.5 Fracture Propagation Models

Experimental findings (Cuss et al., 2014; Harrington et al., 2017) have demonstrated that the advective movement of gas through saturated claystone is accompanied by the formation of gas pressure induced micro-fractures, which occurs at the applied gas pressure significantly below the minimum principal stress. These preferential gas pathways are formed to be highly localized and may vary temporarily and spatially within the material. To account for the fundamental physics involved in the specific gas migration behavior, it is necessary to represent the development of preferential gas pathways in an explicit way. Thus, the fracture theories and potential numerical methods for explicitly simulating the fracturing process are reviewed and discussed in the following section.

3.5.1 Fracture Theories

3.5.1.1 Subcritical Crack Criterion

Microscopic post-observation of claystone after laboratory gas injection test (Harrington et al., 2017) have demonstrated the gas induced micro-fracturing occurs at a scale from micrometer

to millimeter. The development of preferential gas pathways is closely associated with the nucleation, growth and coalescence of microcracks, which is controlled by the changes in local gas pressure and the HM coupling with rock deformation (Skurtveit et al., 2012). For the type-I microcracks occurring in the short-term loading cycle, the microcracks grow when the stress at the crack tip is sufficient for the stress intensity factor (K_I) reaching the critical value (K_{Ic}). Considering the long-term gas injection process and the characteristics of time-dependent deformation in the claystone, the microcracks may propagate under less than critical conditions at the crack tip such that $K_I < K_{Ic}$ (Atkinson and Meredith, 1987). Several mechanisms have been suggested by Atkinson (1984) for subcritical cracks growth, including stress corrosion, dissolution, diffusion, ion-exchange and microplasticity. With regard to the saturated claystone, the liquid water could be an environment agent that weakens the strained bonds at the crack tips, thus facilitates crack propagation. In this case, the crack growth rate can be described with respect to the applied stress, the stress intensity at the crack tip and environmental factors (Atkinson, 1987):

$$\frac{\partial l}{\partial t} = V_1 (K_I)^{n_d} \tag{3.38}$$

where l is the crack length, K_I is the type-I stress intensity factor, V_1 is the material constant, affected by the environment factors such as temperature, humidity; n_d is the subcritical crack growth index, related to crystallographic orientation, stress corrosive reactions and microstructural properties of the rock material.

The type-I stress intensity factor in Eq. (3.38) can be derived using the energy release rate at the crack tip. Consider a vanishing small contour Γ around the crack tip in a two-dimensional (2D) solid, as seen in Figure 3.10, the energy release rate ($\mathcal{G}$) is equal to the energy flux ($\mathcal{F}$) into the crack tip divided by crack velocity (v), such that $\mathcal{G} = \mathcal{F}/v$ (Anderson, 2005). Since gas migration concerns the coupled HM process, the generalized energy release rate at the crack tip, during its smooth propagation can be represented with respect to Eshelby configurational stress tensor, as follows (Dascalu et al., 2008; Ravi-Chandar, 2004):

$$\mathcal{G} = \lim_{\Gamma \to 0} \int_{\Gamma} e_i b_{ij} n_j ds, \; b_{ij} = \psi_s \delta_{ij} - \sigma'_{ij} u_{i,j} \tag{3.39}$$

where b_{ij} are the components of Eshelby configurational stress tensor, e_i is the unit vector along crack propagation direction, n_i is the outward unit vector normal to the contour, ψ_s is the elastic

strain energy. It should be specified that the kinetic effects are not considered in the formulation (3.39), and so the integral is path-independent (Anderson, 2005).

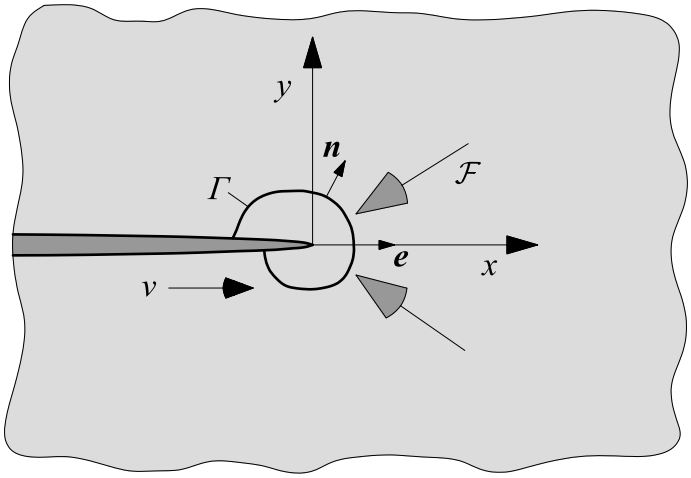

Figure 3.10 Crack tip contour for evaluation of energy release rate (modified from Anderson (2005)), $\mathcal{F}$ is the energy flux into the area bounded by Γ, v is the crack velocity

The above equations (3.38)-(3.39) can be used to obtain the crack propagation law at the microscale. Considering the low stress acting normal to the contained discontinuities in the rock material, extensile fractures are likely to be developed along these pre-existed discontinuities in a preferential manner. It is known from the experimental observations (Cuss et al., 2014; Harrington et al., 2017; Skurtveit et al., 2012) that the interconnection of micro-fractures from the gas inlet to outlet leads to the occurrence of gas breakthrough, because of the highly pressurized gas injection into the saturated claystone, which occurs at applied gas pressure significantly below the minimum principal stress. If we equate the crack propagation with a gas entry event, gas penetrates the saturated claystone when the local tensile stress associated with the capillary pressure exceeds the cohesive strength of the thin water films adsorbed on the surface of clay minerals (Rodwell et al., 1999). The gas-water meniscus in the discontinuities of claystone subjected to high gas pressure is conceptually close in spirit to the notch in mechanical cases, which leads to the stress concentration at the crack tip that can be substantially larger than the applied total stress (Rodwell et al., 1999). By using the subcritical criterion, it is expected that the microcrack may form and propagate under the specific laboratory loading conditions. This mechanism for microcrack propagation has not yet been taken into account in previous numerical models. Considering this mechanism in simulating the gas induced fracturing process will make the model more powerful to represent the gas breakthrough as well as the

corresponding HM behavior.

3.5.1.2 Linear Elastic Fracture Mechanics

The linear elastic fracture mechanics (LEFM) is developed based on the energy criterion in the classical Griffith model, where crack grows from a competition between the released elastic strain energy of material and the surface energy of the fracture (Anderson, 2005). Using either the energy criterion by Irwin (1956) or the stress intensity approach, a critical energy release rate or a critical stress intensity factor exists as the material property that is responsible for the crack propagation. However, the critical value may be not reached at the macroscale in the laboratory condition (Harrington et al., 2013, 2017) where the saturated rock material is loaded under isotropic confinement pressure and applied gas pressure is lower than the confining pressure. Furthermore, the gas induced micro-fracturing is highly localized that presents a dendritic rupture pattern (Cuss et al., 2014; Wiseall et al., 2015), which may not be described by the LEFM. Apart from these physical behaviors in the actual material, the LEFM can lead to stress singularity at the crack tip, which is not suitable to be used in the geomaterials that have finite tensile strength. The stress singularity at crack tip commonly results in numerical instability and mesh sensitivity, which have been extensively discussed in (Murakami, 2012). In order to obviate the convergence issues, a remeshing technique is generally required to refined the mesh around the crack tip (Murakami, 2012), which largely increases the computational cost, especially for the fully coupled HM problems. Because of these presented limitations, the LEFM is not sufficient to describe the gas induced fracturing process in the claystone.

3.5.1.3 Cohesive Zone Model

As a widely referenced approach to analyze the crack growth in the concrete, the cohesive zone model (CZM) by Hillerborg et al. (1976) has been extensively adopted to account for the micro-fracturing process ahead of the crack tip in other materials. Consider a crack by the fluid at pressure p_f, the schematic of CZM along the fracture path and the corresponding traction-separation law are shown in Figure 3.11. The fracture is decomposed into three different zones: totally opened zone, fracture zone and non-damaged zone. In the totally opened zone, the total stress on the crack plane is only due to the fluid and thus is equal to $-p_f \boldsymbol{n}$ (where $\boldsymbol{n}$ is the unit vector normal to the crack plane). In the fracture zone, the boundary condition on the crack plane

is $\boldsymbol{\sigma}\cdot\boldsymbol{n}=\boldsymbol{t}_c^{'}-p_f\boldsymbol{n}$ (i.e., $-p_f<t_{cn}<-p_f+\sigma_t$ where $t_{cn}=\boldsymbol{n}\cdot\boldsymbol{\sigma}\cdot\boldsymbol{n}$ is the traction of total stress normal to the crack plane). When the crack opening is over the critical value δ_c, the total stress is equal to that defined in the totally opened zone. In the non-damaged zone, the two crack lips are in perfect adhesion that no fluid circulation occurs.

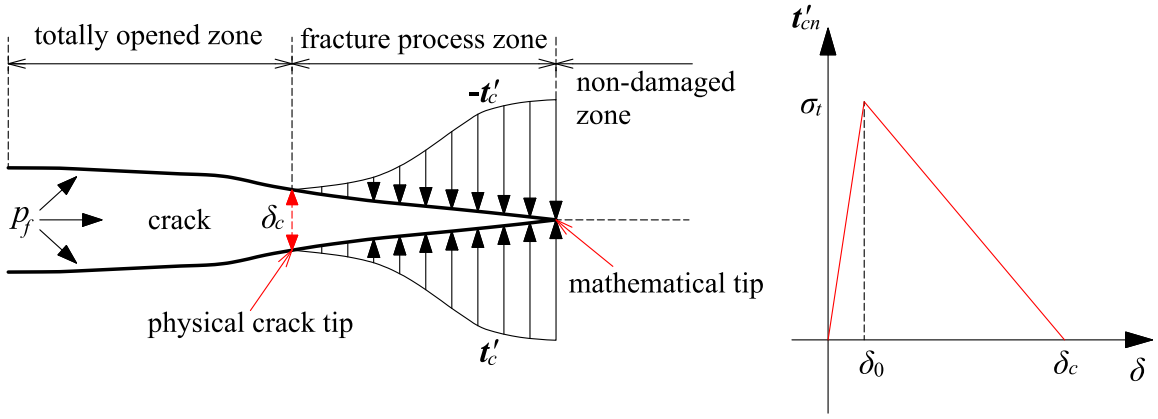

Figure 3.11 Schematic of cohesive zone model under fluid circulation (left) and generalized traction-separation law (right) (modified from Faivre et al. (2016)). Note: $\boldsymbol{t}_c'=\boldsymbol{\sigma}'\cdot\boldsymbol{n}$ is the effective stress traction, δ_0 the separation at failure initiation, δ_c the separation at full failure, σ_t the tensile strength, $t_{cn}'=\boldsymbol{n}\cdot\boldsymbol{\sigma}'\cdot\boldsymbol{n}$ is the effective stress traction normal to crack plane.

Compared with the LEFM, the CZM has introduced a fracture process zone to eliminate the stress singularity at the fracture tip, as seen from Figure 3.11. In this area, the physical crack tip locates the observed macrocrack, while the mathematical tip represents the onset of microcracking. The non-elastic behavior around the fracture tip can be well described by the CZM, thus it seems to be more appropriate to simulate the gas induced fracturing in saturated rocks. Furthermore, the mixed-mode fracture and plastic effects can be also incorporated into the CZM, see Wang (2016). The accuracy and simplicity to capture the moving crack by CZM has led to its widespread use in modelling the hydraulic fracturing in rocks, see e.g., (Faivre et al., 2016; Guo et al., 2017; Nguyen et al., 2017; Wang, 2016), as well as in modelling desiccation cracking in soils (Pouya et al., 2019; Vo et al., 2017). Extending these models to simulate multiphase fluid driven cracking is straightforward, see the work done by (Rethore et al., 2008; Salimzadeh and Khalili, 2015). Through different mathematical treatments on the fractured elements, the CZM can be compatible with various computational methods, such as the finite element method (FEM) with remeshing technique, extended finite element method (XFEM) and discrete element method (DEM). From the above statements, the CZM seems to be a potential method to represent the gas induced fracturing process in saturated claystone, as it covers the main characteristics observed in the laboratory tests, i.e., fluid driven cracking, multiphase flow,

crack interaction, etc. However, considering the fracturing process before fluid pressure reaching the total stress at the macroscale is still a problem since the uniform distribution of total stress in the fractured elements may lead to an elastic response of the material. In addition, the dendritic fracture pattern near the fluid injection inlet may not be represented by the CZM because its fracture paths are predetermined, while these behaviors are controlled by the gas injection rate, fracture aperture and HM coupling with clay fabric in the actual cases. More theoretical works on the designed fracture network and heterogeneous properties of material need to be conducted if the CZM is considered to describe the gas induced fracturing in saturated claystone.

3.5.2 Numerical Methods

The fracture theories described in the Subsection 3.5.1 can be implemented through different numerical methods. In the following part, we focus on the existing and potential approaches that can explicitly represent the development of preferential pathways.

3.5.2.1 Existing Approaches

Since the gas migration in saturated claystone concerns the microcracking process as well as its corresponding macroscopic behaviors, a multiscale approach may appropriately represent the modelling framework. To the best of authors' knowledge, such models with evolving microcracks that are driven by fluid pressure were seldomly reported in previous literatures. Some significant contributions were limited to the mechanical cases, such as the brittle damage model in (Dascalu et al., 2008), the two-scale time-dependent damage models considering subcritical microcracks in (Dascalu et al., 2010; François and Dascalu, 2010; Wrzesniak et al., 2015) and the two-scale thermo-mechanical damage model in (Dascalu and Gbetchi, 2019). In these models, the microcrack tip is assumed to evolve with respect to the middle point of crack and in consequence the microcrack evolution is completely described by its variation of length. Using the assumption of local periodicity condition, the physical process of damage evolution at the macroscale is represented by the microcrack evolving from small length to large length until the cell is fully partitioned by the crack line. As the macroscopic damage law is constructed based on the micro-mechanical energy balance for evolving microcracks, the phenomena of size effect and time effect in fracture are taken into account in the derived damage model. Thus, the microbranching instability is well captured in the damaged zone, as seen from (Atiezo and Dascalu, 2017; Dascalu and Gbetchi, 2019). Although the fluid flow is not included in the two-

scale formulations, it is expected these models can be extended to account for fluid driven cracks by following the classical poromechanics theory in (Coussy, 2004).

Recently, inspired by the derivation work in the thermos-mechanical damage model in (Dascalu and Gbetchi, 2019) and the multiscale framework of HM coupled formulation in (Zhuang et al., 2017), Yang and Fall (2021c) proposed a two-scale time dependent damage model that incorporated gas flow in the asymptotic developments, to explicitly simulate the gas induced micro-fracturing in clayey rock materials. The consideration of subcritical crack at the microscale allows for the reproduction of fracturing process at the applied gas pressure below the minimum principal stress. Other HM behaviors, i.e., gas breakthrough and fracture branching near the gas inlet have been qualitatively observed. However, the two-scale model is limited to the single phase (gas) flow condition. By incorporating water flow in the two-scale formulation, (Yang and Fall, 2021b) developed a two-scale HM damage model to simulate the laboratory gas injection tests conducted on saturated OPA clay and Boom clay. Although the model provided a relative agreement with the experimental results, some important behaviors are still missing, i.e., the gas-water interaction. To account for the water retention curve in the HM framework and to avoid the complexity in formulating the two-scale derivations, a HM damage model was proposed in (Yang and Fall, submitted for publication) to simulate the laboratory and in-situ gas injection experiments. By neglecting the oscillating terms in fluid pressure (Sánchez-Palencia, 1980), the detailed two-scale formulation for fluid flow process was simplified to be a similar form with that in the macroscopic model based on our previous works in (Yang and Fall, 2021b, c). As a consequence the experimentally recorded non-measurable desaturation phenomenon was well reproduced after significant gas flux was observed in the gas outflow boundary.

Although the proposed two-scale time-dependent damage models have shown certain capabilities to reproduce some significant HM behaviors with respect to preferential gas flow in saturated claystone, the models still have some limitations that need to be addressed in the further studies. Since the upscaling from microscale to macroscale is based upon the postulate of incompressible solid grain and porosity, a significant improvement concerns the Biot's poroelasticity theory, which can be included in the asymptotic developments following the method in (Argilaga et al., 2016). In addition, the inertial effects are not taken into account in the damage model that the kinetic energy around the crack tip cannot be represented. Incorporating the kinetic effects into the damage model is anticipated to reproduce the microbranching

behavior in the damaged zone.

3.5.2.2 Potential Approaches

The explicit methods to simulate the hydraulic fracturing and dessication cracking may become the potential approaches to represent gas induced micro-fracturing in saturated claystone, since they convey similar characteristics of fracturing processes. These approaches can be divided into continuum-based, discontinuum-based and hybrid approach according to their specific numerical method.

FEM is a standard continuum-based approach that cannot directly describe the displacement jump of fracture element. A common remedy in FEM is to insert a zero-thickness interface element to predefine the fracture path, and the fracture behavior is generally described by the CZM. This CZM-enriched FEM has been adopted to simulate the fluid driven cracking process in (Nguyen et al., 2017; Segura and Carol, 2010). Compared with the predetermined discontinuity path in interface-enriched FEM, the phase field (PF) method provides a better choice to handle the arbitrary discontinuities in FEM. In the PF, a scalar auxiliary variable is introduced to account for the sharp discontinuities. The nucleation, propagation and branching of cracks are represented by the thermodynamically proposed governing equation (Miehe et al., 2010). Due to its compatibility in combining with conventional coupled HM framework and straightforward manner in describing the fracturing process, the PF has become a popular approach to simulate different failure patterns in rocks, i.e., brittle/quasi-brittle fracture in (Chen et al., 2020; Lee et al., 2016; Wu, 2017; Wu et al., 2020; Yoshioka and Bourdin, 2016), ductile fracture in (Cao et al., 2020; Choo and Sun, 2018; You et al., 2021) and dynamic fracture in (Yang et al., 2021). As another continuous approach to explicitly simulate the fracturing process, the XFEM provided an alternative choice to handle the arbitrary fracture propagation without introducing interface element (Mohammadnejad and Khoei, 2013; Salimzadeh and Khalili, 2015). The sharp displacement is captured by the enriched shape function, thus the remeshing strategy seems to be unnecessary. With the above summary, either the PF or XFEM may be a potential candidate to simulate the arbitrary fracturing process during gas migration within saturated claystone.

Discontinuum-based methods which treat rock mass as separate matrix blocks or particles, are able to describe the fluid driven cracking process at the microscale. Jain and Juanes (2009)

developed a grain-scale mechanistic model for multiphase fluid flow based on the particle flow code (PFC). The simulated results have revealed distinct preferential gas flow modes in the porous medium of different pore radii, where the capillary invasion is likely to occur in coarse-grain sediments, whereas fracturing dominates in fine-grain sediments. This result is consistent with the observed experimental phenomenon that the interconnection of micro-fractures within saturated shale is a prerequisite for gas breakthrough (Skurtveit et al., 2012). It is noted that the fluid interaction in (Jain and Juanes, 2009) is treated in a very simple way. To account for more realistic capillary effects in the saturated claystone, the lattice Boltzmann method (LBM) coupled with the DEM may provide a better solution, as has been done in (Kano et al., 2020; Wang et al., 2020). This coupled LBM-DEM approach may be a potential candidate to investigate the gas migration process in saturated claystone from a grain scale. To consider preferential gas flow mode at the macroscale, the Universal Distinct Element Code (UDEC) coupled with TOUGH may be an appropriate substitute (Lee et al., 2019), as it can include more related behaviors in the model, i.e., fracture propagation, fluid interaction between matrix and fractures.

Due to the characteristics of rock material containing both continuous matrix and discontinuous cracks, the DEM with discrete fracture network (DFN) can be coupled with the FEM to simulate the fracturing process in arbitrary path. However, the implementation is limited to triangular finite elements, which may not properly represent the rock microstructure (Wu et al., 2019). Compared to the FDEM, another hybrid approach, the numerical manifold method (NMM), which combines the FEM and discontinuous deformation analysis (DDA), may better describe the complex rock structure. By incorporating the cohesive elements in the NMM, random polygonal rock micro-grains can be constructed (Wu et al., 2017; Wu et al., 2018). This CZM-enriched NMM has been adopted to tackle the hydraulic fracturing problem (Wu et al., 2019), which may be a potential candidate in the unsaturated cases.

3.6 Conclusions and Recommendations

The review summarizes the current knowledge on modelling of gas migration behavior in saturated rock materials. Specifically, the governing equations, constitutive models, fracture propagation models for simulating the preferential gas flow are summarized. Furthermore, the performances of the pre-existing HM models and the potential approaches are discussed in detail.

Gas flow in saturated host rocks is accompanied by the development of preferential gas

pathways, the number, orientation, width and aperture of which are affected by the local gas pressure, clay fabric deformation and gas-water interaction. The advective gas flow is commonly described by the generalized Darcy's law. The mechanical variable or poroelastic variable has been incorporated into the intrinsic permeability model to simulate the coupled HM process, such as volumetric strain, plastic strain, damage, porosity. The competence of the intrinsic permeability model depends on the contained physical information of rock materials. The EFM or enriched EFM is the most favored one as it conveys more information about the characteristics of fracture sets and accounts for the fracturing mechanism. To describe the gas relative permeability, both the PLM and vG model are commonly used. Compared with the constant gas entry value, the CRM is more representative to consider the effect of gas induced fracture opening on the water retention behavior.

To simulate the mechanical behavior of rock during the gas migration process, linear/nonlinear elastic, elastoplastic and damage models are included in the mechanical processes. The elastoplastic models and elastic-damage models are proposed to simulate the possible shear failure or macroscopic tensile failure under specific conditions, which may not be applicable in most experimental studies. To represent the gas-induced fracturing at the gas pressure significantly lower than the minimum principal stress, a double porosity model seems to provide an alternative choice to tackle the complex fracturing process, and several key experimental behaviors were captured. But the respective physical processes in the dual continuum lead to the production of many model parameters, it is recommended to carefully use the model before finding appropriate physical background for these parameters. In light of these limitations, the enriched EFM seems to be more appropriate, as the introduced parameters are significantly reduced which can also be determined through experimental methods. The capability of enriched EFM is demonstrated by reproducing the coupled HM behaviors in the gas injection tests, e.g., gas flow behavior as well as the anisotropic radial deformation, which might be a good potential to be extended in the field conditions.

Three types of fracture theories are introduced to represent the fracturing process, subcritical crack criterion, linear elastic fracture model (LEFM) and cohesive zone model (CZM). As the gas induced micro-fracturing occurs at gas pressure significantly lower than the macroscopic minimum principal stress, the specific fracture pattern may not be described by the LEFM. To resolve this issue, the subcritical criterion may be more desirable since liquid water

could be an environment agent that weakens the strained bonds at the crack tips, thus facilitates the microcrack propagation. This kind of fracture propagation model has been used to explicitly simulate the gas driven fracturing, but the two-scale formulation leads to the complexity in incorporating the Biot's poroelastic theory. Compared to the other two types of fracture theories, the CZM may be a potential approach, since it has been widely adopted to tackle the hydraulic fracturing problem in rocks. However, considering the non-homogeneous total stress distribution or low stress acting normal to the crack at the initial condition is still an unsolved problem. Currently, the models that can explicitly simulate the gas induced micro-fracturing are relatively few. Some advanced approaches such as PF method, XFEM, DEM, FDEM can be integrated with CZM to provide some promising aspects in simulating the special fracturing process in saturated clayey rocks.

As summarized above, further improvements of the present models may be envisaged to get a deeper understanding of gas migration behavior:

(1) Due to the low stress acting normal to crack plane, the total stress in saturated rocks may present a significantly heterogeneous distribution. Considering the heterogeneity of both stress state and HM properties is expected to improve the model performance in simulating the fracturing process before gas pressure reaches the minimum principal stress.

(2) Shear induced plasticity in compressive stress state is an important factor that contributes to the development of preferential gas pathways, which is necessary to be considered in the fracture models.

(3) Preferential gas flow significantly affects the HM behavior in saturated clayey rocks, and further influences its sealing capacity. Incorporating the self-sealing behavior in the fracture propagation models is necessary to explain the gas migration process when gas pumping is terminated. CZM provides a promising perspective that can include both the fracture propagation law and the fracture sealing behavior in the model, which improves the computational stability. Besides, its strong compatibility with other computational methods, such as PF method, XFEM, DEM, FDEM, yields to desirable numerical tools to simulate the gas induced micro-fracturing in saturated rocks.

3.7 References

Ababou, R., Cañamón, I., Poutrel, A., 2014. Equivalent upscaled hydro-mechanical properties of a damaged and

fractured claystone around a gallery (Meuse/Haute-Marne Underground Research Laboratory). Geological Society Special Publication 400, 339-358.
Aifantis, E.C., 1977. Introducing a multi-porous medium. Dev. Mech 8, 209-211.
Alonso, E.E., Gens, A., Josa, A., 1990. A constitutive model for partially saturated soils. Geotechnique 40, 405-430.
Altmann, S., Tournassat, C., Goutelard, F., Parneix, J.C., Gimmi, T., Maes, N., 2012. Diffusion-driven transport in clayrock formations. Applied Geochemistry 27, 463-478.
Amann-Hildenbrand, A., Krooss, B.M., Harrington, J., Cuss, R., Davy, C., Skoczylas, F., Jacops, E., Maes, N., 2015. Gas Transfer Through Clay Barriers, in: Tournassat, C., Steefel, C.I., Bourg, I.C., Bergaya, F. (Eds.), Developments in Clay Science. Elsevier, pp. 227-267.
Anderson, T.L., 2005. Fracture mechanics: fundamentals and applications, 3rd ed. Taylor & Francis, Boca Raton, FL.
Angeli, M., Soldal, M., Skurtveit, E., Aker, E., 2009. Experimental percolation of supercritical CO2 through a caprock. Energy Procedia 1, 3351-3358.
Argilaga, A., Papachristos, E., Caillerie, D., Dal Pont, S., 2016. Homogenization of a cracked saturated porous medium: Theoretical aspects and numerical implementation. International Journal of Solids and Structures 94-95, 222-237.
Arnedo, D., Alonso, E.E., Olivella, S., 2013. Gas flow in anisotropic claystone: Modelling triaxial experiments. International Journal for Numerical and Analytical Methods in Geomechanics 37, 2239-2256.
Arson, C., Pereira, J.-M., 2013. Influence of damage on pore size distribution and permeability of rocks. International Journal for Numerical and Analytical Methods in Geomechanics 37, 810-831.
Atiezo, M.K., Dascalu, C., 2017. Antiplane two-scale model for dynamic failure. International Journal of Fracture 206, 195-214.
Atkinson, B.K., 1984. Subcritical crack growth in geological materials. Journal of Geophysical Research 89, 4077-4114.
Atkinson, B.K., 1987. Fracture Mechanics of Rock. Academic Press, London, UK.
Atkinson, B.K., Meredith, P.G., 1987. The theory of subcritical crack growth with applications to minerals and rocks. Academic Press, New York.
Bandis, S.C., Lumsden, A.C., Barton, N.R., 1983. Fundamentals of rock joint deformation. International Journal of Rock Mechanics and Mining Sciences & Geomechanics Abstracts 20, 249-268.
Biot, M.A., Willis, D., 1957. The elastic coefficients of the theory of consolidation. Journal of Applied Mechanics 24, 594-601.
Bishop, A.W., 1954. The use of pore-pressure coefficients in practice. Geotechnique 4, 148-152.
Bishop, A.W., 1959. The principle of effective stress. Teknisk ukeblad 39, 859-863.
Brooks, R.H., Corey, A.T., 1964. Hydraulic properties of porous media. Colorado State University, Fort Collins, Colorado.
Bui, T.A., Wong, H., Deleruyelle, F., Xie, L.Z., Tran, D.T., 2017. A thermodynamically consistent model accounting for viscoplastic creep and anisotropic damage in unsaturated rocks. International Journal of Solids and Structures 117, 26-38.
Bui, T.A., Wong, H., Deleruyelle, F., Zhou, A., 2016a. Constitutive modelling of the time-dependent behaviour of partially saturated rocks. Computers and Geotechnics 78, 123-133.
Bui, T.A., Wong, H., Deleruyelle, F., Zhou, A., Lei, X., 2016b. A coupled poroplastic damage model accounting for cracking effects on both hydraulic and mechanical properties of unsaturated media. International Journal for Numerical and Analytical Methods in Geomechanics 40, 625-650.
Cao, Y.J., Shen, W.Q., Shao, J.F., Wang, W., 2020. A novel FFT-based phase field model for damage and cracking behavior of heterogeneous materials. International Journal of Plasticity 133.
Carman, P.C., 1937. Fluid flow through granular beds. Trans. Inst. Chem. Eng. 15, 150-166.
Charlier, R., Collin, F., Pardoen, B., Talandier, J., Radu, J.P.J.P., Gerard, P., 2013. An unsaturated hydro-mechanical modelling of two in-situ experiments in Callovo-Oxfordian argillite. Engineering Geology 165, 46-63.
Chen, B., Sun, Y.N., Barboza, B.R., Barron, A.R., Li, C.F., 2020. Phase-field simulation of hydraulic fracturing with a revised fluid model and hybrid solver. Engineering Fracture Mechanics 229, 16.
Cheng, A.H.D., 1997. Material coefficients of anisotropic poroelasticity. International Journal of Rock Mechanics and Mining Sciences 34, 199-205.
Choo, J., Sun, W., 2018. Coupled phase-field and plasticity modeling of geological materials: From brittle fracture to ductile flow. Computer Methods in Applied Mechanics and Engineering 330, 1-32.
Coussy, O., 2004. Poromechanics. John Wiley & Sons, Chichester, England.
Coussy, O., 2007. Revisiting the constitutive equations of unsaturated porous solids using a Lagrangian saturation concept. International Journal for Numerical and Analytical Methods in Geomechanics 31, 1675-1694.

Coussy, O., Pereira, J.-M., Vaunat, J., 2010. Revisiting the thermodynamics of hardening plasticity for unsaturated soils. Computers and Geotechnics 37, 207-215.
Cuss, R., Harrington, J., Giot, R., Auvray, C., 2014. Experimental observations of mechanical dilation at the onset of gas flow in Callovo-Oxfordian claystone. Geological Society Special Publication 400, 507-519.
Cuss, R.C., Harrington, J.F., Noy, D.J., 2012. Final report of FORGE WP4.1.1: The stress-path permeameter experiment conducted on Callovo-Oxfordian Claystone. British Geological Survey Commissioned Report, CR/12/140.
Dascalu, C., Bilbie, G., Agiasofitou, E.K., 2008. Damage and size effects in elastic solids: A homogenization approach. International Journal of Solids and Structures 45, 409-430.
Dascalu, C., François, B., Keita, O., 2010. A two-scale model for subcritical damage propagation. International Journal of Solids and Structures 47, 493-502.
Dascalu, C., Gbetchi, K., 2019. Dynamic evolution of damage by microcracking with heat dissipation. International Journal of Solids and Structures 174, 128-144.
Dufour, N., Wong, H., Arson, C., Deleruyelle, F., Pereira, J.M., 2012. A thermodynamically consistent framework for saturated viscoplastic rock-materials subject to damage. Mechanics Research Communications 45, 15-21.
Faivre, M., Paul, B., Golfier, F., Giot, R., Massin, P., Colombo, D., 2016. 2D coupled HM-XFEM modeling with cohesive zone model and applications to fluid-driven fracture network. Engineering Fracture Mechanics 159, 115-143.
Fall, M., Nasir, O., Nguyen, T.S., 2014. A coupled hydro-mechanical model for simulation of gas migration in host sedimentary rocks for nuclear waste repositories. Engineering Geology 176, 24-44.
François, B., Dascalu, C., 2010. A two-scale time-dependent damage model based on non-planar growth of micro-cracks. Journal of the Mechanics and Physics of Solids 58, 1928-1946.
Fredlund, D.G., Rahardjo, H., 1993. Soil mechanics for unsaturated soils. John Wiley & Sons, New York.
Gerard, P., Harrington, J., Charlier, R., Collin, F., 2014. Modelling of localised gas preferential pathways in claystone. International Journal of Rock Mechanics and Mining Sciences 67, 104-114.
Gonzalez-Blanco, L., Romero, E., Jommi, C., Li, X., Sillen, X., 2016. Gas migration in a Cenozoic clay: Experimental results and numerical modelling. Geomechanics for Energy and the Environment 6, 81-100.
Guo, J.C., Luo, B., Lu, C., Lai, J., Ren, J.C., 2017. Numerical investigation of hydraulic fracture propagation in a layered reservoir using the cohesive zone method. Engineering Fracture Mechanics 186, 195-207.
Harrington, J.F., Cuss, R.J., Talandier, J., 2017. Gas transport properties through intact and fractured Callovo-Oxfordian mudstones. Geological Society Special Publication 454, 131-154.
Harrington, J.F., Horseman, S.T., 1999. Gas transport properties of clays and mudrocks. Geological Society Special Publication 158, 107-124.
Harrington, J.F., Noy, D.J., Cuss, R.C., 2013. Callovo-Oxfordian Claystone: processes governing advective gas flow. British Geological Survey Commissioned Report, CR/13/088.
Hildenbrand, A., Schlömer, S., Krooss, B.M., 2002. Gas breakthrough experiments on fine-grained sedimentary rocks. Geofluids 2, 3-23.
Hillerborg, A., Modéer, M., Petersson, P.E., 1976. Analysis of crack formation and crack growth in concrete by means of fracture mechanics and finite elements. Cement and Concrete Research 6, 773-781.
Horseman, S.T., Higgo, J.J.W., Alexander, J., Harrington, J.F., 1996. Water, gas and solute movement through argillaceous media. Nuclear Energy Agency, Paris (France).
Horseman, S.T., Volckaert, G., 1996. Disposal of radioactive wastes in argillaceous formations. Engineering Geology Special Publications 11, 179-191.
Irwin, G.R., 1956. Onset of fast crack propagation in high strength steel and aluminum alloys. Naval Research Lab Washington DC.
Jain, A.K., Juanes, R., 2009. Preferential Mode of gas invasion in sediments: Grain-scale mechanistic model of coupled multiphase fluid flow and sediment mechanics. J. Geophys. Res.-Solid Earth 114, 19.
Johnson, L., Marschall, P., Zuidema, P., Gribi, P., 2004. Effects of post-disposal gas generation in a repository for spent fuel, high-level waste and long-lived intermediate level waste sited in opalinus clay. National Cooperative for the Disposal of Radioactive Waste (NAGRA), NTB 04-06.
Kano, Y., Sato, T., Oyama, H., 2020. Numerical study on the formations of gas channels and subsequent bubbles in unconsolidated sandy seabed sediment using a coupled LBM-DEM method. Journal of Natural Gas Science and Engineering 74.
Lee, J., Kim, K.I., Min, K.B., Rutqvist, J., 2019. TOUGH-UDEC: A simulator for coupled multiphase fluid flows, heat transfers and discontinuous deformations in fractured porous media. Computers & Geosciences 126, 120-130.

Lee, S., Wheeler, M.F., Wick, T., 2016. Pressure and fluid-driven fracture propagation in porous media using an adaptive finite element phase field model. Computer Methods in Applied Mechanics and Engineering 305, 111-132.
Leverett, M.C., 1941. Capillary Behavior in Porous Solids. Transactions of the AIME 142, 152-169.
Li, X., Bernier, F., Vietor, T., Lebon, P., 2007. Thermal Impact on the Damaged Zone Around a Radioactive Waste Disposal in Clay Host Rocks. Final Report to EC (Contract Number: FI6W-CT-036449).
Lineham, T., 1989. A laboratory study of gas transport through intact clay samples. UKAEA Harwell Lab.(UK). Chemistry Div.
Lu, G.D., Yang, X.G., Qi, S.C., Li, X.L., Ding, P.P., Zhou, J.W., 2020. A generic framework for overpressure generation in sedimentary sequences under thermal perturbations. Computers and Geotechnics 124, 13.
Mahjoub, M., Rouabhi, A., Tijani, M., Granet, S., M'Jahad, S., Talandier, J., M'Jahad, S., Talandier, J., 2018. Numerical Study of Callovo-Oxfordian Argillite Expansion due to Gas Injection. International Journal of Geomechanics 18.
Marschall, P., Horseman, S., Gimmi, T., 2005. Characterisation of gas transport properties of the Opalinus clay, a potential host rock formation for radioactive waste disposal. Oil and Gas Science and Technology 60, 121-139.
Martinez, M.J., Newell, P., Bishop, J.E., Turner, D.Z., 2013. Coupled multiphase flow and geomechanics model for analysis of joint reactivation during CO2 sequestration operations. International Journal of Greenhouse Gas Control 17, 148-160.
Miehe, C., Welschinger, F., Hofacker, M., 2010. Thermodynamically consistent phase-field models of fracture: Variational principles and multi-field FE implementations. International Journal for Numerical Methods in Engineering 83, 1273-1311.
Mohammadnejad, T., Khoei, A.R., 2013. Hydro-mechanical modeling of cohesive crack propagation in multiphase porous media using the extended finite element method. International Journal for Numerical and Analytical Methods in Geomechanics 37, 1247-1279.
Mualem, Y., 1976. A new model for predicting the hydraulic conductivity of unsaturated porous media. Water Resources Research 12, 513-522.
Mualem, Y., 1978. Hydraulic conductivity of unsaturated porous media: Generalized macroscopic approach. Water Resources Research 14, 325-334.
Murakami, S., 2012. Continuum damage mechanics: a continuum mechanics approach to the analysis of damage and fracture. Springer Netherlands, Dordrecht.
NAGRA, 2008. Effects of post-disposal gas generation in a repository for low- and intermediate-level waste sited in the Opalinus Clay of Northern Switzerland. National Cooperative for the Disposal of Radioactive Waste (NAGRA).
Nasir, O., Fall, M., Evgin, E., 2014. A simulator for modeling of porosity and permeability changes in near field sedimentary host rocks for nuclear waste under climate change influences. Tunnelling and Underground Space Technology 42, 122-135.
Nasir, O., Fall, M., Nguyen, T.S., Evgin, E., 2011. Modelling of the hydro-mechanical response of sedimentary rocks of southern Ontario to past glaciations. Engineering Geology 123, 271-287.
Nguyen, T.S., Le, A.D., 2015. Simultaneous gas and water flow in a damage-susceptible bedded argillaceous rock. Canadian Geotechnical Journal 52, 18-32.
Nguyen, V.P., Lian, H., Rabczuk, T., Bordas, S., 2017. Modelling hydraulic fractures in porous media using flow cohesive interface elements. Engineering Geology 225, 68-82.
Olivella, S., Alonso, E.E., 2008. Gas flow through clay barriers. Géotechnique 58, 157-176.
Ougier-Simonin, A., Renard, F., Boehm, C., Vidal-Gilbert, S., 2016. Microfracturing and microporosity in shales. Earth-Science Reviews 162, 198-226.
Pazdniakou, A., Dymitrowska, M., 2018. Migration of Gas in Water Saturated Clays by Coupled Hydraulic-Mechanical Model. Geofluids 2018, 1-25.
Popp, T., Wiedemann, M., Böhnel, H., Minkley, W., Manthei, G., 2007. Untersuchungen zur Barriereintegrität im Hinblick auf das Ein-Endlager-Konzept. Insitut fur Gebirgsmechanik GmbH, Leipzig, Germany.
Pouya, A., Vo, T.D., Hemmati, S., Tang, A.M., 2019. Modeling soil desiccation cracking by analytical and numerical approaches. International Journal for Numerical and Analytical Methods in Geomechanics 43, 738-763.
Ravi-Chandar, K., 2004. Dynamic fracture. Elsevier, Boston, MA.
Rethore, J., de Borst, R., Abellan, M.A., 2008. A two-scale model for fluid flow in an unsaturated porous medium with cohesive cracks. Computational Mechanics 42, 227-238.
Rodwell, W.R., Harris, A.W., Horseman, S.T., Lalieux, P., Müller, W., Ortiz Amaya, L., Pruess, K., 1999. Gas migration and two-phase flow through engineered and geological barriers for a deep repository for radioactive

waste. Joint EC/NEA Status Report.
Romero, E., Senger, R., Marschall, P., Gómez, R., 2013. Air tests on low-permeability claystone formations. Experimental results and simulations, Springer Series in Geomechanics and Geoengineering, pp. 69-83.
Rozhko, A.Y., 2016. Two-phase fluid-flow modeling in a dilatant crack-like pathway. Journal of Petroleum Science and Engineering 146, 1158-1172.
Rutqvist, J., Tsang, C.F., 2002. A study of caprock hydromechanical changes associated with CO2-injection into a brine formation. Environmental Geology 42, 296-305.
Salimzadeh, S., Khalili, N., 2015. A three-phase XFEM model for hydraulic fracturing with cohesive crack propagation. Computers and Geotechnics 69, 82-92.
Sánchez-Palencia, E., 1980. Non-homogeneous media and vibration theory. Springer, Berlin.
Segura, J.M., Carol, I., 2010. Numerical modelling of pressurized fracture evolution in concrete using zero-thickness interface elements. Engineering Fracture Mechanics 77, 1386-1399.
Senger, R., Romero, E., Ferrari, A., Marschall, P., 2014. Characterization of gas flow through low-permeability claystone: laboratory experiments and two-phase flow analyses. Geological Society Special Publication 400, 531-543.
Senger, R., Romero, E., Marschall, P., 2018. Modeling of Gas Migration Through Low-Permeability Clay Rock Using Information on Pressure and Deformation from Fast Air Injection Tests. Transport in Porous Media 123, 1-17.
Skempton, A.W., 1961. Effective stress in soils, concrete and rocks, pore pressure and suction in soils. Butterworths, 4-16.
Skurtveit, E., Aker, E., Soldal, M., Angeli, M., Wang, Z., 2012. Experimental investigation of CO2 breakthrough and flow mechanisms in shale. Petroleum Geoscience 18, 3-15.
Song, Y., Davy, C.A., Troadec, D., Blanchenet, A.M., Skoczylas, F., Talandier, J., Robinet, J.C., 2015. Multi-scale pore structure of COx claystone: Towards the prediction of fluid transport. Marine and Petroleum Geology 65, 63-82.
Tang, C.A., Tham, L.G., Lee, P.K.K., Yang, T.H., Li, L.C., 2002. Coupled analysis of flow, stress and damage (FSD) in rock failure. International Journal of Rock Mechanics and Mining Sciences 39, 477-489.
Terzaghi, K., 1923. Die Berechnug der Durchlassigkeit des Tones aus dem Verlauf der hydromechanischen Spannungserscheinungen. Sitzungsber. Akad. Wiss.(Wien). Math.-Naturwiss. Kl., Abt. Iia 132, 105-124.
van Genuchten, M.T., 1980. A closed-form equation for predicting the hydraulic conductivity of unsaturated soils. Soil Science Society of America Journal 44, 892-898.
Vo, T.D., Pouya, A., Hemmati, S., Tang, A.M., 2017. Numerical modelling of desiccation cracking of clayey soil using a cohesive fracture method. Computers and Geotechnics 85, 15-27.
Wang, H., 2016. Numerical investigation of fracture spacing and sequencing effects on multiple hydraulic fracture interference and coalescence in brittle and ductile reservoir rocks. Engineering Fracture Mechanics 157, 107-124.
Wang, M., Feng, Y.T., Wang, Y., Qu, T.M., He, W., 2020. A hybrid discrete bubble-lattice Boltzmann-discrete element model for gas-charged sediments. Computational Particle Mechanics 7, 509-522.
Warren, J.E., Root, P.J., 1963. The Behavior of Naturally Fractured Reservoirs. Society of Petroleum Engineers Journal 3, 245-255.
Wilson, R.K., Aifantis, E.C., 1982. On the theory of consolidation with double porosity. International Journal of Engineering Science 20, 1009-1035.
Wiseall, A.C., Cuss, R.J., Graham, C.C., Harrington, J.F., 2015. The visualization of flow paths in experimental studies of clay-rich materials. Mineralogical Magazine 79, 1335-1342.
Witherspoon, P.A., Wang, J.S.Y., Iwai, K., Gale, J.E., 1980. Validity of Cubic Law for fluid flow in a deformable rock fracture. Water Resources Research 16, 1016-1024.
Wrzesniak, A., Dascalu, C., Bésuelle, P., 2015. A two-scale time-dependent model of damage: Influence of micro-cracks friction. European Journal of Mechanics, A/Solids 49, 345-361.
Wu, J.Y., 2017. A unified phase-field theory for the mechanics of damage and quasi-brittle failure. Journal of the Mechanics and Physics of Solids 103, 72-99.
Wu, J.Y., Nguyen, V.P., Zhou, H., Huang, Y.L., 2020. A variationally consistent phase-field anisotropic damage model for fracture. Computer Methods in Applied Mechanics and Engineering 358, 28.
Wu, Z.J., Fan, L.F., Liu, Q.S., Ma, G.W., 2017. Micro-mechanical modeling of the macro-mechanical response and fracture behavior of rock using the numerical manifold method. Engineering Geology 225, 49-60.
Wu, Z.J., Sun, H., Wong, L.N.Y., 2019. A Cohesive Element-Based Numerical Manifold Method for Hydraulic Fracturing Modelling with Voronoi Grains. Rock Mechanics and Rock Engineering 52, 2335-2359.

Wu, Z.J., Xu, X.Y., Liu, Q.S., Yang, Y.T., 2018. A zero-thickness cohesive element-based numerical manifold method for rock mechanical behavior with micro-Voronoi grains. Engineering Analysis with Boundary Elements 96, 94-108.

Xu, W.J., Shao, H., Hesser, J., Wang, W., Schuster, K., Kolditz, O., 2013. Coupled multiphase flow and elasto-plastic modelling of in-situ gas injection experiments in saturated claystone (Mont Terri Rock Laboratory). Engineering Geology 157, 55-68.

Yang, J., Fall, M., 2021a. Coupled hydro-mechanical modelling of dilatancy controlled gas flow and gas induced fracturing in saturated claystone. International Journal of Rock Mechanics and Mining Sciences 138.

Yang, J., Fall, M., 2021b. A two-scale hydro-mechanical-damage model for simulation of preferential gas flow in saturated clayey host rocks for nuclear repository. Computers and Geotechnics 138.

Yang, J., Fall, M., 2021c. A two-scale time dependent damage model for preferential gas flow in clayey rock materials. Mechanics of Materials 158, 103853.

Yang, J., Fall, M., submitted for publication. A coupled hydro-mechanical damage model for simulation of laboratory and in-situ gas injection experiments in saturated claystone.

Yang, J., Fall, M., Guo, G., 2020. A Three-Dimensional Hydro-mechanical Model for Simulation of Dilatancy Controlled Gas Flow in Anisotropic Claystone. Rock Mechanics and Rock Engineering 53, 4091-4116.

Yang, J., Tchelepi, H.A., Kovscek, A.R., 2021. Phase-field modeling of rate-dependent fluid-driven fracture initiation and propagation. International Journal for Numerical and Analytical Methods in Geomechanics 45, 1029-1048.

Yoshioka, K., Bourdin, B., 2016. A variational hydraulic fracturing model coupled to a reservoir simulator. International Journal of Rock Mechanics and Mining Sciences 88, 137-150.

You, T., Waisman, H., Zhu, Q.Z., 2021. Brittle-ductile failure transition in geomaterials modeled by a modified phase-field method with a varying damage-driving energy coefficient. International Journal of Plasticity 136.

Zhuang, X., Wang, Q., Zhu, H., 2017. Multiscale modelling of hydro-mechanical couplings in quasi-brittle materials. International Journal of Fracture 204, 1-27.

Zimmerman, R.W., Hadgu, T., Bodvarsson, G.S., 1996. A new lumped-parameter model for flow in unsaturated dual-porosity media. Advances in Water Resources 19, 317-327.

Chapter 4 Macroscopic HM Modelling of Dilatancy Controlled Gas Flow

4.1 Introduction

Dilatancy controlled gas flow is characterized by the development of gas pressure-induced dilatant pathways, major gas breakthrough and mechanical dilation (increase in sample volume). The aperture of dilatant pathway is a function of the effective stress within the solid matrix. The specific gas transport process occurs at a laboratory condition that the applied gas pressure is significantly lower than the absolute value of the maximum principal stress σ_1 (note: tensile stress is assumed to be positive). To represent the actual physical process of gas migration through saturated claystone, the macroscopic model is developed to capture the experimentally observed phenomena in this chapter. Specifically in Section 4.2, a double porosity model is developed based on the double effective stress concept, in which the volumetric strains of the matrix and fractures are work-conjugated to the respective effective stress level, the volume dilation and gas induced fracturing are well captured in the model. As the 2D axisymmetric model cannot represent the phenomenon of larger fracture opening size close to the gas injection inlet due to the existence of the constant symmetrical axis, also it cannot capture the anisotropic deformation along the radial direction, thus a HM model with three-dimensional (3D) geometry is proposed to capture the anisotropic radial deformation accompanied by the development of gas dilatant pathways in Section 4.3. The simulated results help us get in-depth understanding of the specific gas transport mechanism.

4.2 Paper II: Coupled Hydro-Mechanical Modelling of Dilatancy Controlled Gas Flow and Gas Induced Fracturing in Saturated Claystone

Published in *International Journal of Rock Mechanics and Mining Sciences* 138, 2021, 104584. doi:10.1016/j.ijrmms.2020.104584.

Jianxiong Yang, Mamadou Fall

Department of Civil Engineering, University of Ottawa, Ottawa, ON, Canada

Abstract: Large quantities of gas can be produced during the lifespan of a deep geological repository (DGR) due to several processes that may affect the integrity of the host rock. Therefore, understanding dilatancy controlled gas flow in saturated claystone is important for assessing the safety of a DGR with argillaceous formations as the potential host rocks. In this paper, a coupled hydro-mechanical (HM) model that incorporates double porosity poroelasticity is developed to simulate the gas migration process in saturated claystone. The model accounts for the HM behavior of both the porous medium (which represents the matrix) and the fractured medium (which represents the fractures). Double effective stress principles for each medium are derived from the first law of thermodynamics. The volumetric strains of the matrix and fractures, which are work-conjugated to the respective effective stress level, are explicitly included in the mass balance equations. The developed model is successfully evaluated against three gas injection tests on claystone at the laboratory scale. The main experimental observations, i.e., the development of gas preferential pathways, volume dilation, and gas induced fracturing, are well captured.

Keywords: deep geological repository for nuclear waste; dilatant gas pathway; double porosity; double effective stress; hydro-mechanical processes; gas induced fracturing.

Nomenclature

Latin symbols

a	fracture spacing
a_1, a_2	fitting parameters in mechanical model
A_k, n_k	empirical parameter related to the PSD
b_1, b_2	fitting parameters in hydraulic model
$\boldsymbol{v}_{\kappa s}$	solid velocity in continuum κ in vector format
$\boldsymbol{v}_{\kappa\pi}$	velocity of fluid π in continuum κ in vector format
$\boldsymbol{v}^r_{\kappa\pi}$	relative velocity of fluid π in continuum κ in vector format
$\boldsymbol{v}^D_{\kappa\pi}$	Darcy's velocity of fluid π in continuum κ in vector format
$V_{s(\kappa)}$	solid volume in continuum κ
V_t	total volume of the FPM

$c^{\kappa\pi}$	mass exchange of fluid π in continuum κ
C_s	specific storage coefficient
$\boldsymbol{C}_f$	stiffness tensor of FC in matrix format
D	damage variable
e	fracture aperture
e_T	internal energy
E	Young's modulus
$\boldsymbol{g}$	gravity acceleration in vector format
G	shear modulus of the FPM
G_κ	shear modulus of continuum κ
$\boldsymbol{I}$	identity tensor in matrix format
$k_{r\pi}$	relative permeability of fluid π
$\boldsymbol{k}_f$	intrinsic permeability of FC in matrix format
K	bulk modulus of the FPM
K_s	bulk modulus of solid phase
K_κ	bulk modulus of continuum κ
m	shape parameter in WRC
M	molar mass of gas
p_c	capillary pressure
$\overline{p}_f$	average pore fluid pressure
p_{gev}	gas entry value
$p_p^{'}$	mean pressure in PC
$p_{s(\kappa)}$	intrinsic solid pressure in continuum κ
$p_{\kappa\pi}$	pressure of fluid π in continuum κ
$\boldsymbol{q}$	heat flux in vector format
r	supplied heat
R	ideal gas constant
S_e	effective saturation degree
$S_{\kappa\pi}$	saturation degree of fluid π in continuum κ
T	absolute temperature
$\boldsymbol{u}$	displacement tensor in matrix format
V_κ	volume of pore space in continuum κ
$V_{\kappa\pi}$	volume of fluid π in continuum κ

Greek symbols

α_κ	Biot coefficient of continuum κ
Γ_w	water exchange term between PC and FC
$\varepsilon_{\kappa v}$	volumetric strain of continuum κ
$\boldsymbol{\varepsilon}$	strain tensor of FPM in matrix format
$\boldsymbol{\varepsilon}_\kappa$	strain tensor of continuum κ in matrix format
$\boldsymbol{\varepsilon}_{\kappa\pi}$	strain tensor of fluid π in continuum κ in matrix format
$\boldsymbol{\varepsilon}^I$	isotropic part of strain tensor in matrix format
$\boldsymbol{\varepsilon}^{II}$	deviatoric part of strain tensor in matrix format
μ_π	dynamic viscosity of fluid π
ν	Poisson's ratio
ξ	leakage parameter
ρ	total mass density
$\rho_{\kappa s}$	solid density in continuum κ
$\rho_{\kappa\pi}$	density of fluid π in continuum κ
$\rho^{\kappa s}$	partial mass density of solid in continuum κ
$\rho^{\kappa\pi}$	partial mass density of fluid π in continuum κ
$\boldsymbol{\sigma}$	total stress tensor in matrix format
$\boldsymbol{\sigma}_{(\kappa)}$	local stress tensor in continuum κ in matrix format
$\boldsymbol{\sigma}_\kappa^{(s)}$	partial Cauchy stress tensor in continuum κ in matrix format
$\boldsymbol{\sigma}_\kappa^{'}$	effective stress tensor in continuum κ in matrix format
$\boldsymbol{\sigma}^{\kappa\pi}$	fluid partial Cauchy stress tensor in continuum κ in matrix format
ϕ_{cr}	fitting parameter in hydraulic model
ϕ_t	total porosity of the FPM
ϕ_κ	porosity of continuum κ
$\phi^{\kappa s}$	volume fraction of solid in continuum κ
$\phi^{\kappa\pi}$	volume fraction of fluid π in continuum κ
χ_w	water compressibility

4.2.1 Introduction

Deep geological repositories (DGRs) have been proposed or currently being constructed in several countries, including France, Germany, Switzerland, Canada, and India, as a means of managing the radioactive waste produced by the use of nuclear power. The safe long-term

disposal of nuclear waste in a repository and their isolation from the biosphere are ensured by using a multi-barrier system that consists of a natural barrier (host rocks) and an engineered barrier (Nasir et al., 2013, 2015; Shaw, 2015). The highly consolidated argillaceous formations with low permeability, such as the Callovo-Oxfordian (COx) clay formation in France and the Opalinus (OPA) clay formation in Switzerland, are being investigated as potential host rocks for DGRs (ANDRA, 2012; Johnson et al., 2004; Marschall et al., 2005; NAGRA, 2008). In their initial state, these argillaceous formations are saturated with water (Pazdniakou and Dymitrowska, 2018). However, a large volume of gas can be generated during the lifespan of a DGR due to different processes, such as the corrosion of metal, water radiolysis or microbial degradation, which may affect the integrity of the host rock when the accumulated gas pressure reaches a certain value (Fall et al., 2014; Harrington et al., 2012a; NAGRA, 2008). Therefore, investigating the gas migration process in host rocks is important for assessing the long-term safety of DGRs.

In a clay-based porous medium with low permeability, four kinds of gas migration processes can be found: gas advection-diffusion/dissolution, visco-capillary two-phase flow, dilatancy controlled gas flow, and gas flow controlled by macro-fractures (Harrington et al., 2012a, b; Marschall et al., 2005; NAGRA, 2008). Evidence which shows that gas outflow increases at a rapid but intermittent rate at a certain gas pressure value has been obtained through an increasing number of experimental studies in recent years on gas migration in clay-based porous media (Cuss et al., 2014; Harrington et al., 2012a, 2017). However, the conventional two-phase flow in porous media cannot be used to explain these experimental observations as no significant desaturation occurs in the sample. On the other hand, gas flow controlled by macro-fractures occurs at very high gas production rates, but this is not expected in DGRs since the sourceof gas is insufficient. Besides, gas migration in clays might directly result in a change from a dissolution-diffusion flow to dilatancy controlled flow (Pazdniakou and Dymitrowska, 2018). Thus, a better understanding of dilatancy controlled gas flow is important for explaining the experimental observations in the literature, such as the development of gas preferential pathways, volume dilation, and gas induced fracturing (Cuss et al., 2012, 2014; Harrington et al., 2012a, b, 2013, 2017; Popp et al., 2007).

The mathematical models used to simulate gas migration in saturated claystone are mainly modified two-phase flow models (Senger et al., 2014, 2018), conventional coupled HM models

based on continuum mechanics (Fall et al., 2014; Mahjoub et al., 2018; Nguyen and Le, 2015; Xu et al., 2013), and embedded fracture models (EFMs) (Arnedo et al., 2013; Gerard et al., 2014; Gonzalez-Blanco et al., 2016; Olivella and Alonso, 2008). In terms of the modified two-phase flow models, the mechanical effect on permeability changes is related to the changes in porosity (Senger et al., 2014, 2018). However, the modified two-phase relation may not be adequate enough to describe more complicated phenomena. As for conventional coupled HM models, variables such as damage, plasticity, anisotropy, etc., have been used to capture experimental observations related to dilatancy controlled gas flow (Fall et al., 2014; Mahjoub et al., 2018; Nguyen and Le, 2015; Xu et al., 2013). But the proposed plastic or damage models may be limited to a specific gas fracture cycle test conducted by Popp et al. (2007) as the injected gas pressure exceeds the confining pressure. In contrast, the EFMs offer computational simplicity and flexibility so they have been widely used in coupled HM models to examine the development of dilatant gas pathways (Arnedo et al., 2013; Gerard et al., 2014; Gonzalez-Blanco et al., 2016; Olivella and Alonso, 2008). Actually, the EFM is a strain-based permeability model enriched by the cubic law as the mechanical properties of the embedded fractures are assumed to be the same as those within the sample bulk. Furthermore, the embedded fractures themselves do not occupy the pore space which is not explicitly considered in the governing equations, since the changes in both pores and fractures are integrated into one set of governing equations (Guo and Fall, 2018). As a result, EFMs can only describe the different hydraulic behaviors based on the changes in the permeability of the fractures, and the different mechanical behaviors between the fractures and the matrix may not be well described.

Recently, new numerical methods which include smoothed particle hydrodynamics (SPH), discrete element method (DEM), extended finite element method (XFEM), etc., are used as alternatives for simulating the propagation of fractures in porous media (Pazdniakou and Dymitrowska, 2018; Salimzadeh and Khalili, 2016; Sun et al., 2017). However, most of these methods do not consider the unsaturated condition or are computationally difficult to implement.

In light of the limitations of the pre-existing HM models, a new coupled HM model for gas migration in argillaceous rocks is proposed in this paper. The HM model is constructed based on double porosity poroelasticity, which would include the respective governing equations of the fractures and the matrix. A mechanical constitutive model is developed based on double effective stress, and the gas induced rigidity degradation is adopted in the mechanical behavior of the

fractures, in anticipation of better simulating gas induced fracturing. The model is then evaluated by simulating three gas injection tests in saturated claystone and then compared against the laboratory results. The robustness of the model is demonstrated by its ability to reproduce the main experimental observations, including major gas breakthrough, the development of gas preferential pathways, and volume dilation.

4.2.2 Conceptual Approach and Assumptions

4.2.2.1 Double Porosity Approach

Many researchers have extended Biot's theory of poromechanics to examine fracturing in rock, such as claystone, shale, by using a framework based on the mixture theory for double porosity media (see for example, (Abousleiman and Nguyen, 2005; Aifantis, 1977; Elsworth and Bai, 1992; Nair et al., 2004; Valliappan and Khalili-Naghadeh, 1990)). At the macroscopic level, a fractured porous medium (FPM) is considered to consist of two separate and overlapping porous media: one represents the primary porosity medium, i.e., a porous continuum (PC), while the other one represents the secondary porosity medium, i.e., a fractured continuum (FC), as shown in Figure 4.1. Each porous medium is assumed to have its own poromechanical and physical properties, such as the elastic modulus and Biot's effective stress coefficients. A representative elementary volume (REV) is used to describe the FPM (Bear, 1972). The governing equations are developed against the backdrop that the relation of the effective stress to the effective deformation for each continuum, i.e., the PC and FC, is based on its own constitutive law (Abousleiman and Nguyen, 2005). The total volume V_t, overall bulk modulus K and shear modulus G of the FPM are given as (Abousleiman and Nguyen, 2005; Nair et al., 2004, 2005):

$$V_t = V_{s(p)} + V_p = V_{s(f)} + V_f \tag{4.1}$$

$$\frac{1}{K} = \frac{1}{K_p} + \frac{1}{K_f} \tag{4.2}$$

$$\frac{1}{G} = \frac{1}{G_p} + \frac{1}{G_f} \tag{4.3}$$

where K_p and K_f are the bulk modulus of the PC and the FC respectively; G_p and G_f are the shear modulus of the PC and the FC, respectively.

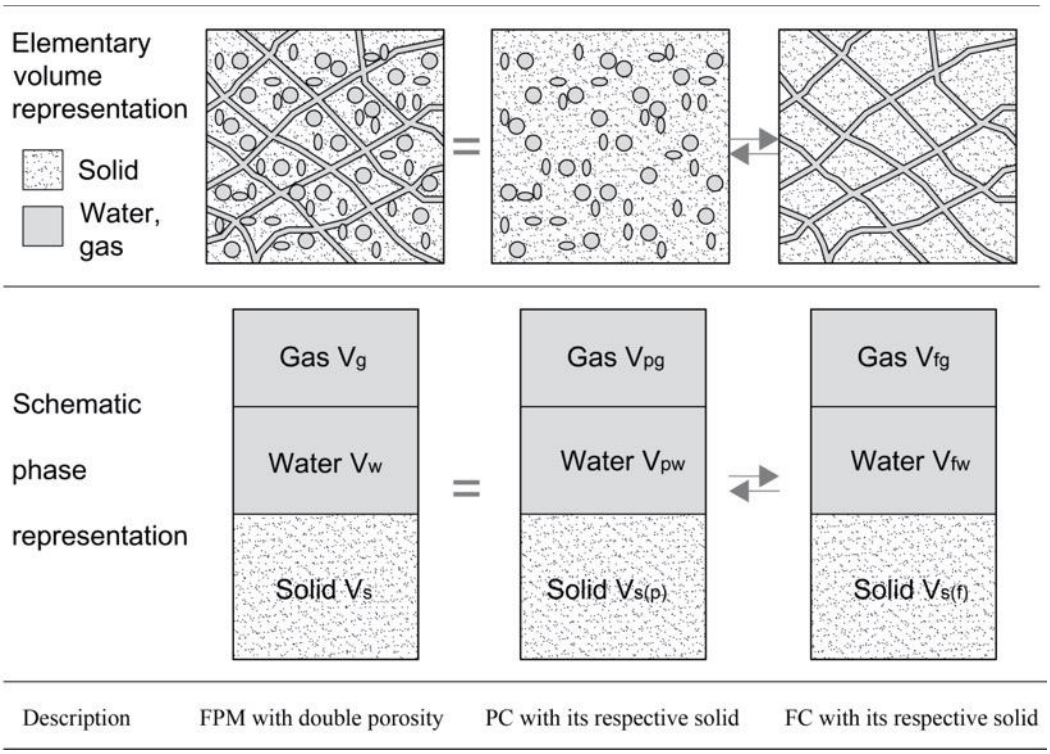

Figure 4.1 Schematic representation of a mixture with double porosity (modified from (Borja and Koliji, 2009; Zhang et al., 2003))

Two different porosity values are assigned to the PC and FC as follows:

$$\phi_p = \frac{V_p}{V_t},\ \phi_f = \frac{V_f}{V_t} \tag{4.4}$$

where ϕ_p and ϕ_f are the porosity of the PC and FC, respectively.

It is widely accepted that fractured rock formations are treated ideally as media with two types of porosity. The primary porosity refers to the pore spaces in the rock matrix inherent to the formation of the rock, while secondary porosity is generated by fractures (Zhang et al., 2003). For partially saturated claystone, the changes in the porosity are influenced by the interaction of the clay with water, the sensitivity of gas induced cracks and the connectivity of pores (Song et al., 2017). The pore size distribution (PSD) of claystone which can be considered as a double porosity distribution consists of natural and fracture porosities. The PSD largely depends on the fracture porosity since the fractures are typically larger than the normal pores in claystone (Arson and Pereira, 2013). As for claystone in an intact (undamaged) state, the PSD could be nearly unimodal, as can be observed in Figure 4.2. When claystone is damaged, the volume component of fractures ϕ_f/ϕ_t increases, and consequently, the amount of micropores ϕ_p/ϕ_t is gradually reduced (Bui et al., 2016), so that the PSD changes from unimodal to bimodal; see Figure 4.2.

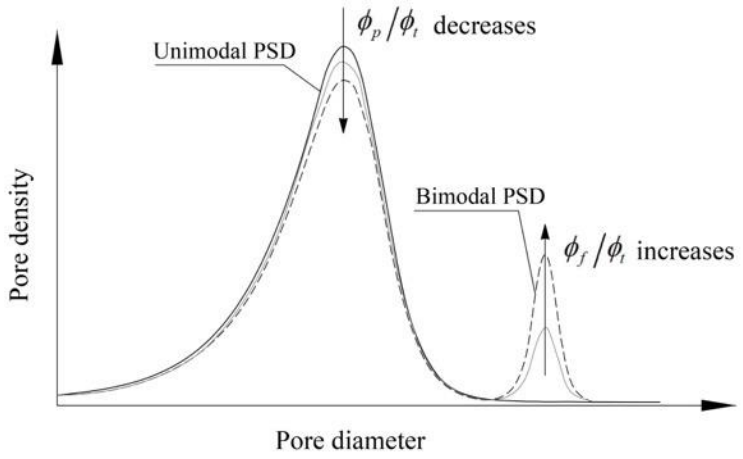

Figure 4.2 Plotted PSD of claystone (modified from (Arson and Pereira, 2013; Bui et al., 2016))

4.2.2.2 Main Assumptions

Prior to deriving the governing equations, a few basic hypotheses with respect to the double porosity model are made as follows:

(i) The rock sample is assumed to be a fractured porous medium (FPM), which consists of two separate but overlapping subcontinua, i.e., a porous continuum (PC) and a fractured continuum (FC).

(ii) The FPM is simplified as a series of squares which is defined as a "matrix" with each side length denoted as a, and the aperture of the orthogonal fractures between the squares is denoted as e, as shown in Figure 4.3. The mechanical properties of the FPM are assumed to be isotropic, and the permeability is anisotropic based on the bedding plane.

(iii) The fluid flow in each subcontinuum is independent, and the interaction between two subcontinua is described by the water exchange and the changes in the porosity between the pores and fractures.

(iv) There is infinitesimal transformation, which implies a small amount of displacement.

(v) Visco-capillary two phase flow takes place in the FC only. Due to the extremely small pores of the clay matrix, full saturation is assumed in the PC during the entire simulation process, so the water flow in the PC is neglected for simplicity. As Figure 4.3 shows, water can flow between the PC and FC depending on the respective pore water pressure.

(vi) As can be seen in Figure 4.3, the original spacing and aperture of the fracture are a and e, respectively, the spacing and aperture after deformation are $a + \Delta a$ and $e + \Delta e$, respectively. The opening/closure of the fractures (represented by $\Delta e - \Delta a$) is based on the interaction

between the dilation of the PC (represented by Δa) and the dilation of the FPM (represented by Δe).

(vii) The PC and FC are subjected to the same total stress, but with different pore fluid pressure, which gives different constitutive relations of the PC and FC, respectively.

(viii) Gas dissolution and water vaporization are neglected, while isothermal conditions are taken into consideration in this paper. Tension is assumed to be positive for stress, while compression is positive for pressure.

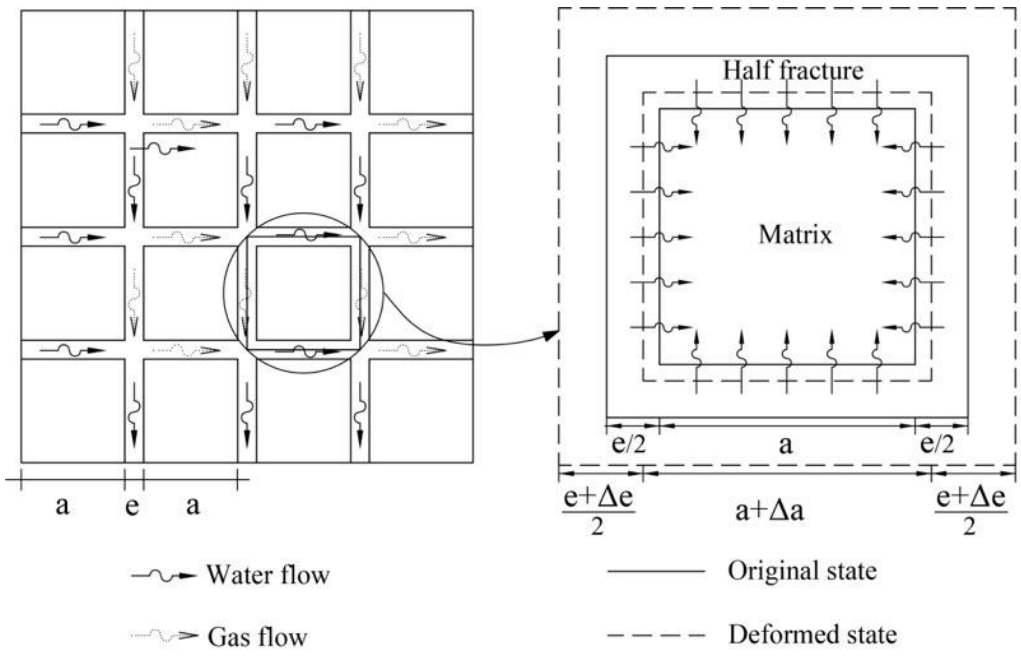

Figure 4.3 Schematic of REV. Notes: a and e are fracture spacings and apertures, Δa and Δe are incremental apertures from dilation of PC and FPM, respectively. (modified from (Guo and Fall, 2018; Wu et al., 2010))

4.2.3 Governing Equations

In the following derivations, it is assumed that REV and double porosity poroelasticity are applicable herein. The porosity of subcontinuum κ, local saturation degree of fluid, volume percentage and partial mass density of each constituent are defined by Eqs. (A.2), (A.3), (A.4) and (A.6) in Appendix A.

Assuming that the mass exchange is limited to fluids, the general mass balance equation for a solid and fluid can be expressed as (Nair et al., 2004, 2005):

$$\frac{\partial \rho^{\kappa s}}{\partial t} + \nabla \cdot (\rho^{\kappa s} \boldsymbol{v}_{\kappa s}) = 0, \ \kappa = f, p \tag{4.5}$$

$$\frac{\partial \rho^{\kappa\pi}}{\partial t} + \nabla \cdot (\rho^{\kappa\pi} \boldsymbol{v}_{\kappa\pi}) - c^{\kappa\pi} = 0,\ \kappa = f, p;\ \pi = w, g \tag{4.6}$$

where the velocity vector of fluid π in the subcontinuum κ $\boldsymbol{v}_{\kappa\pi} = \boldsymbol{v}_{\kappa s} + \boldsymbol{v}^r_{\kappa\pi}$, $\boldsymbol{v}^r_{\kappa\pi}$ is the relative velocity of fluid π with respect to the solid skeleton in the subcontinuum κ, $\boldsymbol{v}_{\kappa s}$ is the respective velocity vector of the solid in the subcontinuum κ, and $c^{\kappa\pi}$ is the mass exchange term of fluid $\pi(\pi = w, g)$ in subcontinuum $\kappa(\kappa = f, p)$ which satisfies the closure condition:

$$\sum_{\kappa = f, p} \sum_{\pi} c^{\kappa\pi} = 0,\ \pi = w, g \tag{4.7}$$

Using Darcy's velocity $\boldsymbol{v}^D_{\kappa\pi} = \phi^{\kappa\pi} \boldsymbol{v}^r_{\kappa\pi}$, and substituting Eqs. (A.4) and (A.6) with Eq. (4.6), the mass balance equation for fluid π can be written as

$$\frac{\partial}{\partial t}(\rho_{\kappa\pi} \phi_\kappa S_{\kappa\pi}) + \nabla \cdot (\rho_{\kappa\pi} \phi_\kappa S_{\kappa\pi} \boldsymbol{v}_{\kappa s}) + \nabla \cdot (\rho_{\kappa\pi} \boldsymbol{v}^D_{\kappa\pi}) - c^{\kappa\pi} = 0 \tag{4.8}$$

4.2.3.1 Mass Balance Equations

Based on the derived mathematical equation, the mass balance equations for the FC and the PC will be obtained respectively as follows.

4.2.3.1.1 Fractured Continuum

The gas balance in the FC can be expressed by using Eq. (4.8):

$$\frac{\partial}{\partial t}(\rho_{fg} \phi_f S_{fg}) + \nabla \cdot (\rho_{fg} \phi_f S_{fg} \boldsymbol{v}_{fs}) + \nabla \cdot (\rho_{fg} \boldsymbol{v}^D_{fg}) = 0 \tag{4.9}$$

where ρ_{fg} and S_{fg} is the density and degree of saturation of the gas in the FC respectively, $\boldsymbol{v}_{fs}$ is the respective solid velocity of the subcontinuum of the FC, which may be related to the overall solid velocity by superimposing the strains from the two subcontinua (Nair et al., 2004), and $\boldsymbol{v}^D_{fg}$ is Darcy's velocity of gas in the FC.

Based on the assumption that there is small deformation (Bear and Bachmat, 1991), the term $\boldsymbol{v}_{fs} \cdot \nabla(\cdot) = 0$ and $\nabla \cdot \boldsymbol{v}_{fs} = \partial \varepsilon_{fv} / \partial t$, Eq. (4.9) can be written as:

$$\rho_{fg} S_{fg} \frac{\partial \phi_f}{\partial t} + \phi_f S_{fg} \frac{\partial \rho_{fg}}{\partial t} + \rho_{fg} \phi_f \frac{\partial S_{fg}}{\partial t} + \rho_{fg} \phi_f S_{fg} \frac{\partial \varepsilon_{fv}}{\partial t} + \nabla \cdot (\rho_{fg} \boldsymbol{v}^D_{fg}) = 0 \tag{4.10}$$

Similarly, the mass balance equation of water in the FC is

$$\rho_{fw} S_{fw} \frac{\partial \phi_f}{\partial t} + \phi_f S_{fw} \frac{\partial \rho_{fw}}{\partial t} + \rho_{fw} \phi_f \frac{\partial S_{fw}}{\partial t} + \rho_{fw} \phi_f S_{fw} \frac{\partial \varepsilon_{fv}}{\partial t} + \nabla \cdot (\rho_{fw} \boldsymbol{v}^D_{fw}) = \Gamma_w \tag{4.11}$$

where ρ_{fw} and S_{fw} are the density and degree of saturation of the water in the fractures

respectively, ε_{fv} and ε_{pv} are the respective volumetric strain of the FC and PC, and Γ_w is a water flow term between the FC and PC.

Following Eq. (A.18) and the equivalent Biot's effective stress parameter provided in Appendix A, the change in the rate of the porosity of FC and PC can be written respectively as:

$$\frac{\partial \phi_f}{\partial t} = (\alpha_f - \phi_f)\frac{\partial \varepsilon_{fv}}{\partial t} \tag{4.12}$$

$$\frac{\partial \phi_p}{\partial t} = (\alpha_p - \phi_p)\frac{\partial \varepsilon_{pv}}{\partial t} \tag{4.13}$$

where ϕ_p is the porosity of the PC, ε_{fv} and ε_{pv} are the volumetric strain of the FC and PC respectively.

The rate of change in water density can be expressed in terms of the water compressibility (χ_w) as follows:

$$\frac{\partial \rho_{\kappa w}}{\partial t} = \rho_{\kappa w}\chi_w \frac{\partial p_{\kappa w}}{\partial t} \tag{4.14}$$

where $p_{\kappa w}$ is the water pressure in the subcontinuum κ, κ represents p and f for the PC and FC, respectively, and χ_w is the water compressibility.

According to the ideal gas law, the rate of change in gas density is

$$\frac{\partial \rho_{fg}}{\partial t} = \frac{M}{RT}\frac{\partial p_{fg}}{\partial t} \tag{4.15}$$

where M is the molar mass of the gas, R is a universal gas constant, and T is the absolute temperature.

In this study, the water retention curve is described by the van Genuchten (vG) model (van Genuchten, 1980), so that if residual degree of saturation in the FC is assumed to be zero and the degree of saturation of water (S_{fw}) is equal to the effective degree of saturation (S_e), then the following relations are obtained:

$$\frac{\partial S_{fg}}{\partial t} = -\frac{\partial S_{fw}}{\partial t} = -\frac{\partial S_e}{\partial t} = C_s \frac{\partial p_c}{\partial t} \tag{4.16}$$

$$C_s = -\frac{\partial S_e}{\partial p_c} = \frac{m}{p_{gev}(1-m)} S_e^{\frac{1}{m}}(1 - S_e^{\frac{1}{m}})^m \tag{4.17}$$

where p_{gev} is the gas entry value; m is a material parameter; p_c is the capillary pressure, such that $p_c = p_{fg} - p_{fw}$; p_{fg} and p_{fw} are the pressure of gas and water in the FC respectively; and C_s

is a specific storage coefficient.

Substituting Eqs. (4.12) and (4.14)-(4.17) into Eqs. (4.10) and (4.11), the final mass balance equation for the gas and water in the FC is written in the following forms respectively:

$$\rho_{fg}\left(\frac{\phi_f S_{fg} M}{\rho_{fg} RT}+\phi_f C_s\right)\frac{\partial p_{fg}}{\partial t}+\nabla\cdot(\rho_{fg}\boldsymbol{v}_{fg}^{D})=\rho_{fg}\phi_f C_s\frac{\partial p_{fw}}{\partial t}-\rho_{fg}S_{fg}\alpha_f\frac{\partial \varepsilon_{fv}}{\partial t} \tag{4.18}$$

$$\rho_{fw}\left(\phi_f S_{fw}\chi_w+\phi_f C_s\right)\frac{\partial p_{fw}}{\partial t}+\nabla\cdot(\rho_{fw}\boldsymbol{v}_{fw}^{D})=\rho_{fw}\phi_f C_s\frac{\partial p_{fg}}{\partial t}-\rho_{fw}S_{fw}\alpha_f\frac{\partial \varepsilon_{fv}}{\partial t}+\Gamma_w \tag{4.19}$$

4.2.3.1.2 Porous Continuum

Due to the extremely small pore size of the PC, Darcy's law for pore water flow is not considered here. The PC remains fully saturated throughout the entire process and water can exchange between the PC and FC depending on the respective pore water pressure. These assumptions are made for computational simplicity, which are also adopted in (Guo and Fall, 2018; Navarro et al., 2015).

Similar to the derivation method in the previous section, the mass balance equation of water in the PC is:

$$\rho_{pw}\frac{\partial \phi_p}{\partial t}+\phi_p\frac{\partial \rho_{pw}}{\partial t}+\rho_{pw}\phi_p\frac{\partial \varepsilon_{pv}}{\partial t}=-\Gamma_w \tag{4.20}$$

Substituting Eqs. (4.13) and (4.14) into Eq. (4.20) gives the final mass balance equation of water as

$$\rho_{pw}\phi_p\chi_w\frac{\partial p_{pw}}{\partial t}=-\rho_{pw}\alpha_p\frac{\partial \varepsilon_{pv}}{\partial t}-\Gamma_w \tag{4.21}$$

where ρ_{pw} and p_{pw} are the density and pressure of water in the PC, respectively.

4.2.3.2 Momentum Balance Equation

When the inertial effects and viscous forces are not taken into consideration, the body loads originate solely from gravity. Then the momentum balance equation for the FPM is

$$\nabla\cdot\dot{\boldsymbol{\sigma}}+\dot{\rho}\boldsymbol{g}=0 \tag{4.22}$$

where $\boldsymbol{\sigma}$ is a total stress tensor, $\boldsymbol{g}$ is the gravity acceleration, and $\rho=(1-\phi_f-\phi_p)\rho_s+(\phi_f S_{fw}+\phi_p)\rho_w+\phi_f S_{fg}\rho_g$, ρ_s is the density of the solid grains.

4.2.4 Constitutive Models

4.2.4.1 Mechanical Processes

The mechanical constitutive model is developed based on double effective stress concept, which has been applied by many researchers (see (Elsworth and Bai, 1992; Guo and Fall, 2018; Nair et al., 2004) for more details). Based on the assumption that there is small deformation and incompressible solid grains, Guo and Fall (2018) derived work-conjugate pairs of stress and strain tensors (double effective stress) based on continuum thermodynamics. As an improvement from their work, the compressibility of the solid grains is taken into account, and the equivalent parameters of the Bishop-like effective stress for the respective media are introduced to the effective stress tensors in the study. Details of the constitutive mechanical models based on the double effective stress concept can be found in Appendix A.

4.2.4.1.1 Porous Continuum

Due to the extremely small pores in the clay matrix, the infiltration of gas is difficult because of the high capillary pressure. The PC is assumed to remain fully saturated during the entire process. Thus, based on Eq. (A.31) in the Appendix, the mechanical behaviour of the PC is governed by

$$\boldsymbol{\sigma}_p^{'} = \boldsymbol{\sigma} + \alpha_p p_{pw} \boldsymbol{I} \tag{4.23}$$

where $\boldsymbol{\sigma}_p'$ is the effective stress of the PC, α_p is the equivalent Biot's coefficient of the PC, and p_{pw} is the pore water pressure in the PC.

Gas injection experiments in samples of clay or clayey rocks showed an important expansion behavior of the samples (Harrington et al., 2012a, b). Sánchez et al. (2005) proposed a simple elastic model to capture the behavior of microstructural swelling and contraction based on the defined microstructural effective stress concept. Though the model only considered the elastic volumetric behavior according to the loading path, it worked very well to reflect the interaction between both pores structures. In this paper, the deformation arising from the PC is assumed to be elastic and volumetric. The increment of the volumetric strain of the PC is defined as a function of mean effective pressure

$$\dot{\varepsilon}_{pv} = \frac{\dot{p}_p^{'}}{K_p} \tag{4.24}$$

where $\dot{\varepsilon}_{pv}$ is the rate of change of the volumetric strain of the PC, $\dot{p}_p^{'}$ is the rate of change of the mean effective pressure, and K_p is the bulk modulus of the PC.

4.2.4.1.2 Fractured Continuum

The FC is assumed to be unsaturated, the effective stress is expressed as:

$$\boldsymbol{\sigma}_f^{'} = \boldsymbol{\sigma} + \alpha_f \bar{p}_f \boldsymbol{I} = \boldsymbol{\sigma} + \alpha_f [S_{fw} p_{fw} + (1 - S_{fw}) p_{fg}] \boldsymbol{I} \tag{4.25}$$

where $\boldsymbol{\sigma}_f'$ is the effective stress of the FC, and $\bar{p}_f$ is the average fluid pressure in fractures.

The development of gas dilatant pathways causes dilation behavior and microcracks can be generated in the process (Cuss et al., 2012; Harrington et al., 2013, 2017), which may result in the deterioration of the material, such as a decrease in strength, rigidity and toughness. To account for these deterioration processes, a mechanical softening variable, D $(0 \le D \le 1)$, is introduced to the mechanical constitutive relation of the FC.

In the damage model found in (Fall et al., 2014), the onset of the mechanical damage is due to the maximum tensile stress or the Mohr-Coulomb criterion in the compressive stress state. Then the damage effect on the intrinsic permeability is considered with different combinations of porosity. This approach appears to be appropriate for describing the mechanical behavior of damaged rock under isotropic pressure by assuming a low gas entry value, of which the damage is almost completely dependent on tensile failure. However, the anisotropic flow behavior and anisotropic mechanical behavior were not taken into consideration. In the joint model developed by Martinez et al. (2013), the effect of joints on the caprock was considered by modifying the bulk material stiffness, which took into account that normal joint stiffness increases with increasing stress. Also, they considered the permeability in the fracture to be anisotropic while that in the matrix was assumed to be isotropic, but these are difficult for implementation in a model which incorporates double effective stress. Mahjoub et al. (2018) assumed in their damage model that the amount of gas in the porous medium has a direct effect on the rigidity of the material. They used the degree of saturation in a damage criterion with an empirical relationship. Although this simplified damage model does not consider thermodynamics, it works very well to describe the onset of microfractures in rock in a gas injection experiment on claystone. In the study, this simplified damage model will be extended to describe the gas induced fracturing behavior of the FC. The saturation degree of gas in the FC, S_{fg}, is introduced to the softening

variable, as follows:

$$\boldsymbol{C}_f = (1-D)\boldsymbol{C}_{f0};\ D(S_{fg}) = a_1[1-10^{-a_2(S_{fg}-S_{fg0})}] \tag{4.26}$$

where $\boldsymbol{C}_f$ is Hooke's elasticity tensor of the damaged FC, $a_1 \in [0,1]$ and $a_2 \geq 0$ are fitting parameters, D is the softening variable.

Following Xu et al. (2013), the mechanical properties of the FC are assumed to be isotropic and homogeneous, while the hydraulic properties of the FC are anisotropic. The changes in permeability due to fracturing are assumed to be isotropic. In reality, it is likely that the HM behavior of the claystone is anisotropic, and the changes in permeability would not only depend on the initial inherent anisotropy, but also on stress re-orientation. However, some simplification is used to reduce the model complexity, more features can be incorporated into the model in the future, such as plasticity or mechanical anisotropy (see e.g., (Arnedo et al., 2013; Nguyen and Le, 2015; Shen et al., 2018; Zhang et al., 2019)).

As the PC is assumed to be volumetrically elastic, the deviatoric strain rate of the FPM is only from the FC, and written as follows:

$$\dot{\boldsymbol{\varepsilon}}_d = \dot{\boldsymbol{\varepsilon}}_{fd} \tag{4.27}$$

where $\dot{\boldsymbol{\varepsilon}}_d$ and $\dot{\boldsymbol{\varepsilon}}_{fd}$ are the deviatoric strain rate of the FPM and the FC, respectively.

Then we have

$$\dot{\boldsymbol{\varepsilon}} = \dot{\boldsymbol{\varepsilon}}_f + \dot{\boldsymbol{\varepsilon}}_p = \dot{\boldsymbol{\varepsilon}}_f + \frac{1}{3}\dot{\varepsilon}_{pv}\boldsymbol{I} \tag{4.28}$$

where $\dot{\boldsymbol{\varepsilon}}$, $\dot{\boldsymbol{\varepsilon}}_f$ and $\dot{\boldsymbol{\varepsilon}}_p$ are the strain rate of the FPM, FC and PC, respectively.

The constitutive relation of the FC can be written as:

$$\dot{\boldsymbol{\sigma}}'_f = C_f : \dot{\boldsymbol{\varepsilon}}_f = (1-D)\boldsymbol{C}_{f0} : \left(\dot{\boldsymbol{\varepsilon}} - 1/3\dot{\varepsilon}_{pv}\boldsymbol{I}\right) \tag{4.29}$$

$$\dot{\boldsymbol{\varepsilon}} = 1/2[\nabla\dot{\boldsymbol{u}} + (\nabla\dot{\boldsymbol{u}})^T] \tag{4.30}$$

$$\boldsymbol{C}_{f0} = \boldsymbol{C}_{f0}(K_f, G_f) \tag{4.31}$$

where K_f and G_f are the bulk and shear moduli of the FC, respectively.

4.2.4.2 Hydraulic Processes

Fluid (water, gas) flow in unsaturated FC is governed by the general Darcy's law, which is written as:

$$\boldsymbol{v}_{f\pi}^{D} = -\frac{k_f k_{r\pi}}{\mu_\pi}(\nabla p_{f\pi} - \rho_\pi \boldsymbol{g}) \tag{4.32}$$

where k_f is the intrinsic permeability of the FC, $k_{r\pi}$ is the relative permeability of fluid π (water, gas), μ_π is the dynamic viscosity, $p_{f\pi}$ is the fluid pressure in the FC, and ρ_π is the fluid density.

4.2.4.2.1 Intrinsic Permeability

As illustrated in Figure 4.3, the rock element can be conceptualized as a hybrid of fractures and matrix blocks and any change in effective stress results in a change in the aperture size of the fractures. A similar conceptual model has been adopted in (Guo and Fall, 2018; Masoudian et al., 2018). Based on the given conceptual model, the intrinsic permeability of the FC can be expressed as:

$$\boldsymbol{k}_f = \boldsymbol{k}_{f0}\left(\frac{\phi_f}{\phi_{f0}}\right)^3\left(\frac{a+\Delta a}{a_0}\right)^2 \tag{4.33}$$

where $\boldsymbol{k}_f$ is the intrinsic permeability of the FC, and the notations with subscript '0' denote their corresponding initial values. The second term of Eq. (4.33), $(\phi_f/\phi_{f0})^3$, is derived from the well-known cubic law (Olivella and Alonso, 2008); more details are referred to (Guo and Fall, 2018).

There are a number of porosity/permeability models that have been developed for fractured porous rock where changes in the pore structure (volume of pores, distribution of pores and cracks) of the medium is related to gas injection (Fall et al., 2014; Nguyen and Le, 2015; Rutqvist and Tsang, 2002). These models adopt an exponential relationship to describe porosity-dependent permeability, which successfully captures the behavior of permeability increase due to gas flow. However, as indicated in (Yang and Aplin, 2010), a slightly more complex equation could better describe the permeability-porosity relationship over a full range of porosity.

Compared to conventional porous media, gas transport through saturated claystone does not cause a measurable desaturation due to the water storage capacity of clayey minerals (Marschall et al., 2005). This phenomenon has been validated in the post-test measurements of desaturation in gas injection tests, thus implying that gas flow is through localized pathway (Cuss et al., 2012, 2014; Harrington et al., 2013, 2017). To better describe the increase in permeability due to gas induced fracturing, the formulation of Eq. (4.33) should reflect the changes in permeability from the initiation to stabilization of fractures. As it is difficult to quantify the fracture spacing term,

an empirical "S" shaped function (Eq. (4.34)) of the changes in porosity is introduced to capture the evolution of the fracture. A similar "S" shaped function has also been adopted in intrinsic permeability models for coal (Chen et al., 2016) and bentonite (Guo and Fall, 2018).

$$f(\phi_f - \phi_{f0}) = \left(\frac{a+\Delta a}{a_0}\right)^2 = b_1\left\{1+\exp\left[b_2\left(1-\frac{\phi_f-\phi_{f0}}{\phi_{cr}}\right)\right]\right\}^{-1} - b_1\left[1+\exp(b_2)\right]^{-1}+1 \tag{4.34}$$

where b_1, b_2 and ϕ_{cr} are fitting parameters.

In order to better understand the transition function above, the assumed parameters are plotted in Figure 4.4. The critical porosity (ϕ_{cr}) is set to 0.01 at which the slope of the function is the steepest and the value of the function is half of the maximum value. b_1 is set to 6 to control the maximum value, while b_2 is set to 5 to control the slope.

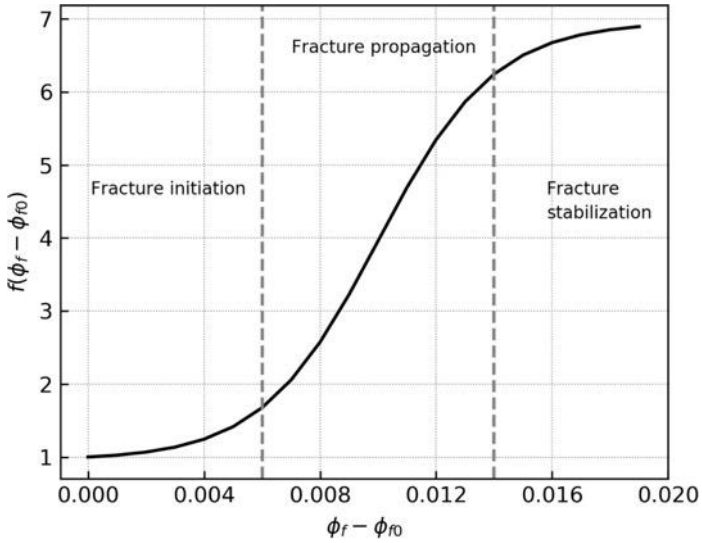

Figure 4.4 Shape of transition function

The physical basis of the proposed "S" shaped function is for interpreting the development of dilatant gas pathways in the gas injection tests. Experimental observations in recent years have proven that there is the formation of microfissures during gas movement through initially saturated claystone (Cuss et al., 2012, 2014; Harrington et al., 2013, 2017). The development of pressure-induced microfissures will cause a rapid increase in permeability, which accelerates the advective movement of gas through the dilatant pathways. A transition function, Eq. (4.34), is proposed to reflect the physical process, in which the transition curve is divided into three stages, i.e., fracture initiation, fracture propagation and fracture stabilization, as can be seen in Figure 4.4.

4.2.4.2.2 Water Retention Curve and Relative Permeability

For the two phase flow processes in the FC, the van Genuchten-Mualem model (Mualem, 1976; van Genuchten, 1980) is applied here to simulate the hydraulic interaction between water and gas. The main parameter in the model is the capillary pressure, written as:

$$p_c = p_{fg} - p_{fw} \tag{4.35}$$

The relationship between the effective water saturation and capillary pressure is expressed as:

$$S_e = \begin{cases} \left[1 + \left(\frac{p_c}{p_{gev}}\right)^{\frac{1}{1-m}}\right]^{-m} & p_c > 0 \\ 1 & p_c \le 0 \end{cases} \tag{4.36}$$

where m is the model parameter, and p_{gev} is the gas entry value.

As the residual degree of saturation in the FC is assumed to be zero, we then have

$$S_e = S_{fw} \tag{4.37}$$

Fracture propagation accompanied with an increase in the porosity of the FC can significantly reduce the gas entry value and accelerate the desaturation process. In this study, the gas entry value of the FC is coupled with intrinsic permeability through the following relation (Arnedo et al., 2013; Olivella and Alonso, 2008):

$$p_{gev} = p_{gev0}(\boldsymbol{k}_{f0}/\boldsymbol{k}_f)^{1/3} \tag{4.38}$$

The relative permeability of the water flow in the FC is given as (Mualem, 1976; van Genuchten, 1980):

$$k_{rw} = \sqrt{S_e}[1-(1-S_e^{1/m})^m]^2 \tag{4.39}$$

The relative permeability of the gas flow in the FC is calculated by adopting a power law, as shown in Eq. (4.40), which is widely used in studies of the research topic at hand (Arnedo et al., 2013; Gerard et al., 2014; Gonzalez-Blanco et al., 2016):

$$k_{rg} = A_k(1-S_e)^{n_k} + \delta \tag{4.40}$$

where δ is a small constant (0.001) to ensure a minimum value of relative permeability, A_k and n_k are fitting parameters.

4.2.4.2.3 Water Exchange Term

According to the conceptual model, after gas infiltrates the rock, water may flow between the FC and PC depending on the respective pore water pressure. Though the Warren-Root type approximation has been adopted to describe the water interaction between matrix and fractures in (Guo and Fall, 2018), the water transfer relation is known to be inaccurate and crude for the long-term scales (Zimmerman et al., 1996). To address the water interaction accompanied by the long-term gas injection process, a more accurate model developed in (Zimmerman et al., 1996) is adopted as follows:

$$\Gamma_w = \xi \rho_{fw} \frac{[(p_{pw} - p_{pw0})^2 - (p_{fw} - p_{fw0})^2]}{2(p_{pw} - p_{pw0})} \tag{4.41}$$

where ξ is a leakage parameter that controls the rate of water flow between the pores and fractures.

4.2.5 Evaluation of the Model

To evaluate the ability of the developed HM model to reproduce experimental observations, the derived governing equations and constitutive equations were first implemented into COMSOL Multiphysics and then validated against three sets of laboratory gas injection tests on claystone. The first experiment involved cyclic testing of gas induced fractures on OPA clay (Popp et al., 2007). The second and the third experiments involved gas injection tests on an intact Callovo-Oxfordian sample (COx-1) (Harrington et al., 2013) and naturally fractured Callovo-Oxfordian sample (COx-4) (Harrington et al., 2017), respectively.

4.2.5.1 Determining Model Parameters

The proposed HM model that incorporates a double porosity concept also has parameters that need to be determined, which is the focus of this section. For clarity, the parameters used in the proposed model can be divided into two categories: basic HM and empirical parameters.

4.2.5.1.1 Basic Hydro-Mechanical Parameters

Basic information on the rock samples used in the gas injection tests, OPA, COx-1 and COx-4, is listed in Table 4-1, and more details can be obtained from (Harrington et al., 2013, 2017; Nguyen and Le, 2015; Popp et al., 2007; Xu et al., 2013). It should be noted that only the length and diameter are available for COx-4 as the sample was sub-sectioned directly after the gas injection test (Harrington et al., 2017), and other information listed in this paper is adopted

from COx-1.

Table 4-1 Basic information of rock samples

Sample	Length, mm	Diameter, mm	Dry density, g/cm^3	Porosity	Degree of Saturation	Source
OPA	150.45	73.59	2.47	0.16	90%	(Nguyen and Le, 2015; Xu et al., 2013)
COx-1	53.9	54.4	2.31	0.146	97%	(Harrington et al., 2013)
COx-4	63.7	54.5	2.31	0.146	97%	(Harrington et al., 2017)

The values of the hydraulic properties of the rock samples are listed in Table 4-2. As mentioned in Harrington et al. (Harrington et al., 2017), COx-4 naturally has fractures, so the permeability value for COx-4 is around one order of a magnitude above that of the intact sample, COx-1. In this work, the adopted values for COx-4, i.e., permeability and shape parameter (m), are those of COx-1. The gas entry value for COx-4 was determined to be 0.8 MPa by using the ideal gas law and the injection pressure response (Harrington et al., 2017).

Table 4-2 Hydraulic properties of rock samples

Sample	Permeability, (m^2)		Gas entry value,	Retention curve	Source
	Parallel, $k_{f0\parallel}$	Perpendicular, $k_{f0\perp}$	p_{gev0}, (MPa)	m	
OPA	3.7×10^{-17}	3.7×10^{-18}	2.5	0.5	(Xu et al., 2013)
COx-1	3.5×10^{-19}	1.4×10^{-20}	1	1/3	(Mahjoub et al., 2018)
COx-4	3.5×10^{-18}	1.4×10^{-19}	0.8	1/3	-

Most of the mechanical parameters in the literature are for single effective stress. It is more challenging to determine the mechanical constants for double porous media. The bulk modulus used for the PC is the same as that based on the single porosity model. However, few studies are available in the literatures that provide the measurements for the individual mechanical parameters of the FC. Cook (1992) and Huang et al. (1995) proposed different methods to determine the fracture poroelastic parameters by measuring fracture spacing and orientation. Jaeger et al. (2007) derived an equation to determine fracture compliance based on the half-length and amount of contact area of the fracture.

Due to variations in the confining pressure, initial stress state or sample preparation method, the rock samples may have different degrees of micro-cracking or macro-cracking (Cuss et al., 2014). However, it is difficult to experimentally measure the individual characteristics of these contained cracks, as it is not the objective of gas injection tests. Therefore, the bulk modulus of the FC is assumed to be 0.9 times that of the PC based on the assumption that the former is softer than the latter. The FC and PC are assumed to have the same solid grain modulus (K_s). The values of the mechanical properties are listed in Table 4-3. The values of COx-4 are the same as those of COx-1.

Table 4-3 Mechanical properties of rock samples (1, Mahjoub et al. (2018); 2, Nguyen and Le (2015); 3, Xu et al. (2013))

Sample	Shear modulus (MPa) $G = E/[2(1+\nu)]$	Bulk modulus of PC (MPa) $K_p = E/[3(1-2\nu)]$	Biot's coefficient of PC, α_p	Bulk modulus of FC (MPa) $K_f = 0.9K_p$	Biot's coefficient of FC, α_f	Source
OPA	984	1812	0.6	1630	0.64	[2, 3]
COx-1	769	1667	0.6	1500	0.64	[1]
COx-4	769	1667	0.6	1500	0.64	-

It is difficult to experimentally measure the porosity of both the PC and FC. According to laboratory tests (mercury porosimetry, nitrogen adsorption/desorption tests) with core samples taken from Benken and Mont Terri in Switzerland, the PSD of OPA clay is classified as: "20% of the porosity consists of micropores (< 1 nm), 50 – 60% of mesopores (1 nm – 25 nm) and 20 – 30% of macropores (> 25 nm)" with respect to the gas accessible porosity (Johnson et al., 2004). A similar percentage of OPA clay macropores (20-30%) has also been reported in (Marschall et al., 2005). The percentage of COx clay macropores in the eastern Paris Basin is measured to be approximately 20-40% (Yven et al., 2007). As we assume that only gas is transported in the FC, and the PC is kept to be fully saturated throughout the entire process, the macropores are therefore regarded as the porosity of the FC. However, the percentage of macropores is a bit different from that of the OPA (20-30%) and COx (20-40%) clay, and this percentage may not maintain the same value due to the variations in experimental measurements. For simplicity, both OPA and COx clays are assumed to have the same percentage of macropores in this work, i.e., approximately 25%. Thus, the initial amount of the porosity of the FC to the total porosity is assumed to be 0.25, for both the OPA and COx clay.

4.2.5.1.2 Empirical Parameters

The empirical parameters for the HM constitutive models are listed in Table 4-4. The values for the different samples vary from each other, which may be caused by several factors.

(1) The heterogeneous distribution of HM properties is an important factor that affects the values of the empirical parameters. It has been experimentally verified in (Cuss et al., 2012, 2014; Harrington et al., 2012a, 2013, 2017; Hildenbrand et al., 2002) that gas flow in claystone is associated with highly localized, time-dependent development of pathways. Within the rock samples of different heterogeneous properties, the developed gas pathways may follow different trajectories. As a result, the introduced empirical parameters, which are used to represent the dynamic, time-dependent process of gas pathways, may also be different for different samples.

(2) The impact of fractures may also affect the value of the empirical parameters. As experimentally validated by Harrington et al. (2017), damage to the sample reduces the gas entry pressure, thus affecting its hydraulic behavior. For intact samples, a high excess gas pressure is required to initiate the opening/closure of dilatant gas pathways. As stated by Cuss et al. (2014), rock samples may have micro-cracking or macro-cracking to different extent due to variations in the confining pressure, initial stress state or sample preparation method. Therefore, these existing cracks within the samples may lead to different values of the empirical parameters.

Table 4-4 Parameters for hydro-mechanical constitutive models

Sample	Softening variable		Intrinsic permeability			Relative permeability		Water exchange term
	a_1	a_2	b_1	b_2	ϕ_{cr}	A_k	n_k	ξ, m*s/kg
OPA	0.8	1.2	29	3	2.0×10^{-3}	1	2	6.5×10^{-13}
COx-1	0.8	2	6	1.8	1.1×10^{-3}	1	3	3×10^{-13}
COx-4	0.8	1	40	8	2.5×10^{-3}	0.5	5	8×10^{-15}

In summary, dilatancy controlled gas flow is a dynamic, localized time-dependent process. More details about the characteristics of this process can be found in (Cuss et al., 2012, 2014; Harrington et al., 2012a, 2013, 2017). At present, both theoretical and experimental methods cannot be easily used to quantitatively evaluate the changes of this process. Therefore, the introduced empirical parameters are determined by fitting the experimental data. To date, it is a widely adopted treatment to simulate gas flow process in host rock, for example, see (Arnedo et al., 2013; Fall et al., 2014; Gerard et al., 2014; Gonzalez-Blanco et al., 2016; Nguyen and Le, 2015; Olivella and Alonso, 2008; Xu et al., 2013) for more details. However, more efforts need to be made in the future to more accurately determine these parameters.

4.2.5.2 Simulation of OPA Test

4.2.5.2.1 Test Description and Boundary Conditions

In the cyclic tests on gas induced fractures in OPA clay, the sample was bonded between two metal plates and sealed with a rubber jacket. A borehole was drilled at the top and bottom of the sample. A hydrostatical load was applied during the testing. Nitrogen was introduced at a controlled pressure through the bottom borehole. The details of the apparatus are schematically shown in Figure 4.5(a). During the testing, the confining pressure was kept constant at 3 MPa, while the gas injection pressure was increased stepwise from 1 MPa to 3.5 MPa. For details on the experimental set up and test description; see (Popp et al., 2007). In the numerical model, an

axisymmetric 2D geometry with labeled boundary number was generated, as shown in Figure 4.5(b). Due to the asymmetry, only half of the sample was modeled. Boundary No. 5 represents the symmetrical axis. Boundary Nos. 3 and 4 represent the borehole conditions, which is set as the roller in the model. The detailed boundary conditions (BCs) for the HM model are listed in Figure 4.5.

The initial gas pressure in the fractures was 0.1 MPa, and initial water pressure in the fractures and pores were set as -1.1 MPa based on the initial gas pressure and the degree of saturation (Nguyen and Le, 2015; Xu et al., 2013). The initial effective stress was determined to be -3.63 MPa. As the gas pressure was applied at $t = 6000$ s, a ramp function was used from 0.1 MPa to 1 MPa to obtain an equilibrium condition from the initial state.

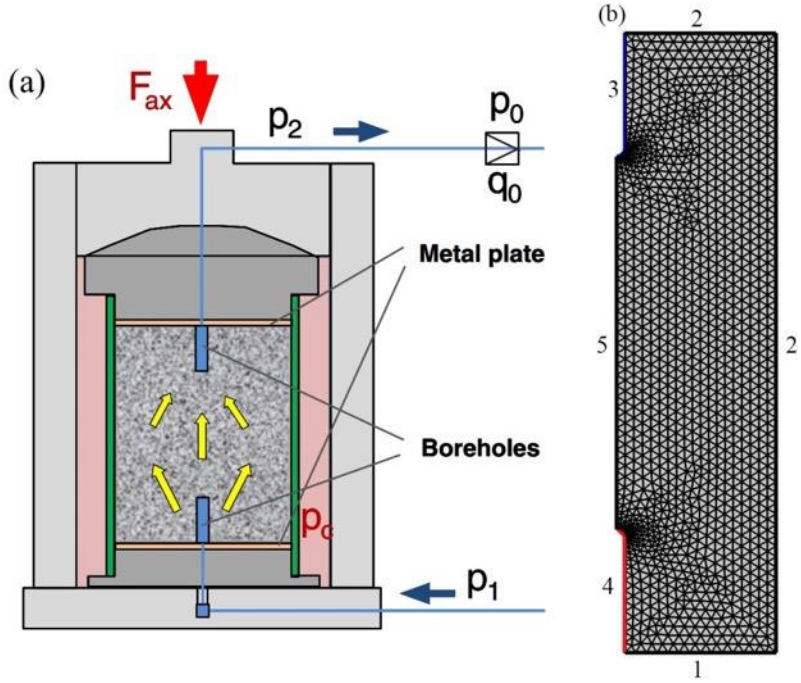

Figure 4.5 (a) Schematic of experimental setup (Popp et al., 2007) and (b) mesh in numerical model

Table 4-5 BCs of HM model of test on OPA

Boundary No.	Hydraulic boundary			Mechanical boundary
	Gas in FC	Water in FC	Water in PC	
1	No flow	No flow	No flow	Roller
2	No flow	No flow	No flow	3 [MPa]
3	0.1 [MPa]	-1.1 [MPa]	No flow	Roller
4	Controlled pressure	No flow	No flow	Roller
5	Axisymmetric			

4.2.5.2.2 Results and Discussion

Figure 4.6 shows the simulated gas outflow rate compared with experimental results, and

Figure 4.7 presents the distribution of gas in the sample with time. In general, the simulated rate of gas flow is in good agreement with the experimental data. However, it can be also found that the model slightly underestimates the flow rate when the gas pressure approaches the gas entry value. This shows that it is difficult to model the dynamic behavior of the gas pathway. Although the gas has already infiltrated the sample when the gas injection pressure is lower than the gas entry value (2.5 MPa), as shown in Figure 4.7(a), no gas outflow can be found, as shown in Figure 4.6, which means that the gas may be trapped in the sample and the continuous gas pathways have not formed yet. After the gas injection pressure exceeds the gas entry value, the gas has already flowed to the outlet borehole of the sample, as shown in Figure 4.7(b). Correspondingly, a continuous flow of gas from the inlet to the outlet can be found after the gas injection pressure exceeds the gas entry value, see Figure 4.6. As stated by Senger et al. (2014), this gas entry value could be representative of the capillary pressure at which a continuous gas pathway is established. When the gas injection pressure exceeds the confining pressure, microcracks and/or macrocracks may form in the sample which leads to a substantial increase in the gas outflow rate, see Figure 4.6. Once the injection pressure decreases to a certain value (1 MPa) that is lower than the gas entry value, the gas pathways appear to be closed immediately, and the gas outflow rate decreases quickly and stabilizes at this low value. Significant amounts of gas may be trapped within the sample, thus causing the non-uniform distribution of the gas pressure (Figure 4.7(d)).

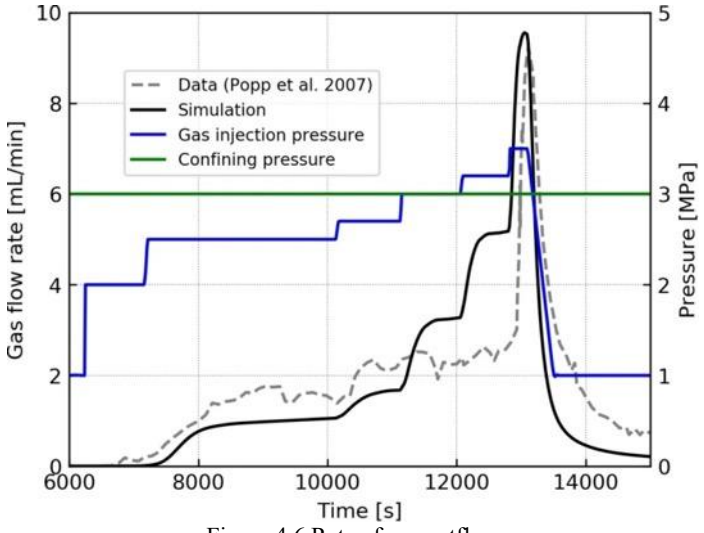

Figure 4.6 Rate of gas outflow

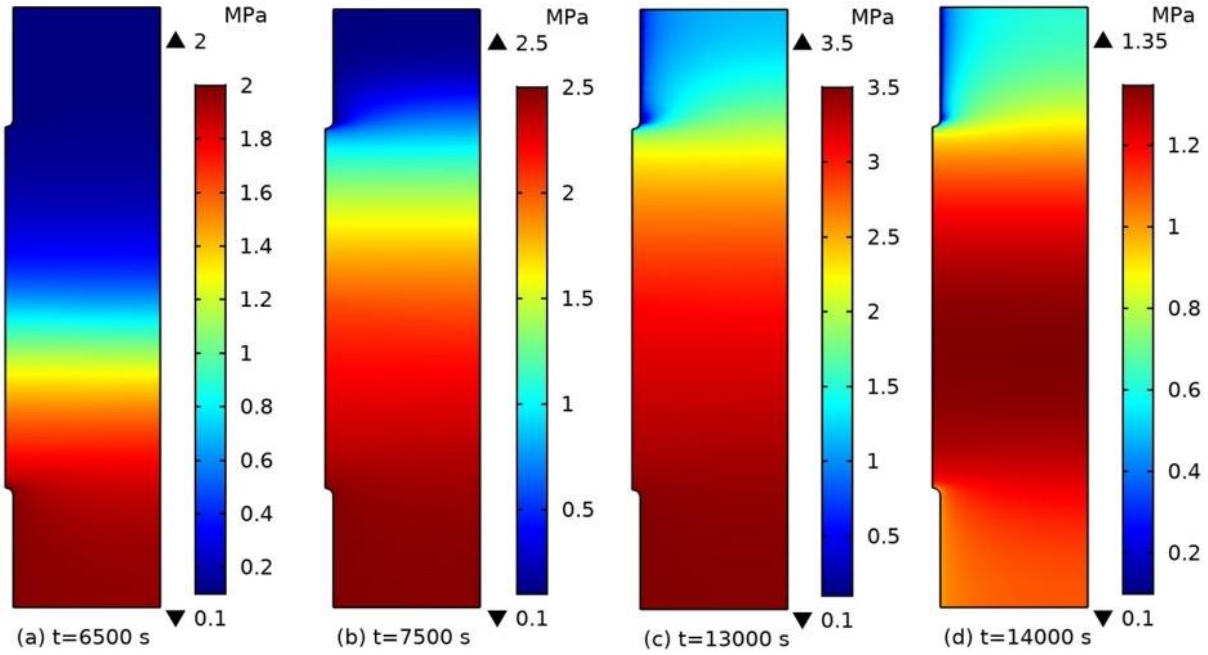

Figure 4.7 Gas distribution in sample with time

Figure 4.8 shows the calculated volumetric strain and the gas entry value at Point A. The volumetric strain of the FC represents fracture opening or fracture closing. According to Eq. (4.28), the total volumetric strain rate is equal to the sum of the volumetric strain rates of the FC and the PC. As the FC is assumed to be softer than the PC and damage takes place as the gas enters the sample, therefore, the stiffness of the FC governs the overall compliance of the FPM, as seen in Eqs. (4.2) and (4.3), thereby influencing the volume expansion due to the dilatancy controlled gas flow. As can be seen in Figure 4.8, the volumetric response of the sample is largely governed by the pore space of the FC. Furthermore, the trend in the change of the volumetric strain of the FC and the total volumetric strain is similar to that of the rate of the gas outflow in Figure 4.6, which increases step by step with increases in the pressure of the gas. This further supports the argument that the gas induced fracturing leads to a substantial increase in gas permeability.

With increases in the gas permeability, the gas entry value decreases based on Eq. (4.38), see Figure 4.8(b), thus accelerating desaturation. The gas flows through the pressure-induced preferential pathways (Harrington et al., 2017) which are governed by the higher gas injection pressure at the inlet borehole, thus allowing the gas to enter from the bottom of the sample. Then, this process is followed by the gas percolation in the top of the sample where the effective pressure is higher and fracture reopening is less likely to occur (Angeli et al., 2009), as can be

seen from the distribution of the gas pressure in Figure 4.7. When the gas injection quickly decreases down to a low pressure at about t=14,000 s, the closure of the developed fractures is accelerated, thus resulting in a lower intrinsic permeability and higher gas entry value (Figure 4.8(b)). Consequently, the gas outflow rate is quickly reduced to a low value, as shown in Figure 4.6.

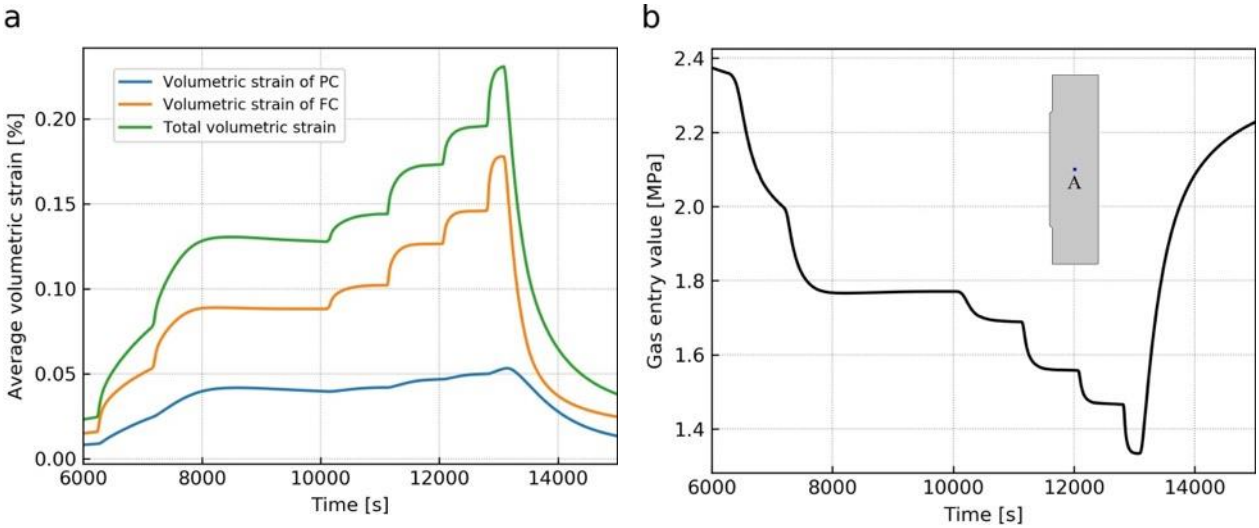

Figure 4.8 (a) Average volumetric strain, (b) Gas entry value at Point A

4.2.5.3 Simulation of COx-1 Test

4.2.5.3.1 Test Description and Boundary Conditions

To conduct the gas injection test on COx-1, helium was used as a safer alternative to hydrogen which was injected into the sample through an injection filter (IF). The water counterpressure was controlled as 4.5 MPa at the backpressure filter (BF), as shown in Fig 10a. A constant confining pressure, i.e., 12.5 MPa, was applied onto the sample. The pressure of the gas injection increased from 6.5 MPa up to 12.5 MPa and then decreased down to 7.5 MPa after several steps.

In the numerical model, the sample, IF and BF, as well as the injection guard-ring (IGR) and the back-pressure guard-ring (BGR) were all taken into account (Figure 4.9). Due to the axisymmetric condition, only half of the sample was modeled, and Boundary No. 6 represents the symmetrical axis. The filters (i.e., the IF, BF, IGR and BGR) were modeled by using an equivalent porous material with high permeability and high porosity. To avoid the convergence problem due to the inconsistent deformation between the filters and the sample, no mechanical conditions were applied to the filters. The detailed boundary conditions of the HM model are

listed in Table 4-6.

The initial water pressure in the fractures and pores was set to 4.5 MPa, which is equal to the pressure in the BF, the initial gas pressure in the fractures was set as 4.5 MPa (Gerard et al., 2014; Mahjoub et al., 2018). The initial effective stress was determined to be -9.62 MPa. To obtain an equilibrium condition from the initial state, a ramp function was provided from 4.5 MPa to 6.5 MPa.

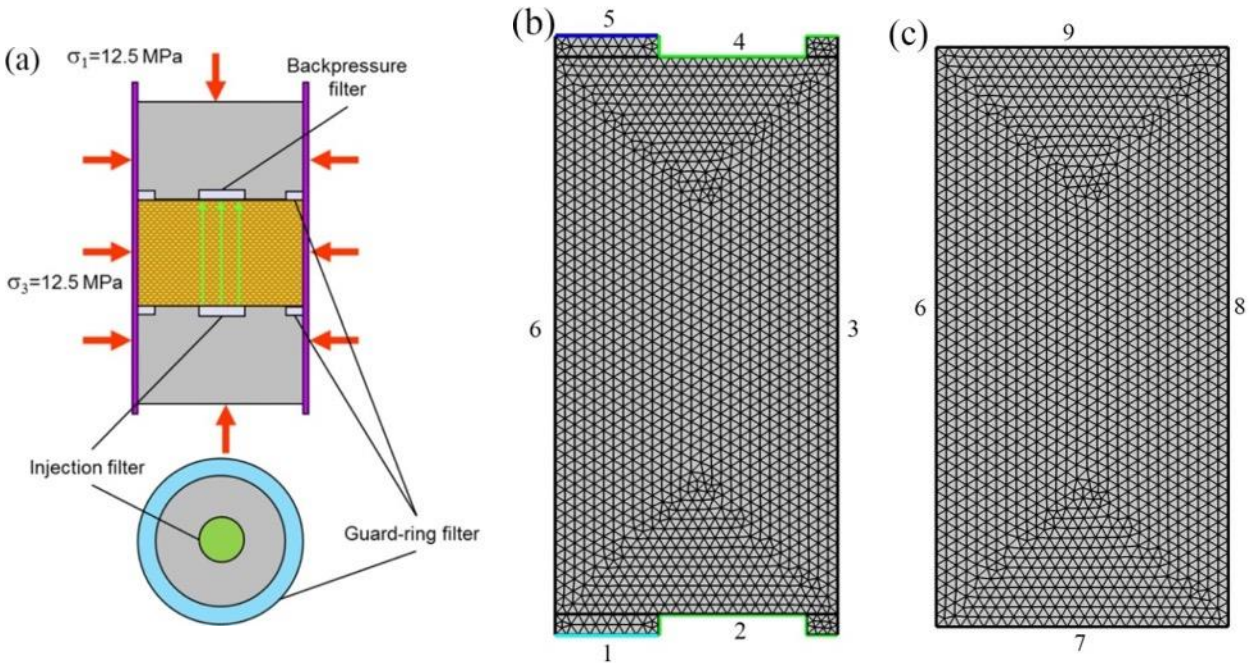

Figure 4.9 Geometry and BCs of the problem: (a) Sketch of laboratory experiment (Harrington et al., 2017), (b) Hydraulic BCs, (c) Mechanical BCs

Table 4-6 BCs of HM model for COx-1 test

Boundary No.	Hydraulic boundary			Mechanical boundary
	Gas in FC	Water in FC	Water in PC	
1	Controlled pressure	No flow	No flow	-
2	No flow	No flow	No flow	-
3	No flow	No flow	No flow	-
4	No flow	No flow	No flow	-
5	4.5 [MPa]	4.5 [MPa]	No flow	-
6	Axisymmetric			
7	-	-	-	Roller
8	-	-	-	12.5 [MPa]
9	-	-	-	12.5 [MPa]

4.2.5.3.2 Results and Discussion

Figure 4.10 is a comparison between the numerically modeled and experimentally obtained gas outflow rate at standard temperature and pressure (STP). In general, the simulated results are in good agreement with the experimental results. It can be also observed that the model

somewhat underestimates the flow rate for low gas injection pressure, and the simulated onset of gas flow is earlier; similar modelling discrepancies have also been reported in (Gerard et al., 2014; Harrington et al., 2013). This highlights the instability of the dynamic behavior of the pathway. The gas outflow rate increases in a stepwise manner that corresponds to the stepwise increase in the gas injection pressure. This shows that gas flow through water saturated claystone is along pressure-induced preferential pathways (Harrington et al., 2017), which are likely to be governed by the increases in gas injection pressure at the inlet of the sample.

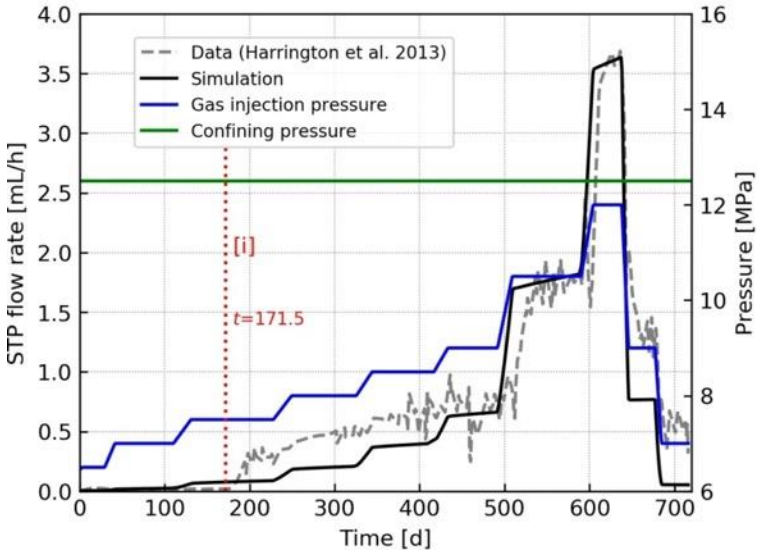

Figure 4.10 Gas outflow rates at STP condition in COx-1 test. Note: [i] represents correlation line and related to onset of major gas breakthrough

Figure 4.11 shows the comparison between the numerically simulated and experimentally obtained results with respect to the IGR and the BGR pressure. The simulated gas pressure for the IGR is modeled well with the experimental data, while the simulated water pressure is closer to the BGR value. Similar results have also been found with the model in (Mahjoub et al., 2018). Although the simulated pore pressure cannot capture the IGR pressure and the BGR by using just one equation, we can still obtain some useful information by analyzing the discrepancies from the following perspectives.

(1) Due to the low gas entry value of COx-1, i.e., 1 MPa, gas enters the sample easily as the excess gas pressure is already 2.5 MPa on the first day of testing. Then the gas injection pressure increases in a stepwise manner, and the major gas breakthrough occurs on day 171.5 and steady state gas flow is formed within the sample. Before the major gas breakthrough occurs, the gas partially reaches the bottom corner of the sample and interacts with the water-saturated IGR. As

gas enters the sink continuously, water is displaced in the sample. The IGR pressure is represented by the pore pressure with increasing saturation of gas, which is slightly lower than the gas pressure; see Figure 4.11(a). After major gas breakthrough occurs, the injection guard is almost fully saturated with gas, and then the IGR pressure is represented by the pore pressure with nearly 100% saturation of gas. Therefore, the plotted IGR pressure changes with the gas injection pressure at the same time.

(2) After major gas breakthrough occurs after 171.5 days, gas propagates through the sample to as far as the BGR, which leads to a sudden increase in the BGR pressure that reaches a peak value of about 5.5 MPa; see Figure 4.11(b). This sudden increase in the BGR pressure implies that there is spontaneous development of new conductive gas pathways. When the steady state gas flow has been achieved, gas moves along the existing pathways at a relative steady state. Then water flows back to the sink until the BGR is saturated with water again. The BGR pressure continues to maintain a value that is almost equal to the backpressure, i.e., 4.5 MPa.

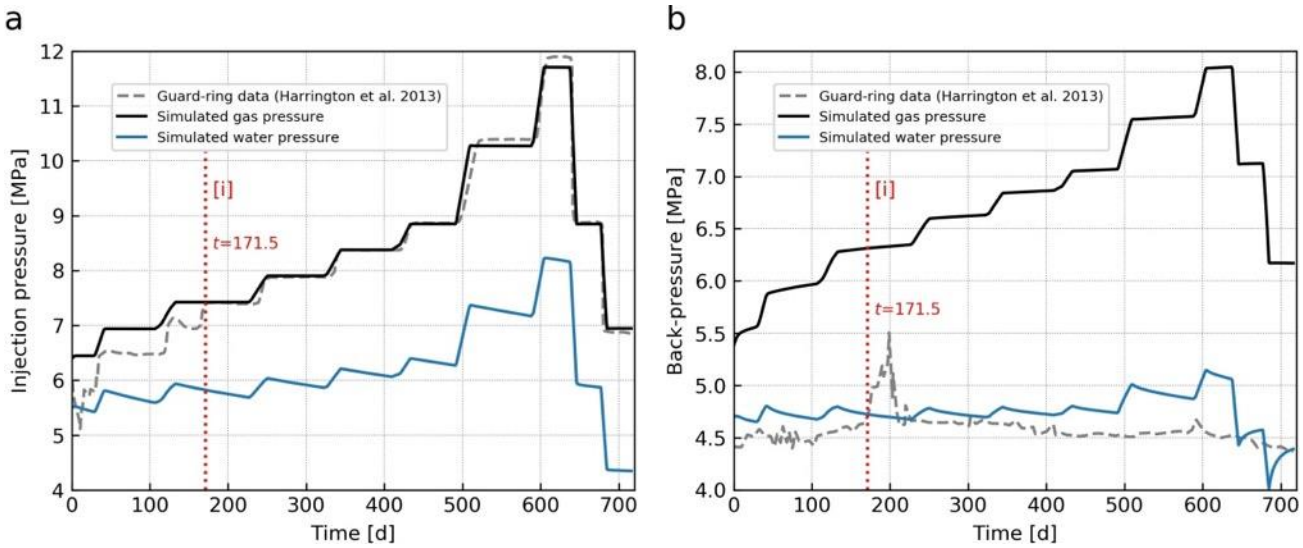

Figure 4.11 (a) Pressure at injection guard-ring, (b) Back guard-ring pressure

Figure 4.12 is a comparison between the numerically modeled and experimentally obtained volumetric strain. It can be observed that there is a satisfactory agreement. A comparison of Figure 4.10 and Figure 4.12 also shows that there is a small but well-defined increase in volume with the flow of gas as experimentally validated in (Cuss et al., 2012; Harrington et al., 2013, 2017). This dilation is not due to the change in volume of the PC, as the total volumetric strain is governed by the volumetric strain of the FC. Furthermore, the trend in the change of the volumetric strain of the FC and the total volumetric strain is very similar to that of the gas

outflow rate in Figure 4.10. This further confirms that the development of fractures leads to a substantial increase in the gas permeability. The simulated result is consistent with the result in (Harrington et al., 2017) who concluded that gas permeability is mainly governed by the presence of fractures in naturally fractured samples.

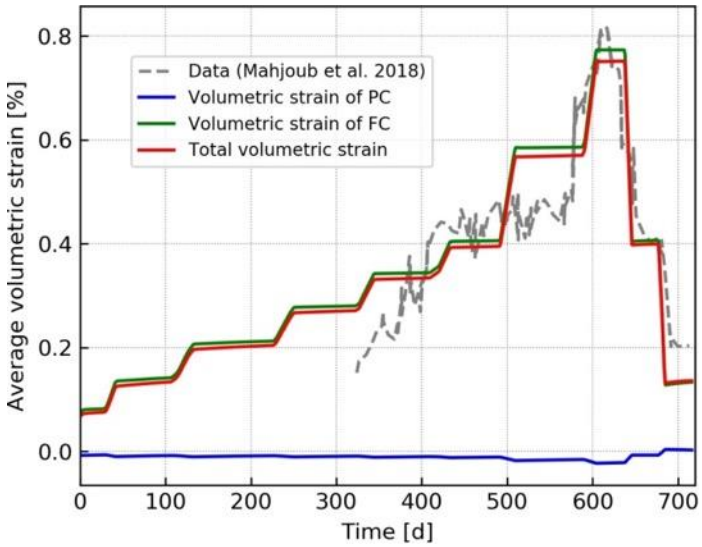

Figure 4.12 Comparison of numerically modeled and experimentally obtained volumetric strain

4.2.5.4 Simulation of COx-4 Test

4.2.5.4.1 Test Description and Boundary Conditions

The testing of COx-4 was conducted under a similar condition as that of COx-1. The experimental set up and the meshed geometry are shown in Figure 4.9. The confined pressure was 12.5 MPa and water pressure was 4.5 MPa in the COx-1 test compared to the 9 MPa confined pressure in COx-4 test, with an applied water pressure in the BF of 1 MPa. The simulation of the gas injection pressure consisted of three pressure ramps from 1 MPa to 7 MPa, and gas was shut-in following the end of the pumping.

The initial water pressure in the fractures and pores was set as 1 MPa, which is equal to the pressure in the BF. The initial gas pressure in the fractures was set as 1 MPa and the initial effective stress was determined to be -8.36 MPa.

4.2.5.4.2 Results and Discussion

Figure 4.13 presents the comparison between the numerically simulated and experimental results with respect to the gas injection pressure and gas outflow rate, respectively. In general,

the simulated results are in good agreement with the experimental findings. Before gas injection is terminated, gas pressure is applied through a ramp function in the model, while the actual gas pressure increases at a constant flow. This constant flow means the applied gas pressure in the vessel may be affected by the mass flow of gas out of the vessel, as gas can flow into the sample depending on the gas entry value and permeability. This is the reason of overestimating the actual gas pressure before gas injection is terminated. The onset of gas breakthrough (at about Day 59.5) is not obvious as the rate of flow is much lower than the peak value.

After reaching the peak value, both the gas pressure and the flow rate show rapid decay and then gradually realize an asymptote value. However, both the simulated values decline more rapidly than found with the experimental results after gas shut in. The following could be some of the reasons for the discrepancies between the numerically modeled and experimentally obtained results: (1) the simulated preferential pathways close more quickly than those in a real situation as the rate of permeability change in reality is slower, and (2) the homogeneous HM properties adopted in the model might not appropriately describe the closure of the developed fractures that may occur in real materials, which further shows that it is difficult to model the unstable dynamic behavior of the pathways.

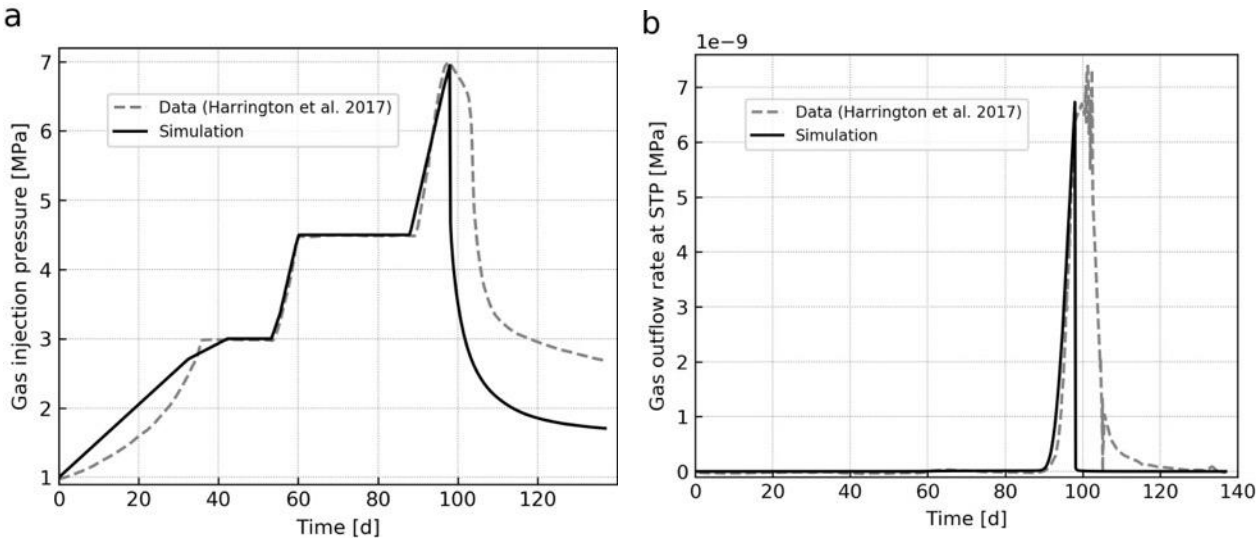

Figure 4.13 (a) Gas injection pressure, (b) Gas outflow rate at STP condition

Figure 4.14 shows the calculated average volumetric strain of the sample. As gas enters the sample, the unloading process leads to sample dilation, and both the volumetric strain of the PC and the FC increase. Furthermore, the total volumetric response of the sample is almost governed by the volumetric strain of the FC. At the third gas injection stage, the volumetric strain of the

FC increases at a more rapid rate than that in the two previous stages, thus leading to a rapid and obvious increase in gas flow rate; see Figure 4.13(b). This phenomenon supports that the dilation of fractures leads to a substantial increase in the gas permeability. This has also been experimentally supported by Harrington et al. (2017), in which the hydraulic behavior is mainly dominated by the fracture properties in the presence of pre-existing fractures. After gas shut-in, a rapid reduction in volumetric strain occurs and compressive strain can even take place due to the rapid reduction in water pressure. With time elapsed, the impact of gas shut-in is reduced and the volumetric strain gradually returns to its original state (or original condition).

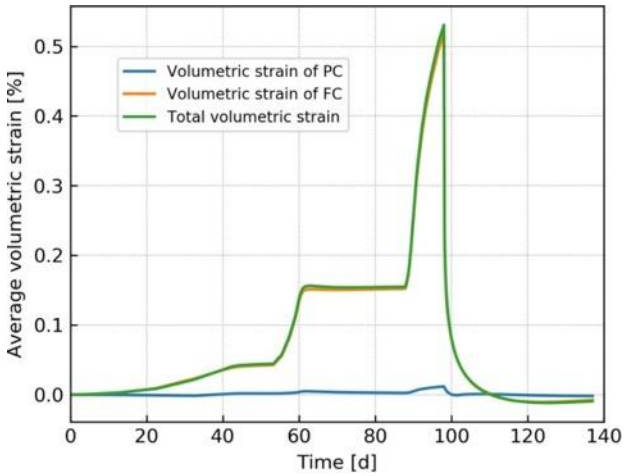

Figure 4.14 Average volumetric strain

Figure 4.15 shows the changes in water pressure in the pores and fractures at Point A after the third period of gas injection. From $t = t_1$ to $t = t_2$ (gas shut-in moment), the water pressure in both the pores and fractures greatly increases as high-pressure gas infiltrates the sample through the developed pathways. Water cannot drain from the matrix immediately because of the small pore size, so some of the load is sustained by the pore water, which leads to the increase in the water pressure. The drainage of water is not sufficient in the fractures to counter the effect of the rapid increase in gas pressure. Therefore, some of the load was transferred to the water, which also leads to an increase in the water pressure in FC. Furthermore, the rate of increase of water pressure in the fractures was larger than that in the pores, which resulted in a higher water pressure in fractures. This pressure difference is the force that drives the flow of water from the fractures to the pores, see Eq. (4.41), thus causing changes in the porosity and dilation of the matrix based on the proposed conceptual model.

From $t = t_2$ to $t = t_3$, the water pressure in the pores and fractures shows a substantial

reduction after gas shut-in. The decline in the rate of water pressure in the fractures is greater than that in the pores, thus leading to a lower water pressure in the fractures. This means that water could flow from the pores to the fractures.

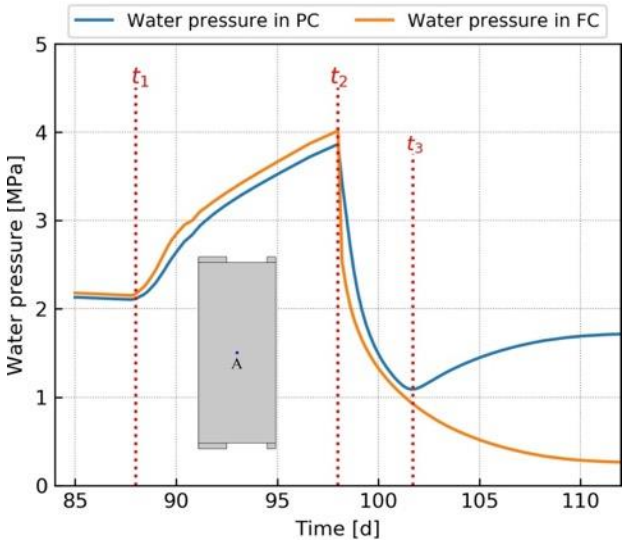

Figure 4.15 Changes in water pressure in pores and fractures at Point A

4.2.6 Conclusions

A coupled HM model that uses an approach of double porosity poroelasticity has been developed to simulate the gas migration process in saturated claystone. The model accounts for the HM behavior of both the porous medium (which is the matrix) and the fractured medium (which represents the fractures). The double effective stress principles for each porous medium are derived from the first law of thermodynamics. This concept can be used to describe the complex HM behavior of rock formation when it is also fractured and/or fissured. The volumetric strains of the matrix and fractures, which are work-conjugated to the respective effective stress level, are explicitly included in the governing equations. By using double porosity and the double effective stress, the PC is assumed to be volumetrically elastic, while the FC is assumed to show elastic damage behavior which considers the decay of the material due to gas induced fracturing. With the proposed conceptual model, the opening/closure of the fractures is caused by the interaction between the dilation of the PC and the dilation of the FPM. The interactions between the PC and FC are coupled by a water exchange term and porosity transformation. An empirical transition function is introduced to describe the rapid increase in permeability due to gas induced fracturing.

The developed model is evaluated against three laboratory experiments, i.e., the cyclic testing of gas induced fractures on OPA clay, and gas injection tests on intact COx-1 and naturally fractured COx-4. In general, the simulated rate of flow is in good agreement with that in all three experimental studies. However, the numerical model either slightly underestimates or overestimates the rate of flow when major gas breakthrough starts, which shows the difficulty of modeling the dynamic behavior of dilatant gas pathways. The volume dilation is well represented by the model in that the total volumetric response is largely governed by the volumetric strain of the fractures, thus governing the corresponding gas flow through the fractures.

In summary, the developed HM model has well captured key experimental observations, i.e., the development of gas preferential pathways, volume dilation, and gas induced fracturing. However, the relationship between the onset of major gas breakthrough and the magnitude of the subsequent flow is challenging to model due to the highly dynamic and unstable gas pathways. Further improvements can be made by introducing a 3D model with a non-symmetrical geometry and heterogeneous HM properties, which is certainly closer to real life cases. Moreover, time-dependent processes such as creeping, fabric alteration, self-healing behavior, etc., can be taken into account to improve the model.

4.2.7 Acknowledgements

The authors gratefully acknowledge funding from a joint program supported by the China Scholarship Council, University of Ottawa and the Natural Sciences and Engineering Research Council of Canada (NSERC). Valuable suggestions from Dr. Guanlong Guo are highly appreciated.

4.2.8 References

Abousleiman, Y., Nguyen, V., 2005. Poromechanics response of inclined wellbore geometry in fractured porous media. Journal of Engineering Mechanics 131, 1170-1183.

Aifantis, E.C., 1977. Introducing a multi-porous medium. Dev. Mech 8, 209-211.

ANDRA, 2012. Référentiel du comportement THM des formations sur le site de Meuse/Haute-Marne, Chatenay-Malabry, France.

Angeli, M., Soldal, M., Skurtveit, E., Aker, E., 2009. Experimental percolation of supercritical CO2 through a caprock. Energy Procedia 1, 3351-3358.

Arnedo, D., Alonso, E.E., Olivella, S., 2013. Gas flow in anisotropic claystone: Modelling triaxial experiments. International Journal for Numerical and Analytical Methods in Geomechanics 37, 2239-2256.

Arson, C., Pereira, J.-M., 2013. Influence of damage on pore size distribution and permeability of rocks. International Journal for Numerical and Analytical Methods in Geomechanics 37, 810-831.

Bear, J., 1972. Dynamics of fluids in porous media. American Elsevier Pub. Co., New York.

Bear, J., Bachmat, Y., 1991. Introduction to Modeling of Transport Phenomena in Porous Media. Springer,

Dordrecht, Netherlands.
Borja, R.I., Koliji, A., 2009. On the effective stress in unsaturated porous continua with double porosity. Journal of the Mechanics and Physics of Solids 57, 1182-1193.
Bui, T.A., Wong, H., Deleruyelle, F., Zhou, A., Lei, X., 2016. A coupled poroplastic damage model accounting for cracking effects on both hydraulic and mechanical properties of unsaturated media. International Journal for Numerical and Analytical Methods in Geomechanics 40, 625-650.
Chen, D., Pan, Z., Shi, J.Q., Si, G., Ye, Z., Zhang, J., 2016. A novel approach for modelling coal permeability during transition from elastic to post-failure state using a modified logistic growth function. International Journal of Coal Geology 163, 132-139.
Cook, N.G.W., 1992. Natural joints in rock: Mechanical, hydraulic and seismic behaviour and properties under normal stress. International Journal of Rock Mechanics and Mining Sciences & Geomechanics Abstracts 29, 198-223.
Cuss, R., Harrington, J., Giot, R., Auvray, C., 2014. Experimental observations of mechanical dilation at the onset of gas flow in Callovo-Oxfordian claystone. Geological Society Special Publication 400, 507-519.
Cuss, R.C., Harrington, J.F., Noy, D.J., 2012. Final report of FORGE WP4.1.1: The stress-path permeameter experiment conducted on Callovo-Oxfordian Claystone. British Geological Survey Commissioned Report, CR/12/140.
Elsworth, D., Bai, M., 1992. Flow-Deformation response of dual-porosity media. Journal of Geotechnical Engineering 118, 107-124.
Fall, M., Nasir, O., Nguyen, T.S., 2014. A coupled hydro-mechanical model for simulation of gas migration in host sedimentary rocks for nuclear waste repositories. Engineering Geology 176, 24-44.
Gerard, P., Harrington, J., Charlier, R., Collin, F., 2014. Modelling of localised gas preferential pathways in claystone. International Journal of Rock Mechanics and Mining Sciences 67, 104-114.
Gonzalez-Blanco, L., Romero, E., Jommi, C., Li, X., Sillen, X., 2016. Gas migration in a Cenozoic clay: Experimental results and numerical modelling. Geomechanics for Energy and the Environment 6, 81-100.
Guo, G., Fall, M., 2018. Modelling of dilatancy-controlled gas flow in saturated bentonite with double porosity and double effective stress concepts. Engineering Geology 243, 253-271.
Harrington, J.F., Cuss, R.J., Talandier, J., 2017. Gas transport properties through intact and fractured Callovo-Oxfordian mudstones. Geological Society Special Publication 454, 131-154.
Harrington, J.F., de la Vaissière, R., Noy, D.J., Cuss, R.J., Talandier, J., 2012a. Gas flow in Callovo-Oxfordian claystone (COx): Results from laboratory and field-scale measurements. Mineralogical Magazine 76, 3303-3318.
Harrington, J.F., Milodowski, A.E., Graham, C.C., Rushton, J.C., Cuss, R.J., 2012b. Evidence for gas-induced pathways in clay using a nanoparticle injection technique. Mineralogical Magazine 76, 3327-3336.
Harrington, J.F., Noy, D.J., Cuss, R.C., 2013. Callovo-Oxfordian Claystone: processes governing advective gas flow. British Geological Survey Commissioned Report, CR/13/088.
Hildenbrand, A., Schlömer, S., Krooss, B.M., 2002. Gas breakthrough experiments on fine-grained sedimentary rocks. Geofluids 2, 3-23.
Huang, T.H., Chang, C.S., Yang, Z.Y., 1995. Elastic moduli for fractured rock mass. Rock Mechanics and Rock Engineering 28, 135-144.
Jaeger, J.C., Cook, N.G.W., Zimmerman, R., 2007. Fundamentals of rock mechanics, 4th ed. Blackwell Pub, Malden, MA.
Johnson, L., Marschall, P., Zuidema, P., Gribi, P., 2004. Effects of post-disposal gas generation in a repository for spent fuel, high-level waste and long-lived intermediate level waste sited in opalinus clay. National Cooperative for the Disposal of Radioactive Waste (NAGRA), NTB 04-06.
Mahjoub, M., Rouabhi, A., Tijani, M., Granet, S., M'Jahad, S., Talandier, J., M'Jahad, S., Talandier, J., 2018. Numerical Study of Callovo-Oxfordian Argillite Expansion due to Gas Injection. International Journal of Geomechanics 18.
Marschall, P., Horseman, S., Gimmi, T., 2005. Characterisation of gas transport properties of the Opalinus clay, a potential host rock formation for radioactive waste disposal. Oil and Gas Science and Technology 60, 121-139.
Martinez, M.J., Newell, P., Bishop, J.E., Turner, D.Z., 2013. Coupled multiphase flow and geomechanics model for analysis of joint reactivation during CO2 sequestration operations. International Journal of Greenhouse Gas Control 17, 148-160.
Masoudian, M.S., Hashemi, M.A., Tasalloti, A., Marshall, A.M., 2018. Elastic-Brittle-Plastic Behaviour of Shale Reservoirs and Its Implications on Fracture Permeability Variation: An Analytical Approach. Rock Mechanics and Rock Engineering 51, 1565-1582.

Mualem, Y., 1976. A new model for predicting the hydraulic conductivity of unsaturated porous media. Water Resources Research 12, 513-522.
NAGRA, 2008. Effects of post-disposal gas generation in a repository for low- and intermediate-level waste sited in the Opalinus Clay of Northern Switzerland. National Cooperative for the Disposal of Radioactive Waste (NAGRA).
Nair, R., Abousleiman, Y., Zaman, M., 2004. A finite element porothermoelastic model for dual-porosity media. International Journal for Numerical and Analytical Methods in Geomechanics 28, 875-898.
Nair, R., Abousleiman, Y., Zaman, M., 2005. Modeling fully coupled oil-gas flow in a dual-porosity medium. International Journal of Geomechanics 5, 326-338.
Nasir, O., Fall, M., Nguyen, S.T., Evgin, E., 2013. Modeling of the thermo-hydro-mechanical-chemical response of sedimentary rocks to past glaciations. International Journal of Rock Mechanics and Mining Sciences 64, 160-174.
Nasir, O., Fall, M., Nguyen, T.S., Evgin, E., 2015. Modeling of the thermohydromechanical-chemical response of Ontario sedimentary rocks to future glaciations. Canadian Geotechnical Journal 52, 836-850.
Navarro, V., Asensio, L., De la Morena, G., Pintado, X., Yustres, Á., 2015. Differentiated intra-and inter-aggregate water content models of mx-80 bentonite. Applied Clay Science 118, 325-336.
Nguyen, T.S., Le, A.D., 2015. Simultaneous gas and water flow in a damage-susceptible bedded argillaceous rock. Canadian Geotechnical Journal 52, 18-32.
Olivella, S., Alonso, E.E., 2008. Gas flow through clay barriers. Géotechnique 58, 157-176.
Pazdniakou, A., Dymitrowska, M., 2018. Migration of Gas in Water Saturated Clays by Coupled Hydraulic-Mechanical Model. Geofluids 2018, 1-25.
Popp, T., Wiedemann, M., Böhnel, H., Minkley, W., Manthei, G., 2007. Untersuchungen zur Barriereintegrität im Hinblick auf das Ein-Endlager-Konzept. Insitut fur Gebirgsmechanik GmbH, Leipzig, Germany.
Rutqvist, J., Tsang, C.F., 2002. A study of caprock hydromechanical changes associated with CO2-injection into a brine formation. Environmental Geology 42, 296-305.
Salimzadeh, S., Khalili, N., 2016. Fully Coupled XFEM Model for Flow and Deformation in Fractured Porous Media with Explicit Fracture Flow. International Journal of Geomechanics 16, 04015091-04015091.
Sánchez, M., Gens, A., do Nascimento Guimarães, L., Olivella, S., 2005. A double structure generalized plasticity model for expansive materials. International Journal for Numerical and Analytical Methods in Geomechanics 29, 751-787.
Senger, R., Romero, E., Ferrari, A., Marschall, P., 2014. Characterization of gas flow through low-permeability claystone: laboratory experiments and two-phase flow analyses. Geological Society Special Publication 400, 531-543.
Senger, R., Romero, E., Marschall, P., 2018. Modeling of Gas Migration Through Low-Permeability Clay Rock Using Information on Pressure and Deformation from Fast Air Injection Tests. Transport in Porous Media 123, 1-17.
Shaw, R.P., 2015. The Fate of Repository Gases (FORGE) project. Geological Society Special Publication 415, 1-7.
Shen, W.L., Bai, J.B., Li, W.F., Wang, X.Y., 2018. Prediction of relative displacement for entry roof with weak plane under the effect of mining abutment stress. Tunnelling and Underground Space Technology 71, 309-317.
Song, Y., Davy, C.A., Bertier, P., Skoczylas, F., Talandier, J., 2017. On the porosity of COx claystone by gas injection. Microporous and Mesoporous Materials 239, 272-286.
Sun, Z.-x., Zhang, X., Xu, Y., Yao, J., Wang, H.-x., Lv, S., Sun, Z.-l., Huang, Y., Cai, M.-y., Huang, X., 2017. Numerical simulation of the heat extraction in EGS with thermal-hydraulic-mechanical coupling method based on discrete fractures model. Energy 120, 20-33.
Valliappan, S., Khalili - Naghadeh, N., 1990. Flow through fissured porous media with deformable matrix. International Journal for Numerical Methods in Engineering 29, 1079-1094.
van Genuchten, M.T., 1980. A closed-form equation for predicting the hydraulic conductivity of unsaturated soils. Soil Science Society of America Journal 44, 892-898.
Wu, Y., Liu, J., Elsworth, D., Miao, X., Mao, X., 2010. Development of anisotropic permeability during coalbed methane production. Journal of Natural Gas Science and Engineering 2, 197-210.
Xu, W.J., Shao, H., Hesser, J., Wang, W., Schuster, K., Kolditz, O., 2013. Coupled multiphase flow and elasto-plastic modelling of in-situ gas injection experiments in saturated claystone (Mont Terri Rock Laboratory). Engineering Geology 157, 55-68.
Yang, Y., Aplin, A.C., 2010. A permeability–porosity relationship for mudstones. Marine and Petroleum Geology 27, 1692-1697.
Yven, B., Sammartino, S., Geraud, Y., Homand, F., Villieras, F., 2007. Mineralogy, texture and porosity of Callovo-

Oxfordian argillites of the Meuse/Haute-Marne region (eastern Paris Basin). Mémoires de la Société géologique de France 178, 73-90.
Zhang, J., Bai, M., Roegiers, J.C., 2003. Dual-porosity poroelastic analyses of wellbore stability. International Journal of Rock Mechanics and Mining Sciences 40, 473-483.
Zhang, Z., Yu, X., Wu, H., Deng, M., Zhang, Z., Yu, X., Wu, H., Deng, M., 2019. Stability Control for Gob-Side Entry Retaining with Supercritical Retained Entry Width in Thick Coal Seam Longwall Mining. Energies 12, 1375-1375.
Zimmerman, R.W., Hadgu, T., Bodvarsson, G.S., 1996. A new lumped-parameter model for flow in unsaturated dual-porosity media. Advances in Water Resources 19, 317-327.

4.3 Paper III: A Three-Dimensional Hydro-Mechanical Model for Simulation of Dilatancy Controlled Gas Flow in Anisotropic Claystone

Published in *Rock Mechanics and Rock Engineering* 53(9), 2020, 4091-4116. doi:10.1007/s00603-020-02152-w.

Jianxiong Yang, Mamadou Fall, Guanlong Guo

Department of Civil Engineering, University of Ottawa, Ottawa, ON, Canada

Abstract: Dilatancy controlled gas flow is characterized by a series of gas pressure induced dilatant pathways in which the pathway aperture is a function of the effective stress within the solid matrix. In this paper, a three-dimensional hydro-mechanical model is presented to simulate the gas migration in initially saturated claystone with considerable anisotropy. The governing equations including mass conservation, momentum balance and energy conservation are presented for the unsaturated rock containing three phases, i.e., gas, water and solid grain. The constitutive model is proposed in which two conceptualized fracture sets with nonlinear mechanical behavior and cubic law controlled permeability are inserted, which have a direct effect on the hydro-mechanical behavior of the equivalent continuum. Lastly, the developed model is validated against three gas injection tests on initially saturated Callovo-Oxfordian claystone. In general, the model is capable of capturing the main features of dilatancy controlled flow, i.e., anisotropic radial deformation, major gas breakthrough, and mechanical volume dilation of the sample. The proposed model offers additional insight into the relation between gas flow, solid matrix deformation and fracture opening/closure, which helps us get in-depth understanding of this gas transport mechanism.

Keywords: Hydro-mechanical process; gas migration; anisotropic deformation; equivalent continuum; deep geological disposal; rock

Nomenclature

Latin symbols

a	fracture spacing
a_s	spacing of fracture set s
A_k, n_k	fitting parameters related to the PSD
$\bar{p}_f$	averaged pore pressure
p_{gev}	gas entry value
p_0	initial air entry value
p_{ref}	reference gas entry value
R	universal gas constant

b_{hs}	hydraulic aperture of fracture set s
C_s	specific storage coefficient
$\mathcal{C}$	equivalent stiffness tensor
D	diameter of the sample
e	internal energy of the mixture
e_s	internal energy of the skeleton
e_α	internal energy of fluid α
E	Young's modulus
f_s	roughness influence factor of fracture set s
$\boldsymbol{g}$	gravitational acceleration
G	shear modulus
h_α	specific enthalpy of fluid α
$\boldsymbol{I}$	second order identity tensor
K_n	normal stiffness of fracture
K_{ni}	initial normal stiffness of fracture
K_s	bulk modulus of solid grain
K_{fs}	shear stiffness of fracture
K_ϕ	unjacketed pore bulk modulus
$\boldsymbol{k}_{in}$	intrinsic permeability tensor
$\boldsymbol{k}_m$	intrinsic permeability tensor of matrix
$\boldsymbol{k}_f$	intrinsic permeability tensor of fracture
$k_{r\alpha}$	relative permeability of fluid α
k_{fs}	permeability through fracture set s
k_{ref}	reference intrinsic permeability
k_0	initial intrinsic permeability of sample
L	sample length
m	shape parameter of van Genuchten model
M	molar mass of gas
n	Eulerian porosity
n_α	volume fraction of fluid α
$\vec{n}$	unit vector normal to fracture plane
$\vec{n}_s$	unit vector normal to plane of fracture set s
N	Biot's skeleton modulus
p_1	axial pressure
p_3	confining pressure
p_α	pressure of fluid α
p_c	capillary pressure
S_α	saturation degree of fluid α
S_e	effective water saturation degree
$\mathbb{S}$	equivalent compliance tensor
$\mathbb{S}_f$	compliance tensor of fracture set
$\mathbb{S}_m$	compliance tensor of matrix
T	absolute temperature
T_s	surface tension on air-water interface
$\mathbb{T}$	transformation matrix
$\boldsymbol{u}$	displacement tensor
u_n	mechanical aperture of fracture
u_{ns}	mechanical aperture of fracture set s
U	interfacial energy
$\boldsymbol{v_s}$	velocity vector of solid
$\boldsymbol{v}_\alpha$	velocity vector of fluid α
$\boldsymbol{v}_\alpha^{\boldsymbol{D}}$	Darcy's velocity of fluid α
V_m	maximum fracture closure

Greek symbols

$\boldsymbol{\alpha}$	Biot's coefficients tensor
β	rotation angle between local and global axis
β_m	rotation angle of bedding plane in matrix
β_{fs}	rotation angle of fracture set s
$\boldsymbol{\varepsilon}$	total strain tensor
ε_v	volumetric strain
$\boldsymbol{\varepsilon}^*$	local strain tensor
μ_α	dynamic viscosity of fluid α
ν	Poisson's ratio
π	equivalent pore pressure
ρ	density of the mixture
ρ_s	density of solid skeleton
ρ_α	density of fluid α
$\boldsymbol{\sigma}$	total stress tensor
$\boldsymbol{\sigma'}$	effective stress tensor
σ_n'	stress traction normal to fracture set
$\boldsymbol{\sigma}^*$	local stress tensor
ϕ	Lagrangian porosity
ϕ_{ref}	reference porosity
χ_w	water compressibility

4.3.1 Introduction

Gas transport processes have gained increasing attention in the research of deep geological repositories (DGRs) for nuclear waste. The safe long-term disposal and isolation of the waste are guaranteed by a multi-barrier system, i.e., engineered barrier and natural barrier system (Abdi et al., 2015; Nasir et al., 2011, 2013; 2015). Each barrier represents an impediment to the waste migration, in which the host rock is the final impediment. However, a significant volume of gas can be generated in the post-closure phase due to several processes, i.e., metal corrosion, water radiolysis or microbial reaction (Shaw, 2015). The integrity of the host rock may be impaired by the accumulated gas pressure (NAGRA, 2008). This situation can be even worse when the gas pressure reaches a certain value to which the micro-fracture or macro-fracture forms (Fall et al., 2014; Harrington et al., 2012b). These gas-induced fractures would enable the easy transport of contaminants, which could jeopardize the biosphere and groundwater. Therefore, the investigation and study of gas migration in host rock is important for assessing DGR safety.

It is widely accepted that there are four kinds of gas transport processes in clay-based porous media, i.e., advection/diffusion of dissolved gas, capillary controlled two phase flow, dilatancy controlled gas flow, and macro-fracture flow (Harrington et al., 2012a, b; Marschall et al., 2005; NAGRA, 2008). The advection/diffusion of dissolved gas is usually a slow transport process in which the efficiency is significantly restricted by the low hydraulic conductivity of the argillaceous rock (Marschall et al., 2005). The conventional capillary-controlled flow process cannot explain some experimental phenomena related to the gas migration process in argillaceous rock, such as gas-induced micro-fracturing, macroscopic volume dilation and associated permeability increase, and the near-zero desaturation occurring after significant gas flux is observed (Angeli et al., 2009; Cuss et al., 2012, 2014; Harrington et al., 2012a, b, 2013, 2017). The ultimate mechanism of gas transport occurs at a condition of high gas production rates such that a macro-fracture is formed to initiate a single-phase (gas) flow process (Marschall et al., 2005). However, this condition is hard to reach in the case of the DGR, where the gas source terms are insufficient (Pazdniakou and Dymitrowska, 2018). Most recent experimental results have demonstrated that gas flow through clay-based porous media is along a series of dilatant pathways that are related to the injected gas pressure, which characterizes the dilatancy controlled gas flow (Angeli et al., 2009; Cuss et al., 2012, 2014; Harrington et al., 2012a, b, 2013, 2017). The aperture of gas pathways is a function of the effective stress within the solid matrix,

which dominates the behavior of fluid flow within the sample (Cuss et al., 2014; Harrington et al., 2017). Therefore, figuring out the mathematical relation between gas flow, solid matrix deformation and fracture opening/closure is important to get an in-depth understanding of the dilatancy controlled gas flow.

To simulate the development of gas preferential pathways, the coupling between unsaturated fluid flow, matrix deformation and fracture aperture have been tackled implicitly or explicitly in several numerical studies, i.e., modified two-phase flow models (Senger et al., 2014, 2018), conventional hydro-mechanical (HM) models (Fall et al., 2014; Mahjoub et al., 2018; Nguyen and Le, 2015; Xu et al., 2013), the embedded fracture models (Arnedo et al., 2013; Gerard et al., 2014; Gonzalez-Blanco et al., 2016; Olivella and Alonso, 2008), and the dilatant crack model (Rozhko, 2016). In terms of modified two-phase flow models, a significant increase in both pore space and intrinsic permeability due to pathway dilation was considered by proposing an effective stress-dependent porosity and corresponding permeability function, which reproduced an overall satisfactory HM response (Senger et al., 2014, 2018). As the model was improved from the standard two-phase flow model, some more complex experimental phenomena, i.e., sudden change of axial deformation related to gas breakthrough and gradual pressure decline following the shut-in were not well captured. By contrast, the conventional HM models were more likely to describe the complex HM response related with the dilatant pathways by introducing features such as anisotropy, plasticity, damage, etc. (Fall et al., 2014; Mahjoub et al., 2018; Nguyen and Le, 2015; Xu et al., 2013). These models have showed the robustness to capture the effect of rigidity degradation on the hydraulic properties such as the intrinsic permeability, gas entry value, which might be an alternative choice to simulate pathway dilation. To simulate the localized gas pathways in a more physical way, the embedded fracture models have been widely integrated into the HM framework (Arnedo et al., 2013; Gerard et al., 2014; Gonzalez-Blanco et al., 2016; Olivella and Alonso, 2008). The conceptualized fracture with strain-controlled permeability was inserted into the coupled HM model, but the fracture shows no mechanical behavior, nor has any mechanical effects on the solid matrix. Correspondingly, the micro-fracturing induced rigidity degradation as well as the anisotropic deformation cannot be represented. In order to address the deficiency of conceptualized fracture, the dilatant crack model was proposed to explicitly simulate the development of gas pathways (Rozhko, 2016). In the model, a single crack-like geometry was inserted into the elastic solid in

which wetting fluid occupies the crack tips and nonwetting fluid occupies the crack central parts, and the dilatancy-controlled fluid flow as well as crack deformation were studied in the model. However, the model with approximated geometry is limited by the complex mathematical treatment on the fracture and the application to real cases of gas injection tests.

At present, several methods have been developed to model the HM behavior of a fractured medium, i.e., finite element method (FEM) with remeshing, the extended finite element method (XFEM), discrete element method (DEM), boundary element method (BEM), the hybrid finite-discrete element method (FDEM), etc. If the domain only contains a limited number of discontinuities, the discrete fractures can be modelled by inserting special zero-thickness interface elements to the standard solid elements (Lei et al., 2017). By defining the fracture geometry as part of the mesh, the coupled HM behavior of interface elements can be properly represented in FEM (Paluszny et al., 2018; Segura and Carol, 2010). In XFEM, the sharp displacement of the fracture elements is captured by adding jump functions to the finite element approximation without remeshing strategy (Faivre et al., 2016). This approach has been adopted for modelling coupled flow-deformation problems, i.e., soil desiccation (Pouya et al., 2019; Vo et al., 2017), hydraulic fracturing (Salimzadeh and Khalili, 2015; Wang, 2016). Compared with the XFEM, the combination of DEM with the discrete fracture network (DFN) gives a more straight representation of fractures, as sharp discontinuities are explicitly modelled as a conformed mesh lattice, which is able to capture the opening/shearing of meshed fractures and the interaction between matrix blocks and fractures (Berre et al., 2018; Fu et al., 2013; Sun et al., 2017). However, great computational efforts are needed for the rock mass with many fractures and blocks, in which the BEM may be a reasonable alternative to provide computational efficiency, accuracy and numerical stability (Asgian, 1989; Dershowitz and Fidelibus, 1999; Fidelibus, 2007; Lenti and Fidelibus, 2003). By combining the BEM with FEM, fluid flow in complex rock fracture networks can be well represented, see Berrone et al. (2018); Xu et al. (2018). As another numerical option, the FDEM can be used to model the transitional behavior of brittle rocks, where the stress-strain evolution is analyzed in FEM while the contact interaction is analyzed in DEM. This synthetic method has been used to tackle engineering problems such as the progressive failure of rock slopes (Vyazmensky et al., 2010), rock blasting (Munjiza et al., 2000), fracture propagation in the excavation damage zone (EDZ) (Lisjak et al., 2014, 2016), etc. Though these methods provide us multiple choices to explicitly account for the fracture

propagation process, these models not only require considerably long computational time, but also are limited in the saturated case or have difficulty for fracture crossings, especially in three-dimensional cases.

In general, tremendous computational efforts have been used to investigate the HM behavior of pre-existing or conceptualized fractures. However, little attention is given in the literature to the anisotropic deformation of the fractured rocks accompanied by the fracture propagation, which is a significant observation in the gas injection tests (Cuss et al., 2014; Cuss et al., 2012). This anisotropic deformation is induced either due to the presence of the fracture sets or by the matrix containing inherent bedding. There appear to be several numerical difficulties to capturing the phenomenon: (1) the anisotropic deformation in the radial direction of a cylindrical sample can only be captured by using a three-dimensional (3D) geometry, which largely increases the computational efforts; (2) serious convergence issues will occur when the problem is related to the gas breakthrough in saturated clayey material (Guo and Fall, 2018, 2019), as this comes to the fracture propagation and self-sealing in unsaturated condition, more details about the problem can be referred to (Angeli et al., 2009; Cuss et al., 2012, 2014; Harrington et al., 2012a, b, 2013, 2017; Skurtveit et al., 2012; Wiseall et al., 2015). To get a balance in simulating the development of gas pathways, simplicity for implementing in real cases of gas injection tests, a 3D HM coupled model based on fundamental physical laws is introduced here to capture more experimental observations, i.e., anisotropic radial deformation, major gas breakthrough, mechanical volume dilation of the sample, etc.

In the remainder of the paper, we will present the mass conservation law, momentum balance equation and energy conservation in Section 4.3.2. In Section 4.3.3, the constitutive framework for unsaturated fractured rocks is proposed. Lastly in Section 4.3.4, the HM model with 3D geometry is proposed and evaluated against three gas injection tests on initially saturated claystone.

4.3.2 Governing Equations

The representative elementary volume (REV) expressed in the following section is extracted from unsaturated fractured rock, in which the matter included consists of a three-phase mixture, i.e., the solid skeleton denoted by s and two fluids, liquid water (w) and gas (g), respectively.

4.3.2.1 Main Assumptions

Prior to derive the governing equations, some basic hypotheses need to be made as follows.

(i) Infinitesimal deformations.

(ii) Isothermal conditions are made.

(iii) Two fluids are assumed to be immiscible and to stay connected in the porous networks, the porous volume is partially saturated by water while the remaining porous space is infiltrated by gas.

(iv) Gas dissolution and water evaporation as well as gas transport by diffusion are neglected for simplicity in this paper. In the post-closure phase of deep geological repository, gas transport capacity by diffusion and/or advection of dissolved gas is significantly restricted by the low hydraulic conductivity of argillaceous rocks, which is several orders of magnitude lower than the transport capacity of two-phase flow (NAGRA, 2008). Moreover, the contribution of gas transport by diffusion and dissolved gas is very low compared with the capacity of dilatancy controlled flow. The latter is the main focus in this paper.

(v) Tensile stress is counted positively, while compression is positive for pressure.

4.3.2.2 Mass Conservation

For a mixture of three phases (solid, water, gas), the phase change is neglected. The mass balance equations for solid phase and fluid phase take the following form (Coussy, 2004):

$$\frac{\partial[\rho_s(1-n)]}{\partial t}+\nabla\cdot[\rho_s(1-n)\boldsymbol{v}_s]=0 \tag{4.42}$$

$$\frac{\partial(\rho_\alpha n S_\alpha)}{\partial t}+\nabla\cdot(\rho_\alpha n S_\alpha \boldsymbol{v}_\alpha)=0\,,\ \alpha=g,w \tag{4.43}$$

where ρ_s and ρ_α $(\alpha=g,w)$ are the intrinsic mass densities of the solid skeleton, fluid, respectively; n is the Eulerian porosity, S_α is the saturation degree of fluid α, $\boldsymbol{v}_s$ and $\boldsymbol{v}_\alpha$ are the velocity vectors of solid and fluid α, respectively.

The term of time derivative of Eulerian porosity contained in the mass balance equations can be obtained by referring to the relationship between Eulerian porosity and Lagrangian porosity (Coussy, 2004, 2007), as follows:

$$\phi=(1+\varepsilon_v)n,\ \dot{\phi}=\dot{n}+\phi_0\dot{\varepsilon}_v \tag{4.44}$$

$$\phi - \phi_0 = \boldsymbol{\alpha} : \boldsymbol{\varepsilon} + (\frac{\pi}{N} - \frac{\pi_0}{N_0}) \tag{4.45}$$

where ϕ is the Lagrangian porosity, ε_v is the volumetric strain of the porous medium, and notation with subscript '0' denotes the corresponding initial value, the overdot represents the time derivative operator, $\boldsymbol{\alpha}$ is the second-order Biot effective stress coefficients tensor, $\boldsymbol{\varepsilon}$ is the strain tensor, N is the Biot's skeleton modulus, π is the equivalent pore pressure, defined by Bui et al. (2017); Coussy (2004)

$$\pi = \bar{p}_f - U = [S_w p_w + (1 - S_w) p_g] - U \tag{4.46}$$

where $\bar{p}_f$ is the averaged pore pressure, $U = \int_{S_w}^{1} p_c dS$ is the interfacial energy, $p_c = p_g - p_w$ is the capillary pressure.

The variables and poroelastic parameters included in the mass balance equations will be further explored in the constitutive models.

4.3.2.3 Momentum Balance

In the study, the inertial and viscous forces are neglected, which means the kinetical effects are zero. The body loads are assumed to solely originate from the gravity. The time derivative of the momentum of all the matter contained in the REV is equal to the sum of external forces acting on the respective matter (Coussy, 2004). Thus, the local equation of momentum balance is represented by:

$$\nabla \cdot \boldsymbol{\sigma} + \rho \boldsymbol{g} = 0 \tag{4.47}$$

where $\boldsymbol{\sigma}$ is the total stress tensor, $\rho = \rho_s (1 - n) + n(\rho_w S_w + \rho_g S_g)$ is the total mass density, $\boldsymbol{g}$ is the gravitational acceleration vector.

4.3.2.4 Energy Conservation

The first law of thermodynamics expresses the energy conservation in a form that the time rate of energy associated with the REV is equal to the sum of the work rate applied by the external forces and the rate of external heat source (Coussy, 2004). When the matter within the REV consists of solid skeleton (s), water (w) and gas (g), the energy balance equation can be represented as (Coussy, 2004):

$$\frac{\partial e}{\partial t}+\nabla\cdot(e\boldsymbol{v}_s)=\boldsymbol{\sigma}:\dot{\boldsymbol{\varepsilon}}-\sum_{\alpha=g,w}\nabla\cdot(\rho_\alpha h_\alpha \boldsymbol{v}_\alpha^{\boldsymbol{D}})+\sum_{\alpha=g,w}(\rho_\alpha \boldsymbol{g}\cdot\boldsymbol{v}_\alpha^{\boldsymbol{D}}) \tag{4.48}$$

where $e=\rho_s(1-n)e_s+\sum_{\alpha=g,w}\rho_\alpha n_\alpha e_\alpha$ is the overall density of internal energy per unit of volume, e_s and e_α represent the specific internal energy of the skeleton and fluid, respectively; $n_\alpha=nS_\alpha$ is the volume fraction of fluid α, $\dot{\boldsymbol{\varepsilon}}$ is the strain rate tensor associated with the velocity $\boldsymbol{v}_s$, or the time derivative of displacement $\boldsymbol{u}$, defined as $\dot{\boldsymbol{\varepsilon}}=\frac{1}{2}[\nabla\boldsymbol{v}_s+(\nabla\boldsymbol{v}_s)^T]=\frac{1}{2}[\nabla\dot{\boldsymbol{u}}+(\nabla\dot{\boldsymbol{u}})^T]$; $\boldsymbol{v}_\alpha^{\boldsymbol{D}}$ is Darcy's velocity of fluid α, defined as $\boldsymbol{v}_\alpha^{\boldsymbol{D}}=n_\alpha(\boldsymbol{v}_\alpha-\boldsymbol{v}_s)$; $h_\alpha=e_\alpha+\frac{p_\alpha}{\rho_\alpha}$ is the fluid-specific enthalpy.

4.3.3 Constitutive Models

4.3.3.1 Mechanical Model

The deformation of fractures contained in the potential host rock for DGRs is an unneglectable part of the performance of the argillaceous rock formations, as the produced gas may significantly migrate through the fractures. Besides, natural clayey rocks usually exhibit specific orientation of distinct bedding planes, which leads to a high anisotropy on the macroscopic scale (Hu et al., 2013). These properties all largely affect the mechanical behavior of clayey rocks, which are characterized by fractures and matrix, respectively. Similar treatment of the equivalent mechanical model containing both behaviors of fractures and matrix is also proposed by Bertrand et al. (2017) and Martinez et al. (2013). The effective stress and strain relation contained in the mechanical model can be expressed as

$$\dot{\boldsymbol{\sigma}}'=\mathbb{C}:\dot{\boldsymbol{\varepsilon}}\Leftrightarrow\dot{\boldsymbol{\varepsilon}}=\mathbb{S}:\dot{\boldsymbol{\sigma}}' \tag{4.49}$$

where $\mathbb{S}$ is the compliance tensor of the equivalent continuum consisting of rock matrix and fractures, $\mathbb{C}$ is the fourth-order effective stiffness tensor; $\boldsymbol{\sigma}'$ is the effective stress tensor, which can be derived based on the thermodynamic framework; more details can be seen in (Coussy, 2004), expressed as follows:

$$\boldsymbol{\sigma}'=\boldsymbol{\sigma}+\boldsymbol{\alpha}\pi=\boldsymbol{\sigma}+\boldsymbol{\alpha}(\bar{p}_f-U) \tag{4.50}$$

Note that if the interfacial energy U is neglected, Eq. (4.50) becomes the Bishop-type effective stress law.

For modelling simplicity, the complex structure of host rock is reduced to a series of matrix separated by fracture sets with constant spacing.

4.3.3.1.1 Characterization of Matrix

The inherent anisotropy of clayey rock due to bedding is a significant property of sedimentary rock, which has been extensively recorded in the gas injection tests (Cuss et al., 2012; Harrington et al., 2013; Popp et al., 2007). This anisotropic characterization of matrix may largely affect the formation of gas preferential pathway, as the bedding plane can make a big difference on the HM properties in different directions. Therefore, the matrix is assumed to be a transverse isotropic material with the z-axis being the axis of rotational material symmetry. With respect to the local bedding plane in the xy plane, the compliance tensor of rock matrix can be expressed in terms of two Young's moduli ($E_{/\!/}$, $E_{\perp}$), two Poisson's ratio ($\nu_{/\!//\!/}$, $\nu_{\perp/\!/}$) and a shear modulus ($G_{/\!/\perp}$) in the following form (Cheng, 1997):

$$\mathbb{S}_m = \begin{bmatrix} \frac{1}{E_{/\!/}} & -\frac{\nu_{/\!//\!/}}{E_{/\!/}} & -\frac{\nu_{\perp/\!/}}{E_{\perp}} & & & \\ -\frac{\nu_{/\!//\!/}}{E_{/\!/}} & \frac{1}{E_{/\!/}} & -\frac{\nu_{\perp/\!/}}{E_{\perp}} & & & \\ -\frac{\nu_{\perp/\!/}}{E_{\perp}} & -\frac{\nu_{\perp/\!/}}{E_{\perp}} & \frac{1}{E_{/\!/}} & & & \\ & & & \frac{1}{G_{/\!//\!/}} & & \\ & & & & \frac{1}{G_{/\!/\perp}} & \\ & & & & & \frac{1}{G_{/\!/\perp}} \end{bmatrix} \tag{4.51}$$

where $E_{/\!/}$ and $E_{\perp}$ are the Young's moduli of intact material parallel to the bedding plane and normal to it respectively; $\nu_{/\!//\!/}$ and $\nu_{\perp/\!/}$ are the Poisson's ratio for effect of the stresses in the bedding plane and in the direction normal to it on the strain in the bedding plane, respectively; $G_{/\!/\perp}$ is the shear modulus of intact material normal to the bedding plane, $G_{/\!//\!/} = E_{/\!/}/2(1+\nu_{/\!//\!/})$ is the shear modulus of intact material in the bedding plane.

4.3.3.1.2 Characterization of Fractures

The mechanical properties of fractures under different loading paths have been extensively studied, by both experimental and numerical methods (Bandis et al., 1983; Cammarata et al.,

2007; Ghaffari et al., 2010; Souley et al., 1995; Yang et al., 2016). In the gas injection experiments, the stiffness of the pre-existing fractures within the rock sample will decrease with the opening of the gas-induced fracturing. To capture the phenomenon, the hyperbolic relationship of the fracture deformability developed in (Bandis et al., 1983) will be applied in this study, as the model satisfies the fact that the fracture stiffness decreases in the gas injection process.

For simplicity, the fractured clayey rock element may be ideally conceptualized by a number of fractures, and each fracture set has a certain parallel direction and fixed spacing, a, as shown in Figure 4.16. The aperture of each fracture set is represented by $u_n = u_{n0} + \Delta u_n$, in which u_{n0} is the initial normal displacement at the initial effective stress field, Δu_n is the change of normal displacement due to local changes in effective stress normal to the fracture plane. In the model, fracture opening is counted positively, V_m is the maximum fracture closure that is negatively expressed in Figure 4.16.

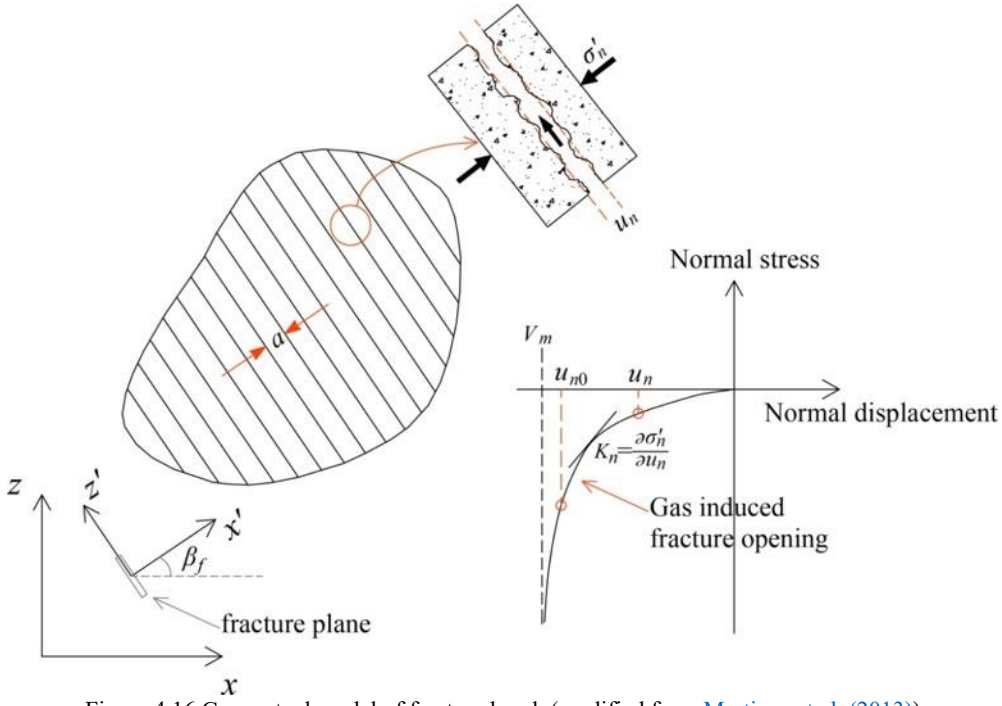

Figure 4.16 Conceptual model of fractured rock (modified from Martinez et al. (2013))

The response of a fracture to normal loading can be described by the hyperbolic model (Bandis et al., 1983; Souley et al., 1995), thus the fracture behavior under normal stress is written as

$$\Delta u_n = \frac{\Delta \sigma_n^{'} V_m}{K_{ni} V_m + \Delta \sigma_n^{'}} \tag{4.52}$$

The fracture stiffness (K_n) normal to the fracture plane can be calculated (Martinez et al., 2013; Souley et al., 1995)

$$K_n = \frac{\partial \Delta \sigma_n^{'}}{\partial \Delta u_n} = \frac{K_{ni}}{(1 - \Delta u_n / V_m)^2} \tag{4.53}$$

where $\sigma_n^{'} = \vec{n} \cdot \boldsymbol{\sigma}^{'} \cdot \vec{n}$ is the traction of effective stress normal to the fracture set, K_{ni} is the initial fracture stiffness and V_m is the maximum aperture of the fracture, which can be used as two fitting parameters for a particular dataset in the numerical implementation, the unit vector normal to the fracture plane can be expressed in terms of Euler angle, β_f shown in Figure 4.16, as follows

$$\vec{n} = (\cos \beta_f, 0, \sin \beta_f) \tag{4.54}$$

Considering a fracture set in the local coordinate system with constant spacing, a , see the $x'z'$ plane in Figure 4.16, the compliance matrix of the persistent fracture can be written as (Amadei and Goodman, 1981)

$$\mathbb{S}_f = \begin{pmatrix} \frac{1}{aK_n} & & & & & \\ & 0 & & & & \\ & & 0 & & & \\ & & & \frac{1}{aK_{fs}} & & \\ & & & & 0 & \\ & & & & & \frac{1}{aK_{fs}} \end{pmatrix} \tag{4.55}$$

where $\mathbb{S}_f$ represents the compliance tensor of the facture set, K_{fs} is the shear stiffness of the fracture.

4.3.3.1.3 Equivalent Continuum

To consider the effect of fracture set on the elastic moduli, a superposition method developed by Yang et al. (2018) may be well applied here, in which the equivalent compliance tensor of the fractured rock is calculated by adding up the individual compliance tensor of intact rock and fracture sets. This method is similar to the method developed by Liu et al. (2009), who

conceptualized the fractured rock as an equivalent continuum consisting of hard spring and soft spring. These methods extend the concept of equivalent continuum proposed by Amadei and Goodman (1981), which has been applied in the production of coalbed recovery (Bertrand et al., 2017) and CO_2 sequestration (Martinez et al., 2013).

By using the superposition method, the determination of the compliance tensor of the equivalent continuum is expressed in Figure 4.17. Noted here the local coordinate system of both bedding plane and fracture set may not correspond to the global coordinate axis, thus a change of compliance tensor of both matrix and the fracture set has to be computed using a rotation matrix, which depends on the angle between the local and global coordinate system, as can be seen in Figure 4.17. The rotation matrix of the bedding plane and the fracture set with respect to the global coordinate axis is expressed as follows

$$\boldsymbol{R} = \begin{pmatrix} \cos\beta & 0 & \sin\beta \\ 0 & 1 & 0 \\ -\sin\beta & 0 & \cos\beta \end{pmatrix} \tag{4.56}$$

where $\beta = \beta_m$ or β_f represents the rotation angle for matrix or fracture set, respectively, $\boldsymbol{R}$ is the corresponding rotation matrix of the bedding plane or the fracture set.

The rotation matrix provides the relationships of stress and strain between local and global coordinate system:

$$\boldsymbol{\sigma}^* = \boldsymbol{R}\boldsymbol{\sigma}\boldsymbol{R}^T \tag{4.57}$$

$$\boldsymbol{\varepsilon}^* = \boldsymbol{R}\boldsymbol{\varepsilon}\boldsymbol{R}^T \tag{4.58}$$

in which $\boldsymbol{\sigma}^*$ and $\boldsymbol{\varepsilon}^*$ are the stress, strain tensor in the local axes system, respectively. We can further obtain the transformation matrix $\mathbb{T}$ if we rearrange Eq. (4.57) in terms of stress components in the following form:

$$\begin{pmatrix} \sigma^*_{xx} \\ \sigma^*_{yy} \\ \sigma^*_{zz} \\ \sigma^*_{xy} \\ \sigma^*_{yz} \\ \sigma^*_{xz} \end{pmatrix} = \mathbb{T} \begin{pmatrix} \sigma_{xx} \\ \sigma_{yy} \\ \sigma_{zz} \\ \sigma_{xy} \\ \sigma_{yz} \\ \sigma_{xz} \end{pmatrix}, \quad \mathbb{T} = \begin{pmatrix} \cos^2\beta & 0 & \sin^2\beta & 0 & 0 & \sin(2\beta) \\ 0 & 1 & 0 & 0 & 0 & 0 \\ \sin^2\beta & 0 & \cos^2\beta & 0 & 0 & -\sin(2\beta) \\ 0 & 0 & 0 & \cos\beta & \sin\beta & 0 \\ 0 & 0 & 0 & -\sin\beta & \cos\beta & 0 \\ -\frac{1}{2}\sin(2\beta) & 0 & \frac{1}{2}\sin(2\beta) & 0 & 0 & \cos(2\beta) \end{pmatrix} \tag{4.59}$$

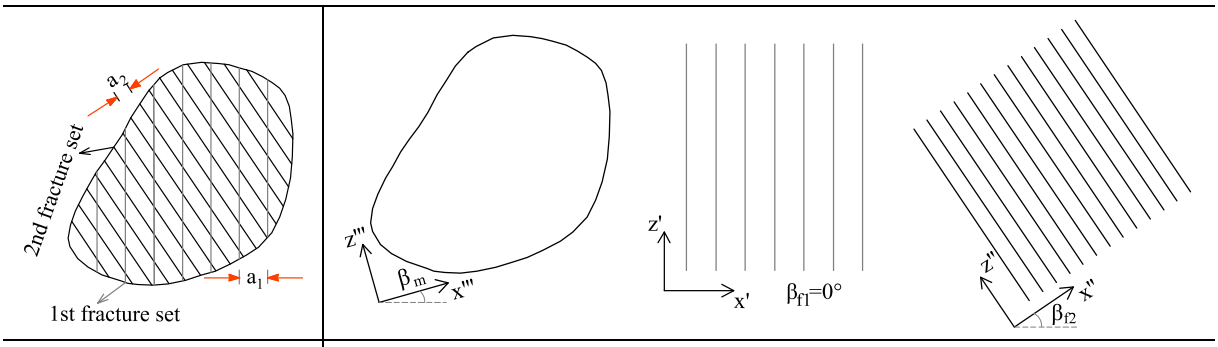

$\mathbb{S}=\mathbb{S}_m^{'}+\mathbb{S}_f^{'}+\mathbb{S}_f^{''}$	$\mathbb{S}_m^{'}=\mathbb{T}^{-1}(\beta_m)\mathbb{S}_m\mathbb{T}(\beta_m)$	$\mathbb{S}_f^{'}=\mathbb{S}_f$	$\mathbb{S}_f^{''}=\mathbb{T}^{-1}(\beta_{f2})\mathbb{S}_f\mathbb{T}(\beta_{f2})$
Fractured rock	Matrix with bedding	The 1st fracture set	The 2nd fracture set

Figure 4.17 Determination of the compliance tensor of the equivalent continuum (modified from Yang et al. (2018))

After the compliance tensor is obtained by the aforementioned superposition method, the elastic stiffness tensor contained in Eq. (4.49) can be easily expressed as the inverse of compliance tensor, $\mathbb{C}=\mathbb{S}^{-1}$. Then it remains to define the explicit form of poro-elastic parameters $\boldsymbol{\alpha}$ and N. Due to the aforementioned characterization of the fractured rock, the Biot's tensor of the equivalent continuum is highly anisotropic and being affected by the evolution of the inserted fracture set, expressed as

$$\boldsymbol{\alpha}=\boldsymbol{I}-\frac{1}{3K_s}\mathbb{C}:\boldsymbol{I} \tag{4.60}$$

where $\boldsymbol{I}$ is the second order identity tensor, K_s is the bulk modulus of solid grain.

For an isotropic material with a homogeneous solid phase, the expression of Biot's modulus is written as $1/N=(\alpha-\phi_0)/K_s$ (Coussy, 2004). Inspired by the micromechanical analysis of anisotropic porous media in (Cheng, 1997) for micro-homogeneous and micro-isotropic material and the unsaturated thermoporoelasticity analysis in (Coussy, 2007) for disconnected porous networks, Aichi and Tokunaga (2012) extend the expression of Biot's modulus to micro-heterogeneous media. In this study, the equivalent continuum is assumed to be micro-homogeneous and micro-isotropic material, two fluids are assumed to be immiscible and to stay connected in the porous networks. The porous volume is partially saturated by water while the remaining porous space is infiltrated by gas. The modulus N is expressed as (Guayacán-Carrillo et al., 2017)

$$\frac{1}{N}=\frac{tr(\boldsymbol{\alpha})}{3K_s}-\frac{\phi_0}{K_\phi} \tag{4.61}$$

where K_ϕ is the unjacketed pore bulk modulus (Aichi and Tokunaga, 2012). The experimental

determination of the modulus K_ϕ is generally very difficult (Ghabezloo et al., 2008); however, it can be simplified to be equal to the modulus of solid grain (K_s) by assuming the porous medium is made up of a homogeneous solid phase (Guayacán-Carrillo et al., 2017). Thus $K_\phi = K_s$ is adopted for simplicity in the study.

4.3.3.2 Hydraulic Constitutive Models

The mass balance equations described in Eqs. (4.42), (4.43) include different variables, i.e., fluid density and water saturation degree, which are linked to the primary variables, i.e., gas pressure, water pressure, and displacement tensor, through some constitutive and equilibrium equations. We will further explore the relations between these variables in this section.

The permeability of the porous material can be largely affected due to the opening/closure of pre-existing fractures, which is a significant characterization of fractured rock, as well as the experimental observation in the gas injection test. The contribution of permeability to the fluid flow within unsaturated rock is governed by the general Darcy's law, expressed as follows,

$$\boldsymbol{v}_\alpha^D = -\frac{\boldsymbol{k}_{in} k_{r\alpha}}{\mu_\alpha}(\nabla p_\alpha - \rho_\alpha \boldsymbol{g}) \tag{4.62}$$

where $\boldsymbol{k}_{in}$ is the intrinsic permeability tensor, $k_{r\alpha}$ is the relative permeability of fluid α, μ_α is the dynamic viscosity of fluid α.

The development of gas preferential pathways activates the opening of the existing fractures, thus increases the value of intrinsic permeability and decreases the gas entry pressure. Accordingly, the relative permeability will be affected indirectly through the coupled variable, i.e., effective saturation degree. The specific model to represent the couplings between the hydraulic variables is described as follows.

4.3.3.2.1 Intrinsic Permeability

In the porous material, fluid flow occurs in the pore space between the solid skeleton, including micro-pores and macro-pores. For the case of fractured rock, the pore space consists of the pores and the existing fractures, in which both of their permeability contribute to the intrinsic permeability of the material. The change in intrinsic permeability of matrix due to porosity change can be described by Kozeny-Carmen model (Carman, 1937), given by

$$\boldsymbol{k}_m = \boldsymbol{k}_{m,0} \frac{\phi^3}{(1-\phi)^2} \frac{(1-\phi_0)^2}{\phi_0^3} \tag{4.63}$$

where $\boldsymbol{k}_m$ is the intrinsic permeability tensor of matrix, notations with subscript '0' denote their corresponding initial values.

According to the conceptualization of the fracture set in this study, a well-known cubic law is adopted to describe the permeability through fracture set s (=1 or 2) oriented parallel to the flow direction k_{fs}.

$$k_{fs} = \frac{b_{hs}^3}{12a_s}, \; s = 1, \; 2 \tag{4.64}$$

where b_{hs} is the hydraulic aperture of the fracture set s (=1 or 2), a_s is the spacing of fracture set s (=1 or 2).

Then the intrinsic permeability of fractured rock can be expressed in terms of the permeability of matrix and fracture as follows,

$$\boldsymbol{k}_{in} = \boldsymbol{k}_m + \boldsymbol{k}_f = \boldsymbol{k}_{m,0} \frac{\phi^3}{(1-\phi)^2} \frac{(1-\phi_0)^2}{\phi_0^3} + \frac{b_{hs}^3}{12a_s}(\boldsymbol{I} - \vec{n}_s \otimes \vec{n}_s), \; s = 1, \; 2 \tag{4.65}$$

where $\boldsymbol{k}_f$ represents the permeability tensor of fracture set, $\boldsymbol{I}$ is the second identity tensor, $\vec{n}_s$ is the unit vector normal to the plane of fracture set s (=1 or 2).

By noting that the hydraulic aperture is generally different with the mechanical aperture in the above equation, the equality is only tenable for smooth fractures (Cappa et al., 2008; Guglielmi et al., 2015; Liu et al., 2013). Fracture roughness and contact area occupied by obstruction are important factors influencing the couplings between the two apertures. Witherspoon et al. (1980) proposed a modified cubic law to adjust the two apertures in the parallel-plate flow concept, which was verified against numerous laboratory experiments (Alvarez et al., 1995; Detournay, 1980). For simplicity, this law will be used in the study, to couple the hydraulic aperture with the mechanical aperture, expressed as follows

$$b_{hs} = b_{hs0} + f_s \Delta u_{ns} \tag{4.66}$$

where b_{hs0} is the initial hydraulic aperture of fracture set s (=1 or 2) at the initial effective stress state, f_s is a factor representing the influence of roughness of fracture set s (=1 or 2) on the tortuosity of flow, Δu_{ns} is the change of aperture in fracture set s (=1 or 2).

4.3.3.2.2 Water Retention Curve

The well-known van Genuchten (vG) model (van Genuchten, 1980) is applied here to simulate the two phase flow process within the rock. The effective water saturation degree S_e can be expressed in terms of capillary pressure as follows,

$$S_e = \begin{cases} \left[1 + \left(\dfrac{p_c}{p_{gev}} \right)^{\frac{1}{1-m}} \right]^{-m} & p_c > 0 \\ 1 & p_c \le 0 \end{cases} \tag{4.67}$$

where m is the model parameter, p_{gev} is the gas entry value, which will be significantly affected by the fracture opening/closure. For the fracture set with aperture b_{hs}, the gas entry value may be written, in view of the Laplace equation, as

$$p_{gev} = \frac{2T_s}{b_{hs}} = \frac{2T_s}{b_{hs0}} \left(\frac{b_{hs0}}{b_{hs}} \right) = \min(p_0 (k_{f0} / k_{fs})^{1/3}),\ s = 1,\ 2 \tag{4.68}$$

where T_s is the surface tension acting on the air-water interface, p_0 is the initial air entry value, the expression ‘ min() ’ in Eq. (4.68) means a function to get the minimum value of two fracture sets, which means gas can penetrate the sample through the largest pore that corresponds to the smallest gas entry value.

The residual saturation degree of both gas and water are assumed to be zero; thus, the water saturation degree S_w is equal to the effective saturation degree, which amounts to writing the following relations:

$$\frac{\partial S_g}{\partial t} = -\frac{\partial S_w}{\partial t} = -\frac{\partial S_e}{\partial t} = C_s \frac{\partial p_c}{\partial t} \tag{4.69}$$

$$C_s = -\frac{\partial S_e}{\partial p_c} = \frac{m}{p_{gev}(1-m)} S_e^{\frac{1}{m}} (1 - S_e^{\frac{1}{m}})^m \tag{4.70}$$

in which C_s is a specific storage coefficient.

4.3.3.2.3 Relative Permeability

The concept of relative permeability with respect to unsaturated fluid flow can be used to capture the dependency of coefficient of permeability on effective water saturation degree. The widely used models are from Brooks and Corey (1964); Mualem (1976); van Genuchten (1980). For simplicity, the model by Brooks and Corey (1964) is extended here to describe the relative

permeability of gaseous phase with respect to the effective saturation degree, which has been widely used in studies of the research topic at hand (Arnedo et al., 2013; Gerard et al., 2014; Gonzalez-Blanco et al., 2016). The generalized power law is expressed as follows,

$$k_{rg} = A_k (1 - S_e)^{n_k} + \delta \tag{4.71}$$

where δ is a small constant (0.001) to ensure a minimum value of relative permeability, similar treatment can be also found in (Guo and Fall, 2018), A_k and n_k are fitting parameters related to the pore size distribution of the material.

For the liquid phase, the relative permeability of the water flow in the rock is given as (Mualem, 1976; van Genuchten, 1980):

$$k_{rw} = \sqrt{S_e}[1 - (1 - S_e^{1/m})^m]^2 \tag{4.72}$$

4.3.3.2.4 Fluid Density Variation

If fluid compressibility is not neglected, then the fluid density varies with the respective fluid pressure in the porous medium. By introducing the water compressibility χ_w, the time derivative of water density can be expressed as

$$\frac{\partial \rho_w}{\partial t} = \rho_w \chi_w \frac{\partial p_w}{\partial t} \tag{4.73}$$

The gas phase within the fractured rock is assumed to obey the ideal gas law, the assumption amounts to writing the time derivative of gas density as follows,

$$\frac{\partial \rho_g}{\partial t} = \frac{M}{RT} \frac{\partial p_g}{\partial t} \tag{4.74}$$

where M is the molar mass of the gas, R is a universal gas constant, and T is the absolute temperature.

4.3.4 Evaluation of the Model

The proposed HM model is implemented in a FEM code, COMSOL Multiphysics, and then validated against three sets of gas injection test on clayey rock. The experimental data used in the study were obtained from the tests conducted on Callovo-Oxfordian claystone (COx) at British Geological Survey (BGS, UK), where the first and second gas injection tests are respectively conducted on intact sample COx-1 and naturally fractured sample COx-4 under isotropic conditions (Harrington et al., 2013, 2017), the third test is conducted on sample SPP_COx-2

under triaxial conditions (Cuss et al., 2012, 2014). In the specific experimental condition of gas injection tests, gas induced fracturing initially occurs in the inlet area, then these fractures gradually propagate along the axial and radial directions and reach the outlet area and sample wall area. This phenomenon can be reflected by the larger fracture opening size close to the gas injection area. However, the 2D axisymmetric model happens to represent an opposite response due to the existence of the constant symmetrical axis. On the other hand, the anisotropic deformation along the radial direction of the sample cannot be represented by using the 2D axisymmetric model. With these considerations, a 3D model with anisotropic HM properties is adopted to fully capture the significant phenomena in the gas injection tests.

The procedures of the experimental tests performed are briefly discussed in the following subsection; detailed experimental explanations of individual tests can be found in (Cuss et al., 2012; Harrington et al., 2013).

4.3.4.1 Experimental Description

A number of gas injection tests on initially saturated COx samples were conducted at BGS to investigate the gas migration mechanism as well as its potential impact on the performance of host rocks. The samples are either subjected to isotropic confining stress conditions (i.e., COx-1 test, COx-4 test) or triaxial stress conditions (see SPP_COx-2 test). Helium was introduced as a substitute gas for hydrogen and was injected into the sample through the injection filter (IF); see Figure 4.18. The water pressure p_w was applied at the backpressure filter (BF) with a constant value. A constant confining pressure p_3 and axial pressure p_1 were applied on the sample through all the gas injection process.

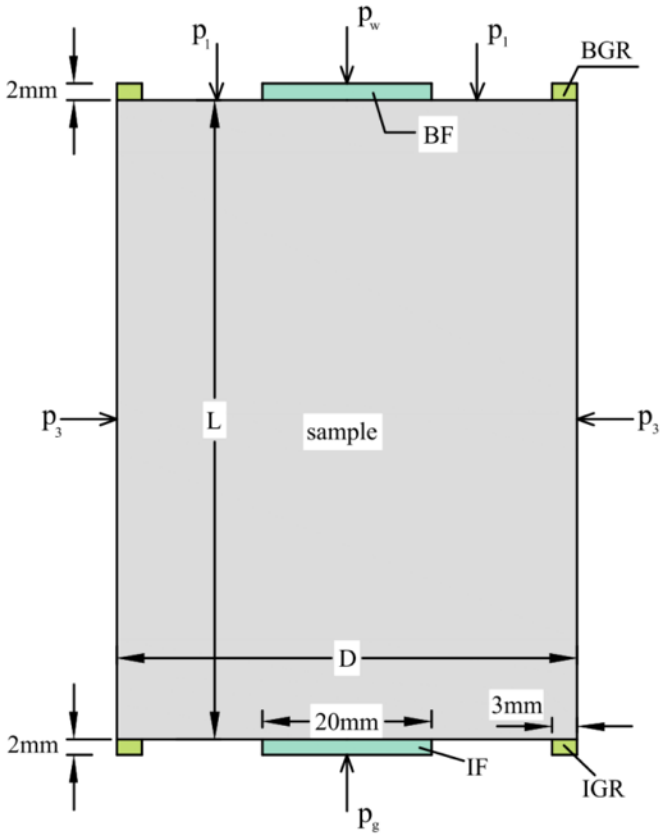

Figure 4.18 Schematic diagram of the experimental system

The gas outflow rate at standard temperature and pressure condition (STP) was recorded. The pressure in the injection guard ring (IGR) as well as in the back guard ring (BGR) was monitored to provide some useful information, i.e., pore pressure evolution and hydraulic anisotropy. The dimensions of IF, BF, IGR and BGR are shown in the Figure 4.18. The sample with diameter D and length L was used for specific experiments.

Sample COx-1 and COx-4 with cylindrical axis perpendicular to the bedding were prepared for the gas injection test under isotropic stress condition ($p_1 = p_3$), while sample SPP_COx-2 with cylindrical axis parallel to the bedding was tested under triaxial stress condition ($p_1 - p_3 = 0.5$ MPa). Sample COx-4 was designated to contain a natural fracture to investigate the gas flow behavior in the fracture. For the SPP_COx-2 test, radial strain at different points of the mid-plane was measured to investigate the anisotropic deformation accompanied with gas flow. Full description of gas injection test as well as the explanation of experimental results can be referred to (Cuss et al., 2012; Harrington et al., 2013, 2017).

4.3.4.2 Model Parameters

Basic information of the rock samples used in the experimental tests is extracted from (Cuss et al., 2014; Harrington et al., 2017), as listed in Table 4-7. As recorded in (Harrington et al., 2017), sample COx-1 and COx-4 were oriented perpendicular to bedding while COx-3 was parallel to bedding. Thus the Euler's angle between the bedding plane and the global axes is obtained as 0°, 0° and 90°, respectively, for COx-1, COx-4 and SPP_COx-2. Noted here, due to limited information of sample COx-4, other data excluding length and diameter listed in this paper is adopted from COx-1.

Table 4-7 Basic information of rock samples

Sample	Length, L (mm)	Diameter, D (mm)	Dry density, g/cm^3	Porosity	Euler's angle, β_m (°)	Source
COx-1	53.9	54.4	2.31	0.146	0	(Harrington et al., 2017)
COx-4	63.7	54.5			0	(Harrington et al., 2017)
SPP_COx-2	82.5	55.9	2.31	0.148	90	(Cuss et al., 2014)

In the mechanical test of SPP_COx-1 conducted by Cuss et al. (2012), anisotropic radial strain was observed in the experiment, which emphasizes the rationality to define the clayey rock as a transverse isotropic material with a higher stiffness value in the direction parallel to the plane of isotropy. Although the elastic constants were measured based on the rule of isotropic material in the experiment, the anisotropic characteristics of COx is considered in the model as it is non-negligible for sedimentary rocks.

The physical properties of the clayey rock sample has been studied by many researchers with emphasis on anisotropy (Belmokhtar et al., 2017; Homand et al., 2006; Pardoen et al., 2015; Wenk et al., 2008), the value of elastic moduli may be different based on the specific loading conditions and experimental apparatus. For simplicity, the isotropic Young's modulus recorded in the experiments will be used as parameters in the plane of isotropy. The value of solid grain modulus is calculated based on the isotropic elastic constants and Biot's coefficient recorded in Mahjoub et al. (2018), who also simulated gas migration process in the COx sample. The degree of elastic anisotropy for all the samples is taken as 1.2 from Wenk et al. (2008) who studied the anisotropy on COx sample, which is originally recorded in (Andra, 2005). The values of shear modulus and Poisson's ratio are extracted from Pardoen et al. (2015), who modelled the shear behavior of cross-anisotropic COx sample. These mechanical parameters, i.e., Young's modulus, shear modulus and Poisson's ratio, are set to the same value for all the samples.

The permeability of sample COx-4 is taken as one order magnitude above that of COx-1 as

COx-4 contains a natural fracture (Harrington et al., 2017). The shape parameter, m, was set to 1/3 for gas migration modelling through all the COx samples, which is similar with the value used by Mahjoub et al. (2018). As gas migration in claystone is a time-dependent dynamic process, it is difficult to capture using the same value set of relative permeability relations for all the samples. Therefore, these constants contained in Eq. (4.71) are used as empirical parameters to better capture this process.

The initial gas entry value, p_0, may be significantly different due to sampling disturbance, pore structure and fracturing degree, etc. Furthermore, this parameter plays a critical role in controlling the gas migration process, but it is not always given for the specific experiment. Therefore, the following reference capillary model given in (Chasset et al., 2011) is applied here to acquire an appropriate initial gas entry value for different COx samples, which is expressed as

$$p_0 = p_{ref}\sqrt{\frac{k_{ref}\phi_0}{\phi_{ref}k_0}} \tag{4.75}$$

where k_0 is the initial intrinsic permeability of the sample, p_{ref}, k_{ref} and ϕ_{ref} refer to the gas entry value, intrinsic permeability and porosity of a representative clayey rock sample with a known capillary curve. The reference properties of the clayey rock sample, i.e., p_{ref}, k_{ref} and ϕ_{ref}, are adopted from the existing experimental data (Charlier et al., 2013), which are given as 15 MPa, 1.33×10^{-20} m^2 and 0.18, respectively.

The detailed HM parameters are summarised in Table 4-8.

Table 4-8 HM parameters of COx sample (1, Mahjoub et al. (2018); 2, Pardoen et al. (2015))

Parameter		COx-1	COx-4	SPP_COx-2
Permeability (m^2)	$k_{0\parallel}$	3.5×10^{-19} [1]	3.5×10^{-18}	5.1×10^{-20} [1]
	$k_{0\perp}$	1.4×10^{-20} [1]	1.4×10^{-19}	2.04×10^{-20} [1]
Initial gas entry value (MPa)	p_0	2.63	0.83	6.95
vG model coefficient	m	1/3 [1]		
Relative permeability coefficient	A_k	1	1	1
Relative permeability coefficient	n_k	1	5	4
Young's modulus (MPa)	$E_\parallel$	2400		
	$E_\perp$	2000 [1]		
Poisson's ratio	$\nu_{\parallel\parallel}$	0.24 [2]		
	$\nu_{\parallel\perp}$	0.33 [2]		
Shear modulus (MPa)	$G_{\parallel\perp}$	1630 [2]		
Bulk modulus of solid grain (MPa)	K_s	4167 [1]		

As stated by Cuss et al. (2014), rock samples may contain micro-fractures or macro-fractures to different extents due to variations in the confining pressure, initial sample size, stress state or sample preparation method. These pre-existing fractures can affect the gas migration

process significantly and need to be considered in the study. On the other hand, to provide predictive results and avoid the convergence problem, only two fracture sets are inserted in the REV. The normal direction of the two fractures is set to be parallel with x-axis and z-axis, respectively. The spacing of the two fracture sets is set to be uniform, i.e., 20 mm, while the initial stiffness value and maximum aperture are used as fitting parameters for the specific dataset in the gas injection test. As we only focus on the fracture opening/closure effect, the shear stiffness of fractures is set to have a same value with the initial normal stiffness. Detailed parameters for the two fracture sets can be found in Table 4-9. Fracture spacing and roughness factor are used as empirical parameters in the calculation to fitting the experimental curve. Similar treatment has been widely adopted in the research topic at hand; for example, see (Fall et al., 2014; Gerard et al., 2014; Gonzalez-Blanco et al., 2016; Nguyen and Le, 2015; Olivella and Alonso, 2008). However, more experimental efforts need to be made in the future to better determine these parameters.

Table 4-9 Facture parameters used in the model

Parameter	COx-1	COx-4	SPP_COx-2
Euler angle of the 1st fracture set, β_{f1} (°)	0		
Euler angle of the 2nd fracture set, β_{f2} (°)	90		
Spacing of the 1st fracture set, a_1 (mm)	20		
Spacing of the 2nd fracture set, a_2 (mm)	20		
Initial normal stiffness of fracture, K_{ni} (GPa/m)	230	300	300
Maximum aperture of fracture, V_m (μm)	-97	-60	-42
Roughness factor of the 1st fracture set, f_1	6.0×10^{-3}	3.6×10^{-2}	2.5×10^{-3}
Roughness factor of the 2nd fracture set, f_2	6.0×10^{-3}	1.0×10^{-2}	3.0×10^{-3}

4.3.4.3 Simulation of COx-1 Test

In the COx-1 test, gas injection pressure p_g increased from 6.5 MPa up to 12 MPa and then decreased down to 7 MPa after several steps. The water pressure p_w was controlled with a constant value, i.e., 4.5 MPa at the BF. The confining pressure was kept at a same value with the axial pressure, i.e., $p_1 = p_3 = 12.5$ MPa.

4.3.4.3.1 Initial and Boundary Conditions

A 3D model is adopted here to simulate the COx-1 test, as the 2D axisymmetric model cannot represent the phenomenon of larger fracture opening close to the gas injection area due to the existence of the constant symmetrical axis. The conceptualized two-fracture sets are set to have uniform parameters, with different normal direction, i.e., along the x-axis for the 1st

fracture set and z-axis for the 2nd fracture set, respectively. The filters, i.e., the IF and BF, the IGR and BGR, are modeled by using an equivalent porous material with high permeability and high porosity. The fine meshed domain including the cylindrical sample and the filters is shown in Figure 4.19(a). To avoid the convergence problem due to the inconsistent deformation between the filters and the sample, mechanical conditions were only applied onto the sample; see Figure 4.19(b). The detailed HM boundary conditions can be referred to Table 4-10.

The initial water pressure in the sample was set to 4.5 MPa, which is equal to the pressure applied on the BF. The initial gas pressure was set to 4.7 MPa which was a little higher than the water pressure to avoid the convergence problem and to initiate the gas flow process. The initial water saturation degree and water-solid interfacial energy are calculated to be 99.3% and 1376 Pa, respectively. Accordingly, the initial equivalent pore pressure is obtained as 4.5 MPa. The initial Biot's tensor is calculated by considering the initial normal stiffness and spacing of the fracture set, which is determined as $\boldsymbol{\alpha}_0 = (0.77 \quad 0.68 \quad 0.78 \quad 0 \quad 0 \quad 0)^{\mathrm{T}}$. The initial effective stress tensor is determined to be $\boldsymbol{\sigma}_0 = (-9.00 \quad -9.42 \quad -8.97 \quad 0 \quad 0 \quad 0)^{\mathrm{T}}$ MPa. From Eq. (4.52), the initial mechanical aperture of the two fracture sets can be calculated as -1.45×10^{-4} m for the 1st set and -1.45×10^{-4} m for the 2nd set, respectively. The two fracture sets are assumed to have a very small initial value of intrinsic permeability, i.e., 2.03×10^{-23} m^2, to initiate the gas flow process in fractures. This value is much smaller than that of the surrounding matrix in the initial state, which represents a nearly closed state when no gas is injected. To obtain an equilibrium condition from the initial state, a ramp function range from 4.6 MPa to 6.5 MPa was provided for the initial gas injection pressure.

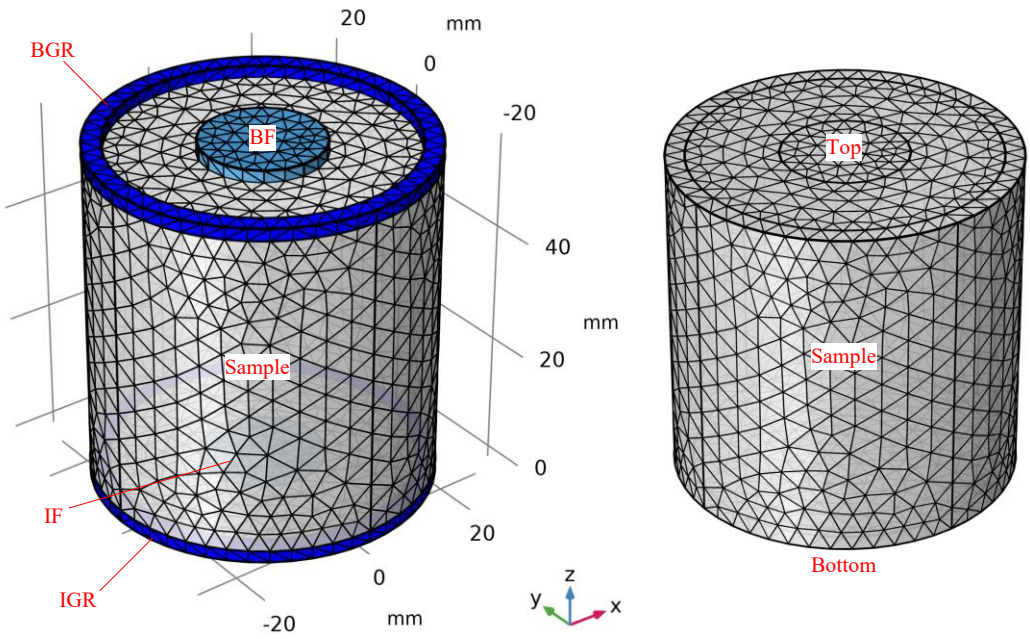

(a) Hydraulic BCs (b) Mechanical BCs

Figure 4.19 Fine meshed geometry of the REV and HM boundary conditions (BCs)

Table 4-10 The HM BCs for COx-1 test

Boundary	Hydraulic boundary		Mechanical boundary
	Gas pressure	Water pressure	
IF bottom	Controlled pressure	No flow	-
BF top	4.7 [MPa]	4.5 [MPa]	-
Remaining area	No flow	No flow	-
Sample bottom	-	-	Roller with three points fixed
Sample top	-	-	12.5 [MPa]
Sample lateral	-	-	12.5 [MPa]

4.3.4.3.2 Results and Discussion

Figure 4.20 presents a comparison between the numerically modeled and experimentally obtained gas outflow rate at STP condition. Figure 4.21 shows the normal displacement of the inserted fracture sets and the corresponding gas entry value at the middle point A. In general, the simulated results are in good agreement with the experimental results. It can be also observed that the model estimates well the flow rate before gas breakthrough occurs, then underestimates it followed the breakthrough and the simulated onset of gas flow is earlier. Similar modelling discrepancies have also been reported in (Gerard et al., 2014; Harrington et al., 2013), which highlights the instability of dynamic gas pathways.

The early onset of gas flow might be attributed to the relatively low gas entry value at an early time, i.e., lower than 1 MPa in the model since day 110, as can be seen in Figure 4.21. Another influence factor is that the fracture opening behavior is related to the gas-induced

unloading phenomenon, which can be represented by the increased fracture aperture step by step that corresponds to the applied gas pressure; see Figure 4.21. This coupled process can be seen from Eqs. (4.52), (4.64), (4.66) and (4.68). As gas is injected from the inlet, gas gradually penetrates the sample that has a direct effect on the sample deformation. The deformation can be represented by the increase of effective stress, which leads to the opening of the two fracture sets; see fracture behavior in Figure 4.16. By the coupled relation between mechanical and hydraulic aperture in Eq. (4.66), the gas entry value decreases with the increasing fracture permeability; see Eqs. (4.64) and (4.68). Thanks to the anisotropic characteristics of claystone, the sample deformation is anisotropic in the radial and axial directions, thus leading to different apertures of the fracture sets, as can be seen in Figure 4.21. Following a major gas breakthrough, the gas migration process is represented by steady state flow along pressure-induced preferential pathways, which can be seen by stepwise gas flux that corresponds to the stepwise increase in the gas injection pressure.

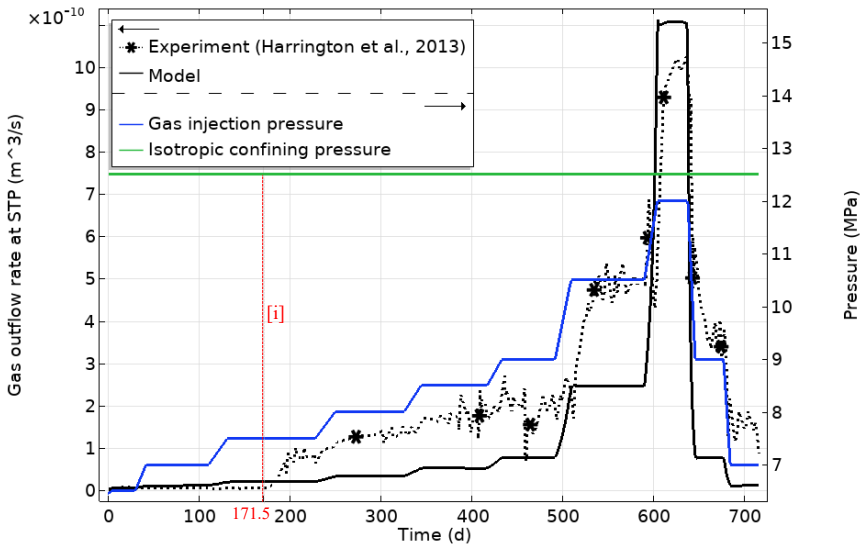

Figure 4.20 Gas outflow rate at STP condition. Note: [i] represents correlation line and related to the onset of major gas breakthrough

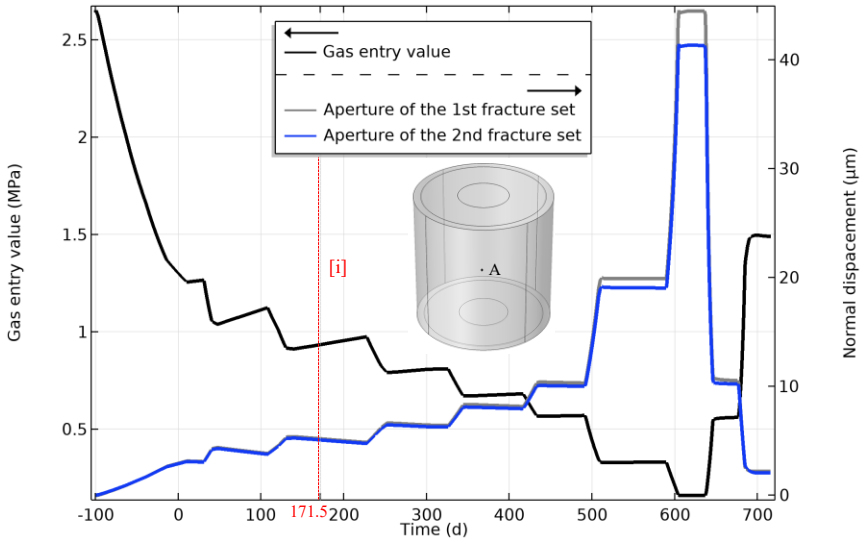

Figure 4.21 Gas entry value and normal displacement of fracture sets at middle point A

Figure 4.22 shows the comparison between modelled pressure and experimental data in the IGR and BGR. As reported by Cuss et al. (2012); Harrington et al. (2013), the pore pressure evolution represented by the observations of guard-ring data is highly complex and no obvious correlation is persistent between IGR and BGR pressure. Thus, it is hard to capture the specific phenomenon by using only one formulation. To get a better explanation of the guard-ring data, the formulations used in the COx-1 test are presented based on the specific experimental interpretation (Harrington et al., 2017; Harrington et al., 2013) and other published modelling work (Mahjoub et al., 2018).

As gas injection process initiates from 6.5 MPa, gas gradually penetrates the sample and reaches the IGR easily along localized pathways, which can be seen by the IGR pressure slightly lower than the gas injection pressure at the initial testing date; see Figure 4.22. As the gas partially interacts with the water-saturated IGR, water is gradually displaced out of the IGR with the increasing gas injection pressure. After the major gas breakthrough occurs, the IGR is almost fully saturated with gas, and then the IGR pressure is represented by the gas pressure. Therefore, the simulated gas pressure in the IGR can well represent the IGR data.

Gas propagates through the sample to as far as the BGR at day 171.5, thus leading to a sudden increase in the BGR pressure; see the red circle in Figure 4.22. This sudden increase indicates the development of new conductive gas pathways. When the gas moves along the existing pathways at a relative steady state, water flows back to the sink until the BGR is saturated with water again. The BGR pressure continues to maintain a constant value, i.e., 4.5

MPa, which is equal to the applied water counterpressure in the BF. Therefore, the simulated water pressure can well represent the BGR pressure.

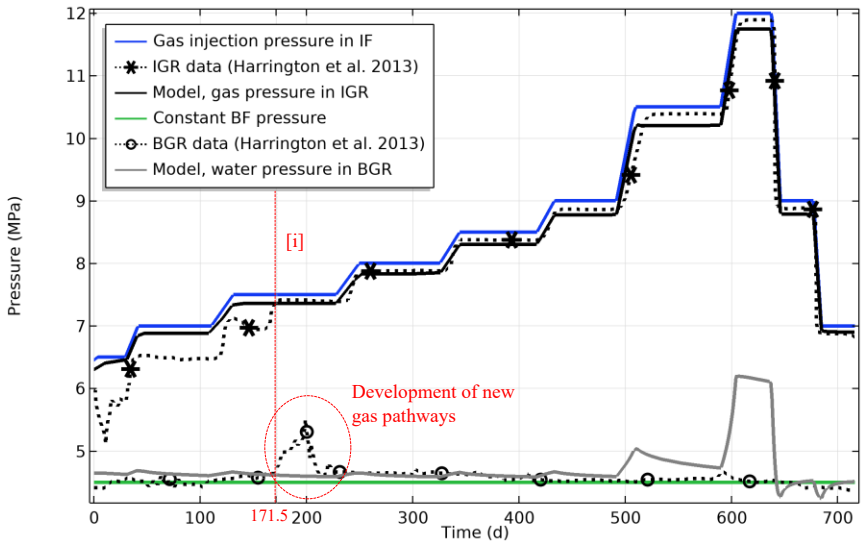

Figure 4.22 Pressure in the IGR and BGR

Figure 4.23 shows the evolution of volumetric strain between simulated results and experimental data, as well as the evolution of vertical intrinsic permeability at different points within the sample. Although the IGR or BGR pressure cannot be represented by the equivalent pore pressure, it acts to have a direct effect on the deformation; see the constitutive relation Eq. (4.50). This direct effect shows a satisfactory agreement between the numerically modeled and experimentally obtained volumetric strain, as shown in Figure 4.23(a). A well-defined increase in volume can be seen in Figure 4.23(a) accompanying the increase of intrinsic permeability (see Figure 4.23(b)), which validates the coupled relation of fracture permeability and mechanical deformation, as captured by the model; see Eqs. (4.52), (4.64) and (4.66). Besides, the area closer to the injection filter shows larger values of vertical intrinsic permeability (see lower point B in Figure 4.23(b)), which represents the inconsistent deformation caused by the gas migration.

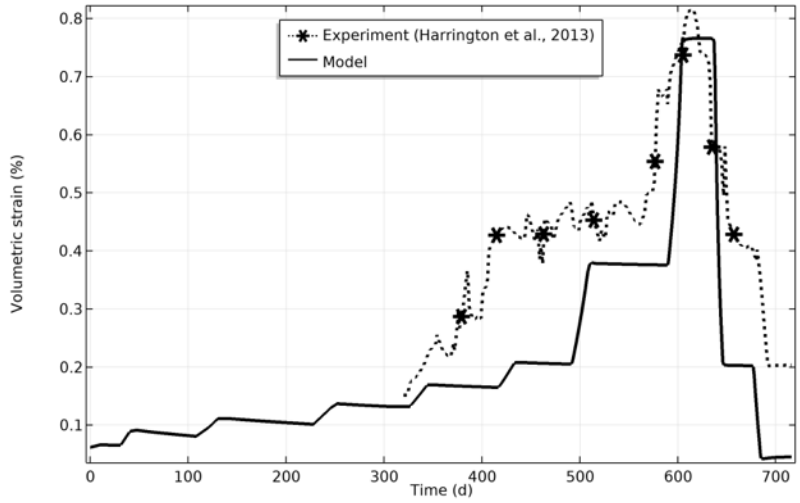

(a) Volumetric strain of the sample

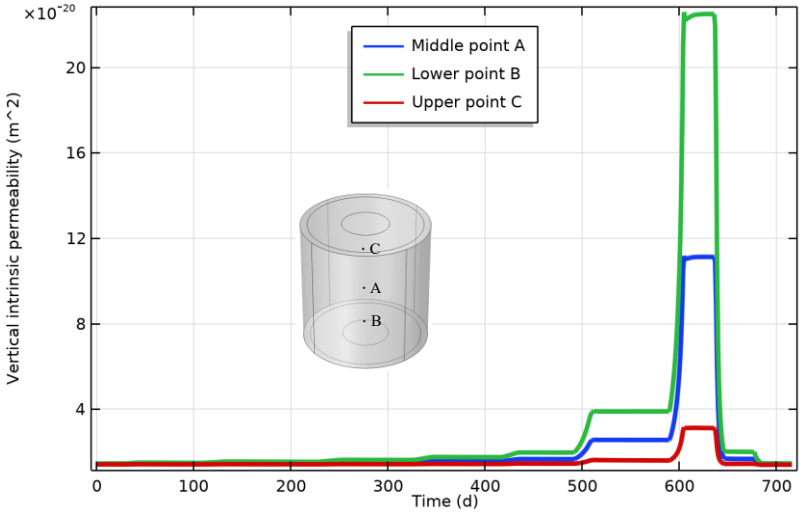

(b) Vertical intrinsic permeability evolution at different points

Figure 4.23 Evolution of volumetric strain and vertical intrinsic permeability

4.3.4.4 Simulation of COx-4 Test

In the COx-4 test, gas injection pressure p_g increased from 1 MPa up to 7 MPa either in constant-flow pressure ramps or in constant-pressure mode over 98 days, and then gas was shut in following the end of the last pumping. The water pressure p_w was controlled with a constant value, i.e., 1 MPa at the BF. The confining pressure was kept at a same value with the axial pressure, i.e., $p_1 = p_3 = 9$ MPa.

4.3.4.4.1 Initial and Boundary Conditions

The COx-4 test is conducted under a similar experimental condition to that in the COx-1 test, but with different confining pressure and gas injection pressure. A 3D model is used to simulate the COx-4 test for same numerical considerations with that in the COx-1 test. The

computational mesh of the domain can be referred to Figure 4.19 as they have the same test apparatus with different sample size and loading conditions. The HM BCs are provided in Table 4-11.

The initial water pressure in the sample was set to 1 MPa, which is equal to the pressure applied on the BF. The initial gas pressure was set to 1.1 MPa to avoid the convergence problem and to initiate the gas flow process. The initial water saturation degree and water-solid interfacial energy are calculated to be 98.7% and 1350 Pa, respectively. Accordingly, the initial equivalent pore pressure is obtained as 1 MPa approximately. The initial Biot's tensor is calculated by considering the initial normal stiffness and spacing of the fracture set, which is determined as $\boldsymbol{\alpha}_0 = (0.75 \quad 0.67 \quad 0.76 \quad 0 \quad 0 \quad 0)^{\mathrm{T}}$. The initial effective stress tensor is determined to be $\boldsymbol{\sigma}_0 = (-8.25 \quad -8.33 \quad -8.24 \quad 0 \quad 0 \quad 0)^{\mathrm{T}}$ MPa. From Eq. (4.52), the initial mechanical aperture of the two fracture sets can be calculated as -1.89×10^{-5} m for the 1st set and -1.88×10^{-5} m for the 2nd set, respectively. The initial intrinsic permeability of two fracture sets are set to have the same value with that in COx-1 test, i.e., 2.03×10^{-23} m^2, which gives an initial value of hydraulic aperture, see Eq. (4.64), to initiate the fluid flow process in fractures.

Table 4-11 The HM BCs for COx-4 test

Boundary	Hydraulic boundary		Mechanical boundary
	Gas pressure	Water pressure	
IF bottom	Controlled pressure	No flow	-
BF top	1.1 [MPa]	1.0 [MPa]	-
Remaining area	No flow	No flow	-
Sample bottom	-	-	Roller with three points fixed
Sample top	-	-	9.0 [MPa]
Sample lateral	-	-	9.0 [MPa]

4.3.4.4.2 Results and Discussion

Figure 4.24 shows a comparison between the simulated and experimental results with respect to the gas injection pressure and gas flux, respectively. The simulated results agree well with the experimental data in general, but the model overestimates the gas flux at the breakthrough timing (approximately at day 59.3), which may be attributed to the relatively large value of fracture opening size in the model. In the simulation of the gas injection process, the increase of gas pressure is applied through three ramp functions, while the actual increase of gas pressure is applied through a constant flow mode; see event of gas pumping in Figure 4.24(a). The discrepancy means that the applied gas pressure may be affected by the gas flux out of the vessel, as gas can penetrate the sample depending on the gas entry value and gas permeability.

This is the reason that gas pressure increases in a linear form in the model, while it is in a nonlinear form in the actual experiment; see Figure 4.24(a).

After reaching the peak value, both the simulated gas pressure and flow rate show rapid decay and then quickly realize an asymptote value, as can be seen in Figure 4.24(b). However, this asymptote value is not fully realized in the experiment, which shows the incapability of forming interconnected gas pathways. The discrepancy represents that the actual gas preferential pathways close more quickly than the fracture closure in the simulated case once gas was shut in, thus leading to less gas flux flowing from the inlet to the outlet and subsequent higher gas pressure in the vessel than that in the simulated case. Further improvements need to be made in future studies to capture the unstable dynamic behavior of gas pathways.

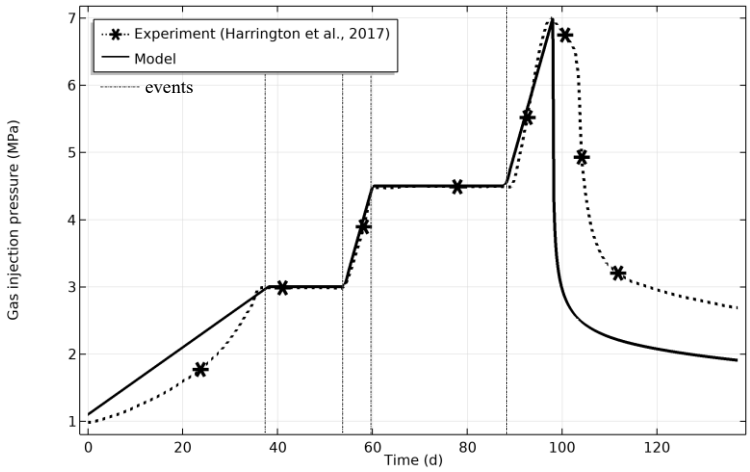

(a) Gas injection pressure

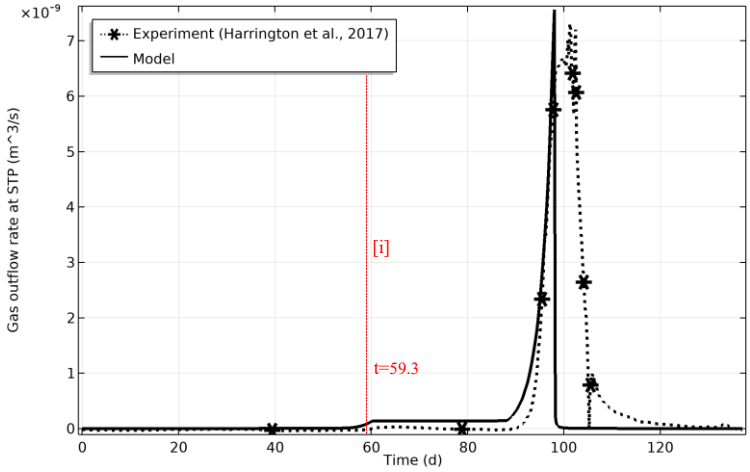

(b) Gas outflow rate

Figure 4.24 Comparison between simulated and experimental results. Note: [i] represents correlation line and related to the onset of gas breakthrough

Figure 4.25 shows the mechanical behavior (i.e., change of aperture and normal stiffness) of

the 1st fracture set in the gas migration process. Accompanying every event of applied gas pressure, the fracture either gradually opens at constant flow mode as it is an unloading process or keeps with the same aperture at constant pressure mode; see Figure 4.25(a). The trend in the change of normal displacement is similar to that in the change of gas injection pressure; see Figure 4.24(a). Corresponding to the fracture opening/closure, the normal stiffness either decreases when fracture continues opening or keeps with the same value when no changes occur on the aperture according to the relation in Eq. (4.53), as can be seen in Figure 4.25(b). After the gas was shut in, the fracture quickly closes and the aperture decreases to a value close to that at the initial state, thus resulting in a rapid increase of normal stiffness; see Figure 4.25(b).

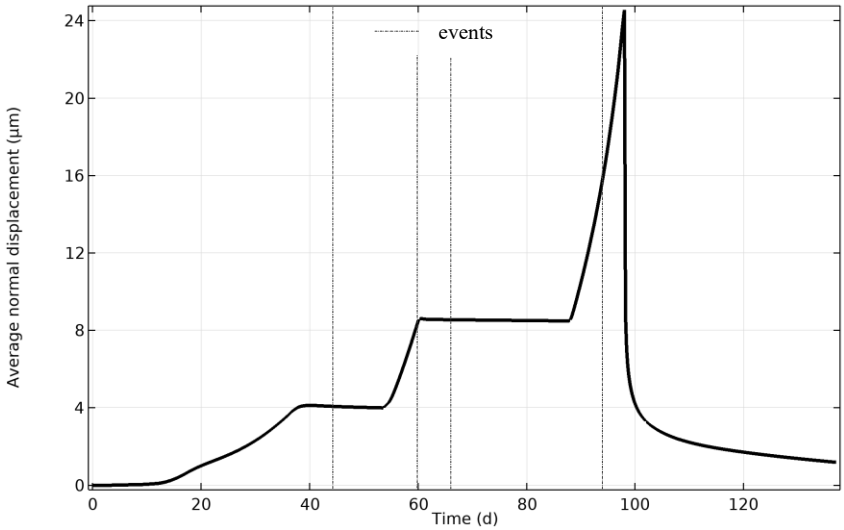

(a) Average normal displacement

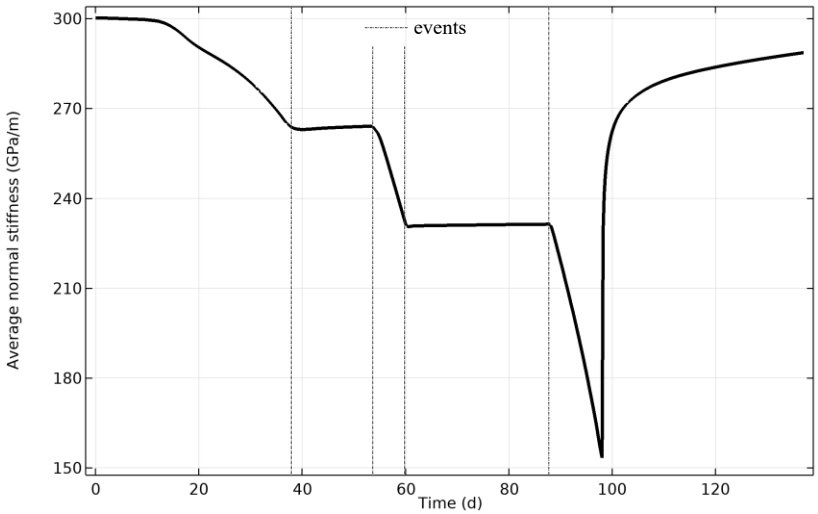

(b) Average normal stiffness

Figure 4.25 Mechanical behavior of the 1st fracture set

4.3.4.5 Simulation of SPP_COx-2 Test

In the SPP_COx-2 test, gas injection pressure p_g increased from 4.5 MPa up to 10.5 MPa either in constant-flow pressure ramps or in constant-pressure mode. The water pressure p_w was controlled with a constant value, i.e., 4.5 MPa at the BF. The axial pressure was kept at a constant value with 0.5 MPa higher than the confining pressure throughout the test, i.e., $p_1 = 13$ MPa, $p_3 = 12.5$ MPa.

4.3.4.5.1 Initial and Boundary Conditions

Aside from the aforementioned numerical considerations in the COx-1 and COx-4 tests, the 2D axisymmetric model also cannot capture the anisotropic deformation along the radial direction, which is a significant phenomenon in the SPP_COx-2 test. Therefore, a 3D model with anisotropic HM properties is also adopted here to simulate the SPP_COx-2 test. The computational mesh of the domain in SPP_COx-2 test is similar to that in COx-1 test, as shown in Figure 4.19. The detailed HM boundary conditions can be referred to in Table 4-12.

The initial water pressure in the sample was set to 4.5 MPa, which is equal to the pressure applied on the BF. The initial gas pressure was set to 5.0 MPa, which was a little higher than the water pressure to avoid the convergence problem and to initiate the gas flow process. Although the initial capillary pressure is calculated to be 0.5 MPa, the corresponding initial water saturation degree is 99.4% which still represents an almost saturated condition of the sample. Accordingly, the initial water-solid interfacial energy and equivalent pore pressure are calculated to be 3178 Pa and 4.5 MPa, respectively. The initial Biot's tensor is calculated by considering the initial normal stiffness and spacing of the fracture set, which is determined as $\boldsymbol{\alpha}_0 = (0.76 \quad 0.67 \quad 0.75 \quad 0 \quad 0 \quad 0)^{\mathrm{T}}$. The initial effective stress tensor is determined to be $\boldsymbol{\sigma}_0 = (-9.08 \quad -9.49 \quad -9.63 \quad 0 \quad 0 \quad 0)^{\mathrm{T}}$ MPa. The initial mechanical aperture of the two fracture sets is calculated to be -1.76×10^{-5} m for the 1st set and -1.82×10^{-5} m for the 2nd set, respectively. The initial intrinsic permeability of two fracture sets is set to have the same value with that in the COx-1 test, i.e., 2.03×10^{-23} m^2, to initiate the fluid flow process in fractures.

Table 4-12 The HM BCs for SPP_COx-2 test

Boundary	Hydraulic boundary		Mechanical boundary
	Gas pressure	Water pressure	
IF bottom	Controlled pressure	No flow	-
BF top	5.0 [MPa]	4.5 [MPa]	-
Remaining area	No flow	No flow	-
Sample bottom	-	-	Roller with three points fixed

Sample top	-	-	13.0 [MPa]
Sample lateral	-	-	12.5 [MPa]

4.3.4.5.2 Results and Discussion

Figure 4.26 shows the comparison of pressure in the IGR and BGR between simulated and experimental results. Although the simulated gas pressure and equivalent pore pressure cannot fully capture the rapid increase of the IGR and BGR pressure, the model still provides some other satisfactory results. In the model, the fracture opening/closure is fully controlled by the normal stress change; see Eq. (4.52). As gas is injected in the IF, gas gradually migrates along the existed fractures with increasing gas pressure. This unloading process leads to the increasing of effective stress, as can be seen from Eq. (4.50), which causes the fracture to open correspondingly. Once the gas penetrates to the IGR area, the gas pressure in the IGR increases nonlinearly, as can be seen in Figure 4.26.

As reported by Cuss et al. (2012, 2014), the evolution of BGR pressure was interpreted as the HM coupled response due to gas penetration. Thus, the equivalent pore pressure may be a good choice to capture the change. Although the response of simulated equivalent pore pressure begins at a similar time with that in the experiment, at about day 255, which is indicative of the start of the coupling process between gas migration and fracture opening. However, the change rate is much smaller than expected due to the aforementioned fracture behavior. Compared with the early stabilized BGR pressure at 6.5 MPa in the experiment, the simulated asymptote value, i.e., 6.1 MPa, is finally reached at around day 310) Further work needs to be done in the future to totally capture the complex evolution of pressure observed in the IGR and BGR.

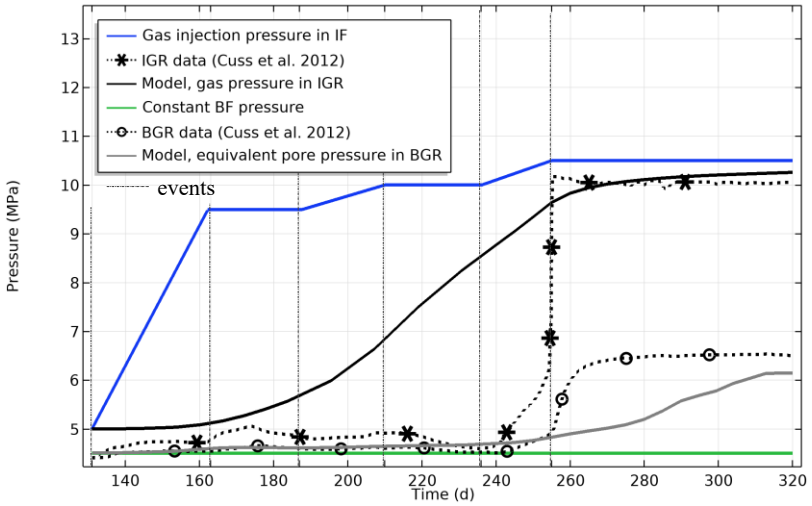

Figure 4.26 Comparison of IGR pressure between simulated and experimental results

Figure 4.27 represents the distribution of gas pressure and gas flux at different times. At the initial state, gas pressure is kept to a uniform value, i.e., 5 MPa, so no gas flux occurs. At the second gas pumping time, i.e., day 187 corresponding to the third event shown in Figure 4.26, gas penetrates the sample through the IF and concentrates in the IF area. At the third gas pumping time, day 236 in the fifth event, gas gradually migrates in both directions. With continuous increasing of gas injection pressure, large amounts of gas flow into the sample and reach the middle area of the sample, accompanied by the sample volume dilation; see Figure 4.27(d). As time elapses, gas almost penetrates the BF area; see Figure 4.27(e). And the preferential gas pathways are along the axial center of sample, as can be seen in Figure 4.27(e), (f), i.e., the more concentrated arrow line in the central area than that in the sidewall area. This phenomenon occurs for two reasons: (1) a straight way from the inlet to the outlet is the shortest distance for gas transport, and (2) the direction of the first pre-inserted fracture set (i.e., β_{f1}=0° in Figure 4.16) is along the sample axis, which provides a preferential pathway for gas movement. This characteristic of gas propagation can be also observed from the symmetry of radial deformation; see Figure 4.29, which has been reported by Cuss et al. (2012).

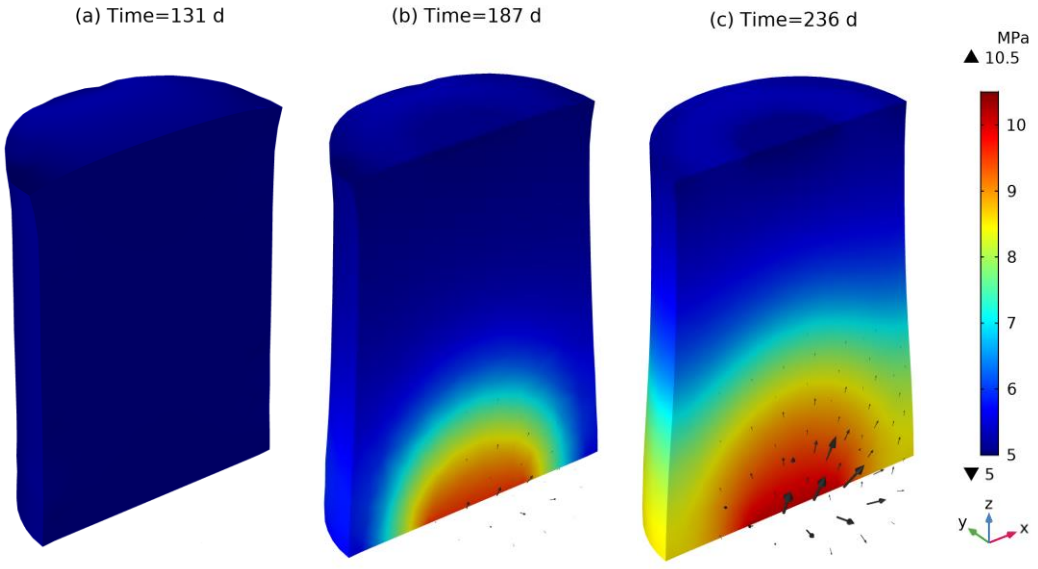

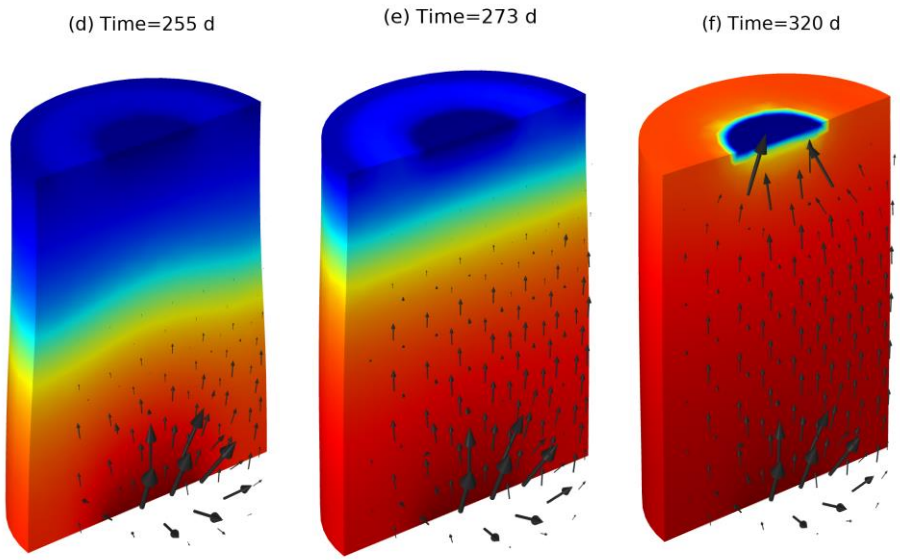

Figure 4.27 The distribution of gas pressure and flux at different time (arrow line represents gas velocity)

Figure 4.28 represents the normal displacement of two fracture sets at middle point A. Based on the general model proposed by Cuss et al. (2012, 2014), the fracture response due to gas injection is also divided into three stages: fracture initiation, acceleration and stabilization. In the stage of fracture initiation, gas gradually enters the sample, and the fracture opening initiates at a slow rate. Due to the anisotropic material properties, the different change in sample deformation causes the different change in normal stress of the fracture set, thus leading to slightly different opening sizes of the two fracture sets. In the acceleration stage, large amounts of gas flow into the sample, which causes the accelerating deformation of fracture in the normal direction. In the last stage of stabilization, fracture behavior becomes stable as gas has already propagated throughout the sample and kept flowing out of the sample at a steady state.

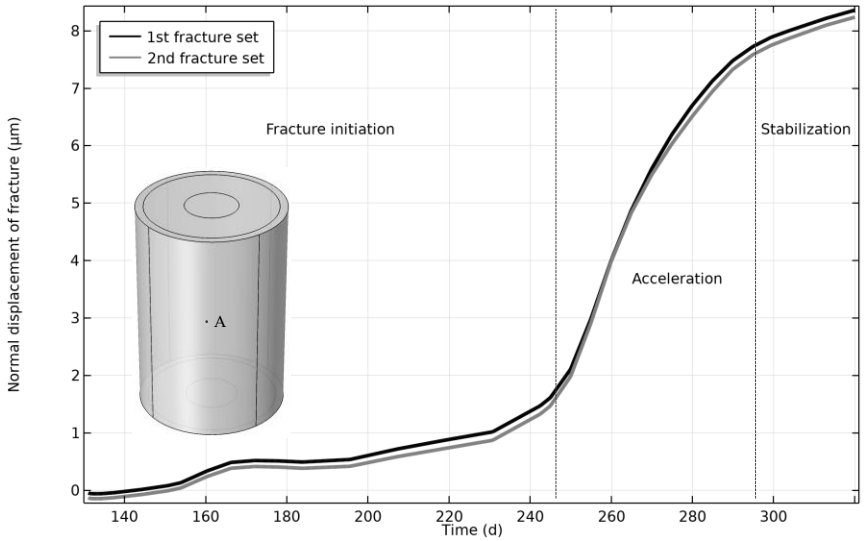

Figure 4.28 Normal displacement of two fracture sets

Figure 4.29 shows the comparison of radial deformation between simulated and experimental results. Figure 4.30 shows the comparison between simulated and experimental results of strain data. Generally, both the simulated displacement and strain results get an overall agreement with the experimental data. Thanks to the inherent bedding of rock matrix and the introduced fracture sets, the determined compliance tensor is significantly anisotropic, see Figure 4.17, thus leading to anisotropic radial deformation. Besides, the symmetric radial deformation also corresponds to the direction of gas flow pathways which are mainly concentrated upon the sample axis area, as can be seen from the gas velocity direction in Figure 4.27(e), (f).

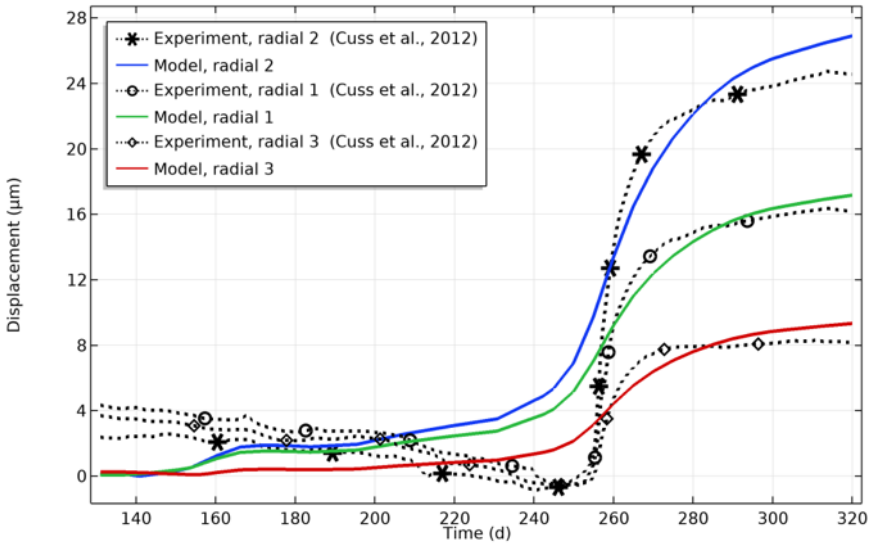

Figure 4.29 The radial deformation of the sample

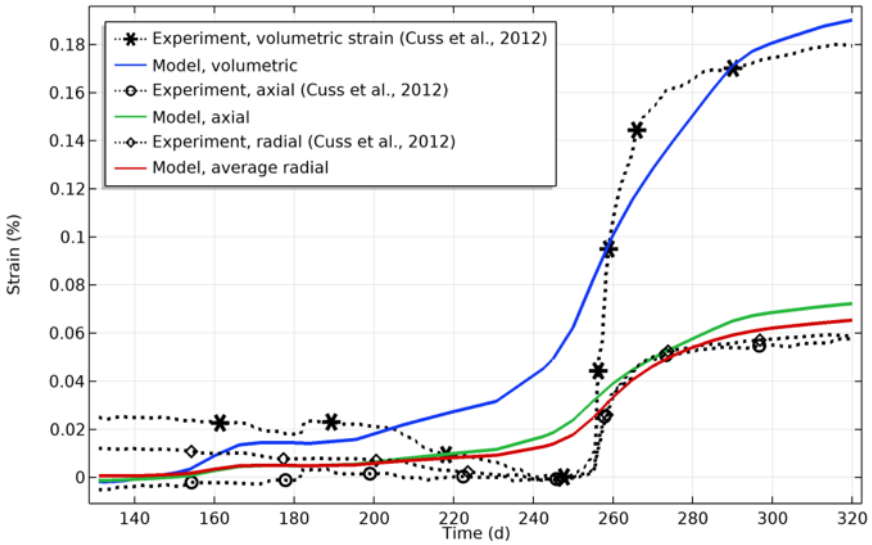

Figure 4.30 Comparison between simulated and experimental results of strain data

4.3.5 Conclusions

A fully coupled hydro-mechanical (HM) model is presented here to simulate the gas migration in initially saturated claystone with considerable anisotropy. The governing equations including mass conservation, momentum balance and energy conservation are presented for the unsaturated rock containing three-phases, i.e., gas, water and solid grain. The constitutive model is proposed by considering the effects of both solid matrix and the fracture set. The fractured rock is regarded as an equivalent continuum consisting of solid matrix and fractures, in which two conceptualized fracture sets are assumed to be pre-existing with constant spacing in the REV. The fracture shows nonlinear mechanical behavior in the normal direction, fracture permeability is controlled by cubic law. The HM behavior of fracture is coupled through the mechanical aperture and hydraulic aperture, which have a superposed effect on the HM behavior of solid matrix. As the 2D axisymmetric model cannot represent the phenomenon of larger fracture opening size close to the gas injection inlet due to the existence of the constant symmetrical axis, also it cannot capture the anisotropic deformation along the radial direction, thus a model with three-dimensional geometry is provided here.

The developed model is evaluated against three laboratory gas injection tests on initially saturated COx claystone, i.e., intact sample COx-1, designated fractured sample COx-4, triaxial condition tested sample SPP_COx-2. In general, the simulated results are in good agreement with that in all three experimental studies. The pressure evolution in the IGR and BGR is specifically represented by the simulated fluid pressure, i.e., gas pressure, water pressure, or

equivalent pore pressure. The fracture opening/closure is governed by the gas injection pressure as it acts to influence the effective stress of the solid matrix. Correspondingly, the normal stiffness of fracture decreases with the aperture opening which has an implicit weakening effect on the compliance tensor of the equivalent continuum, thus leading to the volume dilation. The dual effects of the matrix containing inherent bedding and fracture induced stiffness reduction cause the anisotropic deformation in the radial direction, which is well represented by the proposed 3D model.

In summary, the developed HM model has well captured the key experimental observations, i.e., anisotropic radial deformation, major gas breakthrough, and mechanical volume dilation of the sample, offered additional insight into the mathematical relation between gas flow, solid matrix deformation and fracture opening/closure. However, the numerical model either slightly underestimates or overestimates the gas flux for the whole gas migration process, which shows the difficulty of modeling the dynamic behavior of dilatant gas pathways. Further improvements can be made in future studies by introducing the heterogeneous HM properties, which can better represent the real condition. Moreover, the fracture propagation law as well as thermodynamically consistent damage model can be taken into account to improve the model performance, which will be performed in our future work.

4.3.6 Acknowledgements

The authors gratefully acknowledge funding from a joint program supported by the China Scholarship Council and University of Ottawa. Moreover, the authors thank the Natural Sciences and Engineering Research Council of Canada (NSERC) for financially supporting this research.

4.3.7 References

Abdi, H., Labrie, D., Nguyen, T.S., Barnichon, J.D., Su, G., Evgin, E., Simon, R., Fall, M., 2015. Laboratory investigation on the mechanical behaviour of Tournemire argillite. Canadian Geotechnical Journal 52, 268-282.

Aichi, M., Tokunaga, T., 2012. Material coefficients of multiphase thermoporoelasticity for anisotropic micro-heterogeneous porous media. International Journal of Solids and Structures 49, 3388-3396.

Alvarez, T.A., Cording, E.J., Mikhail, R.A., 1995. Hydromechanical behavior of rock joints: A re-interpretation of published experiments. A a Balkema, Rotterdam.

Amadei, B., Goodman, R.E., 1981. A 3-D constitutive relation for fractured rock masses, Proceedings of the international symposium on the mechanical behavior of structured media, Ottawa, pp. 249-268.

Andra, 2005. Dossier 2005 Argile: Re´fe´rentiel du site de Meuse/Haute-Marne, Tome 2: Caracte´risation comportementale du milieu ge´ologique sous perturbation.

Angeli, M., Soldal, M., Skurtveit, E., Aker, E., 2009. Experimental percolation of supercritical CO2 through a caprock. Energy Procedia 1, 3351-3358.

Arnedo, D., Alonso, E.E., Olivella, S., 2013. Gas flow in anisotropic claystone: Modelling triaxial experiments.

International Journal for Numerical and Analytical Methods in Geomechanics 37, 2239-2256.
Asgian, M., 1989. A numerical model of fluid-flow in deformable naturally fractured rock masses. International Journal of Rock Mechanics and Mining Sciences and 26, 317-328.
Bandis, S.C., Lumsden, A.C., Barton, N.R., 1983. Fundamentals of rock joint deformation. International Journal of Rock Mechanics and Mining Sciences & Geomechanics Abstracts 20, 249-268.
Belmokhtar, M., Delage, P., Ghabezloo, S., Tang, A.-M., Menaceur, H., Conil, N., 2017. Poroelasticity of the Callovo–Oxfordian Claystone. Rock Mechanics and Rock Engineering 50, 871-889.
Berre, I., Doster, F., Keilegavlen, E., 2018. Flow in Fractured Porous Media: A Review of Conceptual Models and Discretization Approaches. Transport in Porous Media 130, 215-236.
Berrone, S., Fidelibus, C., Pieraccini, S., Scialò, S., Vicini, F., 2018. Unsteady advection-diffusion simulations in complex Discrete Fracture Networks with an optimization approach. Journal of Hydrology 566, 332-345.
Bertrand, F., Cerfontaine, B., Collin, F., 2017. A fully coupled hydro-mechanical model for the modeling of coalbed methane recovery. Journal of Natural Gas Science and Engineering 46, 307-325.
Brooks, R.H., Corey, A.T., 1964. Hydraulic properties of porous media. Colorado State University, Fort Collins, Colorado.
Bui, T.A., Wong, H., Deleruyelle, F., Xie, L.Z., Tran, D.T., 2017. A thermodynamically consistent model accounting for viscoplastic creep and anisotropic damage in unsaturated rocks. International Journal of Solids and Structures 117, 26-38.
Cammarata, G., Fidelibus, C., Cravero, M., Barla, G., 2007. The Hydro-Mechanically Coupled Response of Rock Fractures. Rock Mechanics and Rock Engineering 40, 41-61.
Cappa, F., Guglielmi, Y., Rutqvist, J., Tsang, C.-F., Thoraval, A., 2008. Estimation of fracture flow parameters through numerical analysis of hydromechanical pressure pulses. Water Resources Research 44, W11408-W11408.
Carman, P.C., 1937. Fluid flow through granular beds. Trans. Inst. Chem. Eng. 15, 150-166.
Charlier, R., Collin, F., Pardoen, B., Talandier, J., Radu, J.P.J.P., Gerard, P., 2013. An unsaturated hydro-mechanical modelling of two in-situ experiments in Callovo-Oxfordian argillite. Engineering Geology 165, 46-63.
Chasset, C., Jarsjö, J., Erlström, M., Cvetkovic, V., Destouni, G., 2011. Scenario simulations of CO2 injection feasibility, plume migration and storage in a saline aquifer, Scania, Sweden. International Journal of Greenhouse Gas Control 5, 1303-1318.
Cheng, A.H.D., 1997. Material coefficients of anisotropic poroelasticity. International Journal of Rock Mechanics and Mining Sciences 34, 199-205.
Coussy, O., 2004. Poromechanics. John Wiley & Sons, Chichester, England.
Coussy, O., 2007. Revisiting the constitutive equations of unsaturated porous solids using a Lagrangian saturation concept. International Journal for Numerical and Analytical Methods in Geomechanics 31, 1675-1694.
Cuss, R., Harrington, J., Giot, R., Auvray, C., 2014. Experimental observations of mechanical dilation at the onset of gas flow in Callovo-Oxfordian claystone. Geological Society Special Publication 400, 507-519.
Cuss, R.C., Harrington, J.F., Noy, D.J., 2012. Final report of FORGE WP4.1.1: The stress-path permeameter experiment conducted on Callovo-Oxfordian Claystone. British Geological Survey Commissioned Report, CR/12/140.
Dershowitz, W.S., Fidelibus, C., 1999. Derivation of equivalent pipe network analogues for three-dimensional discrete fracture networks by the boundary element method. Water Resources Research 35, 2685-2691.
Detournay, E., 1980. HYDRAULIC CONDUCTIVITY OF CLOSED ROCK FRACTURE: AN EXPERIMENTAL AND ANALYTICAL STUDY. CIM, Montreal, Que, pp. 168-173.
Faivre, M., Paul, B., Golfier, F., Giot, R., Massin, P., Colombo, D., 2016. 2D coupled HM-XFEM modeling with cohesive zone model and applications to fluid-driven fracture network. Engineering Fracture Mechanics 159, 115-143.
Fall, M., Nasir, O., Nguyen, T.S., 2014. A coupled hydro-mechanical model for simulation of gas migration in host sedimentary rocks for nuclear waste repositories. Engineering Geology 176, 24-44.
Fidelibus, C., 2007. The 2D hydro-mechanically coupled response of a rock mass with fractures via a mixed BEM-FEM technique. International Journal for Numerical and Analytical Methods in Geomechanics 31, 1329-1348.
Fu, P., Johnson, S.M., Carrigan, C.R., 2013. An explicitly coupled hydro-geomechanical model for simulating hydraulic fracturing in arbitrary discrete fracture networks. International Journal for Numerical and Analytical Methods in Geomechanics 37, 2278-2300.
Gerard, P., Harrington, J., Charlier, R., Collin, F., 2014. Modelling of localised gas preferential pathways in claystone. International Journal of Rock Mechanics and Mining Sciences 67, 104-114.
Ghabezloo, S., Sulem, J., Guédon, S., Martineau, F., Saint-Marc, J., 2008. Poromechanical behaviour of hardened

cement paste under isotropic loading. Cement and Concrete Research 38, 1424-1437.
Ghaffari, H.O., Sharifzadeh, M., Fall, M., 2010. Analysis of aperture evolution in a rock joint using a complex network approach. International Journal of Rock Mechanics and Mining Sciences 47, 17-29.
Gonzalez-Blanco, L., Romero, E., Jommi, C., Li, X., Sillen, X., 2016. Gas migration in a Cenozoic clay: Experimental results and numerical modelling. Geomechanics for Energy and the Environment 6, 81-100.
Guayacán-Carrillo, L.-M., Ghabezloo, S., Sulem, J., Seyedi, D.M., Armand, G., 2017. Effect of anisotropy and hydro-mechanical couplings on pore pressure evolution during tunnel excavation in low-permeability ground. International Journal of Rock Mechanics and Mining Sciences 97, 1-14.
Guglielmi, Y., Elsworth, D., Cappa, F., Henry, P., Gout, C., Dick, P., Durand, J., 2015. In situ observations on the coupling between hydraulic diffusivity and displacements during fault reactivation in shales. Journal of Geophysical Research: Solid Earth 120, 7729-7748.
Guo, G., Fall, M., 2018. Modelling of dilatancy-controlled gas flow in saturated bentonite with double porosity and double effective stress concepts. Engineering Geology 243, 253-271.
Guo, G., Fall, M., 2019. Modelling of preferential gas flow in heterogeneous and saturated bentonite based on phase field method. Computers and Geotechnics 116, 103206.
Harrington, J.F., Cuss, R.J., Talandier, J., 2017. Gas transport properties through intact and fractured Callovo-Oxfordian mudstones. Geological Society Special Publication 454, 131-154.
Harrington, J.F., de la Vaissière, R., Noy, D.J., Cuss, R.J., Talandier, J., 2012a. Gas flow in Callovo-Oxfordian claystone (COx): Results from laboratory and field-scale measurements. Mineralogical Magazine 76, 3303-3318.
Harrington, J.F., Milodowski, A.E., Graham, C.C., Rushton, J.C., Cuss, R.J., 2012b. Evidence for gas-induced pathways in clay using a nanoparticle injection technique. Mineralogical Magazine 76, 3327-3336.
Harrington, J.F., Noy, D.J., Cuss, R.C., 2013. Callovo-Oxfordian Claystone: processes governing advective gas flow. British Geological Survey Commissioned Report, CR/13/088.
Homand, F., Shao, J.-F., Giraud, A., Auvray, C., Hoxha, D., 2006. Pétrofabrique et propriétés mécaniques des argilites. Comptes Rendus Geoscience 338, 882-891.
Hu, D., Zhou, H., Zhang, F., Shao, J., Zhang, J., 2013. Modeling of inherent anisotropic behavior of partially saturated clayey rocks. Computers and Geotechnics 48, 29-40.
Lei, Q., Latham, J.-P., Tsang, C.-F., 2017. The use of discrete fracture networks for modelling coupled geomechanical and hydrological behaviour of fractured rocks. Computers and Geotechnics 85, 151-176.
Lenti, V., Fidelibus, C., 2003. A BEM solution of steady-state flow problems in discrete fracture networks with minimization of core storage. Computers and Geosciences 29, 1183-1190.
Lisjak, A., Grasselli, G., Vietor, T., 2014. Continuum-discontinuum analysis of failure mechanisms around unsupported circular excavations in anisotropic clay shales. International Journal of Rock Mechanics and Mining Sciences 65, 96-115.
Lisjak, A., Tatone, B.S.A., Mahabadi, O.K., Grasselli, G., Marschall, P., Lanyon, G.W., Vaissière, R.d.l., Shao, H., Leung, H., Nussbaum, C., 2016. Hybrid Finite-Discrete Element Simulation of the EDZ Formation and Mechanical Sealing Process Around a Microtunnel in Opalinus Clay. Rock Mechanics and Rock Engineering 49, 1849-1873.
Liu, H.-H., Rutqvist, J., Berryman, J.G., 2009. On the relationship between stress and elastic strain for porous and fractured rock. International Journal of Rock Mechanics and Mining Sciences 46, 289-296.
Liu, H.-H., Wei, M.-Y., Rutqvist, J., 2013. Normal-stress dependence of fracture hydraulic properties including two-phase flow properties. Hydrogeology Journal 21, 371-382.
Mahjoub, M., Rouabhi, A., Tijani, M., Granet, S., M'Jahad, S., Talandier, J., M'Jahad, S., Talandier, J., 2018. Numerical Study of Callovo-Oxfordian Argillite Expansion due to Gas Injection. International Journal of Geomechanics 18.
Marschall, P., Horseman, S., Gimmi, T., 2005. Characterisation of gas transport properties of the Opalinus clay, a potential host rock formation for radioactive waste disposal. Oil and Gas Science and Technology 60, 121-139.
Martinez, M.J., Newell, P., Bishop, J.E., Turner, D.Z., 2013. Coupled multiphase flow and geomechanics model for analysis of joint reactivation during CO2 sequestration operations. International Journal of Greenhouse Gas Control 17, 148-160.
Mualem, Y., 1976. A new model for predicting the hydraulic conductivity of unsaturated porous media. Water Resources Research 12, 513-522.
Munjiza, A., Latham, J.P., Andrews, K.R.F., 2000. Detonation gas model for combined finite-discrete element simulation of fracture and fragmentation. International Journal for Numerical Methods in Engineering 49, 1495-1520.

NAGRA, 2008. Effects of post-disposal gas generation in a repository for low- and intermediate-level waste sited in the Opalinus Clay of Northern Switzerland. National Cooperative for the Disposal of Radioactive Waste (NAGRA).
Nasir, O., Fall, M., Nguyen, S.T., Evgin, E., 2013. Modeling of the thermo-hydro-mechanical-chemical response of sedimentary rocks to past glaciations. International Journal of Rock Mechanics and Mining Sciences 64, 160-174.
Nasir, O., Fall, M., Nguyen, T.S., Evgin, E., 2011. Modelling of the hydro-mechanical response of sedimentary rocks of southern Ontario to past glaciations. Engineering Geology 123, 271-287.
Nasir, O., Fall, M., Nguyen, T.S., Evgin, E., 2015. Modeling of the thermohydromechanical-chemical response of Ontario sedimentary rocks to future glaciations. Canadian Geotechnical Journal 52, 836-850.
Nguyen, T.S., Le, A.D., 2015. Simultaneous gas and water flow in a damage-susceptible bedded argillaceous rock. Canadian Geotechnical Journal 52, 18-32.
Olivella, S., Alonso, E.E., 2008. Gas flow through clay barriers. Géotechnique 58, 157-176.
Paluszny, A., Salimzadeh, S., Zimmerman, R.W., 2018. Finite-Element Modeling of the Growth and Interaction of Hydraulic Fractures in Poroelastic Rock Formations, Hydraulic Fracture Modeling. Elsevier, pp. 1-19.
Pardoen, B., Seyedi, D.M., Collin, F., 2015. Shear banding modelling in cross-anisotropic rocks. International Journal of Solids and Structures 72, 63-87.
Pazdniakou, A., Dymitrowska, M., 2018. Migration of Gas in Water Saturated Clays by Coupled Hydraulic-Mechanical Model. Geofluids 2018, 1-25.
Popp, T., Wiedemann, M., Böhnel, H., Minkley, W., Manthei, G., 2007. Untersuchungen zur Barriereintegrität im Hinblick auf das Ein-Endlager-Konzept. Insitut fur Gebirgsmechanik GmbH, Leipzig, Germany.
Pouya, A., Vo, T.D., Hemmati, S., Tang, A.M., 2019. Modeling soil desiccation cracking by analytical and numerical approaches. International Journal for Numerical and Analytical Methods in Geomechanics 43, 738-763.
Rozhko, A.Y., 2016. Two-phase fluid-flow modeling in a dilatant crack-like pathway. Journal of Petroleum Science and Engineering 146, 1158-1172.
Salimzadeh, S., Khalili, N., 2015. A three-phase XFEM model for hydraulic fracturing with cohesive crack propagation. Computers and Geotechnics 69, 82-92.
Segura, J.M., Carol, I., 2010. Numerical modelling of pressurized fracture evolution in concrete using zero-thickness interface elements. Engineering Fracture Mechanics 77, 1386-1399.
Senger, R., Romero, E., Ferrari, A., Marschall, P., 2014. Characterization of gas flow through low-permeability claystone: laboratory experiments and two-phase flow analyses. Geological Society Special Publication 400, 531-543.
Senger, R., Romero, E., Marschall, P., 2018. Modeling of Gas Migration Through Low-Permeability Clay Rock Using Information on Pressure and Deformation from Fast Air Injection Tests. Transport in Porous Media 123, 1-17.
Shaw, R.P., 2015. The Fate of Repository Gases (FORGE) project. Geological Society Special Publication 415, 1-7.
Skurtveit, E., Aker, E., Soldal, M., Angeli, M., Wang, Z., 2012. Experimental investigation of CO2 breakthrough and flow mechanisms in shale. Petroleum Geoscience 18, 3-15.
Souley, M., Homand, F., Amadei, B., 1995. An extension to the Saeb and Amadei constitutive model for rock joints to include cyclic loading paths. International Journal of Rock Mechanics and Mining Sciences & Geomechanics Abstracts 32, 101-109.
Sun, Z.-x., Zhang, X., Xu, Y., Yao, J., Wang, H.-x., Lv, S., Sun, Z.-l., Huang, Y., Cai, M.-y., Huang, X., 2017. Numerical simulation of the heat extraction in EGS with thermal-hydraulic-mechanical coupling method based on discrete fractures model. Energy 120, 20-33.
van Genuchten, M.T., 1980. A closed-form equation for predicting the hydraulic conductivity of unsaturated soils. Soil Science Society of America Journal 44, 892-898.
Vo, T.D., Pouya, A., Hemmati, S., Tang, A.M., 2017. Numerical modelling of desiccation cracking of clayey soil using a cohesive fracture method. Computers and Geotechnics 85, 15-27.
Vyazmensky, A., Stead, D., Elmo, D., Moss, A., 2010. Numerical analysis of block caving-induced instability in large open pit slopes: A finite element/discrete element approach. Rock Mechanics and Rock Engineering 43, 21-39.
Wang, H., 2016. Numerical investigation of fracture spacing and sequencing effects on multiple hydraulic fracture interference and coalescence in brittle and ductile reservoir rocks. Engineering Fracture Mechanics 157, 107-124.
Wenk, H.R., Voltolini, M., Mazurek, M., Van Loon, L.R., Vinsot, A., 2008. Preferred Orientations and Anisotropy in Shales: Callovo-Oxfordian Shale (France) and Opalinus Clay (Switzerland). Clays and Clay Minerals 56, 285-

306.
Wiseall, A.C., Cuss, R.J., Graham, C.C., Harrington, J.F., 2015. The visualization of flow paths in experimental studies of clay-rich materials. Mineralogical Magazine 79, 1335-1342.
Witherspoon, P.A., Wang, J.S.Y., Iwai, K., Gale, J.E., 1980. Validity of Cubic Law for fluid flow in a deformable rock fracture. Water Resources Research 16, 1016-1024.
Xu, C., Fidelibus, C., Dowd, P., Wang, Z., Tian, Z., 2018. An iterative procedure for the simulation of the steady-state fluid flow in rock fracture networks. Engineering Geology 242, 160-168.
Xu, W.J., Shao, H., Hesser, J., Wang, W., Schuster, K., Kolditz, O., 2013. Coupled multiphase flow and elasto-plastic modelling of in-situ gas injection experiments in saturated claystone (Mont Terri Rock Laboratory). Engineering Geology 157, 55-68.
Yang, J.P., Chen, W.Z., Wu, G.J., Yang, D.S., 2018. Analytical Estimation of the Equivalent Elastic Compliance Tensor for Fractured Rock Masses. International Journal of Geomechanics 18.
Yang, J.P., Chen, W.Z., Yang, D.S., Tian, H.M., 2016. Estimation of Elastic Moduli of Non-persistent Fractured Rock Masses. Rock Mechanics and Rock Engineering 49, 1977-1983.

Chapter 5 Two-Scale Modelling of Preferential Gas Flow

5.1 Introduction

Although the macroscopic HM framework in Chapter 4 is able to capture the major HM behaviors related to preferential gas flow, the development of gas dilatant pathways is still represented in an implicit way. Despite the significant improvement of Fracture Mechanics to reproduce certain failure characteristics, the theory has limited capacity for capturing complex rupture patterns. The gas induced micro-fracturing in clayey rocks is an example among others. Laboratory observations confirmed that the formation of mode-I micro-fractures occurs at the injected gas pressure significantly lower than the confining pressure and nearly no shear loading is applied. Such specific phenomenon suggests that a HM framework considering micro-crack propagation is appropriate to explicitly simulate the micro-fracturing process. Since it takes place at scales much smaller than the macrostructure, a multiscale approach could be well used to address this issue. Therefore, a two-scale time-dependent damage model is firstly developed under single phase flow condition, to represent the fluid driven fracturing process.

Since the gas induced fracturing occurs in saturated rocks with water, the single phase damage model will be extended to two-phase (water, gas) flow condition. The enriched two-phase flow damage model is expected to explicitly capture the development of gas dilatant pathways under laboratory condition.

5.2 Paper IV: A Two-Scale Time-Dependent Damage Model for Preferential Gas Flow in Clayey Rock Materials

Published in *Mechanics of Materials*, 158, 2021, 103853, doi:10.1016/j.mechmat.2021.103853.

Jianxiong Yang, Mamadou Fall

Department of Civil Engineering, University of Ottawa, Ottawa, ON, Canada

Abstract: Understanding of the gas migration within the host rock is critical for the safety assessment of a deep geological repository for radioactive wastes. However, localized gas flow in clayey host rock materials is a complex behavior associated with dynamic and unstable network of dilatant pathways, which are accompanied by micro-cracking that indicates macroscopic tensile fractures. The subcritical crack propagation at the microscale may represent the mechanism of time dependent damage observed at the macroscale. A two-scale damage model is developed in this study to explicitly simulate the preferential gas flow in clayey rock materials. A homogenization method based on asymptotic developments is employed to deduce the macroscopic damage behavior coupled with the poroelastic system, which initiates from the periodically distributed microstructures with micro-cracks. A time dependent damage evolution law is constructed based on the microscopic phenomena and the corresponding intrinsic permeability model is proposed which implicitly accounts for the fracture opening induced permeability change. The local macroscopic response of the model is analyzed and validated against the experimentally measured direct tensile strength, which illustrates the homogenized elastic and permeability coefficients, and highlights the influence of several parameters, i.e., the initial damage, the microstructural size and the strain rate. Numerical examples are presented in order to illustrate the global macroscopic response, in which a pure mechanical test, i.e., uniaxial tension test is simulated and verified against the laboratory results, then the simulation of preferential gas flow is illustrated together with the comparison of experimental explanation. The numerical results showed that the proposed two-scale model can explicitly simulate the gas induced fracturing, in which the damage propagation and the dilatant gas pathways are well captured.

Keywords: micro-cracks, preferential gas pathways, nuclear waste, coupled processes, time dependent damage, deep geological repository, clayey rock

Nomenclature

Latin symbols

A_t	empirical parameter
b_{ij}	Biot's coefficient tensor
c^*	homogenized specific gas coefficient
C_{ijkl}	stiffness tensor for isotropic solid
C^*_{ijkl}	homogenized stiffness tensor
d	damage variable
d_0	initial damage value
$\mathcal{D}_d$	energy dissipation for damage evolution
$\mathcal{D}_f$	energy dissipation for crack propagation
$\boldsymbol{e}$	unit vector along crack propagation direction in vector format
e_{xij}	macroscopic strain tensor
$\boldsymbol{e}_x$	macroscopic strain tensor in matrix format
e_{yij}	microscopic strain tensor
$\boldsymbol{e}_y$	microscopic strain tensor in matrix format
E	Young's modulus
G_s	thermodynamic potential
$\mathcal{G}^\varepsilon$	energy release rate at the crack tip
$\mathcal{G}_f$	critical fracture energy
k	isotropic intrinsic permeability
k_0	initial intrinsic permeability
k^*_{ij}	homogenized intrinsic permeability tensor
K_0	reference stress intensity factor
K_I	model-I stress intensity factor
K_{Ic}	critical stress intensity factor
l	microcrack length
l_c	size of locally periodic cell
l_q	characteristic length
L_c	size of macrostructure
M	molar mass of gas
n	subcritical growth index
$\boldsymbol{n}$	outward unit vector normal to the circle in vector format
q_{g0}	gas mass flux at outflow boundary
q_i^ε	gas mass flux of heterogeneous porous medium
$\boldsymbol{q}^\varepsilon$	gas mass flux of heterogeneous porous medium in vector format
$q_i^{(r)}$	Y-periodic function of gas mass flux at order r (r=-1, 0, 1 …)
$\boldsymbol{q}^{(r)}$	Y-periodic function of gas mass flux at order r (r=-1, 0, 1 …) in vector format
$Q_i^{(0)}$	macroscopic gas flux
R	universal gas constant
T	absolute temperature
u_i^ε	displacement field of heterogeneous body
$\boldsymbol{u}^\varepsilon$	displacement field of heterogeneous body in vector format
$\boldsymbol{u}^{(r)}$	Y-periodic function of displacement field at order r (r=0, 1, 2 …) in vector format
v_0	reference crack velocity
x_i	macroscopic coordinate
$\boldsymbol{x}$	macroscopic coordinate in vector format
y_i	microscopic coordinate
$\boldsymbol{y}$	microscopic coordinate in vector format
Y_d	damage energy release rate

Greek symbols

α_t	empirical parameter
β_t	empirical parameter
γ_t	fitted linear coefficient
δ_{ij}	Kronecker delta
ε	scale parameter
ζ_i	elementary solution of fluid problem
η	dynamic viscosity of gas
θ	crack orientation angle
λ	Lame coefficient
μ	Lame coefficient
ν	Poisson's ratio
$\boldsymbol{\xi}^{ij}$	characteristic function of elementary deformation modes in vector format
ρ_g	gas density
σ_t	tensile strength
σ_{ij}^ε	total stress field of heterogeneous body

N_i	unit vector normal to crack	$\boldsymbol{\sigma}^{\varepsilon}$	total stress field of heterogeneous body in matrix format
$\boldsymbol{N}$	unit vector normal to crack in vector format	$\sigma_{ij}^{(r)}$	Y -periodic function of total stress tensor at order r (r =-1, 0, 1 …)
p_{cr}	critical gas pressure	$\boldsymbol{\sigma}^{(r)}$	Y -periodic function of total stress tensor at order r (r =-1, 0, 1 …) in matrix format
p^{ε}	gas pressure field of heterogeneous porous medium	ϕ	porosity
$p^{(r)}$	Y -periodic function of gas pressure field at order r (r =0, 1, 2 …)	Σ_{ij}	macroscopic total stress tensor

5.2.1 Introduction

Clayey rock materials, e.g., Opalinus clay, Callovo–Oxfordian claystone, and Boom clay, have been studied as possible geological barriers for nuclear waste disposal due to their thick formation, low permeability and high radionuclide retardation capability (Harrington and Horseman, 1999; Ortiz et al., 2002; Rodwell et al., 1999). During the lifespan of deep geological repositories (DGRs), significant volume of gas may be generated because of metal corrosion, biological degradation, water radiolysis, etc. (Shaw, 2015). The migration of produced gas within the rock materials may jeopardize the stability of DGRs as the gas preferential pathways may form due to the gas induced micro-fractures or macro-fractures (Harrington et al., 2012b, 2017; Wiseall et al., 2015), which in consequence enable the easy transport of the radioactive contaminants and significantly impact the biosphere and groundwater (Johnson et al., 2004).

Recent laboratory experiments have shown that localized gas flow in clayey rocks is a complex behavior, in which it is often associated with dynamic and unstable network of dilatant pathways (Cuss et al., 2014; Harrington et al., 2012a, 2012b, 2013, 2017; Hildenbrand et al., 2002; Wiseall et al., 2015). The dilatant pathways are accompanied by micro-cracking that indicate tensile fractures occur at the macroscopic scale (Cuss et al., 2012, 2014; Hildenbrand et al., 2002), which affects not only the mechanical behavior of the material, e.g., volume dilation and anisotropic deformation, but also the gas flow behavior, e.g., the development of preferential pathways and significant gas outflow at the outlet. Therefore, figuring out the mathematical relation between preferential gas flow and gas induced fracturing may help us better explain the experimental phenomena, which may provide deeper understanding of the real-scale underground disposal problem.

To give some qualitative or quantitative explanations for these laboratory experiments, several numerical research works have been performed to address the preferential gas flow in

clayey rocks. Due to the numerical difficulties caused by a variety of complex physical mechanisms involved, these numerical works are generally conducted from the classical hydro-mechanical (HM) aspects at the macroscopic scale, with none of the works initiated from the multiscale phenomena. For example, Senger et al. (2014, 2018) used modified two-phase flow models to simulate the increase of both pore space and intrinsic permeability due to pathway dilation, but the model cannot capture some more complex phenomena, i.e., gradual decline of gas pressure following the shut-in process and abrupt deformation caused by gas breakthrough. By contrast, the conventional HM models (Fall et al., 2014; Nguyen and Le, 2015; Xu et al., 2013b) may better represent the complex phenomena since some favorable features, e.g., plasticity and damage, may be introduced to capture the influence of rigidity degradation on gas migration. But the proposed plastic or damage model may be limited to a specific gas fracture cycle test conducted by Popp et al. (2007) as the injected gas pressure exceeds the confining pressure, which is a basis for maximum principal stress exceeding the material tensile strength (note: tensile stress is assumed to be positive). To simulate the localized gas pathways under some other general laboratory conditions, the embedded fracture models are proposed (Arnedo et al., 2013; Gerard et al., 2014; Gonzalez-Blanco et al., 2016; Olivella and Alonso, 2008), in which the strain controlled fracture was conceptualized and integrated into the HM model. Since the fracture was not set to have mechanical properties, thus the influence of micro-fracturing on mechanical behavior is not represented. In order to address the deficiency, Rozhko (2016) developed a dilatant crack model to simulate the gas pathways, with a single crack-like geometry inserted into the solid matrix. Although the crack model gets a better representation for both the crack deformation and the gas flow, the approximated geometry is limited by the complex mathematical treatments on the fracture part, e.g., wetting fluid occupies the crack tips while non-wetting fluid occupies central parts of the crack. To make a balance between modelling the fracture behavior and the application to real cases, Yang et al. (2020) developed a three-dimensional (3D) model to account for the influence of HM properties of the fracture sets on the gas migration, which obtained a good outcome for the anisotropic radial deformation as well as the major gas breakthrough. However, the 3D model is still unable to explicitly simulate the gas preferential pathways.

In the recent years, several methods, i.e., finite element method (FEM) with remeshing, discrete element method (DEM), have been developed to simulate the fracturing process in an

explicit way (Fu et al., 2013; Paluszny et al., 2018; Segura and Carol, 2010; Sun et al., 2017). To improve the computational efficiency, the extended finite element method (XFEM) is developed by adding jump functions to the FEM without remeshing strategy, which has been adopted for coupled flow-deformation problems (Faivre et al., 2016; Pouya et al., 2019; Salimzadeh and Khalili, 2015; Wang, 2016). To simulate fluid flow in complex fracture networks, the FEM can be combined with the boundary element method (BEM), to improve numerical stability (Berre et al., 2018; Fidelibus, 2007; Xu et al., 2018a). Some other combined options include the hybrid finite-discrete element method (FDEM), in which the mechanical behavior of matrix is analyzed in the FEM while the interaction of fracture elements is analyzed in the DEM (Lei et al., 2017). This combined method has provided practical utility in geomechanical problems, see Lisjak et al. (2014, 2016); Munjiza et al. (2000); Vyazmensky et al. (2010). Though these methods provided some references in fracture propagation as well as in the area of fluid flow, the characteristic of fracture propagation caused by the microscopic heterogeneities were not involved in the models. For the brittle or quasi-brittle rock materials containing micro-cracks, where the nucleation and development of micro-cracks are typical damage mechanisms (Dascalu et al., 2010b; François and Dascalu, 2010; Wrzesniak et al., 2015), these models cannot represent the micro-cracking induced macroscopic inelastic behavior. In the laboratory gas injection tests on clayey rocks (Cuss et al., 2012; Harrington et al., 2013b; Hildenbrand et al., 2002), gas induced micro-cracking may belong to this category of damage mechanism since the macroscopic maximum principal stress did not exceed the material tensile strength, and nearly no shear stress was externally provided.

In order to better explain the experimental observation in the gas injection tests, the developed mathematical model needs to be initiated from the microscopic phenomena, to study the resultant macroscopic response. Recently, considerable efforts have been made to establish the link between the micro-mechanical phenomena and the resultant macroscopic behavior. For example, the rate dependent damage models accounting for the micro-cracks propagation are developed based on the analytical or numerical upscaling method starting from the microstructural aspects (Bhat et al., 2012; Wang et al., 2015). Following a similar upscaling procedure based on periodicity assumption and asymptotic homogenization, the deduced macroscopic damage models have been used to represent the brittle failure (Dascalu, 2009; Dascalu et al., 2008, 2010a), the subcritical damage propagation (Dascalu et al., 2010b; François

and Dascalu, 2010; Wrzesniak et al., 2015), the dynamic fracture propagation (Atiezo and Dascalu, 2017; Dascalu, 2018), and the coupled thermo-mechanical problem induced by micro-cracking (Dascalu and Gbetchi, 2019). There are some other multi-scale models considering the HM coupling from microscopic phenomena. For example, Frey et al. (2013); van den Eijnden et al. (2016) developed a finite element squared method to simulate the HM coupling in the porous medium, where the strain localization phenomenon is well illustrated. Zhuang et al. (2017) developed a multi-scale model to simulate the hydraulic fracturing phenomenon, where damage propagation and the fluid flow are implicitly represented since their microscopic phenomenon of fluid flow is initiating from the micro-pores.

Based on the above statement, a two-scale time dependent damage model is proposed here to explicitly simulate the gas induced fracturing starting from the microscopic phenomena. Although the laboratory gas injection tests are conducted on initially saturated clayey rocks, nearly zero-desaturation occurs after significant gas mass flux is observed at the outlet (Cuss et al., 2012, 2014; Harrington et al., 2012a, 2013a, 2017). Therefore, to obtain a balance in explicitly capturing the fracturing phenomenon and simply developing the two-scale model, a condition of single phase gas flow is assumed in the study to simplify the problem. Besides, a plane strain deformation mode is adopted in the study. It should be noted that the aim of the study is to explicitly simulate the development of gas preferential pathways initiated from the microscopic phenomena, the quantitative reproduction of the laboratory results is beyond the scope of the present contribution.

The paper is organized as follows. In Section 5.2.2, the two-scale poroelastic fracture problem is formulated for a porous medium with periodic distributed micro-cracks. In Section 5.2.3, we perform the asymptotic homogenization procedure and obtain the homogenized governing equations for the poroelastic system. In Section 5.2.4, a time dependent damage law is developed based on the microscopic phenomena and the corresponding intrinsic permeability model is proposed that implicitly accounts for the fracture opening induced permeability change. The local macroscopic response of the two-scale model is presented and validated in Section 5.2.5. Lastly in Section 5.2.6, numerical examples including uniaxial tension test, and simulation of preferential gas flow together with the comparison of experimental explanations are illustrated.

5.2.2 Two-Scale Poroelastic Fracture Problem

Consider a porous medium containing a large number of micro-cracks, of which the crack length is much smaller than the dimension of the macroscopic structure. The separation of length scales in the homogenization assumption can be stated as

$$l_c \ll L_c \tag{5.1}$$

where l_c is the size of periodic cell at micro-scale, L_c is the characteristic length of the macro-structure at the macro-scale, see Figure 5.1.

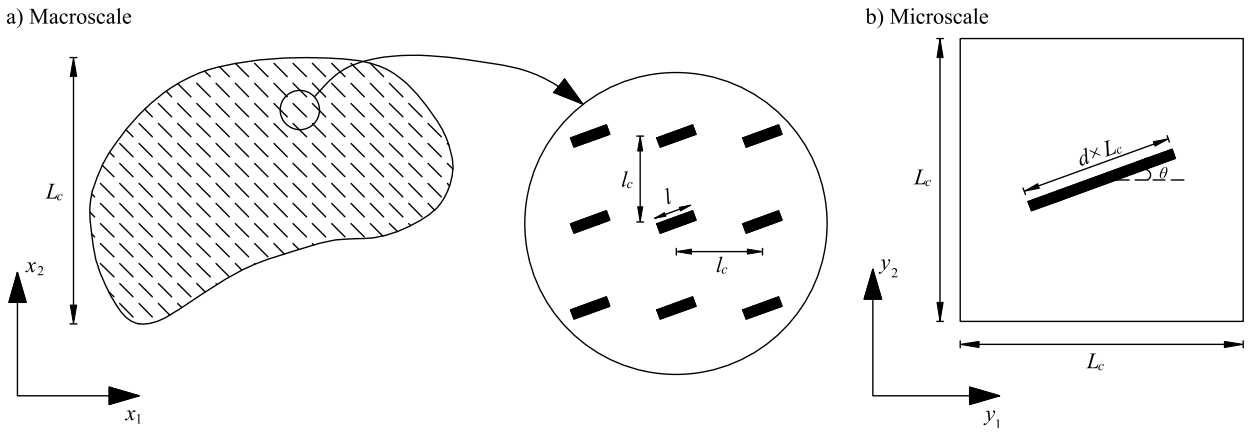

Figure 5.1 (a) Micro-fissured medium with locally periodic microstructure, l is the local micro-fracture length, l_c is the size of a period, and L_c is the characteristic length of the macro-structure. (b) Reference cell of size L_c with rescaled crack length $d \times L_c$. (adapted from Dascalu et al. (2010b))

With this assumption being adopted, the macroscopic properties at the scale of solid body are distinguished from the microscopic properties characterizing the local behavior around the micro-cracks. To simplify the two-scale problem, the distribution of micro-cracks as well as the microstructure is assumed to be locally periodic, as illustrated in Figure 5.1. Each crack is straight with length l and orientated an angle θ with respect to the x_1 direction, which is contained in one microstructure. Together with the locally periodic condition, the micro-cracks can be regarded to be arranged in a parallel type in the macro-structure. It should be specified here that the orientation of micro-cracks can be defined in any given direction and in consequence to derive the corresponding macroscopic response.

A parameter ε representing the ratio between microscopic and macroscopic scales of the solid body, is introduced as follows:

$$\varepsilon = \frac{l_c}{L_c} \ll 1 \tag{5.2}$$

Plane strain deformations are considered in the study, the two-dimensional (2D) solid

domain is denoted by $\mathcal{B}$ and the union of micro-cracks is denoted by $\mathcal{C}$. The normalized damage variable d may be defined as the ratio between the crack length l and the microstructural size l_c, see Figure 5.1(a):

$$d = \frac{l}{l_c} \tag{5.3}$$

The local periodicity assumption ensures that the material behaves periodically over the macroscale domain. When the micro-crack evolves from small length to large length until the microstructure is totally partitioned, the adjacent micro-cracks are interconnected. This physical process represents the damage evolution at macroscale. To link the material behavior at different scales, the following relation between the microscopic and macroscopic spatial coordinates is proposed:

$$y_i = \frac{x_i}{\varepsilon} \tag{5.4}$$

where $x_i (i = 1, 2)$ and y_i denote the components of macroscopic and microscopic coordinates, respectively, as illustrated in Figure 5.2; $\varepsilon \ll 1$ is a scale variable defined in Eq. (5.2). The scaling of this transformation characterizes the field variables at different scales, i.e., displacement and gas pressure fields adopted in the study.

For a field f depending on both scales (x_i and y_i), the differential operator with respect to the spatial coordinates is formulated as:

$$f^{\varepsilon}_{,x_i} = \frac{\partial f}{\partial x_i} + \frac{1}{\varepsilon}\frac{\partial f}{\partial y_i}, \quad f^{\varepsilon}_{,y_i} = \frac{\partial f}{\partial y_i} \tag{5.5}$$

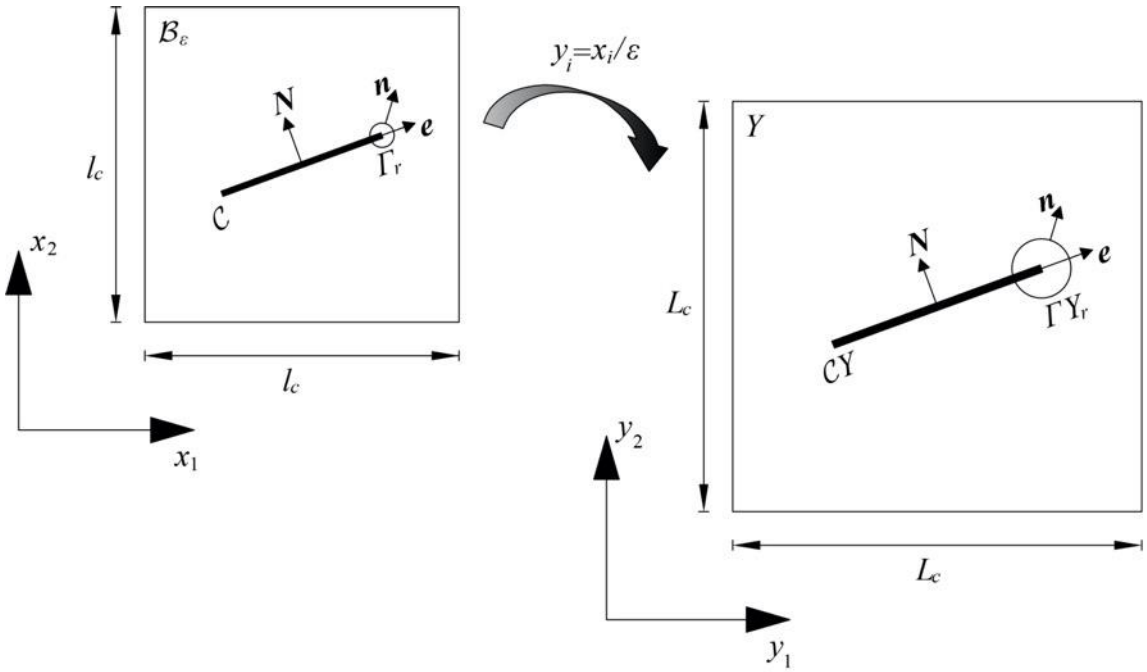

Figure 5.2 Scaling of the microscopic period of the material on the reference cell $Y = [0, L_c] \times [0, L_c]$, which contains the crack $\mathcal{C}Y$ (modified from Wrzesniak et al. (2015))

In the solid part of domain $\mathcal{B}$, the equilibrium equation of the system is formulated by neglecting the volume force, as follows:

$$\frac{\partial \sigma_{ij}^{\varepsilon}}{\partial x_j} = 0 \tag{5.6}$$

where σ_{ij} are the components of total stress tensor.

In order to avoid the additional complexity induced by the change in both volume and micro-pore structure, the pores of the porous material are assumed to be constant and consist of only one fluid, i.e., gas in our study. The mass conservation of gas leads to the following relation:

$$\frac{d}{dt}\left(\rho_g \phi\right) + \frac{\partial q_j^{\varepsilon}}{\partial x_j} = 0 \tag{5.7}$$

where ρ_g is the gas density, ϕ is the porosity of porous material, q_j^{ε} is the gas mass discharge that is given by Darcy's law, as follows,

$$q_j^{\varepsilon} = -\rho_g \frac{k}{\eta} \frac{\partial p^{\varepsilon}}{\partial x_j} \tag{5.8}$$

where p^{ε} is the gas pressure field, η is the dynamic viscosity of gas, k is the isotropic component of intrinsic permeability.

Gas compressibility is taken into account by using the ideal gas law, and the spatial

variation of gas density within the domain is neglected due to the separation of scales (Frey et al., 2013; van den Eijnden et al., 2016). As a result, the gas density is a function of the macroscopic gas pressure, which will be proved in the next section. The following mass balance equation for gas is expressed with respect to the gas pressure field p^ε:

$$\frac{M\phi}{RT}\frac{\partial p^\varepsilon}{\partial t}+\frac{\partial q_j^\varepsilon}{\partial x_j}=0 \tag{5.9}$$

where M is the molar mass of the gas, R is a universal gas constant, T is the absolute temperature.

The constitutive law for isotropic incompressible solid is defined by the following relation,

$$\sigma_{ij}^\varepsilon=\lambda e_{xkk}(\boldsymbol{u}^\varepsilon)\delta_{ij}+2\mu e_{xij}(\boldsymbol{u}^\varepsilon)-b_{ij}p^\varepsilon \tag{5.10}$$

where b_{ij} are the components of Biot's coefficient tensor, which is equal to the Kronecker delta δ_{ij} in the paper for simplicity; λ and μ are the Lame coefficients, the components of strain tensor with respect to the macroscopic scale variable (x_i) are denoted by

$$e_{xkl}(\boldsymbol{u}^\varepsilon)=\frac{1}{2}\left(\frac{\partial u_k^\varepsilon}{\partial x_l}+\frac{\partial u_l^\varepsilon}{\partial x_k}\right) \tag{5.11}$$

Eqs. (5.6) and (5.9) constitute the main governing equations that affect the two-scale poroelastic problem, in which the displacement filed $\boldsymbol{u}^\varepsilon$ and gas pressure field p^ε will be further explored in the next section.

Gas pressure is assumed to be acting on the impermeable crack faces, thus the boundary conditions are expressed as

$$\boldsymbol{\sigma}^\varepsilon\boldsymbol{N}=-p^\varepsilon\boldsymbol{N}\quad;\quad\boldsymbol{q}^\varepsilon\boldsymbol{N}=0 \tag{5.12}$$

where $\boldsymbol{N}$ is the unit vector normal to the crack face, as shown in Figure 5.2.

5.2.3 Asymptotic Developments and Homogenization Analysis

In the following section, the asymptotic homogenization method (Sánchez-Palencia, 1980) is employed to obtain the macroscopic governing equations from the initially described two-scale problem. In the previous section, the locally periodic microstructure with size l_c is constructed with crack length l, see Figure 5.2. By scale transformation, e.g., Eq. (5.4), a reference cell Y of size L_c with contained crack $\mathcal{C}Y$ of length $d\times L_c$ is introduced, as can be seen in Figure 5.2.

Following the homogenization method by Sánchez-Palencia (1980), the displacement $\boldsymbol{u}^\varepsilon$

and gas pressure p^{ε} fields are developed with respect to the parameter ε :

$$\boldsymbol{u}^{\varepsilon} = \boldsymbol{u}^{(0)}(\boldsymbol{x},\boldsymbol{y},t) + \varepsilon \boldsymbol{u}^{(1)}(\boldsymbol{x},\boldsymbol{y},t) + \varepsilon^2 \boldsymbol{u}^{(2)}(\boldsymbol{x},\boldsymbol{y},t) + \ldots \tag{5.13}$$

$$p^{\varepsilon} = p^{(0)}(\boldsymbol{x},\boldsymbol{y},t) + \varepsilon p^{(1)}(\boldsymbol{x},\boldsymbol{y},t) + \varepsilon^2 p^{(2)}(\boldsymbol{x},\boldsymbol{y},t) + \ldots \tag{5.14}$$

where $\boldsymbol{u}^{(i)}(\boldsymbol{x},\boldsymbol{y},t)$, $p^{(i)}(\boldsymbol{x},\boldsymbol{y},t)$, $\boldsymbol{x} \in \mathcal{B}$, $\boldsymbol{y} \in Y$ are smooth functions and Y -periodic in $\boldsymbol{y}$.

Using these developments in the Eqs. (5.8) and (5.10), one obtains:

$$\boldsymbol{\sigma}^{\varepsilon}(\boldsymbol{x},t) = \frac{1}{\varepsilon}\boldsymbol{\sigma}^{(-1)}(\boldsymbol{x},\boldsymbol{y},t) + \boldsymbol{\sigma}^{(0)}(\boldsymbol{x},\boldsymbol{y},t) + \varepsilon\boldsymbol{\sigma}^{(1)}(\boldsymbol{x},\boldsymbol{y},t) + \varepsilon^2\boldsymbol{\sigma}^{(2)}(\boldsymbol{x},\boldsymbol{y},t)\ldots \tag{5.15}$$

$$\boldsymbol{q}^{\varepsilon}(\boldsymbol{x},t) = \frac{1}{\varepsilon}\boldsymbol{q}^{(-1)}(\boldsymbol{x},\boldsymbol{y},t) + \boldsymbol{q}^{(0)}(\boldsymbol{x},\boldsymbol{y},t) + \varepsilon\boldsymbol{q}^{(1)}(\boldsymbol{x},\boldsymbol{y},t) + \varepsilon^2\boldsymbol{q}^{(2)}(\boldsymbol{x},\boldsymbol{y},t)\ldots \tag{5.16}$$

where

$$\sigma_{ij}^{(-1)} = \lambda e_{ykk}(\boldsymbol{u}^{(0)})\delta_{ij} + 2\mu e_{yij}(\boldsymbol{u}^{(0)}) \tag{5.17}$$

$$\sigma_{ij}^{(0)} = \lambda\left(e_{xkk}(\boldsymbol{u}^{(0)}) + e_{ykk}(\boldsymbol{u}^{(1)})\right)\delta_{ij} + 2\mu\left(e_{xij}(\boldsymbol{u}^{(0)}) + e_{yij}(\boldsymbol{u}^{(1)})\right) - b_{ij}p^{(0)} \tag{5.18}$$

$$\sigma_{ij}^{(1)} = \lambda\left(e_{xkk}(\boldsymbol{u}^{(1)}) + e_{ykk}(\boldsymbol{u}^{(2)})\right)\delta_{ij} + 2\mu\left(e_{xij}(\boldsymbol{u}^{(1)}) + e_{yij}(\boldsymbol{u}^{(2)})\right) - b_{ij}p^{(1)} \tag{5.19}$$

and

$$q_j^{(-1)} = -\rho_g \frac{k}{\eta}\frac{\partial p^{(0)}}{\partial y_j}\ ;\ q_j^{(0)} = -\rho_g \frac{k}{\eta}\left(\frac{\partial p^{(0)}}{\partial x_j} + \frac{\partial p^{(1)}}{\partial y_j}\right)\ ;\ q_j^{(1)} = -\rho_g \frac{k}{\eta}\left(\frac{\partial p^{(1)}}{\partial x_j} + \frac{\partial p^{(2)}}{\partial y_j}\right) \tag{5.20}$$

The asymptotic developments of momentum and mass balance equations (5.6), (5.9) lead to the problems of order ε^{α}, with α = -2 , -1, 0, in the following form:

$$\frac{\partial q_j^{(-1)}}{\partial y_j} = 0\ ;\ \frac{\partial \sigma_{ij}^{(-1)}}{\partial y_j} = 0 \tag{5.21}$$

$$\frac{\partial q_j^{(-1)}}{\partial x_j} + \frac{\partial q_j^{(0)}}{\partial y_j} = 0\ ;\ \frac{\partial \sigma_{ij}^{(-1)}}{\partial x_j} + \frac{\partial \sigma_{ij}^{(0)}}{\partial y_j} = 0 \tag{5.22}$$

$$\frac{M\phi}{RT}\frac{\partial p^{(0)}}{\partial t} + \frac{\partial q_j^{(0)}}{\partial x_j} + \frac{\partial q_j^{(1)}}{\partial y_j} = 0\ ;\ \frac{\partial \sigma_{ij}^{(0)}}{\partial x_j} + \frac{\partial \sigma_{ij}^{(1)}}{\partial y_j} = 0 \tag{5.23}$$

Noted here the first term of Eq. (5.23) represents the gas density variation, which is expressed with respect to the macroscopic gas pressure $p^{(0)}$. As has been introduced in Eq. (5.9), this expression is similar to the treatment of water density variation in Frey et al. (2013); van den Eijnden et al. (2016).

Corresponding boundary conditions for different orders of $\boldsymbol{\sigma}^{(m)}$ and $\boldsymbol{q}^{(m)}$ on the crack faces can be obtained from the relation of Eq. (5.12):

$$m=-1\rightarrow\sigma_{ij}^{(-1)}N_j=0\ ;\ q_i^{(-1)}N_i=0 \tag{5.24}$$

$$m=0\rightarrow\left(\sigma_{ij}^{(0)}+b_{ij}p^{(0)}\right)N_j=0\ ;\ q_i^{(0)}N_i=0 \tag{5.25}$$

$$m=1\rightarrow\left(\sigma_{ij}^{(1)}+b_{ij}p^{(1)}\right)N_j=0\ ;\ q_i^{(1)}N_i=0 \tag{5.26}$$

At the order ε^{-2}, the problem for $\boldsymbol{u}^{(0)}$ and $p^{(0)}$ results from Eqs. (5.21) and (5.24) as:

$$\frac{\partial}{\partial y_j}\left(\lambda e_{ykk}(\boldsymbol{u}^{(0)})\delta_{ij}+2\mu e_{yij}(\boldsymbol{u}^{(0)})\right)=0\ ,\ \text{in}\ Y \tag{5.27}$$

$$\left(\lambda e_{ykk}(\boldsymbol{u}^{(0)})\delta_{ij}+2\mu e_{yij}(\boldsymbol{u}^{(0)})\right)N_j=0\ ,\ \text{on}\ \mathcal{C}Y \tag{5.28}$$

and the gas flow equations are simplified by neglecting the spatial variation of gas density, as:

$$\frac{\partial^2 p^{(0)}}{\partial y_1^2}+\frac{\partial^2 p^{(0)}}{\partial y_2^2}=0\ ,\ \text{in}\ Y \tag{5.29}$$

$$\frac{\partial p^{(0)}}{\partial y_j}N_j=0\ ,\ \text{on}\ \mathcal{C}Y \tag{5.30}$$

with periodicity condition applied on the opposite external boundary of the domain Y.

To verify the system of Eqs. (5.27)-(5.30), we can easily find that $\boldsymbol{u}^{(0)}$ and $p^{(0)}$ can only depend on the macroscopic variable $\boldsymbol{x}$. Thus $\boldsymbol{u}^{(0)}=\boldsymbol{u}^{(0)}(\boldsymbol{x},t)$ and $p^{(0)}=p^{(0)}(\boldsymbol{x},t)$ are chosen in the study, which represent the macroscopic displacement and gas pressure fields.

For the problem of $\boldsymbol{u}^{(1)}$ and $p^{(1)}$ at the order ε^{-1}, the deduction can be referred to Eqs. (5.22) and (5.25) as:

$$\frac{\partial}{\partial y_j}\left(\lambda e_{ykk}(\boldsymbol{u}^{(1)})\delta_{ij}+2\mu e_{yij}(\boldsymbol{u}^{(1)})\right)=0\ ,\ \text{in}\ Y \tag{5.31}$$

$$\left(\lambda e_{ykk}(\boldsymbol{u}^{(1)})\delta_{ij}+2\mu e_{yij}(\boldsymbol{u}^{(1)})\right)N_j=-\left(\lambda e_{xkk}(\boldsymbol{u}^{(0)})\delta_{ij}+2\mu e_{xij}(\boldsymbol{u}^{(0)})\right)N_j\ ,\ \text{on}\ \mathcal{C}Y \tag{5.32}$$

and

$$\frac{\partial^2 p^{(1)}}{\partial y_1^2}+\frac{\partial^2 p^{(1)}}{\partial y_2^2}=0\ ,\ \text{in}\ Y \tag{5.33}$$

$$\frac{\partial p^{(1)}}{\partial y_j}N_j=-\frac{\partial p^{(0)}}{\partial x_j}N_j\ ,\ \text{on}\ \mathcal{C}Y \tag{5.34}$$

The general solution of Eqs. (5.31)-(5.32), for the microscopic correction of displacement $\boldsymbol{u}^{(1)}$ is introduced in the following form (Dascalu and Gbetchi, 2019):

$$\boldsymbol{u}^{(1)}(\boldsymbol{x},\boldsymbol{y},t)=\boldsymbol{\xi}^{pq}(\boldsymbol{y})e_{xpq}(\boldsymbol{u}^{(0)}(\boldsymbol{x},t)) \tag{5.35}$$

where $\boldsymbol{\xi}^{pq}$ are termed as the characteristic functions that can be obtained by solving the following unit cell problem:

$$\frac{\partial}{\partial y_j}\left(\lambda e_{ykk}(\boldsymbol{\xi}^{pq})\delta_{ij}+2\mu e_{yij}(\boldsymbol{\xi}^{pq})\right)=0 \text{ , in } Y \tag{5.36}$$

$$\left(\lambda e_{ykk}(\boldsymbol{\xi}^{pq})\delta_{ij}+2\mu e_{yij}(\boldsymbol{\xi}^{pq})\right)N_j=-\left(\lambda\delta_{ij}\delta_{pq}+\mu(\delta_{ip}\delta_{jq}+\delta_{iq}\delta_{jp})\right)N_j \text{ , on } \mathcal{C}Y \tag{5.37}$$

The microscopic corrector of gas pressure $p^{(1)}$ is obtained from Eqs. (5.29)-(5.30), in which the solution should take the following form (Zhuang et al., 2017):

$$p^{(1)}(\boldsymbol{x},\boldsymbol{y},t)=\zeta_j(\boldsymbol{y})\frac{\partial p^{(0)}(\boldsymbol{x},t)}{\partial x_j} \tag{5.38}$$

where ζ_j is the solution of the following unit cell problem:

$$\frac{\partial}{\partial y_j}\left(\delta_{jm}+\frac{\partial \zeta_m}{\partial y_j}\right)=0 \text{ , in } Y \tag{5.39}$$

$$\left(\delta_{jm}+\frac{\partial \zeta_m}{\partial y_j}\right)N_j=0 \text{ , on } \mathcal{C}Y \tag{5.40}$$

Noted here the solutions of the above unit cell problems, i.e., Eqs. (5.36)-(5.37) and (5.39)-(5.40), depend on the normalized micro-crack length d and the crack orientation angle θ, as introduced in Figure 5.1.

At the order ε^0, the problem for displacement and gas pressure fields can be deduced from Eqs. (5.23) and (5.26), as follows

$$\begin{aligned}&\frac{\partial}{\partial x_j}\left(\lambda\left(e_{xkk}(\boldsymbol{u}^{(0)})+e_{ykk}(\boldsymbol{u}^{(1)})\right)\delta_{ij}+2\mu\left(e_{xij}(\boldsymbol{u}^{(0)})+e_{yij}(\boldsymbol{u}^{(1)})\right)-b_{ij}p^{(0)}\right)+\\&\frac{\partial}{\partial y_j}\left(\lambda\left(e_{xkk}(\boldsymbol{u}^{(1)})+e_{ykk}(\boldsymbol{u}^{(2)})\right)\delta_{ij}+2\mu\left(e_{xij}(\boldsymbol{u}^{(1)})+e_{yij}(\boldsymbol{u}^{(2)})\right)-b_{ij}p^{(1)}\right)=0\end{aligned} \text{ , in } Y \tag{5.41}$$

$$\left(\lambda\left(e_{xkk}(\boldsymbol{u}^{(1)})+e_{ykk}(\boldsymbol{u}^{(2)})\right)\delta_{ij}+2\mu\left(e_{xij}(\boldsymbol{u}^{(1)})+e_{yij}(\boldsymbol{u}^{(2)})\right)\right)N_j=0, \text{ on } \mathcal{C}Y \tag{5.42}$$

and

$$\rho_g\frac{k}{\eta}\left(\frac{\partial^2 p^{(0)}}{\partial x_1^2}+\frac{\partial^2 p^{(0)}}{\partial x_2^2}+2\left(\frac{\partial^2 p^{(1)}}{\partial x_1 y_1}+\frac{\partial^2 p^{(1)}}{\partial x_2 y_2}\right)+\frac{\partial^2 p^{(2)}}{\partial y_1^2}+\frac{\partial^2 p^{(2)}}{\partial y_2^2}\right)=\frac{M\phi}{RT}\frac{\partial p^{(0)}}{\partial t}, \text{ in } Y \tag{5.43}$$

$$\left(\frac{\partial p^{(1)}}{\partial x_j}+\frac{\partial p^{(2)}}{\partial y_j}\right)N_j=0, \text{ on } \mathcal{C}Y \tag{5.44}$$

In order to obtain the effective governing equations, the mean value operator is introduced:

$$\langle \cdot \rangle = \frac{1}{|Y|}\int_{Y} \cdot dy \tag{5.45}$$

where $|Y| = L_c^{\,2}$ is the area of Y. By applying the mean value operator to Eqs. (5.41) and (5.43), integrating by parts and making use of the periodicity conditions, we obtain homogenized momentum balance and mass balance relations:

$$\frac{\partial}{\partial x_j}\Sigma_{ij}^{(0)} = 0 \tag{5.46}$$

$$c^* \frac{\partial p^{(0)}}{\partial t} + \frac{\partial Q_i^{(0)}}{\partial x_i} = 0 \tag{5.47}$$

in which the macroscopic stress $\Sigma_{ij} = \langle \sigma_{ij}^{(0)} \rangle$ and macroscopic mass flux $Q_i^{(0)} = \langle q_i^{(0)} \rangle$ are given as follows,

$$\Sigma_{ij} = C_{ijkl}^* e_{xkl}(\boldsymbol{u}^{(0)}) - b_{ij} p^{(0)} \tag{5.48}$$

$$Q_i^{(0)} = -\rho_g \frac{k_{ij}^*}{\eta} \frac{\partial p^{(0)}}{\partial x_j} \tag{5.49}$$

As concerns the expressions of homogenized coefficients occurred in the above macroscopic laws, we compute the effective elastic moduli C_{ijkl}^* from the unit cell problems (5.36) -(5.37), as follows

$$C_{ijkl}^* = \frac{1}{|Y|}\int_{Y} \left(C_{ijkl} + C_{ijmn} e_{ymn}(\boldsymbol{\xi}^{kl}) \right) dy \tag{5.50}$$

and the homogenized specific gas pressure coefficient c^* is expressed with respect to porosity and related gas coefficients:

$$c^* = \frac{1}{|Y|}\int_{Y_s} \frac{M\phi}{RT} dy \tag{5.51}$$

The homogenized permeability components occurred in Eq. (5.49) are obtained as:

$$k_{ij}^* = \frac{1}{|Y|}\int_{Y_s} k\left(\delta_{ij} + \frac{\partial \zeta_j}{\partial y_i} \right) dy \tag{5.52}$$

It can be noticed that the homogenized coefficients C_{ijkl}^* and k_{ij}^* depend on the normalized damage variable d and the crack orientation angle θ. This dependence will further be explored in Section 5.2.5 for local response, with respect to the initial damage d_0, the microstructural size l_c and the loading rate $\dot{e}_{xij}$.

Besides, as the two-scale formulation is deduced under the restrictive assumptions, fracture opening induced permeability change is not included in the model yet, but this is also a considerable contribution for the development of gas preferential pathways. Thus, the intrinsic permeability change induced by fracture opening will be further explored in the following part.

5.2.4 Damage Equations

In order to fulfill the two-scale problem initiated from the micro-crack propagation, the homogenized governing equations and constitutive equations, (5.46)-(5.49), need to be supplemented with an evolution law for the damage variable $d(x_i,t)$. In the meantime, the damage induced permeability change will also be introduced in the following subsection.

5.2.4.1 Damage Evolution Law

The subcritical fracture properties of shales have been experimentally investigated by Swanson (1984), who demonstrated the similar crack growth behavior as that in some other brittle rocks. As a clay-rich rock material, shale presents a large reduction in fracture toughness when contact with water, leading to an enhanced subcritical fracture growth (Chen et al., 2017; Chen et al., 2019). In the laboratory gas injection tests conducted on clayey rocks, gas induced fracturing occurs for the case of injected gas pressure lower than the applied isotropic confining pressures, in which close experimental observations validated the mode I fracturing (Cuss et al., 2012). As has been observed in quasi-brittle/brittle materials such as rocks, the mode I failure due to the subcritical crack propagation at the microscale may represent the mechanism of time dependent damage observed at the macroscale (Miura et al., 2003; Nara and Kaneko, 2006). Furthermore, considerable time dependent creep has been validated during the mechanical test conducted on the SPP_COx-1 (Cuss et al., 2012).

In order to account for the special mechanism that the mode-I micro-crack may propagate for stress intensity factor lower than the critical fracture limit, a subcritical criterion adapted from Charles (1958) is used to formulate the relation between micro-crack growth and mode I stress intensity factor K_I (Dascalu et al., 2010b; François and Dascalu, 2010; Wrzesniak et al., 2015):

$$\frac{dl}{dt} = v_0 \left(\frac{K_I}{K_0} \right)^n \tag{5.53}$$

where K_I is the stress intensity factor under mode I rupture, K_0 is a particular stress intensity

factor for which the velocity of crack propagation is equal to v_0, in which the value of K_0 is likely to be a small fraction (10%-20%) of critical stress intensity factor K_{Ic} (Atkinson and Meredith, 1987); n is the subcritical crack growth index. K_0, v_0 and n are material parameters, which are affected by the rock type, environment such as humidity and temperature (Atkinson, 1987). Many researchers have conducted a lot of experimental tests to obtain the relation between the tensile strength and the critical stress intensity factor K_{Ic}, in which its value for rocks may be approximate as (Li and Zhu, 2002; Xu et al., 2018b; Zhang, 2002):

$$K_{Ic} = \gamma_t \sigma_t \tag{5.54}$$

where σ_t is the tensile strength of rock, γ_t is a fitted linear coefficient, equal to 0.14 $m^{0.5}$.

The crack propagation law should be completed with the reduced dissipation inequality:

$$\mathcal{D}_f = \mathcal{G}^{\varepsilon} \dot{l} \geq 0 \tag{5.55}$$

where $\mathcal{D}_f$ is the energy dissipation associated with the crack propagation, $\mathcal{G}^{\varepsilon}$ is the microscopic energy release rate, $\dot{l}$ represents the crack velocity.

Eqs. (5.53) and (5.55) constitute the general time dependent law for micro-crack propagation. For brittle or quasi-brittle fracture, a Griffith-type energy criterion can be used to consider the cracking initiation: $\dot{l} = 0$ when $\mathcal{G}^{\varepsilon} < \mathcal{G}_f$ and $\dot{l} \geq 0$ when $\mathcal{G}^{\varepsilon} = \mathcal{G}_f$, where $\mathcal{G}_f$ is the critical fracture energy of the material. These damage models have been deduced in Dascalu et al. (2008, 2010a), in which $\mathcal{G}_f$ may be expressed with respect to the crack length l and crack velocity $\dot{l}$ for complex fracture evolution. In the particular case of subcritical propagation law, Eq. (5.53) corresponds to a fracture energy that is associated with crack velocity $\dot{l} = v(\mathcal{G}^{\varepsilon})$, where the time effect is taken into consideration and the micro-cracks may propagate for stress intensity factor lower than the critical value of fracture (Atkinson, 1987; Atkinson and Meredith, 1987; Wrzesniak et al., 2015). The next step is to link the microscopic energy release rate $\mathcal{G}^{\varepsilon}$ and the mode I stress intensity factor K_I, expressed as follows:

$$\mathcal{G}^{\varepsilon} = \frac{1-\nu^2}{E} K_I^2 \tag{5.56}$$

The relation between microscopic and macroscopic energy release rate has been proved in several research papers, see Dascalu et al. (2008, 2010a); Wrzesniak et al. (2015), which is written in the following form:

$$Y_d = \frac{\mathcal{G}^{\varepsilon}}{l_c} = -\frac{1}{2}\frac{dC^*_{ijkl}(d)}{dd} e_{xkl}(\boldsymbol{u}^{(0)}) e_{xij}(\boldsymbol{u}^{(0)}) \tag{5.57}$$

where Y_d is the macroscopic damage energy release rate. Noted here, the microscopic length l_c makes the link between microscopic and macroscopic energy release rate per unit volume. The energy scaling relation will ensure the occurrence of microscopic length l_c in the damage evolution law.

Substituting Eqs. (5.3) and (5.57) into the micro-crack evolution laws (5.53)-(5.55), the macroscopic damage law is obtained as follows:

$$\dot{d} = \frac{1}{l_c} v(l_c Y_d) \tag{5.58}$$

$$\mathcal{D}_d = Y_d \dot{d} \geq 0 \tag{5.59}$$

where $\mathcal{D}_d$ is the dissipation associated with the damage propagation.

Recalling that the damage energy release rate is thermodynamically conjugated with damage, see Bui et al. (2017); Dormieux et al. (2006), one can introduce the macroscopic thermodynamic potential for the porous material under the assumption of incompressible solid grain, as follows:

$$G_s(e_{xij}, d) = \frac{1}{2} C^*_{ijkl}(d) e_{xkl}(\boldsymbol{u}^{(0)}) e_{xij}(\boldsymbol{u}^{(0)}) \tag{5.60}$$

where G_s is the thermodynamic potential associated with the free energy of solid phase, the detailed thermodynamic analysis of the porous material can be found in Coussy (2004), thus we have

$$\Sigma_{ij} = \frac{\partial G_s}{\partial e_{xij}}; \quad Y_d = -\frac{\partial G_s}{\partial d} \tag{5.61}$$

Combining Eqs. (5.56) and (5.57) yields to the expression of mode I stress intensity factor:

$$K_I = \left(-\frac{l_c E}{2(1-\nu^2)} \frac{dC^*_{ijkl}(d)}{dd} e_{xkl}(\boldsymbol{u}^{(0)}) e_{xij}(\boldsymbol{u}^{(0)}) \right)^{\frac{1}{2}} \tag{5.62}$$

Substituting Eqs. (5.58) and (5.62) into the subcritical crack propagation law (5.53) gives us the following macroscopic time dependent damage law:

$$\dot{d} = \frac{v_0}{l_c}\left(\frac{\sqrt{-\frac{l_c E}{2(1-\nu^2)}\frac{dC^*_{ijkl}(d)}{dd}e_{xkl}(\boldsymbol{u}^{(0)})e_{xij}(\boldsymbol{u}^{(0)})}}{K_0}\right)^n \tag{5.63}$$

The damage evolution law accounts for the time effects and size effects due to the dependency on microstructural size l_c, which represents the behavior of macroscopic tensile fractures caused by micro-cracking, as observed in the laboratory gas injection tests conducted on the clayey rock materials (Cuss et al., 2014).

5.2.4.2 Damage Induced Permeability Change

In Section 5.2.3, the homogenized permeability coefficients were analyzed according to the non-flux assumption on the crack face, which is regarded to be reasonable for the solid matrix as the fracture propagation may lead to the pores closing around the dilatant pathways (Cuss et al., 2014). However, the fracture opening induced permeability change is not included yet in the model since it is a significant factor affecting the gas flow in clayey rocks. Normally, the fracture permeability is always several orders larger than the matrix permeability, which dominates the gas migration path in porous media, especially for clayey rocks with very low permeability, see Harrington et al. (2017). Besides, gas migration in clayey rocks is a dynamic and unstable process (Amann-Hildenbrand et al., 2015; Cuss et al., 2012; Gensterblum et al., 2015; Harrington et al., 2012a, 2013b, 2017; Harrington and Horseman, 1999), which makes it difficult to formulate the permeability change based on some simplified assumptions. Therefore, it might be better to include some empirical formulations of permeability change with respect to the solid deformation as well as the damage variable based on the existed experimental data, which is a widely accepted method for the similar research topic at hand, e.g., see Arnedo et al. (2013); Fall et al. (2014); Gerard et al. (2014); Gonzalez-Blanco et al. (2016); Guo and Fall (2018, 2019); Nguyen and Le (2015); Olivella and Alonso (2008); Senger et al. (2018); Xu et al. (2013a); Yang et al. (2020).

Since we assume the constant pore space in the matrix in the beginning, we only focus on the fracture opening induced permeability change in the following part. The relationship between damage and corresponding permeability change has been studied by some researchers, i.e., Arson and Pereira (2013); Shao et al. (2005); Souley et al. (2001); Tang et al. (2002). In the

study, we will start from some idealized permeability-deformation relation to obtain a reasonable formulation.

As shown in Figure 5.3, an idealized stress-strain and permeability-strain curve is displayed, in which the work is adapted from Zhang et al. (2013). Point A is the onset point of volumetric dilation, also referred to be the damage onset point where the permeability begins to increase rapidly. The dilatancy controlled gas flow occurs when the injected gas pressure reaches a certain value (Cuss et al., 2014; Harrington et al., 2017). Before the sample dilation occurs, gas diffusion may be the leading mechanism for gas flow and permeability may decrease as volume constriction occurs. The maximum permeability occurs at a delayed point C corresponding to a residual stress state after the stress reaches the maximum value at point B. The rapid increase of permeability in the regime AC corresponds to the behavior that gas induced micro-cracking occurs, which exhibits the localized damage on the macroscopic level.

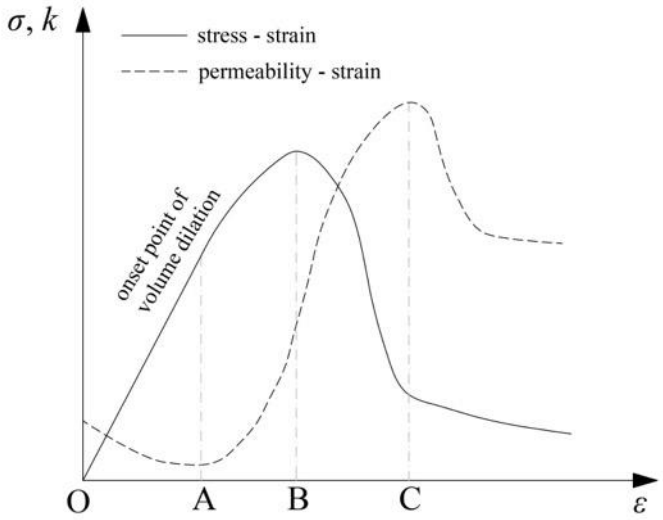

Figure 5.3 Idealized stress and permeability curve with respect to strain for rock (adapted from Zhang et al. (2013))

In the laboratory gas injection tests, mechanical volume dilation and micro-crack propagation are accompanied by the development of gas dilatant pathways. To capture the fracture opening induced permeability change, the influence of both solid structure and volume on the intrinsic permeability should be included. In the introduced two-scale model, the contribution of structure change on the intrinsic permeability is captured by the damage variable d, while the contribution of volume change is represented by the macroscopic volumetric strain e_{xii}. As the term of fracture opening is difficult to be quantified, the fast increase of intrinsic permeability due to gas induced fracturing may be formulated by a function of both e_{xii} and d.

Inspired by the intrinsic permeability model developed in Fall et al. (2014) and Zhuang et al. (2017), the following empirical combination of exponential model with e_{xii} and a power law model with d is introduced, as follows:

$$k = k_0 \exp(A_t e_{xii}) \left(1 + \alpha_t (d/d_0 - 1)^{\beta_t}\right) \tag{5.64}$$

where k is the intrinsic permeability of porous material, as introduced in the relation (5.52); k_0 is the initial intrinsic permeability of undamaged material; A_t, α_t and β_t are empirical parameters used to better capture the experimental phenomena.

5.2.5 Local Macroscopic Response

The objective of local response for the proposed two-scale model is to analyze the local behavior predicted by the time dependent damage model. Firstly, the homogenized elastic and permeability coefficients, i.e., C^*_{ijkl} and k^*_{ij}, are illustrated as a function of the damage variable d by solving the unit cell problems, i.e., Eqs. (5.36)-(5.37) and Eqs. (5.39)-(5.40), respectively, for a large number of normalized micro-crack length. Then the local macroscopic behavior, i.e., stress-strain relation, damage evolution, is presented under the special uniaxial loading condition, by assuming a non-vanishing strain component. The influence of the initial damage value d_0, the microstructural length l_c and the applied strain rate $\dot{e}_{x22}$ is analyzed, which gives a deeper understanding of the two-scale model.

The material parameters used for the computation are mainly referred to Callovo-Oxfordian claystone (COx), which is investigated as a potential host rock for nuclear waste repositories. The elastic stiffness coefficients are obtained from Mahjoub et al. (2018): the Young's modulus $E = 2000$ MPa, the Poisson's ratio $\nu = 0.3$. The initial intrinsic permeability is given by Harrington et al. (2017): $k_0 = 1.8 \times 10^{-21}$ m^2. The tensile strength of the clayey rock is extracted from the uniaxial tension test (Hashiba and Fukui, 2015): $\sigma_t = 1.1$ [MPa], the particular stress intensity factor K_0 is approximated to be 15% of K_{Ic} (Atkinson and Meredith, 1987). The subcritical growth index is taken as $n = 3$ (Wrzesniak et al., 2015), the particular velocity for crack propagation is approximated as $v_0 = 10^{-7}$ m/s (Chen et al., 2017).

To simplify the problem of gas induced fracturing and also to avoid the kinked effects for inclined micro-cracks, only horizontal or vertical micro-cracks are adopted in the study. We

noted that this simplified direction may be extended to inclined orientation by following the method proposed in (François and Dascalu, 2010). The used parameters for local analysis are summarized in Table 5-1.

Table 5-1 Parameters used in the local model

E [MPa]	ν [-]	k_0 [m^2]	σ_t [MPa]	γ_t [m$^{1/2}$]	K_0/K_{Ic} [-]	n [-]	v_0 [m/s]	θ [°]
2000	0.3	1.8×10^{-21}	1.1	0.14	0.15	3	10^{-7}	0 or 90

5.2.5.1 Homogenized Coefficients

The effective coefficients are calculated from the formulae (5.50)-(5.52) expressed with respect to the characteristic functions $\boldsymbol{\xi}^{kl}$ and ζ, which respectively are the solutions of the unit cell problems (5.36)-(5.37) and (5.39)-(5.40) for each damage variable d. In what follows, we consider the elastic solid matrix as well as the permeability of the porous material is isotropic. For given parameters E, ν and k, the effective coefficients can be computed for a large number of $d \in [0, 1]$, and by linear interpolation between continuous data points, we can obtain the interpolation curves in terms of damage variable d, which will be used to calculate the local response in the following part. These calculations are completed by the FEM software COMSOL Multiphysics. In the extreme case of completely cracked cell, i.e., $d=1$, the analytical solutions of the unit cell problem can be obtained to compute the homogenized coefficients at failure limit.

The homogenized elastic coefficients are represented with respect to the damage variable d in Figure 5.4. We note that the presence of micro-cracks induces an overall orthotropic response. For the virgin material with $d=0$, the homogenized coefficients are equal to the initial elastic moduli. While for $d \neq 0$, the presence of crack with different orientations (Figure 5.4(a) horizontal or (b) vertical), i.e., parallel or normal to the loading direction, leads to the nonlinear variation of the effective coefficients with a more abrupt decrease on the rigidity when the cell is close to totally damaged state ($d=1$). With a horizontal crack (direction 11 in Figure 5.4(a)), the stiffness conponent C_{1111} is less affected when loaded in the horizontal direction (11), while the loss of rigidity in C_{2222} and C_{1122} are much more serious when loaded in the vertical direction (22). This characteristic of micro-fracturing induced anisotropy at the macro-scale is experimentally observed in anisotropic rocks (Nara and Kaneko, 2006). For $d=1$, the analytical expression for $C^*_{1111}(d=1)=\dfrac{E}{1-\nu^2}$ is calculated at the last data point in Figure 5.4.

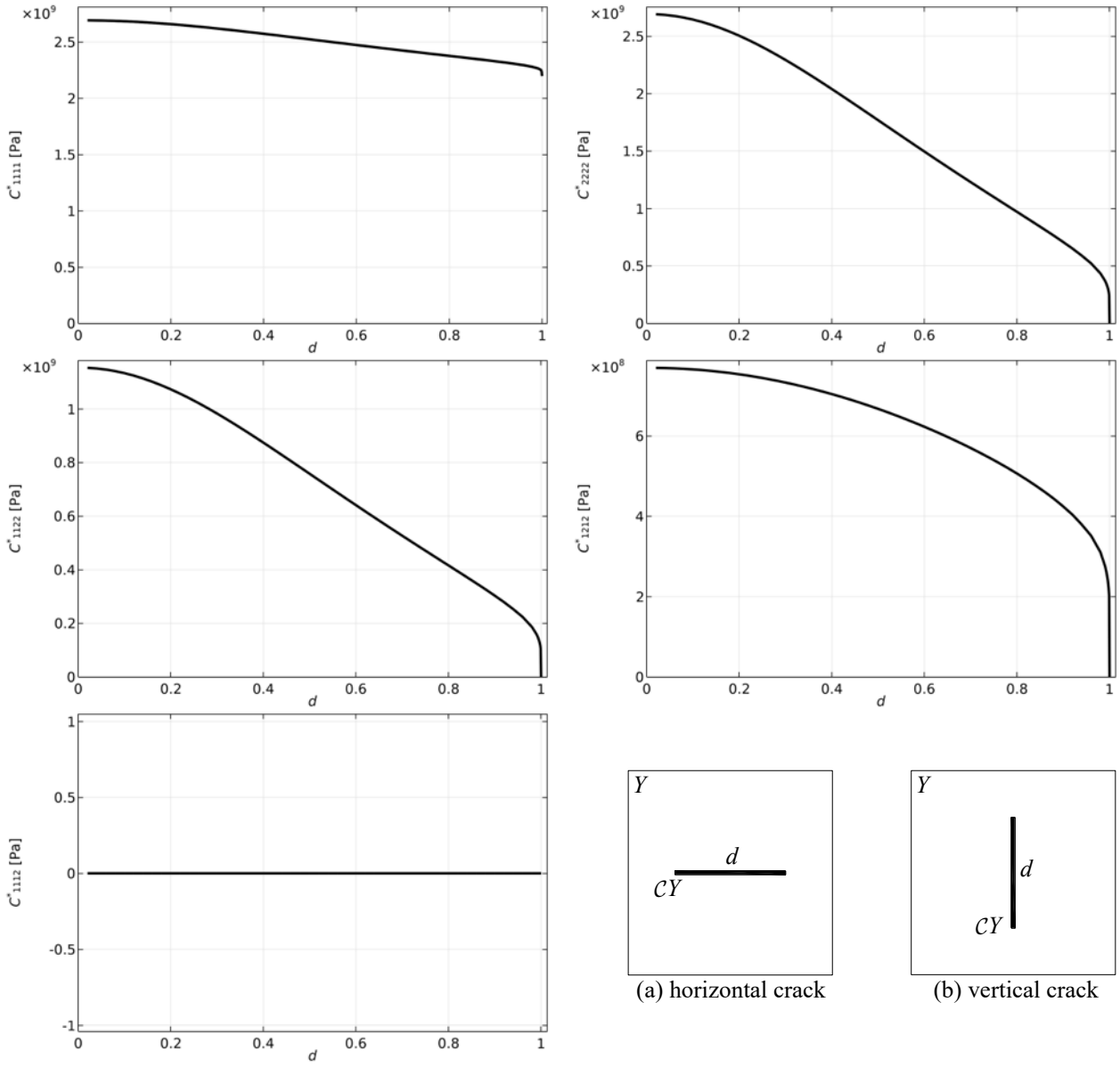

Figure 5.4 Homogenized elastic coefficients versus normalized damage variable for horizontal crack orientation (a). For vertical crack orientation (b), we have the same value for the coefficients except that C_{1111} is replaced by C_{2222} and reciprocally. Y denotes the reference cell and CY denotes the crack.

The homogenized permeability coefficients k_{ij}^* are represented with respect to damage variable d in Figure 5.5, which are normalized with undamaged material permeability $k^*(0)$. The virgin material is assumed to have isotropic intrinsic permeabilities $k_{11}^*(0) = k_{22}^*(0) = k$, $k_{12}^*(0) = 0$. Due to the two-scale simplification of non-fluid flux condition on the crack face, the presence of horizontal crack (direction 11 in Figure 5.4(a)) leads to a constant value of normalized permeability coefficient $k_{11}^*(d)/k_{11}^*(0) = 1$ and a reduction of normalized coefficient $k_{22}^*(d)/k_{22}^*(0)$ in 22 direction. For $d = 1$ with completely damaged cell, the solid

matrix is totally partitioned by the crack, and the continuous fluid flow in 22 direction within the matrix is interrupted. Thus $k_{22}^{*}(1)/k_{22}^{*}(0)=0$, fluid flow only occurs along the crack orientation. This characteristic of micro-fracturing induced anisotropy is experimentally validated in the gas injection tests conducted by Cuss et al. (2014), since the macroscopic fracture dominates the behavior of fluid flow within the clayey rock sample (Harrington et al., 2017).

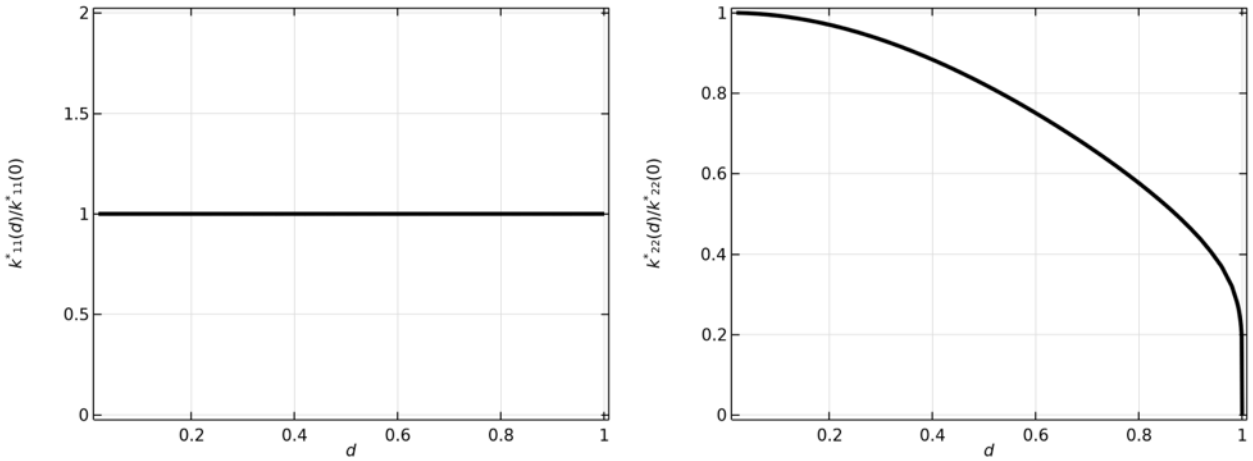

Figure 5.5 Homogenized permeability coefficients versus normalized damage variable for horizontal crack orientation (see Figure 5.4(a)). For vertical crack orientation, we have the same value for the coefficients except that $k_{11}^{*}(d)/k_{11}^{*}(0)$ is replaced by $k_{22}^{*}(d)/k_{22}^{*}(0)$ and reciprocally.

5.2.5.2 Local Response Analysis

In order to analyze the homogenized response of the time dependent damage model, a strain history e_{x22} is imposed as the only non-vanishing strain component, by applying a constant strain rate $\dot{e}_{x22}$. Under this loading condition and assuming a horizontal crack orientation, the local response in stress-strain relation, damage evolution is determined by solving the Eqs. (5.48) and (5.63) numerically.

The parameters for local response analysis are those given in the beginning of Section 5.2.5, which can be referred to Table 5-1. The initial gas pressure is the standard atmospheric pressure that is a gauge pressure in the computation, the gas flow process is not considered in the pure mechanical analysis. The interpolated homogenized coefficients in the previous subsection are used in the numerical computations.

5.2.5.2.1 Influence of the Initial Damage

We first consider the influence of initial damage on the stress and damage evolution, with

different values $d_0 = 0$, $d_0 = 0.1$, $d_0 = 0.2$, $d_0 = 0.3$, respectively. The microstructural length is given as $l_c = 10^{-4}$ m and the applied strain rate is $\dot{e}_{x22} = 10^{-8}$ s^{-1}.

The obtained results are presented in Figure 5.6. As expected, undamaged material has the highest tensile strength, which can sustain higher tensile loading. For higher initial damage value, damage initiates more rapidly with lower strength.

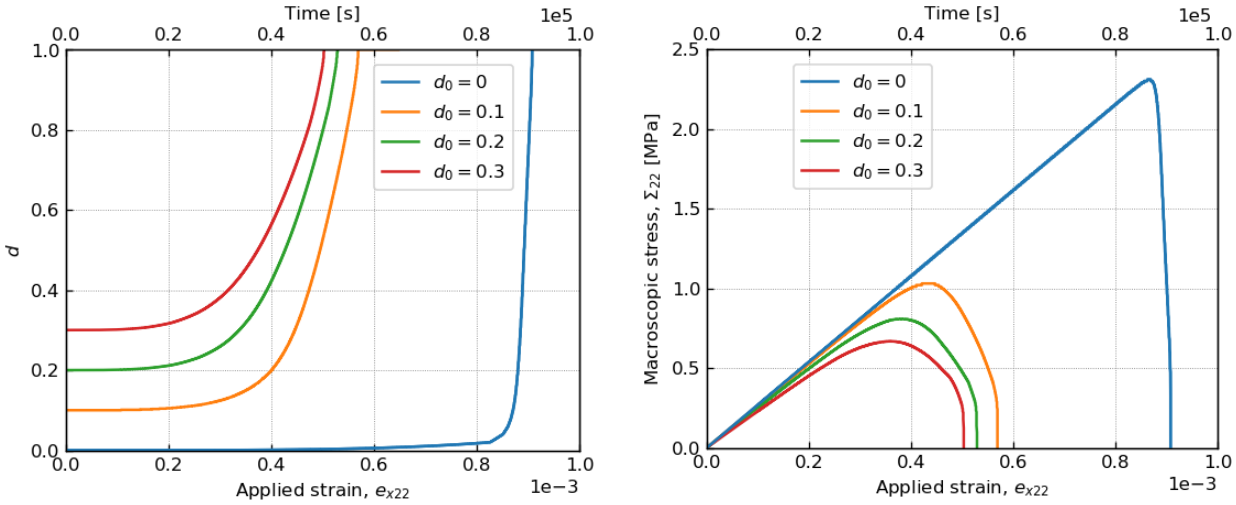

(a) Evolution of damage with applied strain (b) Evolution of macroscopic stress with applied strain

Figure 5.6 Influence of initial damage value ($d_0 = 0$, $d_0 = 0.1$, $d_0 = 0.2$, $d_0 = 0.3$) on the damage and macroscopic stress

5.2.5.2.2 Influence of the Microstructural Size

To study the size effects, different values for the microstructural size are given to analyze the local response. The obtained damage d and stress Σ_{22} are presented in Figure 5.7 for three different microstructural size values: $l_c = 1\times10^{-3}$ m, $l_c = 1\times10^{-4}$ m, $l_c = 1\times10^{-5}$ m. The material is initially undamaged and the applied strain rate is $\dot{e}_{x22} = 10^{-8}$ s^{-1}.

It is observed that larger microstructural size leads to lower material strength. This characteristic may be interpreted as larger microstructure dimension contains bigger sized micro-cracks, thus leading to easier propagation for damage. It is consistent with the result of classical size effect in Fracture Mechanics (Atiezo and Dascalu, 2017), which has been included in the damage model through homogenization analysis.

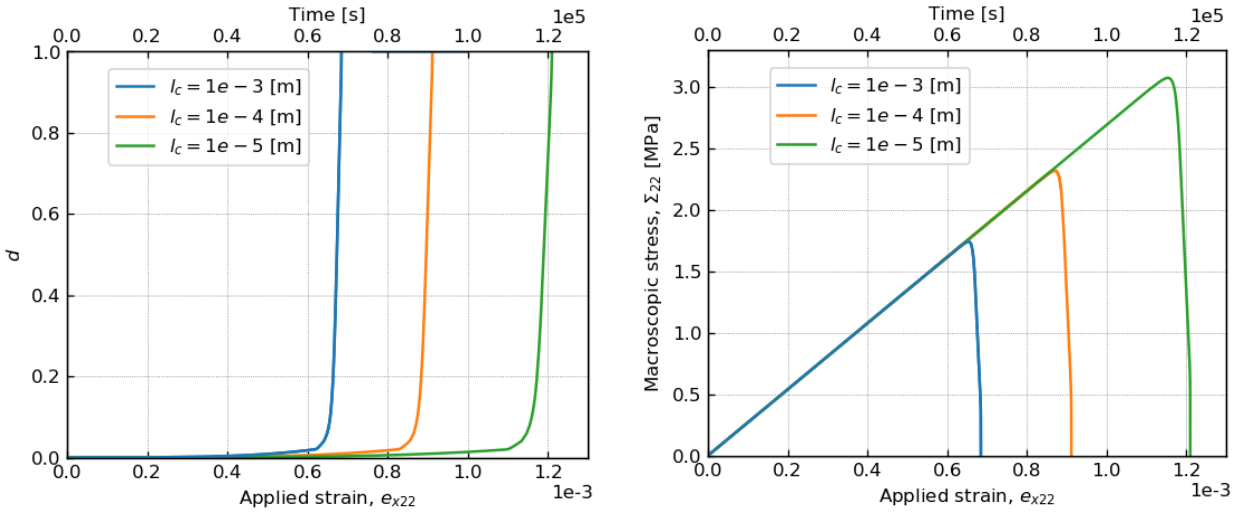

(a) Evolution of damage with applied strain (b) Evolution of macroscopic stress with applied strain

Figure 5.7 Influence of microstructure size ($l_c = 1 \times 10^{-3}$ m, $l_c = 1 \times 10^{-4}$ m, $l_c = 1 \times 10^{-5}$ m) on the damage and macroscopic stress

5.2.5.2.3 Influence of the Strain Rate

The final parametric study concerns the influence of the loading rate. The damage d versus strain e_{x22} and stress Σ_{22} versus strain e_{x22} are presented in Figure 5.8 for three different loading rate conditions: $\dot{e}_{x22} = 5\times10^{-9}$ s^{-1}, $\dot{e}_{x22} = 1\times10^{-8}$ s^{-1}, $\dot{e}_{x22} = 5\times10^{-8}$ s^{-1}. The material is intact and the microstructural length is given as $l_c = 10^{-4}$ m.

The material response depends not only on the time needed for damage propagation, e.g., see Eq. (5.63) and Figure 5.8(a), as well as on the applied loading rate, see Figure 5.8(b). Under lower loading rate condition, the micro-cracks have enough time to develop at a relevant small deformation state compared with higher loading rate condition, and correspondingly the material strength decreases.

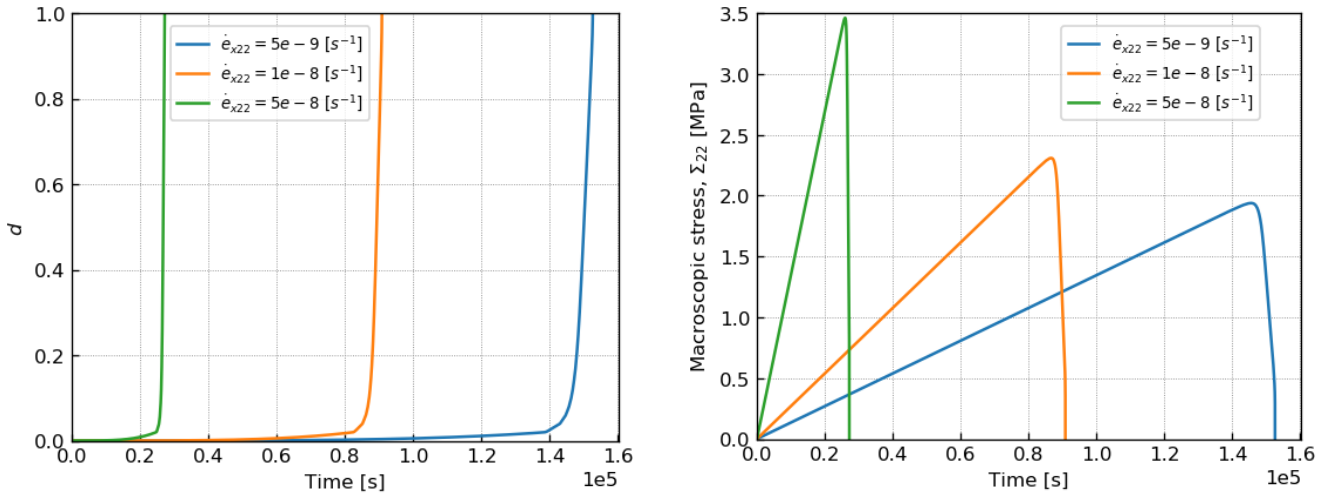

(a) Evolution of damage with applied strain (b) Evolution of macroscopic stress with applied strain

Figure 5.8 Influence of different strain rate ($\dot{e}_{x22} = 5 \times 10^{-9}\ \mathrm{s}^{-1}$, $\dot{e}_{x22} = 1 \times 10^{-8}\ \mathrm{s}^{-1}$, $\dot{e}_{x22} = 5 \times 10^{-8}\ \mathrm{s}^{-1}$) on the damage and macroscopic stress

5.2.5.2.4 Model Prediction

Before analyzing the macroscopic behavior of the two-scale model, the proposed damage law will be used to predict the peak value of axial stress Σ_{22} at failure, which is compared with the experimentally measured direct tensile strength (DTS) of clayey rocks, i.e., mudstone (Hashiba and Fukui, 2015), shale (Gao et al., 2015; Jin et al., 2018; Luo et al., 2018). As has been illustrated in the above analysis, the peak stress is affected by the loading rate, which can be also easily obtained in the uniaxial tension test. For simplicity, the predicted peak stress will be analyzed locally against a large number of loading rate value $\dot{e}_{x22}$, while the data of experimentally measured DTS is relatively few, see Figure 5.9.

In general, the predicted peak stress can represent the failure characteristics of clayey rocks. Due to the variations in the water content, clay minerals, bedding angles and initial damage degree, the recorded DTS of clayey rocks present large difference, especially in the test conducted by Gao et al. (2015), where the DTS of shale is the smallest under a higher loading rate condition. It has to be noted that the strain rate in the uniaxial tension test conducted by Luo et al. (2018) is approximated to be 8.3×10^{-6} /s as the specific dimension of shale sample is not given in the experimental work. More efforts still need to be made in the future to obtain more experimental results on the tensile stress-strain relation of clayey rocks.

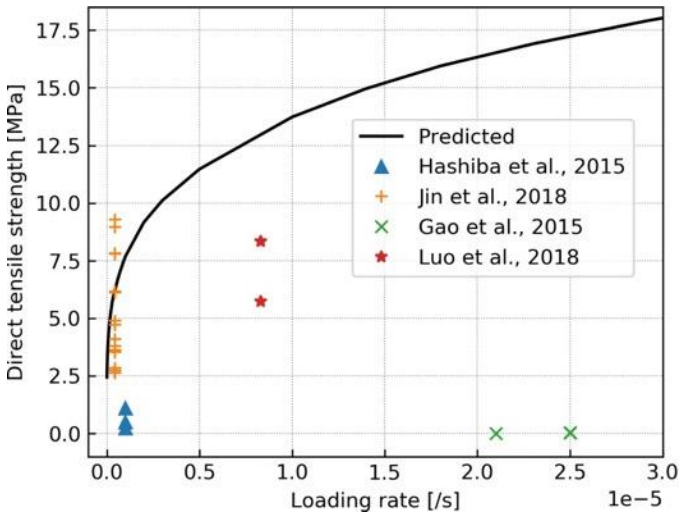

Figure 5.9 Comparison between predicted peak stress and measured DTS in the uniaxial tension test

5.2.6 Numerical Examples

The proposed two-scale model will be discussed in the following part, where the global macroscopic behavior is analyzed in detail. Two numerical examples are considered in the plane strain deformation mode. The first example is the simulation of uniaxial tension test, in which the global stress-strain relation and the failure characteristics are analyzed in detail. Then the basic mechanical model is verified against the laboratory results. In the second example, the preferential gas flow is explicitly simulated, detailed results of damage propagation and preferential gas pathways are illustrated with the comparison of experimental explanations.

The time dependent damage law Eq. (5.63) and the intrinsic permeability law Eq. (5.64) are coupled with the macroscopic momentum balance equation (5.46) and gas mass balance equation (5.47), respectively. The homogenized elastic coefficients $C^*_{ijkl}(d)$ (presented in Figure 5.4) and permeability coefficients $k^*_{ij}(d)/k^*_{ij}(0)$ (see Figure 5.5) are used in the constitutive relations, i.e., Eqs. (5.48) and (5.49). Depending on the specific problem to be studied, these equations are solved based on the applied boundary conditions (BCs).

5.2.6.1 Simulation of Uniaxial Tension Test

Since the uniaxial tension test is a pure mechanical test, thus the influence of gas flow as well as gas pressure is neglected in the simulation. Horizontal crack orientation ($\theta=0$) is assumed for the reference cell in the test, which corresponds to the homogenized elastic coefficients in horizontal direction, see Figure 5.4 for details. The physical parameters used in

the simulation of uniaxial tension test are shown in Table 5-2.

Table 5-2 Parameters in the simulation of uniaxial tension test

E [MPa]	ν [-]	σ_t [MPa]	γ_t [m$^{1/2}$]	K_0/K_{Ic} [-]	n [-]	v_0 [m/s]	θ [°]
2000	0.3	1.1	0.14	0.15	3	10^{-7}	0

5.2.6.1.1 Results Analysis

The initial damage variable is $d_0 = 1\times10^{-6}$, which can be considered to be initially undamaged for the material. The microstructural size is given as $l_c = 1\times10^{-4}$ m. Other used physical parameters are referred to Table 5-2. The specimen dimension is given by 25 mm width and 50 mm height, illustrated in Figure 5.10(a). The displacement $u_2 = u$ is applied in the upper boundary $x_2 = 50$ mm through maintaining a constant strain rate $\dot{e}_{x22} = 1\times10^{-8}$ s^{-1}.

For the initiation of damage propagation, a pre-existing crack line with size of 1 mm is inserted into the geometry, which introduces a displacement discontinuity along the crack. This treatment is similar to that in Dascalu et al. (2008), where several elements with pre-existing crack ($d = 1$) is used for the damage initiation. The pre-existing crack line is positioned laterally at the mid-height of the rock specimen, see Figure 5.10(a). The meshed domain is discretized using triangular elements, gradually refined from the upper/lower boundary to the pre-existing crack area, as seen in Figure 5.10(b). The element size in the refined area is about 0.17 mm and 11741 elements are created for the whole domain, which satisfies the condition that the element size is larger than the microstructural size $l_c = 10^{-4}$ m (Dascalu et al., 2008; Liang et al., 2018).

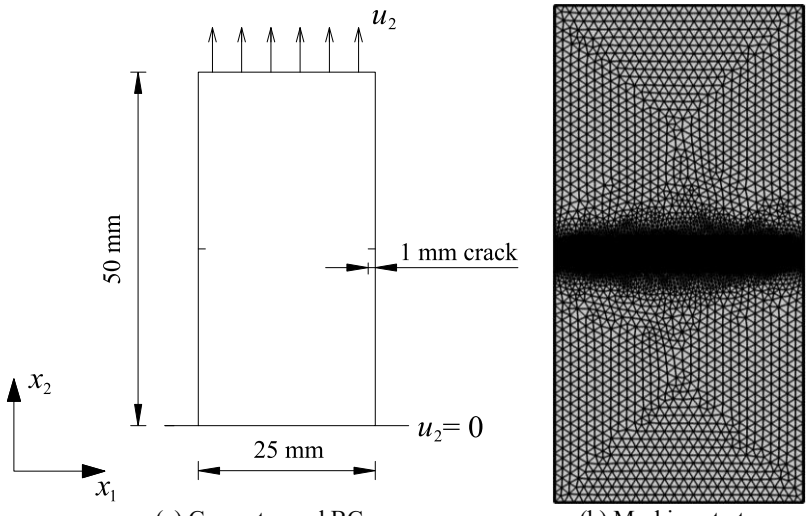

(a) Geometry and BCs (b) Meshing strategy

Figure 5.10 Geometry, BCs and meshed domain for the uniaxial tension test

The obtained global macroscopic response, i.e., stress over the domain with respect to the

applied strain and time, under uniaxial tension condition is illustrated in Figure 5.11. The points, a, b, c, and d on the curve correspond to the states of damage evolution in Figure 5.12. We note that the material softening corresponds to the damage propagation, initiated from the pre-existing crack line.

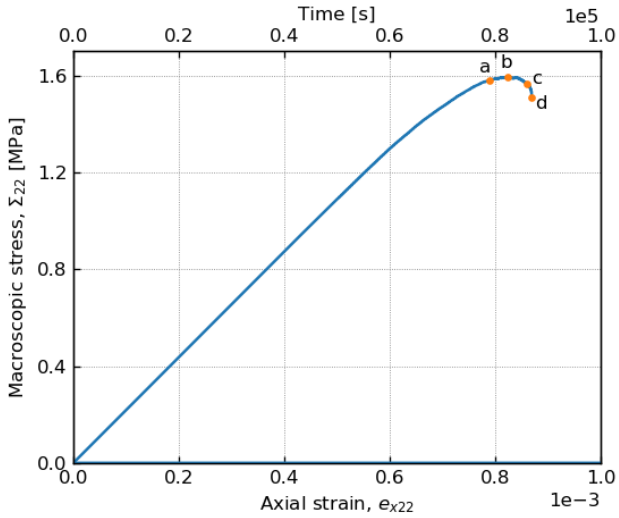

Figure 5.11 Global stress-strain and stress-time response in tension

It can be seen from Figure 5.12 that the damage propagation is almost along the horizontal direction, which is the combined effect of the local periodicity assumption together with the resultant homogenized response.

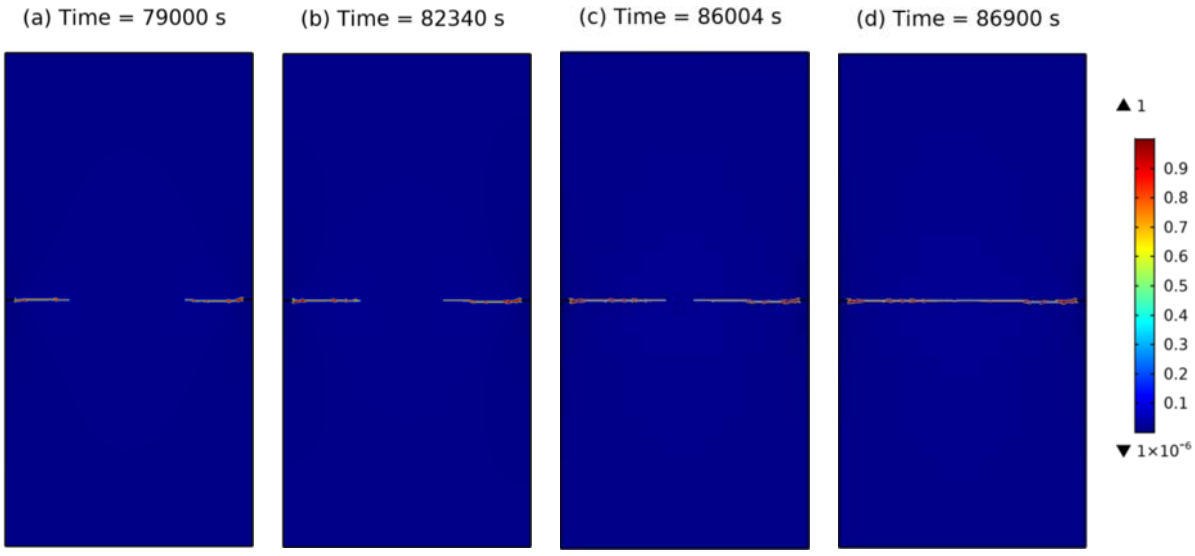

Figure 5.12 Evolution of damage fields corresponding to points a, b, c, and d in global curve

Figure 5.13 presents the damaged shale sample after uniaxial tension test (Gao et al., 2015).

It is clearly seen from the figure that the material presents a failure characteristic along horizontal direction. By comparison of simulated failure mode with the experimental phenomenon, a good agreement is illustrated.

Figure 5.13 Failure characteristics after uniaxial tension test (Gao et al., 2015)

5.2.6.1.2 Model Verification

In the following part, we conduct a quantitative study of uniaxial tension test. The simulated stress-strain results are compared with the experimental data recorded in (Hashiba and Fukui, 2015).

In the computation, the initial damage is chosen to be $d_0 = 0.5$ and the microscopic length is $l_c = 1\times10^{-3}$ m. Other physical parameters used in the model verification are referred to Table 5-2. The sample rock of shale is 25 mm in diameter and 50 mm in height. The applied loading rate in the experiment is 1×10^{-6} /s. The boundary conditions and meshed domain can be referred to Figure 5.10. Using the provided parameters, we obtain the simulated stress-strain curve in Figure 5.14. As seen from the comparison, the two-scale damage model provides a good agreement with the experimental results, which shows the model robustness to reproduce the damage behavior.

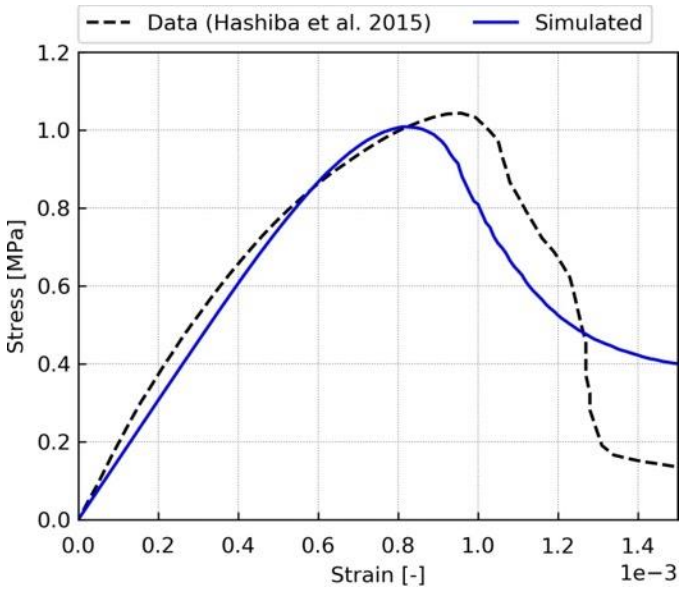

Figure 5.14 Comparison of simulated results with uniaxial tension test results

5.2.6.2 Simulation of Preferential Gas Flow

Considering the direction of gas flow, e.g., from the inlet (lower boundary) to the outlet (upper boundary), vertical crack orientation ($\theta = 90^{\circ}$) is assumed for the reference cell in the computation, which corresponds to the homogenized elastic and permeability coefficients in the vertical direction, see respectively Figure 5.4 and Figure 5.5 for details. Since gas migration in clayey rock is a highly unstable and dynamic process (Cuss et al., 2014; Harrington et al., 2017), the detailed information of intrinsic permeability change with respect to the deformation is not available yet in the gas injection tests, we may use the assumed values of empirical parameters to get a good computational result. Similar treatment by using the parameters in fitting the experimental data has been widely adopted in the research topic at hand, see for example, (Arnedo et al., 2013; Gerard et al., 2014; Gonzalez-Blanco et al., 2016; Nguyen and Le, 2015; Xu et al., 2013b; Yang et al., 2020). The adopted parameters in the simulation are given as: $A_t = 50$, $\alpha_t = 5$, $\beta_t = 2$, and more efforts need to be made to better determine the empirical parameters in the future. The other physical parameters used in the simulation are mainly referred to the sample COx-1 in the gas injection test conducted by Harrington et al. (2013b, 2017), which have been introduced in the beginning of Section 5.2.5. These physical and empirical parameters are summarized in Table 5-3. Since the specimen deformation is caused by externally applied gas pressure, no external loading of strain rate condition is applied on the specimen, detailed initial and boundary conditions are given in the following part.

Table 5-3 Parameters in the simulation of gas flow

E [MPa]	ν [-]	ϕ [-]	k_0 [m^2]	σ_t [MPa]	γ_t [m$^{1/2}$]	K_0/K_{Ic} [-]	n [-]
2000	0.3	0.146	1.8×10^{-21}	1.1	0.14	0.15	3
v_0 [m/s]	l_c [m]	d_0 [-]	θ [°]	A_t [-]	α_t [-]	β_t [-]	
10^{-7}	10^{-4}	0.2	90	50	5	2	

5.2.6.2.1 Initial and Boundary Conditions

The studied domain is a rectangle with dimensions of 25 mm width and 20 mm height, as shown in Figure 5.15. The mesh is gradually refined when it is close to the injection inlet (boundary NO. 3) in order to capture the gas induced fracturing process that initiates from the inlet area. The refined area is discretized with element size of about 0.17 mm and about 13900 triangular elements are meshed for the whole domain.

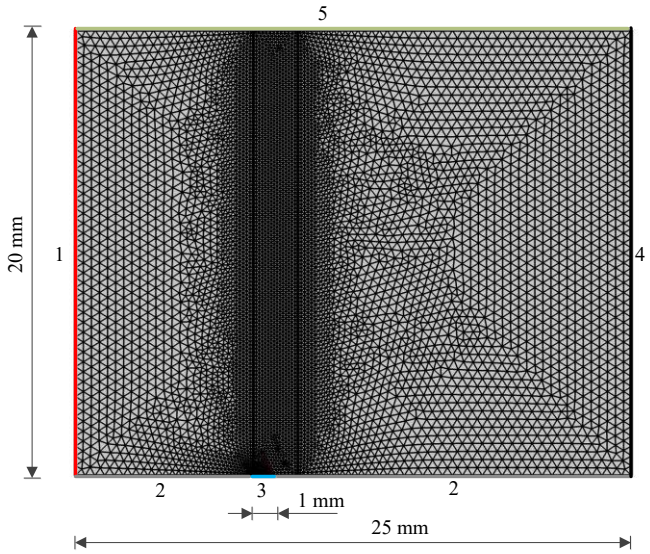

Figure 5.15 Meshed domain and boundary conditions (BCs)

To better represent the gas injection process, the increase of gas pressure at the inlet is applied with constant gas injection rate, in which the inlet is connected with a pump with constant volume. The volume of pump is assumed to be 4×10^{-5} m^3, and the rate of applied gas pressure is about 17.2 kPa/s. The amount of gas flow into the rock specimen depends on the gas pressure inside the pump and the pressure gradient along the specimen. This boundary condition is used as it can well capture the sudden decrease of gas pressure at the inlet after major gas breakthrough occurs. Similar treatment can be also found in Gonzalez-Blanco et al. (2016), in which gas flow in Boom clay is simulated. Helium is chosen to be the safe substitute for

hydrogen, in which the gas behavior follows the ideal gas law. In the gas outlet, the commonly used condition of constant gas pressure is replaced by a type of mass flux condition, as the constant pressure condition is too rigid to describe the gas outflow phenomenon (Guo and Fall, 2018, 2019). The gas pressure inlet (boundary NO. 3) is 8 mm away from the symmetric boundary (boundary NO. 1), with 1 mm wide, as seen in Figure 5.15.

The detailed BCs for gas flow and mechanical loading are provided in Table 5-4.

Table 5-4 Detailed BCs for gas flow and mechanical loading

Boundary NO.	Gas flow boundary	Mechanical boundary
1	Symmetric boundary	
2	No flow	Roller
3	Applied gas pressure	Roller
4	No flow	12.5 MPa confining pressure
5	Mass flux q_{g0}	12.5 MPa confining pressure

The mass flux at the outlet is expressed as:

$$q_{g0} = \begin{cases} \rho_g \dfrac{k_{22}^*}{\eta l_q}\left(p^{(0)} - p_{cr}\right), p^{(0)} > p_{cr} \\ 0, p^{(0)} \le p_{cr} \end{cases} \tag{5.65}$$

where l_q is a characteristic length equal to 1 mm (Guo and Fall, 2018, 2019), and p_{cr} is a critical value of gas pressure, which is set to be slightly higher than the initial gas pressure, to initiate the gas outflow process. This boundary condition can capture the major gas breakthrough phenomenon, where the sudden increase of gas pressure at the outlet occurs. Once the mass flow rate of gas at the outlet exceeds the value at the inlet, gas pumping is terminated.

Isotropic confining pressure was applied at the top and two sides of the specimen, the initial gas pressure was set to 1 MPa. The initial effective stress is determined to be -11.5 MPa. As gas migration within initially fractured COx sample is dominated by the fracture properties (Harrington et al., 2017), the sample is assumed to be initially damaged. The influence of initial damage value on the mechanical behavior has been explored in the Subsection of local response analysis, the increase of initial damage value amounts to speed up the damage propagation process, see Figure 5.6. As there is no existing experimental work to express the relation between fracture properties and damage variable, also the detailed fracture properties were not available in the gas injection tests, thus the initial damage was assumed to get an even value, i.e., $d_0 = 0.2$ in the simulation. A higher $d_0 = 0.8$ is assumed for a small element close to the injection inlet to initiate the damage propagation, see red element in Figure 5.15. Similar treatment can be also

found in Guo and Fall (2019), where an initial fracture with small length was prescribed in the phase field method.

5.2.6.2.2 Modelling Results

Figure 5.16 presents the simulated result of gas pressure at the inlet and outlet, as well as the mass flow rate of gas at the inlet and at the outlet. As can be seen from the figure, although it takes a relevant longer time for gas migration within the sample, gas breakthrough occurs all of a sudden, almost at the time of 13 min. Once the major gas breakthrough occurs, large amounts of gas flow out of the sample and the gas pressure goes up at the outlet abruptly. This phenomenon is consistent with the experimental observations, as detailed in (Cuss et al., 2014; Hildenbrand et al., 2002).

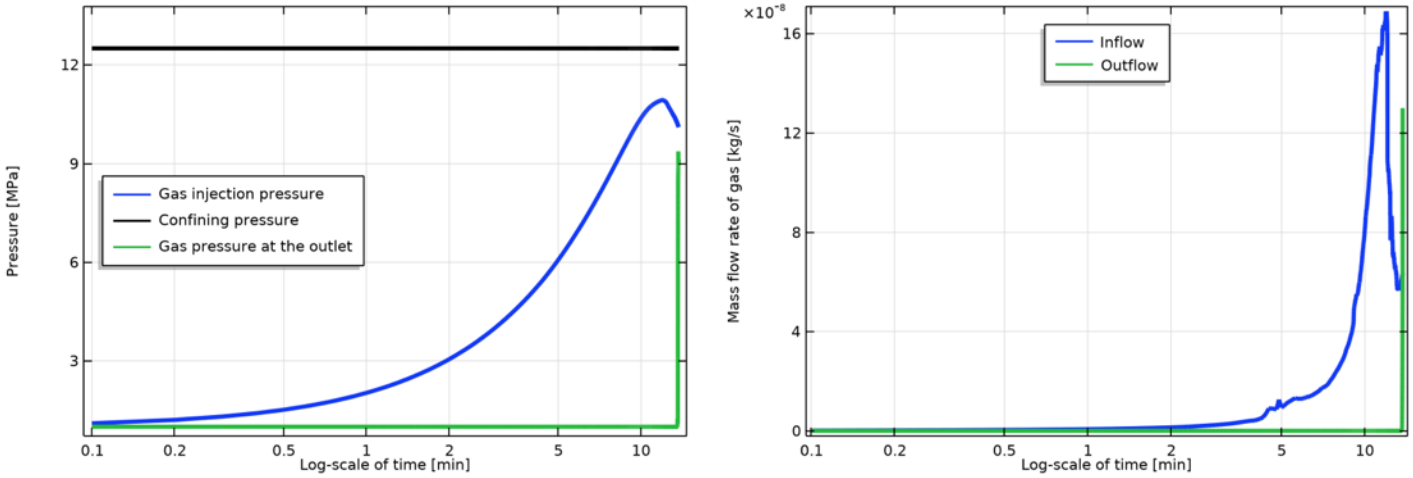

(a) Gas pressure at the inlet and outlet (b) Mass flow rate of gas at the inlet and outlet

Figure 5.16 Simulated gas pressure and mass flow rate at the inlet and outlet

Figure 5.17 presents the distribution of gas pressure inside the domain at different times, Figure 5.18 shows the evolution of damage distribution within the sample. We can see that gas front penetrates to a further area than damage propagates. The penetrated gas causes the volume dilation through the effective stress law, e.g., Eq. (5.48), then the gradually increased strain leads to the damage propagation, see Eq. (5.63).

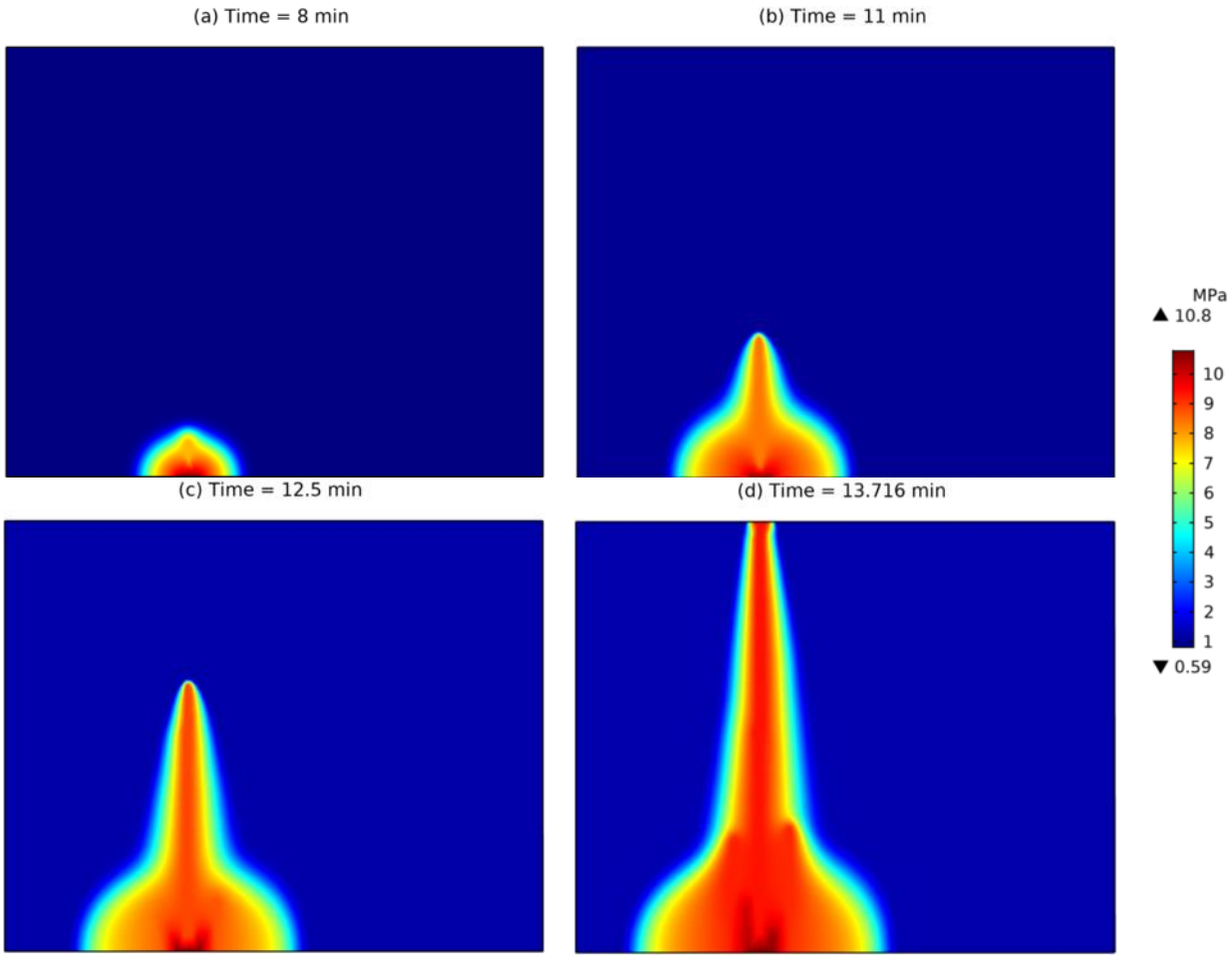

Figure 5.17 Distribution of gas pressure within the sample

Figure 5.19 shows the evolution of gas velocity magnitude within the sample. Thanks to the assumption of vertical crack orientation in the unit cell and the local periodicity assumption, the resultant homogenized response for damage propagation as well as for gas migration is almost along the vertical direction, see Figure 5.18 and Figure 5.19 for more details. This pathway is also the shortest distance for gas transport, which is consistent with the experimental explanation by Cuss et al. (2012) that more gas dilatant pathways are along the central area of the sample since the gas injection inlet and outlet lie in the axial center area. The phenomenon has also been modelled by Yang et al. (2020) who used a 3D model to capture the symmetry of the radial deformation, which validated the concentrated flow pathways in the axial center area of the sample.

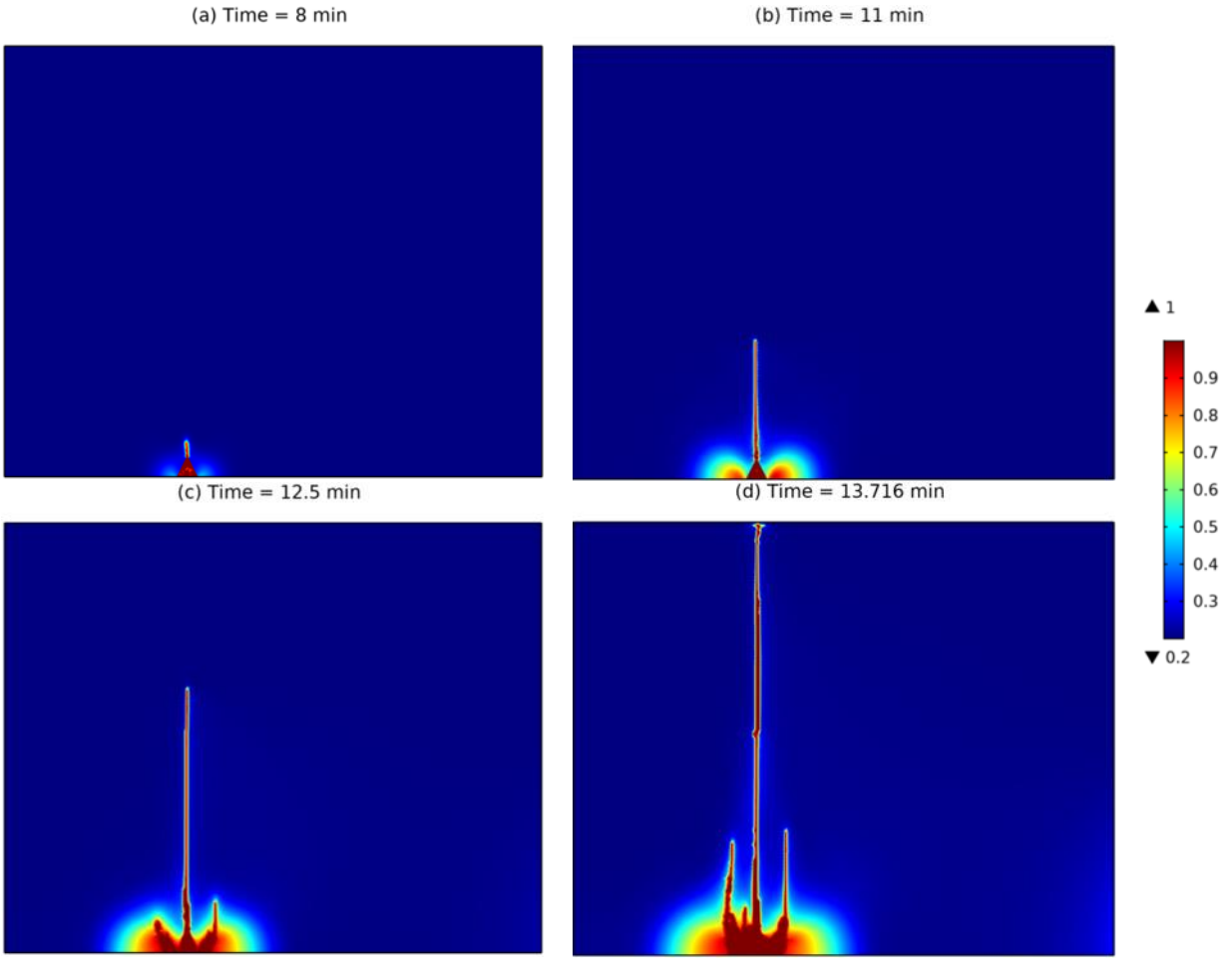

Figure 5.18 Evolution of damage distribution at different times

From the comparison between the damage distribution in Figure 5.18 and the gas flow path in Figure 5.19, we observe that the gas induced fracturing process, which initiates from the gas injection inlet is well captured by the two-scale model. Thanks to the time dependent damage law (e.g., Eq. (5.63)) and the intrinsic permeability model (e.g., Eq. (5.64)), the path for damage propagation and gas migration fits so well, (see Figure 5.18 and Figure 5.19).

Under the condition of the injected gas pressure lower than the applied confining pressure, see Figure 5.16(a), the major gas breakthrough and gas induced fracturing occur in highly localized pathways. The modelling results are consistent with the experimental phenomena, see (Cuss et al., 2014; Harrington et al., 2012a, b, 2013, 2017; Hildenbrand et al., 2002; Wiseall et al., 2015) for more details, and see Figure 5.20 for the comparison of experimental explanation.

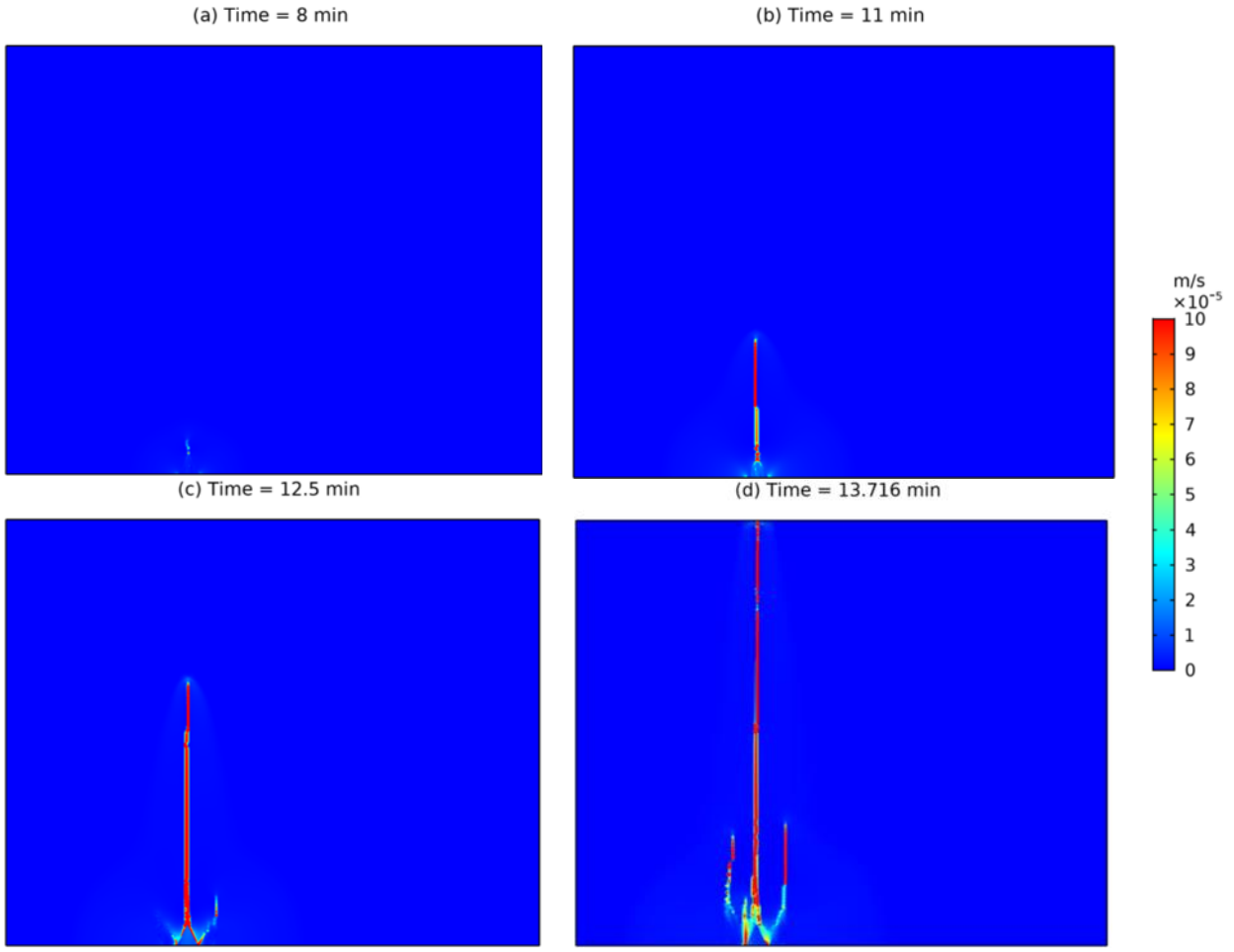

Figure 5.19 Evolution of gas velocity magnitude at different times

Figure 5.20 presents the experimental explanation of gas preferential pathways, which may provide some reference with respect to the modelling results. The large amounts of gas flow into the sample at about 8 minutes, which leads to the damage propagation around the inlet. Although the unstabilized branching occurs at a later time (e.g., 12 min) and gas may penetrate out through anywhere on the outlet boundary, a major preferential gas flow path eventually forms along a vertical direction. This result is consistent with the experimental interpretation, in which dendritic gas pathways gradually formed until totally intersected the sample, see Figure 5.20(a), details are referred to Cuss et al. (2014). Correspondingly, it can be also validated by the experimental observations, where multiple fractures are observed around the injection inlet area, see Figure 5.20(b), as detailed in (Wiseall et al., 2015).

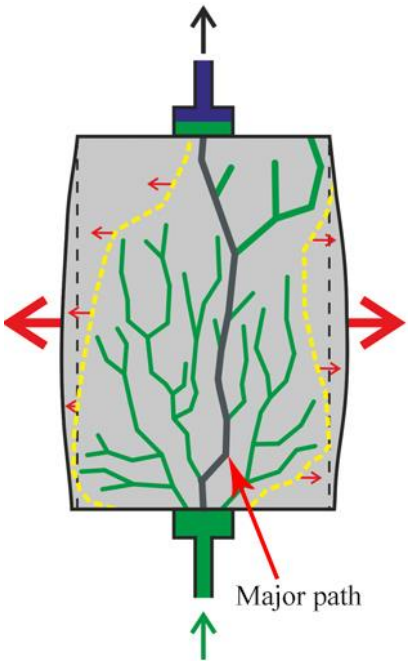

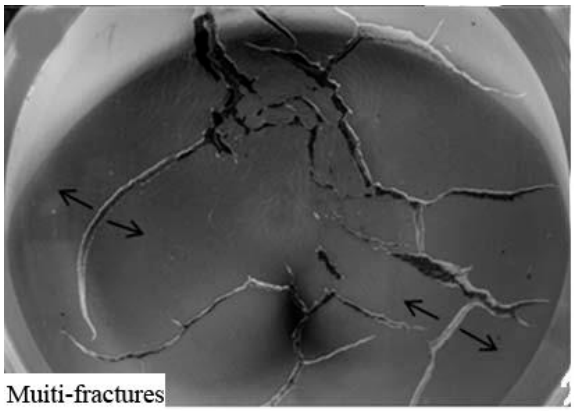

(a) Experimental interpretation of dilatant pathways (adapted from (Cuss et al., 2014))

(b) Experimental observation of gas induced fracturing on clay-rich materials (adapted from (Wiseall et al., 2015))

Figure 5.20 Experimental explanations of preferential gas pathways

Finally we illustrate the evolution of average volumetric strain and damage with respect to time in Figure 5.21. Gas induced mechanical dilation is well simulated, in which the timing for abrupt deformation corresponds to that for large amounts of gas flow into the sample, by comparing the curve with that in Figure 5.16. It can also validate that the gas induced fracturing is highly localized since the average damage variable only increases slightly, while the damage variable reaches the maximum value in the area of gas dilatant pathways, see Figure 5.18.

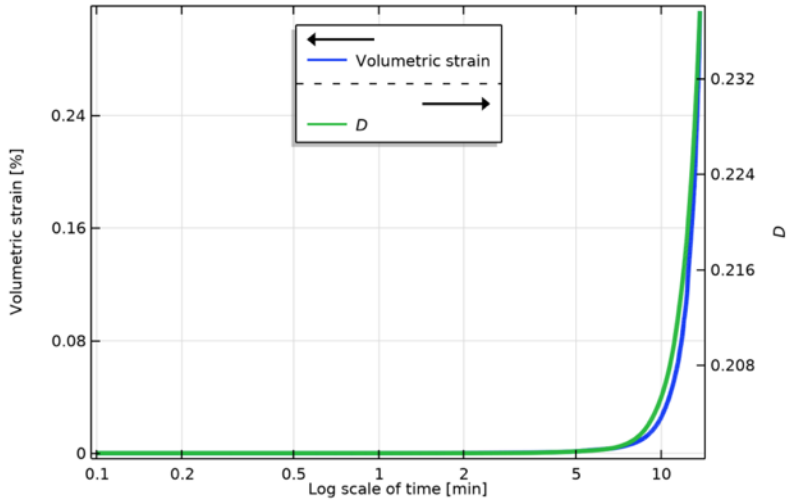

Figure 5.21 Evolution of the average volumetric strain

5.2.7 Conclusions

A two-scale time dependent damage model is developed by using the mathematical homogenization method based on the asymptotic expansions, to explicitly simulate the preferential gas flow in clayey rock materials.

Initiating from the periodically distributed microstructures with micro-cracks, the macroscopic damage behavior coupled with the poroelastic system is deduced by asymptotic homogenization method. The upscaling procedure leads to the homogenized governing equations, i.e., the momentum conservation and gas mass conservation, related to the normalized damage variable that is introduced in the microstructures. Based on the microscopic phenomena observed in the laboratory gas injection tests, a time dependent damage evolution law is constructed and the corresponding intrinsic permeability model is proposed, which accounts for the implicit effect of fracture opening induced permeability change, i.e., mainly along the direction of damage propagation.

The homogenized elastic and permeability coefficients are illustrated with respect to the damage variable, which provide the basis to analyze the macroscopic behavior. The local macroscopic responses of the model, i.e., effective stress-strain and the damage evolution are analyzed by studying the influence of several parameters, i.e., the initial damage, the microstructural size and the strain rate under special strain-driven loading conditions. Based on the local behavior, the damage model is validated against the experimentally measured direct tensile strength that shows its robustness. Numerical examples are presented to illustrate the global macroscopic response, in which the uniaxial tension test is firstly simulated and verified against the experimental results, then the simulation of preferential gas flow is illustrated together with the comparison of experimental explanations. The numerical results showed that the proposed two-scale model can explicitly simulate the gas induced fracturing, in which the damage propagation and the dilatant gas pathways are well captured.

As an initial contribution on the two-scale damage modelling of preferential gas flow, the paper still has its limitations that need to be improved in the future. One of them concerns the extension of single phase (gas) flow to account for two-phase (gas, water) flow, which is a significant aspect in both laboratory and field gas injection tests. The dynamic evolution of both porosity and Biot's effective coefficients with respect to time may be included in the upscaling procedure of the future work since these are important properties for rocks, which may affect the

gas migration pathways. Last but not least, to capture more important experimental phenomena, i.e., anisotropic radial deformation, the extension of the present model to 3D framework would be important, which may be conducted in the future work by following the method proposed in Dascalu et al. (2010a).

5.2.8 Acknowledgements

The authors gratefully acknowledge funding from a joint program supported by the China Scholarship Council and University of Ottawa. Moreover, the authors thank the Natural Sciences and Engineering Research Council of Canada (NSERC) for financially supporting this research. Valuable suggestions from Dr. Guanlong Guo and Dr. Penghai Yin are highly appreciated.

5.2.9 References

Amann-Hildenbrand, A., Krooss, B.M., Harrington, J., Cuss, R., Davy, C., Skoczylas, F., Jacops, E., Maes, N., 2015. Gas Transfer Through Clay Barriers, in: Tournassat, C., Steefel, C.I., Bourg, I.C., Bergaya, F. (Eds.), Developments in Clay Science. Elsevier, pp. 227-267.

Arnedo, D., Alonso, E.E., Olivella, S., 2013. Gas flow in anisotropic claystone: Modelling triaxial experiments. International Journal for Numerical and Analytical Methods in Geomechanics 37, 2239-2256.

Arson, C., Pereira, J.-M., 2013. Influence of damage on pore size distribution and permeability of rocks. International Journal for Numerical and Analytical Methods in Geomechanics 37, 810-831.

Atiezo, M.K., Dascalu, C., 2017. Antiplane two-scale model for dynamic failure. International Journal of Fracture 206, 195-214.

Atkinson, B.K., 1987. Fracture Mechanics of Rock. Academic Press, London, UK.

Atkinson, B.K., Meredith, P.G., 1987. The theory of subcritical crack growth with applications to minerals and rocks. Academic Press, New York.

Berre, I., Doster, F., Keilegavlen, E., 2018. Flow in Fractured Porous Media: A Review of Conceptual Models and Discretization Approaches. Transport in Porous Media 130, 215-236.

Bhat, H.S., Rosakis, A.J., Sammis, C.G., 2012. A Micromechanics Based Constitutive Model for Brittle Failure at High Strain Rates. J. Appl. Mech.-Trans. ASME 79, 12.

Bui, T.A., Wong, H., Deleruyelle, F., Xie, L.Z., Tran, D.T., 2017. A thermodynamically consistent model accounting for viscoplastic creep and anisotropic damage in unsaturated rocks. International Journal of Solids and Structures 117, 26-38.

Charles, R., 1958. Dynamic fatigue of glass. Journal of Applied Physics 29, 1657-1662.

Chen, X.F., Eichhubl, P., Olson, J.E., 2017. Effect of water on critical and subcritical fracture properties of Woodford shale. J. Geophys. Res.-Solid Earth 122, 2736-2750.

Chen, X.F., Eichhubl, P., Olson, J.E., Dewers, T.A., 2019. Effect of Water on Fracture Mechanical Properties of Shales. J. Geophys. Res.-Solid Earth 124, 2428-2444.

Coussy, O., 2004. Poromechanics. John Wiley & Sons, Chichester, England.

Cuss, R., Harrington, J., Giot, R., Auvray, C., 2014. Experimental observations of mechanical dilation at the onset of gas flow in Callovo-Oxfordian claystone. Geological Society Special Publication 400, 507-519.

Cuss, R.C., Harrington, J.F., Noy, D.J., 2012. Final report of FORGE WP4.1.1: The stress-path permeameter experiment conducted on Callovo-Oxfordian Claystone. British Geological Survey Commissioned Report, CR/12/140.

Dascalu, C., 2009. A two-scale damage model with material length. Comptes Rendus - Mecanique 337, 645-652.

Dascalu, C., 2018. Multiscale modeling of rapid failure in brittle solids: Branching instabilities. Mechanics of Materials 116, 77-89.

Dascalu, C., Bilbie, G., Agiasofitou, E.K., 2008. Damage and size effects in elastic solids: A homogenization

approach. International Journal of Solids and Structures 45, 409-430.
Dascalu, C., Dobrovat, A.M., Tricarico, M., 2010a. On a 3D micromechanical damage model. International Journal of Fracture 166, 153-162.
Dascalu, C., François, B., Keita, O., 2010b. A two-scale model for subcritical damage propagation. International Journal of Solids and Structures 47, 493-502.
Dascalu, C., Gbetchi, K., 2019. Dynamic evolution of damage by microcracking with heat dissipation. International Journal of Solids and Structures 174, 128-144.
Dormieux, L., Kondo, D., Ulm, F.J., 2006. A micromechanical analysis of damage propagation in fluid-saturated cracked media. Comptes Rendus - Mecanique 334, 440-446.
Faivre, M., Paul, B., Golfier, F., Giot, R., Massin, P., Colombo, D., 2016. 2D coupled HM-XFEM modeling with cohesive zone model and applications to fluid-driven fracture network. Engineering Fracture Mechanics 159, 115-143.
Fall, M., Nasir, O., Nguyen, T.S., 2014. A coupled hydro-mechanical model for simulation of gas migration in host sedimentary rocks for nuclear waste repositories. Engineering Geology 176, 24-44.
Fidelibus, C., 2007. The 2D hydro-mechanically coupled response of a rock mass with fractures via a mixed BEM-FEM technique. International Journal for Numerical and Analytical Methods in Geomechanics 31, 1329-1348.
François, B., Dascalu, C., 2010. A two-scale time-dependent damage model based on non-planar growth of micro-cracks. Journal of the Mechanics and Physics of Solids 58, 1928-1946.
Frey, J., Chambon, R., Dascalu, C., 2013. A two-scale poromechanical model for cohesive rocks. Acta Geotechnica 8, 107-124.
Fu, P., Johnson, S.M., Carrigan, C.R., 2013. An explicitly coupled hydro-geomechanical model for simulating hydraulic fracturing in arbitrary discrete fracture networks. International Journal for Numerical and Analytical Methods in Geomechanics 37, 2278-2300.
Gao, Q., Tao, J.L., Hu, J.Y., Yu, X., 2015. Laboratory study on the mechanical behaviors of an anisotropic shale rock. Journal of Rock Mechanics and Geotechnical Engineering 7, 213-219.
Gensterblum, Y., Ghanizadeh, A., Cuss, R.J., Amann-Hildenbrand, A., Krooss, B.M., Clarkson, C.R., Harrington, J.F., Zoback, M.D., 2015. Gas transport and storage capacity in shale gas reservoirs - A review. Part A: Transport processes. Journal of Unconventional Oil and Gas Resources 12, 87-122.
Gerard, P., Harrington, J., Charlier, R., Collin, F., 2014. Modelling of localised gas preferential pathways in claystone. International Journal of Rock Mechanics and Mining Sciences 67, 104-114.
Gonzalez-Blanco, L., Romero, E., Jommi, C., Li, X., Sillen, X., 2016. Gas migration in a Cenozoic clay: Experimental results and numerical modelling. Geomechanics for Energy and the Environment 6, 81-100.
Guo, G., Fall, M., 2018. Modelling of dilatancy-controlled gas flow in saturated bentonite with double porosity and double effective stress concepts. Engineering Geology 243, 253-271.
Guo, G., Fall, M., 2019. Modelling of preferential gas flow in heterogeneous and saturated bentonite based on phase field method. Computers and Geotechnics 116, 103206.
Harrington, J., Volckaert, G., Jacobs, E., Maes, N., Areias, L., Charlier, R., Granet, S., 2013a. Summary report: Experiments and modelling of excavation damage zone (EDZ) behaviour in argillaceous and crystalline rocks (Work Package 4). EC FORGE Project Report D4.24-R.
Harrington, J.F., Cuss, R.J., Talandier, J., 2017. Gas transport properties through intact and fractured Callovo-Oxfordian mudstones. Geological Society Special Publication 454, 131-154.
Harrington, J.F., de la Vaissière, R., Noy, D.J., Cuss, R.J., Talandier, J., 2012a. Gas flow in Callovo-Oxfordian claystone (COx): Results from laboratory and field-scale measurements. Mineralogical Magazine 76, 3303-3318.
Harrington, J.F., Horseman, S.T., 1999. Gas transport properties of clays and mudrocks. Geological Society Special Publication 158, 107-124.
Harrington, J.F., Milodowski, A.E., Graham, C.C., Rushton, J.C., Cuss, R.J., 2012b. Evidence for gas-induced pathways in clay using a nanoparticle injection technique. Mineralogical Magazine 76, 3327-3336.
Harrington, J.F., Noy, D.J., Cuss, R.C., 2013b. Callovo-Oxfordian Claystone: processes governing advective gas flow. British Geological Survey Commissioned Report, CR/13/088.
Hashiba, K., Fukui, K., 2015. Effect of Water on the Deformation and Failure of Rock in Uniaxial Tension. Rock Mechanics and Rock Engineering 48, 1751-1761.
Hildenbrand, A., Schlömer, S., Krooss, B.M., 2002. Gas breakthrough experiments on fine-grained sedimentary rocks. Geofluids 2, 3-23.
Jin, Z.F., Li, W.X., Jin, C.R., Hambleton, J., Cusatis, G., 2018. Anisotropic elastic, strength, and fracture properties of Marcellus shale. International Journal of Rock Mechanics and Mining Sciences 109, 124-137.

Johnson, L., Marschall, P., Zuidema, P., Gribi, P., 2004. Effects of post-disposal gas generation in a repository for spent fuel, high-level waste and long-lived intermediate level waste sited in opalinus clay. National Cooperative for the Disposal of Radioactive Waste (NAGRA), NTB 04-06.

Lei, Q., Latham, J.-P., Tsang, C.-F., 2017. The use of discrete fracture networks for modelling coupled geomechanical and hydrological behaviour of fractured rocks. Computers and Geotechnics 85, 151-176.

Li, H., Zhu, Y., 2002. Fracture mechanics of frozen soils. Ocean Press, Beijing, PR China.(in Chinese).

Liang, S., Ren, X., Li, J., 2018. A mesh-size-objective modeling of quasi-brittle material using micro-cell informed damage law. Int. J. Damage Mech. 27, 913-936.

Lisjak, A., Grasselli, G., Vietor, T., 2014. Continuum-discontinuum analysis of failure mechanisms around unsupported circular excavations in anisotropic clay shales. International Journal of Rock Mechanics and Mining Sciences 65, 96-115.

Lisjak, A., Tatone, B.S.A., Mahabadi, O.K., Grasselli, G., Marschall, P., Lanyon, G.W., Vaissière, R.d.l., Shao, H., Leung, H., Nussbaum, C., 2016. Hybrid Finite-Discrete Element Simulation of the EDZ Formation and Mechanical Sealing Process Around a Microtunnel in Opalinus Clay. Rock Mechanics and Rock Engineering 49, 1849-1873.

Luo, Y., Xie, H.P., Ren, L., Zhang, R., Li, C.B., Gao, C., 2018. Linear Elastic Fracture Mechanics Characterization of an Anisotropic Shale. Sci Rep 8, 12.

Mahjoub, M., Rouabhi, A., Tijani, M., Granet, S., M'Jahad, S., Talandier, J., M'Jahad, S., Talandier, J., 2018. Numerical Study of Callovo-Oxfordian Argillite Expansion due to Gas Injection. International Journal of Geomechanics 18.

Miura, K., Okui, Y., Horii, H., 2003. Micromechanics-based prediction of creep failure of hard rock for long-term safety of high-level radioactive waste disposal system. Mechanics of Materials 35, 587-601.

Munjiza, A., Latham, J.P., Andrews, K.R.F., 2000. Detonation gas model for combined finite-discrete element simulation of fracture and fragmentation. International Journal for Numerical Methods in Engineering 49, 1495-1520.

Nara, Y., Kaneko, K., 2006. Sub-critical crack growth in anisotropic rock. International Journal of Rock Mechanics and Mining Sciences 43, 437-453.

Nguyen, T.S., Le, A.D., 2015. Simultaneous gas and water flow in a damage-susceptible bedded argillaceous rock. Canadian Geotechnical Journal 52, 18-32.

Olivella, S., Alonso, E.E., 2008. Gas flow through clay barriers. Géotechnique 58, 157-176.

Ortiz, L., Volckaert, G., Mallants, D., 2002. Gas generation and migration in Boom Clay, a potential host rock formation for nuclear waste storage. Engineering Geology 64, 287-296.

Paluszny, A., Salimzadeh, S., Zimmerman, R.W., 2018. Finite-Element Modeling of the Growth and Interaction of Hydraulic Fractures in Poroelastic Rock Formations, Hydraulic Fracture Modeling. Elsevier, pp. 1-19.

Popp, T., Wiedemann, M., Böhnel, H., Minkley, W., Manthei, G., 2007. Untersuchungen zur Barriereintegrität im Hinblick auf das Ein-Endlager-Konzept. Insitut fur Gebirgsmechanik GmbH, Leipzig, Germany.

Pouya, A., Vo, T.D., Hemmati, S., Tang, A.M., 2019. Modeling soil desiccation cracking by analytical and numerical approaches. International Journal for Numerical and Analytical Methods in Geomechanics 43, 738-763.

Rodwell, W.R., Harris, A.W., Horseman, S.T., Lalieux, P., Müller, W., Ortiz Amaya, L., Pruess, K., 1999. Gas migration and two-phase flow through engineered and geological barriers for a deep repository for radioactive waste. Joint EC/NEA Status Report.

Rozhko, A.Y., 2016. Two-phase fluid-flow modeling in a dilatant crack-like pathway. Journal of Petroleum Science and Engineering 146, 1158-1172.

Salimzadeh, S., Khalili, N., 2015. A three-phase XFEM model for hydraulic fracturing with cohesive crack propagation. Computers and Geotechnics 69, 82-92.

Sánchez-Palencia, E., 1980. Non-homogeneous media and vibration theory. Springer, Berlin.

Segura, J.M., Carol, I., 2010. Numerical modelling of pressurized fracture evolution in concrete using zero-thickness interface elements. Engineering Fracture Mechanics 77, 1386-1399.

Senger, R., Romero, E., Ferrari, A., Marschall, P., 2014. Characterization of gas flow through low-permeability claystone: laboratory experiments and two-phase flow analyses. Geological Society Special Publication 400, 531-543.

Senger, R., Romero, E., Marschall, P., 2018. Modeling of Gas Migration Through Low-Permeability Clay Rock Using Information on Pressure and Deformation from Fast Air Injection Tests. Transport in Porous Media 123, 1-17.

Shao, J.F., Zhou, H., Chau, K.T., 2005. Coupling between anisotropic damage and permeability variation in brittle rocks. International Journal for Numerical and Analytical Methods in Geomechanics 29, 1231-1247.

Shaw, R.P., 2015. The Fate of Repository Gases (FORGE) project. Geological Society Special Publication 415, 1-7.
Souley, M., Homand, F., Pepa, S., Hoxha, D., 2001. Damage-induced permeability changes in granite: a case example at the URL in Canada. International Journal of Rock Mechanics and Mining Sciences 38, 297-310.
Sun, Z.-x., Zhang, X., Xu, Y., Yao, J., Wang, H.-x., Lv, S., Sun, Z.-l., Huang, Y., Cai, M.-y., Huang, X., 2017. Numerical simulation of the heat extraction in EGS with thermal-hydraulic-mechanical coupling method based on discrete fractures model. Energy 120, 20-33.
Swanson, P.L., 1984. Subcritical crack growth and other time- and environment-dependent behavior in crustal rocks. Journal of Geophysical Research 89, 4137-4152.
Tang, C.A., Tham, L.G., Lee, P.K.K., Yang, T.H., Li, L.C., 2002. Coupled analysis of flow, stress and damage (FSD) in rock failure. International Journal of Rock Mechanics and Mining Sciences 39, 477-489.
van den Eijnden, A.P., Besuelle, P., Chambon, R., Collin, E., 2016. A FE2 modelling approach to hydromechanical coupling in cracking-induced localization problems. International Journal of Solids and Structures 97-98, 475-488.
Vyazmensky, A., Stead, D., Elmo, D., Moss, A., 2010. Numerical analysis of block caving-induced instability in large open pit slopes: A finite element/discrete element approach. Rock Mechanics and Rock Engineering 43, 21-39.
Wang, H., 2016. Numerical investigation of fracture spacing and sequencing effects on multiple hydraulic fracture interference and coalescence in brittle and ductile reservoir rocks. Engineering Fracture Mechanics 157, 107-124.
Wang, W., Shao, J.F., Zhu, Q.Z., Xu, W.Y., 2015. A discrete viscoplastic damage model for time-dependent behaviour of quasi-brittle rocks. Int. J. Damage Mech. 24, 21-40.
Wiseall, A.C., Cuss, R.J., Graham, C.C., Harrington, J.F., 2015. The visualization of flow paths in experimental studies of clay-rich materials. Mineralogical Magazine 79, 1335-1342.
Wrzesniak, A., Dascalu, C., Bésuelle, P., 2015. A two-scale time-dependent model of damage: Influence of micro-cracks friction. European Journal of Mechanics, A/Solids 49, 345-361.
Xu, C., Fidelibus, C., Dowd, P., Wang, Z., Tian, Z., 2018a. An iterative procedure for the simulation of the steady-state fluid flow in rock fracture networks. Engineering Geology 242, 160-168.
Xu, W., Shao, H., Marschall, P., Hesser, J., Kolditz, O., 2013a. Analysis of flow path around the sealing section HG-A experiment in the Mont Terri Rock Laboratory. Environmental Earth Sciences 70, 3363-3380.
Xu, W.J., Shao, H., Hesser, J., Wang, W., Schuster, K., Kolditz, O., 2013b. Coupled multiphase flow and elasto-plastic modelling of in-situ gas injection experiments in saturated claystone (Mont Terri Rock Laboratory). Engineering Geology 157, 55-68.
Xu, X., Wu, S., Jin, A., Gao, Y., 2018b. Review of the relationships between crack initiation stress, Mode I fracture toughness and tensile strength of geo-materials. International Journal of Geomechanics 18, 04018136.
Yang, J., Fall, M., Guo, G., 2020. A Three-Dimensional Hydro-mechanical Model for Simulation of Dilatancy Controlled Gas Flow in Anisotropic Claystone. Rock Mechanics and Rock Engineering 53, 4091-4116.
Zhang, R., Jiang, Z., Sun, Q., Zhu, S., 2013. The relationship between the deformation mechanism and permeability on brittle rock. Natural Hazards 66, 1179-1187.
Zhang, Z.X., 2002. An empirical relation between mode I fracture toughness and the tensile strength of rock. International Journal of Rock Mechanics and Mining Sciences 39, 401-406.
Zhuang, X., Wang, Q., Zhu, H., 2017. Multiscale modelling of hydro-mechanical couplings in quasi-brittle materials. International Journal of Fracture 204, 1-27.

5.3 Paper V: A Two-Scale Hydro-Mechanical-Damage Model for Simulation of Preferential Gas Flow in Saturated Clayey Host Rocks for Nuclear Repository

Published in *Computers and Geotechnics*, 138, 2021, 104365, doi:10.1016/j.compgeo.2021.104365.

Jianxiong Yang, Mamadou Fall

Department of Civil Engineering, University of Ottawa, Ottawa, ON, Canada

Abstract: Significant amounts of gases could be generated in the post-phase of radioactive waste repositories, which may deteriorate the integrity of natural host rocks. A safety issue related to the geological disposal facilities concerns the gas migration through saturated host rocks, of which the dominant process is mainly referred to the advective gas flow, accompanied by the formation of micro-fracturing that occurs at the applied gas pressure significantly lower than the minimum principal stress (compressive stress is regarded to be positive here). These fracture formed gas pathways are found to be highly localized and dynamically unstable, which may vary temporally and spatially within the clayey rocks. A multiscale model incorporating the evolving microcracks may be appropriate to address this specific rupture pattern. The model is developed from the periodically distributed microstructures with microcracks in a porous medium. The upscaling method based on the asymptotic expansions leads to the macroscopic hydro-mechanical (HM) governing equations coupled with the normalized microcrack length. Based on the micro-mechanical energy analysis, the time-dependent damage evolution law is constructed that accounts for the subcritical microcrack propagation. The local macroscopic response of the model is analyzed with emphasis on the influence of the microstructural size, the loading rate and the reference crack velocity, which are important factors influencing the localized pathways for gas migration. Two numerical examples of air injection tests on clayey rocks are presented where the highly localized gas pathways are explicitly simulated. The comparison between the model predictions and the experimental results provides in-depth understanding of gas induced fracturing process.

Keywords: nuclear waste repository; advective gas flow; saturated clayey rock; microcracks; time-dependent damage law; localized pathway.

Nomenclature

Latin symbols

A_{ij}^{*}	homogenized hydraulic coefficients
A_k	empirical parameter
b_{ij}	Eshelby configurational stress tensor
$\boldsymbol{b}$	Eshelby configurational stress tensor in matrix format
c_g^{*}	homogenized specific gas pressure coefficient
C_{ijkl}	stiffness tensor for isotropic solid
C_{ijkl}^{*}	homogenized stiffness tensor
d	damage variable
d_0	initial damage value
$\mathcal{D}$	energy dissipation for damage evolution
e_i	unit vector along crack propagation direction
$\boldsymbol{e}$	unit vector along crack propagation direction in vector format
e_{xij}	macroscopic strain tensor
$\boldsymbol{e}_x$	macroscopic strain tensor in matrix format
e_{yij}	microscopic strain tensor
$\boldsymbol{e}_y$	microscopic strain tensor in matrix format
E	Young's modulus
$\mathcal{G}^{\varepsilon}$	energy release rate at the crack tip
$\mathcal{G}_{cr}$	critical energy threshold
$\mathcal{G}_y$	scaled energy release rate in reference cell
$k_{ij,g}$	intrinsic permeability tensor of gas flow
$k_{ij,w}$	intrinsic permeability tensor of water flow
k_{π}	isotropic intrinsic permeability for fluid π
$k_{\pi 0}$	initial intrinsic permeability value for fluid π
$k_{ij,\pi}^{*}$	homogenized intrinsic permeability tensor of fluid π $(\pi = g,\ w)$
K_0	reference stress intensity factor
K_I	model-I stress intensity factor
K_{Ic}	critical stress intensity factor
l	microcrack length
$p_w^{(r)}$	Y-periodic function of water pressure field at order r (r=0, 1, 2 …)
$q_{i,g}^{\varepsilon}$	gas mass flux of heterogeneous porous medium
$\boldsymbol{q}_g^{\varepsilon}$	gas mass flux of heterogeneous porous medium in vector format
$q_{i,w}^{\varepsilon}$	water mass flux of heterogeneous porous medium
$\boldsymbol{q}_w^{\varepsilon}$	water mass flux of heterogeneous porous medium in vector format
$q_{i,g}^{(r)}$	Y-periodic function of gas mass flux at order r (r=-1, 0, 1 …)
$\boldsymbol{q}_g^{(r)}$	Y-periodic function of gas mass flux at order r (r=-1, 0, 1 …) in vector format
$q_{i,w}^{(r)}$	Y-periodic function of water mass flux at order r (r=-1, 0, 1 …)
$\boldsymbol{q}_w^{(r)}$	Y-periodic function of water mass flux at order r (r=-1, 0, 1 …) in vector format
$Q_{i,g}^{(0)}$	macroscopic gas flux
$Q_{i,w}^{(0)}$	macroscopic water flux
R	universal gas constant
T	absolute temperature
T_0	room temperature
u_i^{ε}	displacement field of heterogeneous body
$\boldsymbol{u}^{\varepsilon}$	displacement field of heterogeneous body in vector format
$u_i^{(r)}$	Y-periodic function of displacement field at order r (r=0, 1, 2 …)
$\boldsymbol{u}^{(r)}$	Y-periodic function of displacement field at order r (r=0, 1, 2 …) in vector format
v_0	reference crack velocity
x_i	macroscopic coordinate
$\boldsymbol{x}$	macroscopic coordinate in vector format
y_i	microscopic coordinate
$\boldsymbol{y}$	microscopic coordinate in vector format
Y_d	damage energy release rate

Greek symbols

β_t	empirical parameter
γ_t	fitted linear coefficient
δ_{ij}	Kronecker delta
ε	scale parameter
ζ	elementary solution of fluid problem
η_g	dynamic viscosity of gas

l_c	size of locally periodic cell	η_w	dynamic viscosity of water
L_c	size of macrostructure	λ	Lame coefficient
$L(d)$	correction factor of permeability	μ	Lame coefficient
M	molar mass of gas	ν	Poisson's ratio
n	subcritical growth index	$\boldsymbol{\xi}^{ij}$	characteristic function of elementary deformation modes in vector format
$\boldsymbol{n}$	outward unit vector normal to the circle in vector format	ρ_g	gas density
N_i	unit vector normal to crack	ρ_w	water density
$\boldsymbol{N}$	unit vector normal to crack in vector format	σ_t	tensile strength
N_{si}	unit vector normal to gas boundary	$\sigma_{ij}^{\varepsilon}$	total stress field of heterogeneous body
p_{ig}	gas injection pressure	$\boldsymbol{\sigma}^{\varepsilon}$	total stress field of heterogeneous body in matrix format
p_{og}	gas pressure at outlet	$\sigma_{ij}^{(r)}$	Y -periodic function of total stress at order r (r =-1, 0, 1 …)
p_3	confining pressure	$\boldsymbol{\sigma}^{(r)}$	Y -periodic function of total stress at order r (r =-1, 0, 1 …) in matrix format
p_f^{ε}	fluid pressure field of heterogeneous porous medium	ϕ_g	porosity occupied by gas
p_g^{ε}	gas pressure field of heterogeneous porous medium	ϕ_w	porosity occupied by water
p_w^{ε}	water pressure field of heterogeneous porous medium	ϕ	total porosity
$p_f^{(r)}$	Y -periodic function of fluid pressure field at order r (r =0, 1, 2 …)	$\Sigma_{ij}^{(0)}$	macroscopic total stress tensor
$p_g^{(r)}$	Y -periodic function of gas pressure field at order r (r =0, 1, 2 …)		

5.3.1 Introduction

To properly deal with the radioactive wastes generated from the nuclear power plants, deep geological disposal has been widely investigated as a feasible way to isolate the waste from the accessible biosphere (Norris, 2015). The environmental safety is a key necessity throughout the whole process of depositing the waste, which is guaranteed by a multi-barrier system including an engineered barrier system and a natural barrier system (Rodwell et al., 1999). In the post-phase after the wastes have been emplaced, the geological disposal facilities (GDFs) will be saturated with groundwater (Lu et al., 2020; Pazdniakou and Dymitrowska, 2018). A significant amount of gases can be generated due to water radiolysis, metal corrosion and microbial reaction (Shaw, 2015). This gas production may lead to the formation of free gas phase and in consequence the local gas pressure may increase. As a final impediment to waste migration, the integrity of natural host rocks may be compromised due to the increasing of local gas pressure. Thus understanding gas migration through host rocks is important for the safety evaluation of

GDFs.

Due to the favored properties of clayey rocks, e.g., thick formation, low permeability and good radionuclide capacity, the Callovo-Oxfordian (COx) claystone in France (Harrington et al., 2012a), Opalinus (OPA) Clay in Switzerland (Marschall et al., 2005) and Boom Clay in Belgium (Ortiz et al., 2002), are being investigated as potential host rocks. A number of laboratory gas injection tests (Gonzalez-Blanco et al., 2016; Harrington et al., 2017; Romero et al., 2013) as well as in-situ tests (De La Vaissière et al., 2014; Popp et al., 2007) have been conducted on the saturated clayey rock materials to accurately predict the gas migration behavior. The gas dissolution/diffusion is generally a background process that the transport efficiency is significantly restricted by the low permeability of clayey rocks. Therefore, the dominant process of gas flow that may deteriorate the rock integrity is mainly referred to the gas advective movement through porous rocks, where the transport capacity can be largely improved by the increase of intrinsic permeability and pore structure change. Recent experimental results have demonstrated that the gas advective movement through clayey rocks is accompanied by the formation of gas induced micro-fracturing, which occurs at the applied gas pressure significantly lower than the minimum principal stress (if we consider compressive stress as positive here) (Gonzalez-Blanco et al., 2016; Harrington et al., 2017; Romero et al., 2013). The network of fracture formed pathways for gas flow was found to be highly localized and dynamically unstable, which may vary temporally and spatially within the clayey rocks (Harrington et al., 2017).

Many researchers have been attempting to explain the dynamic gas behavior using numerical models, most of which are focused on reproducing the experimental results based on the coupled hydro-mechanical (HM) relations. To circumvent the explicit simulation of gas fracturing network, the traditional HM models are commonly enriched by incorporating either the plasticity theory, as seen in (Nguyen and Le, 2015; Xu et al., 2013), or damage mechanics as those in (Fall et al., 2014). The intrinsic permeability for gas flow is specifically related to the plastic deformation or damage variable in these models, where some empirical parameters are introduced to calibrate the dynamic gas outflow rate to fit the experimental data. However, the proposed methods for analyzing the irreversible deformation may be limited to the gas fracture cycle test conducted by Popp et al. (2007), in which the gas injection pressure is applied higher than the minimum principal stress. This specific experimental condition makes it possible to

account for the gas induced tensile failure in the macroscopic plastic or damage models. In order to analyze the gas induced fracturing under other general laboratory conditions, a double porosity concept was adopted by Yang and Fall (2021a) to differentiate the fluid flow in matrix and fractures, as well as their corresponding deformations. The fracture opening/closure was implicitly represented by the volumetric deformation of the fractured continuum, which is beneficial to the development of preferential gas pathways. To account for the fracture information in a more physical sense, Yang et al. (2020) developed a three-dimensional (3D) model that incorporates two fracture sets in the rock matrix. Although the stiffness degradation and anisotropic deformation due to fracture opening are well represented, the model is still incapable of explicitly capturing the localized fractures of gas flow pathways.

In the recent years, the development of Fracture Mechanics is able to reproduce the creep failure (e.g., Amitrano and Helmstetter, 2006), brittle/quasi-brittle failure (e.g., Atiezo et al., 2019; Bhat et al., 2012), but the theory still has limited capacity to reproduce complex rupture patterns. The gas induced micro-fracturing in clayey rock materials is an example of these cases. The post-test microscopic observations of clayey rocks confirmed the formation of mode-I micro-fractures in the laboratory gas injection tests, which is an important contribution to gas breakthrough (Skurtveit et al., 2012). The fracture opening/closure was found to be controlled by the variation in local gas pressure and HM coupling with fabric dilation within clayey rocks (Harrington et al., 2017). A model incorporating the subcritical microcracks may be appropriate to represent the gas induced fracturing that occurs at the applied gas pressure below the macroscopic minimum principal stress. Since the microcracking takes place at scales much smaller than the macrostructure, a multiscale approach could be well used to address this issue.

Attempts to model the microcracking phenomenon in the context of Fracture Mechanics can be found in (Atiezo and Dascalu, 2017; Dascalu, 2018), where the dynamic fracture with branching instabilities was analyzed in detail under tensile loading condition. These models were directly developed from the dynamic microcrack propagation law by homogenization method that explicitly contains a microstructural length representing the uniform microcrack spacing, which are able to obtain major features of micro-branching behavior, despite the fact that the models are limited to pure mechanical case. There are some other models capable of incorporating the HM coupling in the multiscale approach, see e.g., (van den Eijnden et al., 2016), where the computational homogenization was included in the FE^2 method to analyze the

cracking induced localization problems in saturated medium. In the homogenization method proposed by Argilaga et al. (2016), an asymptotic expansion form of damage variable was introduced, and the damage evolution was governed by the opening or shearing of cracks. Based on the nonlinear relation of damage variable with respect to the crack opening, the macroscopic poroelastic properties are determined. More recently, Dascalu and Gbetchi (2019) used a similar homogenization method in (Atiezo and Dascalu, 2017) that extends the dynamic microcrack criterion from the mechanical case to the thermo-mechanical (TM) case, which highlighted the localized cooling prior to damage initiation as well as heating effect around the crack tip.

Inspired by the microscale analysis of permeability change on the interface element (van den Eijnden et al., 2016) and the homogenized poroelastic analysis on the crack characteristics (Argilaga et al., 2016), the dynamic microcrack criterion by Dascalu and Gbetchi (2019) may be adapted to the HM case. As a result, the gas induced micro-fracturing behavior can be addressed when a sudden change in stress/strain influences the fluid flow process. In our previous work (Yang and Fall, 2021b), the two-scale model is derived from the asymptotic homogenization method and the time-dependent damage model is constructed from the subcritical microcrack criterion. The model was demonstrated to qualitatively represent the experimental observations, e.g., failure characteristics in the uniaxial tension test and fracture branching near the gas inlet in the numerical example for gas flow process. However, only single phase (gas) flow is included in the two-scale HM framework. As a further improvement, the objective of the current work is to incorporate water flow in the two-scale formulation, which suits the in-situ condition. Besides, the damage evolution law is firstly derived based on the micro-mechanical energy balance. This is necessary to construct some other dynamic crack evolution laws, as have been done in (Dascalu and Gbetchi, 2019). These improvements are meaningful to further incorporate Biot's poroelastic theory as well as the gas-water interaction in the two-scale framework in future work. Lastly, the developed model will be used to quantitatively represent the experimentally observed behaviors by validating against two laboratory gas injection experiments.

In the remainder of the paper, the first part presents the two-scale HM fracture problem for an isotropic solid domain with periodically distributed microcracks. The asymptotic homogenization is detailed and the effective HM governing equations describing the macroscopic porous problem are performed in the second part. As a further step, the mechanical energy analysis is provided to construct the time-dependent damage law for evolving

microcracks. The proposed two-scale damage model allows to analyze the local macroscopic response for stress-strain behavior as well as damage evolution. Two numerical examples of air injection tests on clayey rocks and the comparison with experimental results are given in the last part.

5.3.2 Two-scale HM Fracture Problem

Prior to analyze the HM fracture problem, we adopt the plane strain deformations as well as sign convention of continuum mechanics in the study, such that expansive strain and tensile stress are counted positively, while compression is counted positively for pressure. Now consider a two-dimensional isotropic solid extracted from a porous continuum, which has the isotropic permeability to fluid flow. A large number of periodically distributed microcracks are contained in the solid, as represented in Figure 5.22. The solid domain and the union of microcracks are denoted by $\mathcal{B}$ and $\mathcal{C}$, respectively.

In the porous medium, the pore space is saturated by fluids with pore fluid pressure p_f^{ε} acting on the crack face. The distribution of microcracks as well as the microstructure is assumed to be locally periodic, as illustrated in Figure 5.22. Each crack is straight with length l and parallel to the x_1 axis. A general case of bedding-parallel micro-cracks (Ougier-Simonin et al., 2016) is adopted in the study. For some other types of micro-cracks orientated at an angle with the bedding plane (Padin et al., 2014), they are out of scope in the two-scale problem, as the formation of micro-cracks families is so complicated that may be influenced by stress history, mineral content, internal overpressure, thermal shrinkage or exploitation disturbance.

A parameter ε representing the difference between microscopic and macroscopic scales of the solid body is introduced as follows:

$$\varepsilon = \frac{l_c}{L_c} \tag{5.66}$$

where l_c is the size of periodic cell at micro-scale, L_c is the characteristic length of the macro-structure at macro-scale, see Figure 5.22.

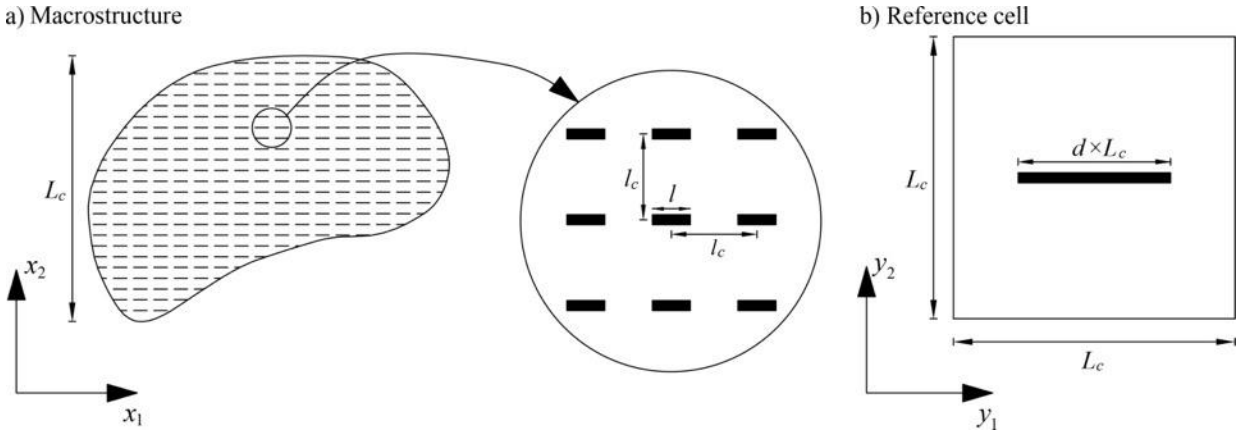

Figure 5.22 (a) Macrostructure of size L_c with periodically distributed micro-fractures, l and l_c are the local length of micro-fracture and micro-period, respectively. (b) Reference cell of size L_c with rescaled crack length $d \times L_c$. (adapted from (Dascalu and Gbetchi, 2019))

In the solid part of domain $\mathcal{B}$, the equilibrium equation of the system is formulated by neglecting the volume force, as follows:

$$\frac{\partial \sigma_{ij}^{\varepsilon}}{\partial x_j} = 0 \tag{5.67}$$

where $\sigma_{ij}^{\varepsilon}$ are the components of total stress tensor.

In order to avoid the additional complexity induced by the pore volume change, the porous material is assumed to have constant porosity, where the pore spaces consist of two disconnected porous networks. Two fluids (gas, water) are assumed to be immiscible and independent in their own network that the interaction between gas and water is delimited by the same internal solid wall (Coussy, 2007), thus the gas-water interaction is neglected in the study. The mass conservation of gas and water can be written in the following form, respectively:

$$\frac{d}{dt}\left(\rho_g \phi_g\right) + \frac{\partial q_{i,g}^{\varepsilon}}{\partial x_i} = 0 \tag{5.68}$$

$$\frac{d}{dt}\left(\rho_w \phi_w\right) + \frac{\partial q_{i,w}^{\varepsilon}}{\partial x_i} = 0 \tag{5.69}$$

where ρ_g and ρ_w are the gas density and water density, respectively; ϕ_g and ϕ_w are the porosity occupied by gas and water, respectively, while they have relations with the total porosity ϕ such that $\phi_g + \phi_w = \phi$; $q_{i,g}^{\varepsilon}$ and $q_{i,w}^{\varepsilon}$ are the mass flux of gas and water, respectively, which are defined by the generalized Darcy's law, as follows,

$$q_{i,g}^{\varepsilon} = -\rho_g \frac{k_{ij,g}}{\eta_g} \frac{\partial p_g^{\varepsilon}}{\partial x_j} \tag{5.70}$$

$$q_{i,w}^{\varepsilon} = -\rho_w \frac{k_{ij,w}}{\eta_w} \frac{\partial p_w^{\varepsilon}}{\partial x_j} \tag{5.71}$$

where p_g^{ε} and p_w^{ε} are the gas pressure and water pressure field, respectively; η_g and η_w are the dynamic viscosity for gas and water, $k_{ij,g}$ and $k_{ij,w}$ are the components of intrinsic permeability tensor for gas and water flow, respectively.

The constitutive law for isotropic incompressible solid is defined by the following relation,

$$\sigma_{ij}^{\varepsilon} = \lambda e_{xkk}(\boldsymbol{u}^{\varepsilon})\delta_{ij} + 2\mu e_{xij}(\boldsymbol{u}^{\varepsilon}) - p_f^{\varepsilon}\delta_{ij} \tag{5.72}$$

where λ and μ are the Lame coefficients, δ_{ij} is the Kronecker delta, p_f^{ε} is the pore fluid pressure. Following Nguyen and Le (2015), the fluid pressure is assumed to be equal to the maximum value between gas and water pressure, defined as follows:

$$p_f^{\varepsilon} = \mathrm{Max}\left(p_g^{\varepsilon}, p_w^{\varepsilon}\right) \tag{5.73}$$

The strain tensor components with respect to the macroscopic scale variable (x_i) is deduced in the framework of small strains, expressed by

$$e_{xkl}(\boldsymbol{u}^{\varepsilon}) = \frac{1}{2}\left(\frac{\partial u_k^{\varepsilon}}{\partial x_l} + \frac{\partial u_l^{\varepsilon}}{\partial x_k}\right) \tag{5.74}$$

Gas phase follows the behavior of ideal gas law and water is assumed to be an incompressible fluid for simplicity. The spatial variation of fluid is neglected due to the separation of scales (van den Eijnden et al., 2016). By adopting these assumptions, the mass balance equations (5.68)-(5.69) becomes:

$$\frac{M\phi_g}{RT}\frac{\partial p_g^{\varepsilon}}{\partial t} + \frac{\partial q_{i,g}^{\varepsilon}}{\partial x_i} = 0 \tag{5.75}$$

$$\frac{\partial q_{i,w}^{\varepsilon}}{\partial x_i} = 0 \tag{5.76}$$

where M and R are the molar mass and universal gas constant, respectively; T represents the absolute temperature.

Eqs. (5.67), (5.75)-(5.76) constitute the main governing equations in the two-scale porous system, in which the displacement $\boldsymbol{u}^{\varepsilon}$, gas pressure p_g^{ε} and water pressure p_w^{ε} fields will be further explored in the next section.

As fluid pressure is acting on the crack face that causes mode-I rupture, we assume the crack face is impermeable for fluid flow. The HM boundary conditions on the crack face may be

expressed as:

$$\boldsymbol{\sigma}^{\varepsilon}\boldsymbol{N} = -p_f^{\varepsilon}\boldsymbol{N} \quad ; \quad \boldsymbol{q}_g^{\varepsilon}\boldsymbol{N} = 0 \quad ; \quad \boldsymbol{q}_w^{\varepsilon}\boldsymbol{N} = 0 \tag{5.77}$$

where $\boldsymbol{N}$ is the unit vector normal to the crack face, as shown in Figure 5.23.

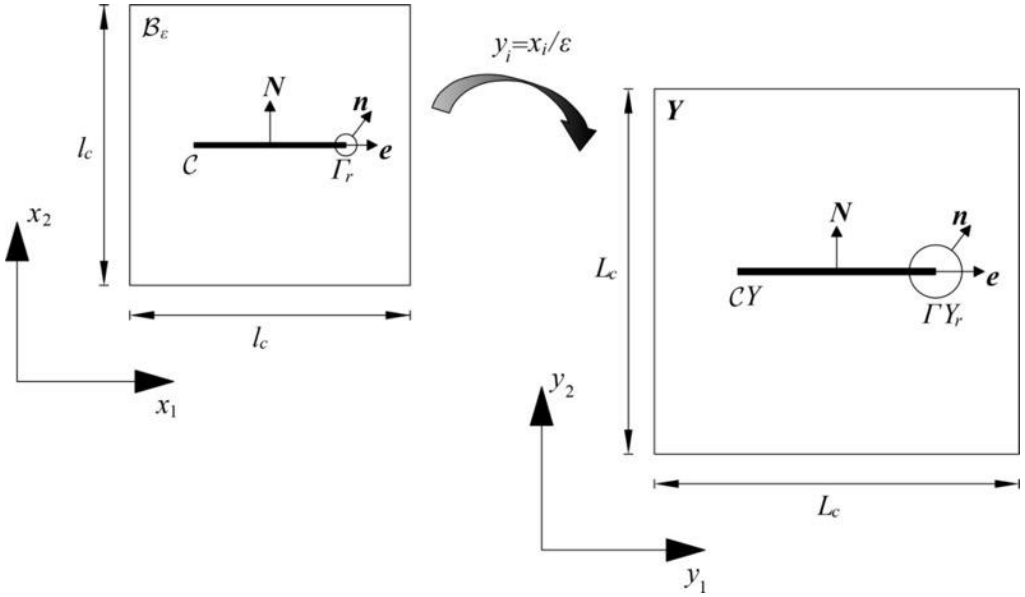

Figure 5.23 Scaling of the local microstructure on the reference cell (modified from (Dascalu and Gbetchi, 2019))

Following Freund (1998), the propagation of microcracks can be described by the energy release rate $\mathcal{G}^{\varepsilon}$, which is expressed with respect to the crack tip, as follows

$$\mathcal{G}^{\varepsilon} = \lim_{r\to 0}\int_{\Gamma_r} \boldsymbol{e}\cdot\boldsymbol{b}(\boldsymbol{u}^{\varepsilon})\boldsymbol{n}ds \tag{5.78}$$

where Γ_r is a closed circular contour with radius r encircling the crack tip, $\boldsymbol{n}$ is the outward unit vector normal to the circle, $\boldsymbol{e}$ is the unit vector along the crack propagation direction, as represented in Figure 5.23. $\boldsymbol{b}(\boldsymbol{u}^{\varepsilon})$ is the Eshelby configurational stress tensor, expressed as (Kienzler and Herrmann, 2000)

$$b_{ij}(\boldsymbol{u}^{\varepsilon}) = \frac{1}{2}C_{klmn}e_{xkl}(\boldsymbol{u}^{\varepsilon})e_{xmn}(\boldsymbol{u}^{\varepsilon})\delta_{ij} - C_{jklm}e_{xlm}(\boldsymbol{u}^{\varepsilon})u^{\varepsilon}_{k,i} \tag{5.79}$$

in which C_{ijkl} are elastic coefficients given by $C_{ijkl} = \lambda\delta_{ij}\delta_{kl} + \mu(\delta_{ik}\delta_{jl} + \delta_{il}\delta_{jk})$.

The integral of Eshelby configurational stress tensor at the crack tip is closely similar to the classical Griffith model where fracture propagation occurs from the competition between released elastic energy and the increased surface energy (Kuhn and Muller, 2010). In the classical fracture mechanics, the crack grows when the energy release rate $\mathcal{G}^{\varepsilon}$ reaches the critical energy threshold $\mathcal{G}_{cr}$. In the paper, a time-dependent propagation law will be proposed to account

for the evolving microcracks, which allows to describe the dynamic behavior of gas induced micro-fracturing in Section 5.3.4, as has been observed in (Cuss et al., 2014; Skurtveit et al., 2012).

5.3.3 Asymptotic Developments and Homogenization Analysis

In the following section, the asymptotic homogenization method by Sánchez-Palencia (1980) is employed to obtain the macroscopic governing equations for the porous system from the initial two-scale problem described previously. Similar techniques have been used in the coupled dynamic thermo-mechanical problems, see e.g., Dascalu and Gbetchi (2019); also in the hydraulic fracturing problems for solid matrix without microcracks, see Zhuang et al. (2017). For the present development, we attempt to deduce the influence of microcracks on the effective elastic and permeability coefficients, as well as to conduct the upscaling of governing equations.

Considering that the microstructural length l_c has been introduced as the size of microscopic period and also the spacing of neighboring microcracks, see Figure 5.22, the damage variable may be expressed as the ratio between the crack length l and the microstructural size l_c:

$$d = \frac{l}{l_c} \tag{5.80}$$

where d is damage variable representing the normalized microcrack length, as can be seen in Figure 5.22(a).

The local periodicity assumption ensures that the material behaves periodically over the macroscale domain, which allows for large-scale spatial variations of the damage variable. The intermittent nature of microcracks corresponds to material showing partly damage, and the microcracking process is represented by the damage variable evolving from a small value to a large value until the structure is completely damaged. To link the material behavior at different scales, the following relation between the microscopic and macroscopic spatial coordinates is proposed:

$$y_i = \frac{x_i}{\varepsilon} \tag{5.81}$$

where $x_i (i = 1, 2)$ and y_i denote the components of macroscopic and microscopic coordinates, respectively, as illustrated in Figure 5.23; ε is a scale variable defined in Eq. (5.66). The scaling

of this transformation characterizes the field variables at different scales.

For a field f depending on both scales (x_i and y_i), the differential operator with respect to the spatial coordinates is formulated as:

$$f^{\varepsilon}_{,x_i} = \frac{\partial f}{\partial x_i} + \frac{1}{\varepsilon}\frac{\partial f}{\partial y_i},\ f^{\varepsilon}_{,y_i} = \frac{\partial f}{\partial y_i} \tag{5.82}$$

The separation of length scales is assumed in the homogenization analysis:

$$l_c \ll L_c \tag{5.83}$$

With this assumption being adopted, the macroscopic properties at the scale of solid body are distinguished from the microscopic properties characterizing the local behavior around the microcracks. Though the variations in microscopic coordinates $\boldsymbol{y}$ do not have much influence on macroscopic coordinates $\boldsymbol{x}$, both variations should be included in the physical fields.

The displacement $\boldsymbol{u}^{\varepsilon}$, gas pressure p_g^{ε} and water pressure p_w^{ε} fields are developed with respect to the scale parameter ε in the form:

$$\boldsymbol{u}^{\varepsilon} = \boldsymbol{u}^{(0)}(\boldsymbol{x},\boldsymbol{y},t) + \varepsilon\boldsymbol{u}^{(1)}(\boldsymbol{x},\boldsymbol{y},t) + \varepsilon^2\boldsymbol{u}^{(2)}(\boldsymbol{x},\boldsymbol{y},t) + \ldots \tag{5.84}$$

$$p_g^{\varepsilon} = p_g^{(0)}(\boldsymbol{x},\boldsymbol{y},t) + \varepsilon p_g^{(1)}(\boldsymbol{x},\boldsymbol{y},t) + \varepsilon^2 p_g^{(2)}(\boldsymbol{x},\boldsymbol{y},t) + \ldots \tag{5.85}$$

$$p_w^{\varepsilon} = p_w^{(0)}(\boldsymbol{x},\boldsymbol{y},t) + \varepsilon p_w^{(1)}(\boldsymbol{x},\boldsymbol{y},t) + \varepsilon^2 p_w^{(2)}(\boldsymbol{x},\boldsymbol{y},t) + \ldots \tag{5.86}$$

where $\boldsymbol{u}^{(i)}(\boldsymbol{x},\boldsymbol{y},t)$, $p_g^{(i)}(\boldsymbol{x},\boldsymbol{y},t)$, $p_w^{(i)}(\boldsymbol{x},\boldsymbol{y},t)$, $\boldsymbol{x}\in\mathcal{B}$, $\boldsymbol{y}\in Y$ are smooth and Y-periodic.

Using the developments of $\boldsymbol{u}^{\varepsilon}$, p_g^{ε} and p_w^{ε} in Eqs. (5.70)-(5.72), we obtain

$$\boldsymbol{\sigma}^{\varepsilon}(\boldsymbol{x},t) = \frac{1}{\varepsilon}\boldsymbol{\sigma}^{(-1)}(\boldsymbol{x},\boldsymbol{y},t) + \boldsymbol{\sigma}^{(0)}(\boldsymbol{x},\boldsymbol{y},t) + \varepsilon\boldsymbol{\sigma}^{(1)}(\boldsymbol{x},\boldsymbol{y},t) + \varepsilon^2\boldsymbol{\sigma}^{(2)}(\boldsymbol{x},\boldsymbol{y},t)\ldots \tag{5.87}$$

$$\boldsymbol{q}_g^{\varepsilon}(\boldsymbol{x},t) = \frac{1}{\varepsilon}\boldsymbol{q}_g^{(-1)}(\boldsymbol{x},\boldsymbol{y},t) + \boldsymbol{q}_g^{(0)}(\boldsymbol{x},\boldsymbol{y},t) + \varepsilon\boldsymbol{q}_g^{(1)}(\boldsymbol{x},\boldsymbol{y},t) + \varepsilon^2\boldsymbol{q}_g^{(2)}(\boldsymbol{x},\boldsymbol{y},t)\ldots \tag{5.88}$$

$$\boldsymbol{q}_w^{\varepsilon}(\boldsymbol{x},t) = \frac{1}{\varepsilon}\boldsymbol{q}_w^{(-1)}(\boldsymbol{x},\boldsymbol{y},t) + \boldsymbol{q}_w^{(0)}(\boldsymbol{x},\boldsymbol{y},t) + \varepsilon\boldsymbol{q}_w^{(1)}(\boldsymbol{x},\boldsymbol{y},t) + \varepsilon^2\boldsymbol{q}_w^{(2)}(\boldsymbol{x},\boldsymbol{y},t)\ldots \tag{5.89}$$

where

$$\sigma_{ij}^{(-1)} = \lambda e_{ykk}(\boldsymbol{u}^{(0)})\delta_{ij} + 2\mu e_{yij}(\boldsymbol{u}^{(0)}) \tag{5.90}$$

$$\sigma_{ij}^{(0)} = \lambda\left(e_{xkk}(\boldsymbol{u}^{(0)})\delta_{ij} + e_{ykk}(\boldsymbol{u}^{(1)})\right)\delta_{ij} + 2\mu\left(e_{xij}(\boldsymbol{u}^{(0)}) + e_{yij}(\boldsymbol{u}^{(1)})\right) - p_f^{(0)}\delta_{ij} \text{ with } p_f^{(0)} = \mathrm{Max}\left(p_g^{(0)}, p_w^{(0)}\right) \tag{5.91}$$

$$\sigma_{ij}^{(1)} = \lambda\left(e_{xkk}(\boldsymbol{u}^{(1)})\delta_{ij} + e_{ykk}(\boldsymbol{u}^{(2)})\right)\delta_{ij} + 2\mu\left(e_{xij}(\boldsymbol{u}^{(1)}) + e_{yij}(\boldsymbol{u}^{(2)})\right) - p_f^{(1)}\delta_{ij} \text{ with } p_f^{(1)} = \mathrm{Max}\left(p_g^{(1)}, p_w^{(1)}\right) \tag{5.92}$$

and

$$q_{i,g}^{(-1)} = -\rho_g \frac{k_{ij,g}}{\eta_g} \frac{\partial p_g^{(0)}}{\partial y_j} \; ; \; q_{i,g}^{(0)} = -\rho_g \frac{k_{ij,g}}{\eta_g} \left(\frac{\partial p_g^{(0)}}{\partial x_j} + \frac{\partial p_g^{(1)}}{\partial y_j} \right) \; ; \; q_{i,g}^{(1)} = -\rho_g \frac{k_{ij,g}}{\eta_g} \left(\frac{\partial p_g^{(1)}}{\partial x_j} + \frac{\partial p_g^{(2)}}{\partial y_j} \right) \tag{5.93}$$

$$q_{i,w}^{(-1)} = -\rho_w \frac{k_{ij,w}}{\eta_w} \frac{\partial p_w^{(0)}}{\partial y_j} \; ; \; q_{i,w}^{(0)} = -\rho_w \frac{k_{ij,w}}{\eta_w} \left(\frac{\partial p_w^{(0)}}{\partial x_j} + \frac{\partial p_w^{(1)}}{\partial y_j} \right) \; ; \; q_{i,w}^{(1)} = -\rho_w \frac{k_{ij,w}}{\eta_w} \left(\frac{\partial p_w^{(1)}}{\partial x_j} + \frac{\partial p_w^{(2)}}{\partial y_j} \right) \tag{5.94}$$

The asymptotic developments of momentum and mass balance equations (5.67), (5.75)-(5.76) lead to the problems for different orders ε^α, with $\alpha = -2,\ -1,\ 0$ in the form:

$$\varepsilon^{-2} \rightarrow \frac{\partial \sigma_{ij}^{(-1)}}{\partial y_j} = 0 \; ; \; \frac{\partial q_{i,g}^{(-1)}}{\partial y_i} = 0 \; ; \; \frac{\partial q_{i,w}^{(-1)}}{\partial y_i} = 0 \tag{5.95}$$

$$\varepsilon^{-1} \rightarrow \frac{\partial \sigma_{ij}^{(-1)}}{\partial x_j} + \frac{\partial \sigma_{ij}^{(0)}}{\partial y_j} = 0 \; ; \; \frac{\partial q_{i,g}^{(-1)}}{\partial x_i} + \frac{\partial q_{i,g}^{(0)}}{\partial y_i} = 0 \; ; \; \frac{\partial q_{i,w}^{(-1)}}{\partial x_i} + \frac{\partial q_{i,w}^{(0)}}{\partial y_i} = 0 \tag{5.96}$$

$$\varepsilon^{0} \rightarrow \frac{\partial \sigma_{ij}^{(0)}}{\partial x_j} + \frac{\partial \sigma_{ij}^{(1)}}{\partial y_j} = 0 \; ; \; \frac{M\phi_g}{RT} \frac{\partial p_g^{(0)}}{\partial t} + \frac{\partial q_{i,g}^{(0)}}{\partial x_i} + \frac{\partial q_{i,g}^{(1)}}{\partial y_i} = 0 \; ; \; \frac{\partial q_{i,w}^{(0)}}{\partial x_i} + \frac{\partial q_{i,w}^{(1)}}{\partial y_i} = 0 \tag{5.97}$$

The corresponding boundary conditions on crack face can be obtained from Eq. (5.77) in terms of different orders $\boldsymbol{\sigma}^{(m)}$, $\boldsymbol{q}_g^{(m)}$ and $\boldsymbol{q}_w^{(m)}$:

$$m = -1 \rightarrow \sigma_{ij}^{(-1)} N_j = 0 \; ; \; q_{i,g}^{(-1)} N_i = 0 \; ; \; q_{i,w}^{(-1)} N_i = 0 \tag{5.98}$$

$$m = 0 \rightarrow \left(\sigma_{ij}^{(0)} + p_f^{(0)} \delta_{ij} \right) N_j = 0 \; ; \; q_{i,g}^{(0)} N_i = 0 \; ; \; q_{i,w}^{(0)} N_i = 0 \tag{5.99}$$

$$m = 1 \rightarrow \left(\sigma_{ij}^{(1)} + p_f^{(1)} \delta_{ij} \right) N_j = 0 \; ; \; q_{i,g}^{(1)} N_i = 0 \; ; \; q_{i,w}^{(1)} N_i = 0 \tag{5.100}$$

In the following part, we attempt to complete the boundary value problems at different orders. Firstly at the order ε^{-2}, the problem for $\boldsymbol{u}^{(0)}$, $p_g^{(0)}$ and $p_w^{(0)}$ results from Eqs. (5.90), (5.93)-(5.95) and (5.98) as:

$$\frac{\partial}{\partial y_j} \left(\lambda e_{ykk}(\boldsymbol{u}^{(0)}) \delta_{ij} + 2\mu e_{yij}(\boldsymbol{u}^{(0)}) \right) = 0, \text{ in } Y \tag{5.101}$$

$$\left(\lambda e_{ykk}(\boldsymbol{u}^{(0)}) \delta_{ij} + 2\mu e_{yij}(\boldsymbol{u}^{(0)}) \right) N_j = 0, \text{ on } \mathcal{C}Y \tag{5.102}$$

and the gas flow equations:

$$\frac{\partial}{\partial y_i} \left(-\frac{\rho_g}{\eta_g} k_{ij,g} \frac{\partial p_g^{(0)}}{\partial y_j} \right) = 0, \text{ in } Y \tag{5.103}$$

$$-\frac{\rho_g}{\eta_g} k_{ij,g} \frac{\partial p_g^{(0)}}{\partial y_j} N_i = 0, \text{ on } \mathcal{C}Y \tag{5.104}$$

as well as water flow equations:

$$\frac{\partial}{\partial y_i}\left(-\frac{\rho_w}{\eta_w}k_{ij,w}\frac{\partial p_w^{(0)}}{\partial y_j}\right)=0,\ \text{in } Y \tag{5.105}$$

$$-\frac{\rho_w}{\eta_w}k_{ij,w}\frac{\partial p_w^{(0)}}{\partial y_j}N_i=0,\ \text{on } \mathcal{C}Y \tag{5.106}$$

It should be specified that the periodicity conditions are applied on the opposite exterior boundaries of domain Y.

In order to fulfill the zero condition on the right member of Eqs. (5.102), (5.104) and (5.106), it is easily found $\boldsymbol{u}^{(0)}$, $p_g^{(0)}$ and $p_w^{(0)}$ only depend on the x variables such that $\boldsymbol{u}^{(0)}=\boldsymbol{u}^{(0)}(\boldsymbol{x},t)$, $p_g^{(0)}=p_g^{(0)}(\boldsymbol{x},t)$ and $p_w^{(0)}=p_w^{(0)}(\boldsymbol{x},t)$, which represent the macroscopic displacement, gas pressure and water pressure fields.

Secondly the next order (ε^{-1}) problem for $\boldsymbol{u}^{(1)}$, $p_g^{(1)}$ and $p_w^{(1)}$ can be deduced from Eqs. (5.91), (5.93)-(5.94), (5.96) and (5.99) as:

$$\frac{\partial}{\partial y_j}\left(\lambda e_{ykk}(\boldsymbol{u}^{(1)})\delta_{ij}+2\mu e_{yij}(\boldsymbol{u}^{(1)})\right)=0,\ \text{in } Y \tag{5.107}$$

$$\left(\lambda e_{ykk}(\boldsymbol{u}^{(1)})\delta_{ij}+2\mu e_{yij}(\boldsymbol{u}^{(1)})\right)N_j=-\left(\lambda e_{xkk}(\boldsymbol{u}^{(0)})\delta_{ij}+2\mu e_{xij}(\boldsymbol{u}^{(0)})\right)N_j,\ \text{on } \mathcal{C}Y \tag{5.108}$$

and

$$\frac{\partial}{\partial y_i}\left(-\frac{\rho_g}{\eta_g}k_{ij,g}\left(\frac{\partial p_g^{(0)}}{\partial x_j}+\frac{\partial p_g^{(1)}}{\partial y_j}\right)\right)=0,\ \text{in } Y \tag{5.109}$$

$$\frac{\rho_g}{\eta_g}k_{ij,g}\left(\frac{\partial p_g^{(0)}}{\partial x_j}+\frac{\partial p_g^{(1)}}{\partial y_j}\right)N_i=0,\ \text{on } \mathcal{C}Y \tag{5.110}$$

and

$$\frac{\partial}{\partial y_i}\left(-\frac{\rho_w}{\eta_w}k_{ij,w}\left(\frac{\partial p_w^{(0)}}{\partial x_j}+\frac{\partial p_w^{(1)}}{\partial y_j}\right)\right)=0,\ \text{in } Y \tag{5.111}$$

$$\frac{\rho_w}{\eta_w}k_{ij,w}\left(\frac{\partial p_w^{(0)}}{\partial x_j}+\frac{\partial p_w^{(1)}}{\partial y_j}\right)N_i=0,\ \text{on } \mathcal{C}Y \tag{5.112}$$

with periodicity conditions applied on the opposite external boundaries of domain Y.

Considering that $\boldsymbol{u}^{(0)}(\boldsymbol{x},t)$ is only depended on $\boldsymbol{x}$, the particular form of crack face condition Eq. (5.108) shows that the solution of Eqs. (5.107)-(5.108) should take the following form (Dascalu et al., 2010a):

$$\boldsymbol{u}^{(1)}(\boldsymbol{x},\boldsymbol{y},t)=\boldsymbol{\xi}^{pq}(\boldsymbol{y})e_{xpq}(\boldsymbol{u}^{(0)}(\boldsymbol{x},t)) \tag{5.113}$$

where $\boldsymbol{\xi}^{pq}(\boldsymbol{y})$ are the elementary solutions of Eqs. (5.114)-(5.115) for the particular macroscopic strain $e_{xij}(\boldsymbol{u}^{(0)})=\delta_{ip}\delta_{jq}$:

$$\frac{\partial}{\partial y_j}\left(\lambda e_{ykk}(\boldsymbol{\xi}^{pq})\delta_{ij}+2\mu e_{yij}(\boldsymbol{\xi}^{pq})\right)=0,\ \text{in } Y \tag{5.114}$$

$$\left(\lambda e_{ykk}(\boldsymbol{\xi}^{pq})\delta_{ij}+2\mu e_{yij}(\boldsymbol{\xi}^{pq})\right)N_j=-\left(\lambda\delta_{ij}\delta_{pq}+\mu(\delta_{ip}\delta_{jq}+\delta_{iq}\delta_{jp})\right)N_j,\ \text{on } \mathcal{C}Y \tag{5.115}$$

With the consideration that gas and water flow in the porous material are characterized by the same hydraulic anisotropy induced by the fracturing process, thus the solutions for Eqs. (5.109)-(5.110) are also feasible for Eqs. (5.111)-(5.112). The microscopic correction of fluid (i.e., gas or water) pressure $p_\pi^{(1)}$ $(\pi=g,w)$ should have a dependence on the macroscopic fluid pressure $p_\pi^{(0)}$, where the form suggested by Zhuang et al. (2017) is adopted, with $N_1=0$, $N_2=1$:

$$p_\pi^{(1)}(\boldsymbol{x},\boldsymbol{y},t)=\zeta(\boldsymbol{y})\frac{\partial p_\pi^{(0)}(\boldsymbol{x},t)}{\partial x_2},\quad \pi=g,w \tag{5.116}$$

where $\zeta(\boldsymbol{y})$ is the component associated to the microscopic fluid pressure. For particular macroscopic fluid pressure $\frac{\partial p_\pi^{(0)}}{\partial x_j}=\delta_{jk}$ and isotropic permeability to fluid flow, $\zeta(\boldsymbol{y})$ can be obtained by solving the following cell problem:

$$\frac{\partial^2\zeta}{\partial y_1^2}+\frac{\partial^2\zeta}{\partial y_2^2}=0,\ \text{in } Y \tag{5.117}$$

$$\frac{\partial\zeta}{\partial y_2}=-1,\ \text{on } CY \tag{5.118}$$

We note that the solution of mechanical cell problems (5.114)-(5.115) depends on the normalized crack length and elastic moduli; while the fluid problem (5.117)-(5.118) is related to the normalized crack length.

Lastly at the order ε^0, we get the following HM problems from (5.92)-(5.94), (5.97) and (5.100):

$$\begin{aligned}&\frac{\partial}{\partial x_j}\left(\lambda\left(e_{xkk}(\boldsymbol{u}^{(0)})\delta_{ij}+e_{ykk}(\boldsymbol{u}^{(1)})\right)\delta_{ij}+2\mu\left(e_{xij}(\boldsymbol{u}^{(0)})+e_{yij}(\boldsymbol{u}^{(1)})\right)-p^{(0)}\delta_{ij}\right)+\\&\frac{\partial}{\partial y_j}\left(\lambda\left(e_{xkk}(\boldsymbol{u}^{(1)})\delta_{ij}+e_{ykk}(\boldsymbol{u}^{(2)})\right)\delta_{ij}+2\mu\left(e_{xij}(\boldsymbol{u}^{(1)})+e_{yij}(\boldsymbol{u}^{(2)})\right)-p^{(1)}\delta_{ij}\right)=0\end{aligned},\ \text{in } Y \tag{5.119}$$

$$\left(\lambda\left(e_{xkk}(\boldsymbol{u}^{(1)})\delta_{ij}+e_{ykk}(\boldsymbol{u}^{(2)})\right)\delta_{ij}+2\mu\left(e_{xij}(\boldsymbol{u}^{(1)})+e_{yij}(\boldsymbol{u}^{(2)})\right)-p^{(1)}\delta_{ij}\right)N_j=0,\ \text{on}\ \mathcal{C}Y \tag{5.120}$$

and

$$\frac{M\phi_g}{RT}\frac{\partial p_g^{(0)}}{\partial t}-\frac{\rho_g}{\eta_g}\left(\frac{\partial}{\partial x_i}\left(k_{ij,g}\left(\frac{\partial p_g^{(0)}}{\partial x_j}+\frac{\partial p_g^{(1)}}{\partial y_j}\right)\right)+\frac{\partial}{\partial y_i}\left(k_{ij,g}\left(\frac{\partial p_g^{(1)}}{\partial x_j}+\frac{\partial p_g^{(2)}}{\partial y_j}\right)\right)\right)=0,\ \text{in}\ Y \tag{5.121}$$

$$\frac{\rho_g}{\eta_g}k_{ij,g}\left(\frac{\partial p_g^{(1)}}{\partial x_j}+\frac{\partial p_g^{(2)}}{\partial y_j}\right)N_i=0,\ \text{on}\ \mathcal{C}Y \tag{5.122}$$

as well as

$$-\frac{\rho_w}{\eta_w}\left(\frac{\partial}{\partial x_i}\left(k_{ij,w}\left(\frac{\partial p_w^{(0)}}{\partial x_j}+\frac{\partial p_w^{(1)}}{\partial y_j}\right)\right)+\frac{\partial}{\partial y_i}\left(k_{ij,w}\left(\frac{\partial p_w^{(1)}}{\partial x_j}+\frac{\partial p_w^{(2)}}{\partial y_j}\right)\right)\right)=0,\ \text{in}\ Y \tag{5.123}$$

$$\frac{\rho_w}{\eta_w}k_{ij,w}\left(\frac{\partial p_w^{(1)}}{\partial x_j}+\frac{\partial p_w^{(2)}}{\partial y_j}\right)N_i=0,\ \text{on}\ \mathcal{C}Y \tag{5.124}$$

By introducing the mean value operator $\langle\cdot\rangle=\frac{1}{|Y|}\int_Y\cdot dy$, where $|Y|=L_c{}^2$ is the area of Y, into Eqs. (5.119), (5.121) and (5.123), integrating by parts and making use of the periodicity conditions, we arrive at the final effective governing equations for the HM problem:

$$\frac{\partial}{\partial x_j}\Sigma_{ij}^{(0)}=0 \tag{5.125}$$

$$c_g^*\frac{\partial p_g^{(0)}}{\partial t}+\frac{\partial Q_{i,g}^{(0)}}{\partial x_i}=0 \tag{5.126}$$

$$\frac{\partial Q_{i,w}^{(0)}}{\partial x_i}=0 \tag{5.127}$$

where the macroscopic total stress $\Sigma_{ij}^{(0)}=\langle\sigma_{ij}^{(0)}\rangle$, the macroscopic gas flux $Q_{i,g}^{(0)}=\langle q_{i,g}^{(0)}\rangle$ and the macroscopic water flux $Q_{i,w}^{(0)}=\langle q_{i,w}^{(0)}\rangle$ are given by

$$\Sigma_{ij}^{(0)}=C_{ijkl}^*e_{xkl}(\boldsymbol{u}^{(0)})-p_f^{(0)}\delta_{ij}\ ;\ Q_{i,g}^{(0)}=-\left\langle\rho_g/\eta_g\right\rangle k_{ij,g}^*\frac{\partial p_g^{(0)}}{\partial x_j}\ ;\ Q_{i,w}^{(0)}=-\left\langle\rho_w/\eta_w\right\rangle k_{ij,w}^*\frac{\partial p_w^{(0)}}{\partial x_j} \tag{5.128}$$

As concerns the homogenized HM coefficients, we express the homogenized elastic moduli C_{ijkl}^* as:

$$C_{ijkl}^*=\frac{1}{|Y|}\int_Y\left(C_{ijkl}+C_{ijmn}e_{ymn}(\boldsymbol{\xi}^{kl})\right)dy \tag{5.129}$$

and the homogenized specific gas pressure coefficient:

$$c_g^* = \frac{1}{|Y|}\int_Y \frac{M\phi_g}{RT} dy \tag{5.130}$$

as well as the homogenized intrinsic permeability:

$$k_{11,\pi}^* = \frac{1}{|Y|}\int_Y k_\pi dy;\ k_{12,\pi}^* = \frac{1}{|Y|}\int_Y k_\pi \frac{\partial \zeta}{\partial y_1} dy;\ k_{22,\pi}^* = \frac{1}{|Y|}\int_Y k_\pi \left(1 + \frac{\partial \zeta}{\partial y_2}\right) dy,\ \ (\pi = g, w) \tag{5.131}$$

It is noted that the homogenized HM coefficients (5.129) and (5.131) can be expressed with respect to the introduced damage variable, which will be numerically explored in Section 5.3.5 for specific initial clayey rock parameters and different microcrack length.

Although the crack growth induced permeability anisotropy is incorporated in Eq. (5.131) at the postulate of impermeable crack face, the crack opening induced permeability change is not considered yet due to its complexity in the two-scale formulation. Besides, the permeability change is commonly regarded as an empirical relation to represent fluid flow in the porous material, see the HM models for the research topic at hand, e.g., (Fall et al., 2014; Nguyen and Le, 2015; Yang and Fall, 2021a; Yang et al., 2020). There are some models coupling the hydraulic aperture and the mechanical aperture of fractures by using the well-known cubic law to represent the permeability change, see e.g., (Cappa et al., 2008; Liu et al., 2013; Yang et al., 2020), but the derived formulations are still limited to the macroscopic case and empirical parameters are also included. To simplify the problem in the study, we adopt an empirical relation that was developed in (Yang and Fall, submitted for publication) to implicitly consider the crack opening induced permeability change, expressed as:

$$k_\pi = k_{\pi 0} L(d) = k_{\pi 0}\left(1 + d \cdot \exp\left(\frac{\beta_t}{\exp(1-d)}\right)\right),\ \ (\pi = g, w) \tag{5.132}$$

where $k_{\pi 0}$ is the initial intrinsic permeability value for fluid π (gas or water); $L(d)$ is a correction factor that calibrates the difference between actual permeability and homogenized permeability, β_t is an empirical parameter. This simplified function will be incorporated into Eq. (5.131) to get the effective response of fluid transport in the porous material.

It should be specified here that the empirical relation (5.132) is proposed in the macroscopic level, to better represent the experimental phenomena related to the development of preferential gas flow. Thus the correction factor $L(d)$ is not effective when deriving the microscopic formulation, such that $L(d) = 1$ in the asymptotic developments. Substituting the empirical relation (5.132) into (5.131), the homogenized intrinsic permeability $k_{ij,\pi}^*$ can be expressed as

$$k^*_{11,\pi} = L(d)k_{\pi 0}A^*_{11};\ k^*_{12,\pi} = L(d)k_{\pi 0}A^*_{12};\ k^*_{22,\pi} = L(d)k_{\pi 0}A^*_{22},\ \ (\pi = g, w) \tag{5.133}$$

in which A^*_{ij} are the components of homogenized hydraulic coefficients, expressed as

$$A^*_{11} = \frac{1}{|Y|}\int_Y 1 dy;\ A^*_{12} = \frac{1}{|Y|}\int_Y \frac{\partial \zeta}{\partial y_1} dy;\ A^*_{22} = \frac{1}{|Y|}\int_Y \left(1 + \frac{\partial \zeta}{\partial y_2}\right) dy \tag{5.134}$$

5.3.4 Time-Dependent Damage Evolution

The homogenized governing equations and constitutive equations presented in the previous section allow us to analyze the gas migration behavior at a given state of non-evolving damage. To supplement the equations (5.125)-(5.128) with evolving damage, energy analysis will be performed based on the formulated two-scale problems.

We assume that the microcrack contained in the microstructure is evolving in mode-I, symmetrically with respect to its middle point (see Figure 5.23), as a result leading to time-dependent damage propagation at the macroscale based on the adopted scale parameter and the periodicity condition in Figure 5.22. To consider the singularity of the fields at crack tips, we will first define a domain $Y_r \subset Y$ representing the cell Y without the interiors of circles ΓY^l_r and ΓY^r_r in Figure 5.23. Besides, CY_r represents the part of crack line CY in domain Y_r. When r is reaching the limit, e.g., $r \to 0$, the fields defined on the cell Y with crack CY are recovered.

The scaled energy release rate in the reference cell is given by (Dascalu et al., 2008)

$$\mathcal{G}_y = \lim_{r\to 0}\int_{\Gamma Y_r} \boldsymbol{e}\cdot\boldsymbol{b}(\boldsymbol{u}^{(1)})\boldsymbol{n} ds_y \tag{5.135}$$

where $\boldsymbol{b}(\boldsymbol{u}^{(1)})$ is the Eshelby configurational stress tensor corresponding to the microscopic displacement $\boldsymbol{u}^{(1)}$, defined as $b_{ij}(\boldsymbol{u}^{(1)}) = \frac{1}{2}C_{klmn}e_{ykl}(\boldsymbol{u}^{(1)})e_{ymn}(\boldsymbol{u}^{(1)})\delta_{ij} - C_{jklm}e_{ylm}(\boldsymbol{u}^{(1)})u^{(1)}_{k,i}$.

Multiplying Eq. (5.101) with $\dot{u}^{(1)}_i$, integrating over Y_r, making use of the periodicity condition and Reynolds transport theorem, we obtain the energy balance:

$$\begin{aligned}&\frac{d}{dt}\int_{Y_r}\frac{1}{2}C_{ijkl}e_{ykl}(\boldsymbol{u}^{(1)})e_{yij}(\boldsymbol{u}^{(1)})dy + \int_{\Gamma Y^r_r \cup \Gamma Y^r_r}\left(\frac{1}{2}C_{ijkl}e_{ykl}(\boldsymbol{u}^{(1)})e_{yij}(\boldsymbol{u}^{(1)})\frac{1}{2}\frac{dd}{dt}L_c\boldsymbol{n}\cdot\boldsymbol{e} + \right.\\ &\left. C_{ijkl}e_{ykl}(\boldsymbol{u}^{(1)})n_j\dot{u}^{(1)}_i\right)ds_y = \int_{CY_r} C_{ijkl}e_{ykl}(\boldsymbol{u}^{(1)})N^+_j[\dot{u}^{(1)}_i]ds_y\end{aligned} \tag{5.136}$$

where $[f] = f^+ - f^-$ denotes the jump across the crack face, with f^+ in the direction of $\boldsymbol{N}$ as illustrated in Figure 5.23.

Following Freund (1998), the singularity of field $\dot{u}^{(1)}_i$ may lead to the local relation

$\dot{u}_i^{(1)} \simeq -\frac{1}{2}\frac{dd}{dt} L_c \frac{\partial u_i^{(1)}}{\partial y_m} e_m$ at crack tips. With this condition, by taking the limit for $r \to 0$, the previous energy balance leads to the following identity:

$$\frac{d}{dt}\int_Y \frac{1}{2} C_{ijkl} e_{ykl}(\boldsymbol{u}^{(1)}) e_{yij}(\boldsymbol{u}^{(1)}) dy + \frac{dd}{dt} L_c \mathcal{G}_y - \int_{CY} C_{ijkl} e_{ykl}(\boldsymbol{u}^{(1)}) N_j[\dot{u}_i^{(1)}] ds_y = 0 \tag{5.137}$$

Consider a modified form of Eq. (5.101) since $\boldsymbol{u}^{(0)}$ does not depend on $\boldsymbol{y}$ variable:

$$\frac{\partial}{\partial y_j}\left(C_{ijkl} e_{xkl}(\boldsymbol{u}^{(0)})\right) = 0 \tag{5.138}$$

Multiplying Eq. (5.138) by $\dot{u}_i^{(1)}$ and integrating over Y while using the periodicity condition, we arrive at:

$$\int_Y C_{ijkl} e_{xkl}(\boldsymbol{u}^{(0)}) e_{yij}(\dot{\boldsymbol{u}}^{(1)}) dy = \int_{CY} C_{ijkl} e_{xkl}(\boldsymbol{u}^{(0)}) N_j[\dot{u}_i^{(1)}] ds_y \tag{5.139}$$

Adding Eq. (5.137) and (5.139), then using the Reynolds transport theorem, we obtain

$$\begin{aligned} &\int_{CY} C_{ijkl}\left(e_{xkl}(\boldsymbol{u}^{(0)}) + e_{ykl}(\boldsymbol{u}^{(1)})\right) N_j[\dot{u}_i^{(1)}] ds_y - \frac{dd}{dt} L_c \mathcal{G}_y - \frac{1}{2}\frac{d}{dt}\int_Y C_{ijkl}\left(e_{xkl}(\boldsymbol{u}^{(0)}) + e_{ykl}(\boldsymbol{u}^{(1)})\right) e_{yij}(\boldsymbol{u}^{(1)}) dy \\ &= \frac{1}{2}\frac{d}{dt}\int_Y C_{ijkl} e_{xkl}(\boldsymbol{u}^{(0)}) e_{yij}(\boldsymbol{u}^{(1)}) dy - \int_Y C_{ijkl} e_{xkl}(\dot{\boldsymbol{u}}^{(0)}) e_{yij}(\boldsymbol{u}^{(1)}) dy \end{aligned} \tag{5.140}$$

Combining Eq. (5.107) with (5.138) gives the following form:

$$\frac{\partial}{\partial y_j}\left(C_{ijkl} e_{xkl}(\boldsymbol{u}^{(0)}) + C_{ijkl} e_{ykl}(\boldsymbol{u}^{(1)})\right) = 0 \tag{5.141}$$

Starting from Eq. (5.141), using a similar procedure to the one that led from (5.138) to (5.139) with the help of crack boundary condition (5.108), we get:

$$\int_Y C_{ijkl}\left(e_{xkl}(\boldsymbol{u}^{(0)}) + e_{ykl}(\boldsymbol{u}^{(1)})\right) e_{yij}(\boldsymbol{u}^{(1)}) dy = \int_{CY} C_{ijkl}\left(e_{xkl}(\boldsymbol{u}^{(0)}) + e_{ykl}(\boldsymbol{u}^{(1)})\right) N_j[u_i^{(1)}] ds_y = 0 \tag{5.142}$$

In order to evaluate the integral $\int_Y C_{ijkl} e_{ykl}(\boldsymbol{u}^{(1)}) dy$ occurred on the right hand side member of Eq. (5.140), we use the specific linear corrector (5.113) together with the expression of homogenized elastic moduli (5.129), to derive the useful relation:

$$\int_Y C_{ijkl} e_{ykl}(\boldsymbol{u}^{(1)}) dy = L_c^2\left(C^*_{ijmn} - C_{ijmn}\right) e_{xmn}(\boldsymbol{u}^{(0)}) \tag{5.143}$$

Substitution of Eqs. (5.142)-(5.143) into (5.140) gives

$$\frac{dd}{dt}\left(\frac{\mathcal{G}_y}{L_c} + \frac{1}{2}\frac{dC^*_{ijkl}}{dd} e_{xkl}(\boldsymbol{u}^{(0)}) e_{xij}(\boldsymbol{u}^{(0)})\right) = 0 \tag{5.144}$$

For evolving microcracks ($\frac{dd}{dt} \neq 0$), Eq. (5.144) establishes a link between scaled fracture energy

$\mathcal{G}_y$ and the macroscopic quantity:

$$Y_d = -\frac{1}{2}\frac{dC^*_{ijkl}(d)}{dd} e_{xkl}(\boldsymbol{u}^{(0)}) e_{xij}(\boldsymbol{u}^{(0)}) \tag{5.145}$$

which generally represents the damage energy release rate.

For a given microcrack propagation criterion, Eq. (5.144) provides the corresponding damage law. Thus, we attempt to incorporate the energy release rate for microcrack growth in the following part. Following Dascalu et al. (2008), the developments of $e_{xkl}(\boldsymbol{u}^{\varepsilon})$ and $\sigma^{\varepsilon}_{jk}$ can be expressed as:

$$e_{xkl}(\boldsymbol{u}^{\varepsilon}) = e_{xkl}(\boldsymbol{u}^{(0)}) + e_{ykl}(\boldsymbol{u}^{(1)}) \tag{5.146}$$

Substitution of Eq. (5.146) into (5.78) with the help of (5.79) provides the fracture energy of microcrack in the following form:

$$\begin{aligned}\mathcal{G}^{\varepsilon} = \lim_{r\to 0}\int_{\Gamma_r} e_i \Bigg(&\frac{1}{2} C_{mnkl}\left(e_{xkl}(\boldsymbol{u}^{(0)}) + e_{ykl}(\boldsymbol{u}^{(1)})\right)\left(e_{xmn}(\boldsymbol{u}^{(0)}) + e_{ymn}(\boldsymbol{u}^{(1)})\right)\delta_{ij} - \\ &C_{ikmn}\left(e_{xmn}(\boldsymbol{u}^{(0)}) + e_{ymn}(\boldsymbol{u}^{(1)})\right)\left(\frac{\partial u^{(0)}_k}{\partial x_j} + \frac{\partial u^{(1)}_k}{\partial y_j}\right)\Bigg) n_j ds\end{aligned} \tag{5.147}$$

Considering the singularity of $\boldsymbol{u}^{(1)}$ at crack tips and $ds = \varepsilon ds_y$, Eq. (5.147) becomes

$$\mathcal{G}^{\varepsilon} = \varepsilon \lim_{r\to 0}\int_{\Gamma_r} e_i \left(\frac{1}{2} C_{mnkl} e_{ykl}(\boldsymbol{u}^{(1)}) e_{ymn}(\boldsymbol{u}^{(1)})\delta_{ij} - C_{ikmn} e_{ymn}(\boldsymbol{u}^{(1)}) \frac{\partial u^{(1)}_k}{\partial y_j}\right) n_j ds \tag{5.148}$$

Comparison between Eq. (5.135) and (5.148) leads to the following correlation for fracture energy:

$$\mathcal{G}^{\varepsilon} = \varepsilon \mathcal{G}_y \tag{5.149}$$

It is noted that the approximated relation (5.149) is derived based on the first order cell solution. For a higher order model that can describe highly oscillated behavior, readers are referred to follow the homogenization procedure in (Smyshlyaev and Cherednichenko, 2000), which will include higher order cell solutions.

Use of Eqs. (5.66), (5.145) and (5.149) into (5.144) allows us to build the following link of energy release rate:

$$\frac{\mathcal{G}^{\varepsilon}}{l_c} - Y_d = 0 \tag{5.150}$$

In the laboratory gas injection tests conducted by Skurtveit et al. (2012), the gas pressure

controlled opening of micro-fractures was found to be the dominating mechanism for gas breakthrough, which occurs at the applied gas pressure significantly below the isotropic confining pressure. For the porous material subjected to constant isotropic confining pressure, the increase of gas pressure is equivalent to an unloading process that leads to expansive behavior of the material. The microscopic imaging (Harrington et al., 2012b) has shown that the gas induced pathway within a clay-based candidate host rock is dynamically and unstably evolved with the formation of micro-fractures. The observed mode-I ruptures at the microscale may represent the mechanism of time-dependent damage at the macroscale. With these considerations in the study, a subcritical law for microcrack propagation by Charles (1958) is adopted in the study, which has been incorporated in many two-scale models to describe the relation between crack growth and model-I stress intensity factor K_I, see e.g., (Dascalu, 2009; Dascalu et al., 2010b; François and Dascalu, 2010; Wrzesniak et al., 2015). This criterion is described as follows:

$$\frac{dl}{dt} = v_0 \left(\frac{K_I}{K_0} \right)^n \tag{5.151}$$

where K_0 is the reference stress intensity factor, n is the subcritical growth index, v_0 is the reference crack velocity. For rock materials, the reported values of reference crack velocity range from 10^{-2} to 10^{-9} m/s (Atkinson, 1984). The reference stress intensity factor is likely to be 15% of critical stress intensity factor (Atkinson and Meredith, 1987), while the subcritical growth index is set to be 3 (Wrzesniak et al., 2015). In order to obtain the mode-I fracture toughness, an approximated empirical relation may be used in the following form (Xu et al., 2018):

$$K_{Ic} = \gamma_t \sigma_t \tag{5.152}$$

in which σ_t is the tensile strength, γ_t is a fitted linear coefficient that is equal to 0.14 $m^{0.5}$ for rock materials (Xu et al., 2018). This empirical relation (5.152) has been validated against various rock types, i.e., sandstone, basalt, shale, detailed experimental results are referred to (Zhang, 2002).

The subcritical law (5.151) considers the time-dependent crack growth that may occur for stress intensity factor below the critical limit (Atkinson and Meredith, 1987), which may be appropriate to represent the mechanism of gas induced micro-fracturing. For exclusively observed mode-I ruptures in the gas injection tests (Cuss et al., 2012), the stress intensity factor

K_I can be derived from the fracture energy $\mathcal{G}^{\varepsilon}$:

$$\mathcal{G}^{\varepsilon} = \frac{1-\nu^2}{E} K_I^2 \tag{5.153}$$

where E and ν are Young's modulus and Poisson's ratio, respectively.

Use of the normalized damage variable (5.80) in (5.151) with the help of (5.150) and (5.153) leads to the final time-dependent damage law as follows:

$$\dot{d} = \frac{v_0}{l_c} \left(\frac{\sqrt{\frac{l_c E Y_d}{(1-\nu^2)}}}{K_0} \right)^n \tag{5.154}$$

The derived damage equation accounts for time effect and size effect, which are significant characteristics for gas induced fracturing. Although the developed fractures within clayey rock materials may present the self-healing behavior with the variation of applied gas pressure (Li et al., 2007), the fracturing process is assumed to be irreversible for simplicity. Thus the damage energy release rate Y_d is replaced by its historical maximum value in the computation.

5.3.5 Local Macroscopic Response

The analysis of homogenized response in a local point is conducted in the following part. Firstly, the homogenized HM coefficients are expressed in terms of the damage variable by solving the cell problems (5.114)-(5.115) and (5.117)-(5.118), respectively for a number of microcrack length. Then we analyze the local macroscopic behavior under specific strain rate loading conditions.

Clayey rocks such as Opalinus (OPA) clay, Boom clay and Callovo-Oxfordian (COx) claystone are commonly investigated as host rocks for nuclear waste repositories due to their favored properties. The intact rocks are simplified to have isotropic HM properties, while the presence of microcracks will lead to the anisotropic response that is analyzed in Subsection 5.3.5.1. The reference parameters for the local analysis are given as: Young's modulus and Poisson's ratio are 2000 MPa and 0.3. The tensile strength of rock is 1.1 MPa (Hashiba and Fukui, 2015). These parameters are summarized in the following table.

Table 5-5 Parameters in the computation of local analysis

E [MPa]	ν [-]	σ_t [MPa]
2000	0.3	1.1

5.3.5.1 Homogenized Coefficients

The homogenized HM coefficients are obtained from the characteristic functions ξ^{kl} and ζ, which are elementary solutions of cell problems (5.114)-(5.115) and (5.117)-(5.118), respectively. The intact material is assumed to have isotropic HM properties. For 11 values of normalized crack length $d \in [0,1]$, these characteristic functions are computed numerically by using the Finite Element software COMSOL Multiphysics. With the help of Eqs. (5.129) and (5.134), the corresponding HM coefficients are interpolated by piecewise cubic polynomial functions between continuous data points. At the extreme case of totally damaged state, the coefficient can be obtained analytically.

The homogenized elastic coefficients $C^*_{ijkl}(d)$ are illustrated in Figure 5.24 with respect to damage variable. The coefficients $C^*_{ijkl}(0)$ correspond to the isotropic behavior of undamaged material, while the presence of microcracks leads to the orthotropic response of damaged material. The homogenized coefficients have a nonlinear dependence of damage variable, with a more abrupt degradation when the material is approaching the totally damaged state $d = 1$. It is noted that the stiffness component $C^*_{1111}(d)$ is less affected by the cracking, in which partial degradation is observed. For the remainder components, their loss of rigidity are much more serious until losing whole rigidity at $d = 1$. Analytical method allows us to obtain the expression of the coefficient $C^*_{1111}(1) = \dfrac{E}{1-\nu^2}$, corresponding to the last data point in Figure 5.24.

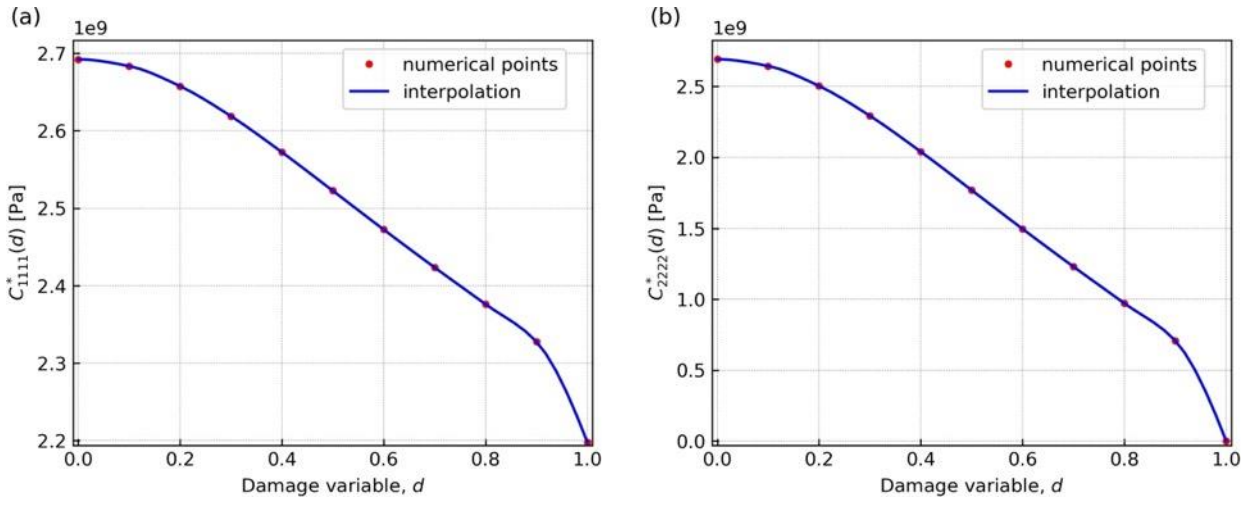

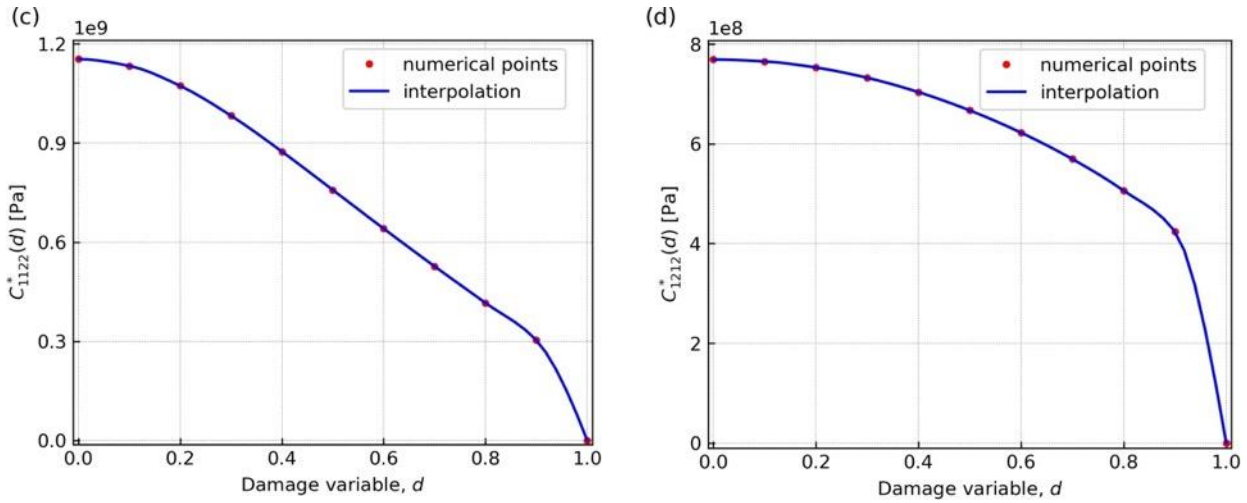

Figure 5.24 Homogenized elastic coefficients versus damage variable: (a) $C^*_{1111}(d)$ vs d, (b) $C^*_{2222}(d)$ vs d, (c) $C^*_{1122}(d)$ vs d, (d) $C^*_{1212}(d)$ vs d.

The homogenized hydraulic coefficient is presented in Figure 5.25 as a function of the damage variable. Considering the isotropic permeability for gas and water flow, we can express the permeability component as $k^*_{11,\pi}(0) = k^*_{22,\pi}(0) = k_{\pi 0}$ and $k^*_{12,\pi}(0) = k^*_{21,\pi}(0) = 0$. The postulate of impermeable crack face at the microscale leads to different hydraulic response, such that the hydraulic coefficient parallel to the crack face $A^*_{11}(d)$ is constant at 1, while the hydraulic coefficient normal to the crack face $A^*_{22}(d)$ has a nonlinear dependence on the damage variable. The other hydraulic coefficient $A^*_{12}(d)$ remains at zero as the orientation of microcracks is not changed during the computation. For increasing damage values, the hydraulic coefficient $A^*_{22}(d)$ is gradually decreasing until reaching $A^*_{22}(1) = 0$, which corresponds to totally partitioned cell that fluid is only transported along the crack face.

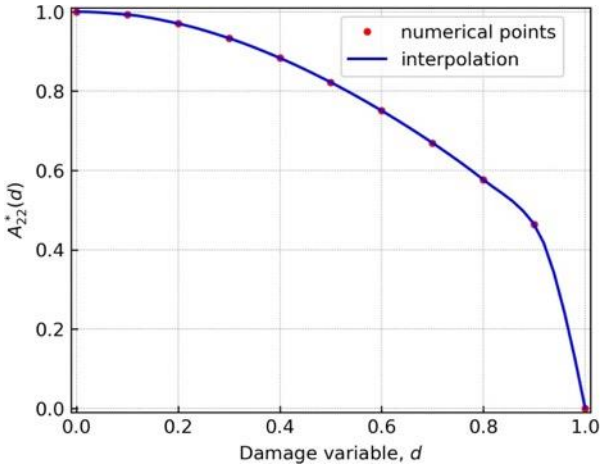

Figure 5.25 Homogenized hydraulic coefficient

5.3.5.2 Local Response Analysis

Before applying the two-scale HM damage model to simulate the preferential gas flow in clayey rocks, the local performance of the time-dependent damage model is first analyzed in the following subsection. We consider a tensile loading condition in the local analysis, where the constant strain rate $\dot{e}_{x22}$ is applied as the only non-vanishing component, fluid pressure as well as fluid flow is neglected for simplicity. Under this condition, the local response in damage evolution is obtained by solving the equation (5.154) with the given macroscopic strain history $e_{x22}(u^{(0)})$. The corresponding homogenized coefficient $C^*_{2222}(d)$ is then derived and in consequence we can compute the macroscopic stress $\Sigma^{(0)}_{x22} = C^*_{2222}(d) e_{x22}(u^{(0)})$. The used parameters in the local computation such as E , ν and σ_t are referred to Table 5-5.

5.3.5.2.1 Influence of the Microstructural Size

We firstly analyze the influence of microstructural size on the evolution of both macroscopic stress and damage. The material is undamaged with a reference crack velocity $v_0 = 1\times10^{-5}$ m/s. The loading rate $\dot{e}_{x22}$ applied in the computation is set to be 1×10^{-6} /s. With time elapsed, we illustrate the evolution of macroscopic stress and damage in Figure 5.26 for three microscopic length values: $l_c = 1\times10^{-6}$ m; $l_c = 1\times10^{-5}$ m; $l_c = 1\times10^{-4}$ m.

For the periodically distributed microcracks in a macroscopic medium, their nucleation and propagation are represented by the damage evolution at the macroscale. As can be seen from Figure 5.26, smaller microstructures are more resistant to damage initiation since the contained microcracks need more time to propagate. This result is consistent with the size effects in classical Fracture Mechanics, which has been retrieved in (Dascalu et al., 2008; Wrzesniak et al., 2015) by using a similar homogenization method.

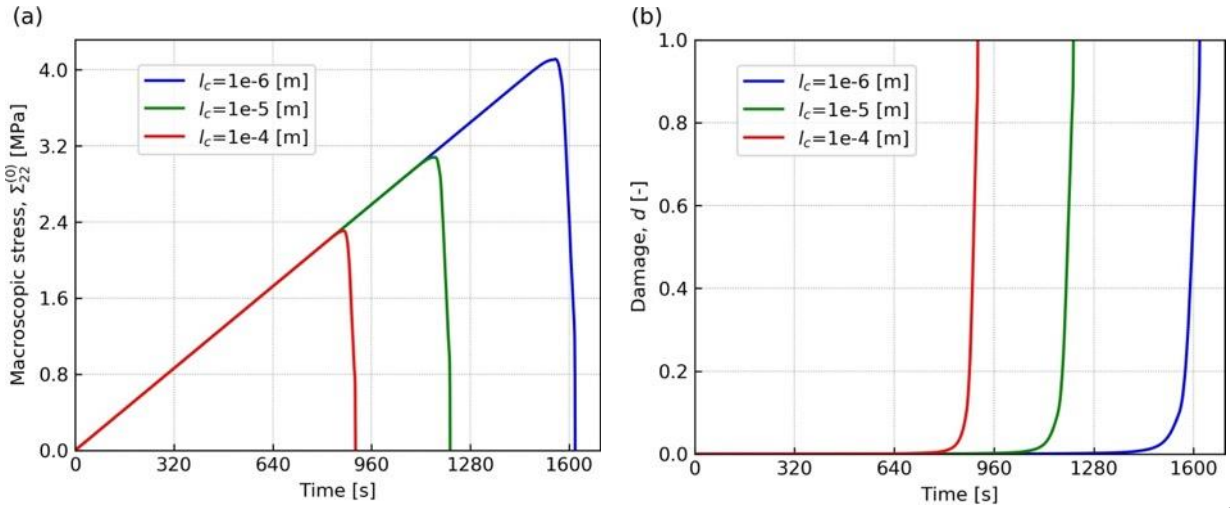

Figure 5.26 Influence of microstructural size on the macroscopic stress (a) and damage (b) for: $l_c = 1 \times 10^{-6}$ m, $l_c = 1 \times 10^{-5}$ m, $l_c = 1 \times 10^{-4}$ m.

For the same strain rate condition $\dot{e}_{x22} = 1 \times 10^{-6}$ /s, the predicted peak stress is presented in Figure 5.27 with respect to different microstructural size values. The influence of microstructural size on the tensile strength is obvious for smaller size value, while the tensile strength gradually reaches an asymptote value for larger microstructural size. This is the consequence of the time-dependent damage law deduced from the subcritical microcrack propagation criterion, in which the microstructural size l_c is included in crack evolution. It expresses the spirit of microcrack length upscaled to distributed damage at the macroscopic level in Fracture Mechanics (Lyakhovsky, 2001).

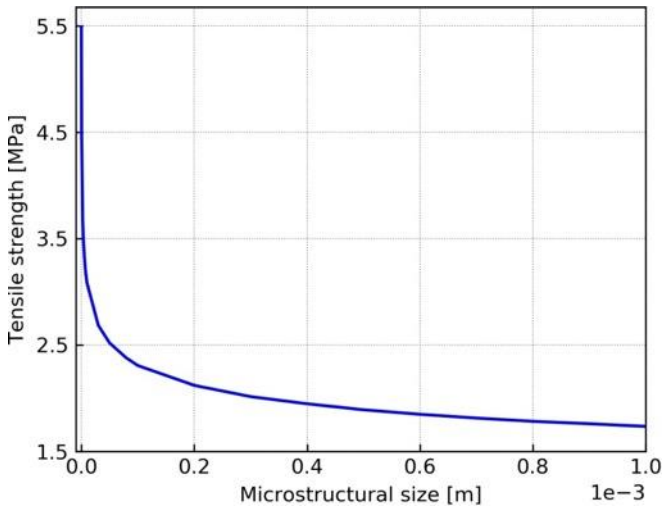

Figure 5.27 Peak stress versus the microstructural size under constant strain rate loading condition

5.3.5.2.2 Influence of the Loading Rate

Now we analyze the influence of loading rate on the mechanical response. The virgin

material has a microstructural size of 0.1 mm and a reference crack velocity of 1×10^{-5} m/s. The evolution of macroscopic stress and damage are illustrated in Figure 5.28 for three strain rates.

As has been observed in the Brazilian tests (Cai et al., 2007), the argillite presented a higher tensile strength with increasing deformation velocity. This dynamic behavior is well represented by the time-dependent damage model, where the higher loading rate causes the fast propagation of microcracks, thus resulting in the quick failure of material. While in the lower loading rate condition, the material has enough time for crack propagation so that the material may not undergo high levels of deformation to reach failure. As a result, the tensile strength decreases correspondingly, which is clearly shown in Figure 5.28.

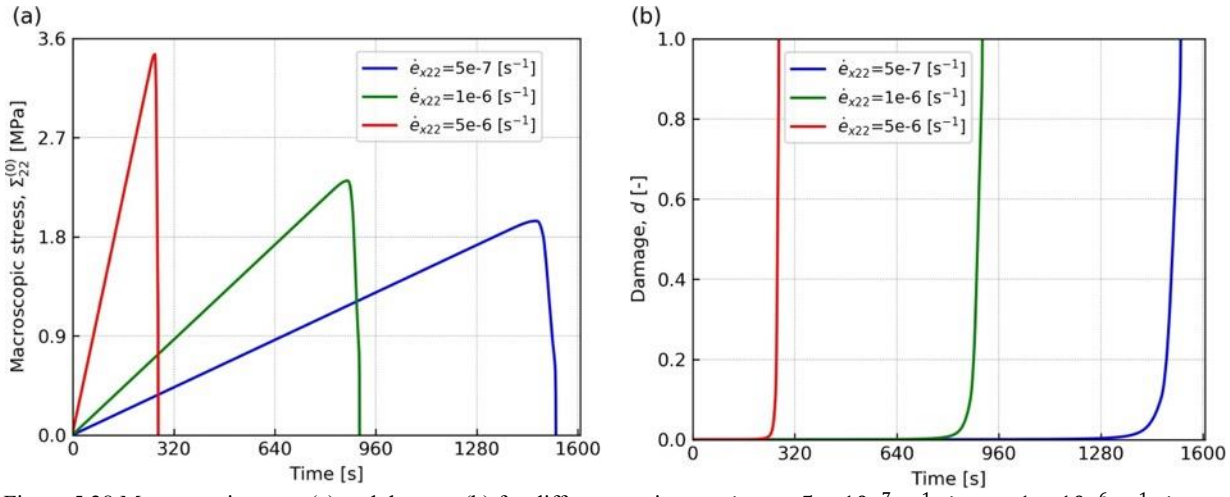

Figure 5.28 Macroscopic stress (a) and damage (b) for different strain rate: $\dot{e}_{x22} = 5 \times 10^{-7}\ s^{-1}$, $\dot{e}_{x22} = 1 \times 10^{-6}\ s^{-1}$, $\dot{e}_{x22} = 5 \times 10^{-6}\ s^{-1}$.

5.3.5.2.3 Influence of the Reference Crack Velocity

We finally analyze the influence of reference crack velocity. The intact material is loaded under constant strain rate condition $\dot{e}_{x22} = 1\times10^{-6}$ /s, and the microscopic length $l_c = 1\times10^{-4}$ m. The local mechanical response is shown in Figure 5.29 for $v_0 = 1\times10^{-6}$ m/s, $v_0 = 1\times10^{-5}$ m/s, $v_0 = 1\times10^{-4}$ m/s.

As expected by the time-dependent damage law (5.154), a larger value of reference crack velocity corresponds to fast damage evolution, in consequence leading to quick failure of the material. Under the condition of same tensile strain rate, the duration of damage evolving dominates the peak stress that the material can sustain. Therefore, the material presents lower tensile strength for higher reference crack velocity, see Figure 5.29.

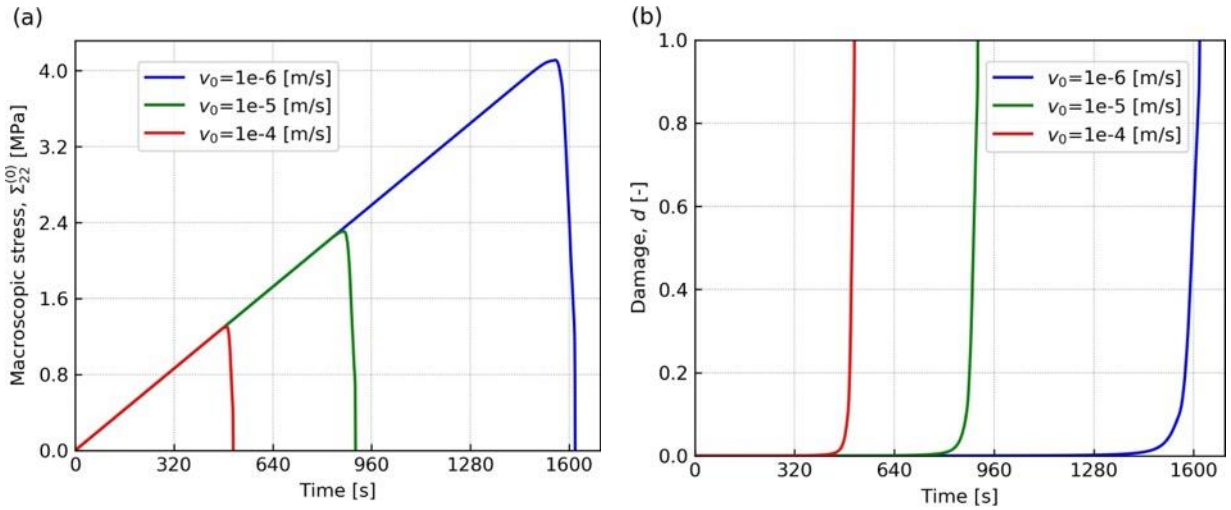

Figure 5.29 Macroscopic stress (a) and damage (b) for different reference crack velocity: $v_0 = 1 \times 10^{-6}$ m/s, $v_0 = 1 \times 10^{-5}$ m/s, $v_0 = 1 \times 10^{-4}$ m/s.

5.3.6 Numerical Examples

In this section, we present two numerical examples of gas injection tests, where the simulated results are compared with the experimental data reported in (Gonzalez-Blanco et al., 2016; Senger et al., 2014). The tests were conducted at the same air injection rate, 100 mL/min for different clayey rock materials, i.e., Boom Clay and OPA Clay in the study. Plane strain conditions are used in the simulation.

5.3.6.1 Model Parameters

Two clayey rock specimens with bedding plane parallel to gas flow were prepared for the tests. The basic parameters of the rock specimen are listed in Table 5-6. Air is used in the test that is considered to be an ideal gas, the rock specimen is initially saturated with water. The reference properties of fluids are summarized in Table 5-7.

Table 5-6 Basic information of clayey rock specimen

Sample	Height [mm]	Diameter [mm]	Porosity [-]	Sources
Boom Clay	20	50	0.363	(Gonzalez-Blanco et al., 2016)
OPA Clay	20	50	0.2	(Senger et al., 2014)

Table 5-7 Fluid properties in the air injection tests

Properties	ρ_w [kg/m^3]	η_w [Pa·s]	ρ_g (air) [kg/m^3]	η_g [Pa·s]	M (air) [g/mol]
Value	1000	0.001	1.2	1.82×10^{-5}	29

As the elastic properties of OPA Clay are not given in the air injection test conducted on sample 'BDR 1_06 14', we extract these elastic parameters recorded in Mont Terri Rock Laboratory (Xu et al., 2013). The behavior of Boom Clay is strongly depending on the in situ conditions that it is generally difficult to make a clear distinction between stiff and soft clays

(Bernier et al., 2007). In the simulation, we use the Young's modulus of Boom Clay that is estimated by Bernier et al. (2007) from the in situ measurements. The tensile strength is inferred from geotechnical properties of the Oligocene Boom Clay (Dehandschutter et al., 2005).

The hydraulic properties recorded in (Senger et al., 2014) and (Gonzalez-Blanco et al., 2016) are used to represent the intrinsic permeability for water flow in OPA Clay and Boom Clay, respectively. The gas permeability of Boom Clay was taken from the gas breakthrough experiments that recorded the effective permeability for steady state gas flow (Hildenbrand et al., 2002). An approximated average value of 2×10^{-20} m^2 is used in the simulation. From the field gas injection tests conducted in the borehole of OPA clay, the intrinsic permeability to gas flow was found to range from 1×10^{-21} m^2 to 6×10^{-20} m^2 (Marschall et al., 2005). A reference value of 1×10^{-20} m^2 was used in the simulation of gas test on OPA clay.

The clayey rock sample is initially saturated and nearly no measurable desaturation occurs after the air injection test, which indicates the highly localized network of gas pathways (Amann-Hildenbrand et al., 2015). Based on this phenomenon, we assume that the available pore spaces for gas flow only accounts for a small percentage (0.1%) of the total pore spaces, thus the porous material can be still considered to be fully saturated. The detailed information of clayey rocks is referred to Table 5-8.

Table 5-8 Basic HM properties of the clayey rock sample (1. Bernier et al. (2007); 2. Gonzalez-Blanco et al. (2016); 3. Dehandschutter et al. (2005); 4. Hildenbrand et al. (2002); 5. Xu et al. (2013); 6. Senger et al. (2014))

Clayey rock	E [MPa]	ν	σ_t [kPa]	k_{w0} [m^2]	k_{g0} [m^2]	ϕ_g/ϕ
Boom Clay	300 [1]	0.33 [2]	100 [3]	4.2×10^{-19} [2]	2×10^{-20} [4]	0.1%
OPA Clay	2500 [5]	0.27 [5]	233 [5]	1.4×10^{-19} [6]	1×10^{-20}	0.1%

The rock samples may contain natural or induced micro-fractures due to the variations in sampling method and stress history (Cuss et al., 2014). The microstructural properties of these contained fractures are seldomly given if the research topic is not focused on the microscopic phenomena. As analyzed in Section 5.3.5.2.1, larger microstructural size corresponds to lower strength, while the increase of reference crack velocity leads to quick damage evolution. Based on the different characteristics of gas dilatant pathways in the two tests, the reference crack velocity is determined to be 1.0×10^{-7} m/s and 1.5×10^{-7} m/s for gas test on Boom Clay and OPA Clay, respectively. The microstructural size of Boom Clay and OPA Clay are 1.0×10^{-6} m and 5.0×10^{-6} m, respectively, which are thousands of magnitude lower than the specimen size L_c, thus the separation of scales assumption (5.83) is verified. The dynamic evolution of intrinsic

permeability is represented by the empirical relation (5.133) that the parameter β_t is determined to better capture the experimental phenomena. The exact values of these parameters are summarized in Table 5-9.

Table 5-9 Parameters related to micro-fractures

Clayey rock	v_0 [m/s]	l_c [m]	β_t
Boom Clay	1.0×10^{-7}	1.0×10^{-6}	4
OPA Clay	1.5×10^{-7}	5.0×10^{-6}	3.5

5.3.6.2 Air Injection Test on Boom Clay

To physically simulate the gas flow process from the inlet to outlet, both the gas injector and recovery system are incorporated in the model, as seen in Figure 5.30. In this way, gas is compressed in the injection vessel to provide the gas injection pressure rather than applying a prescribed boundary condition. The gas containers are idealized as a porous material with large porosity and high permeability, i.e., 1 and 1×10^{-12} m^2 respectively. The volume of gas containers is kept constant during the gas flow process. Air is regarded to follow the ideal gas law at the room temperature (20 ℃) and atmospheric pressure (1 atm).

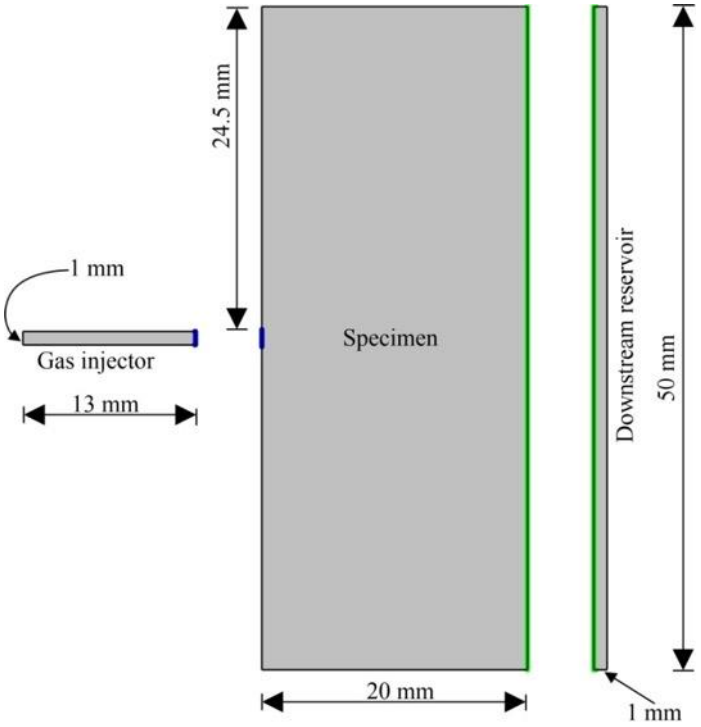

Figure 5.30 Gas injection model setup

5.3.6.2.1 Initial and Boundary Conditions

The geometry of the Boom Clay specimen and the meshed domain are shown in Figure 5.31. The specimen is loaded under isotropic confining pressure condition with p_3=6 MPa, and the left boundary is fixed. The gas inlet is located at the middle position of specimen with 1 mm width. Both the gas inlet and outlet are connected to the gas container, where a mass flux boundary is applied in the container, thus to provide the corresponding gas pressure condition in the inlet and outlet. To reach the maximum gas pressure (4.1 MPa) within 5 minutes, the volume of injection vessel is set to 13 mL. The volume of gas container in the downstream is 50 mL in the simulation. A fast air injection rate of 100 mL/min is applied in the upstream vessel for a continuous time of 5 minutes. After reaching the maximum gas pressure at 5 minutes, air injection process was stopped so that the upstream gas pressure was let to decay.

A finite element mesh is constructed by using the plane strain triangular mesh elements. To capture the trajectory of gas induced fracturing, a refined element size of 0.2 mm is discretizing the sub-domain from the inlet to outlet, as can be seen from Figure 5.31. Both the volume of upstream and downstream vessels is kept constant during the computation.

Initial gas pressure is 0.5 MPa in the upstream and downstream vessels. The initial value of damage variable is set to 1×10^{-6} so that the rock material can be regarded as initially intact. A higher value of damage variable, i.e., d_0=0.1 is applied in the element around the gas inlet area, see the red triangular element in Figure 5.31. The set of different initial damage value is to initiate a non-homogeneous response, similar treatment can be also referred to (Wrzesniak et al., 2015).

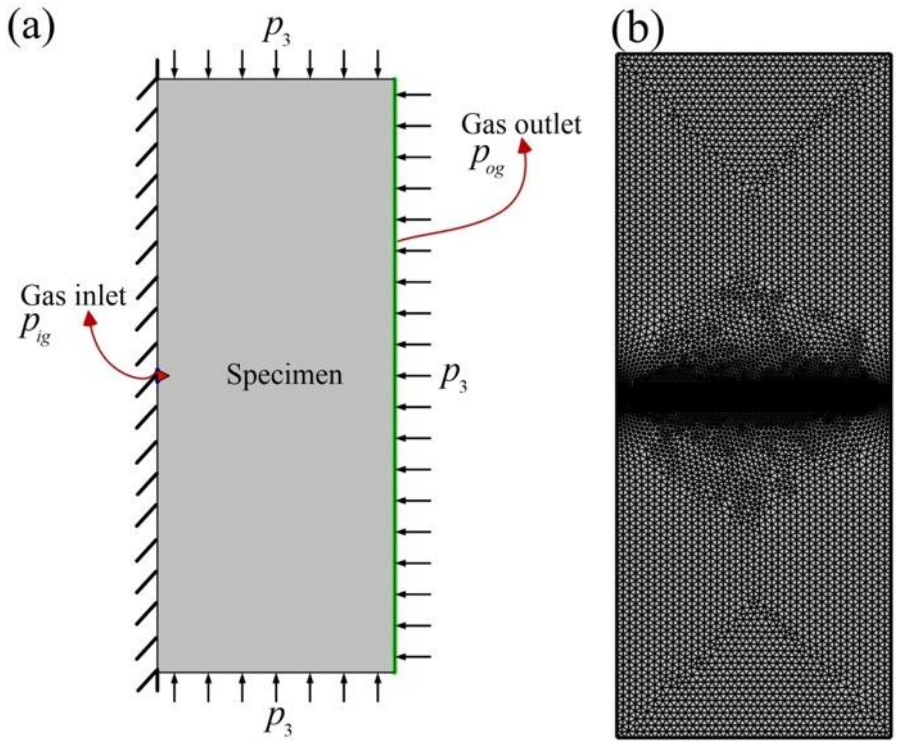

Figure 5.31 (a) Geometry, boundary conditions of rock specimen, (b) meshed domain. Note: p_{ig} is the gas injection pressure, p_{og} the gas pressure at outlet, p_3 the confining pressure.

5.3.6.2.2 Modelling Results

Figure 5.32 illustrates the gas inflow rate at the standard temperature and pressure (STP) condition, together with the damage evolution around the gas inlet area. As gas pressure is applied in the inlet through gas pumping in the injection vessel, gas pressure increases nonlinearly, as can be seen in Figure 5.36. From the mechanical point, gas injection is equivalent to an unloading process that causes the dilational behavior of the material. Due to the low permeability of Boom Clay, gas is firstly transported through the area with higher damage value, triangular element in Figure 5.32. Thanks to the non-homogeneous properties of the material, the fracturing process initiates from the inlet area, see the partially damaged element at t=5 min. Then the gas front gradually penetrates the intact material that leads to the crack front moving from the damaged element to intact parts, as can be seen from the zoomed damage evolution from t=5.9 min to t=6.3 min. As seen from the represented relation of gas inflow rate, the damage propagation is accompanied by the increase of gas inflow rate. When the gas injection rate is applied too quickly that no adequate pathways are developed for gas penetration, gas is likely to flow back to the injector and as a result leads to the oscillated flow behavior in the gas

inlet boundary.

As reported by Harrington et al. (2017), the gas advective movement through clayey rock materials is a dynamic and unstable process that the opening/closure of the gas pathways is related to the local changes in gas pressure and its HM coupling with rock deformation. This unstable gas behavior is clearly represented by the oscillating gas inflow rate in Figure 5.32 when gas induced fracturing occurs.

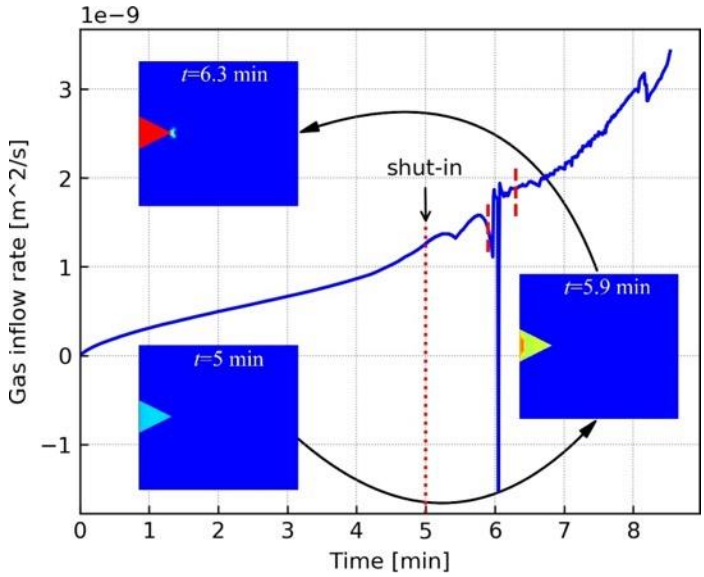

Figure 5.32 Gas inflow rate ($\int_s \frac{Q_{i,g}^{(0)} \cdot N_{si}}{\rho_g} \frac{T}{T_0} ds$) at the STP condition with damage evolution around the gas inlet area. Note: T and T_0 are absolute temperature and room temperature, respectively; N_{si} is the unit vector normal to the gas boundary.

To further study the oscillated gas flow behavior, we evaluate the energy dissipation due to damage evolution in the triangular element of Figure 5.32. The volume density of energy dissipation ($\mathcal{D}$) is given as follows:

$$\mathcal{D}(t) = \int_0^t Y_d(s) \frac{dd}{ds} ds \tag{5.155}$$

The dissipated energy over the triangular element is presented in Figure 5.33 with respect to time. The timing of rapid increase in energy dissipation is at about t=5.9 min, corresponds to the timing for highly oscillated inflow rate in Figure 5.32. After the triangular element is totally damaged, the energy dissipation reaches an asymptote value. By comparison of Figure 5.32 and Figure 5.33, it is demonstrated that the oscillated gas flow behavior is closely associated with the gas induced fracturing in the rock specimen and high compressibility of gas.

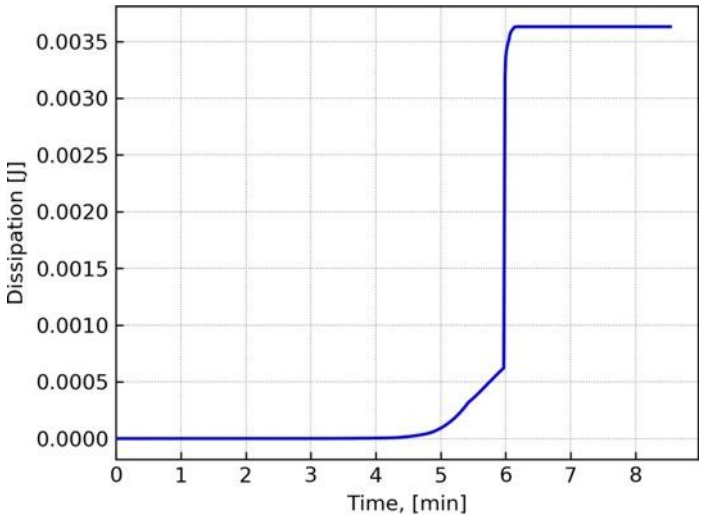

Figure 5.33 Energy dissipation vs time over the triangular element of rock specimen

Figure 5.34 presents the damage distribution in the domain at different time. The effective intrinsic permeability components along horizontal and vertical direction are illustrated in Figure 5.35. Thanks to the adopted microcracks orientation and the local periodicity condition, the resultant homogenized mechanical response leads to a horizontal trajectory of fracturing, as can be clearly seen from Figure 5.34. When the crack front arrives at the position of point A, the quick damage evolution induces a significant hydraulic anisotropy for gas permeability, i.e., an abrupt increase of gas permeability in horizontal direction and a drop in gas permeability along vertical direction, as seen in Figure 5.35. This effect is contributed by the combined action of microcrack induced anisotropy (see Eq. (5.134)) and the fracture opening induced permeability increase (see Eq. (5.132)).

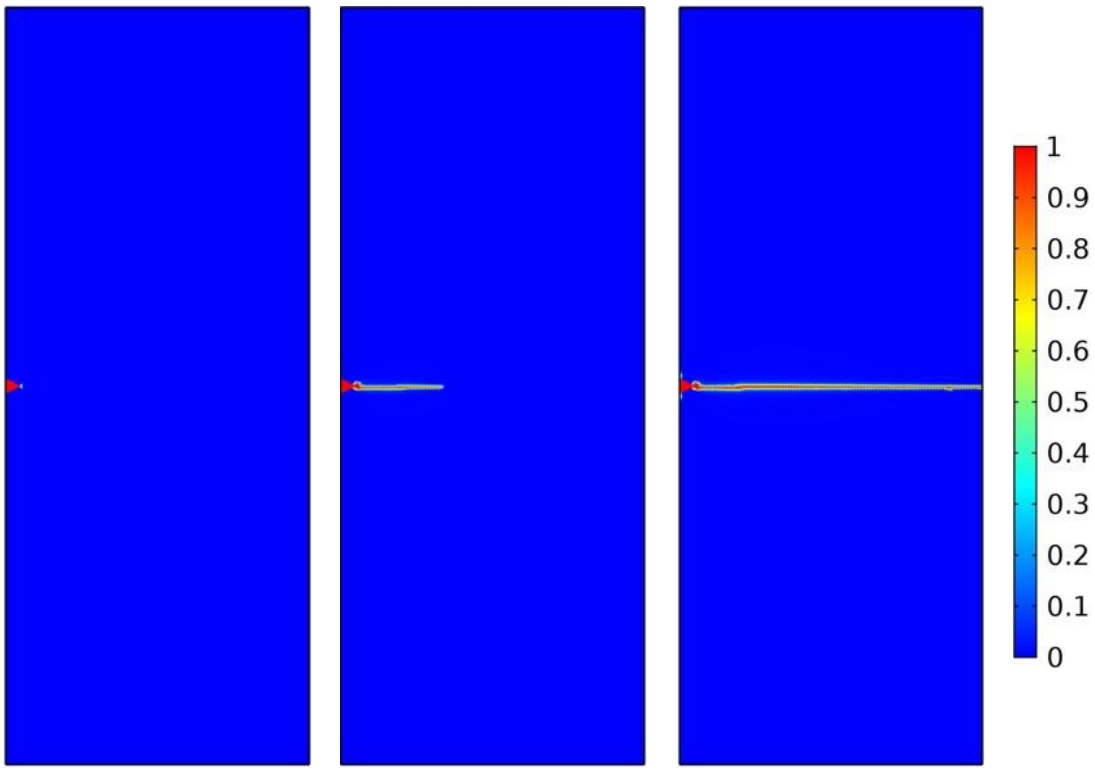

(a) t=6.30 min (b) t=8.00 min (c) t=8.51 min

Figure 5.34 Damage evolution in the Boom Clay at different time: (a) t=6.30 min, (b) t=8.00 min, (c) t=8.51 min.

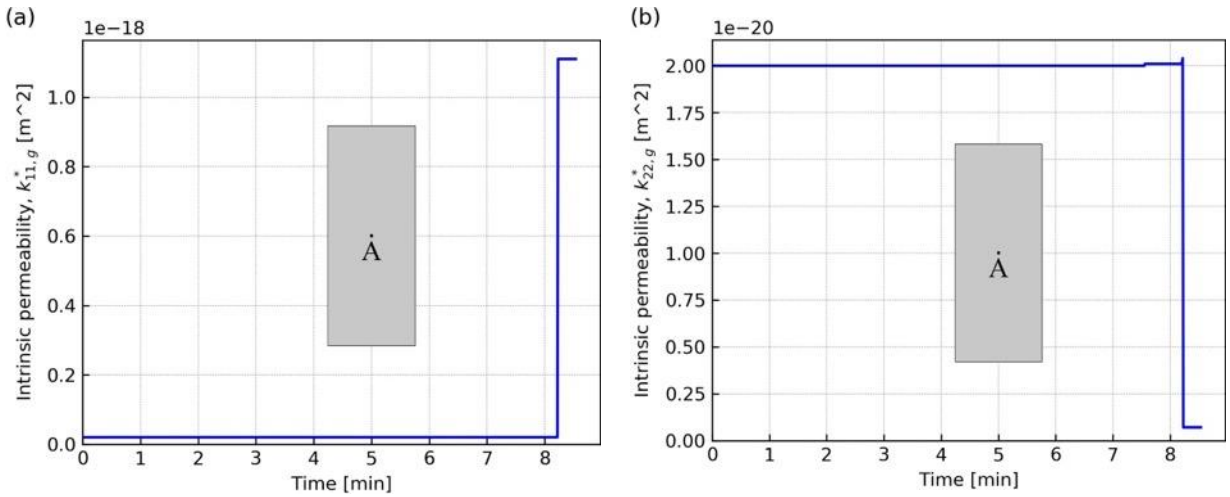

Figure 5.35 Effective intrinsic permeability components at point A: (a) $k^*_{11,g}$, (b) $k^*_{22,g}$.

Lastly, we quantitatively compare the simulated results with the measured value recorded in (Gonzalez-Blanco et al., 2016) in Figure 5.36 and Figure 5.37, where the gas pressure and average axial strain are provided. A similar variation in gas pressure and axial strain can be noticed. From 0-5 min, gas pressure increases nonlinearly that causes the dilational behavior of Boom Clay.

After gas is shut in at 5 min, a significant pressure gradient is still existed within the clayey

rock material due to its low permeability, thus driving the fluid flow along its original path. The combined action of gas flow and volume dilation will lead to the fracture evolving towards the gas outlet and in result causes a more abrupt increase in the axial strain until reaching the maximum value at t=8.51 min. This moment of maximum dilational strain means the crack tip has arrived to as far as the gas outlet area, as can be clearly seen in Figure 5.34. However, the gas front may not reach the outlet yet due to the complicated effects of local gas pressure change, HM coupling related to the clay fabric expansion and gas-water interaction (Harrington et al., 2017). This relative balanced process will sustain for a while that gas pressure decreases slightly (see Figure 5.36) and the axial strain almost kept unchanged, see Figure 5.37 from t=8.51 min to t=36 min.

Once the gas front moves to the outlet area, gas breakthrough will occur in a quite short time period. Large amounts of gas flow out of the specimen and in consequence the dilational axial strain decreases abruptly. As gas outflow pressure p_{og} hits the maximum limit, the release valve will be triggered to control the pressure at a constant value.

When there is no continuous strong driving force to maintain the preferential gas flow, the major pathway may be partly or totally closed depending on the local stress state. Gas will be transported through some other auxiliary pathways that may not pass through the outlet and a considerable amount of gas will be obstructed within the porous medium, thus leading to a significant difference between gas injection pressure and gas outflow pressure, as seen in Figure 5.36. The development of localized gas pathways is possibly referred to a dendritic fracturing network that contains the major and auxiliary pathways, as has been experimentally interpreted and observed in (Cuss et al., 2012, 2014).

It should be specified here that due to the complexity of gas induced fracturing, the model is not able to capture all the experimental phenomena. The dynamic crack propagation is explicitly represented by the model, more work still needs to be done to capture the lagging gas breakthrough phenomenon.

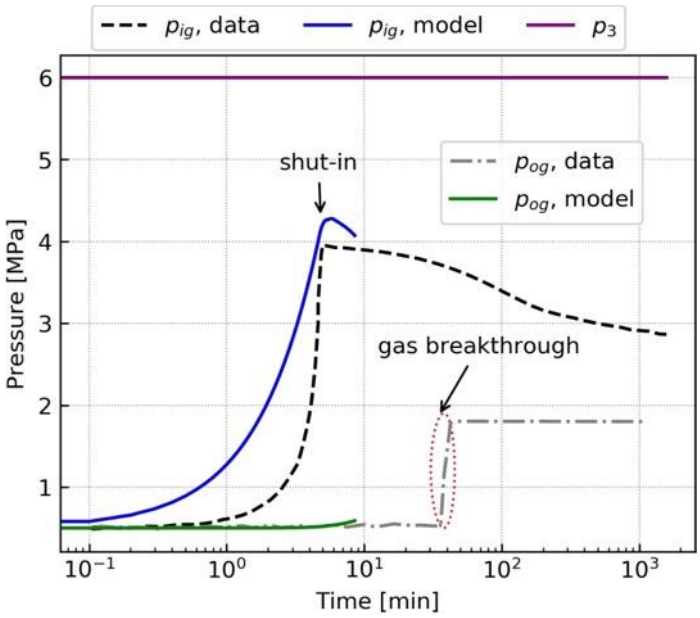

Figure 5.36 Comparison between simulated gas pressure and experimental data from Gonzalez-Blanco et al. (2016). Note: p_{ig} is gas injection pressure, p_{og} is gas pressure at outlet, p_3 is confining pressure.

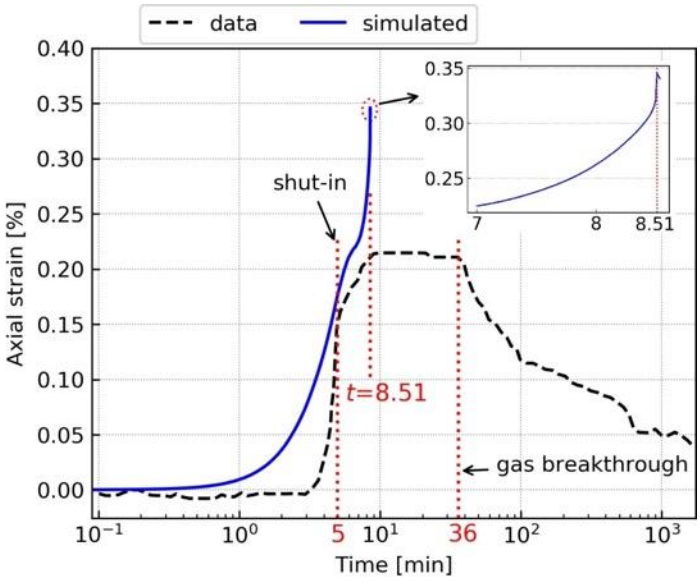

Figure 5.37 Comparison between simulated axial strain and experimental data from Gonzalez-Blanco et al. (2016)

5.3.6.3 Air Injection Test on OPA Clay

The air injection test on OPA Clay is conducted under a similar experimental condition to that for Boom Clay, both of the gas injector and downstream vessel are included. The controlled volume rate for gas pressure was also set to 100 mL/min, while the confining pressure was kept at 15 MPa throughout the whole process. The gas injection pressure was able to increase up to about 13 MPa in a short time period. After the gas was shut in at t=5 min and the gas pressure

reaches the maximum value, the outflow valve was released to keep the outlet pressure at a constant value.

5.3.6.3.1 Initial and Boundary Conditions

To reach the maximum gas pressure at 13 MPa within 4.7 minutes, the volume of gas injector was set to 3.5 mL in the simulation. Ideal gas law is used to provide the gas injection pressure under the gas injection rate of 100 mL/min. The downstream vessel is set to have the same volume for the test on Boom Clay. Since the OPA Clay specimen has the same dimension with the Boom Clay, the computational mesh of the domain can be referred to Figure 5.31. Both the gas containers are kept with a constant volume during the computation.

The initial water pressure is 0.5 MPa, the confining pressure was kept at 15 MPa. To reach a balanced stress state in the initial condition, the initial gas pressure is set to 0.5 MPa. The OPA Clay was initially intact with a small damage value d_0=1×10^{-6}, while a higher value d_0=0.1 was applied in a triangular element around the gas inlet area, see Figure 5.31. The applied boundary conditions are summarized in Table 5-10.

Table 5-10 Stages and the corresponding boundary conditions

Time (min)	Stage	Boundary conditions
0-5	Air injection (100 mL/min)	Gas injection pressure p_{ig} increases from 0.5 MPa to about 13 MPa, the volume of upstream and downstream vessel was constant, confining pressure was 15 MPa.
5-1580	Air dissipation	The confining pressure was 15 MPa, the volume of upstream and downstream vessel was constant, gas is transported along the existed pressure gradient that inlet pressure will decrease and outlet pressure may increase.

5.3.6.3.2 Modelling Results

Figure 5.38 presents the gas inflow from the gas injector to the specimen and gas outflow from the specimen to the downstream vessel. The zoomed image of damage initiation from the inlet area is also provided in Figure 5.38. It is noted that the damage initiation is accompanied by the oscillating mass flux in the inlet as gas can be easily compressed, such a dynamic gas behavior can be also retrieved in the experimental recordings (Harrington et al., 2017). Correspondingly, damage initiation will cause an increase in intrinsic permeability along horizontal direction, see Eq. (5.133), thus leading to the subsequent abrupt increase in mass flux of gas inflow, as can be seen from the gas inflow after the marked timing in Figure 5.38.

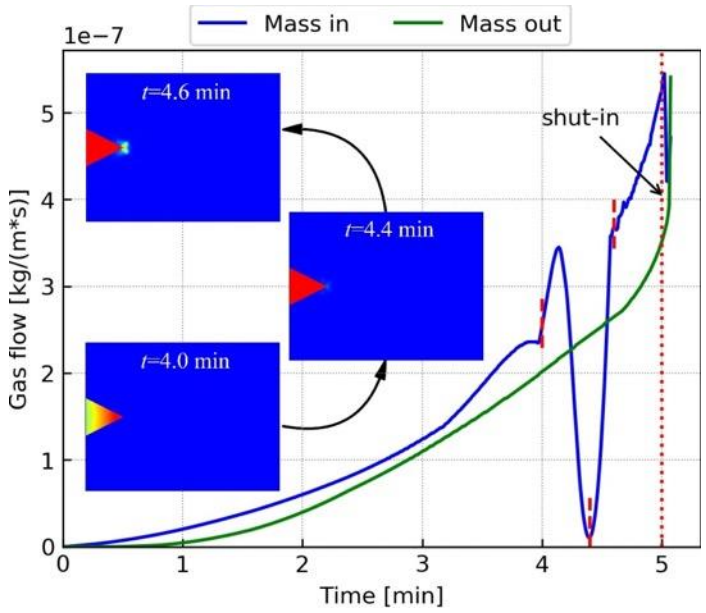

Figure 5.38 Mass ($\int_s Q_{i,g}^{(0)} \cdot N_{si} ds$) of gas flow with damage initiation. Note: N_{si} is unit vector normal to gas flow boundary.

In Figure 5.39, the evolution of simulated gas pressure at different locations is presented. The damage evolution within the OPA Clay at different time is shown in Figure 5.40. As the fast injection rate is applied in the gas injector, gas pressure increases nonlinearly to a maximum value at different locations. After gas shut-in at t=5 min, the gas pressure close to the inlet decreases correspondingly. But a high pressure gradient still exists from the gas inlet to outlet, which will drive the gas front moving towards the outlet. Once the crack front reaches the middle point B, the gas pressure will reach the maximum value at t=5.02 min. Since point C is further away from the gas inlet, it takes a longer time for crack evolving to this area, thus the timing for reaching the maximum value is more delayed.

As can be seen from Figure 5.40, the crack front still does not arrive at the outlet when gas was shut-in at t=5 min. Since a high pressure gradient is still existed, the damage evolution process continues until the crack fully partitions the rock specimen. As a result, gas breakthrough will occur subsequently that causes large amounts of gas flowing out of the specimen, as seen from the rapid increase of gas outflow in Figure 5.38, which causes a drop in gas pressure.

It is noted that the more rapid increase of applied gas pressure will cause a faster dilational behavior of OPA Clay than that in the test of Boom Clay. As has been analyzed in the Section 5.3.5.2.2, a higher strain rate condition will cause the faster propagation of microcracks. Therefore, the damage propagation in OPA Clay from the gas inlet to outlet finishes at an earlier time than the fracturing process ended in Boom Clay, as compared from Figure 5.40 and Figure

5.34.

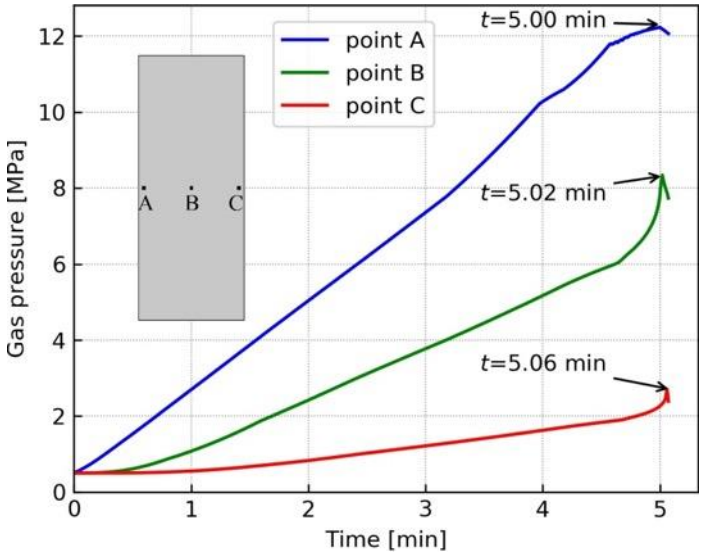

Figure 5.39 Simulated gas pressure evolution at different locations

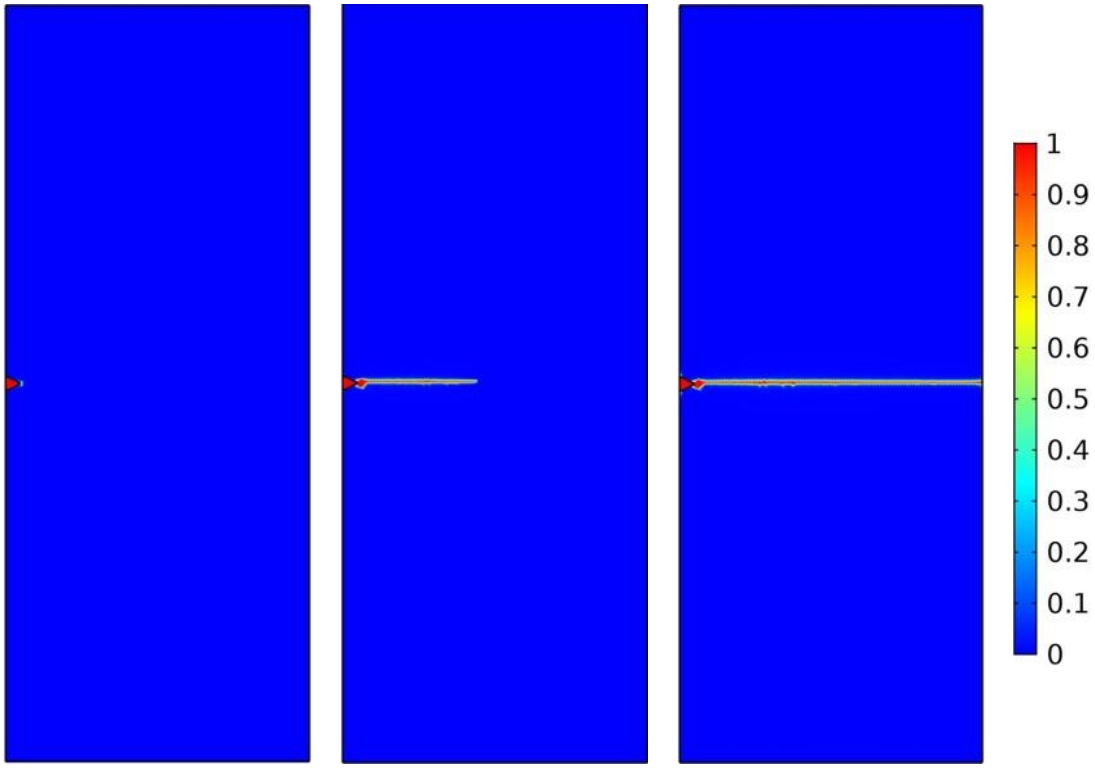

(a) t=4.60 min (b) t=5.00 min (c) t=5.07 min

Figure 5.40 Damage evolution in the OPA Clay at different time: (a) t=4.60 min, (b) t=5.00 min, (c) t=5.07 min.

The comparisons between simulated results and experimental results are illustrated in Figure 5.41. Compared to the long duration of air dissipation process (see Figure 5.41), the duration from crack initiation (about t=4.6 min) to crack completely traversing the material

(about t=5.07 min) is quite short, as seen in Figure 5.40. The crack front and gas front almost evolves simultaneously that they reach the gas outlet at a similar time, as can be seen from the timing for gas breakthrough and maximum axial strain, see Figure 5.41.

It is noted the gas induced fracturing in OPA Clay is significantly different with that occurs in Boom Clay, either in crack evolution or in corresponding gas breakthrough timing, which highlights the dynamically evolved gas pathways. This significant difference is resulted from the arbitrary nature of the pore throat as well as the microstructural properties, as represented by the different microstructural parameters in Table 5-9. Similar phenomenon has also been reported in gas injection test conducted on COx claystone (Harrington et al., 2017). As most laboratory gas experiments are focused on investigating the long-term gas behavior, which may fit in the site conditions for long-term disposal of radioactive wastes. However, the gas induced fracturing as well as the corresponding gas breakthrough seems to be a transient phenomenon, more microscopic experimental work still needs to be done to get in-depth understanding of this complex gas behavior.

After the crack totally traverses the rock specimen at t=5.07 min, the major dilatant gas pathway may be partly closed due to certain amounts of gas flowing out of the specimen. As the partly closed major pathway is not competent for accommodating gas flow, some other auxiliary pathways may be developed around the gas inlet area, see Figure 5.42. This phenomenon is associated with the micro-branching of gas induced fracture, which leads to a long term duration of gas dissipation. Such a deviation in the localized pathways can be retrieved from the experimental interpretations and observations (Cuss et al., 2014; Wiseall et al., 2015). It is quite difficult to use one model to capture the major crack propagation before gas breakthrough as well as to capture the micro-branching instabilities after gas shut-in. More work will be done in the future to better describe the complex behavior of gas induced fracturing phenomenon.

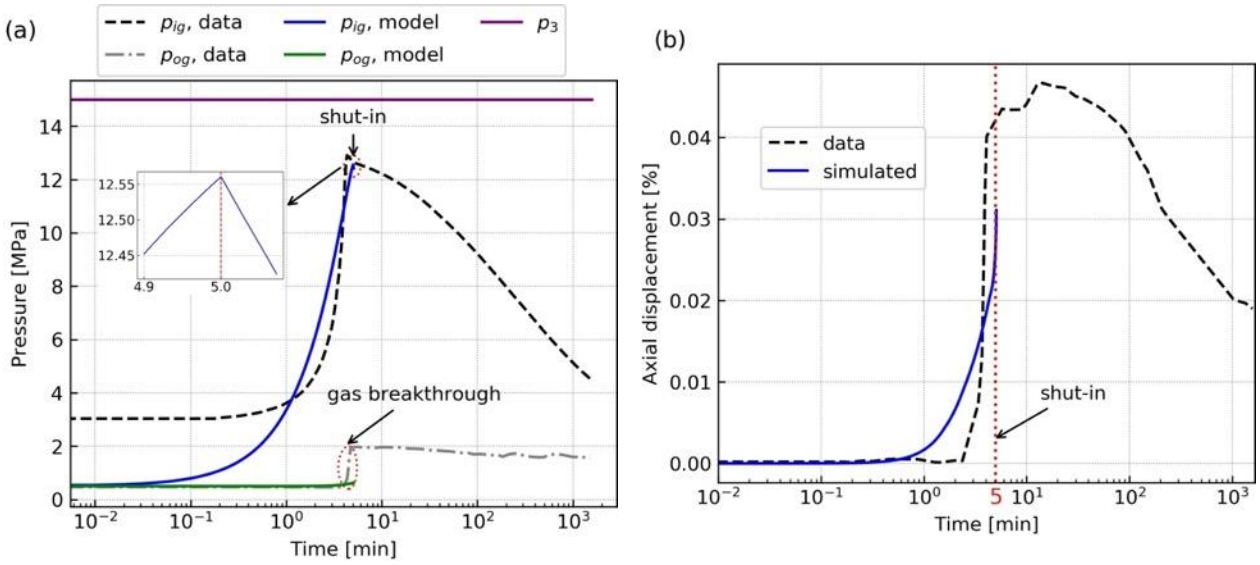

Figure 5.41 Comparison between simulated gas pressure (a) and axial strain (b) with respect to experimental data from Senger et al. (2014). Note: p_{ig} is gas injection pressure, p_{og} the gas pressure at outlet, p_3 the confining pressure.

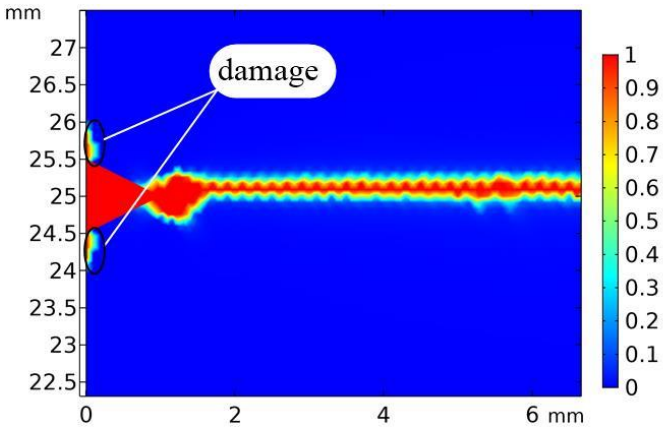

Figure 5.42 Zoomed damage around the gas inlet area at the end

5.3.7 Conclusions

The dominant process of gas migration in saturated clayey rocks is mainly referred to the advective gas flow, accompanied by the formation of micro-fracturing that occurs at the applied gas pressure significantly below the minimum principal stress. To reproduce this specific rupture pattern caused by gas flow, a two-scale time-dependent damage model is developed that accounts for the subcritical microcracks, which may evolve for stress intensity factor below the critical fracture limit. Water flow is also incorporated in the two-scale formulation. The damage evolution law is desired based on the micro-mechanical energy balance.

Starting from a porous medium consists of isotropic solid and periodically distributed microcracks under the postulate of scale separation, the asymptotic homogenization method has

allowed to derive the macroscopic hydro-mechanical (HM) governing equations, of which the homogenized coefficients has a nonlinear dependence on the normalized microcrack length. A time-dependent damage evolution law has been completely obtained from the microscopic mechanical energy analysis for evolving microcracks. The resulting damage model incorporates both the time effect and size effect that will affect the overall HM behavior of clayey rocks, from the development of localized gas pathways to the control of material deformation.

The local effective response has been analyzed for stress-strain behavior as well as damage evolution with highlight on the influence of the microstructural size, the loading rate and the reference crack velocity, which are important factors influencing the localized pathways for gas migration. Two numerical examples of air injection tests on saturated clayey rocks have been performed where the highly localized gas pathways are explicitly simulated. Comparisons between model predictions and the experimental results have shown encouraging agreement for the coupled HM response of clayey rocks subjected to gas pressurization and transport, of which the significant differences in controlling the gas breakthrough and mechanical deformation are resulting from the arbitrary nature of microstructural heterogeneities.

A number of future works may be envisaged from the present work. The model may be used to simulate the microcrack evolving along different directions by following the method in (François and Dascalu, 2010). If readers have interest to investigate the random distribution of microcracks, it is recommended to follow the homogenization method developed in (Willoughby et al., 2012). Last but not least, the model may be used in the field scale application by following the three-dimentional (3D) framework developed in (Dascalu et al., 2010a).

5.3.8 Acknowledgements

The authors thank the Natural Sciences and Engineering Research Council of Canada (NSERC) for financially supporting this research. Specifically, the first author owns a debt of gratitude to his fiancee, Jingjing Wang, who makes a lot of self-sacrifice for the family.

5.3.9 References

Amann-Hildenbrand, A., Krooss, B.M., Harrington, J., Cuss, R., Davy, C., Skoczylas, F., Jacops, E., Maes, N., 2015. Gas Transfer Through Clay Barriers, in: Tournassat, C., Steefel, C.I., Bourg, I.C., Bergaya, F. (Eds.), Developments in Clay Science. Elsevier, pp. 227-267.

Amitrano, D., Helmstetter, A., 2006. Brittle creep, damage, and time to failure in rocks. J. Geophys. Res.-Solid Earth 111, 17.

Argilaga, A., Papachristos, E., Caillerie, D., Dal Pont, S., 2016. Homogenization of a cracked saturated porous medium: Theoretical aspects and numerical implementation. International Journal of Solids and Structures 94-95, 222-237.
Atiezo, M.K., Chen, W., Dascalu, C., 2019. Loading rate effects on dynamic failure of quasi-brittle solids: Simulations with a two-scale damage model. Theoretical and Applied Fracture Mechanics 100, 269-280.
Atiezo, M.K., Dascalu, C., 2017. Antiplane two-scale model for dynamic failure. International Journal of Fracture 206, 195-214.
Atkinson, B.K., 1984. Subcritical crack growth in geological materials. Journal of Geophysical Research 89, 4077-4114.
Atkinson, B.K., Meredith, P.G., 1987. The theory of subcritical crack growth with applications to minerals and rocks. Academic Press, New York.
Bernier, F., Li, X.L., Bastiaens, W., 2007. Twenty-five years' geotechnical observation and testing in the Tertiary Boom Clay formation. Géotechnique 57, 229-237.
Bhat, H.S., Rosakis, A.J., Sammis, C.G., 2012. A Micromechanics Based Constitutive Model for Brittle Failure at High Strain Rates. J. Appl. Mech.-Trans. ASME 79, 12.
Cai, M., Kaiser, P.K., Suorineni, F., Su, K., 2007. A study on the dynamic behavior of the Meuse/Haute-Marne argillite. Physics and Chemistry of the Earth 32, 907-916.
Cappa, F., Guglielmi, Y., Rutqvist, J., Tsang, C.-F., Thoraval, A., 2008. Estimation of fracture flow parameters through numerical analysis of hydromechanical pressure pulses. Water Resources Research 44, W11408-W11408.
Charles, R., 1958. Dynamic fatigue of glass. Journal of Applied Physics 29, 1657-1662.
Coussy, O., 2007. Revisiting the constitutive equations of unsaturated porous solids using a Lagrangian saturation concept. International Journal for Numerical and Analytical Methods in Geomechanics 31, 1675-1694.
Cuss, R., Harrington, J., Giot, R., Auvray, C., 2014. Experimental observations of mechanical dilation at the onset of gas flow in Callovo-Oxfordian claystone. Geological Society Special Publication 400, 507-519.
Cuss, R.C., Harrington, J.F., Noy, D.J., 2012. Final report of FORGE WP4.1.1: The stress-path permeameter experiment conducted on Callovo-Oxfordian Claystone. British Geological Survey Commissioned Report, CR/12/140.
Dascalu, C., 2009. A two-scale damage model with material length. Comptes Rendus - Mecanique 337, 645-652.
Dascalu, C., 2018. Multiscale modeling of rapid failure in brittle solids: Branching instabilities. Mechanics of Materials 116, 77-89.
Dascalu, C., Bilbie, G., Agiasofitou, E.K., 2008. Damage and size effects in elastic solids: A homogenization approach. International Journal of Solids and Structures 45, 409-430.
Dascalu, C., Dobrovat, A.M., Tricarico, M., 2010a. On a 3D micromechanical damage model. International Journal of Fracture 166, 153-162.
Dascalu, C., François, B., Keita, O., 2010b. A two-scale model for subcritical damage propagation. International Journal of Solids and Structures 47, 493-502.
Dascalu, C., Gbetchi, K., 2019. Dynamic evolution of damage by microcracking with heat dissipation. International Journal of Solids and Structures 174, 128-144.
De La Vaissière, R., Gerard, P., Radu, J.-P., Charlier, R., Collin, F., Granet, S., Talandier, J., Piedevache, M., Helmlinger, B., 2014. Gas injection test in the Callovo-Oxfordian claystone: data analysis and numerical modelling. Geological Society, London, Special Publications 400, 427-441.
Dehandschutter, B., Vandycke, S., Sintubin, M., Vandenberghe, N., Wouters, L., 2005. Brittle fractures and ductile shear bands in argillaceous sediments: inferences from Oligocene Boom Clay (Belgium). J. Struct. Geol. 27, 1095-1112.
Fall, M., Nasir, O., Nguyen, T.S., 2014. A coupled hydro-mechanical model for simulation of gas migration in host sedimentary rocks for nuclear waste repositories. Engineering Geology 176, 24-44.
François, B., Dascalu, C., 2010. A two-scale time-dependent damage model based on non-planar growth of micro-cracks. Journal of the Mechanics and Physics of Solids 58, 1928-1946.
Freund, L.B., 1998. Dynamic fracture mechanics. Cambridge University Press, Cambridge, UK.
Gonzalez-Blanco, L., Romero, E., Jommi, C., Li, X., Sillen, X., 2016. Gas migration in a Cenozoic clay: Experimental results and numerical modelling. Geomechanics for Energy and the Environment 6, 81-100.
Harrington, J.F., Cuss, R.J., Talandier, J., 2017. Gas transport properties through intact and fractured Callovo-Oxfordian mudstones. Geological Society Special Publication 454, 131-154.
Harrington, J.F., de la Vaissière, R., Noy, D.J., Cuss, R.J., Talandier, J., 2012a. Gas flow in Callovo-Oxfordian claystone (COx): Results from laboratory and field-scale measurements. Mineralogical Magazine 76, 3303-

3318.
Harrington, J.F., Milodowski, A.E., Graham, C.C., Rushton, J.C., Cuss, R.J., 2012b. Evidence for gas-induced pathways in clay using a nanoparticle injection technique. Mineralogical Magazine 76, 3327-3336.
Hashiba, K., Fukui, K., 2015. Effect of Water on the Deformation and Failure of Rock in Uniaxial Tension. Rock Mechanics and Rock Engineering 48, 1751-1761.
Hildenbrand, A., Schlömer, S., Krooss, B.M., 2002. Gas breakthrough experiments on fine-grained sedimentary rocks. Geofluids 2, 3-23.
Kienzler, R., Herrmann, G., 2000. Mechanics in Material Space: with Applications to Defect and Fracture Mechanics. Springer-Verlag Berlin Heidelberg.
Kuhn, C., Muller, R., 2010. A continuum phase field model for fracture. Engineering Fracture Mechanics 77, 3625-3634.
Li, X., Bernier, F., Vietor, T., Lebon, P., 2007. Thermal Impact on the Damaged Zone Around a Radioactive Waste Disposal in Clay Host Rocks. Final Report to EC (Contract Number: FI6W-CT-036449).
Liu, H.-H., Wei, M.-Y., Rutqvist, J., 2013. Normal-stress dependence of fracture hydraulic properties including two-phase flow properties. Hydrogeology Journal 21, 371-382.
Lu, G.D., Yang, X.G., Qi, S.C., Li, X.L., Ding, P.P., Zhou, J.W., 2020. A generic framework for overpressure generation in sedimentary sequences under thermal perturbations. Computers and Geotechnics 124, 13.
Lyakhovsky, V., 2001. Scaling of fracture length and distributed damage. Geophysical Journal International 144, 114-122.
Marschall, P., Horseman, S., Gimmi, T., 2005. Characterisation of gas transport properties of the Opalinus clay, a potential host rock formation for radioactive waste disposal. Oil and Gas Science and Technology 60, 121-139.
Nguyen, T.S., Le, A.D., 2015. Simultaneous gas and water flow in a damage-susceptible bedded argillaceous rock. Canadian Geotechnical Journal 52, 18-32.
Norris, S., 2015. EC FORGE project: Updated consideration of gas generation and migration in the safety case. Geological Society Special Publication 415, 241-258.
Ortiz, L., Volckaert, G., Mallants, D., 2002. Gas generation and migration in Boom Clay, a potential host rock formation for nuclear waste storage. Engineering Geology 64, 287-296.
Ougier-Simonin, A., Renard, F., Boehm, C., Vidal-Gilbert, S., 2016. Microfracturing and microporosity in shales. Earth-Science Reviews 162, 198-226.
Padin, A., Tutuncu, A.N., Sonnenberg, S., 2014. On the mechanisms of shale microfracture propagation, SPE Hydraulic Fracturing Technology Conference 2014. Society of Petroleum Engineers (SPE), The Woodlands, TX, pp. 612-640.
Pazdniakou, A., Dymitrowska, M., 2018. Migration of Gas in Water Saturated Clays by Coupled Hydraulic-Mechanical Model. Geofluids 2018, 1-25.
Popp, T., Wiedemann, M., Böhnel, H., Minkley, W., Manthei, G., 2007. Untersuchungen zur Barriereintegrität im Hinblick auf das Ein-Endlager-Konzept. Insitut fur Gebirgsmechanik GmbH, Leipzig, Germany.
Rodwell, W.R., Harris, A.W., Horseman, S.T., Lalieux, P., Müller, W., Ortiz Amaya, L., Pruess, K., 1999. Gas migration and two-phase flow through engineered and geological barriers for a deep repository for radioactive waste. Joint EC/NEA Status Report.
Romero, E., Senger, R., Marschall, P., Gómez, R., 2013. Air tests on low-permeability claystone formations. Experimental results and simulations, Springer Series in Geomechanics and Geoengineering, pp. 69-83.
Sánchez-Palencia, E., 1980. Non-homogeneous media and vibration theory. Springer, Berlin.
Senger, R., Romero, E., Ferrari, A., Marschall, P., 2014. Characterization of gas flow through low-permeability claystone: laboratory experiments and two-phase flow analyses. Geological Society Special Publication 400, 531-543.
Shaw, R.P., 2015. The Fate of Repository Gases (FORGE) project. Geological Society Special Publication 415, 1-7.
Skurtveit, E., Aker, E., Soldal, M., Angeli, M., Wang, Z., 2012. Experimental investigation of CO2 breakthrough and flow mechanisms in shale. Petroleum Geoscience 18, 3-15.
Smyshlyaev, V.P., Cherednichenko, K.D., 2000. On rigorous derivation of strain gradient effects in the overall behaviour of periodic heterogeneous media. Journal of the Mechanics and Physics of Solids 48, 1325-1357.
van den Eijnden, A.P., Besuelle, P., Chambon, R., Collin, E., 2016. A FE2 modelling approach to hydromechanical coupling in cracking-induced localization problems. International Journal of Solids and Structures 97-98, 475-488.
Willoughby, N., Parnell, W.J., Hazel, A.L., Abrahams, I.D., 2012. Homogenization methods to approximate the effective response of random fibre-reinforced Composites. International Journal of Solids and Structures 49, 1421-1433.

Wiseall, A.C., Cuss, R.J., Graham, C.C., Harrington, J.F., 2015. The visualization of flow paths in experimental studies of clay-rich materials. Mineralogical Magazine 79, 1335-1342.
Wrzesniak, A., Dascalu, C., Bésuelle, P., 2015. A two-scale time-dependent model of damage: Influence of micro-cracks friction. European Journal of Mechanics, A/Solids 49, 345-361.
Xu, W.J., Shao, H., Hesser, J., Wang, W., Schuster, K., Kolditz, O., 2013. Coupled multiphase flow and elasto-plastic modelling of in-situ gas injection experiments in saturated claystone (Mont Terri Rock Laboratory). Engineering Geology 157, 55-68.
Xu, X., Wu, S., Jin, A., Gao, Y., 2018. Review of the relationships between crack initiation stress, Mode I fracture toughness and tensile strength of geo-materials. International Journal of Geomechanics 18, 04018136.
Yang, J., Fall, M., 2021a. Coupled hydro-mechanical modelling of dilatancy controlled gas flow and gas induced fracturing in saturated claystone. International Journal of Rock Mechanics and Mining Sciences 138.
Yang, J., Fall, M., 2021b. A two-scale time dependent damage model for preferential gas flow in clayey rock materials. Mechanics of Materials 158, 103853.
Yang, J., Fall, M., submitted for publication. Multiscale modelling of gas induced fracturing in anisotropic clayey rocks.
Yang, J., Fall, M., Guo, G., 2020. A Three-Dimensional Hydro-mechanical Model for Simulation of Dilatancy Controlled Gas Flow in Anisotropic Claystone. Rock Mechanics and Rock Engineering 53, 4091-4116.
Zhang, Z.X., 2002. An empirical relation between mode I fracture toughness and the tensile strength of rock. International Journal of Rock Mechanics and Mining Sciences 39, 401-406.
Zhuang, X., Wang, Q., Zhu, H., 2017. Multiscale modelling of hydro-mechanical couplings in quasi-brittle materials. International Journal of Fracture 204, 1-27.

Chapter 6 Paper VI: Coupled Two-Phase Flow and Elasto-Damage Modelling of Laboratory and In-situ Gas Injection Experiments in Saturated Claystone

Submitted for publication

Jianxiong Yang, Mamadou Fall

Department of Civil Engineering, University of Ottawa, Ottawa, ON, Canada

Abstract: Understanding gas migration behavior in host rocks is of importance to the safety evaluation of nuclear waste repositories. In order to investigate gas transport in water saturated argillaceous formations, laboratory and in-situ gas injection experiments were carried out by Harrington et al. (2017) and de la Vaissière et al. (2019a, b), respectively. Experimental results found that gas flow in saturated claystone is through highly localized network of dilatant pathways, whose properties vary temporarily and spatially within the material. For the argillaceous rocks presenting microscopic tensile ruptures due to applied gas pressure, a two-scale approach is well suited to describe the specific gas migration behavior. Considering the low stress acting normal to the contained discontinuities in the rocks, a subcritical criterion for microcrack propagation is proposed to represent the time-dependent damage at the macroscale. The passage from microscale to macroscale is implemented through an asymptotic homogenization method. In this way the microporous damage model is constructed for the isotropic solid containing a large number of periodically distributed microcracks. The solid mechanics is coupled with the fluid flow through pore pressure variation and an intrinsic permeability model, which implicitly accounts for the fracture opening induced permeability change. The developed model is tested against both laboratory and in-situ gas injection experiments conducted on potential host rocks. Some key experimental findings, such as the development of preferential gas pathways and the fully saturated state are explicitly captured by the poroelastic damage model, which helps us get in-depth understanding of this gas transport mechanism.

Keywords: nuclear waste repository; host rock; microcracks; damage; hydro-mechanical processes; preferential gas flow.

Nomenclature

Latin symbols

a	fracture spacing
a_{ijkl}	stiffness tensor for isotropic solid
A_k	empirical parameter
b	fracture aperture
C^*_{ijkl}	homogenized stiffness tensor
C_s	specific storage coefficient
d	damage variable
$\mathcal{D}_d$	energy dissipation for damage evolution
$\mathcal{D}_f$	energy dissipation for crack propagation
e_{xij}	macroscopic strain tensor
e_{yij}	microscopic strain tensor
E	Young's modulus
G_s	thermodynamic potential
$\mathcal{G}^\varepsilon$	energy release rate at the crack tip
$\mathcal{H}$	history maximum value of Y_d^+
$\boldsymbol{I}$	identity tensor in matrix format
$\boldsymbol{k}_0$	initial intrinsic permeability tensor in matrix format
$\boldsymbol{k}_{in}$	intrinsic permeability tensor in matrix format
$\boldsymbol{k}_m$	intrinsic permeability tensor of porous matrix in matrix format
$\boldsymbol{k}_f$	intrinsic permeability tensor of fractures in matrix format
$k_{r\pi}$	relative permeability of fluid π $(\pi = g,\ w)$
K_0	reference stress intensity factor
K_I	model-I stress intensity factor
l	microcrack length
l_c	size of locally periodic cell
l_q	characteristic length
L_c	size of macrostructure
$L(d)$	correction factor of permeability
m	hydraulic parameter
p_f^ε	fluid pressure field of heterogeneous porous medium
p_g^ε	gas pressure field of heterogeneous porous medium
p_w^ε	water pressure field of heterogeneous porous medium
$p_f^{(0)}$	first-order fluid pressure
p_g	gas pressure
p_w	water pressure
q_{g0}	gas mass flux at outflow boundary
q_{ig}	gas injection rate
R	universal gas constant
S_e	effective saturation degree
S_π	saturation degree of fluid π $(\pi = g,\ w)$
T	absolute temperature
u_i^ε	displacement field of heterogeneous body
$\boldsymbol{u}^\varepsilon$	displacement field of heterogeneous body in vector format
$\boldsymbol{u}^{(r)}$	Y-periodic function of displacement field at order r (r=0, 1, 2 …) in vector format
v_0	reference crack velocity
V_{ig}	volume of gas injector
$\boldsymbol{v}_\pi^D$	Darcy's velocity of fluid π $(\pi = g,\ w)$ in vector format
x_i	macroscopic coordinate
$\boldsymbol{x}$	macroscopic coordinate in vector format
y_i	microscopic coordinate
$\boldsymbol{y}$	microscopic coordinate in vector format
Y_d	damage energy release rate
Y_d^+	positive part of damage energy release rate

Greek symbols

β_t	empirical parameter
δ_{ij}	Kronecker delta
ε	scale parameter
μ_π	dynamic viscosity of fluid π $(\pi = g,\ w)$
ν	Poisson's ratio
$\boldsymbol{\xi}^{ij}$	characteristic function of elementary deformation modes in vector format

M	molar mass of gas	ρ_g	gas density
n	parameter in water retention curve	ρ_w	water density
$\vec{n}$	unit vector normal to fracture in vector format	σ_{cr}	critical tensile stress
n_d	subcritical growth index	$\sigma_{ij}^{\varepsilon}$	total stress field of heterogeneous body
$\boldsymbol{N}$	unit vector normal to crack in vector format	$\boldsymbol{\sigma}^{\varepsilon}$	total stress field of heterogeneous body in matrix format
p_0	initial air entry value	$\sigma_{ij}^{(r)}$	Y -periodic function of total stress at order r (r =-1, 0, 1 …)
p_c	capillary pressure	$\boldsymbol{\sigma}^{(r)}$	Y -periodic function of total stress at order r (r =-1, 0, 1 …) in matrix format
p_{cr}	critical gas pressure	σ'_{pa}	principal effective stress
p_{gev}	gas entry value	ϕ	porosity
p_{ig}	gas injection pressure	Σ_{ij}	macroscopic total stress tensor
p_3	confining pressure		

6.1 Introduction

The goal of geological repository is to place and isolate the wastes in the underground space that no one is able to fetch them (Nasir et al., 2013). After the deep geological repositories (DGRs) are sealed and the disposal facilities are re-saturated, large amounts of gases could be generated due to several biological and chemical processes (Rodwell et al., 1999). As free gas phase is formed, the gas pressure will increase and once reach a certain value, the safety function of the DGRs would be impaired by the permeability enhancement of geological barriers, which may lead to the release of radioactive gas (Fall et al., 2014). There are several ways for these gases flowing out of the repository (NAGRA, 2008), i.e., along sealing materials and excavation induced fractures, and pore spaces contained in the host rocks. The host rocks, as a final barrier to the movement of radioactive gases, play an important role in assessing the feasibility of DGRs.

In the last few decades, the thick argillaceous formations have been investigated as a potential host rock for nuclear waste repositories due to its favored properties (Nasir et al., 2011, 2014). As part of these investigations, extensive laboratory and in-situ gas injection tests have been performed on the argillaceous rocks to understand the gas migration behavior. At the laboratory scale, the experiments include to study the hydraulic behavior of Boom Clay (Romero et al., 1999); gas transport properties in the mudrocks (Harrington and Horseman, 1999; Ortiz et al., 2002); the hydro-mechanical (HM) behavior of Callovo-Oxfordian (COx) argillite (Zhang and Rothfuchs, 2004); gas breakthrough experiments on sedimentary rocks (Angeli et al., 2009; Hildenbrand et al., 2002; Skurtveit et al., 2012); gas injection tests on saturated claystone (Cuss

et al., 2014; Harrington et al., 2017; Popp et al., 2007; Romero et al., 2013). In the field studies, the excavation process significantly influences the fluid flow, as the HM properties in the excavation damaged zone (EDZ) or borehole damaged zone (BDZ) such as the porosity, permeability and stiffness are totally different from those of the intact host rock. The in-situ gas injection experiments were either conducted inside the microtunnel (Lanyon et al., 2014) or inside the deposition borehole (De La Vaissière et al., 2014; Svoboda and Smutek, 2015). The field results are generally difficult to be interpreted and the test results are sensitive to minor features, such as the rock bedding or the extent of damaged zone.

A large number of experimental results (Cuss et al., 2014; Harrington et al., 2017) have demonstrated that the classical two-phase flow theory are inappropriate to explain such gas flow behavior as no measurable desaturation occurs after significant gas flux is observed in the gas outlet. Also, the gas induced micro-fracturing occurs at the applied gas pressure below the confining pressure, which does not meet the condition of macroscopic fracture flow. Such gas flow behavior in the saturated claystone is commonly referred to the dilatancy controlled gas flow (Horseman et al., 1996), characterized by the development of highly localized gas pathways (Harrington et al., 2012), volume dilation (Cuss et al., 2014), gas breakthrough (Harrington et al., 2017), etc.

It is challenging to fully capture these behaviors using one model. Most of previous studies focused on the reproduction of experimentally observed phenomena in an implicit way. Essentially, the gas induced tensile ruptures are likely to occur and in consequence utilized by the gas as the preferential pathways, because of the low stress acting on the normal plane of contained discontinuities (Rodwell et al., 1999). To circumvent the difficulty in the explicit simulation of the preferential pathways, the traditional HM models are typically enriched by the damage mechanics (Fall et al., 2014; Pazdniakou and Dymitrowska, 2018) or plastic theory (Nguyen and Le, 2015; Xu et al., 2013). In contrast, the embedded fracture models (EFMs) (Arnedo et al., 2013; Gerard et al., 2014; Gonzalez-Blanco et al., 2016; Olivella and Alonso, 2008) are served as an alternative to describe the fracture in a more physical way as it conveys more fracture information in the model, such as the fracture geometry and aperture. To represent the fracture opening induced stiffness degradation in the claystone, the EFM was enriched by Yang et al. (2020) who used a simplified linear relation to couple the mechanical and hydraulic aperture of fractures, correspondingly the mechanical volume dilation and anisotropic

deformation are well captured.

Many previous models are limited to the single porosity theory, where the fluid flow in the developed fractures is neglected. To address this limitation, Yang and Fall (2021a, b) developed a double porosity model to differentiate the fluid flow in porous matrix and fractures. In this way the gas induced fracturing is implicitly represented by the volumetric strain of the fractured continuum. More recently, Yang and Fall (2021d) developed a two-scale time dependent damage model that accounts for the dynamic evolution of cracks at the microscale, which explicitly describes the development of gas dilatant pathway and the corresponding gas breakthrough phenomenon. But the two-scale model is limited to the single phase (gas) flow condition. Although water flow is also incorporated in the two-scale framework in (Yang and Fall, 2021c), the gas-water interaction is neglected in the study that cannot describe the non-desaturation phenomenon, which is not capable to be applied in the field condition.

To contribute a better understanding of gas induced micro-fracturing as well as the corresponding phenomena, the two-scale model in (Yang and Fall, 2021c) is extended to incorporate gas-water interaction in the current work. Then this model is used to simulate both the laboratory gas injection test (Harrington et al., 2017) and large-scale in-situ gas test (De La Vaissière et al., 2014). Results from the laboratory tests (Harrington et al., 2017) indicated that gas flow through saturated claystone is along highly localized network of dilatant pathways, whose properties vary temporarily and spatially that are influenced by the small-scale heterogeneities within the material.

In the problem for gas test, the isotropic confinement of sample does not allow for the shear failure, while the applied gas pressure lower than the confining pressure does not allow for the macroscopic tensile failure. In order to explicitly represent the development of localized gas pathways, it is proposed to account for the dynamic evolving of subcritical crack at the microscale. Using the asymptotic homogenization method, the microcrack propagation is upscaled to represent the damage evolution at the macroscale. Moreover, the proposed two-scale model is coupled with fluid flow in the porous system, which can capture the non-desaturation phenomenon in the saturated claystone.

The paper mainly focuses on the explicit simulation of localized gas pathways and the corresponding non-desaturation phenomenon, which provides an in-depth understanding of dilatancy controlled gas flow. The remainder of the paper is arranged as follows. The Section 6.2

describes the general framework of poroelastic damage model for preferential gas flow in the host rocks, including a short overview of effective stress theory, model assumption, the detailed construction of two-scale fracture problem and fluid flow equation, as well as the model implementation. In Section 6.3, the developed damage model is used to simulate the laboratory gas injection experiment conducted by the British Geological Survey. Lastly, the Section 6.4 is devoted to simulating the in-situ gas injection experiment where the highly localized gas pathways close to the BDZ are well captured.

6.2 A poroelastic damage model for preferential gas flow

6.2.1 Unified theory of effective stress law

Natural host rocks usually contain pre-existed or induced micro/macro-fractures. The connectivity of cracks in the microporous media significantly influences the HM coupling and the gas migration behavior. The asymptotic homogenization method by Levy (1990) has demonstrated that the behavior of fluid flow in a rigid porous medium with closed cracks is very different from that in case of connected cracks. The velocity of fluid filtration depends on the average pore size of matrix when the fissures are disconnected, while the contribution of porous matrix on fluid flow is negligible when the fissures are connected to form a flow network (Lewandowska and Auriault, 2013). This kind of problem is generally referred to the fluid flow through porous media with double or heterogeneous porosity, which was firstly introduced by Barenblatt et al. (1960) who studied the seepage-deformation problem using the phenomenological approach. Further significant contributions can be referred to the works by Warren and Root (1963); Wilson and Aifantis (1982). The phenomenon-based double porosity models, which are applied to the research topic at hand, can be referred to our recent works, see (Yang and Fall, 2021a; Yang and Fall, 2021b).

Before we introduce the HM response of microporous elastic medium with cracks, we firstly recall the unified theory of effective stress law in the double porosity model (Khalili and Valliappan, 1996). Consider a representative element containing pores and cracks subjected to external principal stresses σ_i, internal pore fluid pressure p_1 and crack fluid pressure p_2, as shown in Figure 6.1. For sake of simplicity, the principal stress σ_2 acting normal to the plane is not shown in the figure. Following (Khalili and Valliappan, 1996), the stresses applied on a fractured porous medium (FPM) can be decomposed into four components, see Figure 6.1.

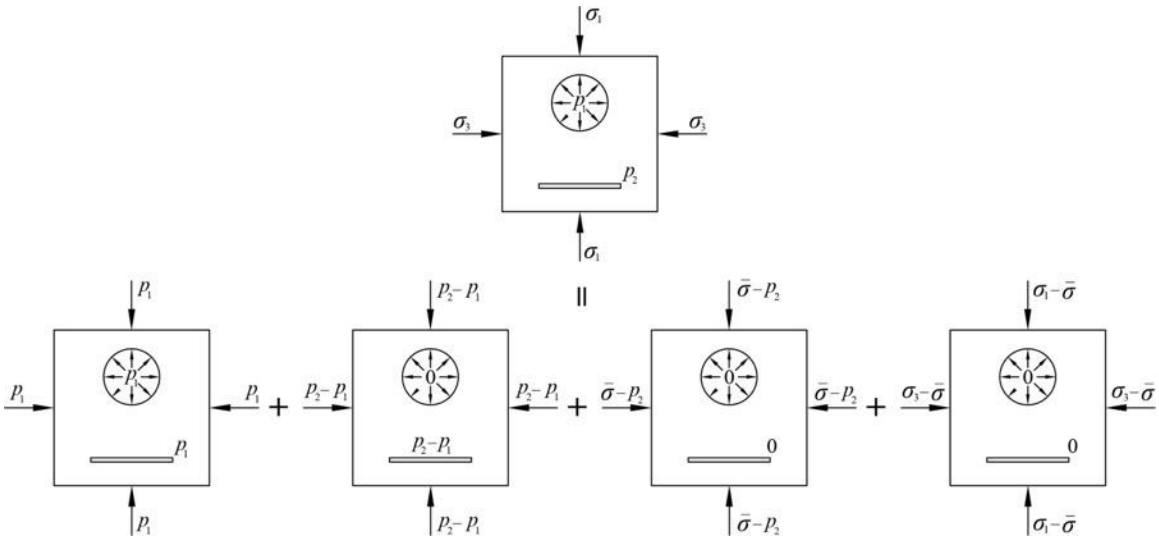

Figure 6.1 Stress decomposition of a fractured porous medium (Khalili and Valliappan, 1996). $\bar{\sigma}$ is the mean stress

Using the equilibrium in total volumetric strain, the following relation is obtained (Khalili and Valliappan, 1996):

$$\varepsilon_V = c(\bar{\sigma} - \alpha_1 p_1 - \alpha_2 p_2) \tag{6.1}$$

where ε_V is the total volumetric strain, c is the drain compressibility of FPM, α_1 and α_2 are effective stress coefficients of porous matrix and fractures, respectively, defined as follows:

$$\alpha_1 = \frac{c_p - c_s}{c},\ \alpha_2 = 1 - \frac{c_p}{c} \tag{6.2}$$

in which c_p and c_s are drained compressibility of porous matrix and solid grains, respectively. It is noted from the above relations that when the crack volume is reduced to zero (i.e., $c_p = c$), Eq. (6.2) yields the effective stress coefficients of a single porosity model, such that $\alpha_1 = 1 - c_s/c$, $\alpha_2 = 0$. In the following part, we consider an extreme case of penny-shaped cracks with small thickness that the crack volume is zero and the solid grains are incompressible. As a result, the Biot's effective stress coefficient becomes to be unity and the effective stress law corresponds to the Bishop-type relation in (Bishop, 1954; Bishop, 1959). For the Biot's theory extended to microporous medium with different geometric cracks, the readers are recommended to refer the works in (Auriault et al., 1990; Lewandowska and Auriault, 2013; Lydzba and Shao, 2000).

6.2.2 Model assumption and simplification

As the two porosity systems act at its own scale range that affects the corresponding macroscopic HM behavior, the determination of microstructural properties is of great importance to predict the fluid flow behavior. Fortunately, the homogenization method applied in materials

with periodic microstructures provided a bridge to analyze the upscaling process and the relationship between microstructural and macroscopic behavior. Two groups of homogenization techniques can be generally identified: the one based on an assumed period representing idealized microstructure (Dormieux et al., 2006b), the other one uses the volume averaging of a statistical ensemble of particles (Yuan and Harrison, 2006). Since the development of fractures is closely associated with the gas migration in porous medium, preferential gas flow will dominate the transport process once the cracks are connected each other. To investigate the gas behavior transiting from capillary flow to preferential flow, our aim is to develop a HM model considering non-connected cracks by using the asymptotic homogenization method. Such a macroscopic model will be used in the field scale to simulate the in-situ gas injection experiments as well as to explain the induced fracturing phenomenon.

The considered microporous medium is presented in Figure 6.2. Due to the small thickness of penny-shaped crack, the crack volume is regarded as negligible. The crack is filtrated by fluid and disconnected in adjacent periods. To simplify the upscaling process using asymptotic homogenization method, major assumptions are made as follows:

(i) Small strain deformation and isothermal condition are adopted. The tensile stress and expansive strain are counted positively in the solid mechanics.

(ii) Due to the arbitrary nature of geomaterials, the detailed information of randomly distributed cracks is difficult to be specified, e.g., orientation, spacing, aperture and toughness. To simplify these information so that the model is able to represent the preferential fluid flow process in the host rocks, the contained microcracks are regarded as belong to the same crack family whose length, orientation and spacing are the same. The cracks are straight in a horizontal direction and distributed periodically in the porous medium.

(iii)The crack length is much smaller than the macroscopic characteristic size. Cracks are disconnected in adjacent periods and the volume of cracks are negligible.

(iv)Although the dissolved gas within pore water plays an important role before free gas phase is formed, the contribution of gas transport by gas dissolution/diffusion is negligible once two-phase capillary flow dominates the flow process, not to mention comparing with the preferential gas flow. Our focus is to investigate the preferential gas flow process due to fracture evolution.

(v) Solid grains are assumed to be incompressible and crack face is impermeable to fluid

flow, which means the mechanical boundary conditions on the cracks are traction free. The filtrated fluid aims to open the crack lips that initiates the fracture propagation process.

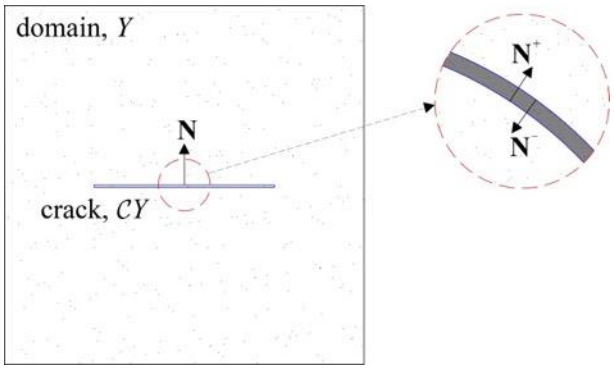

Figure 6.2 Period of a microporous medium with small thickness crack

6.2.3 Solid mechanics

6.2.3.1 Two-scale fracture problem

We consider the quasi-static elasto-damage evolution of the rock material in the following part. The elastic body contains a large number of periodically distributed microcracks, and each crack is assumed to be in a horizontal orientation (parallel to the x_1-axis). The damage variable, d, is defined as the ratio of between the crack length and microstructural size, as seen in Figure 6.3(a).

$$d = \frac{l}{l_c} \tag{6.3}$$

where l is the microcrack length, l_c is the size of microstructure that contains one crack inside.

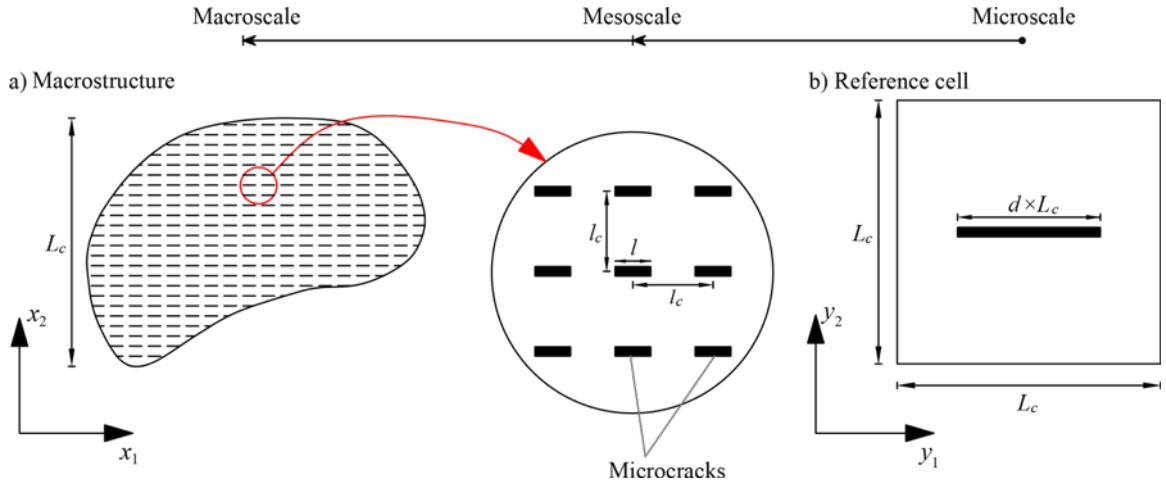

Figure 6.3 (a) A macrostructure containing periodically distributed microcracks. (b) The reference cell with rescaled crack (modified from Yang and Fall (2021d))

The different scales in Figure 6.3 are defined as follows: the microscale refers to the length ranging from micrometer to larger scales, while the macroscale is in the length of centimeters at the core sample level. To make sure the separation of scales, we introduce a scale parameter:

$$\varepsilon = \frac{l_c}{L_c} \ll 1 \tag{6.4}$$

where L_c is the macrostructure size, ε is the scale factor.

In Figure 6.3, the solid domain is denoted by $\mathcal{B}$ and the union of microcracks is denoted by $\mathcal{C}$. Under quasi-static loading condition, neglecting the volume force and the inertial as well as viscous effects yield to the momentum conservation in the solid domain:

$$\frac{\partial \sigma_{ij}^{\varepsilon}}{\partial x_j} = 0 \tag{6.5}$$

Considering the fluid pressure is acting on the microcrack lips to open the fracture, the elasticity constitutive relation for incompressible solid is expressed as:

$$\sigma_{ij}^{\varepsilon} = a_{ijkl} e_{xij}(\boldsymbol{u}^{\varepsilon}) - p_f^{\varepsilon} \delta_{ij} \tag{6.6}$$

where a_{ijkl} is the elasticity tensor for intact material, δ_{ij} is the Kronecker delta, $\sigma_{ij}^{\varepsilon}$ is the total stress field and $\boldsymbol{u}^{\varepsilon}$ the displacement field, p_f^{ε} the fluid pressure field defined by (Nguyen and Le, 2015):

$$p_f^{\varepsilon} = \mathrm{Max}(p_g^{\varepsilon}, p_w^{\varepsilon}) \tag{6.7}$$

in which p_g^{ε} and p_w^{ε} are gas pressure and water pressure fields, respectively.

Based on the postulate of small deformation, the macroscopic strain tensor is:

$$e_{xkl}(\boldsymbol{u}^{\varepsilon}) = \frac{1}{2}\left(\frac{\partial u_k^{\varepsilon}}{\partial x_l} + \frac{\partial u_l^{\varepsilon}}{\partial x_k}\right) \tag{6.8}$$

On the impermeable crack faces, pore fluid pressure is acting on it to cause the fracture opening, thus the boundary condition is represented by:

$$\boldsymbol{\sigma}^{\varepsilon} \boldsymbol{N} = -p_f^{\varepsilon} \boldsymbol{N} \tag{6.9}$$

where $\boldsymbol{N}$ is the unit normal vector on the crack faces.

As can be seen in Figure 6.3(b), a reference cell Y of length L_c is constructed from a locally periodic cell with length l_c, which is a zoomed part from the macrostructure. The macrostructure is referred to the macroscopic coordinates (x_1, x_2), while the spatial information of the reference cell is described by the microscopic coordinates (y_1, y_2). In this way the variations of mechanical fields at different scales are represented by distinct variables. Although the variations in microscopic coordinates do not have significant influences on the macroscopic coordinates,

both variations should be incorporated in the developments. To link the material behavior between microscopic and macroscopic scales, the following coordinate relation is proposed:

$$y_i = \frac{x_i}{\varepsilon} \tag{6.10}$$

The reference cell Y contains one rescaled crack of length $d \times L_c$, represented by CY. Following the asymptotic homogenization method in (Sánchez-Palencia, 1980), we look for expansions of $\boldsymbol{u}^{\varepsilon}$ and $\boldsymbol{\sigma}^{\varepsilon}$ in the form:

$$\boldsymbol{u}^{\varepsilon} = \boldsymbol{u}^{(0)}(\boldsymbol{x},\boldsymbol{y},t) + \varepsilon \boldsymbol{u}^{(1)}(\boldsymbol{x},\boldsymbol{y},t) + \varepsilon^2 \boldsymbol{u}^{(2)}(\boldsymbol{x},\boldsymbol{y},t) + \ldots \tag{6.11}$$

$$\boldsymbol{\sigma}^{\varepsilon}(\boldsymbol{x},t) = \frac{1}{\varepsilon}\boldsymbol{\sigma}^{(-1)}(\boldsymbol{x},\boldsymbol{y},t) + \boldsymbol{\sigma}^{(0)}(\boldsymbol{x},\boldsymbol{y},t) + \varepsilon \boldsymbol{\sigma}^{(1)}(\boldsymbol{x},\boldsymbol{y},t) + \varepsilon^2 \boldsymbol{\sigma}^{(2)}(\boldsymbol{x},\boldsymbol{y},t) \ldots \tag{6.12}$$

where $\boldsymbol{u}^{(i)}(\boldsymbol{x},\boldsymbol{y},t)$, $\boldsymbol{\sigma}^{(i)}(\boldsymbol{x},\boldsymbol{y},t)$, $\boldsymbol{x} \in \mathcal{B}$, $\boldsymbol{y} \in Y$ are smooth functions and Y-periodic in $\boldsymbol{y}$.

Based on our previous works (e.g., Yang and Fall, 2021c, d), the substitution of Eqs. (6.11)-(6.12) in the set of expressions (6.5)-(6.9), leads to the boundary value problems for different orders ε^r in the reference cell Y. It is easily found that the function $\boldsymbol{u}^{(0)}$ can only depend on the macroscopic variable $\boldsymbol{x}$, such that $\boldsymbol{u}^{(0)} = \boldsymbol{u}^{(0)}(\boldsymbol{x},t)$ is chosen to represent the macroscopic displacement field.

For given $\boldsymbol{u}^{(0)}(\boldsymbol{x},t)$ and the crack face condition (6.9), the boundary value problem for $\boldsymbol{u}^{(1)}$ is deduced (Yang and Fall, 2021d):

$$\frac{\partial}{\partial y_j}\left(a_{ijkl} e_{ykl}(\boldsymbol{u}^{(1)})\right) = 0, \text{ in } Y \tag{6.13}$$

$$\left(a_{ijkl} e_{ykl}(\boldsymbol{u}^{(1)})\right) N_j = -\left(a_{ijkl} e_{xkl}(\boldsymbol{u}^{(0)})\right) N_j, \text{ on } CY \tag{6.14}$$

with periodicity condition on the opposite exterior boundary of the cell.

The microscopic correction of displacement $\boldsymbol{u}^{(1)}$ has a linear dependence on the macroscopic deformations, such that $\boldsymbol{u}^{(1)}(\boldsymbol{x},\boldsymbol{y},t) = \boldsymbol{\xi}^{pq}(\boldsymbol{y}) e_{xpq}\left(\boldsymbol{u}^{(0)}(\boldsymbol{x},t)\right)$. Here, the characteristic functions $\boldsymbol{\xi}^{pq}(\boldsymbol{y})$ are elementary solutions of Eqs. (6.13)-(6.14), for particular strain $e_{xpq}\left(\boldsymbol{u}^{(0)}\right) = \delta_{pq}$.

By applying the mean value operator, $\langle \cdot \rangle = \frac{1}{|Y|}\int_Y \cdot dy$, where $|Y| = L_c^2$ is the area of reference cell Y, we can prove (Dascalu et al., 2010; Yang and Fall, 2021d) that the macroscopic stress is

$$\Sigma_{ij}^{(0)} = \langle \sigma_{ij}^{(0)} \rangle = C_{ijkl}^{*}(d) e_{xkl}(\boldsymbol{u}^{(0)}) - p_f^{(0)} \delta_{ij} \tag{6.15}$$

where $p_f^{(0)} = Max(p_g, p_w)$ is the pore fluid pressure, $\sigma_{ij}^{(0)} = a_{ijkl}\left(e_{xkl}\left(\boldsymbol{u}^{(0)}\right) + e_{ykl}\left(\boldsymbol{u}^{(1)}\right)\right)$, and

$$C^*_{ijkl}(d) = \frac{1}{|Y|}\int_Y \left(a_{ijkl} + a_{ijmn} e_{ymn}(\boldsymbol{\xi}^{kl})\right) dy \tag{6.16}$$

are the homogenized elastic coefficients. By introducing the effective relation (6.15) in the momentum conservation, we have the following form:

$$\frac{\partial}{\partial x_j}\left(C^*_{ijkl}(d) e_{xkl}(\boldsymbol{u}^{(0)}) - p_f^{(0)}\delta_{ij}\right) = 0 \tag{6.17}$$

It is noted that the homogenized elastic coefficients depend on the normalized damage variable d for the given crack orientation. A general case of bedding-parallel crack family (Ougier-Simonin et al., 2016) is considered in the study. For the assumed horizontal crack line, the homogenized coefficients C^*_{ijkl} can be computed by solving the cell problems (6.13)-(6.14) for a number of microcrack length. In the following example, the solid matrix is isotropic, of Young's modulus E=2000 MPa and Poisson's ratio ν=0.3.

The Finite Element software COMSOL Multiphysics has been used to compute these homogenized coefficients. For 11 values of normalized microcrack length $d \in [0,1]$, the characteristic functions $\boldsymbol{\xi}^{kl}$ are obtained numerically and then used in the formulation (6.16) to derive the effective coefficients with the help of piecewise cubic polynomial functions between continuous data points, as represented in Figure 6.4 as a function of the damage variable. Thanks to the periodicity condition on the external boundary of the microstructure, the microcracks will be interconnected once the structure is totally partitioned by the crack line. This physical process is represented by the increase of damage value at the macroscale.

As can be seen from Figure 6.4, the presence of microcracks causes the orthotropic response in the homogenized coefficients. The coefficients for d=0 corresponds to the intact material, while for d=1 (completely partitioned part) the analytical solution can be found for $C^*_{1111}(d = 1) = \frac{E}{1-\nu^2}$, which corresponds to the last data point in Figure 6.4. We also note that these coefficients have a nonlinear dependence on the damage variable. When the material is loaded perpendicular to the horizontal crack line, the rigidity degradation is much more serious, see the coefficients $C^*_{2222}(d)$ and $C^*_{1122}(d)$, compared to the crack parallel loading condition (as observed for the coefficient $C^*_{1111}(d)$). This response is referred to the damage induced anisotropy observed at the macroscale, as has been recorded in (Dascalu et al., 2010).

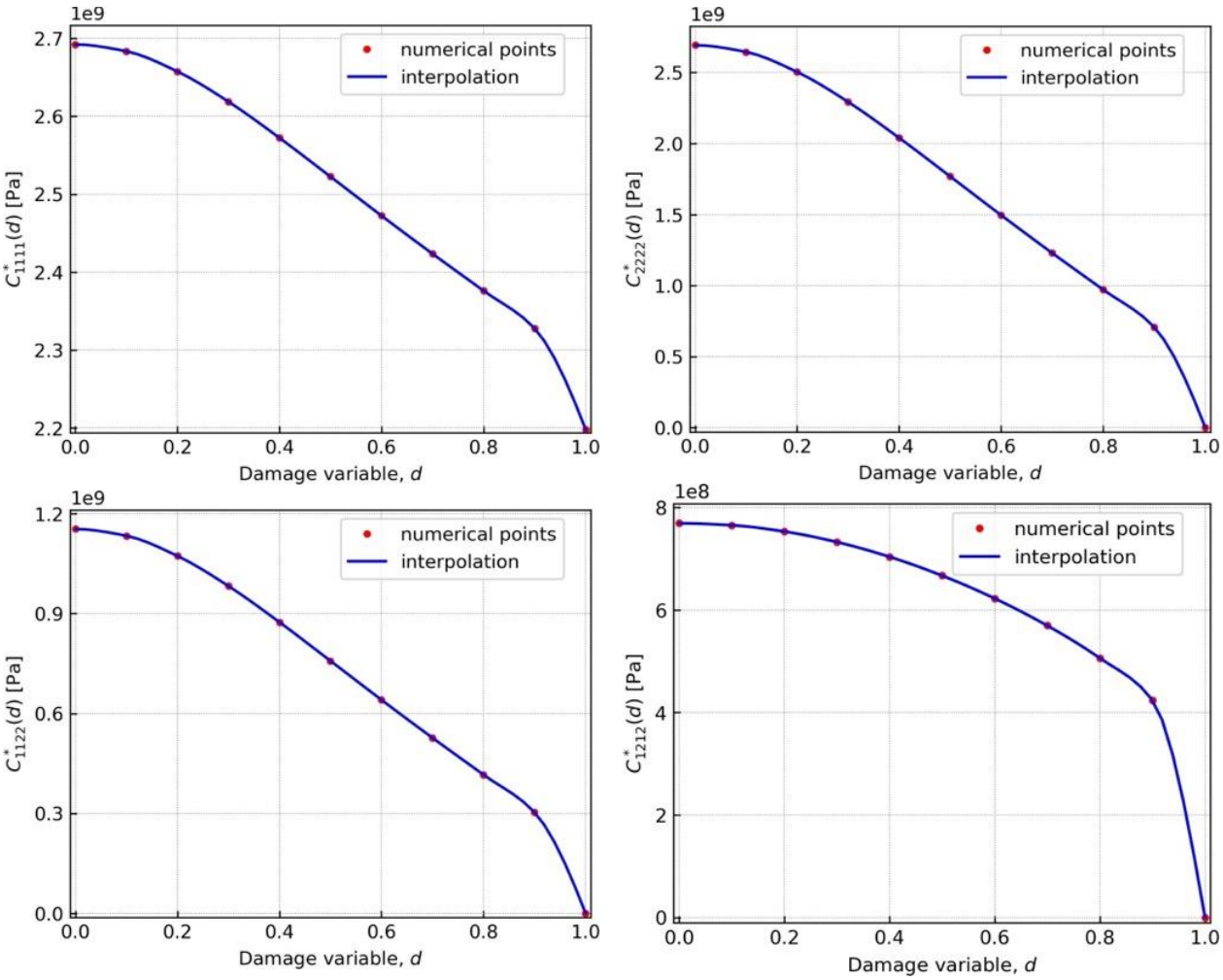

Figure 6.4 Homogenized coefficients for horizontal crack line: E=2000 MPa, ν=0.3

6.2.3.2 Damage equation

The constructed constitutive relation (6.15) describes the stress-strain behavior of rock material at a condition of non-evolving damage. To enrich the equilibrium relation, the evolution of microcracks is taken into account in the following section and correspondingly the macroscopic damage evolution law is deduced.

The tensile failure at microscale due to stress corrosion is generally the dominant mechanism of creep observed at macroscale (Dascalu et al., 2010). These microcracks may evolve for the stress intensity factor lower than the critical fracture limit. The effect of water on the porous rocks results in a time-dependent mechanical deformation (Swanson, 1984), which contributes to the development of subcritical crack growth. In the laboratory gas injection experiments on saturated argillite (Cuss et al., 2014; Cuss et al., 2012), the micro-fracturing

occurs for the applied gas pressure significantly lower than the isotropic confining pressure. Post-observation of the tested COx sample validated the fracture branching for advective gas flow, including major pathway from gas inlet to outlet and auxiliary pathways, as explained by Cuss et al. (2014). To account for the special fracturing process, the subcritical propagation law is proposed for the microcrack evolution (Yang and Fall, 2021d):

$$\frac{dl}{dt} = v_0 \left(\frac{K_I}{K_0} \right)^{n_d} \tag{6.18}$$

where K_I is the mode-I stress intensity factor, K_0 is the stress corrosion limit, v_0 is a characteristic crack speed, n_d is an empirical index for crack growth. This relation should be completed with the dissipation inequality, as follows:

$$\mathcal{D}_f = \mathcal{G}^{\varepsilon} \dot{l} \geq 0 \tag{6.19}$$

in which $\mathcal{D}_f$ is mechanical energy dissipation, $\mathcal{G}^{\varepsilon}$ is the energy release rate.

Since the observed fractures in the gas injection experiments are mainly referred to tensile ruptures (Cuss et al., 2014), the energy release rate can be expressed with respect to the mode-I stress intensity factor:

$$\mathcal{G}^{\varepsilon} = \frac{1-\nu^2}{E} K_I^2 \tag{6.20}$$

It was proved in (Dascalu et al., 2008; Yang and Fall, 2021c) that the damage energy release rate Y_d for evolving microcracks can be linked with $\mathcal{G}^{\varepsilon}$ by using the following relation:

$$Y_d = \frac{\mathcal{G}^{\varepsilon}}{l_c} = -\frac{1}{2} \frac{dC^*_{ijkl}(d)}{dd} e_{xkl}(\boldsymbol{u}^{(0)}) e_{xij}(\boldsymbol{u}^{(0)}) \tag{6.21}$$

Substitution of Eqs. (6.3) and (6.21) into (6.18)-(6.19) leads to the damage law:

$$\dot{d} = \frac{1}{l_c} v(l_c Y_d) \tag{6.22}$$

$$\mathcal{D}_d = Y_d \dot{d} \geq 0 \tag{6.23}$$

where $\mathcal{D}_d$ is the energy dissipation for damage evolution.

To enrich the damage law in the thermodynamic framework, one may introduce the macroscopic thermodynamic potential G_s for incompressible solid grains (Coussy, 2004):

$$G_s(e_{xij}, d) = \frac{1}{2} C^*_{ijkl}(d) e_{xkl}(\boldsymbol{u}^{(0)}) e_{xij}(\boldsymbol{u}^{(0)}) \tag{6.24}$$

which is the potential for thermodynamical forces (Bui et al., 2017; Dormieux et al., 2006a), defined in the following form:

$$\Sigma_{ij} = \frac{\partial G_s}{\partial e_{xij}}; \quad Y_d = -\frac{\partial G_s}{\partial d} \tag{6.25}$$

Using the damage equation (6.22) in the subcritical crack propagation law (6.18) with the help of Eqs. (6.20)-(6.21) yields the time-dependent damage law:

$$\dot{d} = \frac{v_0}{l_c}\left(\frac{\sqrt{-\frac{l_c E}{2(1-\nu^2)}\frac{dC^*_{ijkl}(d)}{dd}e_{xkl}(\boldsymbol{u}^{(0)})e_{xij}(\boldsymbol{u}^{(0)})}}{K_0}\right)^{n_d} \tag{6.26}$$

In this way, Eq. (6.26) can be coupled with the equilibrium equation (6.17) to compute the stress-strain behavior for evolving damage. It is noted that the volumetric energy release rate Y_d is acting as a driving force for damage evolution and its formulation is symmetric with respect to strain tensor in compression or tension. This means the gas induced fracturing can occur when the material is subject to compressible stress state. To avoid the unrealistic failure, only the positive part of fracture driving force is considered. Following Guo and Fall (2021); You et al. (2020), we adopt a stress-based criterion to define the damage initiation in the following form:

$$Y_d^+ = \hat{H}(f_t(\sigma'_{ij}))Y_d, f_t(\sigma'_{ij}) = \sum_{a=1}^{3}\left(\left\langle \sigma'_{pa}\right\rangle_+ / \sigma_{cr}\right)^2 - 1 \tag{6.27}$$

where Y_d^+ is the positive part of damage energy release rate, $\{\sigma'_{pa}\}_{a=1,2,3}$ is the component of principal effective stress, σ_{cr} is the critical tensile stress, $\hat{H}(f_t(\sigma'_{ij}))$ is a term to define crack onset in tensile stress state, given by:

$$\hat{H}(x) = \begin{cases} 1, f_t(\sigma'_{ij}) \geq 0 \\ 0, f_t(\sigma'_{ij}) < 0 \end{cases} \tag{6.28}$$

The developed damage model accounts for time effect and size effect, which are important characteristics observed in the gas injection experiments. Although the clay-rich argillite may show a certain self-sealing capacity for developed fractures, the developed damage model in the work only considers the irreversible fracturing process. For computational simplicity, the positive damage energy release rate Y_d^+ is replaced by its history maximum value $\mathcal{H}$, defined as follows (Miehe et al., 2010):

$$\mathcal{H}(\boldsymbol{x},t) = \max_{\tau\in[0,t]}\left\{Y_d^+(\boldsymbol{x},\tau)\right\} \tag{6.29}$$

Use of relation (6.27)-(6.29) in Eq. (6.26) yields the final damage evolution law:

$$\dot{d} = \frac{v_0}{l_c}\left(\frac{\sqrt{\frac{l_c E}{(1-\nu^2)}\mathcal{H}}}{K_0}\right)^{n_d} \tag{6.30}$$

6.2.4 Fluid flow

Due to the low permeability of argillaceous host rocks, the transport capacity of gas diffusion/dissolution is significantly restricted that can be neglected as a trivial background process, when compared to the transport capacity of two-phase flow (NAGRA, 2008). The main concern of this work is the advective gas flow accompanied by an increase in the intrinsic permeability, such specific transport mechanism is generally referred to the dilatancy controlled gas flow (Horseman et al., 1996). For a porous medium consisting of solid-gas-water mixture, the general mass balance equations for gas and water are recalled:

$$\frac{\partial(\phi\rho_g S_g)}{\partial t} + \nabla\cdot(\rho_g \boldsymbol{v}_g^D) = 0 \tag{6.31}$$

$$\frac{\partial(\phi\rho_w S_w)}{\partial t} + \nabla\cdot(\rho_w \boldsymbol{v}_w^D) = 0 \tag{6.32}$$

where ϕ is the rock porosity, ρ_w and ρ_g are the density for water and gas, respectively; S_w and S_g are the saturation degree of water and gas, respectively; $\boldsymbol{v}_g^D$ and $\boldsymbol{v}_w^D$ are the Darcy's velocity for gas and water.

In the mass conservation equations (6.31)-(6.32), the gas density follows the ideal gas law, water is regarded as incompressible fluid (Lu et al., 2020), thus:

$$\frac{\partial\rho_g}{\partial t} = \frac{M}{RT}\frac{\partial p_g}{\partial t} \tag{6.33}$$

where T is the absolute temperature, M is molar mass of gas, R is universal gas constant.

For the porous material consisting of incompressible solid grains, the porosity change is represented by the volume change:

$$\dot{\phi} = \dot{\varepsilon}_V \tag{6.34}$$

The advective fluid flow is described by the generalized Darcy's law:

$$\boldsymbol{v}_\pi^D = -\frac{\boldsymbol{k}_{in} k_{r\pi}}{\mu_\pi}\nabla p_\pi,\ \pi = g,\ w \tag{6.35}$$

in which $\pi = g, w$ represents the gas and water, respectively; $\boldsymbol{k}_{in}$ is the intrinsic permeability tensor, $k_{r\pi}$ is the relative permeability of fluid π, μ_π is the fluid dynamic viscosity, p_π is the fluid pressure.

The variation of saturation degree of fluid (gas or water) is described by the water retention curve, the main variable is the capillary pressure, $p_c = p_g - p_w$. Assuming the residual saturation degree of both water and gas are zero, so the effective saturation degree, S_e, is equal to the water saturation degree, which can be described by the following relation (van Genuchten, 1980):

$$S_e = \begin{cases} \left[1 + \left(\frac{p_c}{p_{gev}}\right)^n\right]^{\frac{1}{n}-1} & p_c > 0 \\ 1 & p_c \le 0 \end{cases} \tag{6.36}$$

$$\frac{\partial S_g}{\partial t} = -\frac{\partial S_w}{\partial t} = -\frac{\partial S_e}{\partial t} = C_s \frac{\partial p_c}{\partial t} \tag{6.37}$$

$$C_s = -\frac{\partial S_e}{\partial p_c} = \frac{n-1}{p_{gev}} S_e^{\frac{n}{n-1}} (1 - S_e^{\frac{n}{n-1}})^{\frac{n-1}{n}} \tag{6.38}$$

$$p_{gev} = p_0 (\boldsymbol{k}_{in0} / \boldsymbol{k}_{in})^{1/3} \tag{6.39}$$

in which n is the model parameter, C_s is the specific storage coefficient, p_{gev} is the gas entry value that is influenced by the fracture opening/closure, p_0 is the initial air entry value, notations with subscript '0' represent their initial values.

The relative permeability of water is represented by the approach of Mualem (1976), while the generalized power (Brooks and Corey, 1964) is extended to describe the relative permeability of gas, given as follows:

$$k_{rw} = \sqrt{S_e}[1 - (1 - S_e^{1/m})^m]^2 \tag{6.40}$$

$$k_{rg} = (1 - S_e)^3 + o \tag{6.41}$$

where m is a hydraulic parameter, o is a small constant to ensure a minimum permeability for gas flow.

Substituting Eqs. (6.33)-(6.35), (6.37) into (6.31)-(6.32), we obtain the final mass balance equations for gas and water, respectively:

$$\rho_g \left(\frac{\phi S_g M}{\rho_g RT} + \phi C_s\right) \frac{\partial p_g}{\partial t} + \nabla \cdot \left(-\rho_g \frac{\boldsymbol{k}_{in} k_{rg}}{\mu_g} \nabla p_g\right) = \phi \rho_g C_s \frac{\partial p_w}{\partial t} - \rho_g S_g \dot{\varepsilon}_V \tag{6.42}$$

$$\rho_w \phi C_s \frac{\partial p_w}{\partial t} + \nabla \cdot \left(-\rho_w \frac{\boldsymbol{k}_{in} k_{rw}}{\mu_w} \nabla p_w\right) = \phi \rho_w C_s \frac{\partial p_g}{\partial t} - \rho_w S_w \dot{\varepsilon}_V \tag{6.43}$$

Eqs. (6.42)-(6.43) constitute the governing equations for fluid flow, the hydraulic constitutive relations are shown in (6.35)-(6.41). As the fluid flow in the porous medium is closely related to the internal pore structure, of which the variation is dominated by the fracturing

process. To incorporate the fracture opening induced permeability change in the framework, we will introduce an empirical relation in the study, to better represent the laboratory observations. Similar treatments can be also found for the research topic at hand, see e.g., (Fall et al., 2014; Guo and Fall, 2019; Yang and Fall, 2021a; Yang et al., 2020).

Focusing on the porous matrix with the union of microcracks family where the orientation of crack face is parallel to x_1-axis, as seen in Figure 6.3, the effective intrinsic permeability tensor is anisotropic for such a fractured medium. The matrix permeability is equal to its initial value since the porosity is assumed to be constant in the formulation. The cubic law is commonly used to express the fluid flow process through the deformable rock fracture (Witherspoon et al., 1980). As the fracture spacing and aperture are generally difficult to be quantified in the gas flow process, furthermore the corresponding micro-fracturing process commonly causes a significant anisotropy in the permeability change, such that the permeability component increases largely along the direction of fracture propagation while the component perpendicular to the crack face decreases abruptly. The details may be referred to our previous contribution, (e.g., Yang and Fall, 2021d). To explicitly capture the development of gas dilatant pathways, a smooth varied relation used in the two-scale modelling (Yang and Fall, 2021c) is applied here:

$$\boldsymbol{k}_{in} = \boldsymbol{k}_m + \boldsymbol{k}_f = \boldsymbol{k}_m + \frac{b^3}{12a}(\boldsymbol{I} - \vec{n} \otimes \vec{n}) = \boldsymbol{k}_0 \exp(-A_k \varepsilon_v) + \boldsymbol{k}_0 L(d)(\boldsymbol{I} - \vec{n} \otimes \vec{n}) \tag{6.44}$$

$$L(d) = d \cdot \exp\left(\frac{\beta_t}{\exp(1-d)}\right) \tag{6.45}$$

where $\boldsymbol{k}_m$ and $\boldsymbol{k}_f$ are the intrinsic permeability tensor for porous matrix and fractures, respectively; a is the fracture spacing, b is the fracture aperture, $\vec{n}$ is the unit vector normal to the fracture plane, defined by $\vec{n} = (0,1,0)$ in Figure 6.3; $\boldsymbol{k}_0$ is the initial intrinsic permeability of intact material, $L(d)$ is a correction function that calibrates the intrinsic permeability value, A_k and β_t are empirical parameters.

This simplified relation can well represent the fracture opening induced permeability change. When the porous material is initially intact ($d = 0$), the correction factor is zero value that the intrinsic permeability is equal to the matrix permeability. As damage gradually evolves, the crack induced hydraulic anisotropy will directly affect the intrinsic permeability of the fractured continuum, and in consequence contributes to the development of gas dilatant pathways.

6.2.5 Model implementation

The coupled damage-flow model based on the two-scale formulation, is implemented into a finite element software, COMOSL Multiphysics. The damage state and damage induced stiffness softening as well as the permeability change need to be continually updated with the increase in applied gas pressure. The commercial finite element software allows us to conduct the spatial and temporal discretization in a convenient way. In the study, the staggered solution scheme, served as an efficient and stable computational approach, is applied to solve the coupled damage-flow problem. The basic procedures of staggered scheme are summarized in Figure 6.5.

After the example geometry is specified, the model is discretized into a set of representative elements. At each time step with the help of applied HM boundary conditions, the gas pressure, water pressure and displacement vector are firstly solved based on the damage variable calculated at the previous iterative step. Then the history maximum value of damage energy release rate is recorded and as a result the damage variable is determined using the damage evolution law, i.e., Eq. (6.30). If the convergence criterion is met at this state, the solutions of p_g, p_w and $\boldsymbol{u}^{(0)}$ are updated using the converged values. What follows for the algorithm is to move forward to the next time step until the maximum step is reached. If the convergence criterion is violated, the previous steps are iterated until it satisfies the criterion.

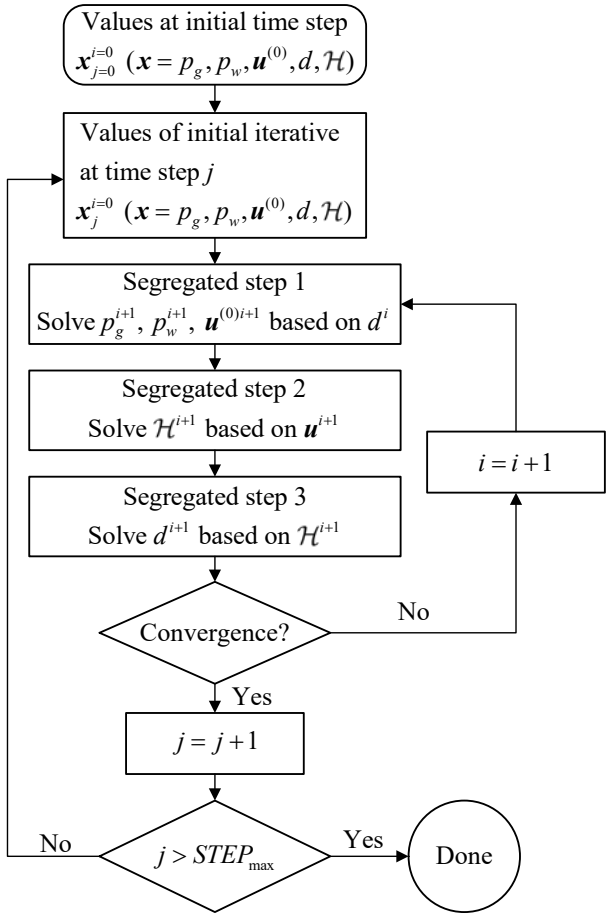

Figure 6.5 Computational solution scheme in the coupled damage-flow model

6.3 Laboratory Gas Injection Experiment

To understand the key processes governing the advective gas flow through saturated host rocks, a series of laboratory gas injection experiments are undertook by the British Geological Survey. In what below we present a test on designated COx-4 sample that contains a natural fracture, as shown in Figure 6.6. Because of the low stress acting on the normal plane of the existed discontinuities, the gas pressure induced tensile fractures are likely to be developed, which act as preferential pathways for the advective gas flow.

Figure 6.6 Naturally fractured COx-4 sample (Harrington et al., 2017)

6.3.1 Experimental description of COx-4 test

The COx-4 sample was prepared to investigate the impact of fracture properties on the gas migration behavior, with the cylindrical axis parallel to the bedding plane. Although the fracture traverses the full length of the core, it can still be regarded to be intact as the cohesion is still existed (Harrington et al., 2017).

The sample was loaded under isotropic confining pressure, p_3 =9 MPa, which was kept to be constant throughout the gas injection process. The helium gas was injected through the injection filter (IF) either in a constant flow rate mode or in a constant pressure mode, while the water pressure was kept constant at the backpressure filter (BF), as seen in Figure 6.7. The IF and BF are porous stainless steel material that is much stiffer than the rock material. The initial gas pressure was same with the water pressure, 1 MPa in the COx-4 test.

Gas injection pressure p_{ig} was applied in a constant flow rate mode for about 38 days' time periods, then kept in a constant pressure mode for about 16 days. After this gas injection cycle, another cycle started for different time of duration, 6 days and 28 days, respectively. About 59.3 days elapsed, gas breakthrough occurs that large amounts of gas flow out of the sample (Harrington et al., 2017; Yang et al., 2020), which means the contained fracture was in a totally opened state. In the next moment, the steady-state gas flow dominates the advective flow process if the continuous gas pressure can be satisfied that no pressure decay occurs.

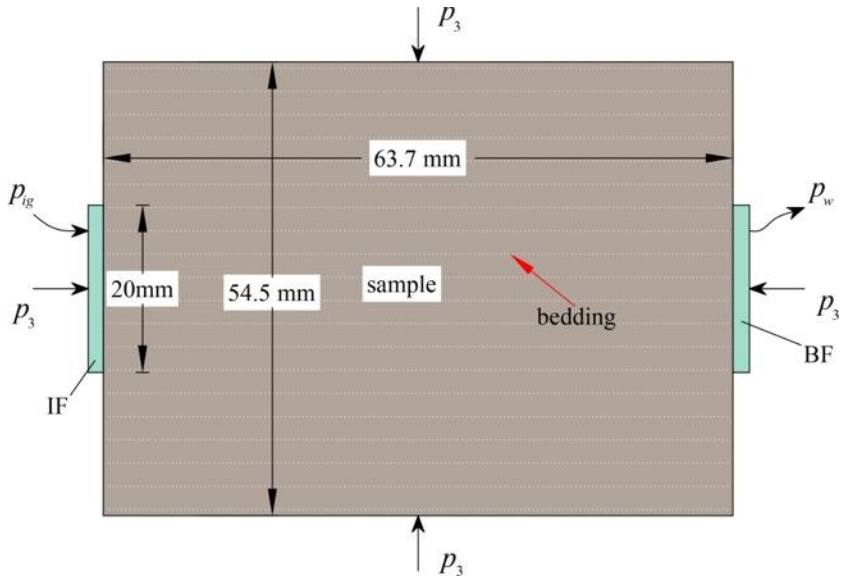

Figure 6.7 Sketch of laboratory experiment (p_3: isotropic confining pressure; IF: injection filter; BF: backpressure filter; p_{ig}: Gas injection pressure)

The detailed gas injection history of COx-4 test is shown in Figure 6.8, where the left one is from the initial gas test day to the end of the test, the right one illustrates the characteristics for the pore pressure difference as well as the gas outflow rate during the period of gas breakthrough. As seen from the figure, the gas breakthrough approximately occurs between t=59 d and t=60 d, which means the gas pathway connected with the outflow boundary. Thus the gas can flow out of the sample continuously that the flow rate keeps at an increasing trend.

It is notified that the fracture is in a totally open state after gas breakthrough, and in consequence the steady state single phase flow dominates the gas migration process. The flow rate value is controlled by the applied gas pressure and the fracture opening size, which may be explained by the theory of parallel planar plate, detailed experimental validation is referred to Witherspoon et al. (1980). Therefore, the flow rate value before gas breakthrough is significantly smaller than that during the parallel flow state.

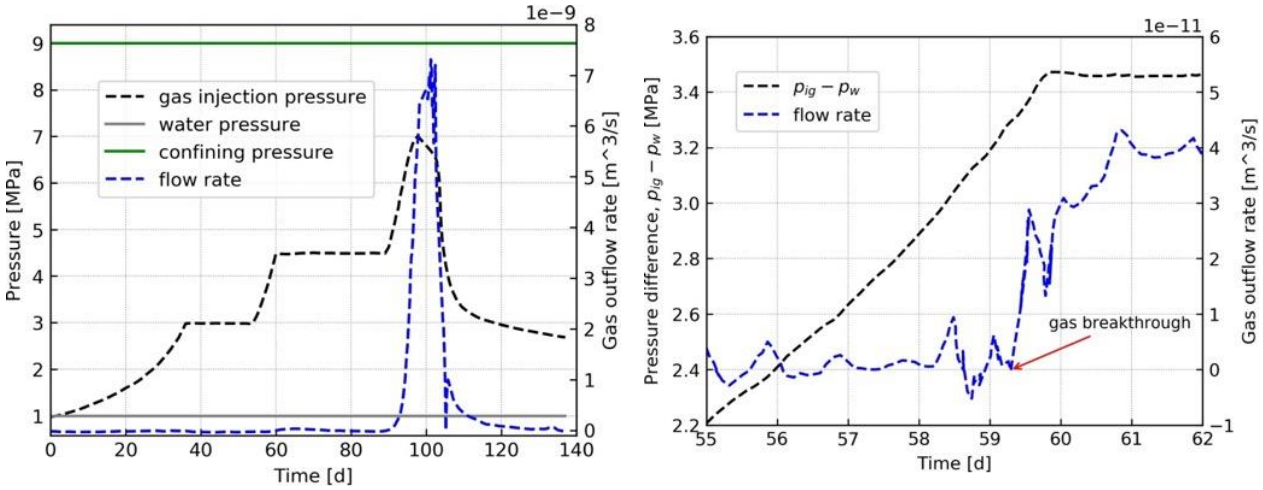

Figure 6.8 Detailed gas injection history in COx-4 test (data reproduced from Harrington et al. (2017))

6.3.2 Model setup

To explicitly simulate the gas induced fracture propagation and the associated HM phenomena, i.e., highly localized gas pathways, gas breakthrough and no measurable desaturation after gas breakthrough, a triangular grid with plane strain deformation mode is used in the computation. As the stepwise increase of gas pressure in the gas inlet is too rigid to describe the actual gas flow (Guo and Fall, 2018, 2019; Yang and Fall, 2021d), the gas injector vessel needs to be considered in the simulation.

Assuming a constant volume of injection vessel, different gas injection rate is applied during these steps. Since the accurate information on the volume of injection vessel is not given, an estimated value (1540 cm^3) from the field gas injection test (De La Vaissière et al., 2014) is adopted. Based on this value in a closed volume, a theoretical calculation is used to derive the specific gas injection rate. The comparison between calculated gas pressure and the experimental data is provided in Figure 6.9, the good agreement allows us to proceed to the simulation of advective gas flow.

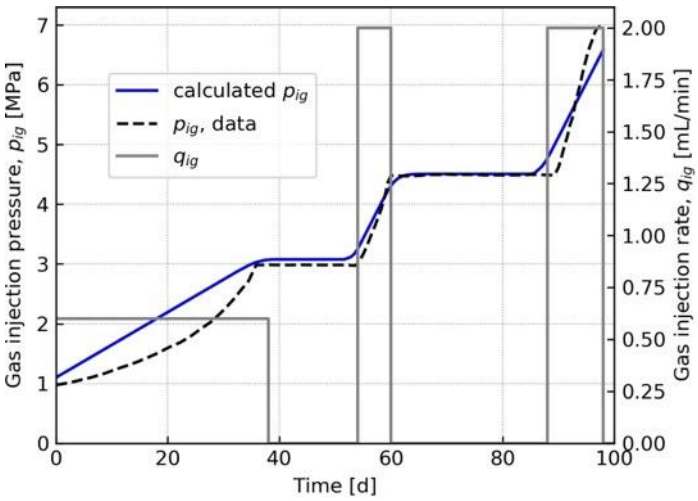

Figure 6.9 The comparison between calculated gas pressure and the experimental data

After the volume of gas injector is known, we incorporate it in the simulation of COx-4 test, as seen in Figure 6.10(a). The COx-4 specimen is loaded under isotropic confining pressure condition with $p_3 = 9$ MPa, the left boundary of specimen is fixed. The volume (V_{ig}) of gas injector is 1540 cm^3 and the applied gas injection rate (q_{ig}) is shown in Figure 6.9. According to the ideal gas law, the variation of gas pressure in the injector vessel is expressed as

$$\frac{\partial p_{ig}}{\partial t} = \frac{RT\rho_g}{MV_{ig}} q_{ig} \tag{6.46}$$

In the simulation, we use a porous material with high permeability (1×10^{-12} m^2) and high porosity (a unit value) to represent the gas injector. The variation of gas injection pressure not only depends on the applied injection rate, but also associates with the gas flow process within the rock material. A constant water pressure, 1 MPa is applied on the right side boundary of specimen, as represented by the green line in Figure 6.10(a). The meshed domain is shown in Figure 6.10(b), with refined area encompassing the potential crack path.

Due to the high compressibility and low viscosity, the fracture opening size for preferential gas flow is generally very small, which has been validated from the microscopic observations by using the nanoparticle injection technique in (Harrington et al., 2012). The gas behavior in the outflow boundary of clay-rich materials is not physically clear, as the gas pathways are dynamically unstable that may switch between open and closed state (Guo and Fall, 2018). A constant gas pressure condition in the outlet is too rigid to describe the actual phenomenon, thus we apply a mass flux boundary condition in the gas outlet. This condition has been adopted in our previous work, see Yang and Fall (2021d), defined by:

$$\boldsymbol{q}_{g0} = \begin{cases} \rho_g \frac{\boldsymbol{k}_{in} k_{rg}}{\mu_g l_q} (p_g - p_{cr}), p_g > p_{cr} \\ 0, p_g < p_{cr} \end{cases} \tag{6.47}$$

where l_q is a characteristic length (1 mm); p_{cr} is a critical pressure.

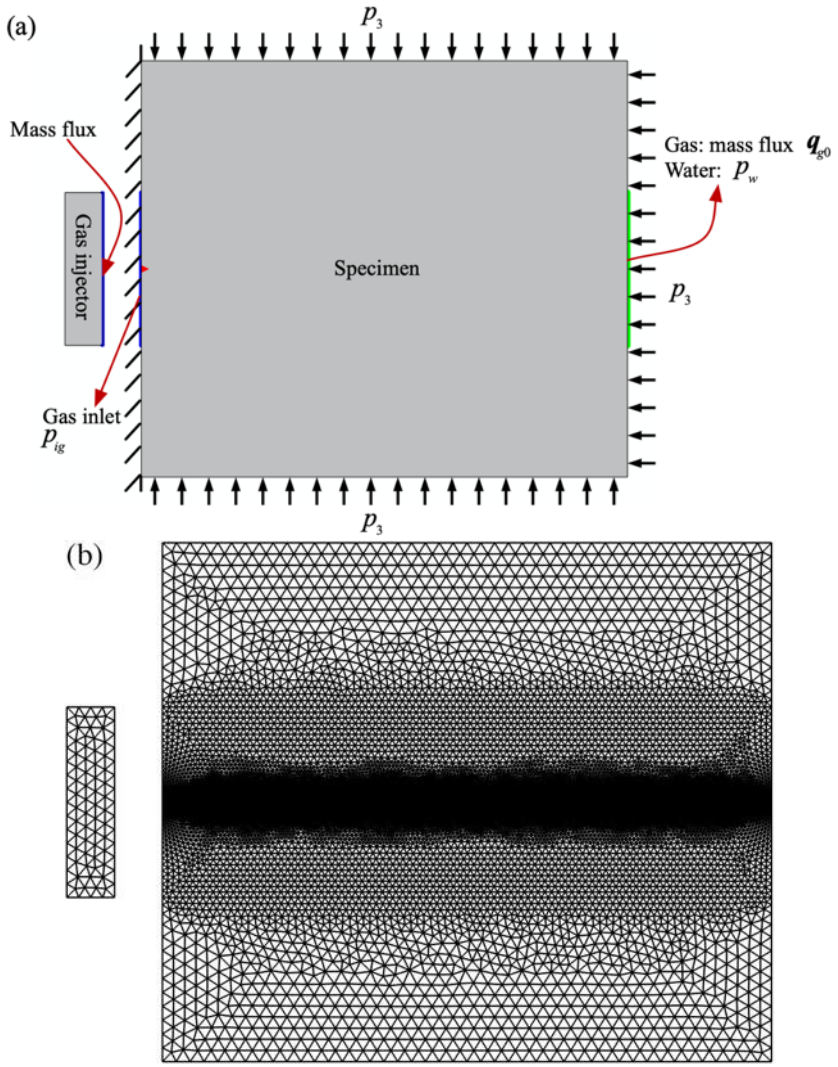

Figure 6.10 (a) Boundary conditions in the COx-4 test. (b) Meshed domain in the simulation of COx-4 test

The initial intrinsic permeability for sample COx-4 is about one order of magnitude above that of intact COx-1 (Harrington et al., 2017) as it contains one natural fracture, thus the permeability parallel to bedding is taken as 1.8×10^{-20} m^2. The hydraulic test gives an permeability anisotropy of 2.5 (Harrington et al., 2017), correspondingly the permeability normal to bedding is 7.2×10^{-21} m^2. The parameters described by the van Genuchten model are adopted from Charlier et al. (2013) who investigated the water retention curve of argillite. The damage parameters related to the microcrack growth are obtained based on the description of our previous work (Yang and Fall, 2021d), where the influence of different crack parameters are

analyzed locally. The empirical parameters A_k and β_t are chosen to get a better phenomenological representation. Detailed reference values are summarized in Table 6-1.

Table 6-1 Parameter values for simulation of COx-4 test

Basic HM properties (Harrington et al., 2017)		Air entry value, p_0 [MPa]	15
Young's modulus, E [MPa]	2000	Damage parameters (based on Yang and Fall (2021d))	
Poisson's ratio, ν [-]	0.3	Crack growth index, n_d [-]	3
Gas helium density, ρ_g [kg/m^3]	0.16	Stress corrosion limit, K_0 [Pa·m]	2.31×10^4
Gas viscosity, μ_g [Pa·s]	1.96×10^{-5}	Microstructural size, l_c [m]	1.0×10^{-5}
Intrinsic permeability parallel, k_{h0} [m^2]	1.8×10^{-20}	Characteristic crack speed, v_0 [m/s]	6.0×10^{-6}
Intrinsic permeability normal, k_{v0} [m^2]	7.2×10^{-21}	Critical tensile stress, σ_{cr} [MPa]	1.1
Porosity, ϕ [-]	0.146	Empirical parameter	
van Genuchten parameters (Charlier et al., 2013)		A_k [-]	1.0
n [-]	1.49	β_t [-]	3.5
m [-]	0.55		

To initiate the gas flow process, the initial gas pressure is set to 1.01 MPa that is slightly higher than the applied water pressure. The initial water saturation degree can still represent a fully saturated condition due to the high air entry value. The initial effective stress is calculated to be -7.99 MPa. The critical gas pressure p_{cr} is set to be slightly higher than the initial gas pressure, 1.1 MPa in the simulation. An initial damage value of 1×10^{-6} is used in the simulation and a higher value (0.1) of initial damage is applied in the element around the gas inlet area, as seen from the red triangular element in Figure 6.10(a). This numerical handling is to initiate a non-homogeneous response, similar treatment can be also found in (Guo and Fall, 2019, 2021; Yang and Fall, 2021d).

6.3.3 Modelling Results

The comparison between simulated gas pressure and experimental data is shown in Figure 6.11. The water saturation degree was obtained averagely for the whole domain, as present in the right image of Figure 6.11. A good agreement was found for the gas injection pressure before gas breakthrough occurs. The unstable behavior in gas outflow pressure at around day 60 represents large amounts of gas flowing out of the boundary, which indicates the gas breakthrough phenomenon. As has been recorded in the post-measurement (Harrington et al., 2017), no measurable desaturation was observed after significant gas flux was monitored in the gas outlet. This phenomenon was well represented by the model, where the average water saturation degree of the sample is very close to unit value, see Figure 6.11.

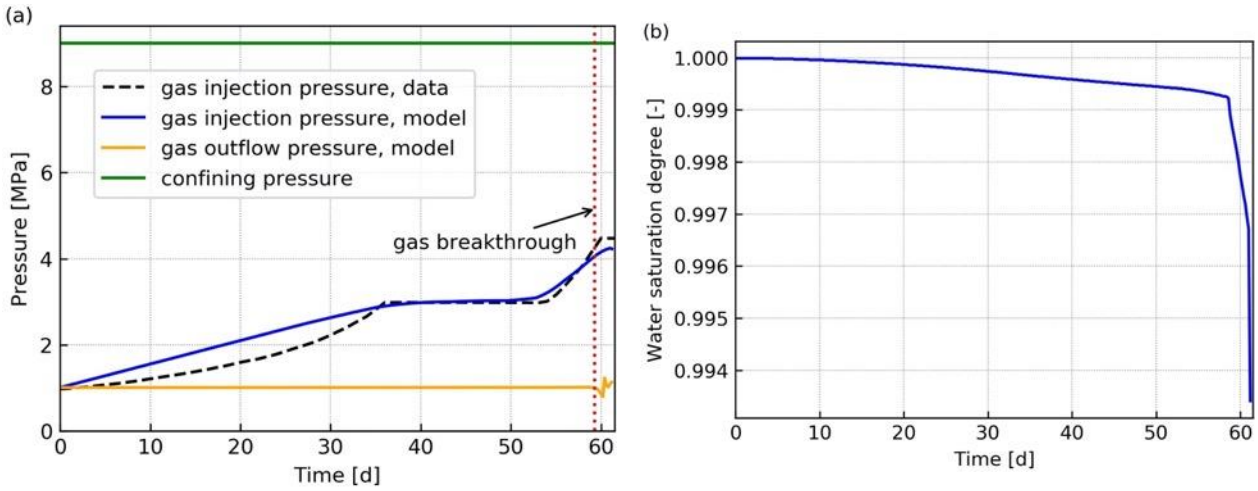

Figure 6.11 (a) Simulated gas injection pressure and (b) average water saturation degree of the sample

Figure 6.12 and Figure 6.13 present the distribution of gas pressure and damage in the COx-4 sample at different time, respectively. Accompanied with each gas pumping rate, gas is injected into the sample and gas pressure is distributed evenly around the inlet, see Figure 6.12(a). As gas pressure increases nonlinearly, the injected gas will cause a dilational behavior of the rock sample. It is analyzed from the local response in (Yang and Fall, 2021d) that this continuous tensile strain will lead to the material failure if the microcracks have enough time to propagate. Due to the non-homogeneous response of the material, the crack firstly evolves from the damaged triangular element, see Figure 6.13(a). Thanks to the assumed periodic condition and crack orientation at microscale, a major horizontal pathway for gas flow is gradually developed towards the outflow boundary, see Figure 6.13(b). According to the mathematical relation (6.44), the damage propagation leads to an increase in the permeability, and in consequence a preferential pathway is developed for gas flow. The preferential gas flow along the localized fracture causes the anisotropic distribution of gas pressure in the domain, as seen in Figure 6.12(b)-(c).

When the gas pumping process continues, the single major pathway is not able to accommodate large amounts of gas penetrating the rock sample, some other auxiliary pathways are developed for gas flow, see Figure 6.13(c)-(d). Following a similar penetrating process, more gas flowing into the sample through these auxiliary pathways, thus creating new gas front, as represented in Figure 6.12(d).

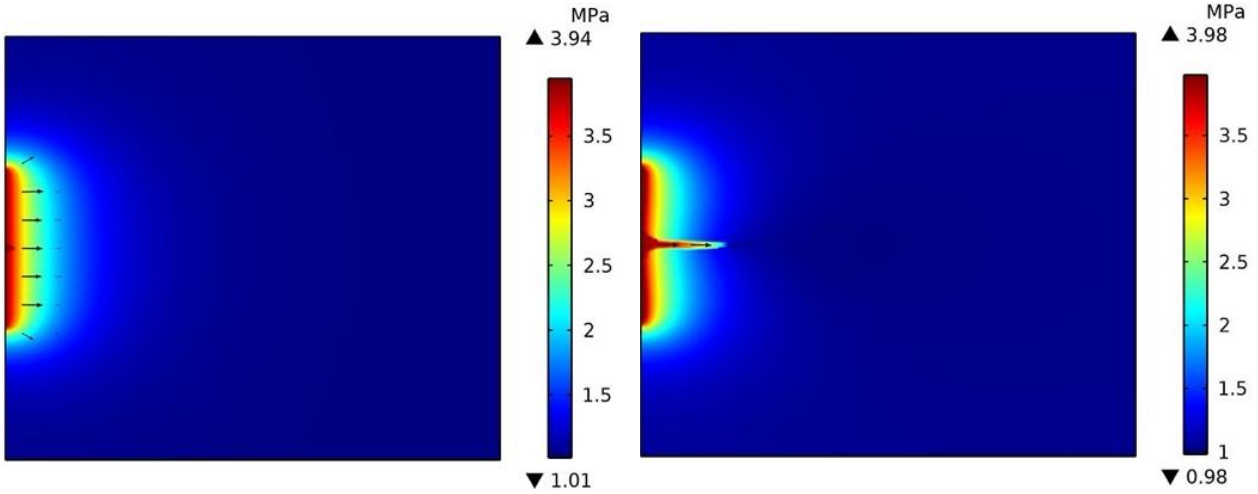

(a) t=58.6 d (b) t=58.8 d

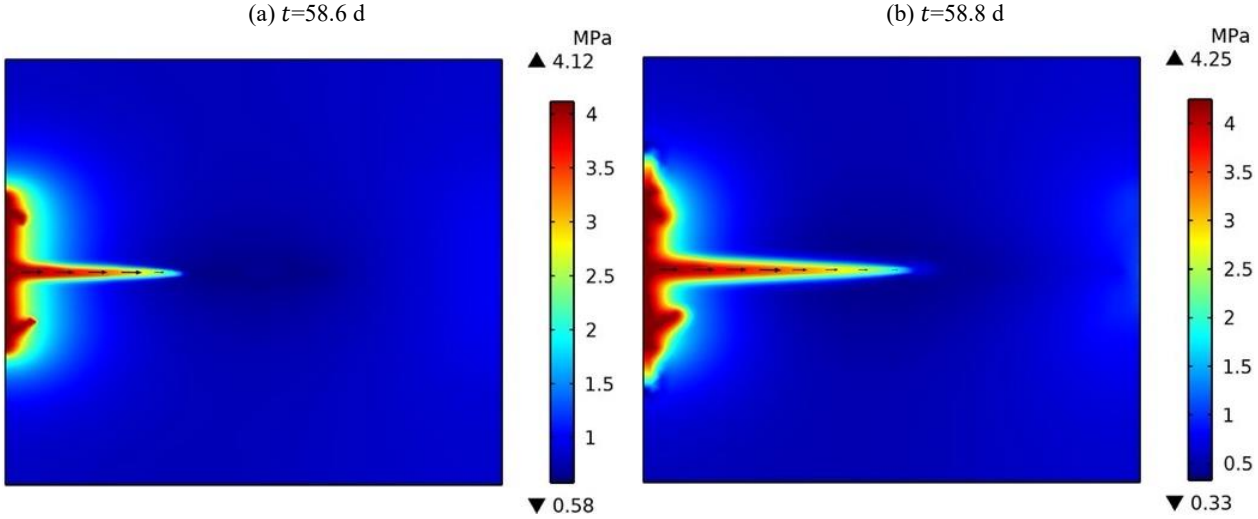

(c) t=59.6 d (d) t=61 d

Figure 6.12 Gas pressure distribution at different time. Note: black arrow is scaled that denotes gas velocity.

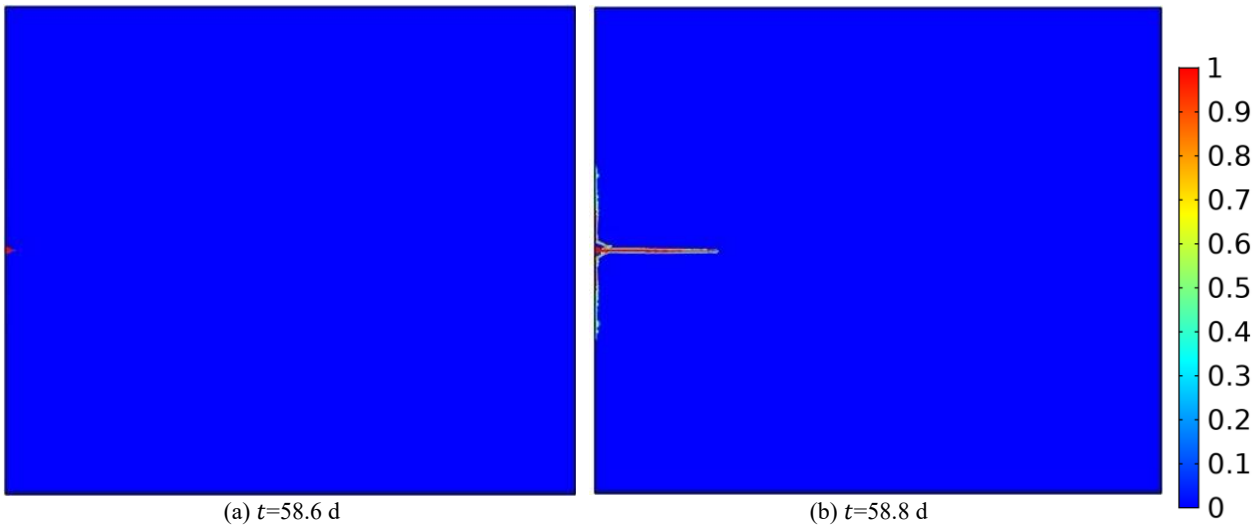

(a) t=58.6 d (b) t=58.8 d

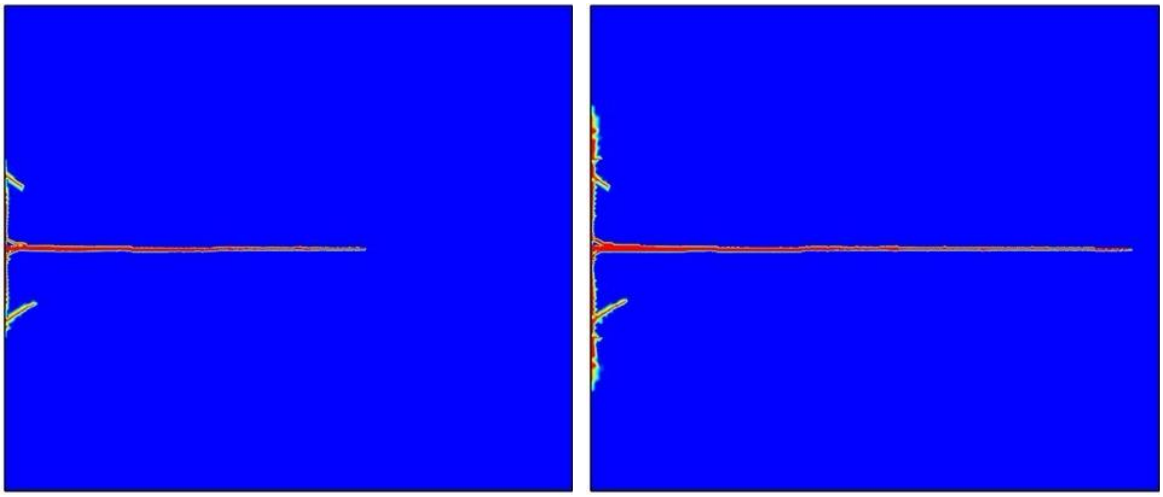

(c) t=59.6 d (d) t=61 d

Figure 6.13 Damage propagation at different time

The horizontal intrinsic permeability and gas entry value at the point A are presented in Figure 6.14, while the distribution of water saturation degree in the domain is shown in Figure 6.15. When the crack front does not arrive at the point, both the permeability and gas entry value keep at the initial value, i.e., 1.8×10^{-20} m^2 and 15 MPa in the test. At about t=59.2 d, the gas front passes through the point area that induces the tensile rupture, then the crack evolves and stabilizes during a short time period. In the localized fracture pathways, the gas-water interaction is so significant that causes an abrupt reduction in the gas entry value and a quick increase in the intrinsic permeability (see Figure 6.14). Correspondingly, the water inside the localized pathways was displaced to a smaller value than that in the surrounding pore spaces, as seen in Figure 6.15. This HM coupled process is described by the mathematical relations (6.17), (6.26), (6.39) and (6.44).

It can be clearly seen from Figure 6.13 and Figure 6.15 that the desaturation mainly occurs inside the dilatant gas pathways. This characteristic is consistent with the experimental observations of the highly localized pathways by using the nanoparticle injection technique in (Harrington et al., 2012).

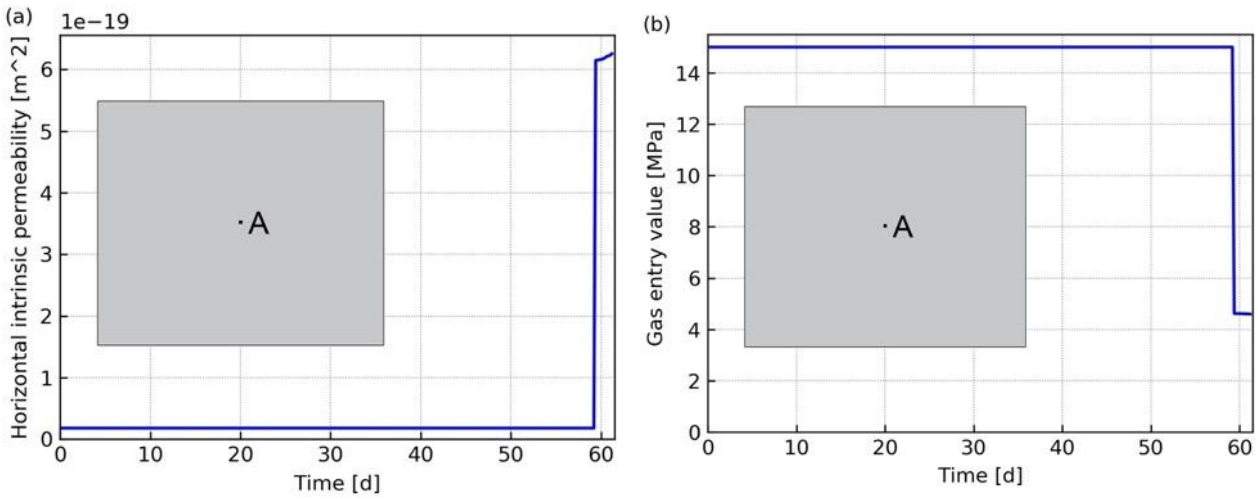

Figure 6.14 (a) Horizontal intrinsic permeability and (b) gas entry value at point A

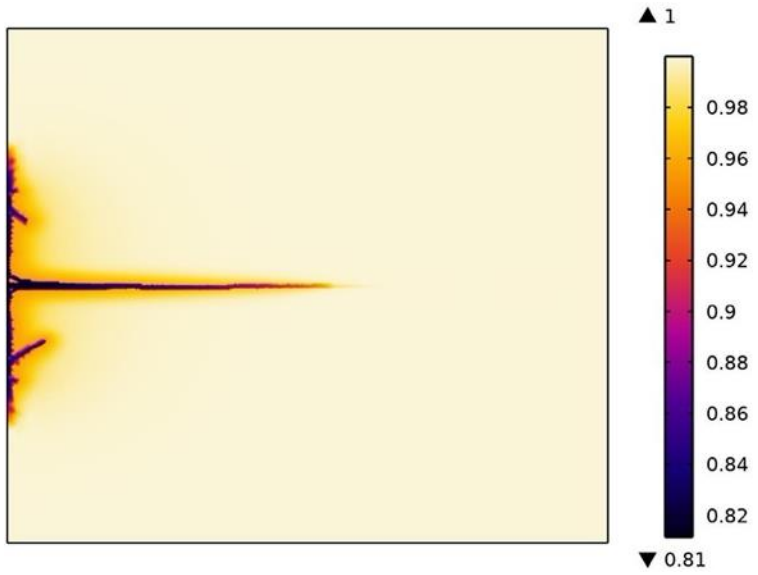

Figure 6.15 Distribution of water saturation degree at the end

Lastly we present the average volumetric strain and damage in Figure 6.16. In the laboratory test (Harrington et al., 2017), the gas induced micro-fracturing occurs at a scale from millimeter to micrometer, which needs to be observed using microscope technique. The characteristic of highly localized pathway corresponds to the little variation in the averaged damage of the whole rock sample.

As recorded by Cuss et al. (2014), the gas induced volume dilation exists in the gas injection test that can not be explained by the pure compression of pore water. In Figure 6.16, the simulated volume change reaches a maximum value of 0.175% in the COx-4 sample. While the observed volume dilation for sample COx-1 and SPP_COx-2 is about 0.8% (Harrington et al., 2013b) and 0.18% (Cuss et al., 2014), respectively. As there is no direct experimental data of

volume change in the COx-4 test, further validation for the dilational behavior in the sample COx-4 needs to be explored in the future.

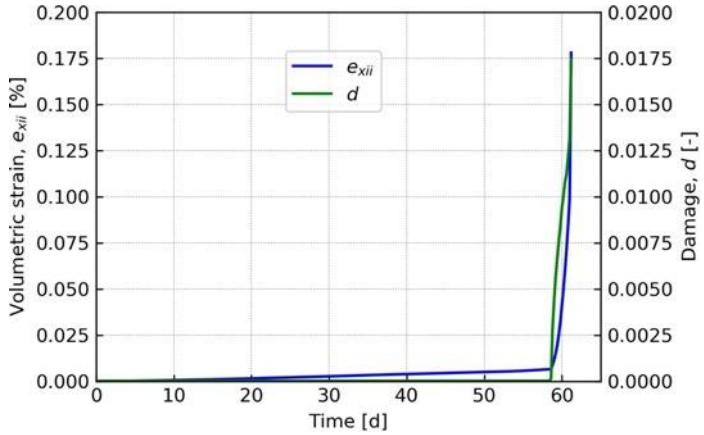

Figure 6.16 Averaged volumetric strain and damage of the sample COx-4

6.4 In-situ Gas Injection Experiment

To investigate the behavior of natural host rocks, the in situ gas injection experiment (PGZ1 test) was conducted in the COx argillite at the Underground Research Laboratory (URL) by Andra (de la Vaissière et al., 2019a, b).

6.4.1 Experimental description of PGZ1 test

The geological layer of COx argillite is at a depth of about 490 m and the experimental layout includes three boreholes, the injection borehole, the measuring borehole and the extensometer borehole, as seen from Figure 6.17. These boreholes were drilled between two parallel galleries, the GED gallery and the GEX gallery. The nitrogen gas was injected from the injection borehole, in which the gas interval (Int. 1) is 1 m long at the central part between the other two measuring intervals (Int. 2 and Int. 3). The different intervals in a same borehole are separated by the packers. The shortest distance between the injection borehole and the extensometer borehole is 1.132 m. Both the injection borehole and measuring borehole are oriented parallel to the maximum principal stress direction (de la Vaissière et al., 2019b).

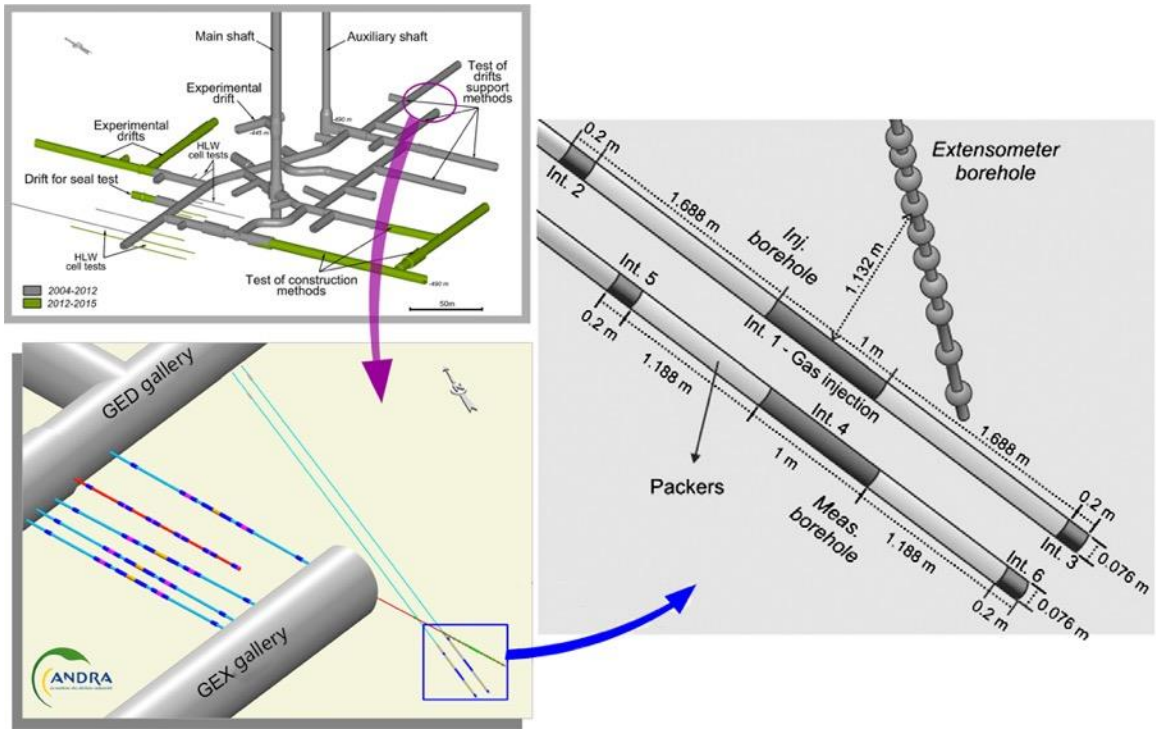

Figure 6.17 Geological layout of in situ gas experiment at the URL (modified from De La Vaissière et al. (2014))

The plane view of the gallery and borehole position is shown in Figure 6.18. The GEX gallery is parallel to the GED gallery with a spacing of 25 m. Two boreholes of 76 mm diameter and 28 m length were drilled parallel in the base wall of the GED gallery with a dip angle of 35.4° to the horizontal plane. The interval 1 (Int. 1) of injection borehole is used for gas injection, while Int. 2 and Int. 3 are used to monitor the pressure change due to gas injection. Similar to the function of Int. 2 and Int. 3, another borehole is also used to recording the pore pressure evolution, located 1 m away from the injection borehole.

The last extensometer borehole was drilled ahead of the GEX gallery with a dip angle of 47.8° to the horizontal plane. It is 23 m long in length and 101.3 mm wide in diameter, which is used to monitor the axial displacement in argillite.

After drilling the boreholes, the system was allowed to evolve freely so that the argillite can be re-saturated, which meets the actual condition for gas generation in the post-phase of DGR. Six pressure sensors were installed in different intervals of two boreholes. Before conducting the GAS1 phase, the hydraulic tests were performed in the interval 1 (Int. 1 in Figure 6.17) to measure the permeability of argillite (De La Vaissière et al., 2014). To aid the dissipation of residual pore water pressure, the nitrogen gas was injected into the Int. 1 to displace the synthetic fluid carefully.

The gas injection was started on 2010/02/01, composed by several periods of controlled gas injection rate and gas shut-in. Thanks to the installed pressure sensors in different intervals, the pore pressure evolution accompanied by the gas injection in the argillite is recorded, as illustrated in Figure 6.19. The build-up of pore pressure in each interval was observed following the start of hydraulic tests on 2009/07/27, which was caused by the perturbation of borehole drilling. When the perturbation was dissipated gradually, the pore pressure underwent a slow decrease until it reached the asymptotic pressure.

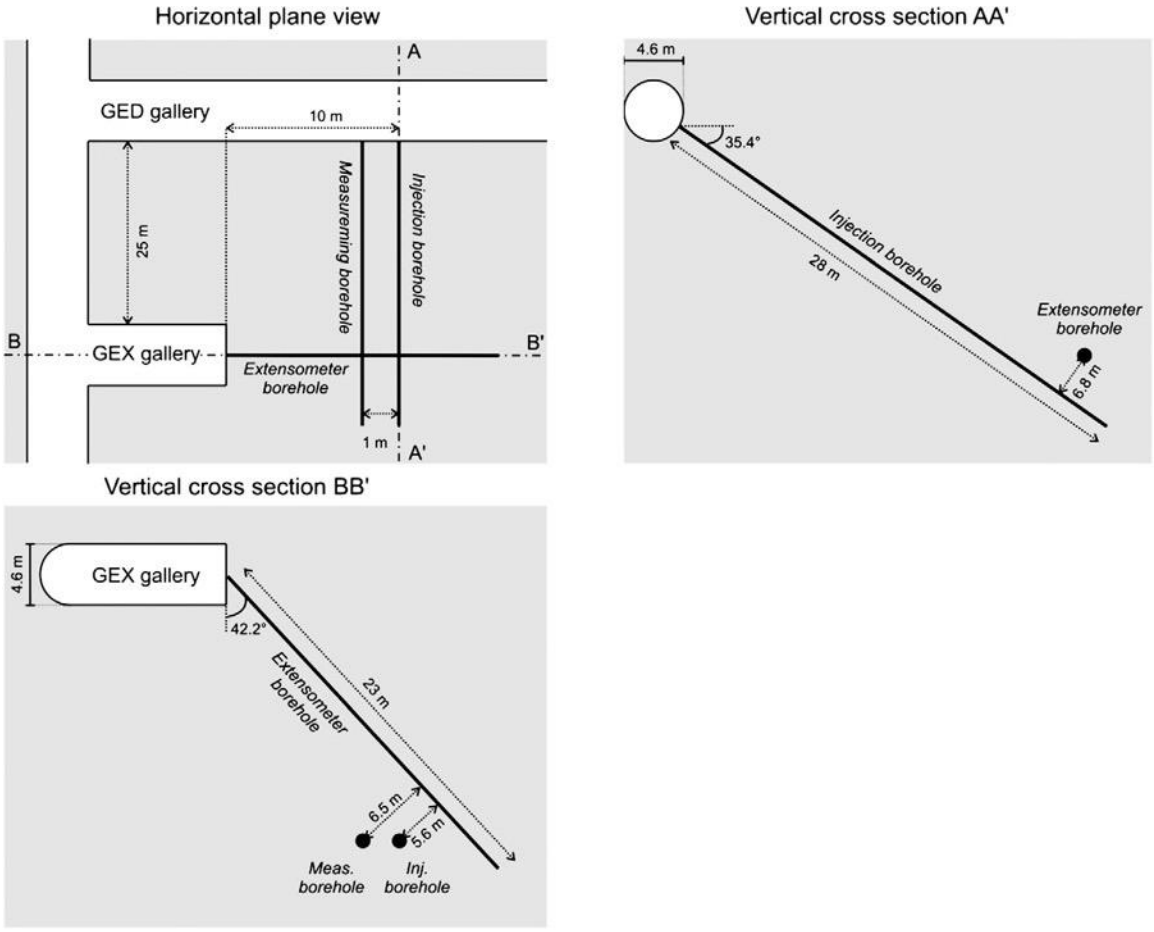

Figure 6.18 Plane view of gallery and borehole position (adapted from Charlier et al. (2013))

During the GAS1 phase, a very small increase of pore pressure was detected in the Int. 4. While for the rest intervals, the pore pressure seemed to be not influenced by the gas injection. This phenomenon was possibly related to the localized gas flow behavior that highly pressurized gas front may not exactly reach the borehole position. A more or less decrease of pore pressure in these intervals might be due to the drainage in the extensometer borehole, as the permeability of filled concrete in the extensometer borehole is much higher than the host rock (Jacops et al.,

2014). The GAS1 phase was lasted for about 424 days and the imposed maximum gas pressure was about 9.1 MPa, as seen in Figure 6.19.

A hydraulic test followed the gas shut-in at the end of GAS1 phase and the second phase (GAS2) was performed on October 2012. During this phase, gas pressure was applied through constant flow rate at 1 mL/min and then switched to constant pressure at 9.8 MPa for about 11 months (de la Vaissière et al., 2019b). Similar to the end of GAS1 phase, a hydraulic test was also performed at the end of GAS2 phase. After that, the third gas injection cycle (GAS3) was continued on August 2014, composed of different constant gas flow rate injection mode and gas recovery mode. The maximum gas pressure during GAS3 phase reached 10.45 MPa.

Detailed discussions in (de la Vaissière et al., 2019b) have shown that conventional two-phase flow with permeability increase occurred in the GAS1 phase, while fracture initiation was mainly limited in the area closer to the gas inlet in the GAS2 phase. Lastly in the GAS3 phase, gas induced fracturing was observed to propagate as far as to the deeper of host rock when the applied gas pressure reached 10.45 MPa, which was still well below the minimum principal stress, about 12.3 MPa detected from a deep borehole, originally measured by Senger et al. (2006), then used in (De La Vaissière et al., 2014).

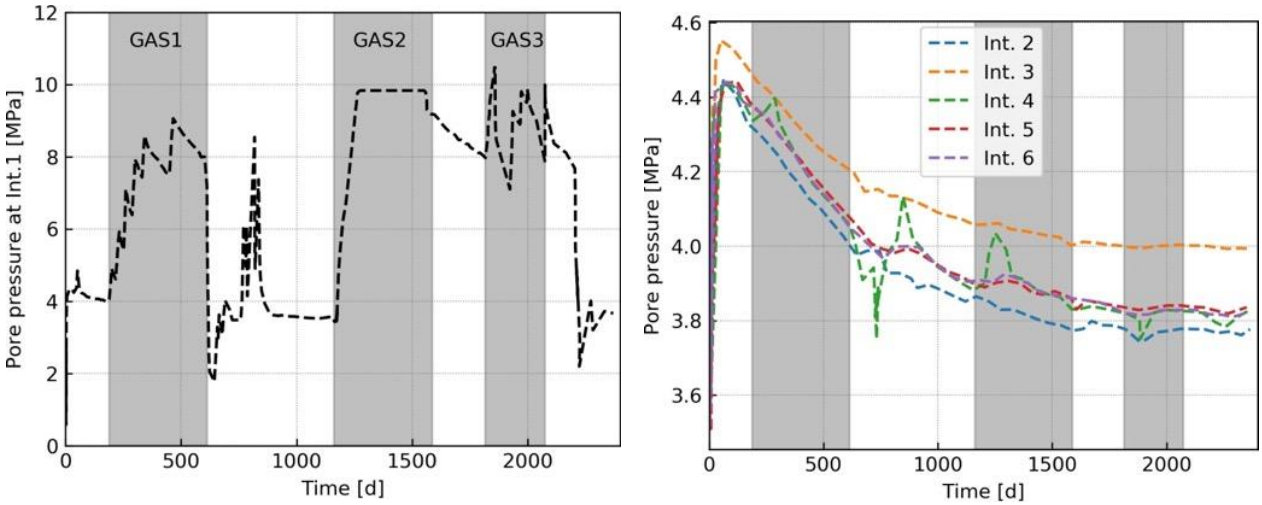

Figure 6.19 Pore pressure evolution in each sensor (data reproduced from (de la Vaissière et al., 2019b))

Since the development and interconnection of fracture networks is closely associated with the preferential gas flow, which is our focus in the study. Thus we further present in Figure 6.20 a detailed gas injection history in the GAS3 phase. GAS3-GRI1 started with a constant flow rate (1 mL/min) for about 2 days, then switched to constant pressure mode that causes abrupt changes in the recorded gas flow rate, as seen from Figure 6.20(b). A stepped constant flow rate was applied

in GAS3-GRI2, accompanied by step-wise increased gas pressure. The third gas injection stage (GAS3-GRI3) with a high constant flow rate (250 mL/min) was performed on 2015/03/31. This stage only lasted for 3 hours and the gas pressure increased abruptly to 9.99 MPa. Observations in (de la Vaissière et al., 2019b) have demonstrated the gas fracture was opened and propagated during GRI1, and was reopened during GRI2 and GRI3.

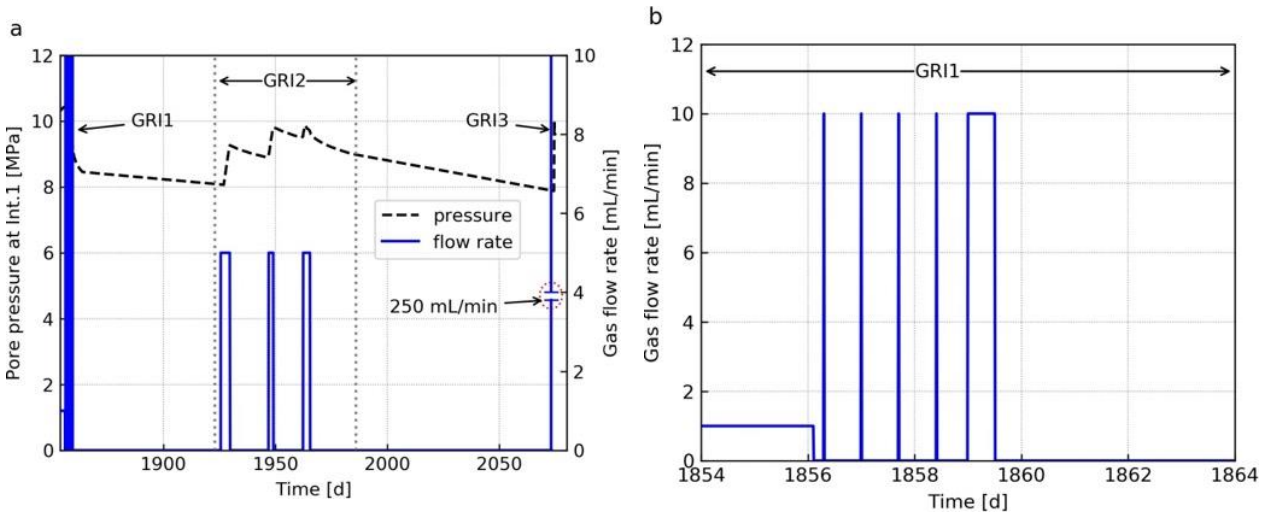

Figure 6.20 (a) Detailed gas injection history in GAS3 phase, (b) Gas flow rate of GAS3-GRI1 (data reproduced from (de la Vaissière et al., 2019b))

The long-term numerical predications of the PGZ1 test in (Harrington et al., 2013a) have shown that the consideration of borehole damaged zone (BDZ) in the model is necessary to better fitting the pore pressure data. More generally, the injected gas would be mainly confined in the BDZ area. Even if gas migrates to the undisturbed argillite, the preferential pathways were restricted to small distance away from the injection interval (De La Vaissière et al., 2014).

6.4.2 Model setup

A 2D plane strain hydro-mechanical model is developed to simulate the in-situ gas injection experiment. The geometry of the problem and the meshed domain are shown in Figure 6.21. According to the structural analysis of geometry model made on borehole and micro-tunnel, no significant scale effect was found for the excavation induced fracture network (Armand et al., 2014), which provided a way to calculate the extent of borehole damaged zone (BDZ). The BDZ is likely to present ellipsoidal shape, the general structure of which is affected by the opening orientation with respect to the subjected principal stresses (Armand et al., 2013, 2014; de la Vaissière et al., 2019b). However, an accurate extent of BDZ around the injection borehole is

difficult to be quantified due to the complex conditions in the field. Considering the borehole axis parallel to the direction of in-situ maximum principal stress, we adopt the BDZ as an ellipsoidal geometry with major and minor axes as approximated 1.8 and 1.3 times of the borehole diameter, respectively. This adoption corresponds to the extent of EDZ in a drift parallel to the maximum in-situ stress direction in (Armand et al., 2014).

Though the gas fractures were experimentally verified in the third gas phase (GAS3) of PGZ1 test, it was not possible to locate the fracture position (de la Vaissière et al., 2019b). Our attention is focused on the formation of gas dilatant pathways around the injection borehole and to capture the corresponding observations in the field, the outer limit of argillite is simplified to be 1.0 m away from the center of borehole. It should be noted that the model limit is made based on the in-situ findings, a more accurate exploration on the limit of gas dilatant pathways needs to be further validated through some other experimental techniques, such as the seismic velocity measurement in (Xu et al., 2013), or borehole inspection in (Guglielmi et al., 2015), etc.

A detailed analysis between gas pressure increase and gas volume was conducted in (De La Vaissière et al., 2014), where the early part of gas injection gave a best fit by using a closed volume of 1150 cm^3. This unchanged value is used for the gas injector volume in the simulation of PGZ1 test, and the applied gas injection rate is referred to Figure 6.19. Similar to the COx-4 test, a mass flux condition, q_{g0}, is applied on all the outer boundary, which means the gas can flow out of the host rock through any direction. There is no water flux through the borehole, the initial water pressure, 4.7 MPa, is applied on the outer edges, see Figure 6.21.

For the mechanical boundary, the borehole is fixed in all directions and a roller condition is applied on BC1. The middle point A on BC3 is fixed in vertical direction. The horizontal loading, equals to the minimum principal stress of 12.3 MPa (De La Vaissière et al., 2014), is applied horizontally on the outer edges (see BC3 in Figure 6.21). The vertical loading is about 1.3 times of horizontal loading (de la Vaissière et al., 2019b), which is applied vertically on the outer edges (see BC2 in Figure 6.21). The domain is meshed using the triangular elements. A refined mesh with an average size of 0.01 m is used to discretize the area encompassing the potential gas flow pathways.

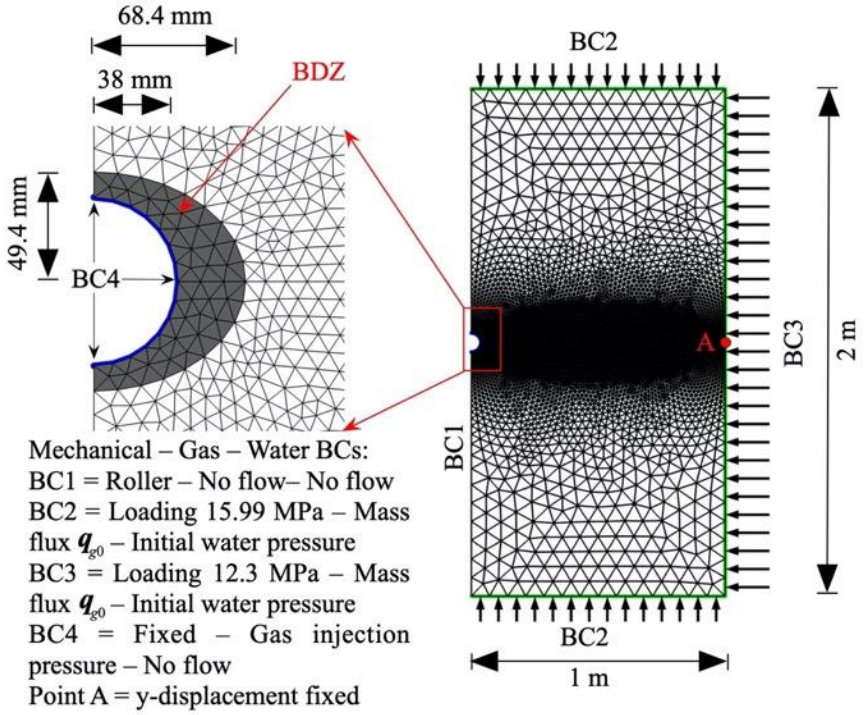

Figure 6.21 Boundary conditions (BCs) and meshed domain in the PGZ1 test

Most of the basic HM parameters and water retention parameters are extracted from Charlier et al. (2013). The intrinsic permeability is set to be same for water and gas flow, 4×10^{-20} m^2 for the permeability parallel to bedding and the hydraulic anisotropy is 3. The difference between BDZ and argillite is represented by different initial damage values. As has been analyzed in (Yang and Fall, 2021d), higher initial damage value leads to faster crack propagation. Thus we set the initial damage value for argillite and BDZ as 1×10^{-6} and 0.2, respectively, which represents the intact and damaged state. The detailed parameters for PGZ1 test are presented in Table 6-2.

It should be specified here that the relation between elastic stiffness components and the damage variable needs to be re-built by solving the cell problems (6.13)-(6.14), for 11 data points. Similar to the procedure in Figure 6.4, the homogenized coefficients are interpolated using piecewise cubic polynomial functions between continuous data points. Then the interpolated function will be substituted into the equilibrium equation (6.17) and damage equation (6.30), to couple with the fluid flow equations (6.36)-(6.45). In this way the HM problem is solved with the given boundary conditions and meshed domain.

Table 6-2 Parameters to simulate the PGZ1 test

Basic HM properties (based on Charlier et al. (2013))	Air entry value, p_0 [MPa]	15

Young's modulus, E [MPa]	4000	Damage parameters (based on Yang and Fall (2021d))	
Poisson's ratio, ν [-]	0.3	Crack growth index, n_d [-]	3
Gas nitrogen density, ρ_g [kg/m^3]	1.13	Stress corrosion limit, K_0 [Pa·m]	2.31×10^{4}
Gas viscosity, μ_g [Pa·s]	1.78×10^{-5}	Microstructural size, l_c [m]	1.0×10^{-8}
Intrinsic permeability parallel, k_{h0} [m^2]	4.0×10^{-20}	Characteristic crack speed, v_0 [m/s]	1.0×10^{-7}
Intrinsic permeability normal, k_{v0} [m^2]	1.33×10^{-20}	Critical tensile stress, σ_{cr} [MPa]	1.1
Porosity, ϕ [-]	0.18	Empirical parameter	
van Genuchten parameters (Charlier et al., 2013)		A_k [-]	5.0
n [-]	1.49	β_t [-]	3.8
m [-]	0.55		

The initial water pressure is 4.7 MPa equals to the measured natural pore pressure at the main level (de la Vaissière et al., 2019b). Since our concern is to investigate the gas induced fracturing in the third gas injection phase (GAS3 in Figure 6.19), we model a process that the gas pressure increases from the initial water pressure value to a finalized pressure value. The initial gas pressure is slightly higher than the applied water pressure, 4.71 MPa in the simulation, and the argillite is still fully saturated due to its high air entry value. The simulated gas injection process starts at t=1800 d, a constant flow rate 0.6 mL/min is applied for a continuous 50 days. Then the gas pressure is applied using a same injection history with that in the in-situ test, denoted by GAS3-GRI1 in Figure 6.20(b), i.e., 1 mL/min in the rest process until fracturing occurs. The critical gas pressure p_{cr} is set to be 4.81 MPa in the simulation.

6.4.3 Numerical results

In order to illustrate the gas induced fracturing around the BDZ, we present the damage evolution at different time in Figure 6.22. Before t=1850 d, the damage mainly occurs inside the BDZ. As gas pressure increases continuously, the crack evolves towards the undisturbed argillite (Figure 6.22(b)) and finally moves as far as to middle area of the domain (Figure 6.22(c)).

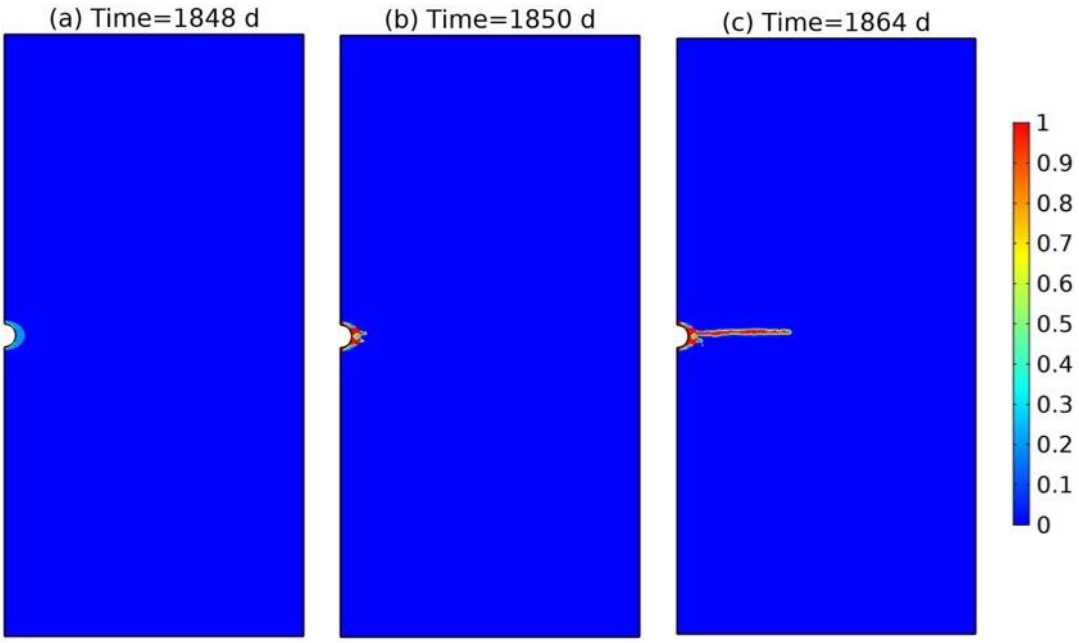

Figure 6.22 Damage evolution in the host rock at different time

The simulated gas pressure at the injection borehole is given in Figure 6.23, together with the computed average value of water saturation degree. Gas pressure increases from 4.71 MPa to the maximum 8.5 MPa in the first pumping cycle, then it decreases slightly when gas induced fracturing occurs in the rock material (see damage distribution in Figure 6.22(b)), even though the gas injection rate is increased to 1 mL/min.

As has been analyzed in (Charlier et al., 2013; De La Vaissière et al., 2014), the high air entry value of claystone avoids the fast desaturation during the gas injection process. The localized fracture network is easily utilized by the highly pressurized gas as preferential pathways to flow out of the porous medium. Once the network is interconnected from the gas inlet to outlet, gas flow in pores is becoming to be single phase flow in fractures. Due to the significant amount of clay minerals in the argillite, the strong cohesive force is acting on water particles that prevent water displacing out of the argillite. Thus the porous rock is still kept in a fully saturated condition, as seen from Figure 6.23(b), which is consistent with the experimental measurement.

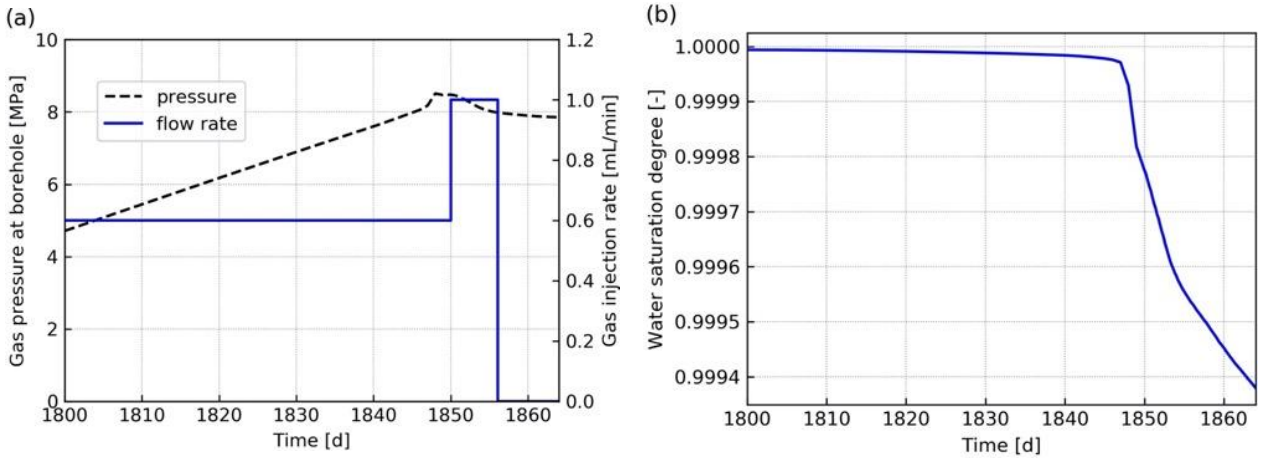

Figure 6.23 (a) Simulated gas pressure at the borehole. (b) Simulated average water saturation degree

To analyze the highly localized gas flow behavior, we present in Figure 6.24 the evolution of horizontal intrinsic permeability and Darcy's velocity magnitude between a damaged and a neighbor undamaged element. It is noted that a significant increase of intrinsic permeability is accompanying the rapid gas flow, as a consequence of the gas induced fracturing (see Figure 6.22). This process is represented by the relation (6.35), (6.44)-(6.45). While for the neighbor undamaged element, the gas flow behavior is not obvious.

Each increase in the Darcy's velocity corresponds to the time the element is damaged. After gas passed through the damaged element, the next undamaged element would be a barrier to impede the movement of gas, in consequence its velocity underwent a slight decrease. As the undamaged element is gradually fractured, the gas velocity would go up again, as seen in Figure 6.24(b). Thus the gas velocity presents a zigzag increasing trend.

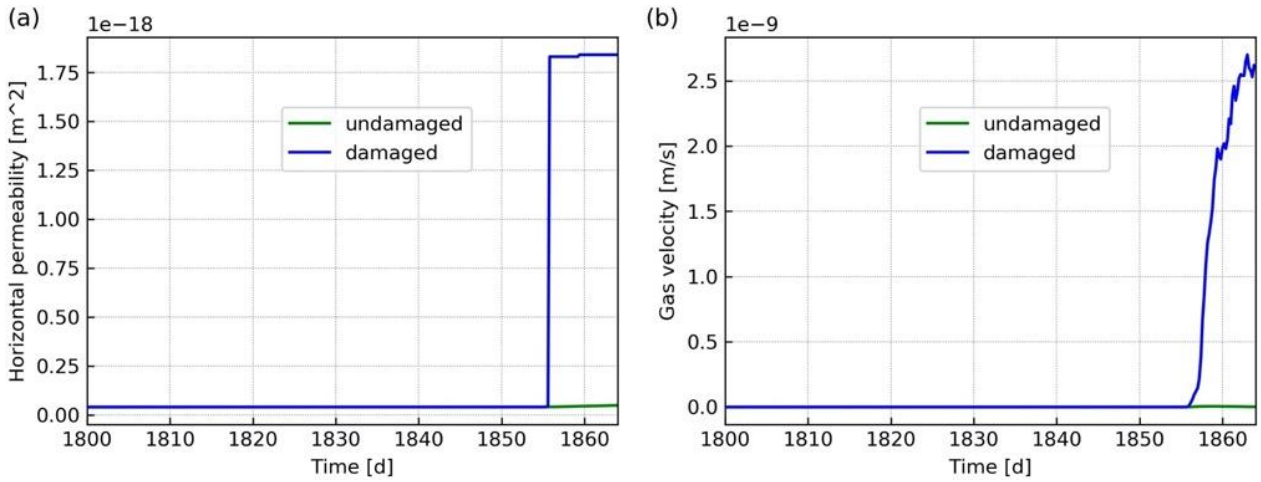

Figure 6.24 (a) Horizontal intrinsic permeability and (b) Darcy's velocity magnitude for damaged and neighbor undamaged elements

To investigate the essential difference between fracture mechanics and the conventional two-phase flow theory, the distribution of water saturation degree in the domain is shown in Figure 6.25, which is found to follow the fracture trajectory in Figure 6.22. Also, it is clearly seen from the figure that the gas seldomly displaces water through the pathways and the porous material can be still considered to be fully saturated, which is an important feature in the dilatancy controlled gas flow. Similar modelling results can be also found in (Guo and Fall, 2019, 2021), where a phase field method was used to capture this specific behavior.

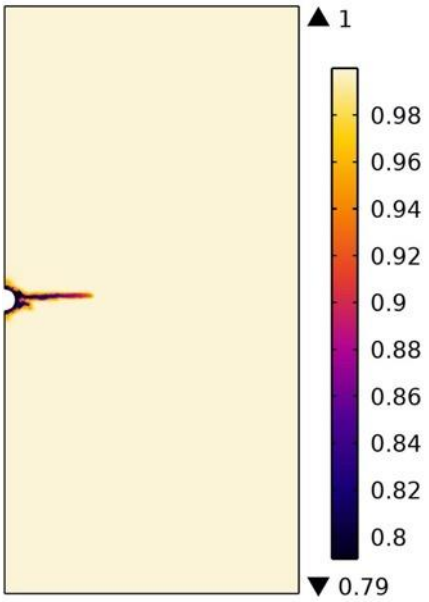

Figure 6.25 Distribution of water saturation degree in the domain

In order to study the pore pressure influenced by the gas injection, we present in Figure 6.26 the evolution of gas pressure at different elements. The point A is located in the damaged element, while point B and C are located away from the gas dilatant pathway. It is noted that the gas pressure at point A is significantly influenced by the gas injection and each drop of gas pressure is associated with the increased fracturing area. Due to the localized gas flow behavior, the highly pressurized gas front does not move to as far as point B and point C, thus the pressure in that area is not influenced by the gas injection.

The nanoparticle injection technique in clay (Harrington et al., 2012) has demonstrated the aperture of gas induced pathways is in a millimeter to micrometer scale, which is much smaller than the field scale. Even if five sensors were installed around the injection interval (see Figure

6.17), it is still difficult to monitor the pressure change influenced by gas migration. This is because any connected larger pores may serve as the preferential pathways for gas flow and in consequence the other areas are barely affected by the highly pressurized gas, as seen from our simulated results in Figure 6.26. This specific feature needs to be taken into account in both theoretical and experimental works in the future.

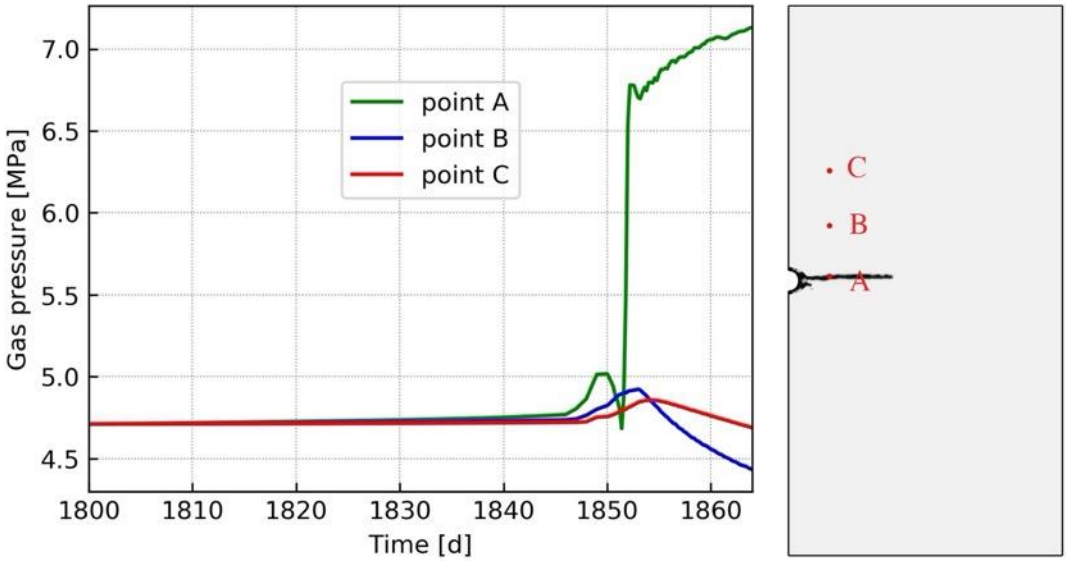

Figure 6.26 Evolution of gas pressure at different elements

6.5 Conclusions

The purpose of this study is to help us get in-depth understanding of dilatancy controlled gas flow, which is accompanied by the formation of micro-fractures that occurs at the applied gas pressure significantly below the minimum principal stress (if we regard compressive stress as positive here). Experimental results have demonstrated the flow is through highly localized network of dilatant pathways, whose properties vary temporarily and spatially within the argillaceous rocks.

In order to explicitly represent the specific gas migration behavior, a poroelastic damage model has been developed in the study. The subcritical propagation law has been applied for the cracks at the microscale, of which the passage to macroscale is implemented through an asymptotic homogenization method. In this way the damage model has been constructed for the isotropic solid containing a large number of periodically distributed microcracks, and the homogenized elastic coefficients have nonlinear dependence on the damage variable. The solid mechanics has been coupled with the fluid flow through pore pressure variation and an intrinsic

permeability model, which implicitly accounts for the fracture opening induced permeability change.

The developed model has been tested against both laboratory and in-situ gas injection experiments conducted on potential host rocks. Comparisons between model predictions and experimental results have shown encouraging agreement. Some key experimental findings, such as the development of preferential gas pathways and the fully saturated state are explicitly captured by the proposed model. Specifically, the preferential gas pathways are more likely to be developed along the pre-existed fractures. If the major pathway is not able to accommodate large amounts of gas penetrating the porous rocks, the other auxiliary pathways are to be developed for gas flow. Reproduction of localized gas pathways in the simulation of in-situ test has allowed us to better describe the experimentally observed phenomena, which provides some helpful guidance in the future works.

6.6 Acknowledgements

The authors thank the Natural Sciences and Engineering Research Council of Canada (NSERC), the China Scholarship Council and the University of Ottawa for financially supporting this research. Moreover, the authors extend their appreciations to CMC Microsystems that provide the computational resources for this study.

6.7 References

Angeli, M., Soldal, M., Skurtveit, E., Aker, E., 2009. Experimental percolation of supercritical CO2 through a caprock. Energy Procedia 1, 3351-3358.

Armand, G., Leveau, F., Nussbaum, C., de La Vaissiere, R., Noiret, A., Jaeggi, D., Landrein, P., Righini, C., 2014. Geometry and Properties of the Excavation-Induced Fractures at the Meuse/Haute-Marne URL Drifts. Rock Mech. Rock Eng. 47, 21-41.

Armand, G., Noiret, A., Zghondi, J., Seyedi, D.M., 2013. Short- and long-term behaviors of drifts in the Callovo-Oxfordian claystone at the Meuse/Haute-Marne Underground Research Laboratory. Journal of Rock Mechanics and Geotechnical Engineering 5, 221-230.

Arnedo, D., Alonso, E.E., Olivella, S., 2013. Gas flow in anisotropic claystone: Modelling triaxial experiments. International Journal for Numerical and Analytical Methods in Geomechanics 37, 2239-2256.

Auriault, J.L., Strzelecki, T., Bauer, J., He, S., 1990. Porous deformable media saturated by a very compressible fluid: quasi-statics. European Journal of Mechanics a-Solids 9, 373-392.

Barenblatt, G.I., Zheltov, I.P., Kochina, I.N., 1960. Basic concepts in the theory of seepage of homogeneous liquids in fissured rocks [strata]. Journal of Applied Mathematics and Mechanics 24, 1286-1303.

Bishop, A.W., 1954. The use of pore-pressure coefficients in practice. Geotechnique 4, 148-152.

Bishop, A.W., 1959. The principle of effective stress. Teknisk ukeblad 39, 859-863.

Brooks, R.H., Corey, A.T., 1964. Hydraulic properties of porous media. Colorado State University, Fort Collins, Colorado.

Bui, T.A., Wong, H., Deleruyelle, F., Xie, L.Z., Tran, D.T., 2017. A thermodynamically consistent model accounting for viscoplastic creep and anisotropic damage in unsaturated rocks. International Journal of Solids and Structures 117, 26-38.
Charlier, R., Collin, F., Pardoen, B., Talandier, J., Radu, J.P.J.P., Gerard, P., 2013. An unsaturated hydro-mechanical modelling of two in-situ experiments in Callovo-Oxfordian argillite. Engineering Geology 165, 46-63.
Coussy, O., 2004. Poromechanics. John Wiley & Sons, Chichester, England.
Cuss, R., Harrington, J., Giot, R., Auvray, C., 2014. Experimental observations of mechanical dilation at the onset of gas flow in Callovo-Oxfordian claystone. Geological Society Special Publication 400, 507-519.
Cuss, R.C., Harrington, J.F., Noy, D.J., 2012. Final report of FORGE WP4.1.1: The stress-path permeameter experiment conducted on Callovo-Oxfordian Claystone. British Geological Survey Commissioned Report, CR/12/140.
Dascalu, C., Bilbie, G., Agiasofitou, E.K., 2008. Damage and size effects in elastic solids: A homogenization approach. International Journal of Solids and Structures 45, 409-430.
Dascalu, C., François, B., Keita, O., 2010. A two-scale model for subcritical damage propagation. International Journal of Solids and Structures 47, 493-502.
de la Vaissière, R., Armand, G., Vu, M.N., Talandier, J., 2019a. Effect of gas flow rate on gas fracturing in Callovo-Oxfordian claystone. Rock Mechanics for Natural Resources and Infrastructure Development, in: da Fontoura, S., Rocca, R.J., Pavón Mendoza, J.F. (Eds.), Proceedings of the 14th International Congress on Rock Mechanics and Rock Engineering. CRC Press, Brazil.
De La Vaissière, R., Gerard, P., Radu, J.-P., Charlier, R., Collin, F., Granet, S., Talandier, J., Piedevache, M., Helmlinger, B., 2014. Gas injection test in the Callovo-Oxfordian claystone: data analysis and numerical modelling. Geological Society, London, Special Publications 400, 427-441.
de la Vaissière, R., Talandier, J., Armand, G., Vu, M.N., Cornet, F.H., 2019b. From two-phase flow to gas fracturing into Callovo-Oxfordian claystone, 53rd U.S. Rock Mechanics/Geomechanics Symposium.
Dormieux, L., Kondo, D., Ulm, F.J., 2006a. A micromechanical analysis of damage propagation in fluid-saturated cracked media. Comptes Rendus - Mecanique 334, 440-446.
Dormieux, L., Kondo, D., Ulm, F.J., 2006b. Microporomechanics. John Wiley and Sons.
Fall, M., Nasir, O., Nguyen, T.S., 2014. A coupled hydro-mechanical model for simulation of gas migration in host sedimentary rocks for nuclear waste repositories. Engineering Geology 176, 24-44.
Gerard, P., Harrington, J., Charlier, R., Collin, F., 2014. Modelling of localised gas preferential pathways in claystone. International Journal of Rock Mechanics and Mining Sciences 67, 104-114.
Gonzalez-Blanco, L., Romero, E., Jommi, C., Li, X., Sillen, X., 2016. Gas migration in a Cenozoic clay: Experimental results and numerical modelling. Geomechanics for Energy and the Environment 6, 81-100.
Guglielmi, Y., Elsworth, D., Cappa, F., Henry, P., Gout, C., Dick, P., Durand, J., 2015. In situ observations on the coupling between hydraulic diffusivity and displacements during fault reactivation in shales. Journal of Geophysical Research: Solid Earth 120, 7729-7748.
Guo, G., Fall, M., 2018. Modelling of dilatancy-controlled gas flow in saturated bentonite with double porosity and double effective stress concepts. Engineering Geology 243, 253-271.
Guo, G., Fall, M., 2019. Modelling of preferential gas flow in heterogeneous and saturated bentonite based on phase field method. Computers and Geotechnics 116, 103206.
Guo, G., Fall, M., 2021. A Thermodynamically Consistent Phase Field Model for Gas Transport in Saturated Bentonite Accounting for Initial Stress State. Transport in Porous Media.
Harrington, J., Volckaert, G., Jacobs, E., Maes, N., Areias, L., Charlier, R., Granet, S., 2013a. Summary report: Experiments and modelling of excavation damage zone (EDZ) behaviour in argillaceous and crystalline rocks (Work Package 4). EC FORGE Project Report D4.24-R.
Harrington, J.F., Cuss, R.J., Talandier, J., 2017. Gas transport properties through intact and fractured Callovo-Oxfordian mudstones. Geological Society Special Publication 454, 131-154.
Harrington, J.F., Horseman, S.T., 1999. Gas transport properties of clays and mudrocks. Geological Society Special Publication 158, 107-124.
Harrington, J.F., Milodowski, A.E., Graham, C.C., Rushton, J.C., Cuss, R.J., 2012. Evidence for gas-induced pathways in clay using a nanoparticle injection technique. Mineralogical Magazine 76, 3327-3336.
Harrington, J.F., Noy, D.J., Cuss, R.C., 2013b. Callovo-Oxfordian Claystone: processes governing advective gas flow. British Geological Survey Commissioned Report, CR/13/088.
Hildenbrand, A., Schlömer, S., Krooss, B.M., 2002. Gas breakthrough experiments on fine-grained sedimentary rocks. Geofluids 2, 3-23.
Horseman, S.T., Higgo, J.J.W., Alexander, J., Harrington, J.F., 1996. Water, gas and solute movement through

argillaceous media. Nuclear Energy Agency, Paris (France).
Jacops, E., Volckaert, G., Maes, N., Charlier, R., Collin, F., Gerard, P., Levasseur, S., Delavaissière, R., Talandier, J., Granet, S., 2014. WP5 Final Report: Experiments and modelling of gas migration processes in undisturbed rocks. FORGE Report D5.19, p. 146pp.
Khalili, N., Valliappan, S., 1996. Unified theory of flow and deformation in double porous media. European Journal of Mechanics, A/Solids 15, 321-336.
Lanyon, G.W., Marschall, P., Trick, T., De La Vaissiere, R., Shao, H., Leung, H., 2014. Self-sealing experiments and gas injection tests in a backfilled microtunnel of the Mont Terri URL, in: Norris, S., Bruno, J., Cathelineau, M., Delage, P., Fairhurst, C., Gaucher, E.C., Hohn, E.H., Kalinichev, A., Lalieux, P., Sellin, P. (Eds.), Clays in Natural and Engineered Barriers for Radioactive Waste Confinement. Geological Soc Publishing House, Bath, pp. 93-106.
Levy, T., 1990. Filtration in a porous fissured rock: influence of the fissures connexity. Eur. J. Mech. B-Fluids 9, 309-327.
Lewandowska, J., Auriault, J.L., 2013. Extension of Biot theory to the problem of saturated microporous elastic media with isolated cracks or/and vugs. International Journal for Numerical and Analytical Methods in Geomechanics 37, 2611-2628.
Lu, G.D., Yang, X.G., Qi, S.C., Li, X.L., Ding, P.P., Zhou, J.W., 2020. A generic framework for overpressure generation in sedimentary sequences under thermal perturbations. Computers and Geotechnics 124, 13.
Lydzba, D., Shao, J.F., 2000. Study of poroelasticity material coefficients as response of microstructure. Mech. Cohesive-Frict. Mater. 5, 149-171.
Miehe, C., Hofacker, M., Welschinger, F., 2010. A phase field model for rate-independent crack propagation: Robust algorithmic implementation based on operator splits. Computer Methods in Applied Mechanics and Engineering 199, 2765-2778.
Mualem, Y., 1976. A new model for predicting the hydraulic conductivity of unsaturated porous media. Water Resources Research 12, 513-522.
NAGRA, 2008. Effects of post-disposal gas generation in a repository for low- and intermediate-level waste sited in the Opalinus Clay of Northern Switzerland. National Cooperative for the Disposal of Radioactive Waste (NAGRA).
Nasir, O., Fall, M., Evgin, E., 2014. A simulator for modeling of porosity and permeability changes in near field sedimentary host rocks for nuclear waste under climate change influences. Tunnelling and Underground Space Technology 42, 122-135.
Nasir, O., Fall, M., Nguyen, S.T., Evgin, E., 2013. Modeling of the thermo-hydro-mechanical-chemical response of sedimentary rocks to past glaciations. International Journal of Rock Mechanics and Mining Sciences 64, 160-174.
Nasir, O., Fall, M., Nguyen, T.S., Evgin, E., 2011. Modelling of the hydro-mechanical response of sedimentary rocks of southern Ontario to past glaciations. Engineering Geology 123, 271-287.
Nguyen, T.S., Le, A.D., 2015. Simultaneous gas and water flow in a damage-susceptible bedded argillaceous rock. Canadian Geotechnical Journal 52, 18-32.
Olivella, S., Alonso, E.E., 2008. Gas flow through clay barriers. Géotechnique 58, 157-176.
Ortiz, L., Volckaert, G., Mallants, D., 2002. Gas generation and migration in Boom Clay, a potential host rock formation for nuclear waste storage. Engineering Geology 64, 287-296.
Ougier-Simonin, A., Renard, F., Boehm, C., Vidal-Gilbert, S., 2016. Microfracturing and microporosity in shales. Earth-Science Reviews 162, 198-226.
Pazdniakou, A., Dymitrowska, M., 2018. Migration of Gas in Water Saturated Clays by Coupled Hydraulic-Mechanical Model. Geofluids 2018, 1-25.
Popp, T., Wiedemann, M., Böhnel, H., Minkley, W., Manthei, G., 2007. Untersuchungen zur Barriereintegrität im Hinblick auf das Ein-Endlager-Konzept. Insitut fur Gebirgsmechanik GmbH, Leipzig, Germany.
Rodwell, W.R., Harris, A.W., Horseman, S.T., Lalieux, P., Müller, W., Ortiz Amaya, L., Pruess, K., 1999. Gas migration and two-phase flow through engineered and geological barriers for a deep repository for radioactive waste. Joint EC/NEA Status Report.
Romero, E., Gens, A., Lloret, A., 1999. Water permeability, water retention and microstructure of unsaturated compacted Boom clay. Engineering Geology 54, 117-127.
Romero, E., Senger, R., Marschall, P., Gómez, R., 2013. Air tests on low-permeability claystone formations. Experimental results and simulations, Springer Series in Geomechanics and Geoengineering, pp. 69-83.
Sánchez-Palencia, E., 1980. Non-homogeneous media and vibration theory. Springer, Berlin.
Senger, R., Enachescu, C., Doe, T., Distinguin, M., Delay, J., Frieg, B., 2006. Design and analysis of a gas threshold

pressure test in a low-permeability clay formation at ANDRA's underground research laboratory, Bure (France), TOUGH Symposium, Lawrence Berkeley National Laboratory, Berkeley, California.
Skurtveit, E., Aker, E., Soldal, M., Angeli, M., Wang, Z., 2012. Experimental investigation of CO2 breakthrough and flow mechanisms in shale. Petroleum Geoscience 18, 3-15.
Svoboda, J., Smutek, J.A.N., 2015. The experimental in-situ study of gas migration in crystalline rock with a focus on the EDZ. Geological Society Special Publication 415, 95-105.
Swanson, P.L., 1984. Subcritical crack growth and other time- and environment-dependent behavior in crustal rocks. Journal of Geophysical Research 89, 4137-4152.
van Genuchten, M.T., 1980. A closed-form equation for predicting the hydraulic conductivity of unsaturated soils. Soil Science Society of America Journal 44, 892-898.
Warren, J.E., Root, P.J., 1963. The Behavior of Naturally Fractured Reservoirs. Society of Petroleum Engineers Journal 3, 245-255.
Wilson, R.K., Aifantis, E.C., 1982. On the theory of consolidation with double porosity. International Journal of Engineering Science 20, 1009-1035.
Witherspoon, P.A., Wang, J.S.Y., Iwai, K., Gale, J.E., 1980. Validity of Cubic Law for fluid flow in a deformable rock fracture. Water Resources Research 16, 1016-1024.
Xu, W.J., Shao, H., Hesser, J., Wang, W., Schuster, K., Kolditz, O., 2013. Coupled multiphase flow and elasto-plastic modelling of in-situ gas injection experiments in saturated claystone (Mont Terri Rock Laboratory). Engineering Geology 157, 55-68.
Yang, J., Fall, M., 2021a. Coupled hydro-mechanical modelling of dilatancy controlled gas flow and gas induced fracturing in saturated claystone. International Journal of Rock Mechanics and Mining Sciences 138.
Yang, J., Fall, M., 2021b. A dual porosity poroelastic model for simulation of gas flow in saturated claystone as a potential host rock for deep geological repositories. Tunnelling and Underground Space Technology 115, 104049.
Yang, J., Fall, M., 2021c. A two-scale hydro-mechanical-damage model for simulation of preferential gas flow in saturated clayey host rocks for nuclear repository. Computers and Geotechnics 138.
Yang, J., Fall, M., 2021d. A two-scale time dependent damage model for preferential gas flow in clayey rock materials. Mechanics of Materials 158, 103853.
Yang, J., Fall, M., Guo, G., 2020. A Three-Dimensional Hydro-mechanical Model for Simulation of Dilatancy Controlled Gas Flow in Anisotropic Claystone. Rock Mechanics and Rock Engineering 53, 4091-4116.
You, T., Zhu, Q.Z., Li, P.F., Shao, J.F., 2020. Incorporation of tension-compression asymmetry into plastic damage phase-field modeling of quasi brittle geomaterials. International Journal of Plasticity 124, 71-95.
Yuan, S.C., Harrison, J.P., 2006. A review of the state of the art in modelling progressive mechanical breakdown and associated fluid flow in intact heterogeneous rocks. International Journal of Rock Mechanics and Mining Sciences 43, 1001-1022.
Zhang, C.L., Rothfuchs, T., 2004. Experimental study of the hydro-mechanical behaviour of the Callovo-Oxfordian argillite. Applied Clay Science 26, 325-336.

Chapter 7 Results Synthesis and Discussion

7.1 Introduction

In the thesis, the coupled HM modelling frameworks of both macroscale and two-scale are developed to represent the experimentally observed behaviors. Specifically, two models, e.g., a double porosity model and an enriched EFM are included in the macroscopic modelling framework, where the laboratory tests, i.e., OPA test, COx-1 test, COx-4 test and SPP_COx-2 test are simulated. In the two-scale modelling framework, a time-dependent damage model under single phase flow condition is adopted to conduct qualitative analysis of gas induced fracturing in clayey rocks, while a damage model with two-phase flow is constructed to simulate the air injection tests conducted on Boom clay and OPA clay. Lastly, the time-dependent damage model is applied in the field gas injection experiment. The numerical results obtained from the two modelling frameworks and from the in-situ test are synthesized and discussed as follows. Based on the discussion, the originality of the PhD work is highlighted at the end of this chapter.

7.2 Numerical Results of the Macroscopic HM Modelling Framework

The double porosity model is developed based on dual-continuum method that the deformation of each continuum is governed by the respective effective stress law, while the enriched EFM is constructed based on equivalent continuum method that the HM behavior of fracture sets has a superposed effect on the behavior of solid matrix.

7.2.1 Evolution of Gas Outflow Rate

Both the double porosity model and enriched EFM perform well to simulate the evolution of gas outflow rate. In general, the simulated results present a good agreement with the experimental results. Due to the dynamic behavior of gas pathways, the model either slightly underestimates or overestimates the flow rate when a major gas breakthrough occurs. After gas breakthrough, the gas outflow rate increases in a stepwise manner that corresponds to the stepwise increase in gas injection pressure, which shows gas flow through water saturated claystone is along pressure-induced pathways.

Once the gas was shut in, the simulated flow rate shows rapid decay and then quickly realizes an asymptote value that is approximately equal to the initial value, while the asymptote is not fully realized in the experiment. This is because the actual gas preferential pathways close

more quickly than the fracture closure in the simulated case, thus leading to large amounts of gas trapped within the rock sample and a subsequent higher pressure gradient than that in the simulated case. Thus, considering the self-sealing behavior of gas pathways in the future is necessary to explain the gas migration process when gas pumping is terminated.

7.2.2 Pore Pressure Evolution in the Guard-Ring

It is hard to capture the pore pressure evolution in the guard-ring by using only one formulation, due to the fact that the gas migration process is highly complex and no obvious correlation is persistent between IGR and BGR pressure.

As the location of IGR is close to IF, gas breakthrough will cause a dendritic fracturing pattern initiating from the gas inlet. After gas breakthrough, several gas pathways will be formed and connected to the IGR and in consequence water in the IGR will be totally displaced by gas. Therefore, the simulated gas pressure in the IGR can better represent the recorded IGR pressure, as captured by the double porosity model and enriched EFM.

In contrast, the location of BGR is closer to the BF, as a result the BGR pressure is more likely to be influenced by the water pressure applied in the BF. For the rock sample with incompact structure (i.e., COx-1 sample), the BGR pressure is influenced by gas pressure when the gas preferential pathways are developed to the BGR area. When steady state gas flow has been achieved that water flows back to the sink in BGR, the BGR pressure becomes to be controlled by the water pressure, as represented in the double porosity model and enriched EFM.

For the rock sample with compact structure (i.e., SPP_COx-2 sample), the BGR pressure is likely to be dominated by the development of localized gas pathways. The BGR pressure seldomly changes before gas breakthrough, while the pressure value undergoes a rapid increase after gas breakthrough, because water in the sink of BGR is partly displaced by highly pressurized gas. This process can be seen from the simulation of SPP_COx-2 test by using the enriched EFM.

7.2.3 Volume Dilation

The volume change recorded in the COx-1 test and SPP_COx-2 test cannot be purely explained by the elastic deformation of sample water alone. The majority of observed deformation is caused by the development of gas dilatant pathways. This volume dilation has

been represented by both the double porosity model and enriched EFM. In the double porosity model, a softening variable is introduced to consider the microcracking process. Based on the experimental phenomenon, gas saturation is assumed to have a direct effect on the material rigidity. The simulated volume change agrees well with the volume dilation in the COx-1 test. However, the simplified damage law seems to be not thermodynamically consistent as the desaturation process is reversible, more theoretical work needs to be done to validate the damage law.

As a comparison, the enriched EFM eases the difficulty in constructing a damage law at a condition of gas pressure significantly lower than the minimum principal stress. The nonlinear mechanical behavior of fracture is incorporated into the model that the normal stiffness of fracture reduces with fracture opening, which has a superposed effect on the deformation of matrix. The effective compliance tensor of rock has been derived using the equivalent continuum method. In this way, the stiffness degradation of material due to gas migration is represented by the enriched EFM, which is closer to the actual physical process. The simulated volume change has a good agreement with the experimental data in the COx-1 test, SPP_COx-2 test.

7.2.4 Anisotropic Radial Deformation

The anisotropic radial deformation cannot be captured by the double porosity model as the mechanical behavior in the PC and FC is isotropic. This behavior can be only represented by the enriched EFM using a 3D geometry. Since gas flow in saturated claystone is through highly localized pathway, which leads to the strong coupling between fluid flow and solid deformation, thus the sample along radial direction presents anisotropic deformation. Thanks to the inherent bedding of rock matrix and the introduced two fracture sets, the determined compliance tensor is significantly anisotropic by using the equivalent continuum method. As a result, the enriched EFM with 3D geometry is able to capture the anisotropic radial deformation.

7.3 Numerical Results of the Two-Scale HM Modelling Framework

The two-scale time-dependent damage model is developed to explicitly simulate the development of gas dilatant pathways, which occurs at the applied gas pressure significantly lower than the isotropic confining pressure and no shear stress is applied.

7.3.1 Evolution of Preferential Gas Pathways

The discrete feature of preferential gas pathways has been successfully described by the two-scale time-dependent damage model. Since the two-scale model is initiated from the microstructures with periodically distributed microcracks, the adjacent microcracks are interconnected when the crack evolves from small length to large length until the cell is totally partitioned, the physical process of which represents the damage evolution at the macroscale. With the adopted postulate that the microcrack trajectory is smooth and a priori known, gas induced micro-fracturing preferentially propagates through the non-homogeneous area with higher initial damage value.

In the two-scale model with single gas flow, unstabilized fracturing behavior around the gas inlet area is reproduced. This behavior is consistent to the experimental interpretation in (Cuss et al., 2014), where the dendritic gas pathways gradually develops until totally intersects the rock sample. The connection of fractures from gas inlet to outlet leads to the phenomenon of gas breakthrough, accompanied by large amounts of gas flowing out of the sample and a rapid drop in gas injection pressure.

In the two-scale model with two-phase flow, simulated results provide relative agreements with respect to the gas injection pressure and axial strain in the air injection tests. The fracture is able to propagate towards the outflow boundary even when the gas pumping is terminated, due to the existed high pressure gradient within the sample. This process is satisfactorily reproduced by the model. Comparisons between model predictions and the experimental results have shown the significant differences in controlling the gas breakthrough and mechanical deformation are resulting from the arbitrary nature of microstructural heterogeneities.

7.3.2 Evolution of Gas Injection Pressure

Under constant injection rate condition, gas injection pressure is mainly controlled by the number, aperture, orientation and length of developed fractures. Before major gas breakthrough occurs, gas injection pressure may start decreasing when large amounts of gas flow into the rock sample, since the claystone can accommodate high pressure gradient. This behavior can be also confirmed from the degassing test conducted on COx-1 sample after gas injection is terminated, as represented by the significant gas bubbles coming out of the sample (Harrington et al., 2017). Therefore, the drop in gas injection pressure generally occurs ahead of gas breakthrough, as seen

in the air injection tests on Boom clay (Gonzalez-Blanco et al., 2016) and OPA clay (Senger et al., 2014).

7.3.3 Influence of Microstructural Features

Local analysis has been performed with respect to microstructural size, reference crack velocity and initial damage value. Larger microstructure dimension contains bigger sized micro-cracks and as a result leads to easier propagation for damage, thus the material strength decreases. A larger value of reference crack velocity corresponds to fast damage evolution, in consequence leading to quick failure of the material, thus the material presents lower tensile strength. For higher initial damage value, damage initiates more rapidly with lower strength. These microstructural properties significantly affect the evolution of gas induced fracturing.

7.4 Numerical Results of the Poroelastic Damage Model

A poroelastic damage model considering two-phase flow has been developed to simulate the laboratory and in-situ gas injection experiments. The preferential gas pathways are more likely to be developed along the pre-existed fractures. If the major pathway is not able to accommodate large amounts of gas penetrating the porous rocks, the other auxiliary pathways are to be developed for gas flow. The gas-water interaction mainly takes place in the localized fracture pathways, in which the water saturation degree is slightly lower than that in the surrounding areas. The rock is still kept fully saturated, which is an important experimental phenomenon.

7.5 Originality of the PhD Work

A coupled HM model using the double porosity poroelasticity approach has been developed to simulate the gas migration process in saturated claystone. In the dual-continuum model, the opening/closure of fractures is represented by the volumetric strain of FC, while the behavior of matrix is described by the PC. The respective volumetric strain of PC and FC is work-conjugated to its corresponding effective stress, which is derived from a new theoretical approach based on the first law of thermodynamics. Thanks to the differentiation of two types of porosity in saturated claystone, the developed double porosity model allows us to describe the gas induced fracturing in an implicit way.

An enriched EFM has been proposed to address the mechanical behavior of fractures in the EFM. A hyperbolic relation of fracture deformability is incorporated into the rock matrix, as a result the fractured rock shows a nonlinear elastic behavior, which can capture the stiffness degradation due to fracture opening. Considering the inherent bedding and fracture induced anisotropy allows us to derive the effective compliance tensor showing significant anisotropy. Lastly, the anisotropic radial deformation during gas migration has been well represented by the enriched EFM with a 3D geometry.

A two-scale HM framework for simulating the deformation-flow problem is originally developed based on the asymptotic homogenization method. Initiating from a porous medium consists of isotropic solid and periodically distributed microcracks, the upscaling procedure has allowed to derive the macroscopic governing equations coupled with the normalized microcrack length under single gas flow condition. The constructed time-dependent damage model has been capable of reproducing a certain failure mode in the uniaxial tension test as well as describing the gas induced fracture branching phenomenon around the gas injection port.

By incorporating water flow in the two-scale HM framework, the enriched model is more powerful to simulate the laboratory gas injection tests conducted on saturated clayey rocks. Furthermore, the time-dependent damage evolution law has been completely derived from the microscopic mechanical energy analysis for evolving microcracks, which is firstly coupled with the HM framework to explicitly represent the gas-driven fracturing in saturated clayey rocks. The developed two-scale damage model with two-phase flow has been able to explain the gas breakthrough and mechanical deformation accompanied with the development of preferential gas pathways.

By neglecting the oscillating terms in fluid pressure (Sánchez-Palencia, 1980), the two-scale HM framework has allowed to incorporate the gas-water interaction in the hydraulic constitutive models. The poroelastic damage model is powerful to reproduce some key experimental findings, such as the development of localized gas pathways and non-desaturation phenomenon in the laboratory and in-situ gas injection experiments.

7.6 References

Cuss, R., Harrington, J., Giot, R., Auvray, C., 2014. Experimental observations of mechanical dilation at the onset of gas flow in Callovo-Oxfordian claystone. Geological Society Special Publication 400, 507-519.

Gonzalez-Blanco, L., Romero, E., Jommi, C., Li, X., Sillen, X., 2016. Gas migration in a Cenozoic clay:

Experimental results and numerical modelling. Geomechanics for Energy and the Environment 6, 81-100.
Harrington, J.F., Cuss, R.J., Talandier, J., 2017. Gas transport properties through intact and fractured Callovo-Oxfordian mudstones. Geological Society Special Publication 454, 131-154.
Sánchez-Palencia, E., 1980. Non-homogeneous media and vibration theory. Springer, Berlin.
Senger, R., Romero, E., Ferrari, A., Marschall, P., 2014. Characterization of gas flow through low-permeability claystone: laboratory experiments and two-phase flow analyses. Geological Society Special Publication 400, 531-543.

Chapter 8 Conclusions and Recommendations

8.1 Conclusions

Gas migration in saturated host rocks is accompanied by a series of characteristic observations, e.g., gas breakthrough, mechanical volume dilation, anisotropic radial deformation, micro-fracture propagation, non-desaturation after gas injection test and self-sealing behaviors. All of these behaviors are recorded at the condition of applied gas pressure significantly lower than the minimum principal stress, and complex couplings are involved in the hydraulic and mechanical processes. In the thesis, two coupled HM frameworks are developed to simulate the gas migration process in saturated host rocks as well as the recorded behaviors. Then, the two-scale framework is extended to the field application.

Two coupled HM models are included in the macroscopic modelling framework. The first one is a double porosity model, which is developed based on dual-continuum method. The rock is regarded as a FPM consisting of two continua, i.e., PC and FC. The mechanical behaviors of PC and FC are governed by the respective effective stress law, which is coupled through total stress equilibrium. The hydraulic behaviors of two continua are coupled through porosity transformation and water exchange term. The treatment in two types of porosity allows us to capture that the opening/closure of the fractures is caused by the interaction between the dilation of the PC and the dilation of the FPM, which is beneficial to describe the gas induced fracturing in an implicit way. The double porosity model has been capable of quantitatively reproducing the dynamic gas flux, pore pressure evolution and mechanical volume dilation.

To ease the difficulty in describing the rigidity degradation due to fracture opening, the nonlinear mechanical behavior of fracture has been incorporated into the matrix behavior in the enriched EFM. The use of equivalent continuum method allows us to derive the effective compliance tensor of rock materials containing inherent bedding and fracture sets, which show significant anisotropy. Considering a 3D geometry in the enriched EFM is able to quantitatively represent the anisotropic radial deformation during gas migration. Apart from this phenomenon, the enriched EFM can well describe some other key behaviors, e.g., dynamic gas flux, volume dilation, pore pressure evolution.

In the two-scale HM framework, initiating from the periodically distributed microstructures with microcracks, the asymptotic homogenization method has allowed to derive the macroscopic

governing equations coupled with the normalized damage variable. The time-dependent damage evolution law has been completely obtained from the microscopic mechanical energy analysis for evolving microcracks. Both time effect and size effect have been incorporated in the damage model that will affect the overall HM behavior of rocks.

Unstabilized fracturing behavior around the gas inlet area has been qualitatively reproduced in the two-scale model under single gas flow condition. The simulated results have demonstrated that the connection of fractures from gas inlet to outlet is a prerequisite for gas breakthrough, accompanied by large amounts of gas flowing out of the sample and a rapid drop in gas injection pressure.

By incorporating water flow in the two-scale framework, the model has shown that the fracture is able to propagate towards the outflow boundary even when the gas pumping is terminated, due to the existed high pressure gradient within the sample. Furthermore, quantitative comparisons between model predictions and experimental results have exlpained that the significant differences in controlling the gas breakthrough and mechanical deformation are resulting from the arbitrary nature of microstructural heterogeneities.

To account for the gas-water interaction in the two-scale framework, a coupled two-phase flow and elasto-damage model has been developed to quantitatively reproduce the laboratory and in-situ gas injection experiments, where the preferential gas pathways are more likely to be developed along the pre-existed fractures. More importantly, simulated results have found that the highly localized fracture pathways are the major places where gas and water interacts each other, and as a result the rock is still kept fully saturated during the whole process.

8.2 Recommendations

In response to the research gaps of current research topic and the limitations of the PhD work, further improvements of the present models may be envisaged to gain a deeper understanding of gas migration behavior:

(1) Due to the discontinuities contained in the rock material, the total stress may present a significantly heterogeneous distribution. Considering the heterogeneity of stress state is expected to improve the model performance in simulating the fracturing process before gas pressure reaches the minimum principal stress.

(2) Shear induced plasticity in compressive stress state is an important factor that

contributes to the development of preferential gas pathways. The plasticity is more likely to occur under the stress anisotropy condition in the gas injection test, thus this effect should be carefully considered based on the measured in-situ stress in the potential DGR.

(3) The two-scale HM framework needs to be further improved to examine the gas migration behavior after gas breakthrough. Once the fractures are formed and connected from gas inlet to outlet, the gas flow behavior has an abrupt transition from visco-capillary flow with enriched intrinsic permeability to steady state gas flow. Thus, considering this behavior is necessary to simulate the gas injection experiments under several gas pumping cycles.

(4) The self-sealing capacity is a specific property of clayey rocks, which has been observed in previous experimental studies. Nevertheless, the fundamental mechanism of self-sealing is still not clear, which may involve complex couplings between clay minerals, capillary water and gas phase. Incorporating the self-sealing behavior in a reliable model is critical to evaluate the long-term performance of host rocks.

(5) The kinetic effects for both solid and fluids are important to reproduce the dynamic microcracking behavior. Taking into account the inertial effects and hydrodynamics involves complex mathematical treatments in the two-scale HM framework, which may be our future work.

(6) The proposed two-scale HM framework focuses on the mode-I type fracture based on some simplifications, such that the trajectory of straight microcrack is a priori know. To better describe the microcrack interaction, type-II and type-III fractures need to be considered at the microscale and then upscaled to derive the macroscopic damage law. An advanced two-scale damage model considering all fracture types could be beneficial to describe the arbitrary fracture propagation in the heterogeneous field.

Appendices

Appendix A Derivation of double effective stress concept

Borja (2006) derived a thermodynamically based effective stress tensor for unsaturated continuum with single porosity based on the mixture theory. Borja and Koliji (2009) then applied this approach to an unsaturated continuum with double porosity. In this study, this approach is extended again to derive a double effective stress concept that assumes small deformation and compressible solid grains. The solid grains are assumed to be located in the subcontinuum κ (which substitutes for m in the original paper) separately, and there is no exchange of solid grains between the two subcontinua.

It is assumed that double porosity poroelasticity is applicable in the following derivation. The relationship between the total volume and subcontinuum volume is assumed as (Nair et al., 2004, 2005):

$$V_t = V_{s(\kappa)} + V_\kappa = V_{s(\kappa)} + \sum_{\pi=w,g} V_{\kappa\pi},\ \kappa = 1,2;\ \pi = w,g \tag{A.1}$$

where V_t is the total volume of the fractured porous medium, and $V_{s(\kappa)}$, $V_{\kappa\pi}$, and V_κ are the volume of the solid, fluid (water, gas) and pore space in the subcontinuum κ, respectively.

The porosity of subcontinuum κ and saturation degree of local fluid π can be defined as:

$$\phi_\kappa = \frac{V_\kappa}{V_t} \tag{A.2}$$

$$S_{\kappa\pi} = \frac{V_{\kappa\pi}}{V_\kappa} \tag{A.3}$$

The volume components of the solid (s) and fluid (π) in the subcontinuum κ are defined as:

$$\phi^{\kappa s} = \frac{V_{s(\kappa)}}{V_t},\ \phi^{\kappa\pi} = \frac{V_{\kappa\pi}}{V_t} = \phi_\kappa S_{\kappa\pi} \tag{A.4}$$

Then the volume components are subjected to the constraint:

$$\phi^{\kappa s} + \phi_\kappa = \phi^{\kappa s} + \sum_{\pi=w,g} \phi^{\kappa\pi} = 1 \tag{A.5}$$

The partial mass density of solid and fluid are taken as

$$\rho^{\kappa s} = \phi^{\kappa s}\rho_{\kappa s},\ \rho^{\kappa\pi} = \phi^{\kappa\pi}\rho_{\kappa\pi} \tag{A.6}$$

where $\rho_{\kappa s}$ and $\rho_{\kappa\pi}$ are the respective intrinsic mass density of the solid and fluid π (water, gas) in the subcontinuum κ.

With the assumption of no solid grain exchange, the mass balance equation of the respective solid in the subcontinuum κ can be expressed as

$$\frac{d\rho^{\kappa s}}{dt} + \rho^{\kappa s}\nabla \cdot \boldsymbol{v}_{\kappa s} = 0 \tag{A.7}$$

where $\boldsymbol{v}_{\kappa s}$ is the respective solid velocity of subcontinuum κ, which may be related to the overall solid velocity by superimposing the strains from the two subcontinua (Nair et al., 2004).

Based on intrinsic bulk relations (Malvern, 1969):

$$\frac{dp_{s(\kappa)}}{dt} = K_s\left(\frac{1}{\rho_{\kappa s}}\frac{d\rho_{\kappa s}}{dt}\right) \tag{A.8}$$

Substituting Eq. (A.8) into Eq. (A.7) yields

$$\frac{d\phi^{\kappa s}}{dt} + \frac{\phi^{\kappa s}}{K_s}\frac{dp_{s(\kappa)}}{dt} + \phi^{\kappa s}\nabla \cdot \boldsymbol{v}_{\kappa s} = 0 \tag{A.9}$$

where $p_{s(\kappa)}$ is the intrinsic pressure of the respective solid in the subcontinuum κ, and K_s is the intrinsic bulk modulus of the solid phase.

For an elastic solid matrix, a functional relation is considered as (Borja, 2006):

$$F_s(\phi^{\kappa s} p_{s(\kappa)}, \rho^{\kappa s}) = 0 \tag{A.10}$$

which is equivalent to the constitutive relation

$$p_{s(\kappa)} = p_{s(\kappa)}(\rho^{\kappa s}, \phi^{\kappa s}) \tag{A.11}$$

Then we have

$$\frac{dp_{s(\kappa)}}{dt} = \frac{\partial p_{s(\kappa)}}{\partial \rho^{\kappa s}}\frac{d\rho^{\kappa s}}{dt} + \frac{\partial p_{s(\kappa)}}{\partial \phi^{\kappa s}}\frac{d\phi^{\kappa s}}{dt} \tag{A.12}$$

With the relation

$$\frac{1}{\rho^{\kappa s}}\frac{d\rho^{\kappa s}}{dt} = -\nabla \cdot \boldsymbol{v}_{\kappa s} = -\dot{\varepsilon}_{\kappa v} \tag{A.13}$$

where $\dot{\varepsilon}_{\kappa v}$ is the volumetric strain rate of the subcontinuum κ.

Substituting Eq. (A.9) and (A.13) into Eq. (A.12) yields

$$\left(1 + \frac{\partial p_{s(\kappa)}}{\partial \phi^{\kappa s}}\frac{\phi^{\kappa s}}{K_s}\right)\frac{dp_{s(\kappa)}}{dt} = -\left(\rho^{\kappa s}\frac{\partial p_{s(\kappa)}}{\partial \rho^{\kappa s}} + \phi^{\kappa s}\frac{\partial p_{s(\kappa)}}{\partial \phi^{\kappa s}}\right)\dot{\varepsilon}_{\kappa v} \tag{A.14}$$

We can further formulate Eq. (A.14) in the following form:

$$\phi^{\kappa s}\frac{dp_{s(\kappa)}}{dt} = -K_{\kappa}\dot{\varepsilon}_{\kappa v} \tag{A.15}$$

where $K_\kappa = \phi^{\kappa s}\left(\rho^{\kappa s}\frac{\partial p_{s(\kappa)}}{\partial \rho^{\kappa s}} + \phi^{\kappa s}\frac{\partial p_{s(\kappa)}}{\partial \phi^{\kappa s}}\right)\Big/\left(1+\frac{\partial p_{s(\kappa)}}{\partial \phi^{\kappa s}}\frac{\phi^{\kappa s}}{K_s}\right)$ is the equivalent elastic bulk modulus of the subcontinuum κ, which has the similar expression as that in (Borja, 2006).

Substituting Eq. (A.15) into Eq. (A.9) gives the solid mass balance in the subcontinuum κ:

$$\frac{d\phi^{\kappa s}}{dt} + (\phi^{\kappa s} - \frac{K_\kappa}{K_s})\dot{\varepsilon}_{\kappa v} = 0 \tag{A.16}$$

According to Eq. (46) in (Borja and Koliji, 2009), the mass balance equation for fluid π (which substitutes α in the original paper) in the subcontinuum κ may be expressed as:

$$\frac{d\phi^{\kappa\pi}}{dt} + \frac{\phi^{\kappa\pi}}{K_{\kappa\pi}}\frac{dp_{\kappa\pi}}{dt} + \phi^{\kappa\pi}\nabla\cdot\boldsymbol{v}_{\kappa s} = c^{\kappa\pi} - \phi^{\kappa\pi}\nabla\cdot\boldsymbol{v}^r_{\kappa\pi} - \boldsymbol{v}^r_{\kappa\pi}\cdot\nabla\phi^{\kappa\pi} - \frac{\phi^{\kappa\pi}}{K_{\kappa\pi}}\boldsymbol{v}^r_{\kappa\pi}\cdot\nabla p_{\kappa\pi} \tag{A.17}$$

where $\boldsymbol{v}^r_{\kappa\pi} = \boldsymbol{v}_{\kappa\pi} - \boldsymbol{v}_{\kappa s}$ is the relative velocity of fluid with respect to the solid velocity in the subcontinuum κ, $\boldsymbol{v}_{\kappa\pi}$ is the fluid velocity; $\phi^{\kappa\pi}$, $K_{\kappa\pi}$, $p_{\kappa\pi}$, and $c^{\kappa\pi}$ are the volume components, bulk modulus, intrinsic pressure and mass density exchange rate of phase π in the subcontinuum κ, respectively.

Considering the definition of porosity in Eq. (A.2) and the constraint in Eq. (A.5), the change in the rate of porosity can be written as:

$$\frac{d\phi_\kappa}{dt} = -\frac{d\phi^{\kappa s}}{dt} = (1 - \frac{K_\kappa}{K_s} - \phi_\kappa)\dot{\varepsilon}_{\kappa v} \tag{A.18}$$

Substituting $\phi^{\kappa\pi}$ with $S_{\kappa\pi}\phi_\kappa$ into Eq. (A.17), and combined with Eq. (A.18), which is written as

$$S_{\kappa\pi}\phi_\kappa\nabla\cdot\boldsymbol{v}^r_{\kappa\pi} = -(1-\frac{K_\kappa}{K_s})S_{\kappa\pi}\dot{\varepsilon}_{\kappa v} - \phi_\kappa\frac{dS_{\kappa\pi}}{dt} - \frac{S_{\kappa\pi}\phi_\kappa}{K_{\kappa\pi}}\frac{dp_{\kappa\pi}}{dt} + c^{\kappa\pi} - \boldsymbol{v}^r_{\kappa\pi}\cdot\nabla(S_{\kappa\pi}\phi_\kappa) - \frac{S_{\kappa\pi}\phi_\kappa}{K_{\kappa\pi}}\boldsymbol{v}^r_{\kappa\pi}\cdot\nabla p_{\kappa\pi} \tag{A.19}$$

For unsaturated double porous media composed of two distinct but overlapping subcontinua, the rate of change in the internal energy density as derived in (Borja and Koliji, 2009) is expressed as:

$$\rho\dot{e}_T = \sum_{\kappa=1}^{2}\boldsymbol{\sigma}^s_{(\kappa)} : \dot{\boldsymbol{\varepsilon}}_{(\kappa)} + \sum_{\kappa=1}^{2}\sum_{\pi=w,g}\boldsymbol{\sigma}^{\kappa\pi} : \dot{\boldsymbol{\varepsilon}}_{\kappa\pi} + \frac{1}{2}\sum_{\kappa=1}^{2}\sum_{\pi=w,g}c^{\kappa\pi}\boldsymbol{v}_{\kappa\pi}\cdot\boldsymbol{v}_{\kappa\pi} + r - \nabla\cdot\boldsymbol{q} \tag{A.20}$$

where ρ is the density of the mixture, $\dot{e}_T$ is the rate of change in the internal energy per unit total mass of the mixture, $\boldsymbol{\sigma}^s_{(\kappa)}$ and $\dot{\boldsymbol{\varepsilon}}_{(\kappa)}$ are the partial Cauchy stress tensor and rate of change in the strain tensor of the respective solid in the subcontinuum κ, $\boldsymbol{\sigma}^{\kappa\pi}$ is the fluid partial Cauchy stress tensor, $\dot{\boldsymbol{\varepsilon}}_{\kappa\pi}$ is strain rate tensor of fluid π in subcontinuum κ, r is the heat supplied per unit

volume of the mixture, and $\boldsymbol{q}$ is the heat flux vector.

Assuming an isotropic fluid, the fluid partial Cauchy stress tensor can be expressed as:

$$\boldsymbol{\sigma}^{\kappa\pi} = -S_{\kappa\pi}\phi_{\kappa}p_{\kappa\pi}\boldsymbol{I} \tag{A.21}$$

Substituting Eqs. (A.19) and (A.21) into Eq. (A.20) gives

$$\rho\dot{e}_T = \boldsymbol{\sigma}_{(\kappa)} : \dot{\boldsymbol{\varepsilon}} - \sum_{\kappa=1}^{2}\sum_{\pi=w,g} p_{\kappa\pi}S_{\kappa\pi}\phi_{\kappa}\nabla\cdot\boldsymbol{v}_{\kappa\pi}^{r} + \frac{1}{2}\sum_{\kappa=1}^{2}\sum_{\pi=w,g} c^{\kappa\pi}\boldsymbol{v}_{\kappa\pi}\cdot\boldsymbol{v}_{\kappa\pi} + r - \nabla\cdot\boldsymbol{q} \tag{A.22}$$

where $\boldsymbol{\sigma}_{(\kappa)}$ is the local stress in subcontinuum κ, $\dot{\boldsymbol{\varepsilon}}$ is the rate of change in the strain tensor.

Local stress equilibrium requires that changes in total stress in adjacent phases must remain in equilibrium (Elsworth and Bai, 1992), such that

$$\boldsymbol{\sigma}_{(\kappa)} = \boldsymbol{\sigma} \tag{A.23}$$

where $\boldsymbol{\sigma}$ is the total stress tensor.

Substituting Eqs. (A.19) and (A.23) into Eq. (A.22) gives

$$\rho\dot{e}_T = \boldsymbol{\sigma} : \dot{\boldsymbol{\varepsilon}} + \sum_{\kappa=1}^{2}\sum_{\pi=w,g}(1-\frac{K_{\kappa}}{K_s})p_{\kappa\pi}S_{\kappa\pi}\dot{\varepsilon}_{\kappa v} - \sum_{\kappa=1}^{2}\sum_{\pi=w,g} p_{\kappa\pi}G_{\kappa\pi} + \frac{1}{2}\sum_{\kappa=1}^{2}\sum_{\pi=w,g} c^{\kappa\pi}\boldsymbol{v}_{\kappa\pi}\cdot\boldsymbol{v}_{\kappa\pi} + r - \nabla\cdot\boldsymbol{q} \tag{A.24}$$

$$G_{\kappa\pi} = -\phi_{\kappa}\frac{dS_{\kappa\pi}}{dt} - \frac{S_{\kappa\pi}\phi_{\kappa}}{K_{\kappa\pi}}\frac{dp_{\kappa\pi}}{dt} + c^{\kappa\pi} - \boldsymbol{v}_{\kappa\pi}^{r}\cdot\nabla(S_{\kappa\pi}\phi_{\kappa}) - \frac{S_{\kappa\pi}\phi_{\kappa}}{K_{\kappa\pi}}\boldsymbol{v}_{\kappa\pi}^{r}\cdot\nabla p_{\kappa\pi} \tag{A.25}$$

Noted here, $G_{\kappa\pi}$ is different from that in the original equation due to the new derivation.

Introducing an equivalent Biot's effective stress parameter (Nair et al., 2004) $\alpha_{(\kappa)} = 1 - K_{\kappa}/K_s$, the second term in Eq. (A.25) can be expressed as:

$$\sum_{\kappa=1}^{2}\sum_{\pi=w,g}(1-\frac{K_{\kappa}}{K_s})p_{\kappa\pi}S_{\kappa\pi}\dot{\varepsilon}_{\kappa v} = \alpha_{(1)}\bar{p}_1\dot{\varepsilon}_{1v} + \alpha_{(2)}\bar{p}_2\dot{\varepsilon}_{2v} \tag{A.26}$$

where $\bar{p}_1 = S_{1w}p_{1w} + S_{1g}p_{1g}$ and $\bar{p}_2 = S_{2w}p_{2w} + S_{2g}p_{2g}$ are the average fluid pressure in Subcontinua 1 and 2, respectively, and $\dot{\varepsilon}_{1v}$ and $\dot{\varepsilon}_{2v}$ are the respective volumetric strain rate of Subcontinua 1 and 2.

The rate of change in the strain tensor, $\dot{\boldsymbol{\varepsilon}}$, can be resolved as the isotropic part, $\dot{\boldsymbol{\varepsilon}}^{I}$, and the deviatoric part, $\dot{\boldsymbol{\varepsilon}}^{II}$:

$$\dot{\boldsymbol{\varepsilon}} = \dot{\boldsymbol{\varepsilon}}^{I} + \dot{\boldsymbol{\varepsilon}}^{II} \tag{A.27}$$

Then considering the two continua, we have

$$\dot{\boldsymbol{\varepsilon}}^{I} = \frac{1}{3}\dot{\boldsymbol{\varepsilon}}_v\boldsymbol{I} = \frac{1}{3}(\dot{\boldsymbol{\varepsilon}}_{1v} + \dot{\boldsymbol{\varepsilon}}_{2v})\boldsymbol{I} \tag{A.28}$$

By substituting Eqs. (A.26), (A.27) and (A.28) into Eq. (A.24), the rate of change in the

internal energy density can be written as

$$\rho\dot{e}_T = \boldsymbol{\sigma}:\dot{\boldsymbol{\varepsilon}}^{II} + \boldsymbol{\sigma}:\frac{1}{3}(\dot{\varepsilon}_{1v}+\dot{\varepsilon}_{2v})\boldsymbol{I} + \alpha_{(1)}\bar{p}_1\dot{\varepsilon}_{1v} + \alpha_{(2)}\bar{p}_2\dot{\varepsilon}_{2v} - \sum_{\kappa=1}^{2}\sum_{\pi=w,g} p_{\kappa\pi}G_{\kappa\pi} + \frac{1}{2}\sum_{\kappa=1}^{2}\sum_{\pi=w,g} c^{\kappa\pi}\boldsymbol{v}_{\kappa\pi}\cdot\boldsymbol{v}_{\kappa\pi} + r - \nabla\cdot\boldsymbol{q} \quad \text{(A.29)}$$

It can be further rewritten as:

$$\rho\dot{e}_T = \boldsymbol{\sigma}:\dot{\boldsymbol{\varepsilon}}^{II} + \frac{1}{3}\boldsymbol{\sigma}_1':\dot{\varepsilon}_{1v}\boldsymbol{I} + \frac{1}{3}\boldsymbol{\sigma}_2':\dot{\varepsilon}_{2v}\boldsymbol{I} - \sum_{\kappa=1}^{2}\sum_{\pi=w,g} p_{\kappa\pi}G_{\kappa\pi} + \frac{1}{2}\sum_{\kappa=1}^{2}\sum_{\pi=w,g} c^{\kappa\pi}\boldsymbol{v}_{\kappa\pi}\cdot\boldsymbol{v}_{\kappa\pi} + r - \nabla\cdot\boldsymbol{q} \quad \text{(A.30)}$$

The effective stress has the form

$$\boldsymbol{\sigma}_1' = \boldsymbol{\sigma} + \alpha_{(1)}\bar{p}_1\boldsymbol{I} \quad \text{(A.31)}$$

$$\boldsymbol{\sigma}_2' = \boldsymbol{\sigma} + \alpha_{(2)}\bar{p}_2\boldsymbol{I} \quad \text{(A.32)}$$

As evident from Eq. (A.30), the derived double effective stress concepts, i.e. $\boldsymbol{\sigma}_1'$ and $\boldsymbol{\sigma}_2'$, are work-conjugated to the respective volumetric strain rates of $\dot{\varepsilon}_{1v}$ and $\dot{\varepsilon}_{2v}$.

Appendix B Mesh independence in the damage model

To verify the effect of element size on the numerical results in the two-scale damage model, we consider a mesh-dependence problem in the following part. The proposed time-dependent damage law belongs to rate dependent models, which is expected to avoid the mesh dependency problem (Bhat et al., 2012). Two meshing schemes are considered for an uniaxial tension test. The used parameters are given as: E =2 GPa, ν =0.3, K_0 =23100 Pa·m, n =3, v_0 =10^{-6} m/s, l_c = 0.1 mm. The homogenized elastic stiffness components are presented with respect to damage variable by linear interpolation between continuous data points, by solving the cell problems. The time-dependent damage law can be referred to Eq. (5.154).

The tested specimen is 25 mm in width and 50 mm in height. A constant strain rate of 10^{-6} /s is applied in the upper boundary. The bottom and right side boundaries are set to be roller. The material is intact with a small initial damage value of 10^{-6}. A V-shaped notch of dimensions 0.2×0.4 mm is adopted at the middle height, to initiate the damage propagation process. The considered meshes are presented in Figure B.1, with refined elements close to the V-notched area in the central area of the domain.

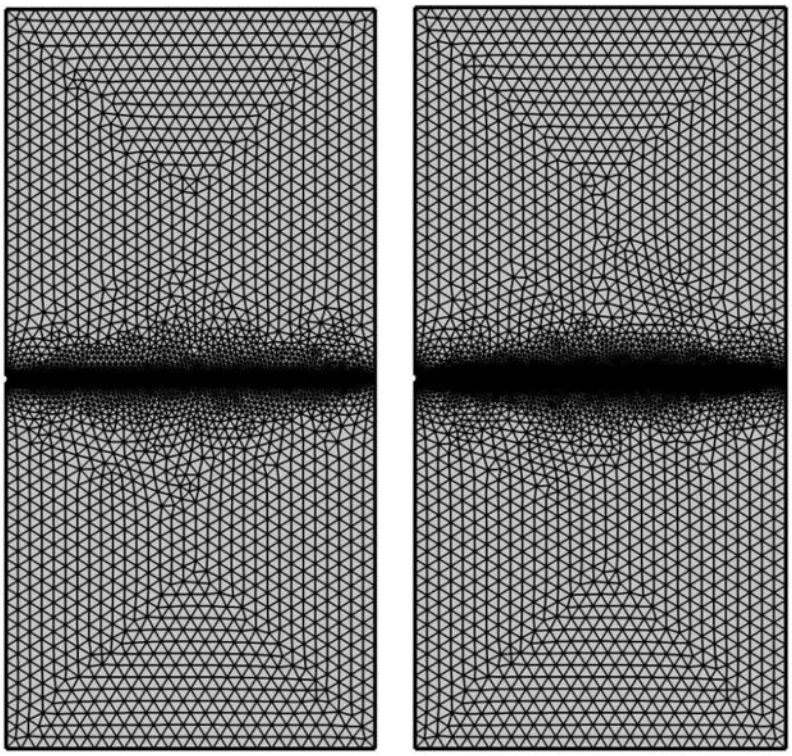

(a) refined mesh 1=0.2 mm (b) refined mesh 2=0.1 mm

Figure B.1 Meshing schemes

The obtained global vertical stress with respect to applied strain is presented in Figure B.2 and the damage map for two different meshes is shown in Figure B.3. We note that both the widths of damage band and the stress-strain curves are almost identical, which allows us to conclude that there is no mesh sensitivity for the time dependent damage propagation.

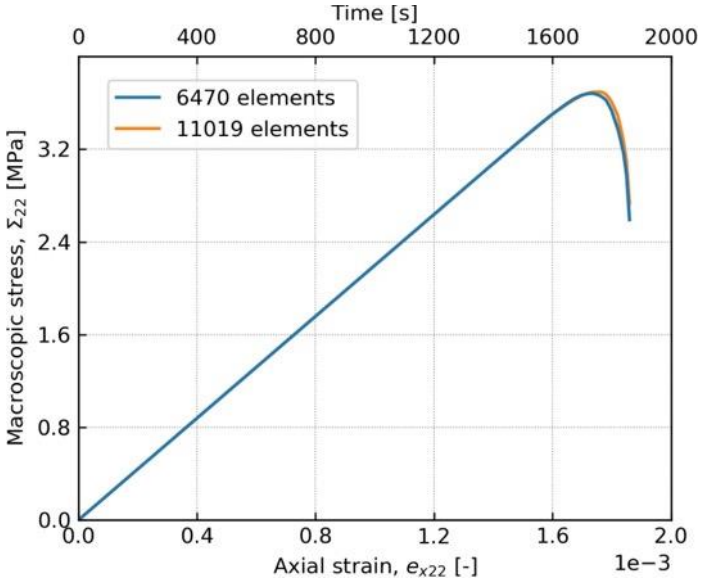

Figure B.2 Global vertical stress vs applied strain and time

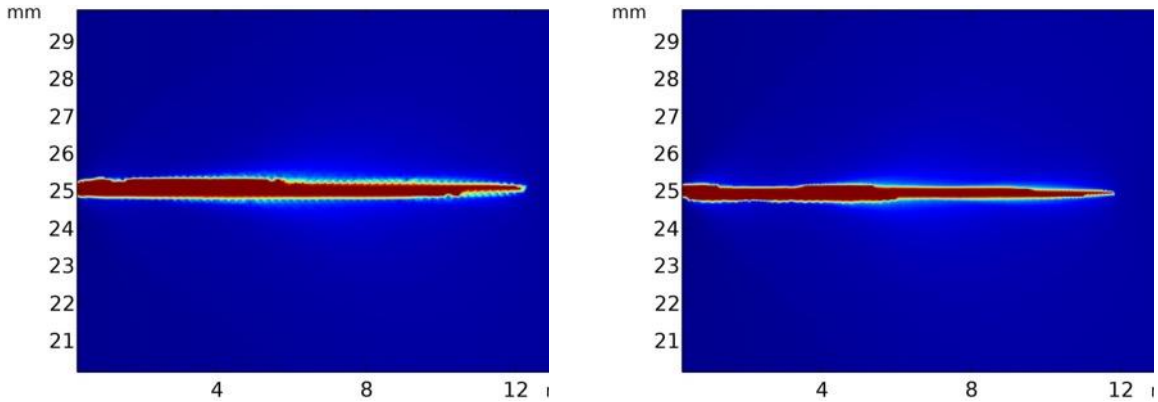

Figure B.3 Damage zones for different mesh sizes: 0.2 mm and 0.1 mm, at t=1800 s

References

Bhat, H.S., Rosakis, A.J., Sammis, C.G., 2012. A Micromechanics Based Constitutive Model for Brittle Failure at High Strain Rates. J. Appl. Mech.-Trans. ASME 79, 12.

Borja, R.I., 2006. On the mechanical energy and effective stress in saturated and unsaturated porous continua. International Journal of Solids and Structures 43, 1764-1786.

Borja, R.I., Koliji, A., 2009. On the effective stress in unsaturated porous continua with double porosity. Journal of the Mechanics and Physics of Solids 57, 1182-1193.

Elsworth, D., Bai, M., 1992. Flow-Deformation response of dual-porosity media. Journal of Geotechnical Engineering 118, 107-124.

Malvern, L.E., 1969. Introduction to the Mechanics of a Continuous Medium. Prentice-Hall, Inc., Englewood Cliffs, NJ.

Nair, R., Abousleiman, Y., Zaman, M., 2004. A finite element porothermoelastic model for dual-porosity media. International Journal for Numerical and Analytical Methods in Geomechanics 28, 875-898.

Nair, R., Abousleiman, Y., Zaman, M., 2005. Modeling fully coupled oil-gas flow in a dual-porosity medium. International Journal of Geomechanics 5, 326-338.